europhysics
conference
abstracts

20th EPS Conference on Controlled Fusion and Plasma Physics

Lisboa, 26–30 July 1993

Editors: J. A. Costa Cabral, M. E. Manso, F. M. Serra,
F. C. Schüller

Contributed Papers, Part III

Published by: European Physical Society

es Editor: Prof. K. Bethge, Frankfurt/M

aging Editor: G. Thomas, Genève

Volume 17C
Part III

europhysics
conference
abstracts

20th EPS Conference on Controlled Fusion and Plasma Physics

LISBOA, 26-30 JULY 1993

Editors: J.A.Costa Cabral, M.E. Manso, F.M. Serra,
F.C. Schüller

CONTRIBUTED PAPERS, PART III

Published by :	The European Physical Society	VOLUME
Series Editor:	Prof. K. Bethge, Frankfurt/M	17C
Managing Editor:	G. Thomas, Genève.	Part III

TOPICS 5-6

20th EPS Conference on Controlled Fusion and Plasma Physics

LISBOA, 26-30 JULY 1993

Editors: J.A.C. Cabral, M.E. Manso, F.M. Serra, F.C. Schüller

CONTRIBUTED PAPERS, PART III

EUROPHYSICS CONFERENCE ABSTRACTS is published by the European Physical Society, c 1993

The Proceedings may be purchased from "Centro de Fusão Nuclear" of "Instituto Superior Técnico", Av. Rovisco Pais, 1096 Lisboa Codex, Portugal.

PREFACE

The 20th EPS Conference on Controlled Fusion and Plasma Physics is Organized, on behalf of the European Physical Society (EPS), by "Sociedade Portuguesa de Física" (SPF) and "Centro de Fusão Nuclear" (CFN) of "Instituto Superior Técnico" (IST) of the Lisbon Technical University.

The Programme, Format and Schedule of the Conference were determined by its International Programme Committee, which also selected the Plenary and Topical Invited Lectures.

The International Programme Committee has also made the selection of the submitted one-page abstracts. Some of these abstracts, of outstanding quality, have been selected, for both poster and oral presentation of the corresponding four-page papers.

In the odd years the Conference is essentially related with Controlled Fusion Research and it has a reduced format. Therefore, the IPC has only been able to accept for conference presentation about 435 abstracts from the almost 620 received.

The Conference Format is: 9 Review Lectures of 45 minutes, 18 Topical Lectures of 30 minutes, 24 Oral Presentations of Contributred Papers of 20 minutes, 4 poster sessions with about 110 posters each and a Special Evening Public Lecture.

Lisboa, June 1993 The Editors

Acknowledgements:

The Conference Organizers acknowledge the financial support of the following Agencies and Institutions:

- Junta Nacional de Investigação Científica e Tecnologica
- Commission of the European Communities
- Fundação Calouste Gulbenkian
- Instituto Superior Técnico
- Câmara Municipal de Lisboa
- Banco Comercial de Lisboa

PROGRAMME COMMITTEE:

F. C. Schüller (Chairman) ..... Netherlands
K. Lackner (Chairman Innsbruck Conference)..... Germany
F. W. Sluijter (Chairman Plasma Phys. Division EPS)..... Netherlands
J. A. Costa Cabral (Chairman Local Org. Committee)..... Portugal
R. Bartiromo..... Italy
C. De Michelis..... France
J.R.Drake..... Sweden
F. Engelmann..... Germany
O. S. Pavlichenko..... Russia
J. Stöckel..... Tchekoslovakia
P. R. Thomas..... United Kingdom
J. Winter..... Germany
H..Wobig..... Germany

LOCAL ORGANIZING COMMITTEE:

C. M. Ferreira..... .....(General Secretary SPF, IST)
C. F. Varandas..... (President CFN, IST)

J. A. Costa Cabral..... (Chairman LOC, IST)
M. E. Manso..... (Secretary, IST)
F. Serra..... (Vice-Secretary, IST)
A.Moreira..... (IST)
A.Praxedes..... (IST)
H. Fernandes..... (IST)
A.Silva..... (IST)
A.Soares..... (IST)

CONTENTS

LIST OF TITLES
PART I
Topic 1: Tokamaks

Poster no
Title
Authors

Volume/Page

Poster no
Title
Authors

Volume/Page

Poster no
Title
Authors

Volume/Page

Poster no — Volume/Page
Title
Authors

Poster no — Volume/Page
Title
Authors

Poster no Volume/Page
Title
Authors

Poster no
Title
Authors

Volume/Page

Poster no
Title
Authors

Volume/Page

Topic 2: Stellarators

Poster no — Volume/Page
Title
Authors

Topic 3: Alternative Confinement Schemes

Poster no — Volume/Page
Title
Authors

Poster no — Volume/Page
Title
Authors

Topic 4: Plasma Edge Physics

Poster no — Volume/Page
Title
Authors

Poster no — Volume/Page
Title
Authors

Poster no
Title
Authors

Volume/Page

Poster no — Volume/Page
Title
Authors

Poster no
Title
Authors

Volume/Page

Poster no
Title
Authors

Volume/Page

Topic 5: Heating and Current Drive

Poster no / Title / Authors — Volume/Page

Poster no
Title
Authors

Volume/Page

Poster no — Volume/Page
Title
Authors

Poster no / Title / Authors — Volume/Page

Poster no — Volume/Page
Title
Authors

Poster no
Title
Authors

Volume/Page

Topic 6: Diagnostics

Poster no
Title
Authors

Volume/Page

Poster no — Volume/Page
Title
Authors

Topic 7: Inertial Confinement Fusion

Topic 8: General Plasma Theory

Poster no / Title / Authors — Volume/Page

Poster no — Volume/Page
Title
Authors

Poster no
Title
Authors

Volume/Page

Contributed Papers received during Printing

Poster no
Title
Authors

Volume/Page

Topic 5

Heating and Current Drive

RF CURRENT DRIVE COMPONENTS IN A TOKAMAK.

P. E. Moroz

Nuclear Engineering and Engineering Physics Department, University of Wisconsin, 1500 Johnson Drive, Madison, WI 53706, USA

Abstract. Theoretical analysis of low frequency current drive in a tokamak is presented. The global model discussed includes kinetic hot plasma effects and collisions. It is found that all kinds of wave-plasma interactions (resonant wave-electron interaction, resonant wave-ion interaction and collisions) can contribute to the current drive. The analysis presented stresses the two new current drive components, the resonant helicity current and the nonresonant collisionless current. Helicity current drive is proportional to the parallel helicity flux and to the wave damping strength, which is defined by the wave-plasma interaction process. The collisionless part of the nonresonant current is proportional to wave damping on ions. However, this is an electron current, and wave-ion interaction just creates necessary polarization of the wave to drive a current. The resistive MHD limit is considered as well, and the correct expression for the RF driven current including the Alfven resonance effect, is given.

Introduction. Steady-state currents can be generated in a tokamak plasma by a variety of means (see, for example, [1]): via low frequency waves, lower-hybrid waves, electron-cyclotron waves, neutral beam injection, minority-species current drive, asymmetric reflection, etc. In spite of great success in driving quasi-steady currents in modern tokamaks (see, for example [2,3]), no method so far can give acceptably high current drive efficiency for the parameters of a future thermonuclear reactor. The most successful method of rf current drive in tokamaks was via the lower-hybrid waves, which, however, has serious limitations in plasma density, temperature and size necessary for a reactor.

Relatively recently, a new concept of current drive based on magnetic helicity has been proposed on the basis of analysis of a system of resistive MHD equations [4-9]. It has been suggested that the circular polarized electromagnetic waves may drive substantial currents due to their intrinsic helicity with greater efficiency than conventional schemes based on the momentum transfer to electrons. For this scheme to work, helicity must be transferred from the wave to the equilibrium magnetic field. In the first publications on this subject, the high current drive efficiency has been obtained under the assumption of full wave helicity conversion to the background magnetic field. However, further studies [6] show that helicity is not conserved during the wave absorption process, and even more [10], that the current drive based on the visco-resistive wave-plasma interactions, in practice, cannot be significant.

In this paper we report on new theoretical results on low frequency RF current drive including helicity current drive and nonresonant collisionless current drive components.

Current drive components. The natural definition of the momentum transfer current comes from a consideration of the momentum balance during the wave absorption process. In steady-state conditions, momentum input is balanced by momentum loss due to collisions, which gives the relation between absorbed power and the induced current:

$$J_M = -\frac{k_\parallel}{n_e e \omega \eta} P_e \equiv -\tilde{\eta} P_e . \qquad (1)$$

We are using the following definitions: e and m are the electric charge and the mass of an electron, n_e is the electron number density, ω and $k_\parallel$ are the wave frequency and the parallel wave number (which is a real number in a tokamak), ν_e is the electron collision frequency , $\eta = m\nu_e/n_e e^2$ is the parallel Spitzer resistivity, and $\tilde{\eta}$ is the current drive efficiency. The absorbed power, P_e, includes all possible absorption mechanisms [11-12], $P_e = P_{LD} + P_{MP} + P_{CR} + P_{COL}$, where P_{LD}, P_{MP}, P_{CR}, and P_{COL} are, respectively, the power absorbed due to Landau damping, TTMP, cross-term effect and collisions. In this paper we do not consider the trapped particle effects which could be, in principle, included through the coefficient depending on the ratio, ζ_e, of phase, $\omega/k_\parallel$, and thermal electron, v_{te}, velocities, similar to Ref. 13.

The RF current drive components additional to the momentum-transfer current, J_M, can be found from the electron momentum equation averaged over the RF period of the wave and over the magnetic surface [14]

$$J_\parallel = \frac{1}{\eta} \left\langle e_\parallel \left[\frac{1}{c} \mathbf{v}_e \times \mathbf{B} + \frac{m}{e} \frac{d_e \mathbf{v}_e}{dt} \right] \right\rangle \qquad (2)$$

In above equation we omitted the terms with the wave electric field, $\mathbf{E}$, pressure, p_e , and viscous stress tensor, $\hat{\pi}_e$, which can be neglected in our approximation . The corresponding components can contribute to the standard ponderomotive force [15], but being a complete gradient of some potential cannot drive an average current. Only the term with the stress tensor, $\hat{\pi}_e$, in a geometry with trapped electrons, for example, such as a tokamak, can lead to an average current – the bootstrap current (see, for example, [16, 17]). The bootstrap current, however, is beyond the scope of this paper. Using Maxwell equations with the hot plasma dielectric, $\hat{\varepsilon}$, and mobility, $\hat{M}_e$, tensors gives the following presentation for the total parallel current, $J_\parallel$:

$$J_\parallel = J_I + J_M + J_P \ , \qquad (3)$$

where

$$J_I = \frac{1}{4c\eta} \, \mathrm{Im}(n_\parallel) \cdot \mathrm{Im} \left[v_e^- (E^-)^* + v_e^+ (E^+)^* - 2 v_{e\parallel} E_\parallel^* \right] , \qquad (4)$$

$$J_M = \frac{1}{4c\eta} \, \mathrm{Re}(n_\parallel) \cdot \mathrm{Re} \left[v_e^- (E^-)^* + v_e^+ (E^+)^* + 2 v_{e\parallel} E_\parallel^* \right] , \qquad (5)$$

$$J_P = -\frac{1}{2\omega n_e e \eta} \, \mathrm{Im} \left[(\mathbf{j}_e \cdot \nabla)\left(E_\parallel^* + \frac{i\omega m}{e} v_{e\parallel}^* \right) \right] , \qquad (6)$$

and $v_e^\pm = v_{ex} \pm i v_{ey}$, $E^\pm = E_x \pm i E_y$. We call the current, J_I , an imaginary current, because it is absent in a tokamak: due to periodicity conditions the parallel wave number, $n_\parallel$, has to be real. However, we still decided to consider this current because it was considered in earlier publications [4-10] in context with the helicity current drive. The current, J_M, is the momentum-transfer current, because it can be written [14] in the form of Eq. (1). The last current component, J_P , we call the polarization current because it depends on the

wave polarization. Estimation of the polarization current component, J_P , in the WKB approximation shows [14] that it includes, among the most important components, the resonant helicity current

$$J_{HEL} = \frac{Rek_{\|}}{2\eta B_o} \frac{|n_{\perp}|^2}{|\varepsilon_3|^2} Im\varepsilon_3 \, Q_{\|} \, , \tag{7}$$

and the nonresonant collisionless current,

$$J_{NR} \approx -\frac{|n_{\perp}|^2 n_{\|}}{8\eta B_o} \frac{\omega^2}{\omega_{pe}^2 \zeta_e^2} Im \left[E^+ (E^-)^* \right] \, , \tag{8}$$

where $Q_{\|}$ is the gauge invariant parallel helicity density flux [14]:

$$Q_{\|} = -\frac{c}{4\omega} \left(|E^-|^2 - |E^+|^2 \right) \, . \tag{9}$$

The helicity current, J_{HEL}, is maximal for the circular polarized waves. In contrast, the nonresonant current, J_{NR} , disappears when the wave is totally circular polarized. Analysis of the polarization factor in Eq. (8) shows [14] that the nonresonant current is proportional to ion absorption. However, J_{NR} is the electron current, and the wave-ion interaction just creates the necessary polarization of the wave to drive a current.

Many previous papers [4-9] considered helicity current drive on the basis of resistive MHD equations. Let us consider the same approximation of a cold plasma with collisions at low frequencies: $\nu_e << \omega << \Omega_i$, $T_e = 0$. In this situation, the collisional terms represent the only contribution to the RF driven current. Using the cold plasma mobility tensor and WKB approximation gives the following presentation for the current drive components corresponding to Eqs. (4-6):

$$J_I = \frac{Im(n_{\|})}{4\eta B_o} \left(|E^-|^2 - |E^+|^2 + \frac{2\Omega_e}{\omega} |E_{\|}|^2 \right) , \tag{10}$$

$$J_M = -\frac{Re(n_{\|})}{4\eta B_o} \frac{\nu_e \omega}{\Omega_e} \left(\frac{|E^-|^2}{\omega + \Omega_i} + \frac{|E^+|^2}{\omega - \Omega_i} + \frac{2\Omega_e^2}{\omega^3} |E_{\|}|^2 \right) , \tag{11}$$

$$J_P = -\frac{Re(n_{\|})}{4\eta B_o} \frac{\nu_e}{\omega} \left[|n_{\perp}|^2 \frac{\omega^2}{2\omega_{pe}^2} \left(|E^-|^2 - |E^+|^2 \right) - \frac{2\Omega_e}{\omega} |E_{\|}|^2 \right] \tag{12}$$

To compare our results with the previous publications we have to take the imaginary current, J_I , into consideration, and also neglect the polarization current contribution and finite $E_{\|}$. Taking into account the relations [6]:

$$Re(n_{\|}) \approx n_A \equiv c / v_A \, , \qquad Im(n_{\|}) \approx \left(\mu + \eta \frac{c^2}{4\pi} \right) \frac{\omega}{2v_A^2} Re(n_{\|}) \, , \tag{13}$$

where $n_A = \omega_{pi} / \Omega_i$, v_A is Alfven velocity, and μ is kinematic viscosity of a plasma, we arrive on the following expression for the total parallel current:

$$J_{\parallel} = -\frac{Re(k_{\parallel})}{\eta B_o} \frac{\omega}{2v_A^2} \left(\mu - \eta \frac{c^2}{4\pi} \right) Q_{\parallel} . \qquad (14)$$

Eq. (14) replicates some results obtained in Ref. [5-7] that viscosity and resistivity make opposite contributions to the driven current. However, in a tokamak, as we have mentioned above, the current J_I is absent, and the total current in the MHD limit is

$$J_{\parallel} = \frac{\omega}{4\pi B_o} n_A^2 Re(k_{\parallel}) \left(1 + \frac{|n_{\perp}|^2}{2n_A^2} \right) Q_{\parallel} , \qquad (15)$$

which is independent on plasma resistivity (due to coincidence that both, wave absorption and plasma resistivity, are proportional to collision frequency), and is proportional to the parallel wave helicity density flux. The second term in parentheses expresses the influence of the Alfven resonance.

Conclusions. Low frequency RF current drive in a tokamak is analyzed. It is shown that the momentum-transfer current is essentially supplemented by an additional, polarization current. The analysis of the polarization current, J_P , in the WKB approximation shows that it can be represented as a sum of different components, including such important components as the nonresonant collisionless current, J_{NR}, and the resonant helicity current, J_{HEL}. The correct expression for the RF driven current in the resistive MHD limit, including the Alfven resonance effect, is given.

Acknowledgment. The author greatly benefited from discussions with Prof. Noah Hershkowitz and other members of the Phaedrus Laboratory for Plasma Science of the University of Wisconsin-Madison. This work was supported by the U.S. Department of Energy Grant DE-FG02-88ER53264.

References.

1. N. J. Fisch, Rev. Mod. Phys. **59**, 175 (1987).
2. F. Rimini, M. Brusati, C. D. Challis, et al., Proc. Eur. Top. Conf. on RF Heating and Cur. Drive of Fus. Dev., Brussels, 1992, **16E**, p.229, EPS, Ed. C. Gormezano (1992).
3. S. Ide, T. Imai, K. Ushigusa, et al., Ibid., p. 261(1992).
4. T. Ohkawa, Comm. on Plasma Phys. and Contr. Fusion **12**, 165 (1989).
5. R. R. Mett, J. A. Tataronis, Phys. Rev. Lett. **63**, 1380 (1989).
6. J. B. Taylor, Phys. Rev. Lett. **63**, 1384 (1989).
7. R. R. Mett, J. A. Tataronis, Phys. Fluids B **2**, 2334 (1990).
8. V. S. Chan, R. L. Miller, T. Ohkawa, Phys. Fluids B **2**, 944 (1990).
9. V. S. Chan, R. L. Miller, T. Ohkawa, Phys. Fluids B **2**, 1441 (1990).
10. P. M. Bellan, M. A. Schalit, Phys. Fluids B **3**, 423 (1991).
11. P. E. Moroz, P. L. Colestock, Plasma Phys. and Contr. Fusion **33**, 417 (1991).
12. P. E. Moroz, N. Hershkowitz, et al., Phys. of Fluids B **4**, 2915 (1992).
13. D. A. Ehst, C. F. F. Karney, Nuclear Fusion **31**, 1933 (1991).
14. P. E. Moroz, to be published in Plasma Phys. and Contr. Fusion (1993).
15. N. C. Lee, G. K. Parks, Phys. Fluids, **26**, 724 (1983).
16. S. P. Hirshman, D. J. Sigmar , Nucl. Fusion **21**, 1079 (1981).
17. S. P. Hirshman , Phys. Fluids **31**, 3150 (1988).

LOW FREQUENCY WAVE HEATING AND CURRENT DRIVE IN TOROIDAL PLASMAS

J. A. Tataronis and A. G. Elfimov
University of Wisconsin - Madison
Madison, WI 53706 USA

1. INTRODUCTION

In this paper, we report on a theoretical study of radio frequency (RF) current drive and heating by low frequency waves in axisymmetric toroidal plasma configurations. Wave induced current can result from both resonant and nonresonant processes. Waves can interact resonantly with a select group of charged particles and produce thereby a net current. Current can also result from nonresonant processes associated with macroscopic wave forces that affect the bulk plasma dynamics rather than a select group of particles. /1-4/ In this paper, our focus is on the nonresonant processes associated with waves in ion cyclotron range of frequencies. Unlike our past studies of nonresonant current drive (NRCD) /1-2/, which were based on the equations of magnetohydrodynamics (MHD), we adopt here a kinetic description of the plasma dynamics. Our key objective is to explore the roles of free and trapped particles, and therefore neoclassical effects, on nonresonant current drive in the tokamak configuration.

2. KINETIC DESCRIPTION OF NRCD

In the MHD frequency limit, the steady-state nonresonant current is computed by averaging Ohm's law over the period of the RF wave, resulting in the expression, $\eta\, \mathbf{j}_0 = \langle \tilde{\mathbf{V}} \times \tilde{\mathbf{B}} \rangle$, where η is the plasma resistivity, $\mathbf{j}_0$ is the driven current density, $\tilde{\mathbf{V}}$ and $\tilde{\mathbf{B}}$ are the fluid velocity and magnetic field of the wave, and the brackets <...> denote an average over the wave period. Only in the presence of nonlinear wave polarization and wave damping does $\tilde{\mathbf{V}} \times \tilde{\mathbf{B}}$ have a non zero average value. /1-4/ In the higher frequency range, the electron force equation with inertia effects neglected gives the time-averaged current density,

$$n_0\, q\, \eta\, \mathbf{j}_0 = q\langle \tilde{n}_e \tilde{\mathbf{E}} \rangle - \langle \tilde{\mathbf{j}}_e \times \tilde{\mathbf{B}} \rangle + \nabla \cdot \langle P_e \rangle \qquad (1)$$

where n_0 and q designate respectively the equilibrium number density and the magnitude of the charge of the electron fluid, $\tilde{\mathbf{E}}$ is the wave electric field, and $[\tilde{n}_e, \tilde{\mathbf{j}}_e, P_e]$ represent respectively the fluctuating electron number density, the fluctuating electron current density and the electron pressure tensor. It is the objective of our study to determine $\mathbf{j}_0$ in axisymmetric toroidal geometry. The linearized Vlasov equation is solved for the electron velocity distribution, which is then used to connect $[\tilde{n}_e, \tilde{\mathbf{j}}_e, P_e]$ to the RF electric field. In toroidal geometry, there are several new effects that could provide additional sources of wave dissipation and current drive. Among them, we specifically treat in this study mode coupling between Fourier harmonics of the electric field, and

wave dissipation on the trapped electrons. These two effects have not been explored in past studies of nonresonant current drive.

We express the electron velocity distribution as a sum of an equilibrium component, $F(\mathbf{r},\mathbf{v})$, and a fluctuating component, $f(\mathbf{r},\mathbf{v},t)$. The Vlasov equation, linearized about the plasma equilibrium state, governs $f(t,\mathbf{r},\mathbf{v})$. To solve the linearized Vlasov equation in axisymmetric tokamak geometry, we use an expansion technique that Nekrasov and Elfimov /5/ introduced. In the equilibrium state, the tokamak plasma is assumed to have concentric magnetic surfaces with circular cross sections. On each magnetic surface, the force lines of the magnetic field are straight with a pitch that varies with the magnetic surface. The spatial coordinates, (ρ,θ,φ), that we use are tied to the circular magnetic surfaces: ρ is the radial coordinate, θ is the azimuthal or poloidal angle and φ is the toroidal angle. Points on a magnetic surface are labeled by values or θ and φ, while magnetic surfaces are labeled by values of ρ. The coordinates in velocity are $(v_\perp,\sigma,v_\parallel)$, where $v_\perp$ and $v_\parallel$ are respectively velocity components perpendicular and parallel to the magnetic field on a magnetic surface, and σ is a polar angle. Because the plasma equilibrium is time independent and axisymmetric, we can assume that all fluctuating variables depend on the toroidal angle and time via the harmonic factor, $\exp[i(n\varphi-\omega t)]$. We thus express $f(\mathbf{r},\mathbf{v},t)$ as $f(\rho,\theta,v_\perp,\sigma,v_\parallel)\exp[i(n\varphi-\omega t)]$. Because the amplitude $f(\rho,\theta,v_\perp,\sigma,v_\parallel)$ is periodic in the polar angle σ, we represent it in Fourier series form,

$$f(\rho,\theta,v_\perp,\sigma,v_\parallel) = f_0(\rho,\theta,v_\perp,v_\parallel) + f_r(\rho,\theta,v_\perp,v_\parallel)\cos(\sigma) + f_b(\rho,\theta,v_\perp,v_\parallel)\sin(\sigma) + \ldots \quad (2)$$

Equations for $f_0(\rho,\theta,v_\perp,v_\parallel)$, and the first harmonic amplitudes, $f_r(\rho,\theta,v_\perp,v_\parallel)$ and $f_b(\rho,\theta,v_\perp,v_\parallel)$, are obtained by substituting Eq. (2) in the linearized Vlasov equation and expanding the resulting equation in terms of two small parameters: the wave frequency divided by the equilibrium cyclotron frequency and inverse aspect ratio of the tokamak geometry. After considerable algebra, the following equation for $f_0(\rho,\theta,v_\perp,v_\parallel)$ is found,

$$v_\parallel\left(\frac{n_\theta}{\rho}\frac{\partial f_0}{\partial\theta} + i\frac{n}{R}n_\varphi f_0\right) - i\omega f_0 - \frac{1}{2}v_\perp\frac{n_\theta}{R}\sin(\theta)\left(v_\perp\frac{\partial f_0}{\partial v_\parallel} - v_\parallel\frac{\partial f_0}{\partial v_\perp}\right) =$$

$$-\frac{q}{m}\frac{\partial F}{\partial v^2}\left\{2v_\parallel\tilde{E}_\parallel - \frac{v_\perp^2}{\omega_c}\left[\frac{1}{\rho}\frac{\partial}{\partial\rho}\left(\rho\tilde{E}_b\right) - \left(\frac{n_\varphi}{\rho}\frac{\partial}{\partial\theta} - i\frac{n}{R}n_\theta\right)\tilde{E}_\rho\right]\right\} \quad (3)$$

where v represents the particle speed, $v \equiv \sqrt{v_\perp^2 + v_\parallel^2}$. The following notation has been introduced in Eq. (3): $R = R_0 + r\cos(\theta)$, $n_\theta(\rho) = (B_\theta/B)$ and $n_\varphi(\rho) = (B_\theta/B)$, and $[\tilde{E}_\parallel,\tilde{E}_b,\tilde{E}_b]$ are the wave electric field components in the parallel, binormal and normal directions, respectively. The equilibrium magnetic field

has poloidal and toroidal components, $B_\theta(\rho,\theta)$ and $B_\varphi(\rho,\theta)$, respectively, and magnitude, $B(\rho,\theta)$. In addition, it has been assumed that the equilibrium velocity distribution is an isotropic Maxwellian, i.e. it depends locally only on the electron speed, v. The first harmonic components of $f(\rho,\theta,v_\perp,\sigma,v_\parallel)$, as defined by Eq. (2), can be expressed in terms of $f_o(\rho,\theta,v_\perp,v_\parallel)$. To lowest order in the parameter, $(1/\omega_c)$, they read,

$$f_r(\rho,\theta,v_\perp,v_\parallel) = -\frac{1}{\omega_c}\left[v_\perp\left(\frac{n_\varphi}{\rho}\frac{\partial f_o}{\partial\theta} - i\frac{n}{R}n_\theta f_o\right) + \frac{n_\varphi}{R}\sin\theta\, v_\parallel \hat{L}\,[f_o] + \frac{q}{m}\frac{\partial F}{\partial v_\perp}E_b\right] \quad (4)$$

$$f_b(\rho,\theta,v_\perp,v_\parallel) = \frac{1}{\omega_c}\left[v_\perp\frac{\partial f_o}{\partial\rho} - \left(\frac{n_\varphi^2}{\rho} + \frac{n_\varphi^2}{R}\cos\theta\right)v_\parallel \hat{L}\,[f_o] + \frac{q}{m}\frac{\partial F}{\partial v_\perp}E_\rho\right] \quad (5)$$

where $\hat{L}\,[f_o]$ is defind as follows, $\hat{L}\,[f_o] \equiv \left(v_\perp\frac{\partial f_o}{\partial v_\parallel} - v_\parallel\frac{\partial f_o}{\partial v_\perp}\right)$.

Equation (3) is a hyperbolic partial differential equation that can be solved explicitly by transforming to characteristic coordinates, (ρ,θ,Λ,v), where Λ is related to the perpendicular kinetic energy of the electron. The coordinate Λ and the electron parallel speed are given by the following expressions,

$$\Lambda \equiv \frac{v_\perp^2}{v_\perp^2+v_\parallel^2}\left(1+\frac{\rho}{R_o}\cos\theta\right) \qquad v_\parallel = s\,v\sqrt{1-\Lambda\frac{R_o}{R_o+\rho\cos\theta}} \quad (6)$$

where s equals plus or minus one, depending on the direction of the electron along the magnetic field line of force. In terms of (ρ,θ,Λ,v), Eq. (3) reads,

$$\frac{\partial f_o}{\partial\theta} + i\lambda f_o = -2\frac{q}{mk_o(\rho)}\frac{\partial F}{\partial v^2}\left[E_\parallel - s\frac{v\Lambda}{2\omega_c}\frac{(\mathbf{k}\times\mathbf{E}_\perp)_\parallel}{\sqrt{1-\Lambda+(\rho/R_o)-2(\rho/R_o)\sin^2(\theta/2)}}\right] \quad (7)$$

where $k_o(\rho)$ replaces the factor, $[n_\varphi(\rho)/R_oQ(\rho)]$, with $Q(\rho)$ representing the tokamak safety factor, $[n_\varphi(\rho)\rho/n_\theta(\rho)R_o]$. The parameter $\lambda(\rho,\theta,\Lambda,v)$ and the function $(\mathbf{k}\times\mathbf{E}_\perp)_\parallel$ are defined respectively as follows,

$$\lambda(\rho,\theta,\Lambda,v) \equiv \frac{nQ(\rho)}{1+(\rho/R_o)\cos\theta} - s\frac{\omega}{k_o(\rho)v}\sqrt{\frac{1+(\rho/R_o)\cos\theta}{1-\Lambda+(\rho/R_o)-2(\rho/R_o)\sin^2(\theta/2)}}$$

$$(\mathbf{k}\times\mathbf{E}_\perp)_\parallel \equiv \left[\frac{1}{\rho}\frac{\partial}{\partial\rho}(\rho E_b) - \left(\frac{n_\varphi}{\rho}\frac{\partial}{\partial\theta} - i\frac{n}{R}n_\theta\right)E_\rho\right]$$

The solution process at this point depends on whether the electrons are trapped or circulating, which in turns depends on the value of the coordinate,

Λ. The electrons are circulating if $0 < \Lambda < 1 - (\rho/R_0)$ and trapped if $1 - (\rho/R_0) < \Lambda < 1 + (\rho/R_0)$. In the remainder of this document, we comment only on the contributions of the circulating electrons. Trapped electron contributions will be treated in detail in a forthcoming publication.

For circulating electrons, Eq. (7) can be solved explicitly for $f_0(\rho,\theta,\Lambda,v)$ in terms of the Jacobi functions and the incomplete elliptic integrals. Our solution of Eq. (7) is based on a Fourier series representation in θ of all fluctuating fields, since they must be periodic in θ,

$$f_0 = \sum_{p'=-\infty}^{\infty} f_{p'} e^{ip'\theta} \qquad E_{\parallel} = \sum_{\ell=\infty}^{\infty} E_{\parallel\ell} e^{i\ell\theta} \qquad (\mathbf{k}\times\mathbf{E}_{\perp})_{\parallel} = \sum_{\ell=\infty}^{\infty} g_{\ell} e^{i\ell\theta} \tag{8}$$

Substituting Eq. (8) in Eq. (7) leads to an expression for the Fourier coefficient $f_{p'}$ in terms of the Fourier coefficients of the electric field components,

$$f_{p'} = i\frac{q}{mk_0 v}\frac{\partial F}{\partial v^2}\sum_{\ell=\infty}^{\infty}\alpha_{\ell}\left(E_{\parallel} + s\frac{v}{2\omega_c}\frac{\Lambda}{1+(\rho/R_0)-\Lambda}g_{\ell}\right) \tag{9}$$

where the coefficient α_{ℓ} has the form,

$$\alpha_{\ell} \equiv \sum_{p=-\infty}^{\infty}\frac{J_{p-p'}(\beta_{\ell})J_{p-\ell}(\beta_{\ell})}{p + \Delta(\omega,\Lambda,v)} \tag{10}$$

In Eq. (10), $J_{p-p'}(\beta_{\ell})$ and $J_{p-\ell}(\beta_{\ell})$ are Bessel functions, and β_{ℓ} and $\Delta(\omega,\Lambda,v)$ are functions that will be specified elsewhere. Two important points should be noted in Eqs. (9) and (10). First, the velocity distribution is coupled to all Fourier harmonics of the electric field. This mode coupling, which results form the spatially inhomogeneous equilibrium of the tokamak, can be a source of additional RF nonresonant current drive processes. Second, the velocity distribution has an infinite number of resonances, which are the zeros of the denominator of α_{ℓ}, $p + \Delta(\omega,\Lambda,v)) = 0$. These resonances, which can be related to the periodic motion of the electrons along the tokamak magnetic field, can contribute to the absorption of the RF waves, and the resonant and nonresonant current drive process in a tokamak plasma.

Although Eq. (8) applies specifically to circulating particles, a similar expression for the trapped particle population is readily derived using the method outlined here.

Work supported by U.S. DOE grant DE-FG02-88ER53264.

/1/ J. A. Tatarons, P. E. Moroz and N. Hershkowitz, Proc. 18th EPS Conf. on Contr. Fusion and Plasma Phys. (Berlin, 1991), **15C-III**, p. 289.
/2/ R. R. Mett and J. A. Tataronis, Phys. Rev. Lett. **63**, 1380 (1989).
/3/ J. B. Taylor, Phys. Rev. Lett. **63**, 1384 (1989).
/4/ V. S. Chan, R. L. Miller, and T. Ohkawa, Phys. Fluids B **2**, 1442 (1990).
/5/ A. G. Elfimov and F. M. Nekrasov, Max-Planck-Institut für Plasmaphysik Report #IPP 4/255, Garching, July 1992.

Pinch Effect of RF Field on Trapped Particles

Masahiko Nakamura
Osaka Institute of Technology
Osaka , 535 , Japan

Introduction

A new method to control radial particle flux is proposed. RF power is coupled to trapped particles to modify their orbit. It is well known that an orbit of a trapped particle (banana orbit) is affected by a DC toroidal electric field , which results in a radially inward shift (Ware pinch). In this presentation , the effect of RF field on trapped particle's orbit is studied. If a trapped particle is accelerated in a parallel direction by RF field (such as LH current drive) during a period with $v_{//} > 0$, its orbit is modified and an inward shift like Ware pinch is obtained. If accelerating power of RF field is much larger than DC toroidal electric field in usual Ohmic discharges, a intense pinch effect is expected.

The effect of perpendicular acceleration (such as ECH) is also studied and it is found that perpendicular acceleration also leads to a pinch effect when RF power is coupled to a trapped particle during a phase with $v_{//} < 0$.

It is shown that a combined effect of parallel and perpendicular acceleration is more effective on a pinch effect because an average pitch angle is conserved.

When coupling conditions are opposite to those described above, radially outward shift contrary to pinch effect is obtained. This effect may be applied to pumping out of impurity ions or He ions.

Effect of parallel acceleration

Electric field of Lower Hybrid wave acts as a DC field for resonant electrons. Trapped particles changes their parallel velocity during 1 cycle of banana orbit , so that the resonant condition can be met during some period of a cycle. When unidirectional wave is injected (as is usual in LHCD) , trapped particles are accelerated only when $v_{//}$ is positive. There is no effect during the

half of the cycle with $v_{//} < 0$. Parallel acceleration has two effects on a banana orbit. (1) The change in $v_{//}$ leads to the change in vertical drift velocity Vd. An orbit of a trapped particle is given by $dr/dt = Vd(\theta)\sin\theta$, where r is a distance from the magnetic axis and θ is a poloidal angle. Because of the change in $v_{//}$, Vd during dr/dt<0 is larger than Vd during dr/dt>0. Thus, net inward shift is obtained. (2) The acceleration changes the pitch angle, resulting in an asymmetry in two (upper and lower) turning points of a banana orbit. Because of this asymmetry of turning points, the period with $dr/dt < 0$ is longer than the period with $dr/dt > 0$. Thus, the orbit of a trapped particle does not close after one cycle of banana orbit, and net inward shift is obtained.

In order to show these effects, the orbit of a trapped particle is calculated with very simple model. The particle is accelerated only when $v_{//} > 0$. For simplicity, the acceleration is modeled by an acceleration due to DC field. i.e. there exist a DC field only when $v_{//} > 0$. Hereafter, this field is notated as $E_{// eff}$. In Fig.1, The result of calculation is shown. It is shown that the shape of the orbit changes gradually and the position moves inward after each cycle. The pinch velocity is given by the radial displacement after one cycle and the bounce time. Dependence of the pinch velocity Vp on $E_{// eff}$. is shown in Fig.2, where $V_{L\ eff}$. is $2\pi R E_{// eff}$.. It is shown that Vp is proportional to $E_{// eff}$. . The value of Vp is nearly the same of the usual Ware pinch velocity. Since $E_{// eff}$. could be much larger than the usual DC field in Ohmic discharge, larger pinch effect is expected.

Because of a continuous acceleration, parallel velocity increases monotonically, while perpendicular velocity remains constant. Then, pitch angle decreases gradually. After a too large acceleration, trapped condition is violated and the trapped particle becomes a transit particle. Since a transit particle shows no pinch effect, large parallel acceleration may result in a decrease or saturation of inward particle flux.

Combined Effect of Parallel and Perpendicular Acceleration

As described above, the change in the pitch angle due to parallel acceleration has an unfavourable effect on inward particle flux. It is desirable that the pitch angle remains constant after one cycle of the banana orbit. Since parallel velocity $v_{//}$ has increased, perpendicular acceleration (heating) is necessary to keep the pitch angle constant. Perpendicular heating such as ECH is suitable for this purpose. When adequate powers for parallel and perpendicular heating are applied, effective pinch effect is expected without any deterioration with high power.

It should be noted that the coupling condition for each acceleration should be chosen appropriately to obtain the inward pinch. Parallel acceleration is necessary during a half period of the orbit with $v_{//} > 0$, as described previously. On the other hand, perpendicular acceleration is necessary during another period with $v_{//} < 0$. When perpendicular heating is applied during the same period, no pinch effect is obtained. Fig.3 shows the orbit with appropriate coupling conditions ; $\Delta K_{//} > 0$ during $v_{//} > 0$, and $\Delta K_{\perp} > 0$ during $v_{//} < 0$, here $\Delta K_{//}$ ($\Delta K_{\perp}$) is the change in parallel (perpendicular) kinetic energy. The orbit is quite similar to that of usual Ware-pinch. In spite of the same applied powers, the orbit is quite different with inappropriate conditions ; (both $\Delta K_{//}$ and $\Delta K_{\perp}$ are positive during the same period with $v_{//} > 0$) . Since the pitch angle is kept constant, no deformation of the orbit is observed. The orbit is nearly the same through several cycles. No inward shift is obtained.

Outward Flux by Inverse Coupling Conditions

When inverse coupling conditions are chosen ($\Delta K_{//} > 0$ during $v_{//} < 0$, and $\Delta K_{\perp} > 0$ during $v_{//} > 0$), outward shift of the orbit is expected. Fig.4 shows the orbit for this condition. The outward velocity is nearly the same of the pinch velocity given in the previous section. This method could be applied to " pumping out " of impurity ions or He ions. It is shown that effective outward particle flux comparable to the diffusive one is obtained with reasonable power.

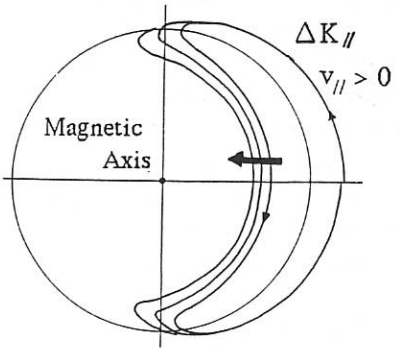

Fig.1
Orbit of a trapped particle with parallel acceleration during $v_{//} > 0$

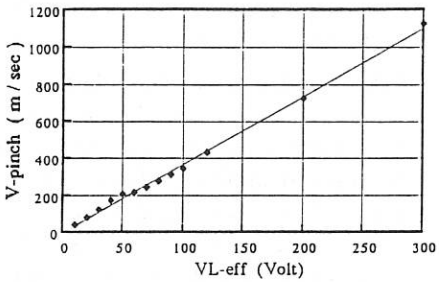

Fig.2
Pinch velocity v.s. $V_{L\,eff}$

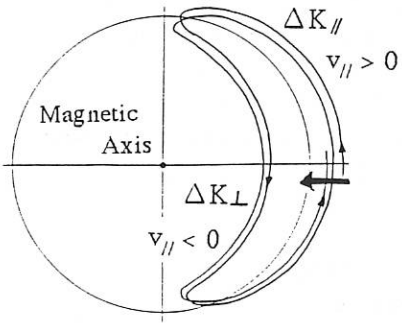

Fig.3
Combined effect of parallel and perpendicular acceleration

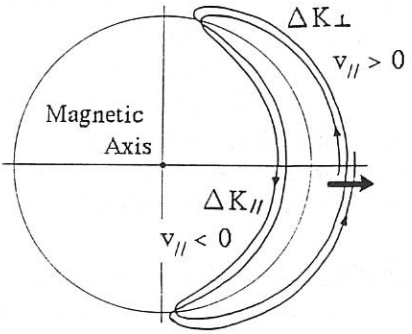

Fig.4
Outward shift by opposite coupling conditions

EFFECTS OF ANOMALOUS RADIAL TRANSPORT ON CURRENT PROFILE

M. Taguchi

College of Industrial Technology, Nihon University,

2-11-1 Shin-ei, Narashino-shi, Chiba-ken 275, Japan

The anomalous radial transport considerably affects the rf current-drive efficiency and the driven-current profile. In this paper, starting from the Fokker-Planck equation in the presence of anomalous radial transport, we derive a radial diffusion-like equation for the rf-driven current density. This equation can be solved by modeling the anomalous transport and the density profile. The anomalous effects on ECCD are also studied by incorporating our method into a ray tracing code.

Radial Diffusion-like Equation for Current Density

A steady-state electron distribution function f in the presence of rf waves and the anomalous radial transport is determined by the Fokker-Planck equation

$$C(f) + L(f) = \frac{\partial}{\partial \mathbf{p}} \cdot \mathbf{S}_{\mathrm{W}}, \tag{1}$$

where C and $-\partial/\partial \mathbf{p} \cdot \mathbf{S}_{\mathrm{W}}$ represent the Coulomb collision operator and the momentum-space diffusion due to rf waves, respectively. We model the anomalous radial transport in the form [1-3]: $L(f) = (\partial/r\partial r)\,[r(D_p \partial f/\partial r + V_p f)]$, where $D_p = D_p(\mathbf{r}, \mathbf{p})$ and $V_p = V_p(\mathbf{r}, \mathbf{p})$ are the momentum-dependent diffusivity and pinch velocity.

Now let us introduce a response function χ_1 satisfying $C(\chi_1 f_0) = \nu_c e v_{\parallel} f_0$, where $v_{\parallel}$ is the parallel velocity to the magnetic field, f_0 is a relativistic Maxwellian, $\nu_c = 4\pi n e^4 \ln\Lambda / m^2 c^3$ is the electron collision frequency normalized to the light speed c with the electron charge $-e$, rest mass m and number density n. This response function χ_1 can be calculated analytically by employing the high-energy form for the collision operator [4]. Using this analytic response function, we can derive the following ordinary differential equation for the rf-driven current density J:

$$\frac{1}{r}\frac{\mathrm{d}}{\mathrm{d}r} r \frac{\mathrm{d}}{\mathrm{d}r}\left(D(r) < J >\right) + \frac{1}{r}\frac{\mathrm{d}}{\mathrm{d}r}\left(rV(r) < J >\right)$$

$$-\nu_c < J >= \nu_c \eta_L < P_d >, \tag{2}$$

where $< \cdot >$ denotes the flux surface average, P_d is the power density dissipated by rf waves, and η_L is the local current-drive efficiency in the absence of the anomalous transport, which can be expressed as [4]

$$\eta_L = -\frac{1}{\nu_c} \frac{< \int \mathbf{S}_W \cdot \frac{\partial \chi_1}{\partial \mathbf{p}} d\mathbf{p} >}{< \int \mathbf{S}_W \cdot \frac{\partial}{\partial \mathbf{p}} (mc^2\gamma)\, d\mathbf{p} >} \tag{3}$$

with $\gamma = 1/\sqrt{1 - v^2/c^2}$. The diffusivity $D(r)$ and the pinch velocity $V(r)$ are defined by

$$\begin{bmatrix} D(r) \\ V(r) \end{bmatrix} = -\frac{1}{e} < \int \begin{bmatrix} D_p \\ V_p - \partial D_p/\partial r \end{bmatrix} \chi_1 f d\mathbf{p} > / < \int v_\parallel f d\mathbf{p} > . \tag{4}$$

This diffusion-like equation (2) shows that the effects of the anomalous radial transport on the rf-driven current can be represented by the diffusivity $D(r)$ and the pinch velocity $V(r)$. Therefore, assuming specific forms of these $D(r)$ and $V(r)$ from theoretically and/or experimentally obtained models, we can calculate the radial current-density profile by solving the diffusion-like equation (2) instead of far more complicated Fokker-Planck equation (1).

Weak Anomalous Case

In the expressions (4) for the diffusivity $D(r)$ and the pinch velocity $V(r)$ the unknown function$f$ is included. In the weak anomalous limit this dependence on f can be removed. We consider this weak anomalous case that the current carrying electrons are relatively well confined. This operation regime will be practically important in future fusion devices since the current-drive scheme may be efficient only in this regime. In the weak anomalous case the diffusivity $D(r)$ and the pinch velocity $V(r)$ can be evaluated perturbatively , and these can be expressed linearly in terms of the momentum-dependent diffusivity D_p and pinch velocity V_p. To obtain these expressions let us consider the following equations:

$$C\left(\begin{bmatrix} \chi_2 \\ \chi_3 \end{bmatrix} f_0\right) = \nu_c \begin{bmatrix} D_p \\ V_p - \partial D_p/\partial r \end{bmatrix} \chi_1 f_0. \tag{5}$$

Then in the similar way to the derivation of (2) we find

$$\begin{bmatrix} D(r) \\ V(r) \end{bmatrix} = - < \int \mathbf{S_W} \cdot \frac{\partial}{\partial \mathbf{p}} \begin{bmatrix} \chi_2 \\ \chi_3 \end{bmatrix} \mathrm{d}\mathbf{p} > / < \int \mathbf{S_W} \cdot \frac{\partial \chi_1}{\partial \mathbf{p}} \mathrm{d}\mathbf{p} >, \tag{6}$$

where we have used the approximate relation $C(f) \simeq (\partial/\partial \mathrm{p}) \cdot \mathbf{S_W}$. For a narrow spectrum of rf waves, the expression (6) is approximated by

$$\begin{bmatrix} D(r) \\ V(r) \end{bmatrix} = - \frac{\mathbf{s} \cdot \frac{\partial}{\partial \mathbf{p}} \begin{bmatrix} \chi_2 \\ \chi_3 \end{bmatrix}}{\mathbf{s} \cdot \frac{\partial \chi_1}{\partial \mathbf{p}}}, \tag{7}$$

where $\mathbf{s} = \mathbf{S_W} / \mid \mathbf{S_W} \mid$ and all the quantities are now evaluated in the position of rf excitation in momentum space. Thus, we do not need the detail form of $\mathbf{S_W}$ and only need the direction and the position of rf excitaion.

The response functions χ_2 and χ_3 can be obtained analytically for a wide range of anomalous transport models. For instance, the response function χ_2 for the model $D_p = D_p(\mathbf{r}, p)$ in the nonrelativistic limit becomes

$$\chi_2 = \frac{ecq}{5+Z} \left(\frac{c}{v}\right)^{1+Z} \int_0^{v/c} D_p x^{Z+7} \mathrm{d}x, \tag{8}$$

where $q = v_{\parallel}/v$ and Z is the effective charge number. In this nonrelativistic limit the response function χ_1 is also obtained in the simple form [4]: $\chi_1 = -ecq(v/c)^4 /(5+Z)$.

Up until now we have neglected the effect of trapped electrons. However, this effect may be taken into account in the weak anomalous limit simply by using the local current-drive efficiency in an inhomogeneous magnetic field in (2).

Anomalous Effect on ECCD

Finally our method is applied to ECCD in a tokamak with circular cross-section. With the local current-drive efficiency and the power density calculated by using a ray tracing code, we solve the diffusion-like equation (2) numerically subject to the boundary condition $< J >|_{r=a} = 0$. In Fig.1, we show the current profile driven by X-mode waves at 2nd harmonic injected from the low-field side, where the anomalous transport and the plasma profiles are modeled by $\bar{D} = D/a^2\nu_c \mid_{r=0} = \text{const.}$

,$V = 0$, $n = n_0[1 - (r/a)^2]$ and $T = T_0[1 - (r/a)^2]^2$. Other parameters are chosen as follows: $a/R = 0.36$, $T_0 = 20$ keV and $N_{\|} = k_{\|}c/\omega = 0.34$. In Fig.2, the ratio of the total current I to that in the absence of anomalous radial transport is depicted as a function of $\bar{D}$. This figure shows that there exists the regime pointed out by Giruzzi[3], where the total current is enhanced by the anomalous effects.

References

[1] J.M. Rax and D. Moreau, Nucl. Fusion 29 (1989) 1751.

[2] M.R. O'Brien, M. Cox and J.S. Mckenzie, Nucl. Fusion 31 (1991) 583.

[3] G. Giruzzi, Phys. Fluids B4 (1992) 1391.

[4] N.J. Fisch, Rev. Mod. Phys. 59 (1987) 175.

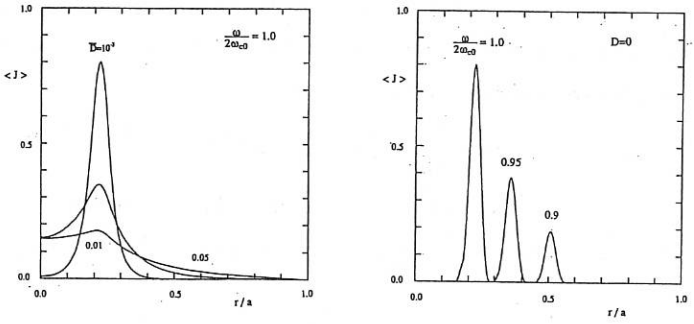

Fig.1 Current profile

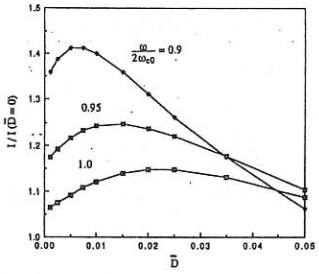

Fig.2

A 2-D Fokker-Planck Solver for the Current Drive Problem

M. Shoucri, I. Shkarofsky

Centre Canadien de Fusion Magnétique
Varennes, Québec, J3X 1S1, Canada

Solution of the 2-D relativistic quasilinear Fokker-Planck equation is of major importance in problems of RF current drive in tokamak plasmas. In many codes coupling ray-tracing and transport, the solution of the Fokker-Planck equation is short-circuited in order to accelerate the calculations, by reducing the 2-D equation to a simpler 1-D equation, or by using some simple formulae relating the current density to the absorbed power in order to calculate the current density. This leads to a value of the current density which is not in very good agreement with the solution of the full 2-D Fokker-Planck equation. We present in this work a fast 2-D Fokker-Planck solver which we hope can be applied for time-dependent current drive problems. The code is 2-D, relativistic, and includes the first Legendre harmonic reaction term. (The inclusion of this term can lead to important differences in the values of the calculated current.) The 2-D equation is discretized using a fully implicit 5-point stencil and solved using the NAG routine D03UAF. Convergence to the steady state can be reached in about 20 to 30 iterations. Preliminary results have been presented in Ref. [1].

1 The Pertinent Equations

We use the normalized variables for the time, velocity and momentum:

$$t \rightarrow t\nu,\ v \rightarrow v/v_t,\ p \rightarrow p/p_t \tag{1}$$

where the thermal velocity unit is defined by the following relations:

$$v_t^2 = \frac{1}{3n_e}\int v^2 f_m(p)\, d\vec{p} \approx \frac{T_e}{m_e}\left(1 - \frac{5}{2}\Theta + \frac{55}{8}\Theta^2\right) \tag{2}$$

where $f_m(p)$ denotes the normalized relativistic Maxwellian distribution:

$$f_m(p) = \frac{1}{(2\pi)^{3/2}} e^{-p^2/(1+\gamma)} \tag{3}$$

with $p = \gamma v, \gamma = (1 + p^2\beta_{th}^2)^{1/2}$ and $\Theta = T_e/m_e c^2 \approx \beta_{th}^2$, $\beta_{th} = v_t/c$.

We will restrict ourselves to cases where $\Theta \ll 1$ (for $T_e \approx 5$ kev we have $\Theta = 0.01$); then $v_t = (T_e/m_e)^{1/2}$. The thermal momentum is given by: $p_t = mv_t$ and the thermal collision frequency is given by: $\nu = n_e\, e^4\, ln\, \Lambda\, /(m^2 v_t^3 4\pi\epsilon_o^2)$. The electric field ϵ is normalized to $E_o = p_t\nu/e$ and the quasilinear diffusion coefficient D for lower hybrid current drive is normalized to $D_o = \nu p_t^2$. Note also that $n_e = n_i\, Z$.

The 2-D Fokker-Planck equation is written in the form:

$$\frac{\partial f}{\partial t} + \nabla .\, \vec{S} = I(f_m, f_1\mu) \tag{4}$$

where $f_1 = \frac{3}{2}\int_{-1}^{1} f\mu d\mu$.

In the spherical coordinates $(p, \mu = \cos\theta)$ we have,

$$\nabla.\vec{S} = \frac{1}{p^2}\frac{\partial}{\partial p}(p^2 S_p) - \frac{1}{p}\frac{\partial}{\partial \mu}(\sqrt{1-\mu^2}S_\mu) \tag{5}$$

where $$S_p = \epsilon\mu f - D\mu\left(\mu\frac{\partial f}{\partial p} + \frac{1-\mu^2}{p}\frac{\partial f}{\partial \mu}\right) - \left(A(p)\frac{\partial f}{\partial p} + F(p)f\right) \tag{6}$$

$$S_\mu = (1-\mu^2)^{1/2}\left[-\epsilon f + D(\mu\frac{\partial f}{\partial p} + \frac{1-\mu^2}{p}\frac{\partial f}{\partial \mu}) + \frac{B_t(p)}{p}\frac{\partial f}{\partial \mu}\right] \tag{7}$$

We consider the case when the background is Maxwellian. In the present work, we compare results obtained using the values of $A(p), F(p)$, $B_t(p)$ and I from Ref. [2], to those obtained using the corresponding values in Ref. [3]. Electron-ion collisions are also included.

We use the grid positions $p_i = (i-1)\Delta p$, $i = 1, ...N1 = 200$, $\mu_j = -1+(j-1)\,\Delta\mu$, $j = 1$, $...N2 = 100$, $\Delta p = p_{\max}/(N1-1)$, $\Delta\mu = 2/(N2-1)$.

The computational domain is $0 \le p \le p_{\max}$ and $-1 \le \mu \le 1$. The electron distribution function is represented by its value at the grid points $f_{i,j}$.

Equation (4) is translated onto our numerical grid in a conservative form as:

$$\frac{f^*_{i,j} - f_{i,j}}{\Delta t} + \frac{1}{p_i^2}\left(\frac{p^2_{i+\frac{1}{2}}S_{pi+\frac{1}{2},j} - p^2_{i-\frac{1}{2}}S_{pi-\frac{1}{2},j}}{\Delta p}\right) - \frac{1}{p_i}\left(\frac{\sqrt{1-\mu^2_{j+\frac{1}{2}}}\;S_{\mu i,j+\frac{1}{2}} - \sqrt{1-\mu^2_{j-\frac{1}{2}}}\;S_{\mu i,j-\frac{1}{2}}}{\Delta\mu}\right)$$

$$= I_{i,j} \tag{8}$$

$f^*_{i,j}$ is the new value of the distribution function. The time differencing assumes a fully implicit discretization for the distribution function f, with the exception of I_{ij} and the values of the distribution function f at the grid points $f_{i+1,j-1}, f_{i+1,j+1}, f_{i-1,j-1}, f_{i-1,j+1}$ which are treated explicitly. This is done this way to derive a five-point stencil for the discretized equation, and benefit from the NAG library D03UAF to invert the matrix derived from the discretization. Details of this discretization have been given in Ref. [1]

In applying the results from Ref. [3], special care was taken in calculating the coefficients involving $\sigma = \sinh^{-1} z$, with $z = \beta_{th}p$, by grouping terms which cancel at low value of p and by using double precision accuracy. For example, we group together terms such as $\gamma\sigma/z - 1, \gamma - \sigma/z, \gamma - \sigma/z - 2\gamma z^2/3, -3\gamma + \sigma(3/z + 2z), -3\gamma\sigma/z^2 + 3/z + z, -3\gamma\sigma/z^2 + 3/z + z - 2z^3/5$ and $\gamma\sigma(6 + 15/z^2) - 15/z - 11z$. We have also calculated the expansions of the groupings for low z and obtained good comparison with the actual expressions.

2 Results

Results obtained using the coefficients $A(p), F(p), B_t(p)$ and I taken from Ref. [2] are denoted by K.-F., and those obtained using the coefficients from Ref. [3] are denoted by B.-K. To make the comparison, we have used the same code, where the values of the coefficients have been successively plugged in the corresponding matrices.

Table I presents the results obtained for the runaway problem using a 200 × 100 grid. These results are calculated with $p_{\max} = 30$. These results are presented for $\beta_{th} = 0.04424$, *i.e.* $T_e = 1$ kev, and $T_i = T_e$. The current is defined by:

$$J = \int v_{\parallel} f d\vec{p} \tag{9}$$

The flux of electrons through the surface of a sphere of radius p gives the runaway rate and is defined by:

$$\Gamma_R = -\frac{\partial}{\partial t}\int f d\vec{p} = \int \nabla . \vec{S} d\vec{p} = 2\pi p^2 \int_{-1}^{+1} d\mu S_p \tag{10}$$

Note that the contribution of the collision term I to Eq. (10) vanishes. Table I gives the results obtained after 30 iterations, with $\Delta t = 0.8$. Note that the addition of the collision term I leads to an electrical conductivity corresponding to the full Spitzer conductivity. The results from (K.-F.) and (B.-K.) are close, the current being slightly higher for the B.-K. coefficients. For the case $\beta_{th} = 0.2$, and for the present numerical parameters, the code with the K.-F. coefficients did not converge to a solution.

Table I

			(K.-F.)		(B.-K.)	
ϵ	β_{th}	Z	J	Γ_R	J	Γ_R
0.01	0.04424	1	0.0745	0.1×10^{-18}	0.08	0.4×10^{-18}
0.03	0.04424	1	0.232	0.41×10^{-7}	0.25	0.11×10^{-6}
0.04	0.04424	1	0.33	0.16×10^{-5}	0.38	0.33×10^{-5}
0.04	0.04424	4	0.105	0.61×10^{-7}	0.11	0.13×10^{-6}
0.01	0.1	1	0.074	0.15×10^{-35}	0.078	0.25×10^{-35}
0.03	0.1	1	0.226	0.44×10^{-8}	0.25	0.42×10^{-8}
0.04	0.1	1	0.32	0.56×10^{-6}	0.35	0.55×10^{-6}
0.03	0.2	1	—		0.22	0.25×10^{-21}
0.04	0.2	1	—		0.28	0.4×10^{-15}

For lower-hybrid waves, we present results where we set in Eqs. (6-7) for the quasilinear diffusion coefficient D:

$$D = \begin{cases} D & \text{for } v_1 \leq \frac{p_{\mu}}{\gamma} \leq v_2 \\ 0 & \text{otherwise.} \end{cases} \tag{11}$$

The results include the cross-effect of the electric field with the R.F. power. The results are calculated for $p_{\max} = 30$, $Z = 1$, $\beta_{th} = 0.054$ ($T_e = 1.5$ kev), and are obtained after 30 iterations, with constant $\Delta t = 1$. We use $v_1 = 4$, $v_2 = 9$, $D = 0.3$, and 200×100 grid points. P is the power absorbed defined by:

$$P = -2\pi \int_{-1}^{1} d\mu \int_{0}^{\infty} \mu D \frac{\partial f}{\partial p_{\parallel}} (\frac{p^3}{\gamma}) dp \tag{12}$$

Table II

	(K.-F.)		(B.-K.)	
ϵ	J	J/P	J	J/P
0.00	0.0064	36.	0.0066	36.
0.005	0.05	200.	0.055	197.
0.01	0.099	300.	0.11	293.
0.02	0.22	397.	0.23	384.

If, for the calculation in Table II, the collision integral I in Eq. (4) is neglected, we get for instance for the result with $\epsilon = 0.02$ a current of only 0.12 with J/P = 300.

If, instead of keeping Δt constant, we allow Δt to increase linearly over 20 iterations to the double of its value, we recover after 20 iterations results very close to those presented in Table II with 30 iterations.

3 Acknowledgments

The authors are grateful to Dr. C. Karney for suggesting the use of the subroutine D03UAF for this problem, and guiding its development through many useful suggestions, and to Dr. D. Ignat for initiating the work and for his interest. The CCFM is a joint venture of Hydro-Québec, Atomic Energy of Canada Limited and the Institut National de la Recherche Scientifique, in which MPB Technologies Inc., and Canatom Inc. also participate. It is principally funded by AECL, Hydro-Québec and INRS.

References

[1] M. Shoucri and I. Shkarofsky, CCFM Report 401 (1993).

[2] C.F.F. Karney and N.J. Fisch Phys. Fluids 28, 116 (1985).

[3] B. Braams and C.F. Karney, Phys. Fluids B1, 1355 (1989).

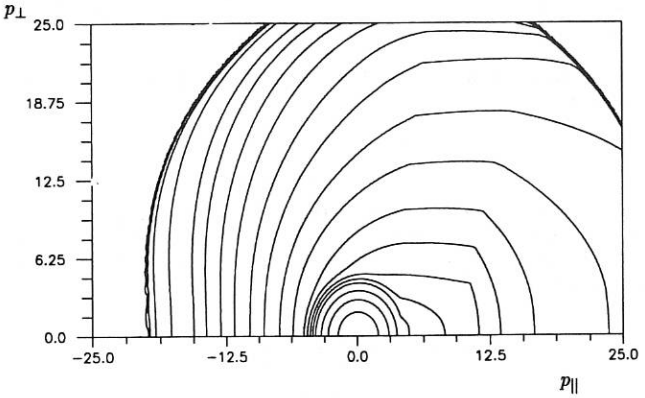

Figure 1: Contour plot of the distribution function calculated for $\epsilon = 0.01, D = 0.3, T_e = 1.5$ kev, $v_1 = 4, v_2 = 9$, using the code with the B.-K. coefficients.

THE EFFECT OF THE STRICTION NONLINEARITY ON ALFVÉN WAVE CONVERSION IN A NONUNIFORM PLASMA

V.I. Lapshin, K.N. Stepanov
Kharkov State University, Kharkov, Ukraine
V.O. Strasser
University of Natal, Durban, South Africa

The effect of the striction nonlinearity on Alfvén wave conversion in an inhomogeneous plasma is investigated. Reduced Maxwell equations describing the propagation of Alfvén wave in a cold inhomogeneous plasma become singular at the Alfvén resonance point. Thermal motion of ion and finite electron inertia remove the singularity, but increase the order of equations leading to new short wave solutions. Analysis shows that all pumping wave energy goes to these new modes. When the effect of finite electron inertia exceeds that of the thermal motion of ions, a small scale wave propagates in the low density direction /1/.

We examine waves propagating almost perpendicular to the steady magnetic field $\vec{B}_0 \parallel \vec{e}_z$ in the plasma with nonuniform density $n(x) = n\,(x/l + 1)$. It is assumed that the wave vector $\vec{k}$ has only two components ($k_y = 0$). The Maxwell equations are

$$(\varepsilon_1 - N_\parallel^2)E_x + \frac{N_\parallel^2 c^2}{\varepsilon_3 \omega^2}\frac{\partial^2}{\partial x^2}E_x + i\varepsilon_2 E_y = 0$$

$$-i\varepsilon_2 E_x + (\varepsilon_1 - N_\parallel^2)E_y + \frac{c^2}{\omega^2}\frac{\partial^2}{\partial x^2}E_y = 0, \qquad (1)$$

here

$$\varepsilon_1 = 1 - \sum_a \frac{\omega_{pa}^2}{\omega^2 - \omega_{ca}^2}: \qquad \varepsilon_2 = -\sum_a \frac{\omega_{pa}^2 \omega_{ca}}{\omega(\omega^2 - \omega_{ca}^2)}: \qquad \varepsilon_3 = 1 - \sum_a \frac{\omega_{pa}^2}{\omega^2}.$$

The striction nonlinearity modifies the plasma density profile as follows /2/:

$$n = n_0 \exp\left(\frac{|E_x|^2}{E_0^2}\right), \qquad \frac{1}{E_0^2} = -\sum_a \frac{e_a^2 n_a}{4 m_a n_e T(\omega^2 - \omega_{ca}^2)}. \tag{2}$$

In the local Alfvén resonance region where $\varepsilon_1 \approx N_z^2$, the quantity E_y changes slowly and the effect of wave conversion may be described by the approximate equation

$$\left(\varepsilon_1 - N_z^2\right) E_x + i\varepsilon_2 E_y + \frac{N_z^2 c^2}{\varepsilon_3 \omega^2} E_x'' = 0, \tag{3}$$

where $E_y = const$. The linearized form of this equation has the following solution

$$E_x(\xi) = -i\frac{\omega}{\omega_{ci}} E_y \left(\frac{l}{\rho_{eff}}\right)^{2/3} W(\xi), \tag{4}$$

where $W(\xi)$ is a solution of the Airy equation $(W'' - \xi W = 1)$,

$$\xi = \frac{x}{\Delta x}, \quad \Delta x = (l\rho_{eff}^2)^{1/3}, \quad \rho_{eff} = -\left(\frac{N_z^2 c^2}{\varepsilon_3 \varepsilon_1 \omega^2}\right).$$

In the local resonance region the electric field is

$$|E_x|_{max} \approx 1.9\frac{\omega}{\omega_{ci}} (l/\rho_{eff})^{2/3} E_y. \tag{5}$$

In the case of strong nonlinearity when $|\varepsilon_1 E_x^2/E_0^2| > |N_z^2 c^2/\varepsilon_3 \omega^2|$ one has from Eq. (3)

$$|E_x| \approx \left(\frac{E_y E_0^2 \omega}{\omega_{ci}}\right)^{1/3}. \tag{6}$$

Using Eq. (3) it is possible to find the shift of the resonance point /2/

$$\delta x = l\frac{|E_x|^2}{E_0^2}. \tag{7}$$

The following plasma and wave parameters were chosen for numerical calculations: $T = 10\ eV$, $n = 10^{13}\ cm^{-3}$, $B_0 = 50\ kG$, $\omega = 0.8\omega_{ci}$, $k_z = 0.156\ cm^{-1}$, $E_y = 16\ V/cm$. These parameters are typical for RF heating

and current drive by fast magnetosonic waves ($\omega \leq \omega_{ci}$) at the plasma edge of large tokamaks. In this case an Alfvén wave is excited at the plasma edge.

Fig. 1 shows the steady electric field strength profile in the resonance region calculated from the system (1) in the linear case, $n = n_0$. This numerical solution is close to solution (4).

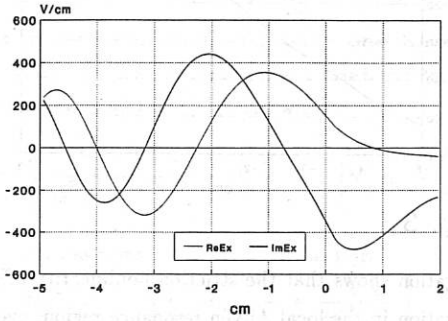

Fig. 1

Fig. 2 presents the result of numerical solution of system (1) in the nonlinear case. The amplitude of the electric field strength is close to the estimate (6). One can see that the striction nonlinearity decreases the electric field strength in the resonance region.

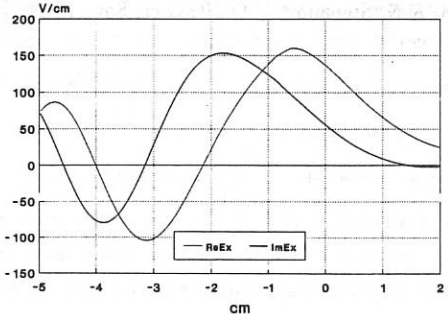

Fig. 2

In fig. 3, the dependence of $\varepsilon_1 - N_z^2$ corresponding to the solution in fig.2 is presented. The shift of the resonance point is close to that given by (7).

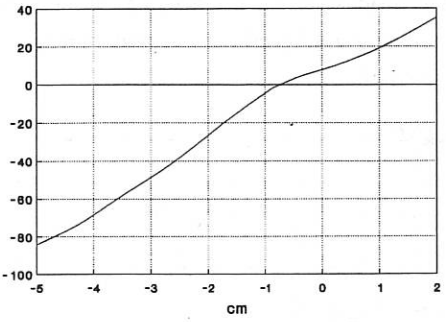

Fig. 3

This investigation shows that the striction nonlinearity affects essentially the wave propagation in the local Alfvén resonance region, even for the comparatively small amplitudes of pumping wave used for RF heating and current drive in tokamaks with ITER parameters.

REFERENCES

/1/ V.V. Dolgopolov, K.N. Stepanov, In coll. Vysokochastotni nagrev plazmy (RF plasma heating), Inst. prikl. fiz. AN SSSR, 105, (1983).

/2/ V.I. Lapshin. K.N. Stepanov. V.O. Strasser. Sov. Phys. Plasma 18. 656. (1992).

ALFVEN WAVE HEATING OF PLASMA IN DEVICES WITH BUMPY MAGNETIC FIELD

Girka I.A., Lapshin V.I., Stepanov K.N.*
Kharkov State University, 310077, Kharkov, Ukraine. *Ukrainean Scientific Center Kharkov Institute of Physics & Technology, 310108, Kharkov, Ukraine.

The report deals with the problem of Alfven waves' (AW) heating of plasma in fusion devices with bumpy magnetic field

$$B_z = B_0 (1 + \varepsilon \cos(k_b z)), \quad B_r = B_0 \frac{\varepsilon'}{k_0} \sin(k_b z), \quad \varepsilon' \equiv \frac{\partial \varepsilon}{\partial r} . \quad (1)$$

External antenna's current contains only one harmonic $\sim \exp(i\varphi)$, $\varphi = m\vartheta + k_z z - \omega t$. It is shown here, that side by side with the main Alfven resonance (AR) $r_A^{(0)}$, in which

$$\varepsilon_1^{(0)}(r) \equiv 1 - \sum_i \frac{\omega_{pi}^2(r)}{\omega^2 - \omega_{ci}^{(0)2}} = N_z^2, \qquad \left[N_z \equiv \frac{c\, k_z}{\omega} \right] \quad (2)$$

two additional resonances $r_A^{(\pm)}$, in which

$$\varepsilon_1^{(0)} = (N_z \pm N_b)^2, \qquad \left[N_b \equiv \frac{c\, k_b}{\omega} = \frac{2\pi c}{\omega L_b} \right] \quad (3)$$

can exist in such devices with week bump ($\varepsilon \ll 1$). Here L_b - bump's space period. It takes place due to the appearence of satellite harmonics in AW field side by side with the main harmonic

$$B_z^{\sim} = \left[B^{(0)}(r) + B^{(+)}(r)\, e^{ik_b z} + B^{(-)}(r)\, e^{-ik_b z} \right] \exp(i\varphi) , \quad (4)$$

here $|B^{(\pm)}| \sim \varepsilon |B^{(0)}|$. $B^{(0)}(r)$ is Maxwell equations' solution in zero approximation ($\varepsilon = 0$). Perturbation theory using makes it possible to derive $B^{(\pm)}$ [1], if r is not close to $r_A^{(\pm)}$. Rapid growth of amplitudes $B^{(\pm)}$ and AW transformation into small-scale kinetic AW take place near by $r_A^{(\pm)}$. Maxwell equations' solution for $B^{(\pm)}$ in the vicinity of $r_A^{(\pm)}$ was obtained with taking into account electron inertia, effect of finity of ion Larmor radius ρ_{Li} and particles collisions analogously to [2-4]. Amplitudes $B^{(\pm)}$ may be expressed through the Airy function $u_0(\xi)$:

$$u_0(\xi) = -\int_0^{\infty} \exp\left[-i \left(t\, \xi + \frac{t^3}{3} \right) \right] dt, \quad (5)$$

$$\xi = k_1 (r - r_A^{(\pm)}) - i\,\eta, \qquad \eta = - k_1\, \varepsilon_1^{(c)} \left[\frac{\partial\, \varepsilon_1^{(0)}}{\partial\, r} \right]^{-1}_{r\,=\,r_A^{(\pm)}},$$

$$k_1 = \left[- \frac{\omega^2}{c^2} \frac{\partial\, \varepsilon_1^{(0)}}{\partial\, r} \frac{\varepsilon_3}{\varepsilon_T\, \varepsilon_3 + \varepsilon_1^{(0)}} \right]^{\frac{1}{3}}_{r\,=\,r_A^{(\pm)}} = |\, k_1\, |\, e^{i\psi}.$$

The value $\varepsilon_1^{(c)}$ provides account of collisions:

$$\varepsilon_1^{(c)} = \sum_{\alpha,\beta} \frac{\omega_{p\alpha}^2\, \nu_{\alpha\beta}}{\omega\, (\omega^2 - \omega_{c\alpha}^2)} \left[\frac{\omega^2 + \omega_{c\alpha}^2}{\omega^2 - \omega_{c\alpha}^2} - \frac{e_\beta\, m_\alpha}{e_\alpha\, m_\beta} \frac{\omega^2 + \omega_{c\alpha}\, \omega_{c\beta}}{\omega^2 - \omega_{c\beta}^2} \right] \qquad (6)$$

Asymptote of $u_0(\xi)$ under large values of argument is as follows

$$u_0(\xi)\,|_{Re\ \xi\ \to\ -\infty} \longrightarrow \frac{i}{\xi} + i \left[\frac{\pi^2}{-\xi} \right]^{\frac{1}{4}} exp\left[i \left[\frac{2}{3} \left(- \xi \right)^{\frac{3}{2}} + \frac{\pi}{4} \right] \right]. \qquad (7)$$

Small-scale kinetic AW (the second addend in (7)) are supposed to damp strongly due to collisions or Landau mechanism when going away from $r_A^{(\pm)}$. AW field's distribution obtained is used for calculation of AW-power $P_r^{(\pm)} + P_z^{(\pm)}$, absorbing in the vicinity of $r_A^{(\pm)}$ in the unit of plasma column length. It consists on the AW field's work over the radial and axial RF currents j_r and j_z

$$P_r^{(\pm)} = \pi\, Re \int_{r_A^{(\pm)} - x}^{r_A^{(\pm)} + x} j_r^*\, E_r^{(\pm)} dr = \frac{\pi\, \omega}{4} \left(\left| \frac{\partial\, \varepsilon_1^{(0)}}{\partial\, r} \right|^{-1} r\, \varepsilon_2^{(0)2} \right)_{r\,=\,r_A^{(\pm)}} |F_1^{(\pm)}|^2, \qquad (8)$$

$$P_z^{(\pm)} = \pi\, Re \int_{r_A^{(\pm)} - x}^{r_A^{(\pm)} + x} j_z^*\, E_z^{(\pm)} dr = \int_{r_A^{(\pm)} - x}^{r_A^{(\pm)} + x} |k_1| \left| \frac{\partial\, u_0}{\partial\, \xi} \right|^2 dr \times$$

$$\times \left(\frac{r\, \omega}{4} \left| \frac{\partial\, \varepsilon_1^{(0)}}{\partial\, r} \right|^{-1} \frac{\varepsilon_2^{(0)2}\, Im\, \varepsilon_3^*\, \varepsilon_1^{(0)}}{|\varepsilon_T\, \varepsilon_3^2 + \varepsilon_1 \varepsilon_3|} \right)_{r\,=\,r_A^{(\pm)}} |F_1^{(\pm)}|^2. \qquad (9)$$

Components of low pressure plasma's tensor ε_{ij} are

$$\varepsilon_{1,2}(r,z) = \varepsilon_{1,2}^{(0)}(r) + \varepsilon_{1,2}^{(1)}(r) \cos(k_0 z) + o(\varepsilon^2), \qquad (10)$$

$$\varepsilon_2^{(0)}(r) \equiv \varepsilon_2(r,z)\,|_{\varepsilon\,=\,0} = - \sum_i \frac{\omega_{pi}^2(r)\, \omega}{(\omega^2 - \omega_{ci}^{(0)2})\, \omega_{ci}^{(0)}}, \qquad (11)$$

$$\varepsilon_1^{(1)} = \left(\frac{\partial\, \omega_{pi}^2}{\partial\, r} \right)_{\varepsilon = 0} \times \frac{1}{r} \int_0^r r\, \varepsilon\, dr \sum_i \frac{1}{\omega^2 - \omega_{ci}^{(0)\,2}} -$$

$$- 4\, \varepsilon \sum_i \frac{\omega_{pi}^2(r)\, \omega_{ci}^{(0)\,2}}{(\omega^2 - \omega_{ci}^{(0)\,2})^2}\,, \qquad (12)$$

$$\varepsilon_2^{(1)} = \left(\frac{\partial\, \ln\, \omega_{pi}^2}{\partial\, r} \right)_{\varepsilon = 0} \frac{1}{r} \int_0^r r\, \varepsilon\, dr\, \varepsilon_2^{(0)} +$$

$$+ \varepsilon \sum_i \frac{\omega_{pi}^2(r)\, \omega\, (\omega^2 - 3\, \omega_{ci}^{(0)2})}{(\omega^2 - \omega_{ci}^{(0)\,2})^2\, \omega_{ci}^{(0)}}\,, \qquad (13)$$

$$\varepsilon_3 = \frac{-\,\omega_{pe}^2}{\omega\,(\omega + i\nu_{ei})} \qquad \left(z_e \equiv \frac{\omega}{\sqrt{2}\,|k_z^{\pm} - k_b|\, v_{Te}} > 1 \right), \qquad (14)$$

$$\varepsilon_3 = \frac{\omega_{pe}^2}{(k_z^{\pm} - k_b)^2\, v_{Te}^2} \left[1 + i\sqrt{\pi}\; z_e\, W(z_e) \right] \quad (z_e < 1)\,. \qquad (15)$$

The value ε_T provides account of $\rho_{Li} = v_{Ti}/\omega_{ci}$ finity,

$$\varepsilon_T = \sum_i \frac{3\, \omega_{pi}^2(r)\, \omega^2\, v_{Ti}^2(r)}{(\omega^2 - \omega_{ci}^{(0)\,2})\,(\omega^2 - 4\, \omega_{ci}^{(0)\,2})\, c^2}\,, \qquad (16)$$

Exciting wave's field value enters to (8),(9) through

$$F_1^{(\pm)} = \left\{ \frac{-1}{2\, \varepsilon_2^{(0)}} \left[i\varepsilon_2^{(1)} E_\vartheta^{(0)} - \frac{c}{\omega}\,(N_b^{\pm} - N_z)\, \frac{\partial}{\partial\, r} \left[\frac{\varepsilon'}{k_0}\, E_r^{(0)} \right] + \varepsilon_1^{(1)} E_r^{(0)} \mp \right. \right. \qquad (17)$$

$$\left. \left. \mp \frac{c\, \varepsilon'\, N_z}{\omega\, r\, k_0}\, \frac{\partial}{\partial\, r}\,(r\, E_r^{(0)}) \mp \frac{i\, c\, m\, \varepsilon'}{\omega\, r\, k_0}\, N_z E_\vartheta^{(0)} \right] - \frac{c\, m}{r\, \varepsilon_2^{(0)}\, \omega}\, B^{(\pm)} - i\, E_\vartheta^{(\pm)} \right\}$$

One can obtain well-known expressions [2-4] for the power $P_r^{(0)}$, absorbing in the main AR, changing in (8),(9) $r_A^{(\pm)} \to r_A^{(0)}$, $E_{r,\vartheta,z}^{(\pm)} \to E_{r,\vartheta,z}^{(0)}$, $(N_z^{\pm} N_b) \to N_z$, $B^{(\pm)} \to B^{(0)}$ and omiting in F_1 (16) addendum in square brackets. P_z contribution to Alfven heating due to satellite harmonics is not small, if $Im\, \varepsilon_3 > Re\, \varepsilon_3$:

$$\frac{P_z}{P_r} \sim \left| \frac{\varepsilon_1}{\varepsilon_1 + \varepsilon_T \varepsilon_3} \right| \frac{Im\ \varepsilon_3}{|\varepsilon_3|} \quad (18)$$

The values $P_r^{(\pm)}$ are proportional to ε^2 and they usually are small as compared with $P_r^{(0)}$. But in some cases power $P_r^{(\pm)}$ can prove to be more essential, then $P_r^{(0)}$.

a) AR (2) displaces at the plasma edge, if k_z is small. At the same time AR $r = r_A^{(\pm)}$ can be located in the plasma core, if k_b is large. $P_r^{(\pm)} > P_r^{(0)}$ if k_b is large, so far as $P_r^{(\pm)} \sim n(r_A^{(\pm)})\,(k_z \pm k_b)^2\,|F_1^{(\pm)}|^2$ and $P_r^{(0)} \sim n(r_A^{(0)})\,k_z^2 |F_1^{(0)}|^2$. In this case $B^{(0)}$ penetrate in plasma well due to k_z smallness. Field $B^{(0)}$ corresponds to the fast magnetosonic wave (FMSW) in the region of high density $\left(\frac{\omega_{pi}^2}{\omega_{ci}(\omega + \omega_{ci})} > N_z^2 \right)$. These FMSW interact linearly in the bumpy magneic field with AW, whose axial wavenumber is $(k_z \pm k_b)$. These FMSW are absorbed resonancely near by the $r_A^{(\pm)}$ due to this interaction.

The wave $B^{(0)}$ can be the eigen mode with week damping for the device. It leads to satellite harmonics' $B^{(\pm)}$ increasing. The powers $P_{r,z}^{(\pm)}$ and $P_{r,z}^{(0)}$ increase consequently.

Values $P_{r,z}^{(\pm)}$ can also increase, when AW with axial wavenumber $(k_z \pm k_b)$ is the eigen mode for the device. Two last addendum in (16) $\left[\frac{c\,m}{\omega\, r\, \varepsilon_2^{(0)}} B^{(\pm)} - i\, E_\vartheta^{(\pm)} \right]_{r=r_A^{(\pm)}}$ increase resonancely in this case.

b) Condition $N_z^2 > \varepsilon_1^{(0)}$ is true everywhere in low density plasma. That is why the main AR does not exist. The AR $r = r_A^{(-)}$ can exist in this case. This AR provides excited field's absorption. This absorption can be increased, if satellite wave $B^{(-)}$ is the eigen mode for the device.

The work is supported by State Committee of Science & Technology of Ukraine (Contract N 8303 of Programme 9.2).

References

1. Girka I.A., Stepanov K.N. Ukr. Phys. Journal. 1992. V. 37. P. 69.
2. Dolgopolov V.V., Stepanov K.N. Nucl. Fusion. 1965. V. 5. P. 276.
3. Grekov D.L., et al. Fizika Plasmy. 1981. V. 7. P. 752.
4. Girka I.A., Stepanov K.N. Ukr. Phys. Journal. 1990. V. 35. P. 1680.

INTERACTION OF LOWER-HYBRID WITH FAST IONS IN JET

M.C.R. Andrade*, M. Brusati, L.G. Eriksson, C. Gormezano,
E. Righi, F.Rimini, G. Sadler
JET Joint Undertaking, Abingdon, Oxon, OX14 3EA, UK
*Instituto de Física-Universidade de São Paulo-CP20516,São Paulo-SP, Brazil

It is predicted by theory [1] that the fast minority ions in the plasma, generated during minority heating experiments with ion cyclotron waves (ICRH), can interact with Lower-Hybrid waves (LH), through Landau Damping, in the direction perpendicular to the toroidal magnetic field when the resonance condition, $v_\perp=\omega/k_\perp=c/n_\perp$, is fulfilled. $v_\perp$,$k_\perp$ and $n_\perp$ are the perpendicular components of the ion velocity, the wave vector and refractive index of the wave respectively, and ω is its frequency. The LH-fast ion interaction, which simulates the interaction of α particles (~3.5MeV) with LH, is competitive with parallel electron Landau Damping thus reducing the current drive efficiency of an LHCD system. Recent studies, however, have indicated that the energy exchange between α particles and LH waves in a reactor scenario, where very high density and electron temperature occur, might improve the accessibility of the wave to the core of the plasma [2].

A 1-D Fokker-Planck equation [3], including the ICRH and LH quasi-linear diffusion coefficients, describes the interaction between LH and fast ions and their slowing-down over a Maxwellian plasma. This interaction requires both ICRH and LH power deposition profiles on the fast ion population to be superimposed.

The first experimental evidence of the interaction of LH waves with fast ions at JET is presented in this work. LH experiments at JET were performed in low density plasmas with 1 to 2 MW of LH power in 2.6 to 3.3T limiter plasmas and 2 and 3 MA of plasma current. These experiments were carried out in order to optimise LHCD current drive efficiency. Heating of hydrogen minority with minority concentration ranging from 5 to 15% in deuterium plasmas was done using 4 to 6 MW of ICRH power with the cyclotron resonance layer ranging between the plasma centre and r=40cm in relation to the magnetic axis. The central electron density was approximately $n_e(0)=2.5\times10^{19}$ m^{-3} in order to enhance LH wave penetration for current drive studies and central electron temperatures were ranging from 5 to 8 keV. Between 1 to 2 MW of LH power at 3.7GHz were launched with power spectrum centred at a parallel refractive index $n_{||}=1.8$. LH wave propagation leads to $n_\perp$ values in the range of 10 to 25. In this case, the fast ion resonance energy, ($E_{fi}=0.5m_i(c/n_\perp)^2$), ranges from 0.75 to 4.7 MeV.

Diagnostics: Observations on the absorption of LH waves by the fast minority ions were mainly based on the analysis of the fast ion energy, and on the γ ray and neutron rates.

Fast Ion Energy: The fast ion energy content (W_p), defined as the perpendicular energy in excess of the isotropic component, is related to the anisotropic high energy tail generated during ICRH heating [4], which increases preferably the perpendicular velocity component of the minority ions. There is however a component of their parallel energy above the thermal level due to pitch angle scattering or because of the variation of the magnetic field along the particle orbit. It can be obtained from the diamagnetic energy $W_{DIA}=3/2W_\perp$, measured by the

diamagnetic loop, and the MHD energy, $W_{MHD}=3/4(W_{\perp}+2W_{\parallel})$, obtained from MHD equilibrium calculations resulting in $W_f=4/3(W_{DIA}-W_{MHD})$. A possible off-set between W_{DIA} and W_{MHD} is accounted in order to obtain $W_f=0$ for an isotropic distribution in absence of fast ion tails.

γ Rays and Neutron rate: The fast minority ions can interact either with the main ions in the plasma or with impurity ions. The unstable products originated from these reactions emit γ rays whose spectrum and flux rate can be measured to estimate the fast ion minority density as well as their threshold in energy in order to excite such reactions [5]. In this work we present the γ rays count rate in reactions between fast ions with ^{9}Be, one of the main impurities in JET plasmas. These reactions have a threshold in energy of 1 MeV, and the energy of γ rays released during this process is 3.5 MeV. The neutron rate measures the D-D reaction rate in the plasma and in most of the cases this rate increases when LH is coupled to the plasma.

NPA: The new neutral particle analyser at JET which can diagnose minority ions with energy ranging from 286 keV to 1.0 MeV shows that there is an increase in the fast particle flux for all energies when LH is present. Further analysis still has to be carried out since impurity and minority concentrations, which are difficult to be measured accurately, are critical elements in the data analysis.

Experimental results: Time dependence of plasma parameters for a typical JET pulse where LH coupling to the fast ions was observed, is shown in fig1. Approximately 25% of increase in W_f (200 kJ) is observed for #27760 (Fig.1d) when 2MW of LH power is applied in addition to 3.0 MW of ICRH at 48 MHz. This gives an estimate of approximately 10% for the LH power damped on the fast ion population which is in reasonable agreement with the 8% obtained from code simulations carried out for this shot. Time dependent code simulations including the presence of ICRH only [6] for #27760, do not reproduce the fast increase on the fast ion energy content as it is observed experimentally, suggesting that the step on the fast ion energy is related to the presence of LH. An increase, of more than a factor 2, in the γ count rate is observed after 8.5s in #27760, after LH is switched on (Fig.2). The electron temperature measured by the LIDAR diagnostics remains approximately constant and the higher γ rays rate observed cannot be accounted by an increase in Z_{eff} , which remains approximately 3.8. Therefore the possible cause of this increase, is the increase of the fast ion population when LH is launched in the plasma. The neutron rate, which is a measure for the D-D reaction rate, also increases after 8.54s (Fig.1e).

Finally, Figs 3a and 3b show the analysis on the Fourier analysis (FFT) of shots where LH power is modulated with a frequency of 1 Hz. The results are shown for shots #24898 and #24909 where the hydrogen minority cyclotron layer was respectively 40 cm and 10 cm outboard of the magnetic axis. In the first pulse the resonance is outside the q=1 surface and represents the off-axis heating case. In both shots the plasma parameters are similar but the FFT for #24898 of the fast ion energy gives a peak in its spectrum around 1Hz, not evident in #24909. As shown in fig.4, the fast electron profile, as deduced from the FEB camera [7] is hollow and peaked at r~50 cm. This indicates that damping of LH waves on the minority ions takes place when the cyclotron resonance layer is close to the region where the fast electrons are located.

Conclusions: The first experimental evidence at JET on the interaction of fast minority ions with LH is reported in this work. An increase of approximately 20% on the fast ion energy content was observed in the presence of LH, with an estimated LH absorbed power of approximately 10% for 2 MW of LH power and plasma densities of 2.0×10^{19} m^{-3} with central temperatures $T_e(0)$~6 keV. γ ray and neutron rates also show that absorption of LH waves by the fast minority ions is taking place. FFT analysis confirms a better damping of the wave when ICRH heating and maximum of fast electrons population coincides. This condition would be somewhat relaxed when α particles are considered due to large orbit effects. The next JET operational campaign, where 10 MW of LH are expected to be coupled to the plasma, will provide further information on the interaction between α particles and LH waves, as simulated with ICRH minority fast ions.

References:

/1/ E. Barbato, Proc. 17th EPS Conf., Amsterdam 3,1163 (1990).

/2/ N. Fisch, J.M. Rax, Phys. Rev. Lett. 62, 612 (1992).

/3/ T.H.Stix, Nuclear Fusion 15,737 (1975).

/4/D.Start et al., JET Report - JET-P(89)84.

/5/ G. Sadler et al, Fusion Technology 18,556 (1990).

/6/ L.Eriksson, submitted to Nuclear Fusion.

/7/ P. Froissard et al., Proc. 18th EPS Conf., Berlin 3, 383 (1991).

Aknowledgements: We aknowledge the useful contributions of Dr. E. Barbato from ENEA-FRASCATI on the theoretical discussions of this work and the financial support given by the Brazilian Council CNPq, by the Commission of European Communities and by JET Joint Undertaking.

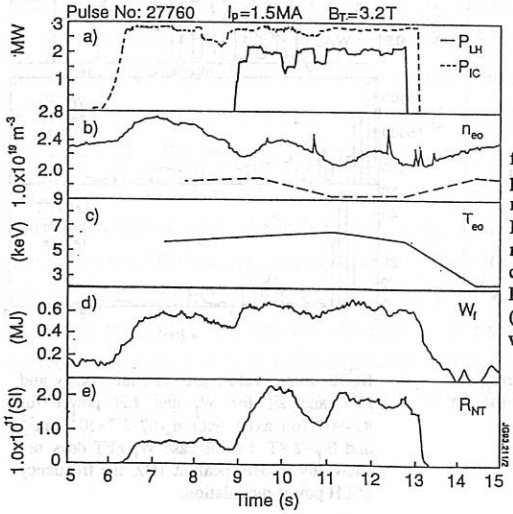

fig.1: Time evolution of the main plasma parameters, fast ion energy W_f and neutron rate (RNT) for #27760. a) — LH power, --- ICRH power, b) — central electron density $n_e(0)$ (interferometer),---$n_e(0)$ from LIDAR, c) central electron temperature $T_e(0)$ from LIDAR, d) increase on the fast ion energy (W_f) after 8.5 s e)increase on the neutron rate when LH is coupled to the plasma.

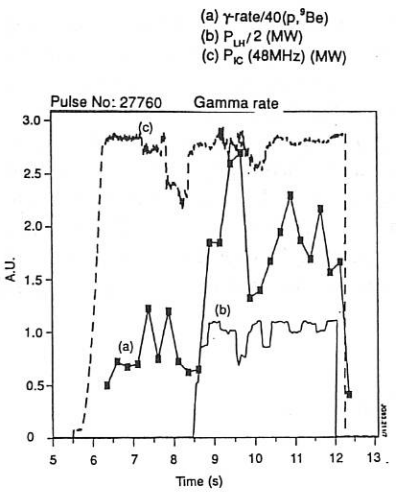

fig.2: Gamma rays rate for #27760. An increase higher than a factor two is observed after LH is launched in the plasma (8.5s).

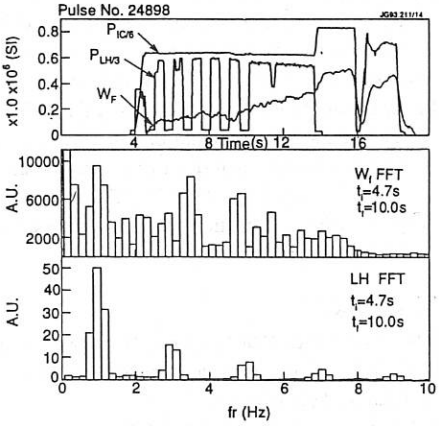

fig.3a: Time evolution of fast ion energy and FFT analysis for W_f and LH for #24898 (off axis) with $n_e(0)\sim2.7\times10^{19}m^{-3}$ and B_T=2.6T. There is a peak on the W_f spectrum around 1 Hz, the frequency of LH power modulation. Peaks in upper frequencies seem still to follow LH Fourier spectrum.

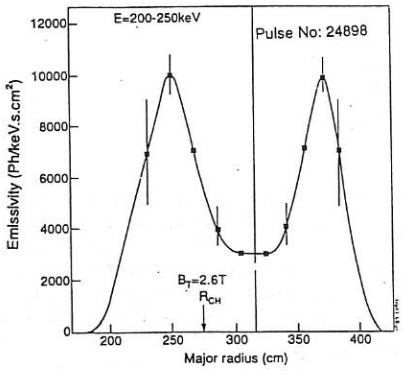

fig.4: Fast electron profile (FEB camera), for #24898 peaked at r~50 cm, close to the ion cyclotron resonance layer (r~40cm)

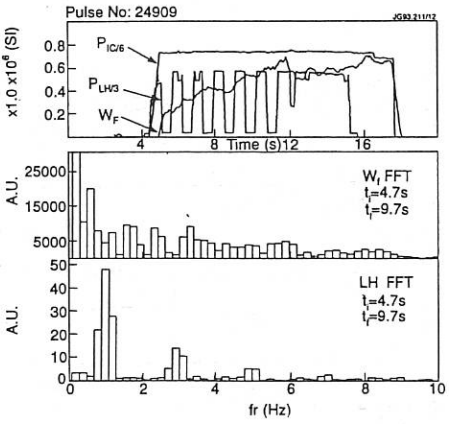

fig.3b: Time evolution of fast ion energy and FFT analysis for W_f and LH power for #24909 (on axis) with $n_e(0)\sim2.7\times10^{19}$ m^{-3} and B_T=2.8T. In this case W_f FFT does not show any evident peak at 1Hz, the frequency of LH power modulation.

MODELLING OF LHCD AND COMPARISON WITH EXPERIMENTAL RESULTS IN JET

Y.F. Baranov, M. Brusati, A. Ekedahl, P. Froissard,
C. Gormezano, M. Lennholm, F. Rimini
JET Joint Undertaking, Abingdon, UK, OX14 3EA

ABSTRACT. A new code has been developed for the simulation of LHCD in JET. The model which includes stochastic radial diffusion of electrons and scattering of Lower Hybrid waves is validated by comparing its results with the current drive efficiency derived from the LHCD experiments in JET, and by simulating the hard X-ray bremsstrahlung emission from fast electrons and comparing it with the experimentally measured emission. Good agreement has been found for both LH only cases and LH plus electric field.

LH WAVE PROPAGATION

The ray-trajectory method is used to simulate propagation and absorption of Lower Hybrid waves. The equations describing the ray trajectory of a wave are presented in /1/. The dispersion relation for LH waves includes electromagnetic part and thermal corrections. Collisional and Landau damping by electrons is taken into account. The calculations are carried out for the equilibrium magnetic field topology.

SCATTERING OF LOWER HYBRID WAVES BY DENSITY FLUCTUATIONS

Scattering of the slow LH waves by low frequency density fluctuations is taken into account using a theory proposed by Ott /2/. The spectrum of the fluctuations is approximated by a Gaussian function $S(k)=(1/\pi k_0^2)<\delta n/n>^2 \exp(-k^2/k_0^2)$ where k is a wave vector of the fluctuations, which is perpendicular to the magnetic field. The characteristic wave scalelength k_0^{-1} is assumed to be of the order of the ion Larmor radius ρ_i (all calculations were carried out for $k_0^{-1}=3\rho_i$). The amplitude of the fluctuations is distributed in space according to: $<\delta n/n>^2=\Delta r\rho_i/a^2$, where r is the radial coordinate and a the minor radius. The parameter Δ is introduced to investigate the influence of the fluctuation amplitude on the distribution of the driven current. The best agreement between the experimental data and results of calculations is observed for $0.25\leq\Delta\leq1$. The scattering of the waves is modelled in the framework of the ray-trajectory approach using Monte Carlo method. The scattering length 1_s for a slow wave with a given $k_\perp$ can be calculated according to /3/. It is assumed that, during each small step $\Delta s \ll 1_s$ along the trajectory, $\vec{k}_\perp$ is deflected by an angle $\Delta\Theta=\pi/2(\Delta s/1_s)^{1/2}$ with the average value $<\Delta\Theta>=0$.

FOKKER-PLANCK EQUATION

The electron distribution function $F(p_{||},r)$ is calculated via numerical solution of the relativistic 2-D (in $p_{||}$ and r) Fokker Planck (FP) equation:

$$\frac{\partial F}{\partial t} = \frac{\partial}{\partial p_{||}} D_{ql}(p_{||},r) \frac{\partial F}{\partial p_{||}} + \upsilon_o \frac{\partial}{\partial p_{||}} \frac{P_e^3}{P_{||}^3} \left(p_{||} F + mT(p_{||},r) \frac{\partial F}{\partial p_{||}} \right) + \frac{1}{r} \frac{\partial}{\partial r} r D_{rr}(p_{||},r) \frac{\partial F}{\partial r} + \frac{eE(r)}{m} \frac{\partial F}{\partial p_{||}}$$ where

$p_{||}$ is a parallel momentum, p_e the momentum of thermal electrons, E(r) the toroidal electric field, $\upsilon_o = C(5+Z_{ef})\omega_{pe}^4 \log\Lambda/(8\pi n_e v_e^3)$, n_e the electron density, Z_{eff} the effective charge of the plasma, $D_{ql}(p_{||},r)$ the coefficient of the quasilinear diffusion and $D_{rr}(p_{||},r)$ the coefficient of the radial diffusion. It is assumed that fast electron diffusion is connected with the stochasticity of the magnetic field. In the framework of this model $D_{rr}=D_m v/v_e$, where v and v_e are the parallel velocity of fast electrons and velocity of thermal electrons, respectively. A factor C=0.55 is introduced into the expression for υ_o to reproduce the current drive efficiency derived from experimental results as well as observed hard X-ray emission. It should be noted that the comparison between 2-D (in $v_{||}$ and $v_\perp$) and 1-D nonrelativistic calculations gives C≈0.4 /4/. It is assumed that the electron distribution function is spread in the perpendicular direction due to pitch angle scattering. In the plateau region i.e. for $v_1(r) < v < v_2(r)$ (v_1, v_2 are lower and upper boundary of parallel phase velocity of LH waves, respectively), the characteristic temperature $T_\perp = 2T_b((v-v1)/(v2-v1))^2$, and for $v>v2$, $T_\perp = 2T_b$, where T_b is defined in /5/ (formula(37)). Parameter $T(p_{||},r)$ in FP equation is chosen to be $T(p_{||},r)=T_e(r)$ for $v < v_2(r)$, and $T(p_{||},r) = T_\perp(r)$ for $v>v_2(r)$.

CALCULATION OF THE LHCD

The ray tracing and Fokker-Planck equations are solved iteratively to get the stationary solution. All relevant parameters are taken from experimental data. The magnetic field topology calculated by three moments equilibrium code is adjusted to match the JET reconstructed equilibrium.

The wave spectrum $P(n_{||})$ for Lower Hybrid waves launched by the antenna is divided into 89 equal intervals. To simulate the height of the grill, the ray trajectories are launched from K different poloidal positions ($25< K <40$) for each fixed $n_{||}$ with initial power $P(n_{||})$.

FEB DATA SIMULATION

The Fast Electron Bremsstrahlung (FEB) diagnostic is a multichord system designed to detect hard X-ray emission in the range 100 keV upwards /6/. The X-ray emission spectrum is analyzed on 4 equal energy windows between 100 and 300 keV to produce 4 line integrated emissivity profiles.

The FEB signal is calculated using the simulated electron distribution function. The local suprathermal emissivity for a photon of energy ε at an angle ϕ' with respect to the local magnetic field direction, is given by:

$$\frac{dN}{d\varepsilon dV dt d\Omega}(\varepsilon,\phi',r) = \iiint v_s f_s(p,r)\left[\sum_i Z_i^2 n_i(r)\frac{d\sigma_{ei}}{d\varepsilon d\Omega}(p,\varepsilon,\phi',Z_i)+n_e(r)\frac{d\sigma_{ee}}{dk d\Omega}(p,\varepsilon,\phi')\right] d^3p$$

where $f_s(p,r) = F(p_{||};r)(1/2\pi m T_\perp(p_{||},r))\exp(-p_\perp^2/(2\pi m T_\perp(p_{||},r)))$, $n_i(r)$ ion density, v_s-suprathermal electron velocity, $d\sigma_{ei}$ is the electron-ion Bremsstrahlung cross-section calculated according to the Bethe-Heitler-Elwert formula, and $d\sigma_{ee}$ is the electron-electron Bremsstrahlung cross-section calculated with the Haug-Elwert formula (both are in the Born approximation) /7/.

The line averaged emissivity along the FEB sightline is deduced from local emissivity. The photon temperature is obtained by fitting the line averaged emissivity spectrum.

RESULTS OF THE CALCULATIONS AND COMPARISON WITH THE EXPERIMENTAL DATA

The results of modelling of LHCD with LH only for three shots (#27745,#24955,#24918) with different densities and temperatures are chosen for the comparison with experimental data. The main parameters of the shots are listed below:

	1(MA)	B_T(T)	$n_{eo}(10^{19}m^{-3})$	T_{eo}(keV)	P_{LH}(MW)	Z_{ef}	V_{res}(V)
#27745	3.1	3.3	1.4	7.8	1.8	3.8	0.38
#24955	1.5	3.1	3.0	2.3	2.3	1.7	0.2
#24918	0.37	2.5	1.8	1.4	1.8	1.6	0.

All calculations are done for fixed values $D_m=0.5m^2/s$ and $\Delta=0.25$, unless indicated. Fig. 1 shows the calculated LH driven current density $J_{RF}(r)$ and dissipated RF power density $P_{RF}(r)$ for a high temperature, low density plasma in a residual electric field (shot #27745). Profiles for the calculated and experimentally observed brightness and temperature of hard X-ray emission are shown in Fig. 2 and Fig. 3, respectively. For all three shots reasonable agreement between measured and simulated data is observed. For some cases, where LHCD is combined with ICRH, the calculated photon temperature is significantly lower than the measured one. The discrepancy in these cases can be attributed to synergistic effects between IC waves and the fast electron tail, produced by LH waves /8/.

In conclusion the comparison between the experimental data and the numerical simulations shows that the code describes well LHCD in JET. This comparison stands well for large excursions in electron temperature: 1.4 to 7.8 keV and in electron density: 1.4 to 3 $10^{19}m^{-3}$. The code is based on the model, which incorporates the stochastic diffusion of fast electrons with $D_{rr}\sim v$, scattering of the LH waves by low frequency fluctuations and analytical approximation for $T_\perp$.

Authors are grateful to Dr.V.Parail for very fruitful discussions.

REFERENCES

/1/ Yu.F.Baranov, A.R.Esterkin, Sov.J.Plasma Phys. 16, 665 (1990).

/2/ E.Ott, Phys. Fluids 22, 1732 (1979).

/3/ P.T.Bonoli, E.Ott, Phys. Fluids 25, 359 (1982).

/4/ C.F.F.Karney, N.J.Fisch, Phys. Fluids 22, 1817 (1979).

/5/ V.Fuchs, et al., Phys. Fluids 28, 3619 (1985).

/6/ P.Froissard, et al., 18th EPS Conf. Proc., Berlin 1991, part 3, p 389.

/7/ H.W.Koch, F.W.Motz, Rev. Mod. Phys. 31, 920 (1959).

/8/ C.Gormezano, 10th Topical Conf. on RF Power in Plasmas. Boston 1993.

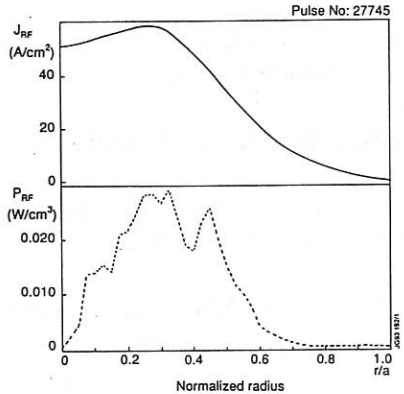

Fig. 1. Current density (a) and dissipated power density (b) profiles (shot #27745).

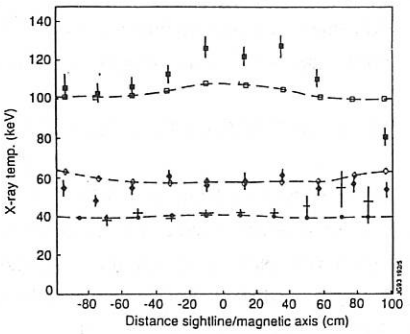

Fig. 3. Photon temperature profiles
■-measured, □-calculated (shot #27745)
◆-measured, ◊-calculated (shot #24955)
†-measured, •-calculated (shot #24918)

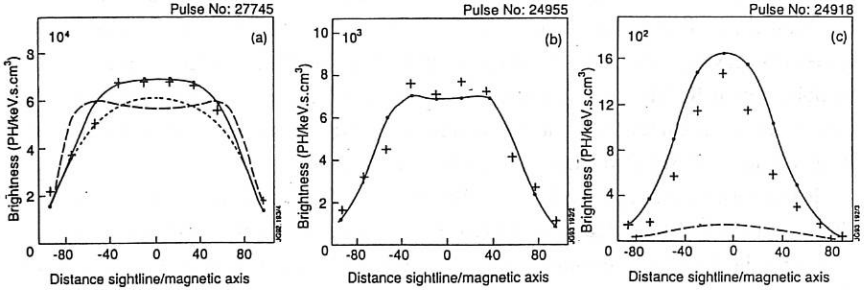

Fig. 2. Brightness profiles for the photon energy window 200÷250KeV. Crosses-experimental data. Solid lines-Δ=.25, D_m=.5m^2/s, a) dashed line-Δ=0, D_m=0, dotted line -Δ=0, D_m=.5m^2/s, c) $T_\perp = T_b ((v-v1)/(v2-v1))^2$ for v>v1.

On the Applicability of the Eikonal Description of LH Waves

G. V. Pereverzev[1]

Max-Planck-Institut für Plasmaphysik, Garching, Germany, EURATOM Association

1. Introduction.

The zero approximation of the method of geometric optics (GO), or more simply ray tracing, is widely used for describing wave propagation in tokamak plasmas. However, the approach is far from being really justified. The applicability criterion, $\lambda \ll L$ (λ is the wavelength, L is the medium inhomogeneity length), which is usually used gives a *necessary* but not sufficient condition for applying ray tracing [1]. Even fulfilment of the condition $\lambda \ll L$ by a large margin does not, in general, ensure the applicability of GO. For example, in Ref. [2] a case is considered which shows that ray tracing is not always valid even in the electron cyclotron range of frequencies. An underlying physical mechanism which causes a departure of the approximate GO solution from the exact wave field is diffraction.

This report treats the applicability of GO to the case of lower hybrid (LH) waves. It is shown that for the characteristic parameters of LH current drive the ray tracing technique is hardly applicable even for the first passage of the wave along the minor radius. With increasing number of passages, the reliability of the approach becomes still more doubtful.

2. Concept of the Fresnel volume [1].

In accordance with [1] we use the Huygens-Fresnel principle and consider two adjacent rays, both starting on the constant phase surface Q at the plasma edge and arriving at the same point

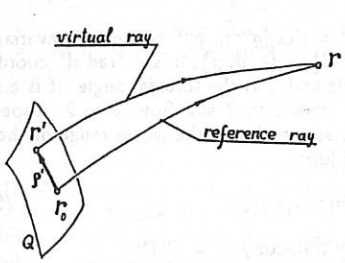

Fig. 1. The reference ray and a virtual ray.

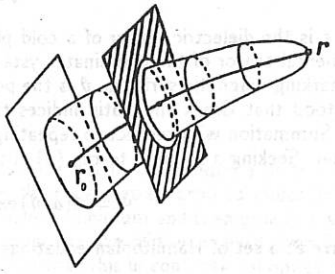

Fig. 2. The Fresnel volume as a 3D region enclosed by the boundary of the first Fresnel zone moving along the reference ray.

$\mathbf{r}$ in the plasma interior, as shown in Fig. 1. The difference $\Delta\psi(\mathbf{r}') = |\psi_{virt}(\mathbf{r}', \mathbf{r}) - \psi_{ref}(\mathbf{r}_0, \mathbf{r})|$ between the wave phase $\psi_{virt}(\mathbf{r}', \mathbf{r})$ computed along a virtual ray ($\mathbf{r}' \to \mathbf{r}$) and the phase $\psi_{ref}(\mathbf{r}_0, \mathbf{r})$ along the reference ray ($\mathbf{r}_0 \to \mathbf{r}$) characterizes the contribution of the point $\mathbf{r}'$ to creating an image at the observation point $\mathbf{r}$. As is known, the field at the point $\mathbf{r}$ is essentially

[1]Permanent address: I.V.Kurchatov Institute of Atomic Energy, Moscow, Russia

created by the first Fresnel zone, i.e. such a manifold of points $\mathbf{r}' \in Q$ that $\Delta\psi(\mathbf{r}') \leq \pi$. The inputs of the kth Fresnel zone $(k-1)\pi \leq \Delta\psi(\mathbf{r}') \leq k\pi$ and the $k+1$ zone nearly cancel each other. In turn, the resultant field from the entire (if it is large enough) surface Q is twice as small as the field of the first Fresnel zone. On the other hand, if we restrict the area of the surface Q by making the aperture smaller than the first Fresnel zone, this obstructs the field in the point $\mathbf{r}$.

It is also instructive to introduce the concept of the three-dimensional Fresnel zone or Fresnel *volume*. The idea is illustrated by Fig. 2, which shows that the Fresnel volume is obtained by movement of the surface Q and the correspondent first Fresnel zone along the reference ray. The physical significance of the concept is that the Fresnel volume can be viewed as a physical object of finite thickness correspondent to an infinitely thin mathematical ray (trajectory of the Hamiltonian set of equations).

Two heuristic criteria of GO applicability are formulated in [1]. We reproduce these criteria in a form modified to the goals of the current study:
(*) The ray tracing technique is only applicable over that part of the reference ray where the size of the first Fresnel zone is less than that of the launching waveguide.
(**) The Fresnel volumes of the two different rays used to describe the wave pattern of the same antenna and reaching one and the same point in the plasma must not significantly penetrate one another.

3. Lower hybrid waves.

The theory briefly described in the previous section was developed for the Helmholtz wave equation. In order to apply this theory to LH waves, consider the equation for the potential Φ of electrostatic waves in a plasma:

$$\operatorname{div} \hat{\varepsilon} \operatorname{grad} \Phi = \frac{1}{\sqrt{g}} \frac{\partial}{\partial x^\alpha} \sqrt{g} g^{\gamma\beta} \varepsilon_\gamma^\alpha \frac{\partial \Phi}{\partial x^\beta} = 0, \tag{1}$$

where $\hat{\varepsilon}$ is the dielectric tensor of a cold plasma, $g^{-1} = \det||g^{\alpha\beta}||$, $g^{\alpha\beta}$ is the contravariant fundamental tensor of the coordinate system $\{x^1, x^2, x^3\} = \{a, \vartheta, \varphi\}$, a is a "radial" coordinate marking magnetic surfaces, ϑ is the poloidal angle and φ is the toroidal angle. It is also understood that Greek and Latin indices take values from 1 to 3 and from 1 to 2, respectively. Summation with respect to repeating indices is assumed over the whole range of their variation. Seeking a solution to Eq. (1) in the eikonal form

$$\Phi = A(a, \vartheta) \exp\{in\varphi + inS(a, \vartheta)\}, \tag{2}$$

we arrive at a set of Hamiltonian equations for the ray trajectory $x^j = q^j(t)$:

$$\frac{dq^j}{dt} = \frac{\partial H}{\partial p_j}, \qquad \frac{dp_j}{dt} = -\frac{\partial H}{\partial q^j}, \qquad \frac{dS_0}{dt} = p_j \frac{\partial H}{\partial p_j}, \tag{3}$$

with the Hamiltonian function

$$H = H(a, \vartheta, p_\alpha) = p_\alpha p_\beta g^{\alpha\gamma} \varepsilon_\gamma^\beta = 0, \tag{4}$$

and

$$p_1 = \frac{\partial S}{\partial a}, \qquad p_2 = \frac{\partial S}{\partial \vartheta}, \qquad p_3 = 1. \tag{5}$$

A perfect analogy exists between the time variable in the Helmholtz equation and the toroidal angle φ in Eq. (1). Therefore, we can replace the 3D eikonal $\psi(\mathbf{r})$ of the previous section with the 2D eikonal $S_0(t)$ and repeat all the observations made there. Consequently, the concept of the Fresnel volumes can be used without any changes.

Assume that the surface Q of a constant phase coincides with some magnetic surface at the plasma edge. The poloidal sizes of the low Fresnel zones in this surface are shown in Fig. 3 for parameters of the JET tokamak. It is supposed that the reference ray starts in the equatorial plane and only one passage along the minor radius is considered. It is seen that after a rapid increase the sizes of all Fresnel zones tend to saturate but then increase again. Only at the very beginning of the reference ray is the size of the first Fresnel zone less than the poloidal aperture of a single waveguide array (dashed horizontal line in Fig. 3).

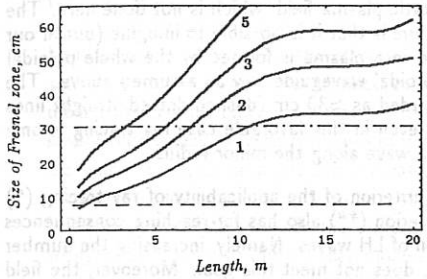

Fig. 3. Poloidal sizes of the 1st, 2nd, 3rd and 5th Fresnel zones as functions of the length along the reference ray. The plasma parameters are $n_e(r) = 3(1 - 0.8r^2/a^2) \cdot 10^{19}$ m^{-3}, $q(r) = 1 + 2r^2/a^2$, $f = 3.7$ GHz, $N_{\|} = 2$, $B = 3.3$ T, $R_0 = 2.96$ m, $a = 1.25$ m, $b/a = 1.68$.

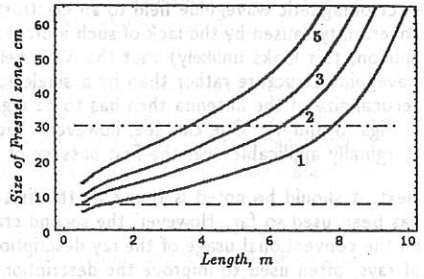

Fig. 4. The same as in Fig. 3, but for $R_0 = 2.35$ m, $a = 0.8$ m, $b/a = 1$.

The same dependences for the same plasma parameters but in the geometry of the TORE SUPRA tokamak are shown in Fig. 4. Here the sizes the Fresnel zones grow to values ≥ 1.5 m at $l = 12$ m. Further along the ray trajectory they have a minimum and then growth resumes. This behavior is not shown in the figure, because even the size of the smallest, first Fresnel zone does not decrease below 50 cm. The effect is similar to this in conventional optics, where the ray description fails in a small vicinity of the focus and is then recovered again. In terms of our consideration, this means that the dimensions of all Fresnel zones are infinite at the focal point. The saturation of the curves in Fig. 3 and the non-monotonic behavior of the Fresnel zone dimensions in TORE SUPRA indicate the trend of recovery of the Fresnel diffraction region after the reference ray passes beyond a caustic, but, in fact, such a restitution does not occur.

It is seen from the two figures that only a very small initial piece of the trajectory lies in the region of the Fresnel diffraction where the ray tracing technique is really justified. Along the major part of the ray Fraunhofer diffraction dominates and the ray approximation is hardly

applicable. Consideration of the Fresnel zones in itself cannot give a quantitative measure of the discrepancy, but this can be done while still remaining within the limits of the ray approach as in [3]. A different mode of attacking this problem is based on the paraxial WKB method [4], which describes the Fresnel and Fraunhofer diffraction zones equally well. The latter method was used in [5]. Figure 2 of Ref. [5] is obtained for the same plasma parameters as Fig. 4 of the current report and gives a quantitative idea of the error of the ray approach. It shows that the channel width in which the LH energy is propagated can be broadened due to the diffraction by a factor of ten or more. It has also to be noted that, in the reality, the picture of the field distortion must be stronger than that presented in [5] because the case of the Gaussian beam considered there is least subject to the diffractional broadening.

4. Discussion.

The analysis performed above is not complete. A full analysis would require matching an electromagnetic waveguide field to an electrostatic plasma field, which is not done here. The uncertainty caused by the lack of such a procedure is that it is possible to imagine (but in our opinion, this looks unlikely) that the wave field in a plasma is formed by the whole poloidal waveguide structure rather than by a single toroidal waveguide row as assumed above. The vertical size of the antenna then has to be regarded as $\approx$30 cm (dashed-dotted straight lines in Figs. 3 and 4). One can see, however, that even in this favorable case ray tracing is only marginally applicable over the first passage of a wave along the minor radius.

Next, it should be noted is that only the first criterion of the applicability of ray tracing (*) has been used so far. However, the second criterion (**) also has far-reaching consequences on the conventional usage of the ray description of LH waves. Namely, increasing the number of rays, often used to improve the description, does not meet this goal. Moreover, the field structure obtained by multiple-ray tracing is, in general, farther from an exact wave solution than that given by a single ray.

It has also to be mentioned that only the main contribution to the phase advance along a ray trajectory has been considered here. There are additional mechanisms which can make the applicability of ray tracing still more problematic. These are plasma gyrotropy, which appears in the first approximation of GO, electromagnetic corrections not described by the simplified wave equation (1) and wave absorption. For example, it is clear that if the wave absorption along a virtual ray (Fig. 1) differs from that along the reference ray, then the inputs of the adjacent Fresnel zones to the image creation in the observation point do not cancel each other, which results in a further deflection from the ray picture.

We remark, in conlusion, that although we have considered only usual space, a similar approach can be applied for spectral space as well. The distortion of the ray description in Fourier space results in spectrum broadening and can help to solve the spectral gap problem.

References

1. Yu. A. Kravtsov and Yu. I. Orlov, Geometrical Optics of Inhomogeneous Media (Springer Series on Wave Phenomena; Vol. 6), Springer-Verlag, Berlin-Heidelberg 1990.
2. G. V. Pereverzev and F. Leuterer, this conference, Report 5/53.
3. R. A. Cairns and V. Fuchs, The Effect of Poloidal Antenna Width on Lower Hybrid Ray Propagation, Internal Report CCFM, Varennes, October 7, 1992.
4. G. V. Pereverzev, Paraxial WKB Solution of a Scalar Wave Equation, Internal Report, IPP, 4/260, April 1993.
5. G. V. Pereverzev, Nucl. Fusion **32** (1992) 1091.

MODELING OF THE HARD X-RAY EMISSION DURING LOWER-HYBRID CURRENT DRIVE

J. P. Bizarro[a)], Y. Peysson, P. T. Bonoli[b)], J. Carrasco, T. Dudok de Wit, V. Fuchs[c)], G. T. Hoang, X. Litaudon, D. Moreau, C. Pocheau, and I. P. Shkarofsky[d)]
Département de Recherches sur la Fusion Contrôlée, Association Euratom-CEA, Centre d'Etudes de Cadarache, 13108 St. Paul lez Durance Cedex, France

The present communication is based on a paper that is to appear in the literature [1], and reports results concerning a detailed investigation showing the ability of combined ray tracing and Fokker-Planck codes to predict the hard x-ray (HXR) emission during lower hybrid current drive in situations where toroidally induced ray stochasticity [2] is important. Such results have been obtained using a well-known and documented ray-tracing and Fokker-Planck code [2]. Although the validity of geometrical optics can be questioned when stochastic effects prevail, it has been suggested [2,3] that if a sufficently large number of rays is used, ray tracing still accurately and reliably describes the dynamics of the launched power spectrum in the wave phase space. In particular, the steady-state values and time responses of parameters that depend on the characteristics of the suprathermal electron population created by the LH wave, like the loop voltage and the internal inductance, have been well simulated [2], which indicates that the models involved are consistent with the experimental phenomenology. However, a more stringent test on the validity of such models is still possible, and that is to see how well they reproduce the features of the HXR emission observed during LH current drive, which are intimately related to the distribution of suprathermal electrons in configuration and momentum spaces [4,5]. The study performed below has been carried out using the same plasma and LH wave characteristics that have been used elsewhere [2,3].

A point to be assessed here is the effect radial diffusion of suprathermal electrons may have on the prediction of the HXR emission. The simulation code deals with radial diffusion of suprathermal electrons by diffusing the LH-driven current density, $J_{LH}(\rho)$, so the diffusion coefficient is an eigenvalue of a boundary value problem consistent with a global conservation law given by the Fokker-Planck equation [6]. Here, ρ designates the normalized radial flux surface coordinate, with $\rho = 1$ at the plasma minor radius. Since the radial diffusion calculation is not performed on the electron distribution function itself, but rather on its current density moment, some assumptions have to be made in order to link the diffused LH-driven current density, $J^*_{LH}(\rho)$, with the diffused profile for the suprathermal electron distribution function, $f^*_{st}(\rho,\mu,p)$, if the influence of radial diffusion on the predicted HXR emission is to be assessed. Numerical studies using a three-dimensional Fokker-Planck analysis have shown [7] that radial diffusion does not significantly distort the electron distribution function in momentum space: the effective perpendicular temperature is not appreciably modified and the shape of the LH-generated plateau is conserved. Suprathermal electrons are therefore radially redistributed by essentially changing the plateau level on each flux surface. So, it is reasonable to consider that the $J^*_{LH}(\rho)$ and $f^*_{st}(\rho,\mu,p)$ profiles have roughly the same form,

$f^*_{st}(\rho,\mu,p) \equiv \chi(\mu,p)\, J^*_{LH}(\rho)$, and that the suprathermal electron density in momentum space is conserved. For the plasma considered here, collisional slowing down prevails in the inner half of the discharge, so radial diffusion is felt mainly in the outer half [2]. This can be seen in Fig.1, which shows $J_{LH}(\rho)$ and $J^*_{LH}(\rho)$, the latter resulting from a diffusion calculation that has given a diffusion coefficient $D \approx 1.2\ m^2/s$, which is consistent with time responses for the loop voltage and the internal inductance [2].

The x-ray photon emission is studied in the range $30\ keV \leq h\nu \leq 700\ keV$, using the TORE SUPRA HXR diagnostic, which probes the plasma in a poloidal cross-section along five lines-of-sight which are labelled A, B, C, D, E and which intersect the equatorial mid-plane at (R-R0)/a ≈ +0.20, 0.00, -0.33, -0.52, -0.71, where R is the distance from the tokamak axis [5]. The simulations are performed considering only the electron-ion bremsstrahlung emission, with fully stripped carbon ($Z_c = 6$) considered as the only relevant impurity. For the plasma of interest here ($Z_{eff} \approx 2.8$), the electron-electron contribution, which is less than 10%, is neglected. The spherical symmetry of the problem is taken advantage of by expanding the cross-sections and the electron distribution function in series of Legendre polynomials. For lines-of-sight D and E, which intersect the inner wall, corrections due to radiation scattering by the wall have been considered. Such corrections have been evaluated by means of a Monte-Carlo code that solves the photon transport equation inside the wall.

The measured and predicted HXR spectra are depicted in Fig.2. Before applying the LH power, low-level signals are detected up to 50 keV. Once the LH pulse is on, a large increase in the counting rate is observed and the HXR spectra extend up to $h\nu \approx 400$ keV. For all lines-of-sight, the measured HXR spectrum decreases rapidly when the photon energy increases, and a significant spread of the experimental data, represented by the error bars, occurs for $h\nu \geq 250$ keV, indicating that the signals have dropped to the noise level. It is worth noting that, even without taking into account radial diffusion of suprathermal electrons and radiation scattering by the inner wall, both the energy dependence and the magnitude of the measured HXR spectra are fairly well predicted in the range $30\ keV \leq h\nu \leq 250\ keV$, except for line-of-sight E. Corrections due to radial diffusion of suprathermal electrons are important only for lines-of-sight D and E, in particular for the last one. The effect of radiation scattering by the inner wall is negligible for line-of-sight D and significant (about 40%) for line-of-sight E. The measured and predicted values of the "photon temperature" T_{ph} for the different lines-of-sight [4], calculated in the interval $75\ keV \leq h\nu \leq 225\ keV$, are given in Fig. 3 and compare well with each other.

Notwithstanding some discrepancies that remain to be explained, a fair agreement exists between the measured and predicted HXR data, demonstrating the ability of combined ray-tracing and Fokker-Planck calculations to predict the HXR emission during LH current drive in tokamaks when toroidally induced ray stochasticity is important. Furthermore, it has been shown that both radial diffusion of suprathermal electrons and radiation scattering by the inner wall play, in general, a non-negligible role in explaining the experimentally observed features of the HXR emission. It may thus be concluded that combined ray-tracing and Fokker-Planck codes do contain the basic ingredients to

correctly model the physics of LH current drive in tokamaks. Obviously, a number of improvements can still be introduced in order to obtain a finer fitting between measurements and predictions.

REFERENCES

[a]Permanent address: Centro de Fusão Nuclear, Associação Euratom-IST, Instituto Superior Técnico, 1096 Lisboa Codex, Portugal.
[b]Plasma Fusion Center, Massachusetts Institute of Technology, Cambridge, Massachusetts 02139.
[c]Centre Canadien de Fusion Magnétique, Varennes, Québec J3X 1S1, Canada.
[d]MPB Technologies Inc., Pointe claire, Québec H9R 1E9, Canada.
[1] J. P. Bizarro, Y. Peysson, et al., Phys. Fluids B **5** (1993) in press.
[2] J. P. Bizarro, D. Moreau, Phys. Fluids B **5** (1993) 1227.
[3] J. P. Bizarro, Nucl. Fusion **33** (1993) No. 5 or 6 (also in this conference).
[4] S. von Goeler, J. Stevens, et al., Nucl. Fusion **25** (1985) 1515.
[5] Y. Peysson, J. P. Bizarro, et al., Proc. 18th Eur. conf. on Control. Fusion and Plasma Phys. (1991) Berlin, Vol.15C, Part IV, p.345.
[6] V. Fuchs, I. P. Shkarofsky, et al., Nucl. Fusion **29** (1989) 1479.
[7] G. Giruzzi, Plasma Phys. Controlled Fusion **35**, A123 (1993).

FIGURE CAPTIONS

FIG. 1. Predicted nondiffused and diffused LH-driven current density profiles.

FIG. 2. Measured and predicted HXR spectra. (a) Line-of-sight A. (b) Line-of-sight B. (c) Line-of-sight C. (d) Line-of-sight D. (e) Line-of-sight E. The black (white) squares correspond to the measured HXR spectra in the Ohmic-LH (Ohmic) steady state. Dashed lines (crosses) correspond to the predicted HXR spectra without (with) corrections due to radial diffusion of suprathermal electrons. In Fig.4 (e), the dotted line corresponds to the predicted spectrum scattered by the inner wall and the dot-dashed line to the predicted HXR spectrum with corrections due to radial diffusion of suprathermal electrons and to radiation scattering by the inner wall.

FIG. 3. Measured and predicted "photon temperatures".

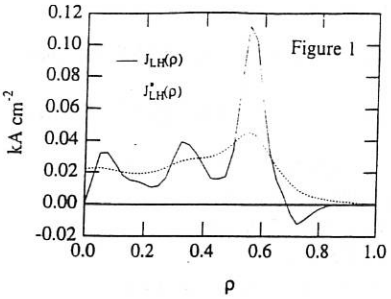
Figure 1
$J_{LH}(\rho)$
$J^{*}_{LH}(\rho)$
kA cm^{-2}
0.12
0.10
0.08
0.06
0.04
0.02
0.00
-0.02
0.0
0.2
0.4
0.6
0.8
1.0
ρ

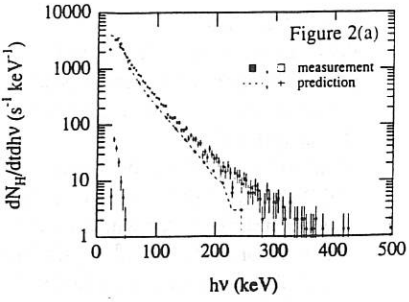
Figure 2(a)
measurement
prediction
$dN_H/dtdh\nu$ (s^{-1} keV^{-1})
10000
1000
100
10
1
0
100
200
300
400
500
hν (keV)

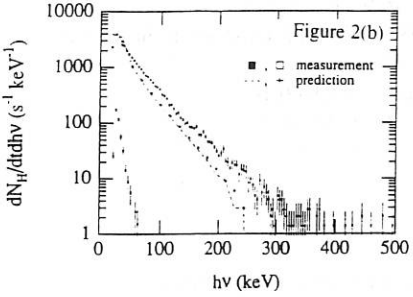
Figure 2(b)
measurement
prediction
$dN_H/dtdh\nu$ (s^{-1} keV^{-1})
10000
1000
100
10
1
0
100
200
300
400
500
hν (keV)

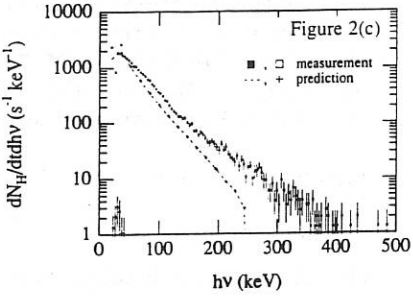
Figure 2(c)
measurement
prediction
$dN_H/dtdh\nu$ (s^{-1} keV^{-1})
10000
1000
100
10
1
0
100
200
300
400
500
hν (keV)

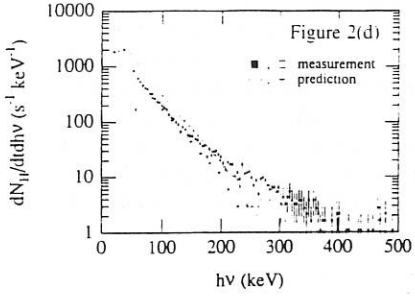
Figure 2(d)
measurement
prediction
$dN_H/dtdh\nu$ (s^{-1} keV^{-1})
10000
1000
100
10
1
0
100
200
300
400
500
hν (keV)

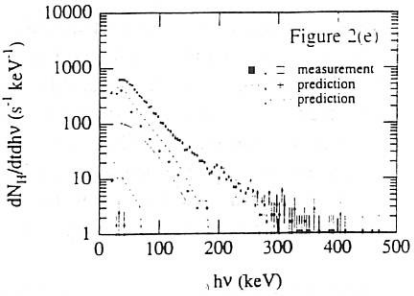
Figure 2(e)
measurement
prediction
prediction
$dN_H/dtdh\nu$ (s^{-1} keV^{-1})
10000
1000
100
10
1
0
100
200
300
400
500
hν (keV)

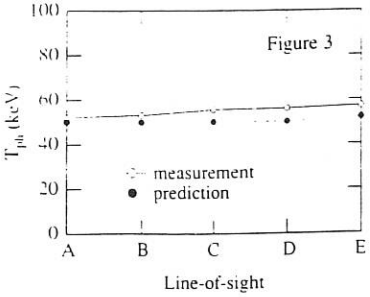
Figure 3
T_{ph} (keV)
100
80
60
40
20
0
measurement
prediction
A
B
C
D
E
Line-of-sight

INTERACTION BETWEEN L.H. WAVES AND THERMONUCLEAR PROTONS

C. DOLOC & G. MARTIN
Ass. Euratom CEA / CEN Cadarache / B.P. 1 / 13108 SAINT-PAUL / FRANCE

1°) EXPERIMENTAL RESULTS :

Thermonuclear protons created by deuterium fusion reactions in Tore-Supra are detected by a silicon detector [1] located in a vertical port , in the vicinity of the plasma . Composed of 16 active strips behind a central collimator (pin-hole camera) , it allows to obtain simultaneously energy and pitch-angle resolution : 100 keV and 3 degrees respectively . Usual spectra exhibit a central thermonuclear peak at 3 MeV with a small broadening about 160 keV due to Doppler effect .

During current drive experiments , with several megawatts of lower hybrid power at 3.7 GHz , protons with an energy higher (or lower) than the usual three MeV are observed on the detector spectra . Typical examples are drawn on the first figure . Several typical shots have been chosen , with different toroidal field and plasma current (values on figure) . The 3 MeV line is easily spotted in the middle of each spectrum ; two additional structures appear beetween 2 and 5 MeV (one of them is sometimes hidden by the thermonuclear line) , with positions depending on plasma parameters .

Fig 1 : PROTON SPECTRA

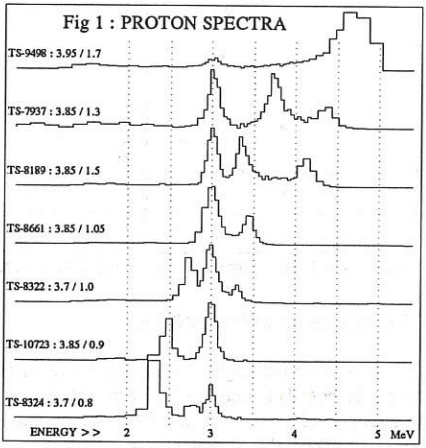

1-A) PROTON ENERGY :

A systematic study of their energy has been performed for a large set of plasmas . All results are plotted on figure 2 as a function of the plasma current : closed points represent the lowest energy peak and open ones the highest . The main tendencies are :

♣ The energy does not change with L.H. power or electron density . The various points in each small cloud on the figure correspond to different values for both parameters : L.H. from 1 to 4 MW and n_e from 3 to 5 10^{19} m^{-3} .

♣ It changes mainly with the plasma current and toroidal field values . Increasing rapidely for low currents (< 1.2 MA) it saturate for higher values . Both peaks follow the same pattern , with almost a constant gap . Even a very small change in B_t produce a large effect , especially with high I_p . In the shaded area , additional peaks might be hidden below the 3 MeV line .

Fig 2 : Peak Energy vs Plasma Current

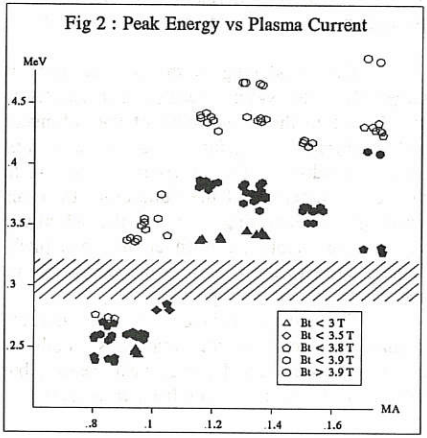

1-B) PROTON FLUXES :

The number of protons observed for the additional peaks changes also with the plasma parameters (see figures 3 for examples) :

♣ It increases almost linearly with L.H. injected power (curves 3-A) . On the contrary , the 3 MeV peak does not change much , due to the low impact of these waves on the ion temperature .

♣ It decrease quite rapidely with density (curves 3-B) : almost no signal is observed above 5 10^{19} m^{-3} central ; the 3 MeV signal increases with density as fusion rate goes as n^2 .

♣ The current dependence is less clear : a maximum is observed for low density plasmas , which tend to disappear at higher density (curves 3-C) . The low statistic of the counting makes difficult to obtain a clear pictures for these last shots .

♣ The behaviour of the two peaks is qualitatively the same , but their ratio might vary from one case to the other . The second one is in general smaller that the first .

Figures 3 : Proton fluxes -> A.U. : (Closed points -> 1st peak // Open points -> 2nd peak)

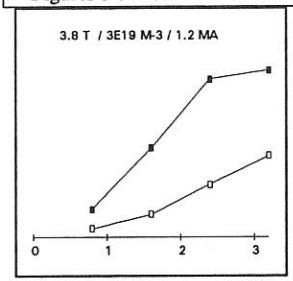

Fig 3-A : L.H. power (MW)

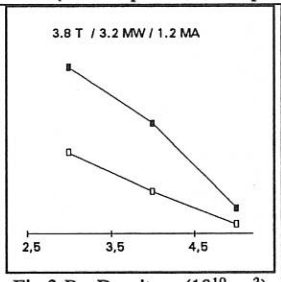

Fig 3-B : Density n (10^{19} m^{-3})

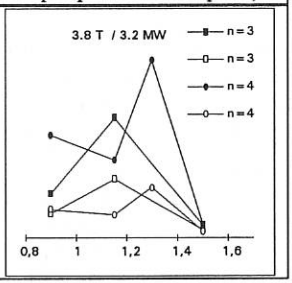

Fig 3-C : Plasma current (MA)

1-C) PROTON PITCH-ANGLE :

Some pitch-angle resolution concerning these protons is obtained with the system , composed of 16 independant detectors , each one looking at a different direction relative to the toroidal magnetic field , i.e. with a different pitch-angle . The figure 4 shows some flux profiles for the various peaks : the thermonuclear one in thick line , the first additional peak just below and the second reversed . Two adjacent strips are separated by approximatly 2 degrees in pitch-angle .

The broadening of the 3 MeV peak is larger than the system resolution (resolution mainly due to the finite width of the collimator and Rutherford diffusion in the 6 μm steel vacuum window) . On the contrary , the width of the two others is of the same order than this resolution , indicating that all the additional protons are mainly observed at only one pitch-angle , close to the one from the fattest banana trajectory (**[F]** on the figure 5) .

The actual position of the maxima changes with main plasma parameters , both for the 3 MeV line and the additional peaks , but they are generaly quite close from each other .

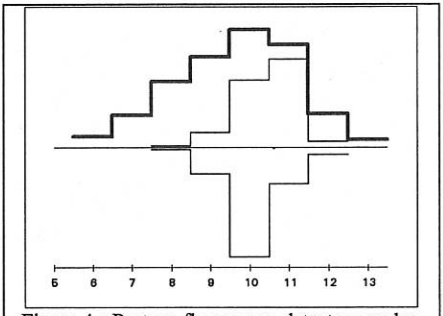

Figure 4 : Protons flux versus detector number

2°) PRELIMINARY MODEL :

A first qualitative model has been developed to explain the energy of these particles , based on fusion products trajectories and ion/L.H. interaction .

2-A) PROTON TRAJECTORIES :

Usual behavior of fusion protons created in the plasma can be summarized by (figure 5) :

♣ Created randomly in the plasma (more in central hottest parts) , some are confined on closed trajectories [C] and some are lost on open ones [O] : they might be seen with their full birth energy of 3 MeV in the dectector .

♣ The confined protons loose slowly their energy by collision with plasma electrons . The induced energy drag does not modify their behavior : they stay confined .

♣ An increase in energy or a change in pitch-angle can switch them from a confined topology to an unconfined one : this transition occurs mainly through the fatest banana [F] orbit . In usual conditions , this change does not occur .

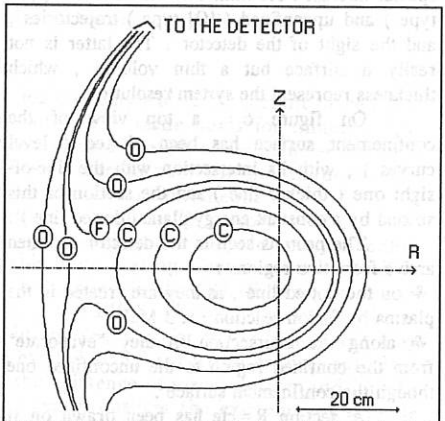

Figure 5 : Typical proton trajectories (adiabatic)

2-B) INTERACTION BETWEEN L.H. WAVES AND PROTONS :

As confined protons loose slowly their energy on plasma electrons , they can interact with lower hybrid waves by a Landau type process , when their velocity matches the perpendicular waves velocity . Cold dispersion relation indicates that perpendicular index values between 10 and 15 are present in the plasma : interaction occurs for ions with $v_\perp > c/n_\perp$, i.e. $E_\perp > 2$ Mev .

Twice per Larmor revolution (20 ns) a resonant condition is then fulfilled between the waves and the protons : $v_{\perp k} = c/n_\perp$, where $v_{\perp k}$ is the projection of the perpendicular (to B) particle velocity on the wave vector $k_\perp$. During this brief interaction ($<<$ 1 ns) , energy is exchanged at a high rate (the electric field of the waves is of several kV/cm) , giving an energetic kick of the order of plus or minus one keV to the proton (actual value depends on field strengh , i.e. L.H. injected power , density , magnetic field , ...) . The global effect is then a diffusive process in the energy space , with a typical diffusion coefficient $D \cong 100$ MeV^2/s . As the energy drag dE/dt from the plasma is about 40 to 100 MeV/s , the particles can reach energies of several MeV above their initial one (typical value $\cong$ D/(dE/dt)) .

This model of interaction explains both evolution of the signal intensity with L.H. power and density : as the former increases the diffusion coefficient does the same , so more protons can reach a high energy during their confined life ; and as the latter increases the slowing down time decreases , reducing their probability to diffuse towards higher energy (density has also an effect on the waves : the perpendicular index increases , thus allowing interaction with lower energy ions , but L.H. power can then hardly reach the plasma center) . But it does not explain the peak structure of the spectrum : a continuous tail would be expected . For this , a more refined view of the trajectories topology is needed .

2-C) THE PEAK STRUCTURE :

A given particle trajectory in the torus can be caracterize by three parameters (in an

axisymetric configuration, i.e. without toroidal ripple): the large radius where it intersect the equatorial plane, the pitch-angle at this point, and the poloidal Larmor radius: $\rho = mv/qB_p(a)$, function of energy , particle type and Ip .

In this 3-D space , two surfaces are of special interest : the limit between confined ([C] type) and unconfined ([O] type) trajectories , and the sight of the detector . The latter is not really a surface but a thin volume , which thickness represent the system resolution .

On figure 6 , a top view of the confinement surface has been plotted (level curves) , with its intersection with the line-of-sight one (thicker line) and the section of this second by a constant energy plane (dotted line) .

The protons seen in the detector can then arrive from two regions :

♣ on the dotted line , as they are created in the plasma by fusion reaction , at 3 MeV ;

♣ along the intersection as they "evaporate" from the confined region to the unconfined one though the confinement surface .

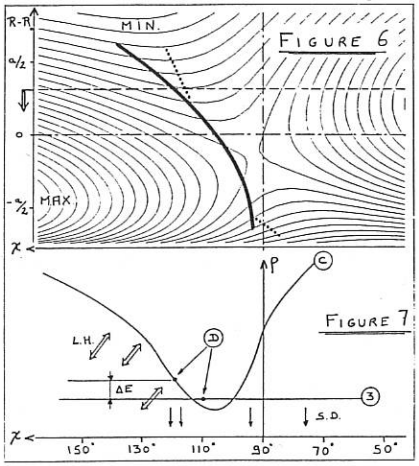

A section R=cte has been drawn on figure 7 (dashed line from figure 6) , with the confinement limit [C] , the 3 MeV plane [3] and the detector points [D] for evaporating and 3 MeV protons . The effect of slowing down and L.H. diffusion are represented by simple and double arrows respectively (the two effect are almost without effect on R) . It is clear that to be lost in the detector , a proton born at 3 MeV must gain a precise amount of energy ΔE . As this ΔE depends on the position of the considered radial section , the density profile of confined protons will induce an energy profile on the detector . This density profile present a maximum in small radius ($\cong$ a/4) : there are then two maximum in large radius $\cong$ R0$\pm$a/4 , which might induce two maxima in the spectra . A complete and quantitative evaluation is still to be done , but the main tendencies are obtained :

♣ The structure depend only on the trajectories , i.e. the magnetic fields , and not on L.H. power .

♣ As the plasma current decreases , the evaporation line , fixed in ρ space , corresponds to lower and lower energies , explaining the displacement of the peaks with Ip .

3°) CONCLUSIONS :

A strong interaction between confined fusion products and lower hybrid waves , observed on Tore-Supra plasmas as been qualitatively understood with simple models of particles trajectories and wave induced diffusion . To enhance the comprehension of the phenomena , two ways will be followed :

♣ to develop the models to obtain quantitative results . Many parameters must be taken in account : profiles , ripple , ...

♣ to increase the detector pitch angle resolution to check the fattest banana hypothesis .

Despite the fact that the energy gain per proton is fairly large (up to 1.5 MeV) , the total amount of power taken from the LH waves is insignificant , because of the their very small number ($< 10^{12}$) . It is known that for future Tokamaks , with a large alpha population in the same energy range , this phenomena might absorb a important part of the LH power used to drive the plasma current : the frequency must thus be increased to avoid high perpendicular indexes .

[1] G.MARTIN et al. - Fusion Profile Measurement on Tore-Supra - 17th EPS Conf. - AMSTERDAM - 1990

LOWER HYBRID CURRENT DRIVE IN THE PRESENCE OF ION CYCLOTRON WAVES

Abhay K. Ram, Abraham Bers
Plasma Fusion Center, M.I.T.,Cambridge, Massachusetts, USA
Vladimir Fuchs
Centre Canadien de Fusion Magnetique, Varennes, Québec, Canada

INTRODUCTION

The theoretical and experimental basis for lower hybrid (LH) current drive (CD) has been well established over the past decade. The same holds for minority ion-cyclotron heating (ICH) by waves in the ion cyclotron range of frequencies (ICRF). In a series of experiments on JET it has been observed that the non-inductive CD efficiency is enhanced when the LHCD waves are used simultaneously with ICH [1]. The theoretical study reported here was motivated by these JET experiments.

In the experiments, the ICRF spectrum, generated by a monopole antenna configuration, is symmetric in $k_\parallel$ and, thus, incapable of generating a net current by itself in a Maxwellian plasma. Consequently, any enhancement in the CD efficiency is due to the interaction of ICRF waves with the asymmetric LHCD electron distribution function. Two aspects of the experimental conditions required for the enhancement play an important role in our studies. First, the excited ICRF spectrum ensures sufficient ICRF power at low values of $k_\parallel$'s. Second, the existence of ion cyclotron and ion-ion hybrid resonaces inside the plasma near the center ensures the existence of a mode conversion layer inside the plasma. Thus, the incident ICRF power, propagated by fast Alfvén waves (FAW), can, in principle, mode convert to ion-Bernstein waves (IBW's). This mode conversion is efficient for small $k_\parallel$'s and for small minority concentrations.

Modeling studies show that the LH energy and momentum deposition onto the electrons is typically localized and off-center in a tokamak. Since the symmetric ICRF spectrum cannot generate a net current in a Maxwellian plasma, in order to enhance the current drive efficiency ICRF waves have to interact with energetic electrons on the same flux surfaces where LHW's are Landau damped and generate current. Consequently, in our effort to arrive at an understanding of the JET observations, we simplify our analysis to a single flux surface where the LH absorption is a maximum. Since the experimental conditions permit mode conversion, we have studied the effects of both FAW's and IBW's on LH generated energetic electron distribution functions.

We have previously shown that, for JET-like conditions, the FAW's have little effect on the suprathermal electrons, whereas the IBW's can significantly modify the LH generated electron distribution function thereby enhancing the current drive efficiency [2,3]. In this paper we present results obtained from a relativistic, two-dimensional Fokker-Planck code [4] describing the combined effect of LH and IB waves on electrons. We establish a general dependence of the current drive efficiency and the perpendicular temperature of the suprathermal electrons on the strength of the IBW diffusion coefficient and on the plasma temperature. We find that current drive efficiencies and electron perpendicular temperatures reported for JET experiments fall within the range of values given by our Fokker-Planck analysis.

MODE CONVERSION TO AND PROPAGATION OF ION-BERNSTEIN WAVES

The relativistic evolution of the flux surface averaged, and gyro-angle averaged, electron distribution function is given by the Fokker-Planck equation:

$$\frac{\partial}{\partial t} f_o = \frac{\partial}{\partial p_\parallel} \left\{ \left(D^{LH} + D^{IB} \right) \frac{\partial}{\partial p_\parallel} f_o \right\} + \left(\frac{\partial}{\partial t} f_o \right)_{collisional} \qquad (1)$$

where the D's are the appropriate quasilinear diffusion coefficients [2,3] and $p_\parallel$ is the component of the electron momentum along the magnetic field. In our evaluation of the diffusion coefficient for LHW's and IBW's we make use of the full hot Maxwellian plasma dispersion tensor to determine $k_\perp$ and the electric field polarizations. These diffusion coefficients are then used to find the steady-state solution of Eq. (1) using the numerical code CQL3D [4].

For IBW's to modify the LH generated electron distribution function it is necessary that D^{IB} be comparable to the collisional diffusion of the suprathermals, and that the spectrum of IBW's overlap the spectrum of LHW's. The magnitude of D^{IB} depends on the amount of power that is mode converted to IBW's. Mode conversion calculations based on [5] show that, for JET-type parameters with a hydrogen minority in a deuterium plasma, less than 20% of the incident FAW power, is mode converted to IBW's [2]. The mode conversion coefficient C decreases with increasing minority concentration $\eta = n_H/n_e$ [2], with increasing $k_\parallel$, and with increasing minority temperature:

Table I C (%) as a function of minority temperature and $k_\parallel$ for $\eta = 0.02$

T_H (keV)	4	7	10	20
C ($k_\parallel = 1\text{m}^{-1}$)	13.4	10.8	8.8	4.5
C ($k_\parallel = 4\text{m}^{-1}$)	3.6	1.7	1.0	0.3

Since low $k_\parallel$'s undergo mode conversion more effectively, a significant portion of the IBW power spectrum is at values of $v_\parallel$ that lie above the LH spectrum. However, D_o^{IB} [2] decreases rapidly for IBW phase velocities that are higher than the LHW phase velocities (see Fig. 1). Thus, it would appear that D^{IB} is small and would not have any significant overlap with the LH spectrum.

However, these problems are satisfactorily aleviated by the dramatic effect of toroidicity on the propagation of IBW's [6]. Both the electric field amplitudes and $k_\parallel$'s are significantly enhanced along the IBW rays away from mode conversion. The electric field amplitudes can increase by factors ranging from 3 to about 10. This leads to a considerable increase in D^{IB} from its value at mode conversion. The upshifted $k_\parallel$'s allow the IBW's to interact with the LH generated electron tail. The variations in $k_\parallel$'s and electric field amplitudes typically occur over short radial distances of propagation of IBW's [6]. An additional benefit of the toroidal effect on IBW's is that, with the mode conversion layer centrally located in the plasma, $k_\parallel$'s are upshifting as the IBW's propagate towards the flux surface of maximum LHW absorption.

RESULTS

In the Fokker-Planck simulation studies we assume the following parameters on the flux surface under consideration: an electron density n_e of 2×10^{19} m^{-3}, a hydrogen-deuterium plasma with a 2% hydrogen minority, $f_{LH} = 3.7$ GHz, $f_{IC} = 35$ MHz, the local toroidal magnetic field of 3.4 Tesla, and a major radius of $R = 3$m. In Fig. 1 we plot, for a plasma temperature of 7 keV, $v_{te}D_o^{IB}$, with D_o given in [2,3], as a function of $v_\parallel/v_{te}$ for different values of $v_\perp/v_{te}$ ($v_{te} = \sqrt{T_e/m_e}$ is the electron thermal velocity). For the same parameters the lower hybrid diffusion coefficient is: $D_{LH} \approx 0.22\,(|E_{kz}^{LH}|^2/|E_{ky}^{IB}|^2)\,((\Delta k_\parallel)_{IB}/(\Delta k_\parallel)_{LH})\,D_o^{IB}$ where $\Delta k_\parallel$ denotes the spectrum width in $k_\parallel$ for the corresponding waves.

The complete evaluation of the diffusion coefficients also requires the evaluation of $\overline{D} \equiv D/D_o$ [2,3] which depends on the external input power, the spectrum in $k_\parallel$ of the waves, and, in the case of IBW's, the mode conversion coefficient. For LHW's

we find that for 1MW of input power, the flux-surface averaged $\overline{D}/D_c \approx 10$ (where $D_c = m_e v_{te} \nu_o$ with m_e being the electron rest mass, and ν_o being the electron-electron collision frequency. For 3MW of ICRF power we estimate that the flux surface averaged $\overline{D}/D_c$ for IBW's can range from approximately 1 to approximately 50.

We evaluate the current drive efficiencies for various parameters by obtaining the steady-state solution of Eq. (1). We assume that the LH spectrum extends form $3.5 v_{te}$ (Landau damping limit) to $0.56c$ (corresponding to $n_\parallel = 1.8$ for the incident LH spectrum), where c is the speed of light. The IBW spectrum is assumed to extend from $0.5c$ to the boundary of the computation region (set at an electron energy of 1 MeV). In the table below we summarize the results for the current drive efficiency and the perpendicular temperature on the LH generated plateau:

T_e (keV)	1	2	4	4	4	7	7	7	10	10	10
$(\overline{D}/D_c)_{IB}$	0	0	0	2	10	0	2	10	0	2	10
γ_{cd}	0.22	0.26	0.33	0.61	1.34	0.41	0.46	0.56	0.49	0.5	0.54
$T_\perp/T_e$	34	18	9	26	40	5	8	13	2.5	4	5

Here $\gamma_{cd} = n_e RI/P_d$ is the current drive efficiency in units of 10^{20} A/W m^2 (n_e is the electron density, I is the current, and P_d is the power dissipated. The table shows the change in γ_{cd} due to IBW's for different strengths of the IBW diffusion coefficient and at different plasma temperatures. At low temperatures ($T_e = 4$ keV) the CD efficiency in the presence of IBW's increases with the strength of the IBW diffusion coefficient and the CD efficiency is enhanced considerably over the values of the efficiency obtained by LHW's alone. As the temperature of the plasma is increased the effect of the IBW's diminishes till eventually around $T_e = 10$ keV the CD efficiency is not modified significantly in the presence of IBW's. The perpendicular temperature of the LH generated suprathermal electrons also increases in the presence of IBW's with the increase being more significant at lower plasma temperatures.

The increase in the current drive efficiency in the presence of IBW's is due to a modification, by the IBW's, of the energetic electron tail generated by LHW's. To illustrate this effect we compare, in Fig. 2, the electron parallel distribution function for the case of LH only with the distribution function for LH+IBW with both evaluated at a plasma temperature of 7 keV. The value of $\overline{D}/D_c$ for both waves is 10. The IBW's generate a larger number of energetic electrons than in the case of LHW's alone, thereby raising the plateau and extending the distribution function to higher momenta as seen in Fig. 2 The electron distribution function decreases at higher momenta due to a decrease in the IBW diffusion coefficient as shown in Fig. 1.

The table above also shows an increase in the CD efficiency as a function of the electron temperature for the case of LHW's only. This dependence of LHCD efficiency on the plasma temperature has been discussed before [7].

In conclusion, we find that an increase in the current drive efficiency with an asymmeteric lower hybrid spectrum lauched into a plasma which is being heated by a symmetric ICRF spectrum can be explained by the interaction of IBW's with the energetic electron tails generated by LHW's. The increase in the CD efficiency due to IBW's is larger at lower plasma temperatures. The corresponding increase in the perpendicular temperature reflects an increase in the population of the suprathermal electrons. Mode conversion and Fokker-Planck calculations show that a smaller minority concetrations and an incident ICRF power spectrum peaked and more concentrated at low values of $k_\parallel$'s would lead to higher CD efficiencies.

This work is supported in part by DOE Grant No. DE-FG02-91ER-54109 and by DOE Contract No. W-7405-ENG-48. The CCFM is supported in part by Atomic Energy of Canada Ltd., Hydro-Quebec, and Institut National de la Recherche Scientifique.

REFERENCES

1. C. Gormezano, M. Brusati, A. Ekedahl, P. Froissard, J. Jacquinot, and F. Rimini, Proceedings of the IAEA Technical Meeting on Fast Wave Current in Reactor Scale Tokamaks (Synergy and Complementarity with LHCD and ECRH), Arles, France, September 23-25, 1991. Eds. D. Moreau, A. Bécoulet, and Y. Peysson, p. 244.
2. A. K. Ram, A. Bers, V. Fuchs, R. W. Harvey, in Proceedings of the 10th Topical Conference on Radio Frequency Power in Plasmas, Boston, MA, April 1-3, 1993 (to be published).
3. A. K. Ram, A. Bers, V. Fuchs, R. W. Harvey, M. G. McCoy, Proceedings of the Europhysics Topical Conference on Radiofrequency Heating and Current Drive of Fusion Devices, Brussels, Belgium, July 7-10, 1992, Eds. C. Gormezano, P. U. Lamalle, R. R. Weynants, pp. 201–204.
4. M.G. McCoy, G.D. Kerbel, R.W. Harvey, AIP Conf. Proc. 159, 77 (1987); R.W. Harvey, M.G. McCoy, G.D. Kerbel, AIP Conf. Proc. 159, 49 (1987).
5. V. Fuchs and A. Bers, Phys. Fluids 31, 3702 (1988).
6. A. K. Ram and A. Bers, Phys. Fluids B3, 1059 (1991).
7. R. W. Harvey, M. G. McCoy, A. K. Ram, A. Bers, V. Fuchs, Proceedings of the Europhysics Topical Conference on Radiofrequency Heating and Current Drive of Fusion Devices, Brussels, Belgium, July 7-10, 1992, Eds. C. Gormezano, P. U. Lamalle, R. R. Weynants, pp. 205–208.

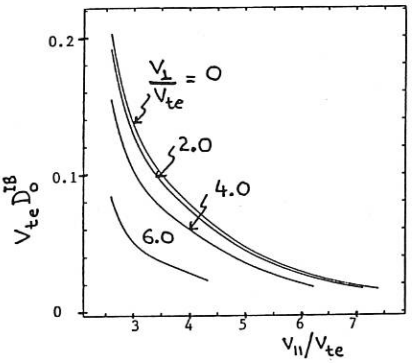

FIGURE 1

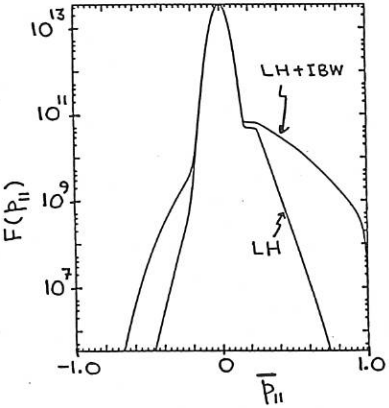

FIGURE 2

ACCESSIBILITY FOR LOWER HYBRID WAVES IN PBX-M[1]

H. Takahashi, S. Batha[1], R. Bell, S. Bernabei, M. Chance, T. K. Chu, J. Dunlap[2], A. England[2], G. Gettelfinger, N. Greenough, J. Harris[2], R. Hatcher, S. Hirshman[2], D. Ignat, R. Isler[2], S. Jardin, S. Jones[3], R. Kaita, S. Kaye, J. Kesner[3], H. Kugel, B. LeBlanc, F. Levinton[1], S. Luckhardt[3], J. Manickam, M. Okabayashi, M. Ono, F. Paoletti[3], S. Paul, F. Perkins, A. Post-Zwicker[2], N. Sauthoff, L. Schmitz[4], S. Sesnic, Y. Sun, W. Tighe, G. Tynan[4], E. Valeo, and S. von Goeler
Plasma Physics Laboratory, Princeton University, Princeton, NJ, USA
([1]Fusion Physics & Technology, [2]ORNL, [3]MIT, [4]UCLA)

The Lower Hybrid Current Drive (LHCD) experiments on the PBX-M tokamak attempt to modify the current profile in order to find high performance operating regimes.[4] Successful current and safety factor (q) profile modification has been reported.[6,7] Transport of LHCD generated fast electrons by MHD activity[7] and by diffusion[2] has been studied. Relationship between current deposition location and MHD behavior has been examined.[1] Understanding the wave damping mechanism in the face of 'spectral gap' is an important issue for the current profile control, and is discussed here. A traditional explanation based upon upshifting[8] of the wave parallel refractive index ($n_\parallel$) is examined. Another mechanism is also considered, based upon the 2-D velocity space dynamics coupled with a compound wave spectrum, here consisting of forward- and backward-running waves. The runaway critical speed relative to the phase speeds of these waves plays an important role.

The power spectrum ($P_{LH}(n_\parallel)$) of the 4.6 GHz 32-waveguide grill,[9] computed by a Brambilla code,[10] is shown in Fig. 1 for several settings of the phase angle between adjacent waveguides. Each phase setting produces a lobe in the positive $n_\parallel$ range representing forward waves, and a generally smaller lobe in the negative range representing backward waves. The distance in $n_\parallel$ between the lobes is a structural constant of the grill, and is ~ 8.3 here. As a result, the faster the forward waves are, the slower the conjugate backward waves are. The phase speed of forward waves is, however, much faster than the electron thermal speed (v_e) in our experiments (on-axis electron temperature, $T_e(0) \sim 0.8-1.3$ keV), and there is a spectral gap between v_e and the wave speed. In the Landau damping process in the 1-D velocity space, the gap must be filled with a *contiguous* spectrum of waves for the thermal electrons to be brought to resonance with high phase-speed waves. There are also much smaller side lobes. All lobes are narrow ($\Delta n_\parallel \leq 0.5$) owing to the large number of waveguides in the grill. This means that our spectrum is not contiguous, even when all lobes are 'mapped' onto the positive $n_\parallel$ side, i.e., there are also gaps in the wave spectrum itself.

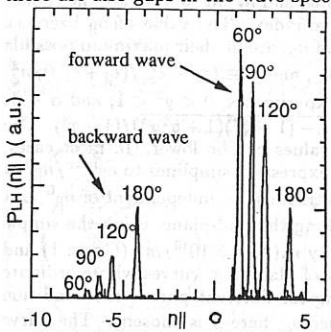

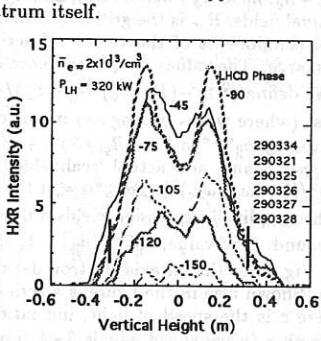

(Left) Fig. 1: An $n_\parallel$ spectrum of PBX-M LHCD system; (Right) Fig. 2: A vertical slice of a 2-D HXR camera image through the central region of an ohmically heated bean-shaped plasma. The data was taken in similar discharges over a period 30–45 ms into the LHCD pulse.

A novel 2-D tangentially viewing Hard X-radiation (HXR) camera[3] is used to study the profile of LHCD generated fast electrons. A vertical 'slice' of a 2-D image is shown in Fig. 2 for a series of phases ('phase scan'). Approximate locations of the 'classical' accessibility limit, i.e., the mode conversion point for waves with the grill-imposed $n_\parallel{}^0$, are indicated by short vertical lines on the $-75°$ curve. High phase angles, $-120°$ and $-150°$, are classically accessible to the plasma center. Off-axis peaks were observed for low phase angles up to $-90°$ *inside* the classical accessibility limit. This is evidence that the $n_\parallel$ upshift occurred. The peaks appeared

[1]Supported by USDOE Contract No. DE-AC02-76-CHO-3073

at approximately the same location regardless of the phase. But the amplitude of the peaks was strongly dependent on the phase. Theory predicts the current deposition location varying slowly with the phasing (see next paragraph) under conditions for which the $n_{||}$ upshift determines the ultimate wave accessiblity. The experimental results in this respect are not inconsistent with such predictions. But it appears puzzling that more inaccessible low phase angle cases generated a stronger HXR signal.

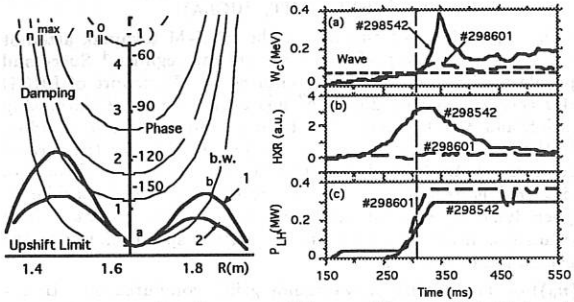

(Left) Fig. 3 Upshift accessibility limit: For profiles the parabola raised to α is used, where α is 1 for n_e and 2 for T_e, $T_e(0)$ is 1 keV. For B_θ/B_ϕ, a model equilibrium with I_p = 180 kA was used; (Right) Fig. 4 Runaway critical energy, HXR from escaping runaways, and LHCD power waveforms.

We first examine the $n_{||}$-upshift caused by toroidal effects. A ray-tracing analysis predicted[5] that, in some cases, especially in bean-shaped plasmas, upshift was sufficient to fill the gap completely and thus to damp the waves. But it predicted also that, in other cases, notably in low density (n_e) circular plasmas, upshift was enough only for the waves to propagate beyond the classical accessibility limit, but not to fill the gap and damp the wave. Inclusion of scattering of the lower hybrid waves by a density turbulence, based upon a theory by Andrews and Perkins,[11] resulted in increased upshift, but the qualitative conclusions remained the same. The upper bound of $n_{||}$ upshift can be estimated by a simple analysis following Kupfer and Moreau.[12] Using the nomenclature of reference[8] and taking the middle two terms of Eq. (15) of that reference, an 'electrostatic' approximation to the dispersion relation is $n_\perp^2+(n_{||}{}^2-\epsilon_\perp)(\epsilon_{||}+\epsilon_\perp)/\epsilon_\perp+\epsilon_{xy}^2/\epsilon_\perp = 0$, where $\epsilon_\perp$, $\epsilon_{||}$, and ϵ_{xy} are the elements of the cold plasma dielectric tensor. We have geometric relationships, $n_\perp{}^2 \approx n_r^2+n_\theta^2$, $n_{||} \approx n_\phi+n_\theta(B_\theta/B_\phi)$, and $n_\phi = n_{||}{}^0(R_{gr}/R)$, where B_θ and B_ϕ are the azimuthal and toroidal fields, R_{gr} is the grill major radius, and n_r, n_θ and n_ϕ are the radial, azimuthal and toroidal components of the vector refractive index. The value of $n_{||}$ becomes large when n_θ becomes large. The values of n_θ, and hence of $n_{||}$, are at their maximum possible values when $n_r = 0$. We define $g^2 \equiv -(B_\theta/B_\phi)^2(\epsilon_{||}+\epsilon_\perp)/\epsilon_\perp$, and $\alpha \equiv (\epsilon_\perp-\epsilon_{xy}^2/(\epsilon_{||}+\epsilon_\perp))/n_\phi^2$. In the region of interest (where waves propagate) in our experiments, $0 < g^2 < 1$, and $\alpha < 1$. The maximum $n_{||}$ is given by $n_{||}{}^{max}/n_{||}{}^0 = (R_{gr}/R)(1+\sqrt{1-(1-g^2)(1+g^2\alpha)})/(1-g^2)$. The expression gives the *upper bound*, and actual 'realizable' values can be lower. In most cases, $g^2 \approx (B_\theta/B_\phi)^2(\omega_{pe}/\omega)^2/(1+(\omega_{pe}/\omega_{ce})^2)$. For $g^2\alpha \ll 1$ the expression simplifies to $n_{||}{}^{max}/n_{||}{}^0 = (R_{gr}/R)/(1-\mid g \mid)$. The simplified expression yields a universal curve, independent of $n_{||}{}^0$, but overstates the upper bound. The value, $n_{||}{}^{max}/n_{||}{}^0 - 1$, along the mid-plane, using the simple expression is shown in Fig. 3 for the on-axis electron density $n_e(0) = 3{\cdot}10^{19}/m^3$ (Curve 1) and $1.2{\cdot}10^{19}/m^3$ (Curve 2). Shown also in the figure is a series of 'damping' curves whose ordinate is $c/(3v_e n_{||}{}^0) - 1$, where c is the speed of light, indicating for different phases the condition for strong Landau damping (wave speed equals 3–4 times v_e; here 3 is chosen). The curve labeled, 'b.w.,' is for $n_{||} = -6.2$, close to the backward waves of the $-90°$ phase. The waves would damp strongly over the range where the upshift limit curve and a damping curve overlap (e.g., between 'a' and 'b' on the b.w. curve). The 'damping region' would first appear in the mid-radius range, and only gradually expand, as $n_{||}{}^0$ (or T_e or n_e) increases. When the two curves do not intersect, the vertical distance between them represents a spectral gap remaining after maximum upshift is attained. The Curve 1 and damping curves represent approximately the phase scan discussed earlier, showing that the gap existed for all cases except the $-150°$ phase and backward waves. The gap is, however, smallest in the mid-radius region, and current

would be driven there if the gap is bridged by *some* mechanisms. Many other cases, notably low n_e, low current circular plasmas, had a gap similar to, or greater than, those between the Curve 2 and damping curves. Yet, a drop in the loop voltage (V_l) indicated that current was driven. These observations led to the question as to what fills the remaining spectral gap in these cases.

We now compare two nearly identical target discharges in which an LHCD pulse, similar in power, but different in waveform, was applied. The current deposition (inferred from 2-D HXR camera images — not shown) was very different in its spatial profile and time evolution. The LHCD phase was $-90°$ ($n_\parallel \sim 2.1$) for the both discharges. In one discharge (#298601) a nearly square waveform pulse was applied, but in the other (#298542) there was a long ($\sim$ 100 ms) low-power ($\sim$ 12 kW) pedestal ahead of the higher-power main pulse. The waveforms are shown in Fig. 4(c). Both discharges had neutral beam injection (NBI) heating over 250 – 580 ms with an absorbed power ($\sim$ 350 kW) comparable to $P_{LH} \sim$ 300 kW. In #298601 the HXR camera image was characterized by persistent 'hollowness' in the center between off-axis peaks. This implies sustained localization of off-axis current drive, a desirable characteristic for current profile control. In #298542 the profile was centrally peaked and rapidly grew toward its maximum value. Most of the rise occured *during the low-power pedestal.* The HXR emission produced by escaping runaway electrons was monitored by a scintilator. We examine its signals shown in Fig. 4(b) in the early part of the LHCD pulse. The background level was removed from either data by using the signal from a third discharge (#298559 — not shown) that had only NBI heating, but no LHCD. There was no increase in the scintilator signal attributable to LHCD for #298601. There was a rapid increase, after a delay ($\sim$ 50 ms), of the signal during the pedestal for #298542. The minimal power that caused the signal rise suggests that the process was probably not limited by the availability of the wave power. The critical energy (W_c) for a test electron to runaway in the presence of an electric field (E) is plotted in Fig. 4(a). The critical energy here is the value computed from Eq. (2.13) of Knoepfel and Spong[16] times $(2 + Z_{eff})/3$, where Z_{eff} is the effective ionic charge. The density representative of mid-radius regions was used. The value, $Z_{eff} = 4$, was assumed for these target discharges which had a relatively high loop voltage ($V_l \sim 1.5V$). Shown also in the figure is the energy corresponding to $n_\parallel{}^0$. The W_c values are below the wave 'energy' for the both discharges initially, indicating that, *if* there are electrons with energies beyond the runaway critical energy, E field can cause them to runaway. Since the target discharges were not runaway discharges, it is likely that the waves carried thermal electrons to the runaway critical energy. In many other situations, small changes in plasma parameters, notably V_l and n_e, often resulted in a very different current deposition profile and evolution. This 'volatility' of the results does not appear to be amenable to an easy explanation in terms of the wave propagation characteristics, such as *changes* in the classical or upshifted accessibility limit.

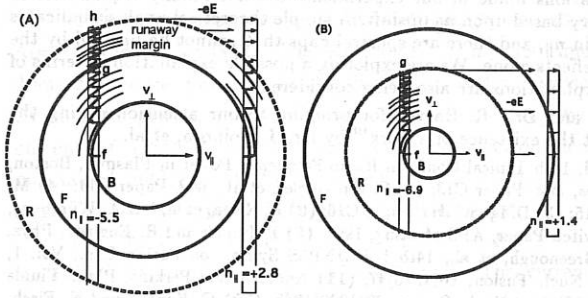

Fig. 5: (A) Runaway critical energy greater than either wave phase speed. The backward waves can feed electrons to the forward and upshifted waves; (B) Runaway critical energy intervenes between the wave phase speeds. The backward waves do not feed electrons to the forward waves, but to runaway population.

There have been many ideas advanced to explain how the spectral gap may be bridged. They include an extension of the imposed wave spectrum to higher $n_\parallel$ values by some unspecified mechanisms, and additional upshift due to some causes other than toroidal effects. We consider here effects of the backward waves. The model is of speculative nature and needs quantitative computational verification and further experimental tests. Electrons can gain speed beyond

the wave speed under the combined influence of lower hybrid waves and pitch angle scattering. This 2-D mechanism was studied intensively following a publication by Karney and Fisch.[13] In the presence of low phase-speed backward waves, the mechanism may serve as a means of supplying fast electrons to higher phase-speed forward waves. In the wave resonance zones, represented by a pair of vertical lines in Fig. 5 (A), electrons are accelerated by the wave field, and are then distributed along constant energy circles through pitch angle scattering. Two solid line circles, F and B, represent such a trajectory passing through the phase speed of the forward and backward waves, respectively. Those electrons, that gain speed from the backward waves and reach a point between f and g, can pitch angle scatter and interact with upshifted forward waves, and those that reach a point beyond g can resonate with the forward waves. The dashed line circle, R, represents a critical energy for electrons to runaway with a substantial probability in the presence of an E field (the boundary shape is in detail not a simple circle[14]). Those electrons, that reach h can become runaways, but the number of such electrons is small, when the 'runaway margin,' i.e., the distance between F and R, is large. In this model, it is crucial whether R is beyond both F and B as shown in (A), or R intervenes between F and B as shown in (B). Now, referring to (B), those electrons, that reach g can become runaways. The runaways can interact with the forward waves, but the forward waves are now rendered irrelevant, because the electrons continue to gain speed from the field. (Appert, et al.[18] has shown that a strong enhancement of the runaway production can occur through the 2-D dynamics.) Owing to the difference in the wave phase speeds, those electrons resonant with the backward waves are exponentially more numerous, and suffer far more frequent pitch angle scattering, compared to those electrons resonant with the forward waves. An inspection of the shape of the velocity space 'stream lines' computed by Karney and Fisch[13] shows that the bulk of the particle flux moves in the direction opposite the waves, and suggests that the backward waves may be effective in supplying electrons to the forward waves. (In a so-called compound wave spectrum[17] the high $n_{\|}$ *forward* waves can play a similar role.) It is the electrons that fill up the spectral gap in this model, rather than a contiguous spectrum of waves, although the $n_{\|}$ upshift of both the forward and backward waves also play an important role in bridging the gap. The runaway critical speed ($\propto n_e/E$), relative to the forward wave speed, can change quickly during a discharge, depending upon how far and quickly E is depressed by the current drive, and how n_e evolves. This may be a reason for the sensitivity of our current profile control experiments to date. Tailoring the waveform during the discharge may be useful, not only of the LHCD power, but also of the phase setting, taking advantage of the PBX-M LHCD system capability for rapid phase change.[9] Recently, Colborn, et al.[19] considered, based in part on CQL3D code results, broad side-lobes and backward lobes that would bridge the full extent of the spectral gap contiguously. In such a situation, only pitch angle scattering along constant energy circles, but not the acceleration mechanism, is required to bridge the gap.

In summary, some observations made in our experiments are not readily explainable in terms of the conventional theory based upon $n_{\|}$ upshift. A simple theoretical analysis indicates that there is an upper bound in $n_{\|}$, and there are spectral gaps that cannot be bridged by the $n_{\|}$ upshift caused by toroidal effects alone. We are exploring a possible explanation in terms of the backward waves. Other explanations are also being considered.

We thank Dr. P. Bonoli and Dr. R. Harvey for bringing to our attention during the preparation of this manuscript the existence of a work[19] by Dr. J. Colborn, et al.

REFERENCES : **(1)** R. Bell, 10th Topical Conf. on Radio Frequency Power in Plasmas, Boston, 1993, Invited Paper; **(2)** S. Jones, *ibid*, Paper C13; **(3)** S. von Goeler, et al., *ibid*, Paper C14; **(4)** M. Okabayashi, et al., *ibid*, Paper C15; **(5)** D. Ignat, *ibid*, Paper C16; **(6)** R. Kaita, et al, IAEA, Würzburg, 1992; **(7)** S. Bernabei, et al., Invited Paper, APS Meeting, 1992; **(8)** P. Bonoli and R. Englade, Phys. Fluids, **29**(1986)2937; **(9)** N. Greenough, et al., 14th IEEE/NPSS Symp. on Fusion Eng., Vol. 1, p126, 1991; **(10)** M. Brambilla, Nucl. Fusion, **16**(1976)47; **(11)** Andrews and Perkins, Phys. Fluids **26**(1983)2537; **(12)** Kupfer and Moreau, Nucl. Fusion, **32**(1992)1845; **(13)** C. Karney and N. Fisch, Phys. of Fluids, **22**(1979)1817; **(14)** Karney and N. Fisch, Phys. of Fluids, **29**(1986)180; **(15)** J. Kesner, MIT Report PFC/JA-92-24, 1993; **(16)** H. Knoepfel and D. Spong, Nucl. Fusion, **19**(1979)785; **(17)** F. Soeldner, et al.,IAEA Washingon, 1990; **(18)** K. Appert, et al., EPS Conference, Aachen, p329, 1983; **(19)** J. Colborn, et al., submitted to Phys. Fluids.

Current Drive Efficiency of Long-Duration and High-Density Discharge in TRIAM-1M

T. Yamagajo, Y. Kobaru*, S. Kawasaki, E. Jotaki, K. Makino, K. Nakamura, Y. Nakamura, S.-I. Itoh and S. Itoh

Advanced Fusion Research center, Research Institute for Applied Mechanics, Kyushu University 87, Kasuga 816, Japan

INTRODUCTION

Experiments of non-inductive current drive plasma have been carried out by using high frequency (8.2GHz) lower hybrid waves in the superconducting tokamak TRIAM-1M (R=0.84m). Fairly high density plasma ($\bar{n}_e$>10^{19}m^{-3}) has been maintained for 23s [1]. In shorter pulse LHCD discharges, current drive efficiency has been conventionally estimated as $\eta_{CD} = \bar{n}_e I_p R/P_{RF}$. By using this figure of merit η_{CD}, its dependences on machine and plasma parameters (i.e. $\Delta\phi$, B_t and $\bar{n}_e$) at the initial stage of the discharge are examined.

However, it is uncertain that η_{CD} is an available figure of merit for the extrapolation to the plasma sustained for a long time. Then, temporal evolutions of the plasma parameters are measured and the current drive figure of merit during the long duration (≥10s) discharge is studied. The plasma current and the line averaged electron density are maintained constant for about 4s. Nevertheless, they begin to decrease and η_{CD} decreases accordingly. The cause of the deterioration of η_{CD} and the correlation between η_{CD} and the confinement of the bulk electrons are investigated.

CURRENT DRIVE EFFICIENCY OF INITIAL STAGE

A typical waveforms of LHCD discharge are shown in Fig.1, where B_t=7T, $\Delta\phi$=90° and P_{RF}=94kW. The RF power is injected into the OH target plasma at 20msec after the initiation of the discharge. After 300msec, the loop voltage drops to 0V and the plasma current becomes to be driven fully by the RF wave. The plasma current of I_p>55kA and the line averaged electron density of $\bar{n}_e$>2.0x10^{19}m^{-3} are maintained until 4s. At first, the dependences of η_{CD} on $\Delta\phi$, B_t and $\bar{n}_e$ at the initial stage of the discharge (0.3s≤t≤4.0s) are investigated.

The η_{CD} is plotted against $\Delta\phi$ in Fig.2, where P_{RF}=130kW, B_t=7T, I_p=18.03~52.13kA and $\bar{n}_e$=1.24~1.89x10^{19}m^{-3}. The current drive figure of merit has a maximum value of 0.7x10^{19}m^{-2}A/W at around $\Delta\phi$=90°. The corresponding $\langle 1/N_{//}^2 \rangle$ (square inverse of the refractive index weighted by the power spectrum [2]) is also shown in Fig.2, and it takes the highest value at $\Delta\phi$=86°. This result agrees with the theoretical prediction that η_{CD} is proportional to $\langle 1/N_{//}^2 \rangle$. The radial profile of the

hard X-ray emission from the high energy electrons is peaked in the central part of the plasma at $\Delta\phi$=90°. This indicates that current carrying high energy electrons exist within the inner region of the plasma column for the effective LHCD.

The increase in B_t is expected to improve η_{CD} because of the improvement of wave accessibility of the plasma to LH waves. The dependence of η_{CD} on B_t is examined, where $\Delta\phi$=90° P_{RF}=94kW, I_p=28.7~58.2kA and $\bar{n}_e$=1.61~1.96x$10^{19}m^{-3}$. As B_t increases from 5 to 7T, η_{CD} increases from 0.48 to 0.90x$10^{19}m^{-2}$A/W.

We also investigate the dependence of η_{CD} on $\bar{n}_e$, where B_t=7T, $\Delta\phi$=90° and P_{RF}=130kW. As $\bar{n}_e$ increases from 1.5 to 2.3x$10^{19}m^{-3}$, η_{CD} increases from 0.66 to 0.98x$10^{19}m^{-2}$A/W in spite of the deterioration of the accessibility (Fig.3). It has been thought that there were two most possible reasons for the improvement of η_{CD} with increase in $\bar{n}_e$. One of them is the decrease in the effective ionic charge Z_{eff} with $\bar{n}_e$ [3]. Another is the improvement of the confinement of the high energy tail electrons due to the increase in $\bar{n}_e$ [4]. However, the absolute value of η_{CD} obtained from the experiments is smaller than the predicted one from the simple quasilinear Fokker-Planck theory, and the effect of the impurities cannot fully explain this. Then it is expected that the confinement of the high energy tail electrons play an important role for the effective LHCD. It is reported that the confinement time of the high energy tail electrons τ_{et} can be taken as approximately equal to the bulk electron confinement time τ_{eb}. In TRIAM-1M, lower bound of the energy confinement time of the bulk electrons is estimated to be about 1.1msec for 8.2GHz LHCD at the initial stage of the discharge. Theoretical curve [4] is also shown in Fig.3 assuming that Z_{eff}=4, τ_{et}=1,2,5msec and T_e=1keV.

TEMPORAL EVOLUTION OF η_{CD}

Temporal evolution of η_{CD}, I_p and $\bar{n}_e$ up to 20s during the long pulse discharge are investigated, where B_t=7T, $\Delta\phi$=90° and P_{RF}=130kW. The initial gas puff allows us to maintain the plasma current of I_p>57.7kA and the line averaged electron density of $\bar{n}_e$>1.5x$10^{19}m^{-3}$ until 4s with η_{CD}>0.66x$10^{19}m^{-2}$A/W. However they begin to decrease, and η_{CD} decreases accordingly. The decay rates of I_p, $\bar{n}_e$ and η_{CD} are found dI_p/dt=-5.40kA/s, $d\bar{n}_e/dt$=-0.13x$10^{19}m^{-3}$/s and $d\eta_{CD}/dt$=-0.10x$10^{19}m^{-2}$A/Ws, respectively. Later η_{CD} drops to less than 0.57x$10^{19}m^{-2}$A/W at 8s and remains constant until the RF power is finally stopped at 20s.

In association with the plasma current decrease, increase in the high Z impurities is observed spectroscopically. The lower bound of effective ionic charge Z_{eff} is evaluated to be 4.0 at 1s and rises up to 6.0 at 10s at the plasma center [5]. This observation corresponds to the results from hard X-ray measurement. During the decrease of the plasma current, the radial profile of high energy X-ray emission (E≥100keV) becomes more peaked and the effective X-ray temperature rises in the inner region of the plasma column. From 8s to the end of the discharge, the high energy

X-ray emission profile returns to the original shape and remains almost constant. This fact indicates that the impurity contamination occurs during the plasma current decrease.

The η_{CD} of the later part of the discharge (8s ~ 15s) is plotted against $\bar{n}_e$ in Fig.4. Theoretical estimations for τ_{et}=1,2msec, Z_{eff}=6 and T_e=0.6keV are also drawn. It is found that η_{CD} has a different dependence on $\bar{n}_e$ between the initial and the final stage of the discharge. This has a relationship with the plasma conditions such as Z_{eff}, $\bar{n}_e$ and T_e. Plasma parameters, $<1/N_{//}^2>$ and η_{CD} at 1s and 8s are shown in Table 1. We evaluated the deterioration of η_{CD} as follows. The decreasing rate of the current drive figure of merit $\eta_{CD}(8s)/\eta_{CD}(1s)$ is 0.48. According to the fact that η_{CD} is proportional to $1/(5+Z_{eff})$, the expected decreasing rate of η_{CD} is about 0.82. The decrease in $\bar{n}_e$ improves the accessibility. Then $<1/N_{//}^2>$ changes from 0.291 at 1s to 0.283 at 8s. So the expected increasing rate of the figure of merit is 1.03. The deterioration of η_{CD} cannot be explained fully by the effect of Z_{eff} and the accessibility. The fast electron loss may be a candidate. Since we cannot discriminate τ_{et} from τ_{eb}, the data at present are not conclusive. The effect of the density profile is also to be investigated.

Table 1

time(s)	I_p(kA)	$\bar{n}_e(10^{19}m^{-3})$	Te(0)(keV)	Z_{eff}	$<1/N_{//}^2>$	$\eta_{CD}(10^{19}m^{-2}A/W)$
1s	60.5	1.81	1.0	4.0	0.291	0.80
8s	38.5	1.32	0.6	6.0	0.283	0.38

REFERENCES

[1] S. Itoh, et al., IAEA-CN-56/E-3-6-2 (1992).

[2] J. E. Stevens, et al., Nucl. Fusion 28 (1988) 217.

[3] K. Ushigusa, et al., Nucl. Fusion 29 (1989) 1052.

[4] S. C. Luckhardt, Nucl. Fusion 27 (1987) 1914.

[5] M. Takashiri, et al., Impurity Behavior of LHCD Discharge in TRIAM-1M, this conference.

[*] Present address: Canon Inc.

FIGURE CAPTIONS

Fig.1 Temporal evolution of I_p, V_L, $\bar{n}_e$, η_{CD} and MoXIII line intensity.

Fig.2 Dependence of η_{CD} on $\Delta\phi$. Solid curve is the calculated $<1/N_{//}^2>$.

Fig.3 Dependence of η_{CD} on $\bar{n}_e$ at 1s ~ 4s. Solid curve is for η_{CD} calculated with Z_{eff}=4, τ_{et}=1,2,5msec and T_e=1keV.

Fig.4 Dependence of η_{CD} on $\bar{n}_e$ at 8s ~ 15s. Solid curve is for η_{CD} calculated with Z_{eff}=6, τ_{et}=1,2msec and T_e=0.6keV.

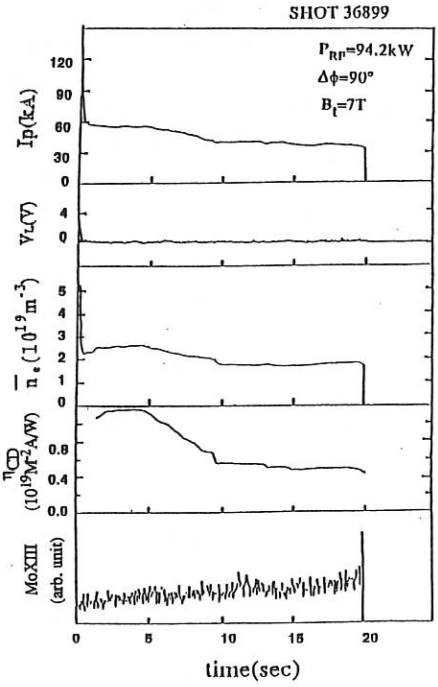

Fig.1

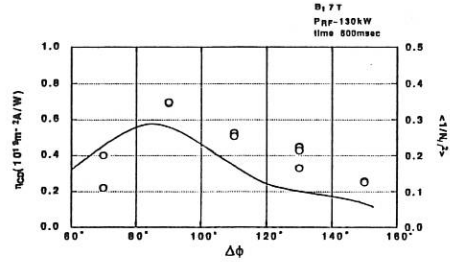

Fig.2

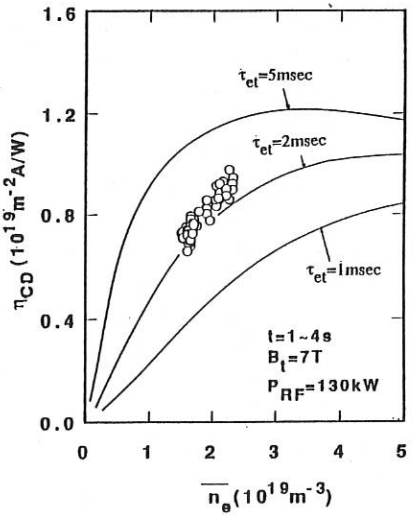

Fig.3

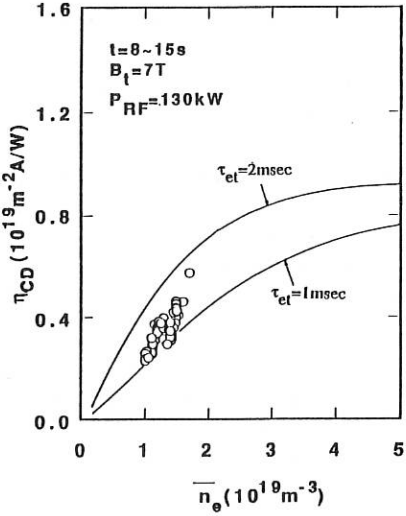

Fig.4

LOWER HYBRID CURRENT DRIVE EXPERIMENTS IN JT-60U

Y. Ikeda, K.Ushigusa, O.Naito, M.Seki, T. Kondoh and T. Imai

Japan Atomic Energy Research Institute, Naka Fusion Establishment,
Naka-gun, Naka-machi, Ibaraki-ken, Japan

Introduction

A new 48x4 multijunction grill for Lower Hybrid Current Drive (LHCD) has been installed on JT-60U to inject high power up to 7MW and totally 10MW in addition to the 24x4 multijunction grill (grill-I). This new grill (grill-II) consists of 4 (toroidal) x4 (poloidal) multijunction modules, each of which has 12 sub-waveguides in the toroidal direction following a oversized waveguide [1]. The wave spectrum is controlled by the operational frequency with $N_{\parallel}^{peak}$ = 1.4 to 2.2 at 2.23GHz to 1.74 GHz in the grill-II. In the first campaign of combination with these grills, high power LHCD experiments up to 8.3 MW at 2GHz were carried out and 3 MA of RF driven current was obtained.

Coupling and Conditioning of Grill-II

It is very important to simplify the LHCD grill structure because a huge number of waveguides should be required to inject several tens MW with high wave directivity in next generation tokamaks. A multijuntion technique with a oversized waveguide has been employed on the grill-II. A very low reflection coefficient should be required to excite a appropriate wave spectrum against the multi-reflection in the sub-waveguides and oversized waveguides. Figure 1 shows the reflection coefficients ρ of the each poloidal row in the grill-II at 2GHz as a function of the plasma-wall distance δp when the wall-grill distance δg is set about 15 mm. On the 1st to 3rd rows, a very low reflection coefficient $\rho \sim 3$ % was obtained at $\delta p < 100$ mm, while the reflection coefficient on the 4th row was still ~ 25 % at the same shot. The poor coupling in the 4th row may be due to the shape discrepancy in the curvature between the grill front and the first wall, because a good coupling on the 4th row was obtained by setting the grill at $\delta g \sim 5$ mm as shown in Fig.2, where $\delta p \sim 70$mm. Then, the plasma-wall and the wall-grill distances were usually set at δp=60~100 mm and δg=5~10 mm, respectively.

A high injected power ~7MW was easily obtained on the grill-II within two weeks operation after a few weeks baking at 250°C. The associated power density is ~30MW/m^2 which is consistent with the empirical scaling law [2]. Total injected power into plasmas was reached up to 8.3 MW for one second by using both the grill-I and the grill-II. The maximum power of the grill-II was limited by the capability of the klystron, and there was no hot spot phenomena on the divertor plates measured by a CCD camera. In the conditioning of the grill-II, few RF breakdowns at the window occurred as far as the good coupling was obtained. We believe that the high temperature baking is effective to reduce the outgassing and suppress RF breakdown at the window.

Current Drive Efficiency

The current drive experiment was performed in the hydrogen divertor discharge with the plasma parameters of Ip = 1.2 ~3.5 MA, $\bar{n}e$ = 1~2x10^{19}m^{-3}, Bt=3~4 T and Rp ~3.4 m.

Figure 3 shows the drop of the surface voltage ($\Delta v/v$) during LH injection as a function of injected power at $\bar{n}e \sim 1x10^{19}$ m^{-3}. The operational frequency was 2GHz for both grills, and the expected $N_{||}^{peak}$ were 1.4 and 1.6 for the grill-I and grill-II, respectively. The data at $P_{LH} < 5$ MW were obtained by using the grill-II alone. The negative surface voltage $\Delta v/v > 1$ was obtained for all plasma current discharges. A zero surface voltage for Ip= 1.2 MA was achieved at $P_{LH} \sim 2.5$ MW. In the range of Ip= 2 ~3.5 MA, $\Delta v/v \sim 1$ was achieved at $P_{LH} \sim 5$MW. These results indicate that the surface voltage drops easily at the higher plasma current discharge at Ip >2MA. A large reduction of the internal inductance l_i was observed during the LH injection at the higher plasma current discharge. Figure 4 shows the time evolution of l_i during LH injection on various plasma current discharges at $\bar{n}e \sim 1x10^{19}$ m^{-3} by using the grill-II. The injected power P_{LH} are ~ 4MW for Ip=2MA, and ~7MW for Ip=3~3.5 MA, respectively. The internal inductance increases and decreases at Ip=2 MA and Ip>3 MA, respectively. These results indicate that the current profile driven by LH power becomes flatter at the higher plasma current discharge. The hard x-ray measurement also indicates the broadening of the emission in the radial profile at the high plasma current discharge. Since the surface voltage depends on Ip and dli/dt, the current drive efficient should be estimated by taking account of the reduction of the internal inductance. Figure 5 shows the typical full LHCD discharge at the plasma current of 3MA, where P_{LH} ~7MW and $\bar{n}e \sim 1.3x10^{19} m^{-3}$. The surface voltage becomes negative at about -0.2 V and the change of l_i is ~0.07 s^{-1} during LH injection. The corresponding inductive voltage is ~0.2 v which is estimated by using a relationship between the surface voltage and dli/dt in the OH discharge on assuming that the relationship in the OH discharge is the same as in the LHCD discharge. Then, the current drive efficiency is estimated about $2x10^{-19}$ A/m^2W taking into account of dli/dt. In this experimental campaign, a large reduction in l_i during LH injection is always observed at Ip >2MA, and a full current drive discharge was obtained under $\Delta v/v > 1$. Even though the inverse DC field was applied on the LHCD discharge at Ip >2MA, the current drive efficiency was not sensitive to the plasma current and was about $2x10^{19}$ A/m^2W for the various plasma current Ip =1.2 ~3MA.

Discussion

It is first approach to employ the oversized waveguide in the multijunction module. The wave spectrum of the module can be controlled by the operational frequency. By using one module in the toroidal direction, the validity of the wave spectrum in the module was demonstrated in the change of l_i at Ip=1.2 MA. The internal inductance was increased in the case of frequency at 2GHz ($N_{||}^{peak}$=1.6), and decreased at f= 1.74GHz ($N_{||}^{peak}$=2.2). These behaviors were similar $N_{||}$ dependence obtained by using the grill-I, in which the $N_{||}$ is controlled by the phasing between adjacent standard-sized modules as reported in Ref[3]. Therefore, the oversized multijunction module may excite an expecting wave spectrum.

In the grill-II, the effect on the change in l_i was sensitive to the phasing between the toroidal modules at the higher plasma current discharge. The internal inductance did not increase when the phasing control system did not work well as shown in Fig 6. The solid and dotted lines show the time evolution of l_i before and after adjustment of the phasing control system Since the number of the sub-waveguides in the module (twelve) is larger than the toroidal module number (four) in the grill-II, the wave spectrum is separated into lower-$N_{||}$ and higher-$N_{||}$ around the $N_{||}^{peak}$ at an inappropriate phasing. The wave spectrum may be separated before phase adjustment, and the deposition zone of LH waves may be shifted more toward the periphery as reported in ASDEX [4]. Therefore, it is noted that a fine control of the phasing is required to obtain the peaked current profile at the higher plasma current discharge in using the oversized multijunction grill.

The current drive efficiency in this campaign is slightly smaller than that of the previous data ($2.5x10^{19}$ A/m^2W) by the grill-I. One of the reason of this discrepancy is due

to the higher $N_{\parallel}^{peak}$ of the grill-II than that of the grill-I, because the current drive efficiency roughly depends on the $(1/N_{\parallel}^{peak})^2$. The other is the effect of the inverse DC field due to the reduction in l_i at the high plasma current discharge. The inverse DC field may decrease the current drive efficiency. A slight phasing miss-adjustment may also degrade the wave directivity. These effects on the current drive efficiency will be studied in detail in next campaign.

Summary

High power LHCD experiments have been carried out in JT-60U by using a 48x4 multijunction grill. On the most of the rows in the grill-II, a good coupling was obtained at the reflection coefficient of ~3% at the plasma-wall distance of ~100 mm. The sharp fitting between the first wall and the grill front is key to achieve a good coupling for whole rows in the grill.

3MA of RF driven current was successfully produced by injecting P_{LH} ~7 MW at $\bar{n}e$~$1.3x10^{19}m^{-3}$. The current drive efficiency was about $2x10^{19}A/m^2W$. The current drive efficiency is not sensitive to the plasma current. A large reduction of the internal inductance was observed at the high plasma current discharge. It seemed that a small amount of power fraction with high $N_{\parallel}$ causes the flattening of deposition profile.

In next campaign the effect of the wave spectrum on the current profile will be investigated to achieve higher current drive efficiency and to demonstrate profile controllability at the high plasma current discharge..

References

[1] Ikeda, Y., et al.,Proc. 14th Symp. on Fusion Engineering, San Diego, 1991,Vol 1,122-125.
[2] Tonon, G., et al., Plasma Phys. Control. Fusion 35(1993) A105-A122.
[3] Ushigusha, K., et al., this conference.
[4] Söldner, F.X., et al.,17th EPS-Conf.,Amsterdam 1990, part 3, 1323.

Figure Captions

Fig. 1: Reflection coefficient as a function of the plasma - wall distance δp. The grill is located at ~15mm behind the first wall.

Fig. 2: Reflection coefficient on the 4th row as a function of the wall - grill distance δg. The plasma position is at δp~70mm.

Fig. 3: The reduction of the surface voltage ($\Delta v/v$) as a function of injected power P_{LH} for various plasma current I_P = 1.2 ~ 3.5 MA and $\bar{n}e$ ~$1x10^{19}m^{-3}$.

Fig. 4: Time evolution of l_i during LH injection on various plasma current discharge.

Fig. 5: Typical LHCD discharge at I_P=3MA.

Fig. 6: Effect of the phasing adjustment in the grill-II on the change in l_i. The solid and dotted lines show the time evolution of l_i before and after phasing adjustment.

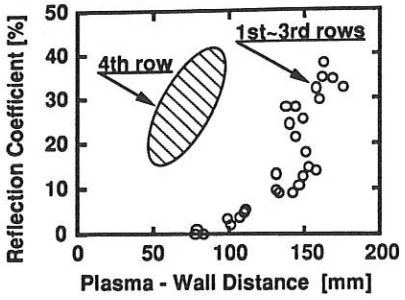

Fig.1

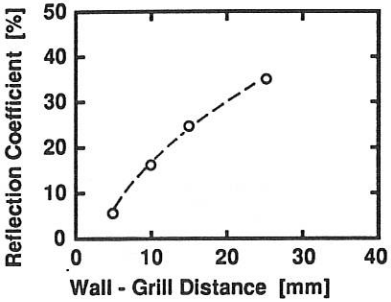

Fig.2

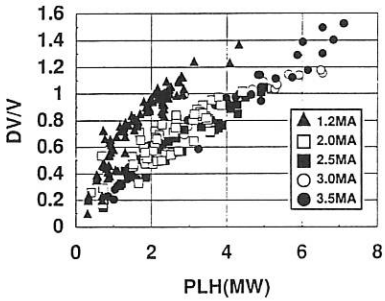

Fig.3

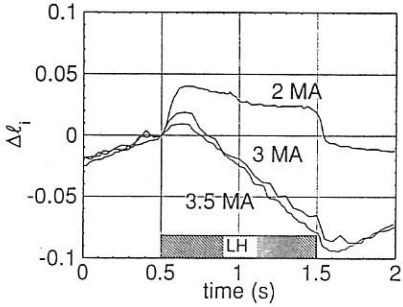

Fig.4

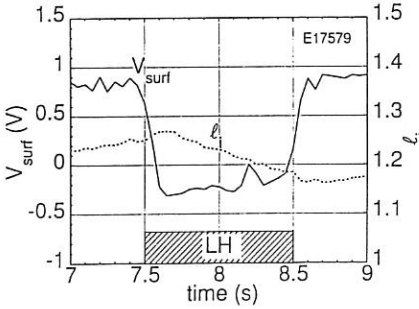

Fig.5

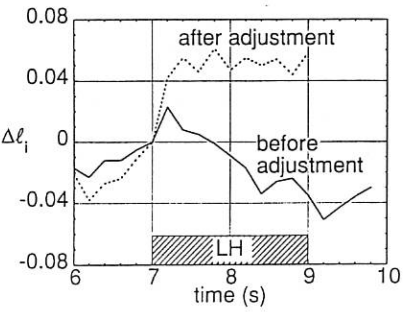

Fig.6

Current Profile Control by Non-Inductive Current Drive in JT-60U

K. Ushigusa, M. Matsuoka, Y. Kamada, O. Naito,
Y. Neyatani, Y. Ikeda, S. Ishida, T. Kondoh, M. Nagami

Japan Atomic Energy Research Institute
Naka Fusion Research Establishment
Naka-machi, Naka-gun, Ibraki-ken 311-01, Japan

Abstract

By increasing an internal inductance in target plasma and adjusting beam deposition profile, high beta plasmas with β_p = 2.5 - 4.0 and the normalized beta β_N = 2.5 - 3.5 were maintained without β_p collapse. High β_N plasmas have a favorable confinement ($\tau_E/\tau_E^{ITER\text{-}P89}$ = 1.5 - 2.0 in ELMy H-mode) with a high fraction of non-inductive current. Comparison of co and counter neutral beam current drive (NBCD) in high β_N discharges indicated an importance of additional driven current in bootstrap current dominated discharges. By adding NBCD in high β_N plasmas, almost full CD plasmas were obtained where almost half of the plasma current was driven by the boostrap current. Capability of current profile control by lower hybrid current drive (LHCD) was confirmed in JT-60U. Optimization of a seed current profile by using LHCD and NBCD in bootstrap current dominated discharges will be soon examined.

Current Profile and the High β_N Performance

Study of additional non-inductive current drive in bootstrap current dominated discharges are important to realize a steady state tokamak reactor. Although a high D-D fusion reaction rate with a certain fraction of bootstrap current were demonstrated in recent study of high β_p plasma with a high toroidal field of 4.4T in JT-60U[1], the high β_p plasma were often terminated by the β_p-collapse[2]. To achieve higher β_p plasmas in steady state, a current profile control in high β_p plasmas by non-inductive current drive such as NBCD and LHCD were examined in JT-60U.

In Fig.1, β_p are plotted against the safety factor q_{eff} for various operation modes. High β_p plasmas were obtained by strong central heating (P_{NB} > 25MW) in a relatively low current (I_p < 2.5MA) and a high toroidal field (B_T > 4T). Upper boundary of poloidal beta in the high β_p plasmas is limited by the β_p collapse which are shown as a solid circles in Fig.1. The β_p limit decreases with decreasing qeff. In order to obtain higher β_p plasma, a target plasma with a high plasma internal inductance l_i was produced by

increasing the plasma volume during the initial current ramp-up phase. Correlation between l_i and the energy confinement time in JT-60U was reported already in Ref.[3]. To realize broader pressure profile, an off-axis NBI ($P_{NB} \leq 15MW$) was injected into such high l_i target plasmas with a very low current ($I_p \leq 0.6MA$) and low toroidal field ($B_T \sim 1.5T$). By employing such optimizations, high β_p plasmas with $\beta_p = 2.5 - 4$, which is higher than the β_p-limit in usual high β_p experiments, were achieved as shown in Fig.1 (squares with cross). It should be emphasized that these optimized plasmas (we call this as the high β_N H-mode for simplicity) satisfy simultaneously several important requirements for a steady state tokamak reactor. At the first, the high β_N H-mode is the ELMy H-mode with $\tau_E/\tau_E^{ITER-P89} = 1.5 - 2.0$ and the improved confinement is maintained for long enough compared to the energy confinement time. The poloidal beta is large enough ($\beta_p = 2.5 - 4.0$) to generate a large amount of the bootstrap current. The normalized beta is close to the required value for a steady state reactor; $\beta_N = \beta_T(\%)/(I_p(MA)/a(m)B_T(T)) = 2.5 - 3.5$. Detail of MHD behaviors on the β_p - q_{eff} plot as shown in Fig. 1 is given in Ref[2].

Co and counter NBCD in high β_N H-mode plasmas were examined to see an effect of non-inductive current drive on bootstrap current dominated discharges. Results are shown in Fig. 2 where 10 - 12MW of nearly perpendicular beam was injected in the plasma with $I_p = 0.4MA$, $B_T = 1.5T$, $q_{eff} = 14$, $n_e = 1.1 \times 10^{19} m^{-3}$. In the case of co NBCD, $\beta_p = 3.7$ and $\beta_N = 2.5$ with $\tau_E/\tau_E^{ITER-P89} = 1.7$ were maintained during co-beam injection. The ACCOME code[4] predicts that almost all plasma current was driven non-inductively; the beam driven current is 0.2 - 0.3MA and the bootstrap current is ~0.2MA. In the case of counter-NBCD, confinement improvement is low ($\tau_E/\tau_E^{ITER-P89} < 1.2$), the achieved beta is low ($\beta_p = 1.8$, $\beta_N = 1.2$) and consequently the bootstrap current is low ($I_{BS} \sim 0.1MA$). Strong MHD activities which appear in $\beta_p > 2$ may correlate with β_p limit in the counter-NBCD case. From the time evolution of l_i shown in the 3rd and 4th traces in Fig.2, which is estimated by the diamagnetic β_p and the Shafranov Λ, the co-NBCD case has a lower dl_i/dt than the counter-NBCD. This suggests that the peaked current profile is realized in the co-NBCD case compared to the counter-NBCD. Current profile modification by injecting co and counter NBCD is also discussed in Ref.[5]. These results indicate an importance of additional non-inductively driven current profile to the bootstrap current dominated discharges.

Current Profile Control by LHCD

LHCD is one of the most powerful tool to drive non-inductive current and to control current profile. By adding a new large simplified-multijunction launcher (toroidally 48 and poloidally 4 waveguide array) to the already installed 24x4 multijunction launcher, JT-60U has a capability to inject ~10MW of LHCD power. Up to now, 8.3MW of LH

power was injected and a negative surface voltage was achieved in 3.5MA discharge at the density of $n_e \sim 10^{19}m^{-3}$[6].

In order to confirm the capability to control the current profile in JT-60U, 5s pulse of LH power ($P_{LH} \sim 1MW$) with different refractive index along the magnetic field $N_{||}$ was injected into 1.2MA discharge at $n_e \sim 10^{19}m^{-3}$ with $B_T = 4T$ as shown in Fig. 3. Results indicate that the plasma internal inductance can be controlled by changing the launched $N_{||}$. Centrally peaked hard x-ray profile was observed in low $N_{||}$ injection, while high $N_{||}$ injection shows a hollow hard x-ray profile, and these results are consistent qualitatively with the time evolution of the internal inductance.

Similar capability was observed in the 48x4 simplified multijunction launcher. Since the 48x4 launcher has only 4 module toroidally, where each module consists of 12 sub-waveguides, the phase adjustment between adjacent modules does not have a capability to change the launched peak $N_{||}$ widely. To change $N_{||}$ widely in 48x4 multijunction launcher, we changed the launched wave frequency from 1.74GHz to 2.23GHz and observed decrease and increase in l_i at 1.74GHz and 2.23GHz, respectively.

Driven current profile in LHCD is strongly affected by the plasma parameters and the launched wave conditions. By increasing the plasma current from 1.2MA to 3.5MA, it was found that RF driven current tends to be broad at high current. This is partly thought to be due to the higher electron temperature at higher current. The RF driven current is also affected by the wave accessibility condition. It was confirmed that the internal inductance during LHCD tends to decrease when the wave accessibility condition $N_{||}^{acc}$ approaches to the launched peak $N_{||}$. Fine tuning of phasing between adjacent modules is also required to realize LHCD plasmas with a high internal inductance. A small side lobe with a higher peak $N_{||}$ than the main lobe in the launched wave spectrum, which is caused by a small error on adjacent phasing control in 48x4 multijunction launcher, affected drastically on the time evolution of l_i during LHCD. Similar effect was reported in ASDEX experiments, where a large decrease in l_i was observed when a small power of higher $N_{||}$ wave was superimposed in LHCD plasmas with lower $N_{||}$ waves.

Summary and Near Future Experiments

By controlling the target current profile and the beam deposition profile, a bootstrap dominated discharge with a high β_p, a high β_N, an ELMy H-mode and a high confinement improvement factor was maintained simulteneously in nearly steady state. By adding co-NBCD, almost fully non-inductive discharge was realized in high β_N plasmas. An importance of non-inductively driven current profile in bootstrap dominated discharges was presented. Capability of current profile control by LHCD were confirmed in JT-60U. Based on these results, active control of current profile in high β_p or high β_N plasmas will be performed soon by using ~10MW of LHCD. Since 10MW of LHCD

power is large enough to drive a similar current at the similar density with the high β_p experiments, completely OH free discharge can be possible. Preliminary experiments of NBCD in bootstrap dominated plasma with OH free discharge were successfully performed.

References

[1] O. Naito et al., in this conference.
[2] Y. Neyatani et al., in this conference.
[3] Y. Kamada et al., Proc. 14th IAEA Conf., Würzburg, 1992, CN-56/A-7-13.
[4] K. Tani et al., J. Comp. Phys. 98(1992)332.
[5] M. Matsuoka et al., in this conference.
[6] Y. Ikeda et al., in this conference.

Fig. 1 The poloidal beta β_p against the safety factor q_{eff} for various operation modes.

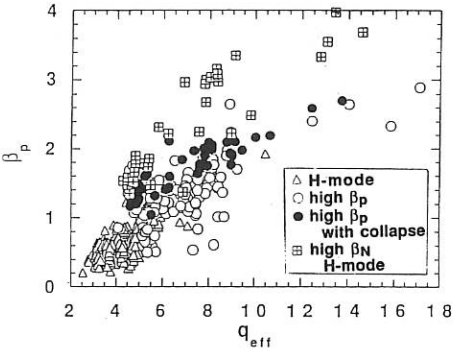

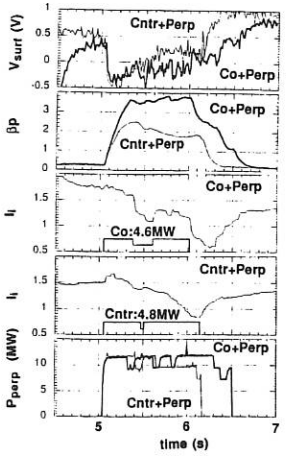

Fig. 2 Comparison of co and counter NBCD in high β_N discharge. I_p = 0.4MA, B_T = 1.5T, $n_e = 1.1 \times 10^{19} m^{-3}$.

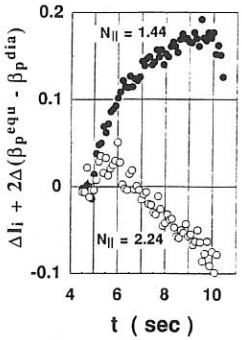

Fig. 3 Control of the internal inductance by LHCD with different $N_{||}$ injection. I_p = 1.2MA, B_T = 4T, $n_e = 10^{19} m^{-3}$, f = 2GHz, P_{LH} = 1MW and 24x4 multijunction launcher.

TIME EVOLUTION OF THE POWER SPECTRUM DURING LOWER-HYBRID CURRENT DRIVE IN TOKAMAKS

J. P. BIZARRO
Centro de Fusão Nuclear, Associação Euratom-IST, Instituto Superior Técnico,
1096 Lisboa Codex, Portugal

The present communication is based on a paper that is to appear in the literature [1], and reports results concerning the time evolution of the power spectrum during lower-hybrid (LH) current drive in tokamaks in a situation where toroidally induced ray stochasticity is important [2]. Such results have been obtained using a well-known and documented ray tracing and Fokker-Planck code [2]. Moreover, accurate representations of the poloidal extent of the antenna and of its radiated power spectrum have been used, thus ensuring that the initial conditions provided to the ray tracing calculation correctly reproduce the injected LH power both in poloidal angle, θ, and in parallel wave index, $n_{//}$. Notwithstanding the fact that questions may arise concerning the validity of geometrical optics when stochastic effects are important, it has been demonstrated that, in this situation, models based on ray tracing can quantitatively reproduce experimental data in a reliable manner provided a sufficiently large number of rays is used [2,3]. In this case, ray tracing may be regarded as a Monte Carlo-like method for describing the LH wave propagation and absorption.

In what follows, the plasma characteristics are: helium gas, major radius $R_0 = 2.34$ m, minor radius $a = 0.78$ m, magnetic field on axis $B_0 = 3.9$ T, central electron density $n_{e0} = 5.3 \times 10^{19}$ m^{-3}, volume-averaged electron density $\langle n_e \rangle = 3.3 \times 10^{19}$ m^{-3}, central electron temperature $T_{e0} = 3.1$ keV, volume-averaged electron temperature $\langle T_e \rangle = 1.5$ keV, ion effective charge $Z_{eff} = 2.8$, loop voltage $V_{loop} = 0.57$ V, and plasma current $I_p = 1.6$ MA, 19% of which is of noninductive nature. The wave frequency is $\omega/2\pi = 3.7$ GHz and the total LH injected power is $P_{in} = 2.46$ MW. The power P_{in} is equally divided into the four θ values corresponding to the poloidal locations of the four rows of waveguides that form the antenna, which is installed in the low-field side of the equatorial mid-plane and which extends roughly 0.38 radians in the θ direction. The same power spectrum is launched from each θ value, and only the two main lobes of the spectrum radiated by the antenna are retained. The negative lobe ($n_{//} < 0$) is peaked at $n_{//}^m = -5.62$ and is described using 21 rays uniformly distributed with a spacing $\Delta n_{//}^m = 1.6 \times 10^{-2}$, whereas the positive lobe ($n_{//} > 0$) is peaked at $n_{//}^p = 1.59$ and is described using 100 rays uniformly distributed with a spacing $\Delta n_{//}^p = 3.9 \times 10^{-3}$. This makes a total of 84 rays traced with $n_{//} < 0$ and 400 rays traced with $n_{//} > 0$. The negative and positive lobes can thus be considered to be described using grids whose effective spacings are

$\Delta n^m_{//eff} = \Delta n^m_{//}/4 = 4.0\times10^{-3}$ and $\Delta n^p_{//eff} = \Delta n^p_{//}/4 = 9.8\times10^{-4}$, respectively. Practically all the power in the positive lobe (68% of P_{in}) is injected with $n_{//}$ values that are not accessible to the plasma center, since for the present set of parameters central penetration of the LH wave requires $|n_{//}| \gtrsim 1.7$. With such strong accessibility constraints, the onset of ray stochasticicy is favored, and the rays launched within the positive lobe propagate inside the plasma for a long time before significant absorption takes place. Therefore, the set of parameters given above corresponds to a situation where stochastic effects induced by toroidicity are important. The effective grid spacings $\Delta n^m_{//eff}$ and $\Delta n^p_{//eff}$ have been chosen so to be appropriate for the different types of dynamics followed by the two lobes and to obey robustness criteria obtained by performing sensitivity studies [2]. Indeed, and as discussed below, the negative lobe is not affected by stochastic effects, while the positive lobe is strongly affected by such effects. So, the following criteria apply: $\Delta n^m_{//eff} \lesssim 10^{-1}$ and $\Delta n^p_{//eff} \lesssim 10^{-3}$.

The trajectories followed by the rays before complete damping occurs, projected in the (ρ,θ) polar plane, are depicted in Fig. 1. Here, ρ stands for the normalized radial flux coordinate. It is striking to see how differently the two lobes behave. The reasons for this are well understood and have to do with the fact that the dynamics of the high-$|n_{//}|$ negative lobe is characterized by strong wave damping, whereas the dynamics of the low-$|n_{//}|$ positive lobe is typical of a weak damping situation dominated by stochastic effects. The rays launched with $n_{//} < 0$ propagate coherently, in contrast with the rays launched with $n_{//} > 0$, which suffer a stochastic divergence and end up completely filling the tokamak cavity. Moreover, the rays with $n_{//} > 0$ do go through the central regions of the plasma, even if initially most of them have $|n_{//}| \lesssim 1.7$. Only apparently this can be considered as surprising, since it has been well established that ray stochasticity can greatly alter the accessibility constraints on the launched power spectrum [2]. It is most interesting in studying the dynamics of the latter to explicitly calculate the time evolution of the LH power spectral density, $S_{LH}(\tau,n_{//})$, which is reported in Fig. 2. Here, τ designates a normalized time variable. The characteristic damping times are very different for the negative and positive lobes. Furthermore, the first essentially keeps its shape and propagates in a regular manner, while the second is distorted and broadened. Such distinct behaviors reflect themselves in the way the LH power is damped on the plasma electron population. The absorbed power density per unit interval of $n_{//}$ due to electron Landau damping, $W_{ELD}(\rho,n_{//})$, can be seen in Fig. 3. Quite naturally, the power deposition pattern associated with the negative lobe is highly localized, as compared to the extended pattern associated with the positive lobe. The picture that may thus be retained when the ray dynamics is dominated by stochastic effects is that of a diffusion of the LH energy density in the $(\rho,n_{//})$ space. The absorbed and the launched power spectra,

$S_{ELD}(n_{//}) = (2\pi a)^2 R_0 \int_0^1 W_{ELD}(\rho', n_{//})\, \rho'\, d\rho'$ and $S_{LH}(0, n_{//})$ respectively, are compared in Fig. 4. The negative lobe essentially keeps its form, while being slightly broadened and upshifted in $|n_{//}|$. As expected, the major modifications take place for the positive lobe, which strongly spreads towards the high-$|n_{//}|$ side.

In conclusion, the analysis that has been presented clearly illustrates the influence of the balance between the wave damping and the stochastic divergence of nearby ray trajectories in governing the power spectrum dynamics and in establishing the characteristics of the LH power deposition patterns. When strong wave damping prevails, the launched power spectrum behaves regularly: the LH power deposition is localized and the absorbed power spectrum is very similar in shape to the launched one, although some broadening and shifting in parallel wave index generally occur. If the wave damping is weak and stochastic effects are important, the rays end up completely covering the plasma cross section and the power spectrum dynamics becomes diffusive-like: the LH power deposition turns out to be extended and the absorbed power spectrum is much broader than the launched one, as a result of strong spreading towards the high absolute values of parallel wave index.

REFERENCES

[1] BIZARRO, J. P., Nucl. Fusion **33** (1993) No. 5 or 6.

[2] BIZARRO, J. P., MOREAU, D., Phys. Fluids B **5** (1993) No. 4.

[3] BIZARRO, J. P., PEYSSON, Y., et al., Phys. Fluids B **5** (1993) in press (also in this conference).

FIGURES

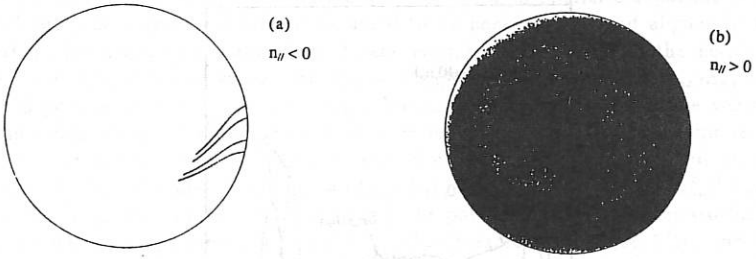

FIG. 1. Projection of the ray trajectories in the (ρ,θ) polar plane for: (a) $n_{//} < 0$ and (b) $n_{//} > 0$. The outer circle corresponds to $\rho = 1.1$.

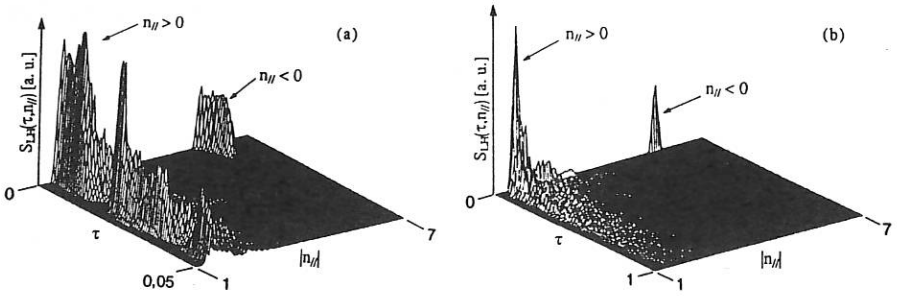

FIG. 2. Time evolution of the LH power spectral density up to: (a) $\tau = 0.05$ and (b) $\tau = 1$.

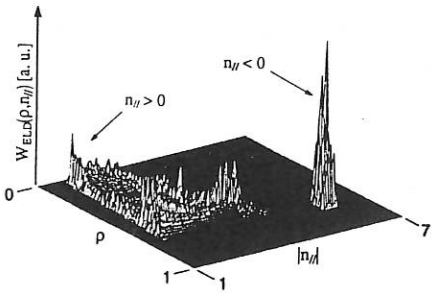

FIG. 3. Absorbed power density per unit interval of $n_{//}$ due to electron Landau damping.

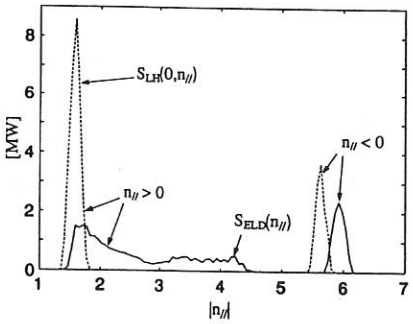

FIG. 4. Absorbed and launched power spectra.

STOCHASTIC E × B TRANSPORT OF FAST ELECTRONS IN THE PRESENCE OF LOWER HYBRID WAVES

J.A. Heikkinen[a] and S.K. Sipilä

Helsinki University of Technology, Nuclear Engineering Laboratory, SF-02150 Espoo, Finland

Introduction

Several numerical studies have been undertaken for the test particle problem where the particle diffusion is based on the $\mathbf{E}\times\mathbf{B}$ drift in a given turbulent spectrum of electrostatic fluctuations [1]–[4]. In these studies, the parallel motion is assumed to be decoupled from the perpendicular $\mathbf{E}\times\mathbf{B}$ drift motion, neglecting the effects of finite parallel wavenumber and stochasticity in the velocity space. For lower hybrid waves, the parallel motion is not decoupled from the $\mathbf{E}\times\mathbf{B}$ drift as the parallel wavenumber is finite. The parallel motion should therefore be included in the test particle simulations. This is of importance because, in the case of lower hybrid heating, $\langle E^2\rangle/B^2$ is much smaller than $\omega^2/k_\perp^2$. The latter would imply zero diffusion according to the two-dimensional simulations. Specifically, in the test particle simulations of particle transport caused by lower hybrid waves, we have to consider the topology of the stochastic regions and the direction of the diffusion as a function of the direction of the wave vectors in the xy-plane. The agreement of the diffusion with the quasilinear estimates as well as the trajectories for the nonresonant electrons are of interest.

Guiding centre equations

The numerical study is based on the nonrelativistic guiding centre equations

$$\begin{aligned} \frac{dz}{dt} &= v, & \frac{dv}{dt} &= \frac{q}{m_e}\sum_n E_{nz}\cos(\Psi_n), \\ \frac{dx}{dt} &= \frac{1}{B}\sum_n E_{ny}\cos(\Psi_n), & \frac{dy}{dt} &= -\frac{1}{B}\sum_n E_{nx}\cos(\Psi_n), \end{aligned} \tag{1}$$

where $\Psi_n = k_{nz}z + k_{nx}x + k_{ny}y - \omega t$ is the phase of the n th Fourier component of the electric field. The magnetic field B is assumed to be homogeneous and aligned in the z direction. We neglect the toroidal effects and consider the diffusion in the xy-plane. For the lower hybrid waves we assume $E_{ny} = (k_{ny}/k_{nz})E_{nz}$, $E_{nx} = (k_{nx}/k_{nz})E_{nz}$ and use the dispersion relation $k_{nz}/k_n = \omega/\omega_{pe}$. We assume an equidistant phase velocity spectrum $\omega/k_{jz} = v_p + v_d j/N$ centered at $v = v_p$, where $2N+1$ is the number of the modes. In our calculations, we normalize time with respect to ω^{-1} and spatial coordinates to k_{0z}^{-1}. We also define $A_n = (E_{n\perp}/B)/(\omega/k_{0z})$, $E_{n\perp} = (E_{nx}^2 + E_{ny}^2)^{1/2}$ and $\tan\theta_n = E_{nx}/E_{ny}$. According to Equations (1), the particle motion becomes stochastic when the overlapping parameter $\epsilon = qN^2E_{nz}/mk_{nz}v_d^2$ exceeds the value $1/16$, and the condition $|(v - v_p)/v_p| < N + v_{tr}/\Delta v_{ph}$ is satisfied for the parallel velocity, trapping velocity v_{tr} and mode separation $\Delta v_{ph} = v_d/N$.

The implicit Gear's stiff method [5] based on backward differentiation formula up to order five is used for numerical solution of Eqs. (1). This method is accurate for times $(v_d/v_p)t/N \leq 100 - 200$. For $v_d/v_p = 10$ and $N = 10$, Equations (1) can be integrated

accurately up to $t = 8000 - 10000$ with a reasonable tolerance $10^{-12} - 10^{-9}$ depending on the other parameters in the calculations. For the lower hybrid waves with $\omega/2\pi = 3 \times 10^9$ s^{-1}, this time is of the order of 1μ s. During that time the particles can diffuse a length of the order of 1 mm according to the quasilinear estimates.

Nonregular and stochastic orbits

We have found periodic orbits in all the cases where the parallel phase velocities of the modes as well as the mode amplitudes are equal. Nondrifting periodic orbits are also found when the perpendicular components of the mode wave vectors are parallel. An oscillatory motion due to the $\mathbf{E} \times \mathbf{B}$ drift, perpendicular to the common wave vector direction, is obtained in this case. For diverse directions of the wave vectors with overlapping modes and nonequal phase velocities, the trajectories are shown to be stochastic even at such low amplitudes as $A_n \sim 10^{-4}$. To study the particle diffusion, we concentrate in the following on simulations with more than two modes.

Assuming 10 MW power for LHCD and taking this power to be radiated uniformly through the magnetic surface at $\rho/a = 0.4$ with $a = 1$ m and $R = 3$ m for the minor and major radii, we find $E_{nz} \sim 3000$ V/m with $k_{nz} = 1.5$ cm^{-1} and $\omega/2\pi = 3.7$ GHz. Assuming $\omega_{pe}/\omega = 10$, this corresponds to $A_n \sim 7 \times 10^{-5}$ with $B = 3$ T. In the case of single pass absorption, the wave trajectories are directed inwards radially, but due to the toroidal effects the wave vectors of the modes may have a significant poloidal component [6]. We now investigate the particle transport in the cases where the wave vectors of the modes are uniformly positioned inside a cone centered in the positive x direction, i.e., $\theta_n = \pi/2 - \Delta\theta + (n-1)\Delta\theta/N$, where $2N+1$ is the number of the modes and $\Delta\theta$ measures the spread of the poloidal wave vector components in the units of polar angle. We have taken $\omega_{pe}/\omega = 10$, $\Omega_e/\omega = 20$, $v_d/v_p = 0.1$.

Figure 1 shows the stroboscopic sections of four particles when $2N + 1 = 7$, $A_n = 1.5 \times 10^{-4}$ for each mode and $\Delta\theta = 0.3$. The four particles have been started at $z = 0$, 2, $4\pi/2.7$ and $8\pi/2.7$, respectively. The trajectories are stochastic in the region bounded in the y direction. In the x direction, the particles appear to diffuse freely. This result is similar to the case of two standing waves studied in Ref. [1] , where a stochastic region in a band in y was reported. In this study, the parallel motion was decoupled, and the stochasticity was not observed at such low amplitudes as in our case.

The anisotropic nature of the diffusion can be clearly seen in Fig. 2, where the variances $\langle \delta x^2 \rangle = \sum_{i=1}^{M} [x_i(t) - x_i(0)]^2/M$ and $\langle \delta y^2 \rangle = \sum_{i=1}^{M} [y_i(t) - y_i(0)]^2/M$ are plotted for an ensemble of $M = 20$ particles. The ensemble consists of particles initially distributed uniformly in a finite z region with the common initial velocity $v(0) = 0$. The spatial spread in the y direction appears to be rapidly saturated while the spread in x increases steadily. The estimate $\hat{D}_{xx} = \lim_{t\to\infty} \langle \delta x^2 \rangle / 2t$ for the diffusion coefficient from the numerical calculations can be compared with the quasilinear estimate. In the present case, the latter can be approximated (in normalized units) as $D_{xx} = (\pi/2)\langle A_y^2 \rangle N/(v_d/v_p)$, where

$$\langle A_y^2 \rangle = \frac{1}{2}\left[1 - \frac{\sin(2N+1)(\Delta\theta/N)}{(2N+1)\sin(\Delta\theta/N)}\right] \frac{\hat{E}_\perp^2/B^2}{(\omega/k_{0z})^2} \tag{2}$$

with $E_{ny} = \hat{E}_\perp \cos\theta_n$ for each n. We have written $\langle E_y^2 \rangle = \sum_{n=-N}^{N} E_{ny}^2(k_{nz})/(2N+1)$. With the parameters of Fig. 2a, we find $D_{xx} = 4 \times 10^{-8}$. In comparing this number with

$\hat{D}_{xx} = 8 \times 10^{-9}$ obtained from the simulation, we find them to agree within an order of magnitude. The quasilinear estimate, however, turns out to be larger by a factor of 5.

In the present simulation, the number of modes is finite, and the test particle ensemble covers only a small part of the possible initial positions in the zv-phase space. A more rigorous comparison should be done with a much larger number of test particles and modes. However, we note that our result of a very weak diffusion in y, in the present case with well directed ensemble of wave vectors in the x direction, appears to be in accordance with the quasilinear theory if we note that the velocity diffusion in v appears as an incoherent oscillation in y and x about a slowly varying average which diffuses due to the action of $D_{xx} - D_{xv}^2/D_{vv}$ in x and due to the action of $D_{yy} - D_{yv}^2/D_{vv}$ in y [6]. In our case of almost standing waves in the y direction, D_{xv} and $D_{yy} - D_{yv}^2/D_{vv}$ tend to almost vanish when the wave vector directions of all modes approach the x direction. Therefore, the diffusion in y is strongly suppressed in this limit while D_{xx} should estimate diffusion in x.

Figure 2b shows the x and y variances for $\Delta\theta = 0.8$. The result shows an increase of $\hat{D}_{xx}$ for increasing $\Delta\theta$ in agreement with the quasilinear theory. We find $\hat{D}_{xx} = 2.5 \times 10^{-8}$ and 5×10^{-8}, $D_{xx} = 10^{-7}$ and 2.2×10^{-7} for $\Delta\theta = 0.5$ and 0.8, respectively. In addition, it can be seen that the diffusion in y appears to be enhanced for these larger values of $\Delta\theta$ in agreement with the theory. For the case $\Delta\theta = \pi$, symmetric diffusion takes place with equal diffusion coefficients in x and y. We note, however, that smaller diffusion coefficients than the quasilinear estimate were found in this case, too.

From the obtained values of the diffusion coefficient we may estimate the typical length Δx which the trajectories can move in x during an average collision time ν_0^{-1}, which for $n_e = 2 \times 10^{19}$ m^{-3} and $T_e = 5$ keV is of the order of 10^{-4} s for the electrons. We find $\Delta x = (2\hat{D}_{xx}\nu_0^{-1}\omega)^{1/2} \sim 0.2$ with $\omega/2\pi = 3.7 \times 10^9$ s^{-1} and $\hat{D}_{xx} = 10^{-8}$. This corresponds to a diffusion coefficient of about 0.05 m^2/s with $k_{0z} = 1.5$ cm^{-1} and to a length of 3 mm, which is $20 - 30$ times larger than the typical banana width of the fast electron orbits in toroidal geometry. This hardly exceeds diffusion by other sources which may predict values of the order of 1 m^2/s for the diffusion coefficient. However, it should be noted that the convection arising from anisotropic spectra of wave vectors in the poloidal direction [6] may give higher losses of fast electrons.

The results for the diffusion in the configuration space clearly indicate the importance of including the parallel motion. Stochastic orbits perpendicular to the magnetic field are obtained even at such low amplitudes as with lower hybrid waves on tokamaks. For almost coinciding wave vectors, the wave-induced diffusion can be strongly anisotropic, which should be accounted for in the Fokker–Planck calculations.

References

[a] Permanent address: Technical Research Centre of Finland, Nuclear Engineering Laboratory, P.O. Box 208, SF-02151 Espoo, Finland

[1] KLEVA R.G. and DRAKE J.F. (1984) *Phys. Fluids* **27**, 1686.

[2] HORTON W. (1985) *Plasma Phys.* **27**, 937.

[3] MISGUICH J.H. and NAKACH R. (1991) *Phys. Rev. A* 44, 3869.

[4] PETTINI M., VULPIANI A., MISGUICH J.H., DE LEENER H., ORBAN J. and BALESCU R. (1988) *Phys. Rev. A* **38**, 344.

[5] HINDMARSH A.C. (1974) *GEAR, Ordinary Differential Equation System Solver*, Lawrence Livermore Laboratory, Report UCID–30001, Revision 3.
[6] KUPFER K. and BERS A. (1991) *Phys. Fluids B* **3**, 2783.

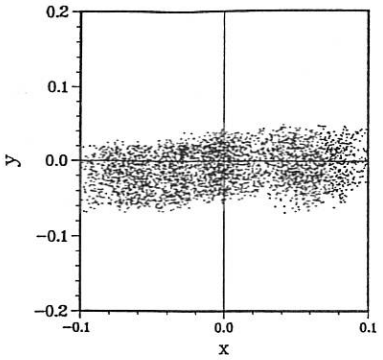

FIG. 1 Stroboscopic sections of a trajectory of four particles with $z = 0$, 2, $4\pi/2.7$ and $8\pi/2.7$ and $v = 0$ at $t = 0$ for the case of 7 modes with $A_j = 1.5 \times 10^{-3}$ for $j = 1, \ldots 7$ and $\Delta\theta = 0.3$. The dots are recorded at the end of each period ($t = T_0, 2T_0, 3T_0, \ldots$); $T_0 = 5.33$.

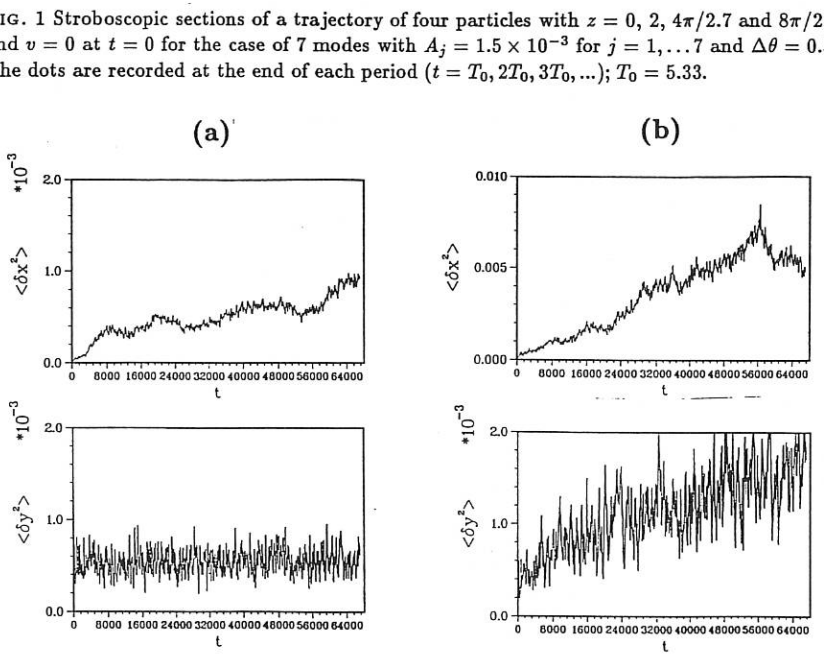

FIG. 2 The variances $\langle \delta x^2 \rangle$ and $\langle \delta y^2 \rangle$ as a function of time for an ensemble of 20 particles uniformly distributed in the region $0 < z < 2\pi/0.9$ with $v = 0$ at $t = 0$. (a) $\Delta\theta = 0.3$, (b) $\Delta\theta = 0.8$. Other parameters are the same as in Fig. 1.

DIFFUSION OF THERMONUCLEAR ALPHA PARTICLES UNDER THE INFLUENCE OF INTENSE LH WAVES

L. KRLÍN and P. PAVLO
Institute of Plasma Physics, Czech Academy of Sciences,
182 11, P.O. Box 17, Prague 8, Czech Republic

Abstract

Recently, a new mechanism was proposed by Fisch and Rax which should lead to amplification of lower hybrid (LH) waves at the expense of alpha particles energy, improving thus the LH current drive efficiency. The present contribution investigates the possibility of achieving the conditions on which this mechanism - based on the spatial diffusion of fusion alpha particles - could become operative.

1 Introduction

It had been generally accepted that for an efficient LH current drive, the resonant interaction of LHW with alpha particles should be better avoided. The simplest way for this is to increase LHW frequency up to or above 5 GHz (see e.g. [1]).

Recent papers of Fisch and Rax [2,3,4] have studied this problem in a rather untraditional way. They consider the regime of a strong LHW - alpha particles interaction. They have found that on certain conditions, this interaction can be used to the amplification of considered LHW. Their mechanism is based on a special feature of the induced diffusion of alpha particles in the energy-configuration space. The model is further based on the possibility of launching of LHW with sufficiently large k_θ component.

The complete solution of this problem requires a full velocity-space description of the LHW - alpha particles and plasma interaction. Nevertheless, some interesting results can be obtained from simplified models. In what follows, we discuss the problem of launching of LHW capable to reach deeper regions of a tokamak plasma, and the effect of the quasilinear flattening of the velocity distribution function of alpha particles on the global energy balance. Further, we discuss analytically the model of Fisch and Rax in the frame of the quasilinear lines of diffusion constraint.

2 Propagation and absorption of LHW with large k_θ component

The propagation and absorption of lower hybrid waves by electrons and alpha particles has been calculated using the codes described in detail in [1]. The equilibrium configuration of the magnetic field (for prescribed initial radial profiles of the electron density and electron and ion temperatures) was obtained from the code ASTRA [5].

The parameters of plasma were chosen to match those of the last ITER definition: the minor radius 2.15 m, elongation 2.2, triangularity 0.42, the major radius 6 m, the toroidal magnetic field on the axis 4.85 T, density profile $n_e(r) = 1 \times 10^{20} \times (1 - 0.95x^2)^{0.5}$ (m^{-3}), temperature profile $T(r) = 31 \times (1 - 0.95x^2)^{0.5}$ (keV), $x = r_{eqv}/a_{eqv}$.

Since the mechanism described in Introduction requires that the alpha particles interact with the lower hybrid waves, the frequency has to be chosen below 5 GHz (see e.g. [1]). Moreover, it is desirable that the rays form a ring around the plasma, and that in the region where there is already a significant production of fusion alphas. To find the best candidates for the purpose, we have performed a preliminary study, launching waves systematically from top to bottom around the outer surface of the torus. The refractive index was chosen 1.8, and the calculations were performed for the generator

frequency of 5, 3 and 2 GHz, with initial $k_\theta = 0$; see Fig. 1. The dashed portions of each curve correspond to the spatial points where any ray will be most probably damped because the phase velocity v_{ph} falls down to $1.5 \times v_{Te}$ (thermal velocity); full lines show that either accessibility limit is reached, or the ray has turned back (the latter case is indicated by asterisks). Fig. 1 shows firstly that the lower the frequency the worse the penetration and, secondly, that there are but two regions where the waves penetrate deep enough - just below the equatorial and close to the top. These regions can be made wider if the initial k_θ is optimized for each launching position - see dash-dot line in Fig. 1.

Fig. 1. Penetration depth

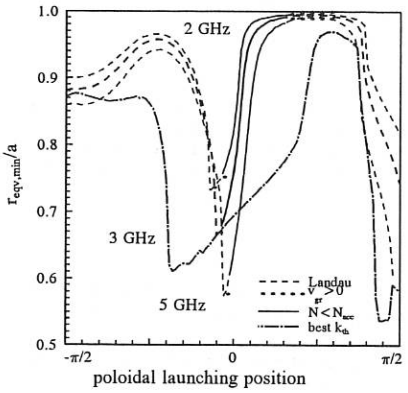

Fig. 2. Absorbed/generated power

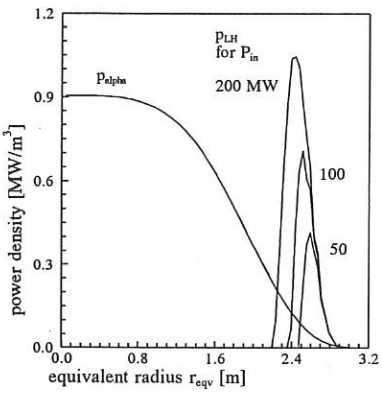

As a compromise between the required depth of penetration and the necessity of interaction with alphas, we have chosen the frequency to be 3 GHz, and a side launch.

Fig. 2 shows the power density profiles for 50, 100 and 200 MW of LH input power, launched at the poloidal angle 0.15 rad and $k_\theta = 0$. The input spectrum was rectangular, centered at $N_{par} = 1.65$, extremely narrow (full width 0.05), and a zero height of the launching structure, so as to get the deepest penetration of LHW. Final height of the grill, non-rectangular spectrum, spread in k_θ due to fluctuations and other effects will in fact make the penetration even worse.

Obviously, for acceptable input powers about 100 MW, the LH waves will be completely damped before they could be noticeably enhanced by alpha particles. The part of the fusion power released in alpha particles corresponding to the above profiles of density and temperature is also shown in Fig. 2 (50:50 D-T mixture is assumed). To sustain LHW, the power absorbed by electrons would have to be compensated by alphas which does not seem possible. Consequently, the waves launched from the plasma periphery cannot significantly profit from the mechanism under study.

It should be noted that it is predominantly the damping by electrons and the behaviour of rays what prevents the waves from reaching the hotter part of the plasma column. The damping by alphas is not very significant, even if the tendency toward saturation of the absorption is modified by by acceleration of an increasing number of alphas over their initial energy with the increasing power, see Tab 1.

This numerical simulation can be considered as a pendant to the analytical study of the same problem, given in [6] and [2].

3 Analytical study of space-velocity induced LHW diffusion and generalized quasilinear lines of diffusion constraint

In what follows we consider the toroidal geometry with coordinates r, θ, φ. For this geometry, we use the system of canonical coordinates and momenta, Q_1, Q_2, Q_3, J_1, J_2, J_3, described in [7]. Here, Q_1 is the angle of the cyclotron rotation, Q_2 is the poloidal angle od the guiding center of a particle, and

$Q_3 = \varphi$ is the toroidal angle of the guiding center. The canonically conjugated system of momenta is $J_1 = \frac{mv_\perp^2}{2\omega_c} = \rho_c^2 \frac{eB_\varphi}{2}$; $J_2 = \frac{eB_\varphi r_D^2}{2}$; $J_3 = p_\varphi$, where $\omega_c = \frac{eB_\varphi}{m}$, r_D is the radius of the guiding center, B_φ is the toroidal magnetic field, p_φ is the toroidal momentum and ω_c, B_φ are taken in the guiding center position. ρ_c is the cyclotron radius.

Considering the motion of a particle in the tokamak magnetic field as integrable, and taking LHW into its electrostatic wave approximation, the Hamiltonian, describing the particle-wave interaction has the form

$$H = H_0(J_1, J_2, J_3) + e\varphi_0 \exp(i\mathbf{k}.\mathbf{r}(Q_i, J_i) - i\omega t) \tag{1}$$

where H_0 is the integrable part, φ_0 is the potential of the wave and $\mathbf{k}$ and ω is the wave vector and angular frequency of the wave, respectively, and $\mathbf{r}$ is the space vector. Taking $\mathbf{k}$ as $\mathbf{k}(k_r, k_\theta, k_\parallel)$, expanding (1) into the Bessel functions, neglecting $k_r \ll k_\theta$ and using the resonance condition

$$-i\omega + in(\dot{Q_1} + \dot{Q_2}) + ik_\parallel R_0 \dot{Q_3} = 0 \tag{2}$$

where $\dot{x} = \frac{dx}{dt}$, we obtain from the canonical equations the following expressions

$$\frac{dJ_1}{dJ_2} = \frac{n}{n + k_\theta r_D}; \qquad \frac{dJ_1}{dJ_3} = \frac{n}{k_\parallel R_0}; \qquad \frac{dJ_2}{dJ_3} = \frac{k_\theta r_D + n}{k_\parallel R_0}. \tag{3}$$

Using the results from our canonical formulation [7], we obtain for $k_\theta r_d \gg n$ the relation $dr = \frac{dW_\perp}{\omega_c n m} k_\theta$ where $W_\perp = \omega_c J_1$. This is already the result, obtained by Fisch and Rax [3] and which determines the coupling between the change of the perpendicular energy of the particle, $dW_\perp$ and the shift of the guiding center, dr.

We shall now show that the same result will appear - as a special case - from the quasilinear lines of diffusion constraint. Quasilinear lines of diffusion were first mentioned by Kennel and Engelmann [8]. Formal generalization for toroidal configurations were performed by Kaufman [9] and Becoulet et al. [10]. Their consequences for the radial transport of banana particles were discussed in [11].

For the determination of the generalized lines of diffusion, the unperturbed Hamiltonian H_0 requires specification. Choosing it in the form [10], considering the resonance condition (2), and using the usual procedure for the determination of the quasilinear lines of diffusion constraint (see e.g. [10]), we obtain

$$\Delta W_\perp - \frac{n\omega_c}{k_\theta r_D + n} [1 - \frac{k_\parallel v_\parallel}{\omega} [\frac{k_\theta B_P}{k_\parallel B_T}(1 + \frac{n}{k_\theta r_0}) + 1]] \Delta r, \tag{4}$$

where B_T and B_P is the toroidal and poloidal magnetic field, respectively.

Neglecting the term, proportional to $\frac{k_\parallel v_\parallel}{\omega}$, we obtain the result of Fisch and Rax [3]. The foregoing, more exact solution therefore offers further possibility of the transport of the transformation of alpha particle energy, now its parallel component. For LHW, $\frac{k_\parallel v_\parallel}{\omega} \approx 0.1$; the effect is therefore rather weak. Nevertheless, for fast waves this term can be larger, and the mentioned effect more expressive.

Till now we have considered the approximation $k_\theta \gg k_r$. From our general canonical approach follows that the radial electric field, $E_r = -k_r \varphi_0$ induces the radial shift also. Labeling the shift, caused by the poloidal field as Δr_p and by the radial field as Δr_r, their mutual relation is $\frac{\Delta r_p}{\Delta r_r} \approx \frac{r_D}{\rho_c}$. The effect of Fisch and Rax caused by the poloidal field therefore dominates over the effect of the radial field. Nevertheless, due to the difficulties with the generating of large k_θ field deeper in the plasma, the effect of E_r can be of some importance.

Initial input power [MW]	50 MW	100 MW	200 MW
Power at $r/a = 0.81$ [MW]	13.7 MW	42.9 MW	154.8 MW
Electrons $[kW/m^3]$	191.0	632.0	875.0
Alphas $[kW/m^3]$	2.4	3.4	4.5
Fast alphas share	25%	29%	33%

Table 1: Absorbed power densities at $r/a = 0.81$.

In the foregoing, the effect of the inhomogeneity of the magnetic field has been neglected. Indeed, $\Delta W_\perp$ must be expressed as $\Delta W_\perp = \omega_c \Delta J_1 + J_1 \frac{\partial \omega_c}{\partial r} \Delta r$. For usual tokamak gradients, the significance of the last term for toroidally untrapped particles is small. Larger effects can be expected by the radial shift of bananas.

According to the foregoing, the induced radial diffusion of alpha particles is accompanied by the transport of alpha particle's energy into LHW (and vice versa). Nevertheless, the ability of the feeding of the LH wave depends not only on the total amount of the transformable energy, but also on the diffusion velocity of particles.

Let us consider the simplest expression of Fisch and Rax [3] for the energy-space constraint (in their notation) $W_\perp + aX = const$, where X is the space coordinate and $a = \frac{m_\alpha \omega_c \omega}{k_\theta}$. Let $^{\prime}\tau$ is the characteristic time for the lost of the correlation , both for the diffusion in the velocity and configuration space. Defining the diffusion coefficient for the energy as $D_{W_\perp}$ and for the coordinate as D_X, where $D_{W_\perp} =< \frac{(\Delta W_\perp)^2}{\tau} >$; $D_X =< \frac{(\Delta X)^2}{\tau} >$ and where $<>$ labels the averaging, we obtain a simple relation between this two diffusion coefficients as $D_{W_\perp} = a^2 D_X$. Supposing that the region of RF fields forms a slab of the thickness of Δl, estimating the time element Δt, which is necessary for the space diffusion through Δl, and labeling the maximum of the available and transformable energy as $\Delta W_{\perp,max}$, then the transformable power density $p_{RF,\alpha}$ is $p_{RF,\alpha} \approx \frac{D_{W_\perp}}{a \Delta l}$.

The power density, describing the transformation of the energy between LHW and alpha particles therefore decreases with the increase of a.

4 Conclusion

In the present work, the possibility to utilize a part of the fusion alpha particles energy to improve the driven current efficiency was investigated. It was shown that the damping by electrons prevents the waves from reaching hot enough regions of the plasma column and the waves are damped before they could have been amplified. The mechanism of enhancing LH waves would necessitate the excitation of these ways deep inside instead of launching them at the plasma boundary.

The analytical approach, based on the discussion of the generalized lines of diffusion constraint, revealed the possibility of the energy transformation also for the parallel component of the energy. Moreover, it was shown that the induced radial diffusion can be caused by the radial component of the electric field, and the effect of the inhomogeneity of the magnetic field has been also investigated. The transformable power depends on the diffusion coefficients both in the velocity and in the radius.

References

[1] Pavlo P., Krlín L., Tlučhoř Z.: Nucl. Fusion 31 (1991), 711.

[2] Fisch N.J., Rax J.-M.: Nucl. Fusion 32 (1992), 549.

[3] Fisch N.J., Rax J.-M.: Phys.Rev.Lett. 69 (1992), 612.

[4] Fisch N.J.: Plasma Phys. Control. Fusion 35 (1993), A91.

[5] Pereverzev, G. V., Yushmanov, P. N., Dnestrovskiy, A. Yu. et al., Rep. IPP Garching No. 5/42 (1991).

[6] Krlín L., Pavlo P., Tlučhoř Z.: 16th Conf. Plasma Phys. and Thermonucl. Fusion, Budapest 1985, Vol. 9F, Part I, 88.

[7] Gášek Z., Krlín L., Tlučhoř Z.: Czech.J.Phys.B 37 (1987), 571.

[8] Kennel C.F., Engelmann F.: Phys.Fluids 9 (1966), 2377.

[9] Kaufman A.N.: Phys. Fluids 15 (1972), 1063.

[10] Becoulet A., Gambier D.J., Samain A.: Phys. Fluids B 3 (1991), 137.

[11] Krlín L.: Czech.J.Phys. 43 (1993), 43.; 19th Conf. Plasma Phys. and Thermonucl. Fusion, Innsbruck 1992, Vol.II, 1013.

BEAM-DRIVEN AND BOOTSTRAP CURRENTS IN JT-60 UPGRADE

M. Matsuoka, S. Ishida, Y. Kamada, M. Kikuchi, M. Kuriyama
K. Nagashima, O. Naito, and K. Ushigusa
Japan Atomic Energy Research Institute, Naka Fusion Research Establishment
Naka-machi, Naka-gun, Ibaraki-ken 311-01, Japan

ABSTRACT

We recently performed beam-driven current-drive experiments with a low fraction of bootstrap currents in a wide range of plasma parameters in JT-60 upgrade. The evidence of current profile modification by the beam-driven current with tangential neutral beam injectors. A high β_N, high β_p and ELMy H-mode plasma with possibly fully non-inductive current-drive by beam-driven and bootstrap currents was maintained for a considerably long duration with the combined injection of quasi-perpendicular and co-tangential beams.

NEUTRAL BEAM CURRENT DRIVE

Experimental Procedure

Recently re-oriented tangential beams [1] from quasi-perpendicular beams were used in this experiment. A pair of upper and lower units are co-directed and another pair of units are counter-directed with a tangency radius of 2.86 m. Figure 1 shows the beam traces to a poloidal cross section and two plasma configurations used in the experiment. Since the beams do not path through the plasma center, the beam-driven current will flow in the off-axis region.

Every two successive plasma shots were operated with the same plasma parameters but with different beam directions. Figure 2 shows a typical pair of shots; in the first (second) shot shown by solid (dotted) lines, counter- (co-) directed beams were injected first and later co- (counter-) directed beams were injected. Both upper and lower deuterium beams with 90 keV of beam energy were injected into a standard plasma. The difference in the loop voltage clearly indicates the presence of beam-driven current. The amount of beam-driven current I_{NB} can be estimated by the relation

$$I_{NB}=(I_P-I_{BS})\times\frac{V_{COUNTER}-V_{CO}}{V_{COUNTER}+V_{CO}} ,$$

where I_P and I_{BS} are the plasma and bootstrap currents, respectively. The bootstrap current was estimated using ACCOME, a steady-state non-inductive current analysis code [2]. To minimize the experimental uncertainty coming from the bootstrap current, perpendicular beams were not superposed except short pulse beams for T_i measurement by charge exchange recombination spectroscopy. The bootstrap current was estimated to be less than 6% of the plasma current in this experiment. $V_{COUNTER}$ and V_{CO} are resistive loop voltages with counter- and co-beams, respectively. The resistive loop voltage was evaluated by considering the contribution of the time-evolution of the internal inductance on the surface loop voltage. The internal inductance was obtained from magnetics measurement. Since the orbits of the produced energetic ions are not identical with co- and counter- beams, parallel and anti-parallel beam-driven current may not be the same amount. Such an effect is ignored in the present analysis. Instead, a beam-driven current as low as 6% of the plasma current can be distinguished still with good accuracy by this method.

Modification of Current Profile

The time-evolution of the internal inductance ℓ_i is compared in Fig. 3, where ℓ_i of the counter beam injection shot shifts up by 0.05 to match the values at the beam initiation. Only lower deuterium beam with 80 keV of beam energy was injected into the elongated plasma in these shots. Since the lower beam was injected into the upshifted plasma, the beam-driven current should be highly hollow. Figure 4 shows the driven-current density profiles by

ACCOME code for both Fig. 2 (standard) and Fig. 3 (elongated) cases. The code predicts no beam-driven current at $\rho<0.3$ for the latter case. As expected, ℓ_i decreased with the co-beam and vice versa with the counter-beam. The deviation of ℓ_i at the end of two-second beam injection between two shots was about 0.08, which is consistent with the steady-state limit 0.10 predicted by the numerical code.

The concept of current-profile control by neutral beams was proposed in the reference [3], where a beam angle is real-time controlled by a magnetic field prior to neutralization. The present fundamental experiment supports such a scenario.

Comparison with Numerical Result

Beam-driven currents obtained experimentally are compared with those obtained numerically in Fig. 5. The experiments were performed in the wide range of operating parameters; $\overline{n}_e$=0.13~1.5×10^{19} m^{-3}, I_p=0.5, 1.5 MA, beam energy: 40~90 keV, beam power: 1.0~3.6 MW, working gas: hydrogen and deuterium. In the hydrogen operation, hydrogen beams and prefill were used together with helium puff during discharge. Though the scatter of the experimental data is large, we see that the experimental result is consistent with theory over the very wide range more than one order, except the cases with very low plasma density ($\overline{n}_e$ =0.13~0.14×10^{19} m^{-3}). One of the most possible explanation for the very low density case is due to any enhanced loss mechanism of energetic ions.

DRIVEN-CURRENTS IN HIGH NORMALIZED BETA SHOTS

In a recent high normalized beta β_N experiment, we achieved to maintain the high β_N state for the duration ten times longer than the energy confinement time with the combined injection of the quasi-perpendicular and co-tangential beams. The high β_N state finished simply by the termination of the co-tangential beams. The main plasma parameters obtained at the same time are;β_p~3.5, β_N~2.5, ELMy H-mode with *H-factor*=1.7 at I_p=0.4 MA, B_T=1 T, P_{NB}=13 MW, q_{eff}=13. Such a good performance was not maintained with the combined injection of the quasi-perpendicular and counter-tangential beams [4].

Figure 6 shows the cross section of the high β_N plasma and beam traces. Since the central part of the elongated plasma moved outward due to the Shafranov shift, both upper and lower tangential beams contributed to drive beam-driven current near the plasma center. Note that the *e*-folding full width of the tangential beams are about 50 cm, which is also shown in Fig. 6.

Figure 7 shows the plasma profiles and the calculated beam-driven and bootstrap current profiles of the shot. The high β_N shot is characterized by the broader pressure profile than that of the high β_p but low β_N shots, in which the strong β_p-related collapse observed. The density profile shown has uncertainty since we derived it from only two-code FIR interferometry, but the broader profile was also confirmed by the soft X-ray emission profile.

A numerical calculation predicts the large driven-currents in this shot; 270 kA of beam-driven current and 150 kA of bootstrap current, the sum of which is almost equal to the plasma current. The calculated beam-driven current is peaked at the plasma center. This provides a favorable total profile of the driven-currents except the edge region from the view point of MHD stability. In the shot with the combined injection of the quasi-perpendicular and counter-tangential beams, the beam-driven current was in the anti-parallel direction at the plasma center. In addition, the ohmic current was induced at the plasma edge to compensate the anti-drive and to keep the total plasma current constant. The total driven-current profile was, therefore, unfavorable for MHD stability. The better plasma performance with the co-beams than with the counter-beams may be explained by these mechanisms.

CONCLUDING REMARKS

We performed a neutral-beam current-drive experiment with wide plasma parameters. The plasma current profile was modified by the off-axis beam as predicted. The observed beam-driven current is consistent with theory except the case with very low plasma density. A high β_N , high β_p and ELMy H-mode plasma with possibly fully non-inductive current-drive was maintained for a considerably long duration with the combined injection of quasi-perpendicular and co-tangential beams. These experimental facts suggest that neutral

beams can be used as a tool to modify the current profile and thus to improve the plasma performance.

The authors would like to acknowledge the members of the JT-60 Team for their cooperation and helpful discussions.

REFERENCES

[1] M. Kuriyama et al., Proc. 13th Sympo. on Fusion Eng., Vol. 2, IEEE (1989) 996.
[2] K. Tani et al., J. Comp. Phys. **98** (1992) 332.
[3] S. Yamamoto et al., in Plasma Phys. and Cont. Nuclear Fusion Research 1986, (proc. 11th Int. Conf. Kyoto, 1986), Vol. 2, IAEA Vienna (1987) 267.
[4] K. Ushigusa et al., this conference.

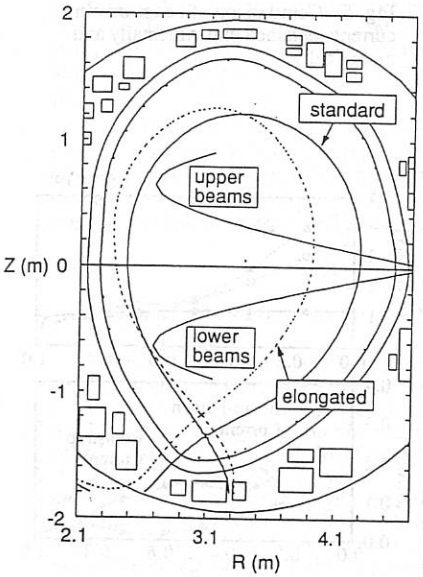

Fig. 1 Beam traces to a poloidal cross section and two plasma configurations used in the experiment.

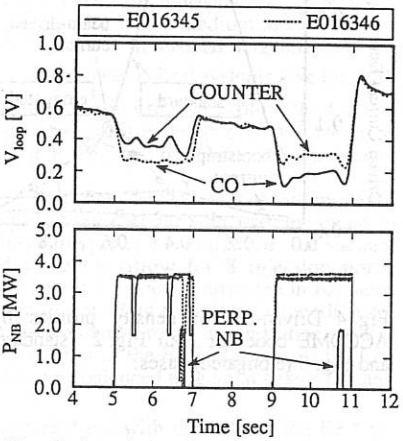

Fig. 2 A typical pair of shots; in the first (second) shot shown by solid (dotted) lines, counter- (co-) directed beams were injected first and later co- (counter-) directed beams were injected.

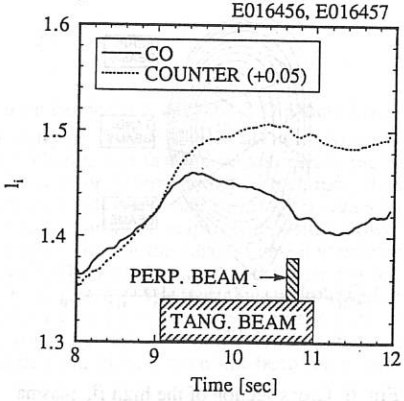

Fig. 3 Time-evolution of the internal inductance ℓ_i with co- and counter- beams.

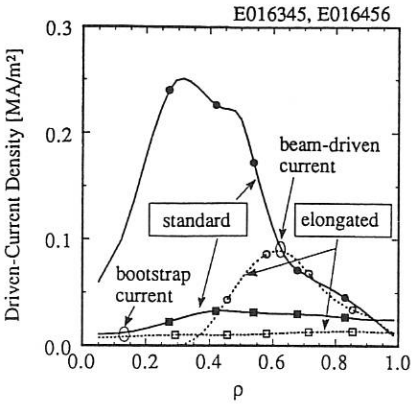

Fig. 4 Driven-current density profiles by ACCOME code for both Fig. 2 (standard) and Fig. 3 (elongated) cases.

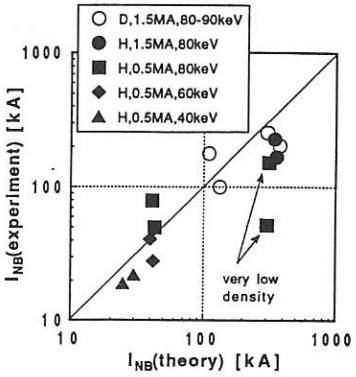

Fig. 5 Comparison of beam-driven currents obtained experimentally and numerically.

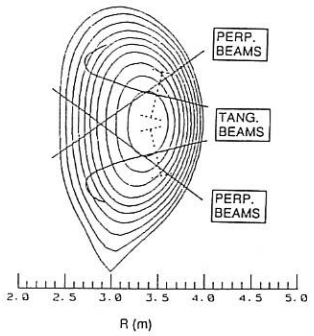

Fig. 6 Cross section of the high β_N plasma and beam traces. Dotted lines indicate the *e*-folding full width of the tangential beams.

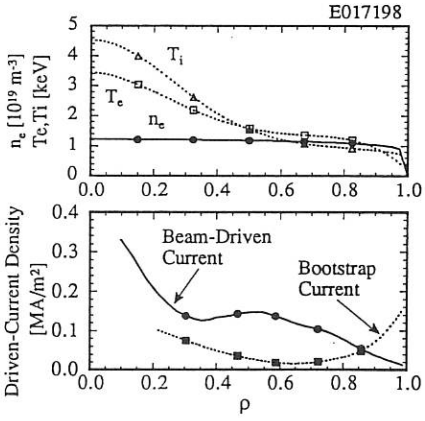

Fig. 7 Plasma profiles and calculated beam-driven and bootstrap current profiles of the high β_N shot.

NBI Physics studies in TJ-II

M. Liniers, J. Guasp, C. Alejaldre, A.Pérez-Navarro
Asociación EURATOM/CIEMAT, 28040 Madrid, Spain.

Introduction

Neutral beam injection is intended to constitute the main plasma heating device in the second stage of TJ-II experimental programme. TJ-II is a medium size stellarator (major radius =1.5 m, average plasma radius = 0.1 to 0.2 m, toroidal magnetic field = 1 T), with helical magnetic axis. Theoretical studies for these helical systems give higher β limits than in stellarators with circular magnetic axis. In order to explore the finite β effects on the heliac configuration, the first experimental stage with only 400 kW ECR heating (53.2 GHz, 2nd harmonic, X-mode) will be followed by 2 MW of neutral beam injection.

The vacuum vessel has a seemingly conplicated helical shape which determines to a large extent the injection geometry. In Fig. 1, beams #1 through #4 correspond to tangential injection and beams #5 and #6 to "quasi- perpendicular" injection. The vacuum vessel and support structure have been designed to allow for 8 injection ports, corresponding to horizontal, almost tangential beams that can be arranged in balanced couples, and another 8 ports (two per period) corresponding to "quasi- perpendicular" injection. The choice of injection angle is dictated by shine-through minimization: near to paralel injection is most favorable at the low densities of the ECR plasmas, so the first stage of the NBI heating will be carried out with two balanced tangential beams (#1 and #4 in Fig. 1)[1].

Beam trasmission studies have been carried out with the help of the DENSB code[2]. For a beam such as #1 in Fig. 1, the main beam limiting apertures are the injection port (rectangular in shape, 27x34 cm, vertically elongated), and the inner edge of the first tooidal field coil. Assuming a beamline length of 3 m and a beamlet divergence of 1.3° the transmission through these apertures is 85 %.

Beam absorption studies

Beam absorption calculations have been carried out with the 3-D Monte Carlo code FAFNER[3], adapted to the peculiar geometry of TJ-II. FAFNER allows evaluation of the scraper losses, shine-through, charge exchange and fast ion losses, giving radial profiles of fast ion generation and absorbed power on plasma ions and electrons. The code has been adapted at CIEMAT to estimate the loads due to shine through neutrals on the inside of the vacuum vessel and scrapers, and produce maps of deposited power densities onto those surfaces. An adequate representation of the vacuum vessel geometry is essential to the study of the fast ion losses in TJ-II due to the fact that there are regions where the plasma comes really close to the chamber walls. The particles are followed in real space coordinates, and the magnetic field, its gradients, and the magnetic surface average radius are interpolated in a "helical toroidal" grid from files previously generated with vacuum field line codes. Radial electric field effects have not been taken into account.

Beam power absorption as a function of the injection energy has been studied for three different plasma densities: low ($n_e(0)=2.0x10^{13}$ cm^{-3}), medium ($n_e(0)=5.8x10^{13}$ cm^{-3}) and high ($n_e(0)=1.1x10^{14}$ cm^{-3}).The results are shown in Figs. 2, 3 and 4.

Although the power available decreases with energy at all plasma densities, due to the shine through losses, the final absorbed power is roughly independent of energy for the medium and high density cases (Fig.2). Charge exchange losses are especially importatnt at the low densities (Fig. 3). Fast ion losses increase with density (Fig4). A slight improvement is observed for higher injection energies.

Ion generation profiles are well centered in the plasma for densities up to $1.1x10^{14}$ cm^{-3} (Fig. 5). The beam power density on the plasma ions and electrons is plotted in Fig. 6. In spite of the rounded ion capture profiles, and the assumed parabolic plasma density and temperature profiles, the power deposition profiles are very peaked for the range of densities studied. A more detailed study in which the fast ion birth points are selected inside circular sectors of variable radii, shows that fast ion losses are accountable for this fact: a large fraction of the ions deposited outside half the plasma radius are lost to the vessel wall, and those which stay in the plasma spend most of their time at the innermost region of the plasma.

This behaviour leads to a large contribution to the β from the fast ion component. This contribution may be calculated with the help of FAFNER. A stationary state of the beam can be constructed by adding the contribution of the followed particles at different times in a sequence from their birth to their complete thermalization. Fig. 7 presents the results of the fast component calculation for three different plasma densities. The largest contribution from the fast component occurs at the low densities, when the slowing down time of the ions is longer.

Summary

Neutral beam injection with two tangential balanced beams of 1 MW has been studied for the TJ-II plasmas. The chosen geometry gives acceptable transmission and beam deposition at the low densities of the ECR plasmas. At low plasma density, where shine through and charge exchange losses dominate, injection energies between 25-35 keV give better absorption. At medium and high densities fast ion losses take over, and a slight improvement can be observed for injection energies above 35 keV.

Power deposition profiles are very peaked on account of the large fraction of the outermost captured ions that are lost to the vacuum vessel wall. The fast ion contribution to the b has been estimated. This contribution approaches 25% at low density, when the energy content of the fast component is larger.

References

1.- Asociación Euratom-Ciemat, "Proposal for 2 MW Neutral Beam injection heating for the TJ-II flexible heliac".
Application for Euratom preferential support, Phase I, May 1992.
2.-F.P. Penningsfeld, "DENSB code". Report IPP 4/229, IPP Garching, 1986.
3.-G.C. Lister, "FAFNER, a fully 3-D Neutral Beam Injection code using Monte Carlo methods". Report IPP 4/222, IPP Garching, January 1985

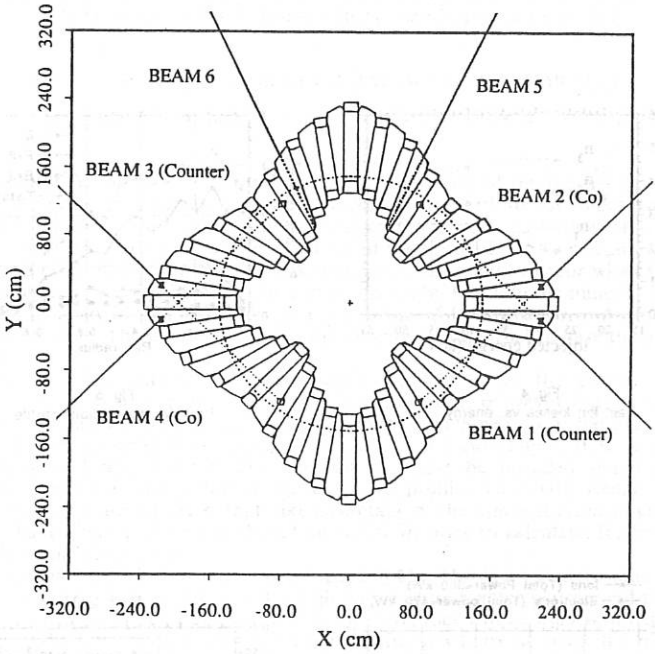

Figure 1: Geometry of Neutral beam injection into TJ-II

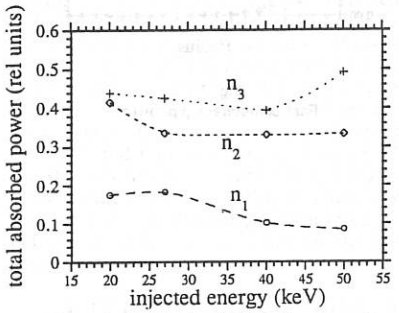

Figure 2: Power absorbed by the plasma ions and electrons as a function of injection energy for low, medium and high density.

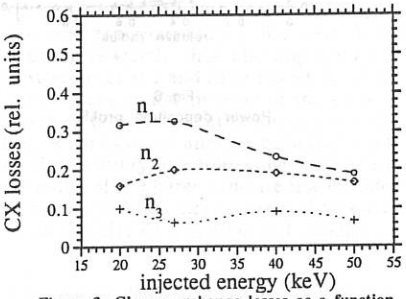

Figure 3: Charge exchange losses as a function of injection energy for the low, medium and high density cases

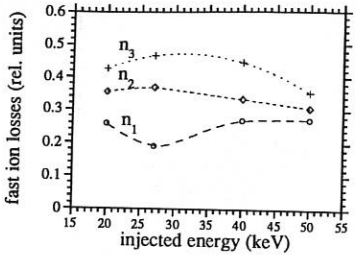

Fig. 4
Fast ion losses vs. energy

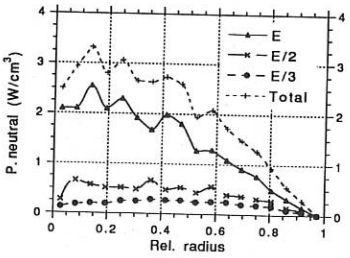

Fig. 5
Particle generation profile

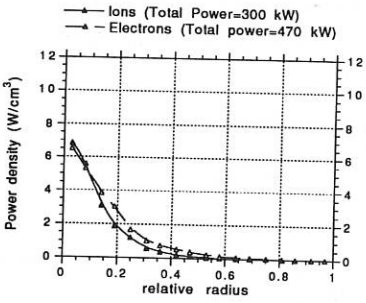

Fig. 6
Power deposition profile

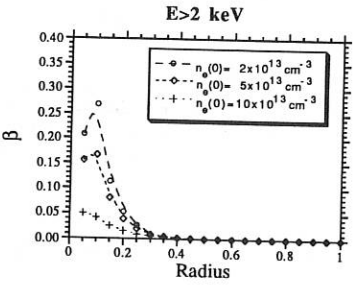

Fig. 7
Fast component β profile

A Simultaneous Description of Fast Wave e-TTMP And Ion Current Drive Effects on Shear in a Tokamak: Theory and Experiments in JET.

V.P. BHATNAGAR, G. BOSIA, J. JACQUINOT, F. PORCELLI.
JET Joint Undertaking, Abingdon, OXON, OX14 3EA (U.K.)

1. INTRODUCTION. A controlled local modification of the plasma-current profile, the safety factor q or shear (dq/dr) in a tokamak can lead to an improvement in its performance [1]. For example, enhanced confinement in JET discharges with deep pellet injection is found to be associated with a reversal of the shear [2]. Also, a significant control over the sawteeth behaviour in the JET tokamak has been found to occur when the shear at the q = 1 surface is modified by a dipolar-current driven by ICRF in the minority-ion heating regime [3]. This could give a handle on the ejection of fast particles and hence on burn control in a reactor. The above sawtooth control may also be used to ease the ash removal in a reactor.

When an ICRH antenna array is phased ($\Delta\phi \neq 0$ or π), the excited asymmetric $k_{//}$-spectrum can drive non inductive currents by interaction of waves both with electrons (TTMP and e-Landau damping) and ions at minority (fundamental) or harmonic cyclotron resonances depending upon the scenario. Therefore, in any modeling of ICRF current drive, both (electron and ion) current drive mechanisms must be included simultaneously to correctly represent the non inductive current drive profile. To devise scenarios of shear control by minority current drive, that take advantage of the inherent electron current drive as well, we have developed a model based on earlier theories to calculate, for the first time, the two effects simultaneously.

For current drive physics see a review paper [4]. The fast magnetosonic waves can penetrate to the centre of a high density, high temperature reactor plasma and they are not subject to any density limits. For electron current drive, they can be used with parallel phase velocity up to the speed of light enjoying a higher efficiency (current drive efficiency $\propto v_{//}^2$) at the Landau resonance ($\omega = k_{//} v_{//}$). The ion current drive can modify the gradient of the current profile (see below) adequately for sawteeth control at modest power levels. Our TTMP and e-LD current drive calculations have previously been discussed in [5]. In this paper, we concentrate on the minority current drive physics of the calculation although the results include both mechanisms.

The minority-ion current drive was first discussed by Fisch [6]. The resonant condition $\omega - \omega_{ci} = k_{//} \cdot v_{//i}$ suggests that the sign of the driven current reverses on the two sides of the minority cyclotron layer in a tokamak when the damping is not too strong. Since the effect is local, it can be used to advantage to modify the gradient of the plasma current density especially near the q = 1 surface. Both theoretically and experimentally, it has been found that two different mechanism can be used to control the sawteeth while allowing q on axis to drop below unity: (i) stabilization by minority fast-ion pressure and (ii) a reduction of the local (q = 1) magnetic shear [7]. Note that the latter effect requires phasing of the antenna array such as to excite asymmetric $k_{//}$-spectrum. Result of the present calculation provide the e-TTMP and minority current drive profile which form an input to another code that study the stability of resistive internal kink modes (sawtooth instability) encompassing both effects of fast-ion pressure and local magnetic shear [7]. Results of the latter code are not included here, though simulations [7] using minority CD profiles similar to those presented here (see below), show that sawteeth can be stablised ($\tau \cong 1$s) or destablised ($\tau \leq 100$ms) depending on the antenna phasing.

2. CURRENT DRIVE MODEL. To evaluate current drive, Fokker-Planck equation has to be solved together with the linear-wave field by a full-wave solution in the toroidal geometry. We use the ray tracing technique instead, which contains the essential physics including the effects of poloidal field on $k_{//}$. But, eigenmodes in a weak damping case are not described. We solve the phased, planar antenna-plasma coupling problem by a full-wave solution in the edge plasma region which fixes the initial conditions for ray tracing [8]. The

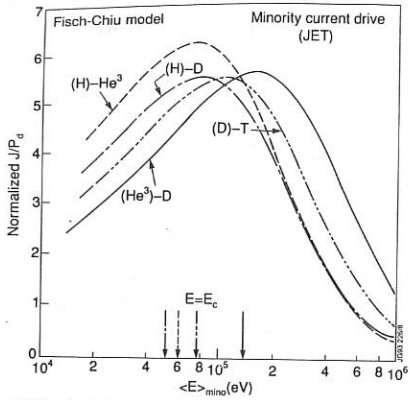

FIG. 1. Normalised minority CD efficiency factors.

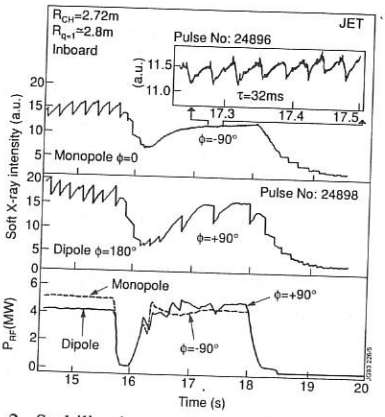

FIG. 2. Stabilisation and destabilisation of sawteeth in a minority CD experiment.

ray tracing solution in a 3-D tokamak geometry is then carried out in the central hot plasma region where the absorption takes place. The electron current drive efficiencies at each step of ray tracing are calculated by analytic fits, that include the effect of electron trapping and Z_{eff} etc. [9], to more complete Fokker Planck numerical codes. To calculate the minority ion current drive efficiencies, a flux-surface averaged ion power deposition profile is first generated with the ray tracing procedure. For the resulting power density on each flux surface, the minority ion energy distribution function is obtained by Stix [10] model. The Fisch efficiency factors [6] modified by Chiu [11] are used that take into account the back electron current, electron trapping, majority-ion rotation and Z_{eff}. Although the relative effect of minority-ion trapping, when rays access different regions of the plasma cross section, is taken into account, the actual transfer of particle from non-trapped to trapped regions and the resulting increased cancellation of minority current (Ohkawa effect) is not included. The normalized current drive efficiency $\eta = j_n/p_n$ used for e-TTMP current drive are given in [9] whereas the minority ion current drive normalised efficiencies calculated here are shown in Fig. 1 (see section 3) for several minority scenarios. Here, j_n and p_n are respectively the normalized current density and absorbed power density. However, note that v_{th} is defined as $\sqrt{T_e/m}$. In practical units, we find that

$$\frac{I(A)}{P(W)} = 3.05 \cdot 10^{18} \cdot \frac{T_e(keV)}{R(m) n_e(m^{-3}) \ln \Lambda} \cdot \eta$$

where R is the major radius and $\ln \Lambda$ is the Coulomb logrithm. Finally, the flux-surface averaged electron and minority ion current drive profiles in a non circular tokamak plasma are generated.

3. RESULTS . Normalised minority ion current drive efficiencies (η) mentioned above plotted as a function of minority ion average energy $<E>$ are shown in Fig. 1 for several minority scenarios. Note that η peaks when the $<E>$ is close to the critical energy E_c at which the minority ion relaxes roughly equally both on bakground electrons and ions. This was noted by Fisch [6] as the condition for maximum minority CD since the relative drift between minority and majority ions depends on the variation of the collision frequency ν with minority energy which is strongest at $E = E_c$. For $E \ll E_c$ minority ions collide heavily with majority and for $E \gg E_c$ they collide principally with electrons resulting in lower ∇v and lower η. Note that electrons will be dragged by drifting minority ions resulting in a return electron current. This will cancel the ion current when $Z_m = Z_{eff}$. But, due to electron trapping in the toroidal geometry, there is still a net ion current off axis despite cancellation on axis. Further, at higher energy, increased trapping of minority ions moving in the CD direction effectively

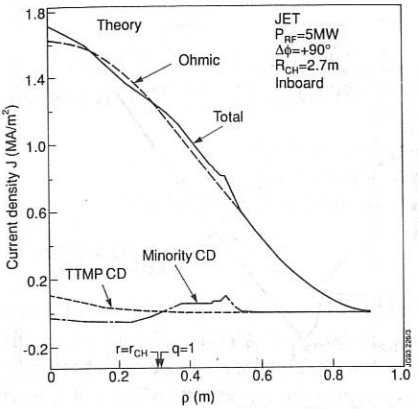

FIG. 3(a). Ray tracing CD profiles for data of Fig. 2; $\phi = +90°$ (stabilisation).

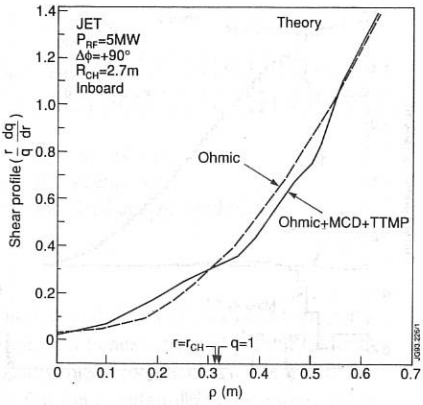

FIG. 3(b). Corresponding shear profile showing flattening near the q = 1 surface.

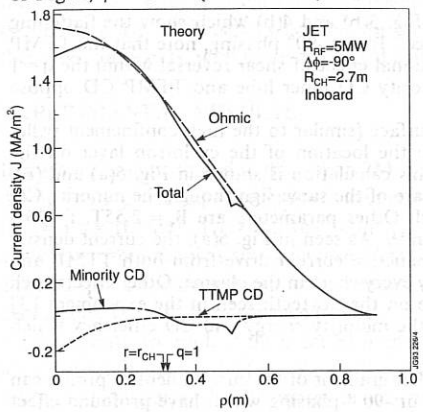

FIG. 4(a). Steepening of J near the q = 1 surface; $\phi = -90°$ (destabilisation).

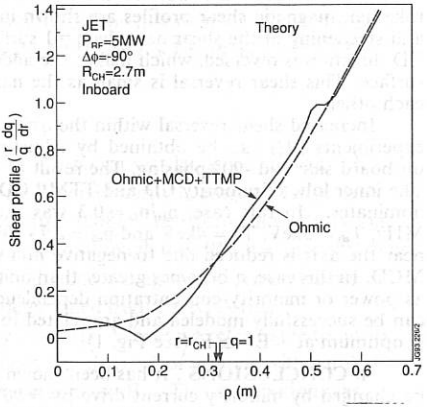

FIG. 4(b). Steepening of the shear near the q = 1 surface; $\phi = -90°$.

increases current in the opposite direction (Ohkawa effect) reducing current drive. The latter effect is not included here. This ion trapping effect is less significant when the cyclotron layer is located on the high field side.

In Fig. 2, we show the stabilisation of sawteeth at $P_{RF} \cong 5$MW at $+90°$ phasing where the minority cyclotron layer is located near the q = 1 surface on the high field side. For parameters and other details see Ref. 3. Note that in the early phase of the discharge, the dipole phasing and off-axis heating did not produce monster sawteeth. When the phase is reversed to -90°, there is a dramatic destabilisation of sawteeth with period $\tau \cong 32$ms. As simulated in [7], the stabilisation or destabilisation occurs due to the flattening or steepening of the current density profile (J) at the q = 1 surface. The local change in the gradient of J is produced by the minority current drive.

Using the present ray tracing CD code, the J profile flattening and steepening at the q = 1 surface for $+90°$ and -90° antenna phasing respectively has been shown to be due to the combined effect of TTMP and minority CD. See Fig. 3(a) and 4(a). The parameters used are those of the experimental case shown in Fig. 2. The TTMP CD peaks at the centre whereas the minority CD changes sign at the cyclotron layer position. The corresponding

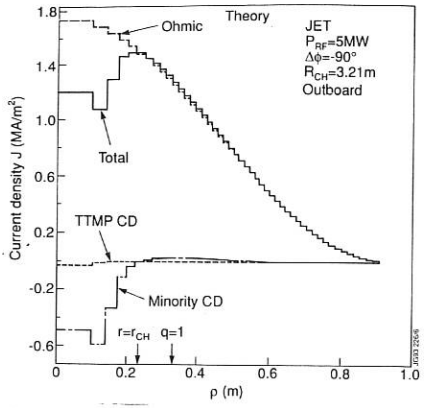

FIG. 5(a). A proposed scenario to produce strong shear reversal inside the q = 1 surface.

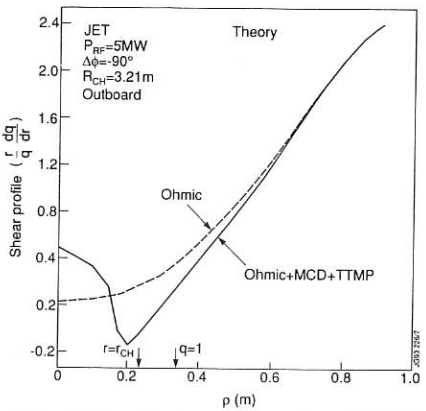

FIG. 5(b). Corresponding shear profile showing its inversion.

tokamak magnetic shear profiles are shown in Fig. 3(b) and 4(b) which show the flattening and steepening of the shear near the q = 1 surface. In the -90° phasing, note that the TTMP CD direction is reversed, which makes the additional effect of shear reversal within the q = 1 surface. This shear reversal is small as the minority CD inner lobe and TTMP CD oppose each other.

Increased shear reversal within the q = 1 surface (similar to the high confinement pellet experiments [2]) can be obtained by adjusting the location of the cyclotron layer on the outboard side and -90° phasing. The result of this calculation is shown in Fig. 5(a) and (b). The inner lobe of minority CD and TTMP CD are of the same sign though the minority CD dominates. In this case, $n_H/n_D = 0.3$ was used. Other parameters are $B_\phi = 2.55T$, $f = 36.5$ MHz, $T_{e0} = 5keV$, $T_{i0} = 4keV$ and $n_{e0} = 2.7 \cdot 10^{19} m^{-3}$. As seen in Fig. 5(a), the current density near the axis is reduced due to negative non inductive current drive from both TTMP and MCD. In this case, q becomes greater than unity everywhere in the plasma. Other effects such as power or minority concentration dependence on the sawteeth seen in the experiment [3] can be successfully modeled and are related to the minority energy and CD efficiency which is optimum at $< E > \cong E_c$ (see Fig. 1).

4. CONCLUSIONS . It has been shown that gradient of the current density profile can be changed by minority current drive by +90° or -90 ° phasing which have profound effect on sawteeth. Further, scenarios can be found that make the shear reversal possible inside the q = 1 region with the fast wave current drive at modest power levels. In other cases, one can make q > 1 every where in the plasma.

ACKNOWLEDGEMENT. We wish to thank our colleagues in the JET team and especially J.J. Ellis and D.F.H. Start for their expert help.

REFERENCES.

[1] REBUT P.H. et al, Proc. 12th IAEA Conf., Nice, France, 2 (1989) 191.
[2] HUGON M. et al, Nuclear Fusion, 32 (1992) 33.
[3] START, D.F.H. et al, Proc. 19th EPS Conf. Innsbruck, 16C (1992) part II, 897
[4] FISCH, N.J., Rev. Modern Phys, 59 (1987) 175.
[5] BHATNAGAR, V.P. et al, Proc. Int. Theory Workshop, Varenna, Italy, (1990) 243.
[6] FISCH, N.J., Nuclear Fusion, 21 (1981) 15.
[7] PORCELLI, F. et al, Proc. 19th EPS Conf.,Innsbruck, 16C (1992) part II, 901.
[8] BHATNAGAR, V.P. et al, Nuclear Fusion 24 (1984) 995.
[9] EHST, D. et al, Nuclear Fusion, 31 (1991) 1933.
[10] STIX, T.H., Nuclear Fusion, 22, (1975) 737.
[11] CHIU, S.C. et al, Nuclear Fusion, 23, (1983) 499.

FOKKER-PLANCK SIMULATION OF NEUTRAL PARTICLE FLUXES OBSERVED DURING ICRH ON JET

*C D Warrick, *M R O'Brien and *M Cox
JET Joint Undertaking, Abingdon, UK
*UKAEA/EURATOM Fusion Association, Culham, Abingdon, UK

INTRODUCTION

An understanding of the behaviour of fast (MeV) ion distributions in tokamaks is important since large populations of fusion products will be present in next step and reactor tokamaks. A Neutral Particle Analyser (NPA), viewing vertically and perpendicular to the magnetic field at R = 3.07m, has been used to measure such fast ion populations in the energy range of 0.28 to 1.04MeV on JET (R/a ≈ 3m/1.2m) [1]. Measurements were made of hydrogen minority in a ^{3}helium plasma where the position of the ion cyclotron resonance was varied during the pulse. This paper describes comparisons of the ion distributions deduced from these measurements, with those calculated using the CLIC ion Fokker-Planck code [2].

EXPERIMENTAL RESULTS

In the experiment studied in this paper, 7MW of ICRH power was launched (f = 42.6MHz, dipole phasing with $k_{||} \sim 7m^{-1}$) for fundamental hydrogen minority heating in ^{3}He plasma ($n_{e0} = 3.5 \times 10^{19}m^{-3}$, $T_{e0} = 8.5$ keV, $Z_{eff} \sim 2$, $n_H/n_{He} \sim 0.08$). The hydrogen minority ion cyclotron resonance was swept between 2.8m and 3.6m (through the NPA line of sight) over a period of ~ 10s during the shot. The variation in the line averaged hydrogen minority ion distribution with ICRH resonance position was determined from the NPA flux measurements, for each of the eight NPA energy channels. Where we refer to the minority ion distribution, denoted $\bar{f}(E_\perp, E_{||} \approx 0)$, we mean the "density" of protons with parallel energy ~ 0 and perpendicular energy in a narrow range about $E_\perp$. This distribution was calculated using the energy dependence of the cross sections of the major charge exchange processes and the (beryllium and carbon) impurity concentrations calculated by a charge state equilibrium code that models the relevant atomic processes. The neutral flux at a given energy, has a 'one-to-one' mapping with the line averaged distribution at that energy. Values of $\bar{f}(E_\perp, E_{||} \approx 0)$ from four of these channels are shown in Figure 1 together with CLIC code predictions described later. The line averaged distribution is largest when the resonance position is slightly to the low field side of the NPA line of sight (which is almost coincident with the magnetic axis). In the lower energy channels (<0.52MeV) the distribution falls off more quickly for low field resonance positions. These measurements are averaged over 500ms, spanning many sawteeth.

CLIC CODE RESULTS

The line averaged minority ion distribution inferred from the NPA has been compared to that calculated using the CLIC ion Fokker-Planck code [2]. The minority ion distribution function $f(v, \theta_0)$ (v is the speed and θ_0 is the pitch angle on the outside of the flux surface)

is calculated by solving the 'bounce-averaged' Fokker-Planck equation including collisions and ICRH. The effect of minority ion self collisions as well as collisions with electrons, majority ions and impurities are included. The ICRH operator models the full quasi-linear diffusion coefficient in velocity space using the wave field and spectrum values given by a ray tracing code and takes full account of trapped particle effects including the Airy function dependence of the diffusion coefficient for ions bouncing near to the resonance.

Runs of CLIC for several flux surfaces (between r = 10cm and 70cm) were performed for each of five different resonance locations spread around the NPA line of sight, taking into account variations in plasma parameters such as T_{e0} and n_{e0}. It should be noted that the code does not take account of plasma elongation (κ= 1.4 at the edge in this shot, but smaller near the magnetic axis) but assumes circular flux surfaces. However, this is unlikely to contribute any significant error in the results. The ion distribution function $f(v_{\perp_0}, v_{\parallel_0})$ derived for each of these runs was plotted as a contour map in $v_{\perp_0}$ and $v_{\parallel_0}$ space ($v_{\perp_0}$= $v\sin\theta_0$ and $v_{\parallel_0}$=$v\cos\theta_0$). Figure 2 shows these contours for a flux surface of radius r = 30cm in a central resonance case. Lines indicating the location of the trapped/passing particle boundary and the line of sight of the NPA (ie picking out those ions which bounce at 3.07m and therefore contribute to the neutral flux) are highlighted on this graph. As the resonance is scanned, the velocity space 'ridge' moves through the detector line of sight so that, at each energy, the particle flux has a peaked profile with respect to the resonance location. The width of this profile is determined by the width of the 'ridge'. Values of $f(v, \theta^*)$ (θ^* = pitch angle corresponding to ions bouncing in the NPA line of sight) for each of the eight NPA energies are calculated and, by summing these over all the flux surfaces, values of the line averaged distribution $\bar{f}(E_\perp, 0)$ for each energy at each resonance position are determined. These results are compared to the experimental ones for four energies in Figure 1.

For low energies, the CLIC profile is much broader than the experimental results indicate. However, at energies approaching 1MeV, a clear peak in the CLIC profiles is noted, slightly outboard of the NPA line of sight, and of a similar width to that measured. Indeed, CLIC data at an energy (~ 1.8 MeV) above that detectable by the NPA show further peaking.

DISCUSSION

It is clear that the NPA measurements show a peak in the value of $\bar{f}(E_\perp, 0)$ where the resonance crosses the NPA line of sight. This profile falls away in a Gaussian like manner as the resonance moves away from this position. This behaviour is reproduced at higher energies by the CLIC code and is explained as follows. As shown in Figure 2, the ion distribution peaks sharply at the pitch angle where the bounce points of the trapped ions coincide with the ICRH resonance layer. This is because these protons linger in the resonance region and are thus heated more strongly than ions which simply pass through the resonance. Thus the population of energetic ions visible to the NPA (ie those with small parallel energies) is a maximum when the NPA line of sight coincides with the resonant

major radius. The fall-off in $\bar{f}(E_\perp,0)$ as the line of sight and resonance differ, is a result of the sharp localisation in pitch angle shown in Figure 2.

The reason for the much broader profiles predicted by CLIC at lower energies is thought to be due to the following. As Figure 2 shows, the ion distribution is less peaked in pitch angle at lower velocities. This is due to broadening by pitch angle scattering as the initially energetic heated ions are collisionally slowed down giving a distribution less sharply peaked at the resonant pitch angle at lower energies. This explanation does not, however, resolve the discrepancy between experimental and simulated data. Possible explanations include:

- The ICRH wave parameters used in the code (predicted by ray tracing) may differ from those in the experiment.
- Collisional slowing down of the energetic ions may be stronger than the code calculates (ie an anomalous deceleration of the ions), meaning that pitch-angle scattering does not have time to broaden the distribution function.
- The CLIC distributions are from steady-state calculations. Since the sawtooth period is comparable to the collision time, sawteeth may expel the fast ions [3] before pitch angle scattering has had time to broaden the distribution at low energies. Thus, the fast ion population may be more peaked than that calculated by CLIC at lower energies.

It should be noted that the code does not include any transport effects, but these would be expected to broaden the profiles further.

In conclusion, NPA flux measurements at high energies (~ 1 MeV) have been successfully modelled using the CLIC ion Fokker-Planck code. However, CLIC predicts broader profiles than the NPA at lower energies. The reason for this discrepancy is as yet not fully understood. Further studies are continuing.

REFERENCES

[1] A Gondhalekar et al., IAEA Technical Committee Meeting on Alpha Particles in Fusion Research, May 1993, Trieste.
[2] M Cox and D F H Start, 1987 Int. Conf. on Plasma Physics, Kiev, Vol. 1, p232.
[3] F M Marcus et al., Plasma Physics and Controlled Fusion **33** (1991) p277.

ACKNOWLEDGEMENTS

This work was carried out as part of a JET Task Agreement and was funded jointly by the UK Department of Trade and Industry and EURATOM. The authors wish to acknowledge the considerable assistance of D F H Start and A Gondhaleker in these studies.

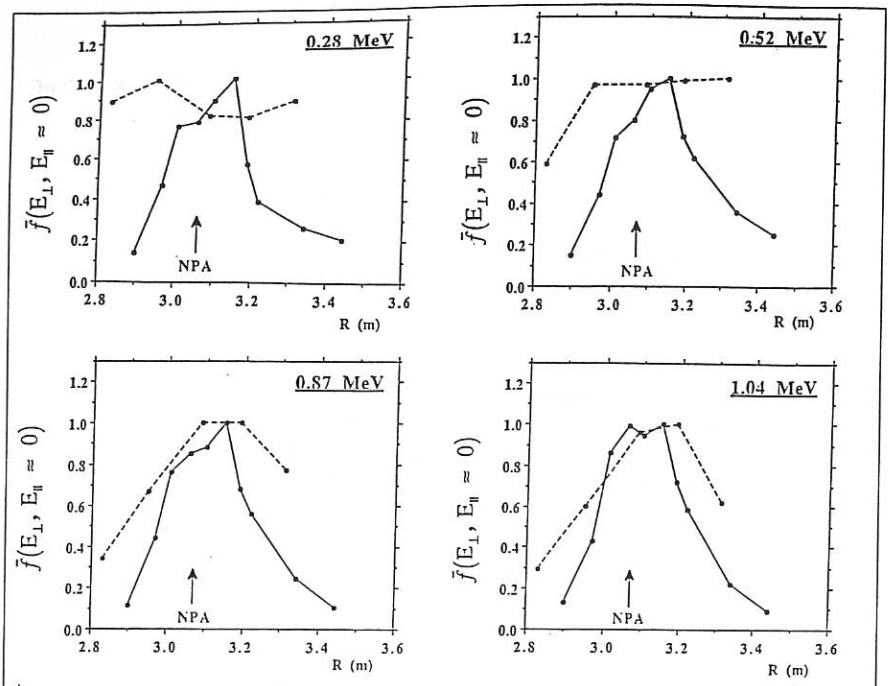

Figure 1 : Comparison of $\bar{f}(E_\perp, E_\parallel \approx 0)$ profiles derived experimentally (——) and simulated using the CLIC code (- - -).

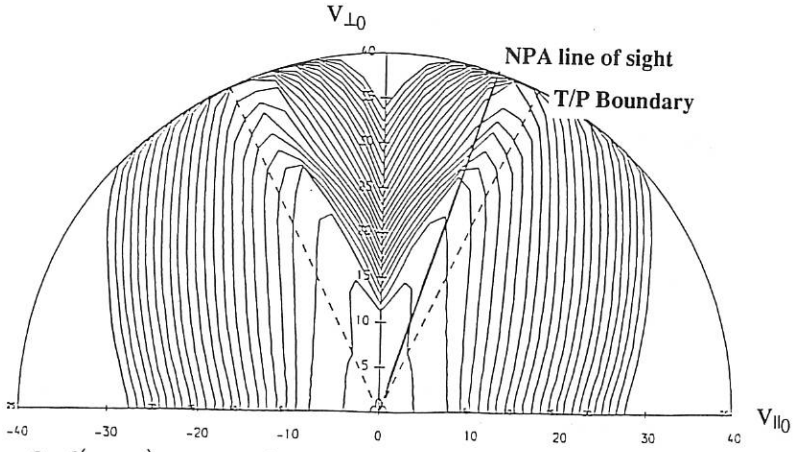

Figure 2 : $f(v_{\perp_0}, v_{\parallel_0})$ contours calculated from CLIC for a flux surface of radius r = 30cm, with the resonance at a central (2cm outboard) location. The maximum speed equates to an energy of ~10MeV.

Combination of Fundamental and Second Harmonic Minority Ion Cyclotron Resonance Heating on ASDEX Upgrade

J.-M. Noterdaeme, C. Hoffmann, M. Brambilla, K. Büchl, A. Eberhagen, C. Fuchs, O. Gehre, J. Gernhardt, O. Gruber, A. Kallenbach, W. Köppendörfer, W. Poschenrieder, N. Salmon, W. Schneider, F. Wesner, ICRH Team, ASDEX Upgrade Team

Max-Planck-Institut für Plasmaphysik
Euratom Association - D 85748 Garching - Fed.Rep.Germany

ABSTRACT
Second harmonic heating of an H component at concentrations between 3-25% in He and D majority gases has been successfully combined with fundamental heating. Even at low concentrations, the second harmonic heating is as efficient as the fundamental (minority) heating, because of coupling to the energetic H tail.

INTRODUCTION

The combination of fundamental heating and second harmonic heating of the same species is, to say the least, not a common scenario : few ICRH systems have the necessary wide frequency range to investigate this combination and at first sight the optimal conditions for both heating methods do not seem to overlap. Indeed : fundamental heating needs a small concentration of the resonant species to optimize the absorption, while second harmonic heating is usually performed at high concentration, since its absorption is proportional to the β ($\propto nT$) of the resonant particles, thus favoring a high density of those particles.
But the absorption at the second harmonic is a finite larmor radius effect, such that good absorption can also be obtained at sufficiently high temperature, for particles with large perpendicular energy. Heating of small concentrations of particles resonant at the second harmonic is thus in principle possible if a tail can be produced (by the second harmonic heating itself or by other means) and has been reported for JT-60 [1] in ohmic plasmas and in plasmas additionally heated by NI for H concentrations in the 10 % range. In the low minority concentration regime, fundamental heating can efficiently initiate or support the production of fast particles, providing optimal conditions for the second harmonic heating.
In the high concentration regime, there is a limit, for very large concentration, above which fundamental heating can no longer be used successfully. This limit depends on the antenna spectrum (higher n_ϕ allow a higher concentration) and on the plasma temperature. Using second harmonic heating then can provide the increased temperature for operation of fundamental heating at higher concentrations.

SYSTEM CAPABILITIES

ASDEX Upgrade [2] is a divertor tokamak with R=1.65m, a=0.5m, b=0.8m. Four generators with a frequency range from 30 to 120 MHz are available for a total ICRH power of up to 8 MW. The large frequency range allows the combination of different heating methods. Four antennas, located on the low magnetic field side consist each of two loops. They are operated 180° out-of-phase, resulting in a toroidal spectrum peaking near $n_\phi = 14$. First results with ICRH on ASDEX Upgrade are reported in [3] and [4].
For the experiments presented here ($B_t = 2T$ and $I_p = 600$ kA), H second harmonic heating (at 60 MHz) was performed and combined with H fundamental heating (at 30 MHz) in He discharges with an H concentration in the 5% range, and D discharges with a H concentration in the 15-25 % range. The H concentration is estimated from mass spectrometric measurement of the gas in the divertor exhaust during the discharge. This estimate is consistent in the case of (H)D with the ratio of the hydrogen isotope fluxes from the divertor plates, as measured from the hydrogen α lines.

TIME EVOLUTION OF THE PLASMA ENERGY
WITH SECOND HARMONIC HEATING, WITH AND WITHOUT PREHEATING

Without ICRH, the transport losses of the resonant ions are compensated in steady state by the electron-ion energy transfer term. When second harmonic heating is switched on, the power is absorbed by the resonant ions and by the electrons. The absorption on the resonant ions depends on the *energy of the resonant ions* and the *second harmonic power density*. For low energy ions and low power density, the power initially absorbed by the resonant ions is small (compared to the change in the losses and in the electron-ion energy transfer term), and increasing their energy will be a slow process (compared to the confinement time). If the increase in losses and transfer to the other particles is larger than the increase in absorbed power with increasing temperature, a change in energy could even be prevented altogether. At higher energy of the resonant ions or higher power density, their initial power absorption will be higher and the energy increase can be fast.

Fig. 1 shows the comparison of the energy increase for H second harmonic heating at the level of 200 kW, with and without H preheating of the minority at the fundamental frequency (300 kW at 30 MHz) for two consecutive shots in D (H concentration 15 %). Without preheating, no energy increase can be observed on the 100 ms timescale. On the other hand the H_α signal rise is a factor 50 % higher, despite an identical line averaged density (within 3 %), indicating enhanced plasma-wall interaction. The energy increase is correlated with the preheating, a *higher initial energy of the ions* leading to a faster increase in energy. Similar results are obtained at much lower H concentrations using H in He.

Fig. 2 shows three consecutive discharges in D (H concentration 25 %), with longer pulses of second harmonic power, at 200 and 300 kW, and without preheating (the time before the heating at the fundamental is added is 300 ms, and we discuss here only the phase up to the switch on of the fundamental heating).

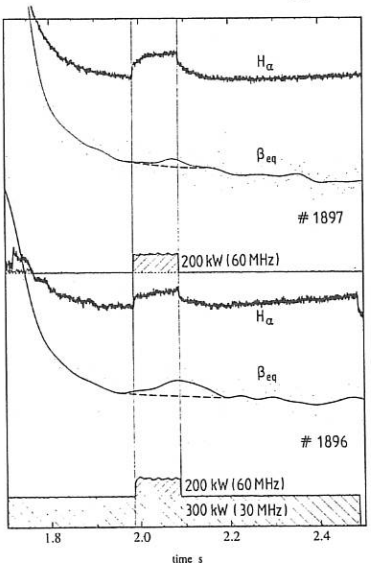

Fig. 1. Time traces for 2 consecutive discharges with 200 kW of second harmonic power (60 MHz), with and without preheating (300 kW at 30 MHz)

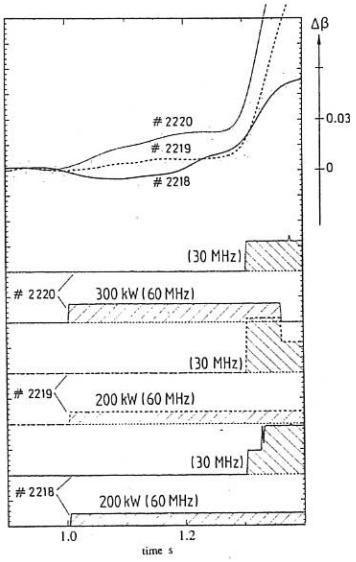

Fig. 2. Time traces for 3 consecutive discharges without initial preheating (30 MHz heating starts at 1.3s), but with different levels of second harmonic power

The first discharge at 200 kW shows an increase after 200 ms time, the second at the same power but marginally higher density does not show an energy increase within the 300 ms and the third at 300 kW a clear increase from the start. In this case, the increase is correlated with *sufficient second harmonic power*. Thus, at least at those concentrations, even without preheating, the second harmonic heating is able to bootstrap itself, as expected if the heating pulse is long enough, and the power level high enough. No data is yet available at the lower minority concentrations in He.

INDICATION OF A THRESHOLD

The energy increase obtained on a short time scale (100ms) with the second harmonic heating (H in He and D) seems to show a threshold behaviour depending on the level of preheating with 30 MHz. Fig. 3 includes points with second harmonic heating up to 200 kW (to stay below the level at which the second harmonic alone seems bootstrap itself) and power levels at the fundamental frequency between below 800 kW (to avoid effects due to the H-mode transition). The energy increase is normalized to the second harmonic power level and corrected by 0.75. The correction of the second harmonic power with 0.75 is to assist in the comparison with incremental confinement times (of the order of 30-40 ms) obtained with fundamental (minority) heating in L-mode (where an absorption coefficient of 0.75 has been measured). Fig 3. shows that below about 300 kW of preheating there is no increase, above this level the increase corresponds to an incremental confinement of around 60 ms.

The data does not allow a conclusion on the fact whether or not there is a difference of threshold between H in He (H concentration around 5 %), and H in D (H concentration around 15 %). It has further to clarified as to whether only the total power plays a role (as in the case of Fig. 2), for example for a combination where the total power is above 300 kW, but the fundamental power below 300 kW.

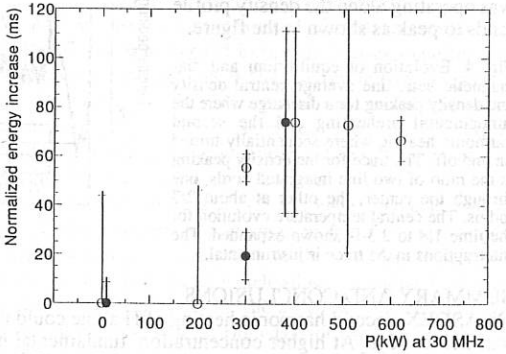

Fig. 3. Energy increase after 100 ms, normalized to the second harmonic power power, as a function of the preheating power. The open circles are for H in He, and the closed ones for H in D.

SEQUENTIAL USE OF SECOND HARMONIC AND FUNDAMENTAL HEATING

Fig. 4 shows a discharge where preheating with 300 kW of fundamental heating was combined with 300 kW of second harmonic heating at very low H concentration. The H concentration in He varied from typically 3% to 6% during the pulse. The additional β increase obtained with the 300 kW at 60 MHz is as large as the first increase with the 300 kW fundamental heating. After 300 ms of combined heating, the fundamental heating was switched off. Even now, with second harmonic heating alone, the β increase with the 60 MHz is similar to that of the original 30 MHz. The fundamental heating is then turned on again 600 ms later for 300 ms of combined heating.

Comparison of diamagnetic β and equilibrium β seems to indicate an increased perpendicular tail energy during the periods of combined heating, as expected if the second harmonic couples to the high energy particles in the tail and preferentially increases their energy.

Some additional observations are worth underlining.The evolution of the density is for ICRF heated plasmas often a good indicator of how good the central absorption is (for reduced central absorption, the interaction with the edge tends to increase, resulting in a density increase, whereas power with good central absorption leads to a reduction in energy and particle

confinement and thus to a decrease in density). At turn-on of the fundamental heating the density decreases (A), the addition of second harmonic leads briefly to a density increase (B). The turn-off of the fundamental heating leads to a density increase (C, C'), indicating a worsening of the conditions for the second harmonic. The turn-on of the fundamental heating leads to a decrease (D), confirming that the conditions improve. Note that during the first period of combined heating, after the brief density increase the density decreases suddenly (E), this time is correlated with an increase in the diamagnetic signal and a change in sawtooth appearance. During the periods where the second harmonic was operating alone the density profile tends to peak as shown in the figure.

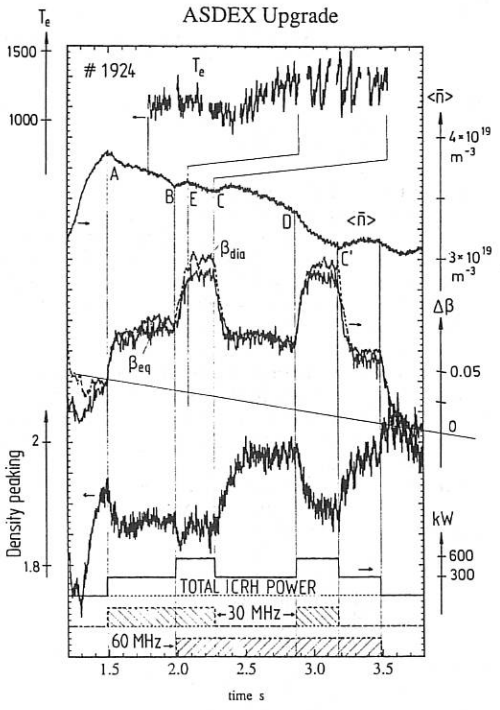

Fig. 4. Evolution of equilibrium and diamagnetic beta, line average central density and density peaking for a discharge where the fundamental preheating and the second harmonic heating where sequentially turned on and off. The trace for the density peaking is the ratio of two line integrated cords, one through the center, the other at about 2/3 radius. The central temperature evolution for the time 1.8 to 2.3 is shown expanded. The interruptions in the trace is instrumental.

SUMMARY AND CONCLUSIONS

On ASDEX, second harmonic heating of H alone could not be used when the H concentration was below 10%. At higher concentration, fundamental heating did not work. In neither case was the combination of both methods tried. On ASDEX Upgrade, the second harmonic has been combined with fundamental heating and works successfully at concentrations as low as 3% and up to at least 25%. The addition of fundamental minority heating improves the conditions for second harmonic heating at low minority concentrations. It would be interesting to use second harmonic power as preheating to improve the conditions for the fundamental heating at even higher concentrations.

The combination of both methods extends the range in which each method can be applied. Since fundamental heating and second harmonic act on different parts of the distribution function of the ions, active control of this distribution function may be performed over a wide range of experimental conditions, increasing the experimental flexibility.

REFERENCES

1. H.Kimura et al., ICRF heating experiments in JT-60 and JT-60U, RF Heating and CD of Fusion Plasmas (EPS Conf., Brussels, 1992),Vol 16E, 93.
2. W. Köppendörfer et al., ASDEX Upgrade, Fus. Techn. (12th Symp., Jülich, 1982) Vol. 1, 187.
3. J.-M. Noterdaeme et al., First results of ICRH on ASDEX Upgrade, RF Power to Plasmas (10th AIP Conf., Boston, 1993) to be published.
4. M. Kaufmann, Edge Physics and H-mode studies on ASDEX Upgrade, Controlled Fusion and Plasma Heating, (invited paper, 20th EPS Conf., Lisbon, 1993) to be published in Plasma Phys. Contr. Fus.

ICRF HEATING EXPERIMENTS IN THE W7-AS STELLARATOR USING A NARROW $K_{||}$ SPECTRUM ANTENNA

M. Ballico, G. Cattanei, V. Plyusnin*, W7-AS team & ICRH team
Max-Planck-Institut für Plasmaphysik, Garching 85747, GERMANY
* NSC Kharkov Institute of Physics & Technology 310108 Kharkov UKRAINE

ABSTRACT

First experimental results using a toroidally broad ICRH antenna on the W7-AS modular stellarator are presented. The antenna, which is located on the high-field side in the elliptical section, has been designed to launch only a narrow $k_{||}$ spectrum to the plasma. As consequence it should be able to radiate the same power into the plasma with a voltage at the antenna surface a factor of $2 \sim 3$ lower than an equivalent double strap antenna. This is expected to reduce the production of fast ions in the SOL and the impurities influx. The antenna is not provided with a Faraday screen, allowing the flexibility to launch preferentially the the FW or the IBW by a simple change of the phasing of the feeders currents. Results are presented indicating that although the dominant field component of the antenna should be $\tilde{b}_{||}$, an unexpected high loading, possibly attributable to launching of the IBW masks the intended 2nd harmonic FW heating.

INTRODUCTION

Previous ICRH experiments [1] in W7-AS have used a conventional double strap antenna on the low-field side with an optically closed Faraday screen. Second harmonic heating experiments at both 2.5 and 1.25 T showed no clear evidence of heating even at the maximum coupled power of 300 kW. In the D(H) and He(H) minority heating at 2.5 T an initial increase of the total stored energy, with a relatively low efficency $\frac{dW}{dt}/P_{IC} = 0.2$, is soon counteracted by a large metallic impurity influx and consequent radiative cooling. A large amount of unconfined fast ion population and a RF-induced density and impurities rise were also observed.

In order to minimize these deleterious effects a broad antenna [3] has been designed, which by removing the unwanted part of the $k_{||}$ spectrum reduces the antenna near fields. The broad antenna extends 1 m toroidally and 40 cm poloidally. It is earthed to the vessel wall at both ends and is fed independently at 4 positions (A,B,C,D in fig.1) which allows changing both the $k_{||}$ spectrum and the polarisation of the electric field radiated by the antenna. The vacuum $\tilde{b}_z$ field profile in fig.2 is notable in the absence of field peaking at the edges of the antenna strap, and around the image currents in the antenna side-limiters, which in a conventional antenna lead to a spectrum rich in high axial wavenumbers. The vacuum $\tilde{b}_z$ field decreases exponentially away from the antenna surface with the expected $|k_r| \approx |k_{||}| \approx 6m^{-1}$, ensuring that the FW launching efficiency has a weak dependence on the antenna-plasma separation. When the current in two toroidally adjacent feeders is $\pi/2$ out of phase this antenna also gives a very directive narrow spectrum which can be used for current drive generation.

Due to stress limitations on the field coils of W7-AS, operation of the machine has been restricted to half-field operation regime at 1.25T, which, given the generator tunability 30 MHz$<$ f $<$ 120 MHz, allows only hydrogen plasma 2nd harmonic ICRF heating. Two typical target plasmas were used:

(i) 400 kW ECRH plasma, characterized by hot ($\approx$ 1 keV) electrons , cold ($\approx$ 200 eV) ions and relatively low density. The ECRH cutoff at $6 \times 10^{19} \mathrm{m}^{-3}$ makes density control critical, especially if the density rises during the ICRH pulse.

(ii) 800kW NBI plasma, with high density and ions and electrons strongly coupled, with a temperature $\approx$ 400eV. Because of the low electron temperature, these discharges are sensitive to radiation collapse due to enhanced impurities influx or strong gas puffing.

EXPERIMENTAL RESULTS

Initial experiments were performed feeding only the bottom two ports (B & D) of the antenna, and relying on a half wavelength resonant line on each of the top two ports to provide the desired π phasing up/down and left/right. Although the currents in the 4 ports of the antenna were equal, and the phasings correct in vacuum, during the plasma the currents in the top half of the antenna fell to less than 10% of those in the bottom half. This is attributable to the high measured 6 $\Omega \leq$ R $\leq 12\Omega$ plasma loading (much higher than expected for preferencial FW coupling) reducing the Q of the resonant circuit below the value needed for correct feeding the upper half of the antenna. Up to 500kW was coupled to an ECRH plasma in this regime, always to be accompanied by a strong density increase. The initial rate of density increase was proportional to the coupled power however no significant impurities influx was observed. The plasma loading was independent of power over 5-500kW.

Following these experiments, the antenna feeding system was revised to actively feed all 4 ports of the antenna, by T-junctions at the voltage maxima, thus also providing a useful impedance transformation. This ensured that the desired antenna phasing was maintained throughout the plasma. The plasma loading was observed to range between 8 $\Omega \leq$ R $\leq$ 16 Ω and was, for the standard ι = .34 limiter plasma, independent of power. However when the limiter was open (31 cm) and ι =.5 a power dependence of the loading i.e. decreasing from 16 Ω (P=10 kW) to 10 Ω (P > 100 kW) was observed. During the RF pulse both the plasma density and the total stored energy increased while T_e and T_i remained almost unchanged. The practical power limit during ECRH discharges is due to the RF induced density rise, which eventually increases the density beyond the ECRH cutoff and terminates the discharge. It was observed, however, that below some power limit (P $\leq$ 200 kW) the density ceased to increase before the end of the RF pulse, and could be decreased to the initial value by the feed-back control of the gas valve fig.3. The maximum power for which the density rise could be controlled was increased by a power ramp at the beginning of the RF pulse. Over about 200 kW, however, this technique became impractical due to the limitation in the power ramp length (t $\leq$ 100 ms). Although in vacuum the RF power is limited by thermal outgassing and consequent arcing only at 280kW (33kV) and can last for over 600ms, during NBI discharges, the power was always limited to 150kW (12kV) for 100 ms, decreasing with pulse length, due to arcing in the connections to the antenna (not in the antenna itself, which was observed by a video camera). The observation that both the reactive and resistive antenna loading depends on edge and not on line density indicates a coupling mainly to the edge plasma. Langmuir probe measurements made in the SOL toroidally opposite the antenna showed an increase in the plasma potential by 30 V for 60 kW of ICRH power although no change in either the edge density or electron temperature was observed. This suggests that the power is being deposited in the edge region near to the antenna. Some evidence of FW eigenmodes excitation was observed in the antenna loading and in the RF probe signals after ECRH switch-off when the line density was still high but the plasma temperature was decreased fig.4.

DISCUSSION

The central observation in the first experimental results from the broad antenna is the very large antenna loading which remains large even at very low values of the line density and of the total stored energy where FW loading should be negligible.

This loading is much larger than can be theoretically expected for the FW even at the maximum stored energy (R < 2 Ω). The predicted fraction of the RF power launched in the FW should be under 10%.

The absence of power dependent loading indicates against loading due to Langmuir currents to the antenna surface as seen in comparable experiments with unshielded antennas. [2,6] .

The strong dependence of the loading from the scrape-off density indicates IBW launching by the parallel currents as the best candidate for the large loading observed. The increase (almost twice) in the loading after changing the antenna feeding scheme can thus be explained by assuming that the mirror currents in the plasma decrease the value of the parallel inductance and hence increase the ratio of toroidal to poloidal currents in the antenna. The upper and lower parts of the antenna can in this case be considered as separate.

Numerical comparison with theory is difficult due to the sensitivity of IBW to the exact values of the density in the region very close to the antenna ($n_e \leq 3 \times 10^{16} \mathrm{m}^{-3}$). However, although the large loading could be consistent with some choice of the unknown density at the antenna, the theoretical model [3] failed to predict the large decrease in the parallel inductance.

The increase in the line density, without evidence of bulk heating is similar to the results of several IBW experiments [4,5] .

The presence of modes, both on magnetic probes and above a large background loading of the antenna, when the stored energy is low (low damping), is consistent with only a small part of the RF power going in the FW which is only seen during sharp eigenmodes.

REFERENCES

[1] M. Ballico et. al., Radio Frequency Power in Plasmas, Charleston, S.C. 1991, AIP Conference Procedings 244

[2] M. Ballico et. al., J. Plas. Phys. and Cont. Fus. Vol.30, pp1331 to 1338 (1988)

[3] G. Cattanei, Topical Conf. on RF heating and Current drive of Fus. Dev.,Europhysics conf.(1992) abs.,vol.16e,p121

[4] T.Seki et. al., Nuc. Fus.,Vol.32,No.12 (1992)

[5] R. I. Pinsker et. al. in Radio-frequency power in plasmas, Proc. 8th Top. conf. Irvine, C.A., (1989), Am. Phys. Soc. N.Y. pp350

[6] G.G.Borg et. al., Nuc. Fus.,Vol.32,No.5,(1992)

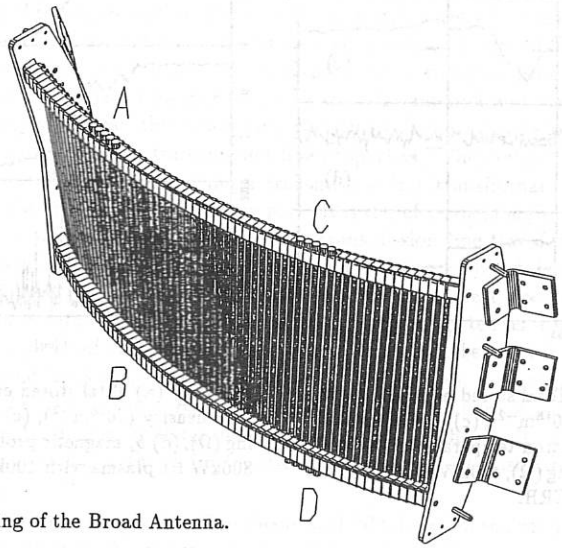

Figure 1: Drawing of the Broad Antenna.

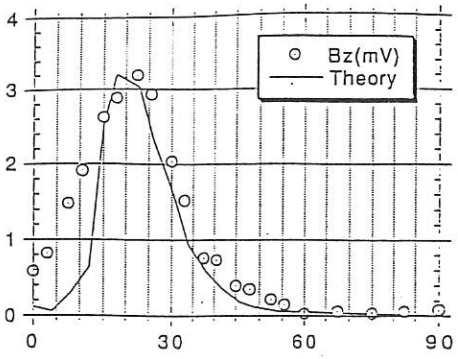

Figure 2: Profile of $\bar{b}_z$ vs. z (cm) along the midplane of the antenna for π phasing feeding at A & B.

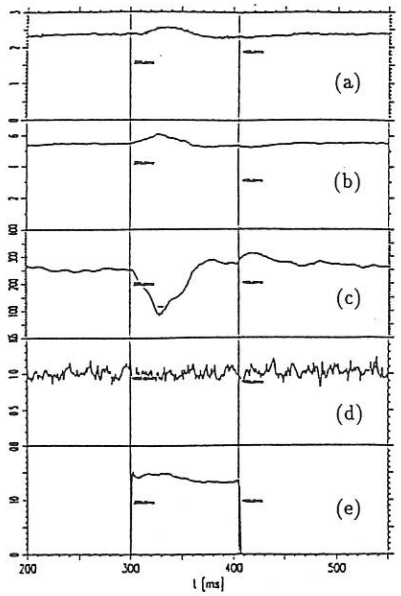

Figure 3: (a) Total stored energy (kJ), (b) Line density (10^{18}m^{-2}), (c) Gas Flux (a.u.), (d) Soft-X electron temperature (keV), (e) Antenna loading (Ω), 400kW ECRH plasma with 100kW ICRH.

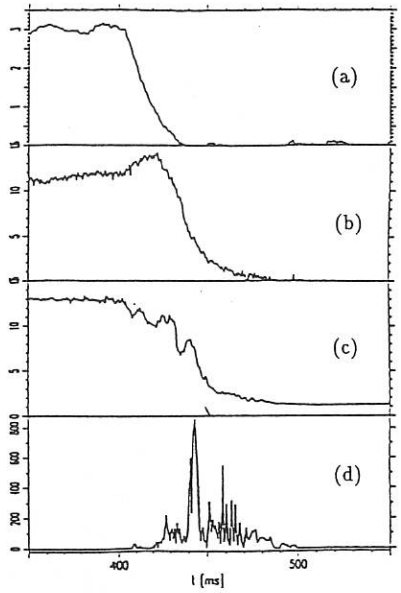

Figure 4: (a) Total stored energy (kJ), (b) Line density (10^{18}m^{-2}), (c) Antenna loading (Ω), (d) $\bar{b}_z$ magnetic probe signal (a.u.), 800kW NI plasma with 100kW ICRH.

COMPARISON OF THEORETICAL AND CALCULATED ICRH ANTENNA RESISTANCE ON ASDEX UPGRADE

C. Hoffmann, F. Hofmeister, J.-M. Noterdaeme, M. Brambilla, C. Fuchs, O. Gehre, ASDEX-Upgrade Team and ICRH Team

Max-Planck-Institut für Plasmaphysik, EURATOM Association, D-85748 Garching, Fed. Rep. of Germany

1 Introduction The progress in the understanding of the coupling of electromagnetic waves in the ion cyclotron range of frequencies to high temperature plasmas is based on the experience gained in using ICRH antennas on Tokamaks and Stellarators, and on theoretical predictions that are made with antenna-plasma coupling codes. The measurement of crucial parameters like the antenna resistance allows in return to validate the simplifications that necessarily have to be made in any theoretical model. For ASDEX Upgrade[1], a finite Larmor radius code in slab geometry (FELICE[2]) was used. It includes a sophisticated, self consistent antenna model, with the simplification that the distance between central and return conductor is taken to be constant.

2 Definition of the antenna resistance In order to compare experimental findings with theory a common definition for the antenna resistance is necessary. There are various ways to define an antenna resistance. In Fig.1 the HF-generator, the antenna, and the impedance matching network are schematically depicted [4]. The complex impedance at the antenna base, point A in Fig.1, consists of the imaginary part resulting from the capacitive and inductive properties of the conducting structures of the antenna and the real part due to mainly the radiation loss and a small fraction of transmission line losses. The antenna base impedance is one possible choice for a common definition. Yet for an assessment of the radiation properties of a particular antenna and comparison with others it has disadvantages: the conducting structures of the antenna possess besides capacitive and inductive, also transmission line properties. The complex resistance at the antenna base therefore results from a transmission line transformation both of the real radiation resistance and the imaginary part. It is therefore meaningful to discard the imaginary part of the antenna impedance by a transmission line transformation. This procedure constitutes the definition for the antenna resistance, which is used here and will be denoted by R_{eff}. It yet requires that the imaginary part does not vary with changing plasma parameters. The transformation can be depicted as a substitution of the antenna by a piece of transmission line, with the same characteristic impedance as the feeding line and the length determined by the transformation terminating in a purely real load. The definition reads: $R_{eff} = (2 \cdot Z_0^2 \cdot P/V_{max}^2)$, where V_{max} is the voltage maximum of the standing wave along the transmission line, P the resulting power flowing towards the antenna and Z_0 the characteristic impedance of the transmission line, which is in our case $Z_0 = 25\Omega$.

3 Measuring the density profile The theoretical calculation of the coupling resistance is crucially determined by the density profile in the vicinity of the antenna. On AUG this profile was now experimentally determined. Fig.2 shows the 8 sightlines of the infrared

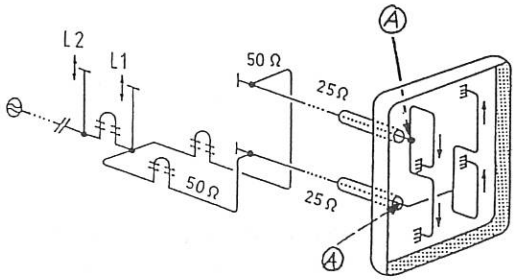

Figure 1: *Schematic drawing of the generator, antenna and impedance matching network of the ICRH-system on AUG*

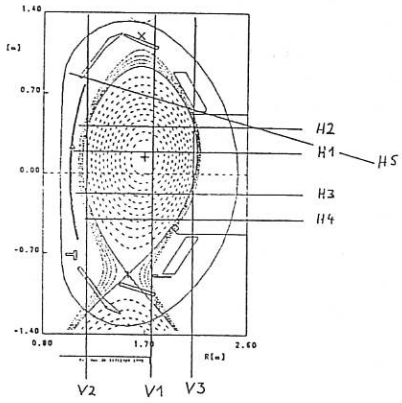

Figure 2: *The infrared interferometer consists of 8 chords looking in the directions drawn. The infrared laser works at 195μm. The vertical outer channel V3 and the five horizontal channels H1-5 are used to infer the complete profiles shown in Fig.5. Channel V3 together with shifting the plasma position is used to extract a refined edge density profile.*

interferometer system[5]. For a sufficiently exact resolution of the edge density this number of integrals is far too small. Therefore experiments were conducted, where the plasma was displaced radially. Assuming that the density does not change in a co-moving reference frame, the vertical sight line through the outer plasma edge taken at *different* times is the analogue to narrowly spaced vertical sight-lines in the edge taken at *one* time. The small edge region can be approximated by a simple geometry. The geometry is chosen to be analytically integrable. Our choice are circular flux surfaces with equal curvature radius but different centers, see Fig.3. The centers of these circles are not even close to the geometric or magnetic center of the plasma. The origin of the coordinate system in the moving plasma is taken to be the center of that circle that is tangent to the separatrix. The coordinate of the centers of the surfaces is denoted by $\tilde{r}$. A parabolic model in $\tilde{r}$ for the edge density is assumed: $n(\tilde{r}) = a + b \cdot \tilde{r} + c\tilde{r}^2$. The coefficients a, b, c result from the inversion of the following linear system containing the line integrals $N(R_i)$:

$$N(R_i) = a + b \cdot \left[R_i - \frac{1}{2Z_i}\kappa(R_k, Z_i)\right] + c \cdot \left[R_i^2 + R_k^2 - \frac{R_i}{Z_i} \cdot \kappa(R_k, Z_i) - \frac{1}{3}Z_i^2\right] \quad (1)$$

where R_k is the curvature radius, R_i the position of the sightline in the co-moving frame, Z_i the integration limit in the Z-direction: $Z_i = \sqrt{R_k^2 - [R_k - (\tilde{r}_{outside} - \tilde{r}_i)]^2}$ and $\tilde{r}_{outside}$ being the center of that circle that is tangent to the antenna limiter. $\kappa(R_k, Z_i)$ is the

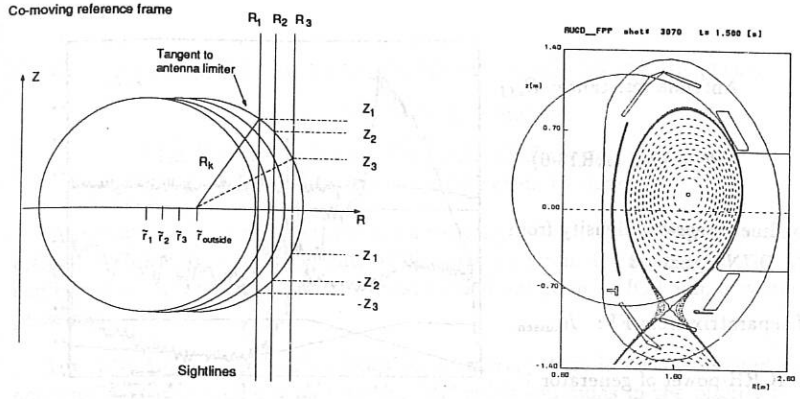

Figure 3: *Left: Approximate geometry in the plasma edge (the distances between $\tilde{r}_i$ are smaller in reality), Right: comparison with true flux surfaces.*

integral of a circle: $\kappa(R_k, Z_i) = Z_i\sqrt{R_k^2 - Z_i^2} + R_k^2 \arcsin(Z_i/R_k)$. For discharge 1781 for example the edge density upon inversion was calculated as $0.91 - 11 \cdot \tilde{r} - 111 \cdot \tilde{r}^2 [10^{19}\mathrm{m}^{-3}]$. The density profile over the whole domain is supplied by another author[3], using the full flux geometry calculated from magnetic measurements and the subset of DCN-channels mentioned in the caption of Fig.2. The full profile together with the improved edge density profile is then used as input to the FELICE code to calculate wave propagation and absorption and subsequently the antenna resistance.

4 Experimental Results The relation among antenna resistance and distance between antenna limiter and separatrix was established for two separate groups of experimental data. The first is a shot by shot survey where this distance is constant in the flat top phase of the discharge when the resistance is measured. Fig. 5 shows the relation for L- and H-Mode shots as well as for different plasma currents. The comparable L- and H-Mode results for $I_p = 600$kA exhibit a 20% decrease of the antenna resistance in H-Mode. Fig.4 displays the rich features that are contained in the time development of the antenna resistance of antenna 1 together with the geometrical information on the distance between separatrix and antenna limiter (R_{aussen}), the line-integrated density seen by channel V3 of the infrared interferometer, the H_α-signal in the edge and the power delivered by HF-Generator 1. The linear ramp-up of the ICRH-power leads to a linear rise in the coupling resistance. With the onset of the inward motion of the plasma the antenna resistance drops. Yet shortly afterwards there is an H-Mode transition that introduces some complicated dynamics of both density and resistance. With continued inward motion the decrease of the antenna resistance is resumed. At the turning point of the motion the resistance rises again. Its subsequent oscillation is correlated with on- and off-switching of the neighbouring ICRH-system 2. It remains to be analyzed whether the influence of system 2 on system 1 is due to changing plasma conditions that are induced by the switching such as a change of the near antenna density, or whether this influence is a direct electromagnetic coupling, reflected in the voltage measured in system 1.

5 Comparison with theory Comparison between experiment and theory, Fig. 5 and 6, depends strongly on the definition for the distance. In the theoretical calculation the distance between Faraday screen and separatrix was varied. The experimental points were set up using the distance between separatrix and antenna limiter. This distance differs from the other by the distance between antenna limiter and the Faraday screen plus half of the thickness of the Faraday rods. The density profiles derived from the DCN measurement were cast into an analytical form as an input to the FELICE calculation:

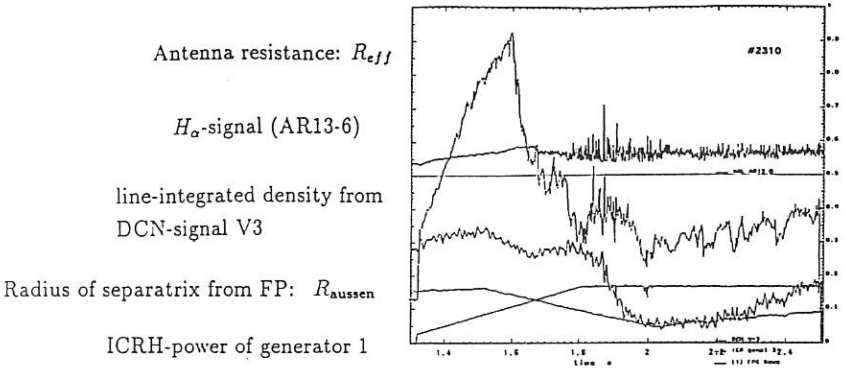

Figure 4: *Antenna resistance of ICRH-system 1 for discharge 2310, where the plasma column was moved away and towards the antenna. 130 ms after initiating the plasma motion an H-Mode transition occurs.*

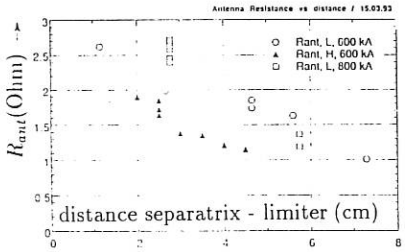

Figure 5 *Comparison of the antenna resistance in L- and H-Mode for varying distances between separatrix and antenna limiter for two different plasma currents.*

L-Mode: $n_{edge} = 1 \cdot 10^{19}\mathrm{m}^{-3}$, $n_{central} = 4 \cdot 10^{19}\mathrm{m}^{-3}$
H-Mode: $n_{edge} = 0.2 \cdot 10^{19}\mathrm{m}^{-3}$, $n_{central} = 8 \cdot 10^{19}\mathrm{m}^{-3}$

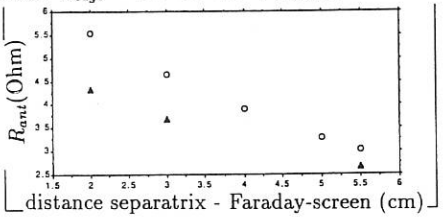

Figure 6 *Theoretical calculation of the antenna resistance, varying the distance for L-Mode (o) and H-Mode (▲) density profiles.*

L-Mode: $n(\tilde{r}) = n_{edge} + (n_{central} - n_{edge})(1 - \tilde{r}^{2.5})$
H-Mode: $n(\tilde{r}) = n_{edge} + n_{central}(1 - 0.5\tilde{r} + 2.1\tilde{r}^2 - 17.1\tilde{r}^3 + 43.2\tilde{r}^4 - 38.\tilde{r}^5 + 9.4\tilde{r}^6)$
The distance between central and return conductor was taken to be 15 cm. Both experiment and theory agree upon the fact that the effects of plasma quantities on the antenna resistance, in particular the distance between plasma and antenna and the plasma edge density are prominent. Only through a series of experiments with fixed parameters it will be possible to decide how crude or otherwise acceptable the approximation of a constant distance between central and return conductor in the present antenna model is. On the other hand the sensitivity of the antenna resistance to changing plasma edge parameters inspires future work to focus on the antenna resistance as a plasma diagnostic.

References

/1/ J.-M. Noterdaeme et al., First Results of ICRH on ASDEX Upgrade, RF power to plasmas, 10th AIP Conf. Boston, 1993, to be published.

/2/ M. Brambilla, Modelling Heating and Current Drive in the Ion Cyclotron Frequency Range, Plasma Phys. and Contr. Fusion, **35**, 1993), p.A141.

/3/ J.C. Fuchs, Tomographic methods on AUG, private comm.

/4/ F. Hofmeister al., Acquisition of technical data and matching procedures for the ICRH System on ASDEX Upgrade, SOFT 92.

/5/ O. Gehre, Measurement of electron density profiles on ASDEX by HCN Interferometry, Proc. Basic & adv. diagnostic techniques, Varenna, 1986.

SELF-CONSISTENT MODELING OF IC MINORITY HEATING.

M. Brambilla, C. Hoffmann

Max-Planck Institut für Plasmaphysik-Euratom Association
D-8046 Garching bei München, Germany

Abstract. We have developed a numerically efficient procedure to evaluate the dielectric tensor and the coefficients of the wave equations for a plasma not in thermal equilibrium. An application to the quasilinear description of ICR minority heating is presented.

Introduction. To model h.f. heating and current drive in fusion–oriented plasmas, one should ideally couple a code solving Maxwell's equations in the plasma to a code solving the Fokker-Planck quasilinear equations in two velocity and one spatial dimensions (assuming averaging over magnetic surfaces to be justified). This very ambitious task is still on the border of what is computationally feasible. To get reliable results with reduced computational effort, two lines of action are open. On the one hand, semi–analytic solutions of the kinetic equations can be used; in the case of minority IC heating accurate solutions of this kind have been obtained by Stix [1]. On the other hand, one should develop methods to evaluate the coefficients of the wave equations as efficiently as possible. The direct numerical integration of the required multiple integrals over the velocity distribution functions starting from the numerical solution of the FP equation has been pioneered by Koch [2], and refined by Van Eester [3].

Generalized Plasma Dispersion Functions. We have chosen a complementary approach, which assumes that a representation of the distribution functions of the form

$$F_\alpha(v_\perp, v_\parallel) = \frac{e^{-v_\perp^2/\alpha_\perp^2}}{\pi\alpha_\perp^2} \frac{e^{-v_\parallel^2/\alpha_\parallel^2}}{\sqrt{\pi}\alpha_\parallel} \Psi(v_\perp^2, v_\parallel) \qquad (1)$$

is available (a sum of terms of this form is obviously admissible). As in [2]–[3], we consider here as a first step the effects of deviations from thermal equilibrium on the local dispersion relation (LDR) of the plasma. This makes sense, since the same integrals required in the local dielectric tensor $\underline{\underline{\epsilon}}$ appear in the coefficients of the wave equations as well (cfr. e.g. [4]). Moreover, a detailed investigation of the LDR is in any case a necessary preliminary to the solution of the wave equations.

We have developed two methods to compute $\underline{\underline{\epsilon}}$. The first does not make any assumption on the wavelength, but relies on $\Psi(v_\perp^2, v_\parallel)$ being factorized, or a sum of factorized terms. In the second approach $\Psi(v_\perp^2, v_\parallel)$ is arbitrary, and the dielectric tensor is expanded in powers of $\lambda = k_\perp^2 \alpha_\perp^2 / 2\Omega^2$ using Neumann's series for products of Bessel functions. Although convergent for all real λ, this approach is numerically efficient only if the perpendicular wavelength is not much shorter than the thermal ion Larmor radius. In particular, this method is well suited to the small Larmor radius (FLR) approximation, which in the ion cyclotron frequency domain is valid for all waves with the exception of ion Bernstein waves of order larger than 2.

The FLR expansion naturally leads to introduce the following *Generalised Plasma Dispersion Functions* (GPDF's):

$$\tilde{Z}^{(k)}(x) = \frac{1}{\sqrt{\pi}} \int_{-\infty}^{+\infty} \frac{e^{-u^2}}{u-x}\, g^{(k)}(u)\, du \qquad \tilde{W}^{(k)}(x) = \frac{1}{\sqrt{\pi}} \int_{-\infty}^{+\infty} \frac{e^{-u^2}}{u-x}\, \frac{dg^{(k)}}{du}\, du \tag{2}$$

where $u = v_\parallel/\alpha_\parallel$, $w = v_\perp/\alpha_\perp$, and

$$g^{(k)}(u) = \frac{2}{k!} \int_o^\infty w^{2k+1}\, e^{-w^2}\, \Psi(w,u)\, dw \tag{3}$$

The two functions $\tilde{Z}^{(k)}$ and $\tilde{W}^{(k)}$ are related to each other through

$$\tilde{Z}'^{(k)}(x) = -2\left(\mu_0^{(k)} + x\,\tilde{Z}^{(k)}(x)\right) + \tilde{W}^{(k)}(x) \tag{4}$$

where we have introduced the moments over parallel velocities

$$\mu_n^{(k)} = \frac{1}{\sqrt{\pi}} \int_{-\infty}^{+\infty} u^n\, e^{-u^2}\, g^{(k)}(u)\, du \tag{5}$$

The "reduced" distributions $g^{(k)}(u)$ can be evaluated using Gauss–Hermite or Gauss–Laguerre quadrature. The evaluation of $Z^{(k)}$ is greatly facilitated by the simple trick of rewriting Eq. (2) in the form

$$\tilde{Z}^{(k)}(\zeta) = \frac{1}{\sqrt{\pi}} \int_{-\infty}^{+\infty} \left(\frac{g^{(k)}(u) - g^{(k)}(\zeta)}{u-\zeta}\right) e^{-u^2}\, du + g^{(k)}(\zeta)\, Z(\zeta) \tag{6}$$

where Z is the PDF of the Maxwellian plasma. The first integral is always regular, and can again be evaluated efficiently with Gauss–Hermite quadrature formulas. The singularity for real $\zeta = x$ is fully taken care of by the function Z, for which fast and accurate algorithms are available [5]. For large argument, moreover, $|\zeta| \gg 1$, an asymptotic expansion of the GPDF is easily derived:

$$\tilde{Z}^{(k)}(\zeta) \simeq -\frac{1}{\zeta} \sum_{n=0}^{\infty} \frac{\mu_n^{(k)}}{\zeta^n} + i\sigma\sqrt{\pi}\, e^{-\zeta^2} g^{(k)}(\zeta) \tag{7}$$

where σ depends on the sign of $\mathrm{Im}\,(\zeta)$ according to Landau's prescription.

For lack of space, we omit here the full dielectric tensor, and we only mention that in the FLR approximation only GPDF's of order 0, 1, and 2, are needed. In the examples, all FLR terms where consistently taken into account.

An example. With $\alpha_\parallel^2 = \alpha_\perp^2 = kT_M/m$, and suffixes M and i referring to the majority and minority species, respectively, the Stix solution [1] of the quasilinear FP equation for the case of ICR minority heating can be compactly written

$$F_i(v) = \frac{F_o}{\pi^{3/2}} \exp\left\{-\left(\alpha + \frac{\beta}{1+q\gamma^{2/3}v^2}\right) v^2\right\} \tag{8}$$

where

$$\alpha = \frac{\tau\epsilon}{\epsilon + D} \qquad \beta = \frac{1+\tau\epsilon}{1+\epsilon+D} - \alpha \qquad \gamma = k_1 \frac{\epsilon + D}{1+\epsilon+D} \tag{9}$$

Here $v^2 = u^2 + w^2$, F_o is the normalisation constant, $\tau = T_M/Te$; moreover $k_1 = (4/3\sqrt{\pi})\,(A_M/A_i)^{1/2}$, $q \simeq 0.4135$, and $\epsilon = (n_e/Z_M^2\, n_M)\,[(m_e/m_M)\tau]^{1/2} \ll 1$. Finally

$$D = 6.208\ 10^{-3} \left(\frac{A_i}{A_M}\right)^{1/2} \frac{Z_i Z_M}{A_i A_M} \frac{T_M^{1/2}}{10^{-20} n_e} \frac{W_i}{10^{-20}\, n_i} \tag{10}$$

is the normalised quasilinear diffusion coefficient. W_i is the power deposited in the minority in W/cm^{-3}, temperatures are in keV, densities in m^{-3}. Equation (8) can be interpreted in terms of a two–population distribution, the temperatures of the "bulk" and "tail" being respectively

$$T_i^{bulk} = T_M \frac{1+\epsilon+D}{1+\epsilon(T_M/T_e)} \qquad T_i^{tail} = T_e \left(1 + \frac{D}{\epsilon}\right) \tag{11}$$

If $D \gg \epsilon$ and $T_M/T_e = O(1)$, T_i^{bulk} depends only on the majority temperature, while T_i^{tail} depends only on the electron temperature.

In Fig. 1 the functions $-x\tilde{Z}^{(k)}(x)/\mu_o^{(k)}$ with $k = 0$, 1 and 2, evaluated for the distribution (8) for a typical ASDEX-Upgrade situation, are compared to the PDF for the two–Maxwellian distribution (11) with the same energy content. The latter is much more easily evaluated, but gives a rather poor approximation just for $|x| = O(1)$, where most of the IC absorption takes place. In Fig. 2 we have compared the dispersion relation around the minority IC resonance in the Ohmic limit with Maxwellian distribution, and when $W_i = 2$ W/cm^{-3}. For the parameters chosen ($n_e = 8 \cdot 10^{19}$ m^{-3}, 5% H$^+$ in D$^+$, $T_e = T_M = 2$ keV, $B_o = 3$ T, $f = 45$ MHz, $n_\parallel = 5$), the ohmic case is in the mode–conversion regime, with the evanescence region before the ion–ion resonance fully separated from the cyclotron resonance. In the heated case the increased average energy of the minority, 8.36 keV ($T_i^{bulk} = 2.38$ keV, $T_i^{tail} = 25.5$ keV), causes a transition into the minority regime. A substantial increase of the first transit absorption and a suppression of mode conversion to Bernstein waves are to be expected.

Conclusions. The example illustrates the relevance of quasilinear effects in the estimation of the heating efficiency, and stresses the importance of adequate approximations of the distribution functions for a really consistent evaluation of these effects. The procedure developed for this purpose is computationally efficient, so that it can hopefully be used also in the solution of full–wave problems. It is also easily extended to other situations, for the investigation of wave propagation and instabilities in plasmas not in thermal equilibrium.

[1] T.H. Stix, *Nucl. Fus.* **15** (1975) 737.
[2] R. Koch, *Phys. Letters* **A 157** (1991) 399.
[3] D. Van Eester, *Plasma Phys. Contr. Fus.* **35** (1993) 441.
[4] M. Brambilla, *Plasma Phys. Contr. Fus.* **31** (1989) 723.
[5] W. Gautschi,*SIAM Rev.* 9 (1967) 24.

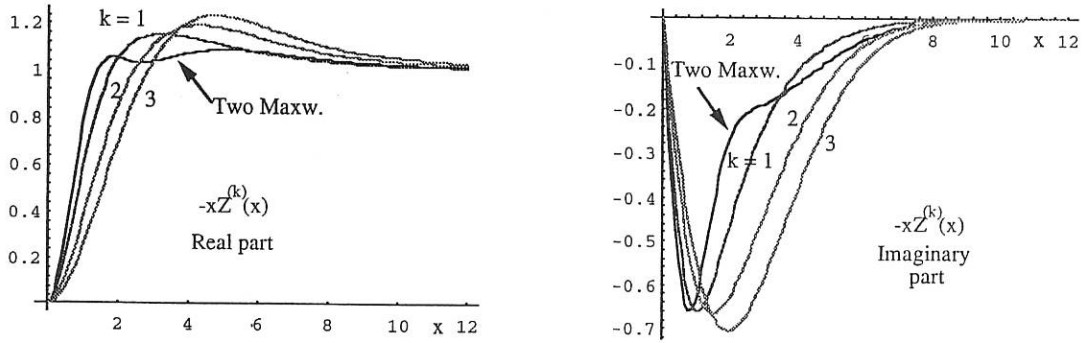

Fig. 1 - Generalised Plasma dispersion functions for the Stix ICR heated minority distribution functions. Plasma parameters given in the text, $W_i = 2$ W/cm^3.

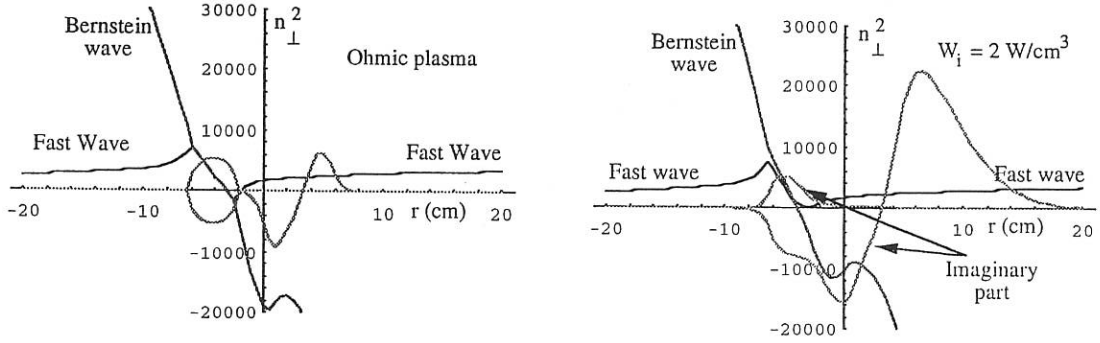

Fig. 2 - Dispersion relation near the H^+ cyclotron resonance, plasma parameters given in the text.

Solution of the Nonlocal Wave Equation of an IBW Mode Conversion Problem

H. Werthmann[1] and M. Brambilla
Max Planck Institute for Plasma Physics
Boltzmann-Str. 2, D-8046 Garching b. München

1. Introduction

The object of this work is the theoretical investigation of an Ion Bernstein Wave (IBW) heating scheme, based on the excitation of higher order IBWs by mode conversion of externally launched slow cold-plasma waves at low harmonics of the ion cyclotron frequency. The investigation of the conversion efficiency requires the solution of the wave equation within the mode conversion layer, which at these frequencies is located in the scrape-off of a TOKAMAK. The wavelength of an IBW is of the same order of magnitude as the thermal ion-gyroradius, so that the relevant wave equation of a strongly dispersive plane stratified plasma is of an integro-differential type. We have integrated it using a Galerkin finite element method. Numerical solutions show that conversion is complete if damping can be avoided. To investigate the effect of local damping on the conversion efficiency, we have derived an explicit expression for the power dissipated per unit volume by an IBW propagating in an inhomogeneous plasma slab, which is suitable for numerical calculation of power deposition profiles.

In contrast to vacuum waves IBWs are essentially longitudinally polarised, so that they cannot be excited directly at the plasma edge. In the heating scheme under investigation, mode conversion of an externally launched slow wave (SW) into an IBW in the vicinity of the cold lower hybrid resonance is used as a coupling mechanism [1]. The latter is illustrated in Fig. 1, which shows the solution of the local dispersion relation, i.e. the refractive index in perpendicular direction $n_\perp$, plotted versus the radial coordinate x in the scrape-off range between the limiter at x_a and a point x_b near the wall. The plot was calculated for a parallel refractive index $n_\parallel = 7$, a wave frequency ω of 438 MHz and exponentially decaying density and temperature profiles with e-folding lengths of 1.80 cm and 10.65 cm, respectively. The mode conversion layer, where three modes exist simultaneously, is imbedded between the SW and the IBW branch. To make the heating scheme operative, the IBW should propagate further into the plasma and deposit its energy via electron Landau damping or Ion-Cyclotron-Resonance damping.

2. Basic System of Equations

To close the wave equation, $\frac{c^2}{\omega^2}\underline{\nabla} \times (\underline{\nabla} \times \underline{E}) = \underline{E} + \frac{4\pi i}{\omega}\underline{J}$, the electric current density $\underline{J}$ must be expressed in terms of the electric wave field $\underline{E}$. Assuming the validity of the linear Vlasov equation, the constitutive relation $\underline{J} = \underline{\mathcal{F}}[\underline{E}]$ is a linear functional of $\underline{E}$. Though being in general nonlocal, for modes of which the perpendicular wavelength is much larger than the thermal gyroradii this linear functional can be approximated through a local, i.e. differential expression. Since however the wavelength of an IBW is of the same order of magnitude as the ion gyroradius, the fully nonlocal constitutive relation has to be taken into account to solve the mode conversion problem.

To model the scrape-off in front of a launcher we assume a plane stratified plasma with equilibrium parameters varying in x-direction and the static magnetic field parallel to the z-direction.

[1]The work of one of the authors (H.W.) has been financed by the Friedrich-Schiedel-Stiftung für Energietechnik.

Then the constitutive relation relevant for this so called slab-geometry can be written as a relation between the x-dependent amplitudes of corresponding Fourier-modes of the electric wave field and the current density [2]-[3],

$$\underline{J}(x;k_y,k_\parallel) = \int_{-\infty}^{\infty} dx'\ \underline{\underline{\sigma}}(x,x';k_y,k_\parallel)\cdot\underline{E}(x';k_y,k_\parallel)\ . \tag{1}$$

The tensorial kernel $\underline{\underline{\sigma}}(x,x';k_y,k_\parallel)$ is given by a two-fold inverse Fourier transformation of the conductivity kernel in Fourier space, which is in turn represented by an integral expression,

$$\underline{\underline{\sigma}}(x,x';k_y,k_\parallel) = \int_{-\infty}^{\infty} dk_x e^{ik_x x}\int_{-\infty}^{\infty} dk'_x e^{-ik'_x x'}\int_{-\infty}^{\infty} dx'' e^{i(k'_x-k_x)x''}\underline{\underline{\sigma}}(k_\perp,k'_\perp;\psi,\psi';k_\parallel;x'') \tag{2}$$

In the equation above, $k_\perp$ and $k'_\perp$ denote perpendicular wave numbers and the arguments $\psi = \arctan(k_y/k_x)$ and $\psi' = \arctan(k_y/k'_x)$ angles in $\underline{k}$-space. The tensor $\underline{\underline{\sigma}}(k_\perp,k'_\perp;\psi,\psi';k_\parallel;x'')$, the x''-variation of which is solely due to the spatial variation of the equilibrium plasma parameters, and its derivation through integration along characteristics of the linear Vlasov equation are given explicitely in [3].

3. The Galerkin Finite Element Method

To solve the nonlocal wave equation, we use a Galerkin finite element (FEL) method. The method is based on the weak formulation of this equation, obtained by integrating the scalar product of the wave equation with vector-functions of an appropriate class of test-functions $\{\underline{F}^i\}$ over the x-intervall $[x_a,x_b]$. Integration by parts brings in a boundary-term $(c^2/\omega^2)\ \underline{e}^1\cdot[\underline{F}^i\times(\nabla\times\underline{E})]_{x=x_a}^{x_b}$, which allows the specification of boundary conditions for the system.

The next step of the FEL solution procedure is the Ansatz that the electric wave field is a linear combination of the given set of test functions. On each mesh element within the intervall $[x_a,x_b]$ we use cubic hermitian polynomials as test functions, cfr. [4]. This choice has the advantage that the continuity of the electric and magnetic field of a wave solution at the boundaries of finite elements is assured, and as a consequence, guarantees good convergence properties. Substituting the Galerkin Ansatz into the weak wave equation leads to a linear algebraic system, which can be written formally as $\underline{\underline{S}}\cdot\underline{\epsilon} = \underline{b}$. Here $\underline{\epsilon}$ denotes the vector of the unknown coefficients of the Galerkin Ansatz, i.e. the values of the electric field and its first derivative at the grid points, $\underline{\underline{S}}$ is the so called stiffness-matrix and $\underline{b}$ a vector of given quantities that has to be specified through boundary conditions. Hence, the formal solution of the wave equation involves the inversion of the stiffness matrix, $\underline{\epsilon} = \underline{\underline{S}}^{-1}\cdot\underline{b}$. However, since we are faced with the inversion of an integral operator, the structure of $\underline{\underline{S}}$ is no more block-tridiagonal as in the purely differential case. The band of the stiffness matrix encompasses now additional blocks due to nonlocal terms. Moreover, the boundary conditions must be treated in a special way, so that they are physically and mathematically compatible with the integral nature of the wave equation. This is assured by the assumption that the electric field can be represented by WKB solutions in layers adjacent to the intervall $[x_a,x_b]$, having a width of a few ion gyroradii. Then the boundary conditions appropriate to the mode conversion problem are specified by analogy with a scattering problem.

The FEL solution must match with WKB modes at $x = x_a$ and $x = x_b$, where for given ω and given parallel wave number $k_\parallel$ the polarization and $k_\perp$ of the latter can be determined with the help of the local dispersion relation, cfr. fig. 1. There are only three WKB modes involved in the conversion problem, the externally launched SW, a reflected SW and a transmitted IBW with amplitudes $C_{\rm in}(\rm SW)$, $C_{\rm refl}(\rm SW)$ and $C_{\rm trans}(\rm IBW)$, respectively. Setting the amplitude $C_{\rm in}(\rm SW)$ of the incident wave to a unit amplitude specifies the driving vector $\underline{b}$ of the algebraic system. $C_{\rm refl}(\rm SW)$ and $C_{\rm trans}(\rm IBW)$ are unknown quantities which are formally absorbed in the vector $\underline{\epsilon}$, so that we supplement the algebraic system $\underline{\underline{S}}\cdot\underline{\epsilon} = \underline{b}$ by continuity equations at $x = x_a, x_b$.

The explicit evaluation of the stiffness-matrix arising from the nonlocal constitutive relation (1) requires a five-fold integration. With the mild assumption that the gradient-lenghts of the equilibrium plasma parameter vary on length-scales much larger than the thermal gyroradii, we can perform four integrations analytically. The last integral, the inversion of $\underline{\underline{S}}$ and the solution of the algebraic system are carried out numerically. An example of a mode conversion solution, corresponding to the local dispersion relation plotted in fig. 1, is shown in fig. 2 for a refractive index in y-direction of $n_y = 5$. Within the mode conversion layer occurs a complicated superposition of the three simoultaneously existing modes, whereas outside the SW and the IBW can be identified easily.

4. The Power Balance

We have formulated a local WKB power balance using the conductivity kernel given by eq. (2). As results we obtain explicit expressions for the kinetic correction $\underline{S}^{\text{kin}}$ to the e.m. Poynting flux and the locally from a wave by the plasma particles dissipated power P^{abs}. The kinetic contribution to the Poynting flux $\underline{S}^{\text{kin}}$ is due to a coherent motion of the particles in the e.m. wave field.

The dimensionless global power balance, relevant for the mode conversion problem, is of the form $T + R + A = 1$, where T, R and A denote the transmission, reflexion and absorption coefficients for the power of the externally excited SW. Since the WKB approximation is valid at $x = x_a, x_b$ we can extract the reflexion and the transmission coefficient from the asymptotic WKB analysis. For the numerical example shown in fig. 2, we obtain $T \approx 98.6\%$, $R \approx 0.0\%$ and from the identity $A = 1 - T - R$ an absorption coefficient $A \approx 1.4\%$ (due to a little electron Landau damping). Here and in similar cases the vanishing reflexion coefficient indicates that conversion is complete if significant damping can be avoided. The systematic study of the influence of local damping on the conversion efficiency is still in progress.

A local power balance is needed on the other hand to calculate power deposition profiles and to evaluate the absorption coefficent A directly. The latter can then be used together with the asymptotic expressions for T and R to confirm the conservation of energy for a specific numerical solution of the wave equation. For this purpose we have derived an expression for the local dissipated power, valid also within the conversion layer:

$$P^{\text{abs}} = \pi \sum_{k_y, k_y'} e^{i(k_y - k_y')y} \sum_{k_\parallel} \int_{-\infty}^{\infty} dk_x e^{ik_x x} \int_{-\infty}^{\infty} dk_x' e^{-ik_x' x} \times \tag{3}$$

$$\tilde{\underline{E}}^*(k_x', k_y', k_\parallel) \cdot \left[\underline{\underline{\sigma}}(k_\perp'', k_\perp; \psi'', \psi; k_\parallel; x)\right]^{\text{H}} \cdot \tilde{\underline{E}}(k_x, k_y, k_\parallel) \, .$$

Here an appropriately defined hermitian part of the tensor $\underline{\underline{\sigma}}(k_\perp'', k_\perp; \psi'', \psi; k_\parallel; x)$ is saturated with the Fourier amplitudes of the electric wave field.

Expression (3) for the local dissipated power consists of two contributions. The first, which might be called the Stix-term, is positive definite and describes an irreversible energy exchange due to an interaction of single particles with the e.m. wave field [5]. It reduces in the appropriate limit to the expression for P^{abs} of a homogeneous plasma in terms of the antihermitian part of the dielectric tensor as given in [6]. The second contribution to P^{abs}, which is proportional to density- and temperature-gradients, could be called the diamagnetic term, and is due to an irreversible energy exchange via an interaction between the e.m. wave field and the diamagnetic drift motion. It has therefore the character of a collective effect, to which also non-resonant particles contribute.

The diamagnetic term is not positive definite, so that the local power dissipation can become negative. In case of $P^{\text{abs}} < 0$, energy is transfered irreversibly from the plasma particles to

the e.m. wave field. In particular, it should be possible to recover criteria for marginal stability of linear drift waves through the condition $P^{\text{abs}} = 0$. In fact we could reproduce precisely in that way a well-known criterion for marginal stability of a density gradient driven electrostatic oscillation, the so called universal instability, as given in [7].

References

[1] M. Ono, *Course and Workshop on Application of RF Waves to Tokamak Plasmas*, Varenna, Vol. I, p. 185, 1985

[2] O. Sauter, Ph.D. thesis, Ecole Polytechnique Federale de Lausanne, 1992

[3] M. Brambilla, Plasma Physics and Controlled Fusion **33**, p. 1029, 1991

[4] K. Appert, Computer Physics Communications **40**, p. 73, 1986

[5] H. Werthmann, M. Brambilla, 19^{th} *EPS Conference Innsbruck*, Vol. 2, p. 925, 1992

[6] T. H. Stix, *The Theory of Plasma Waves*, McGraw-Hill, N.Y., Ch. 3., 1961

[7] N. A. Krall, M. N. Rosenbluth, Physics of Fluids Vol. **8**, p. 1488, 1965

Fig. 1. The dispersion relation.

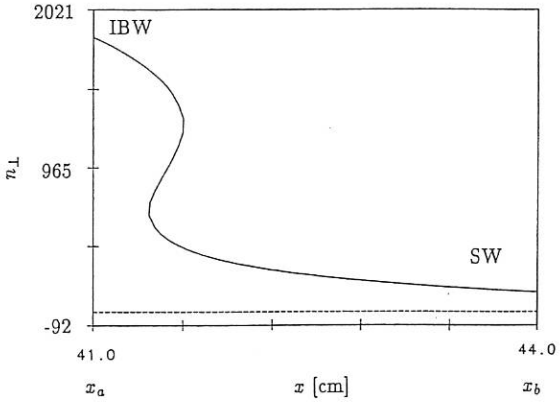

Fig. 2. The x-component of the electric wave field.

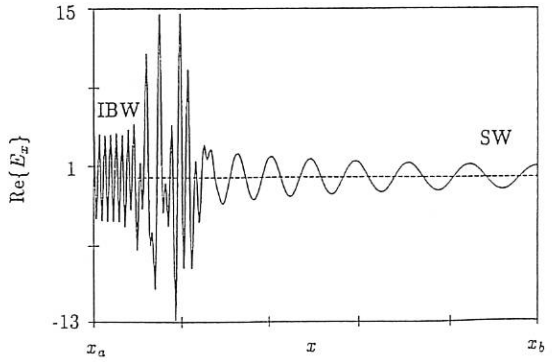

SIMULATION OF ENHANCED TOKAMAK PERFORMANCE ON DIII-D USING FAST WAVE CURRENT DRIVE*

J.S. deGrassie, Y.R. Lin-Liu, C.C. Petty, R.I. Pinsker, V.S. Chan, R. Prater, H. St.John, F.W. Baity,† R.H. Goulding,† and D.H. Hoffman†

General Atomics, San Diego, California, U.S.A.

INTRODUCTION

The fast magnetosonic wave is now recognized to be a leading candidate for noninductive current drive for the tokamak reactor due to the ability of the wave to penetrate to the hot dense core region. Fast wave current drive (FWCD) experiments on DIII-D have realized up to 120 kA of rf current drive, with up to 40% of the plasma current driven noninductively [1]. The success of these experiments at 60 MHz with a 2 MW transmitter source capability has led to a major upgrade of the FWCD system. Two additional transmitters, 30 to 120 MHz, with a 2 MW source capability each, will be added together with two new four-strap antennas in early 1994.

Another major thrust of the DIII-D program is to develop advanced tokamak modes of operation, simultaneously demonstrating improvements in confinement and stability in quasi-steady-state operation. In some of the initial advanced tokamak experiments on DIII-D with neutral beam heated (NBI) discharges it has been demonstrated that energy confinement time can be improved by rapidly elongating the plasma to force the current density profile to be more centrally peaked [2]. However, this high-ℓ_i phase of the discharge with the commensurate improvement in confinement is transient as the current density profile relaxes. By applying FWCD to the core of such a κ-ramped discharge it may be possible to sustain the high internal inductance and elevated confinement.

Using computational tools validated on the initial DIII-D FWCD experiments we find that such a high-ℓ_i advanced tokamak discharge should be capable of sustainment at the 1 MA level with the upgraded capability of the FWCD system.

DIII-D FWCD UPGRADE TO 6 MW

Figure 1 shows a schematic diagram of the FWCD system as it will be following the upgrade to a 6 MW generator source capability. That portion indicated as existing now has been described extensively [3–5]. This existing system consists of one transmitter, 2 MW, 30 to 60 MHz, driving a four-strap antenna with peak $k_{\parallel} \simeq 8.9$ m^{-1} at the antenna in current drive operation where a $\pi/2$ phase shift is set between adjacent straps.

For the upgrade portion, two new modular four-strap antennas [6,7] will be installed in DIII-D. These antennas will have partial water cooling with a power handling capability of 4 MW (each) for a 10 sec pulse. In current drive phasing the peak spectral component at the antenna is $k_{\parallel} \simeq 10$ m^{-1}. Two new transmitters will drive the two new antennas, one on each antenna initially. These transmitters are similar to those used on ASDEX-U [8], operating over 30 to 120 MHz, with a perfectly matched output power capability of 2.5 MW at the low frequency end, and 1.5 MW at the high frequency end. The power from one transmitter must be divided equally among the four straps with proper phasing between the straps. Part of the solution on DIII-D is to couple pairs of straps on an antenna into resonant loops which force these coupled straps to either be in or out of phase, depending on the length of the loops.

The transmission system will utilize the same successful techniques developed on DIII-D [3,4] for tuning and matching under current drive phasing, but with some significant improvements. An antenna decoupler [9] will be incorporated to recirculate the power coupled from one set of straps to another during operatkon with current drive phasing. This is necessary because

*This is a report of work sponsored by the U.S. Department of Energy under Contract Nos. DE-AC03-89ER51114 and DE-AC05-84OR215400.

†Oak Ridge National Laboratory, Oak Ridge, Tennessee, U.S.A.

of the mutual inductances between the straps, which otherwise results in a power imbalance in the main lines feeding the resonant loops. Another improvement will be to use phase shifters within the resonant loops, allowing the resonance frequency, and thus the operating frequency, to be changed on a shot to shot basis.

ADVANCED TOKAMAK SIMULATION

The computational tools used in this simulation are the transport code ONETWO[10] and the rf package FASTWAVE [11]. Recently ONETWO has been upgraded [12] to allow 1-1/2D transport and magnetohydrodynamic (MHD) coupled simulation calculations in which the kinetic and current profiles are evolved according to the choice of transport model; as the pressure profile evolves, the two dimensional MHD equilibrium is self-consistently calculated. In FASTWAVE the antenna spectrum is modeled by up to 20 discrete rays, with ray propagation assumed to be a straight line with a toroidal upshift. The power deposition and current drive profiles are calculated using a slab model [12], and these profiles are spread in the vertical direction by a width chosen to simulate the full-wave calculations.

The code results have been benchmarked against the experimental data on DIII–D. Figure 2 shows data from fast wave current drive experiments [1] along with the results of a code computation. The code simulations also agree with the basic scalings seen experimentally; current drive efficiency increases with electron temperature and the driven current increases with the deposited power per plasma particle, P/n.

DIII–D κ-ramp experiments have resulted in an improvement in energy confinement of 1.5 to 1.8 relative to the JET/DIII–D H–mode thermal confinement scaling [2]. In these NBI heated experiments the elongation κ is rapidly increased (200 msec) from 1.3 to 2.2 while the input power (7.5 MW) and plasma current (1 MA) are held constant. Internal inductance values of 1.8 have been obtained transiently in this manner. It is of interest to maintain this centrally peaked current profile using FWCD and test whether the enhanced confinement can be maintained noninductively.

For this FWCD-maintained high ℓ_i study we take the target plasma from the actual experimental parameters of a DIII–D κ-ramped discharge. The discharge is in the H–mode, with $n_e(0) = 5.3 \times 10^{19}$ m^{-3}, $T_e(0) = 3.9$ keV, $T_i(0) = 3.8$ keV, $Z_{eff} = 1.3$, $\kappa = 2.2$, and $\ell_i = 1.8$. The applied fast wave power is taken from the parameters of the 6 MW upgraded capability: 1.6 MW at 60 MHz on the original antenna ($n_\parallel$ peak $\simeq 7$) and 1.5 MW at 120 MHz on each of the two new antennas ($n_\parallel$ peak $\simeq 4$). Moderate NBI at 2.5 MW is also applied to provide ion heating and some additional noninductive current drive. The profiles of Z_{eff}, n_e, and χ_i are taken as those of the target plasma and held constant throughout the simulation. The electron thermal conductivity $n\chi_e$ is selected to give τ_E consistent with the enhanced confinement observed in the experiment; $n\chi_e = 5 \times 10^{19}$/m-sec. The Hirshman-Sigmar neoclassical formulation [14] is used along with a sawtooth mixing model [15]. The transport code evolves the T_e, T_i, and J profiles consistent with the calculated FW and NBI deposition profiles. As the pressure profile evolves, the 2D free boundary MHD equilibrium is self-consistently calculated.

At the end of a 2 sec FW and NBI pulse, $T_e(0) = 7.5$ keV, $T_i(0) = 4.0$ keV, and the loop voltage is nearly zero, less than 10 mV. Figure 3 shows the current profile at this time, together with the various elements making up the noninductive current drive. Table I gives a summary of the results of this simulation; FWCD is 0.37 MA ($\gamma_{FWCD} = 0.063$), NBCD is 0.09 MA, and the bootstrap current is 0.5 MA, with the remaining 0.08 MA driven Ohmically. The internal inductance has dropped to 1.4 due to current profile broadening arising from the bootstrap current at the edge.

This simulation is not an optimization of what might be obtained with the new FWCD capability. We have found similar levels of current drive for other FWCD operating scenarios, for example, for lower frequency on the new antennas. Systematic simulation parametric studies will be performed. The important result is that noninductive current drive approaching the 1 MA level, including bootstrap current, could be within reach on DIII–D next year, when the upgraded operating mode is combined with enhanced confinement resulting from an elongation ramp. The kink stability analysis for the final equilibrium is yet to be done, but from past

experience it should be stable to the $n = 1$ external kink with the DIII–D wall geometry, and unstable to a benign internal kink [16].

REFERENCES.

[1] R.I. Pinsker *et al.*, *Direct Electron Heating and Current Drive With Fast Waves in DIII–D*, in *Plasma Physics and Controlled Nuclear Fusion Research*, Proc. 14th Int. Conf. Würsburg, 1992 (International Atomic Energy Agency, Vienna, to be published).

[2] L.L. Lao *et al.*, *High Internal Inductance Improved Confinement H–Mode Discharges Obtained with an Elongation Ramp Technique in the DIII–D Tokamak*, submitted to Phys. Rev. Lett.

[3] R.I. Pinsker *et al.*, *30–60 MHz FWCD System on DIII–D: Power Division, Phase Control and Tuning for a Four-Element Antenna Array*, in Proc. 14th IEEE/NPSS Symp on Fusion Engineering, San Diego (1991), Vol. 1, p. 115.

[4] M.J. Mayberry *et al.*, *Fast Wave Current Drive Antenna Performance on DIII–D*, in Proc. 9th Top. Conf. on RF Power in Plasmas, Charleston (1991), p. 276.

[5] R.H. Goulding *et al.*, *Design and Performance of Fast Wave Current Drive Systems in the ICRF, ibid.*, p. 285.

[6] F.W. Baity *et al.*, *The Technology of Fast Wave Current Drive Antennas*, to be published in J. Fusion Eng. (1993).

[7] J.S. deGrassie *et al.*, *Fast Wave Current Drive System Design for DIII–D*, in Proc. 17th Symp. on Fusion Technology, Rome (1992), to be published.

[8] F. Hofmeister, *Acquisition of Technical Data and Matching Procedures for the ICRH System on ASDEX Upgrade, ibid.*, to be published.

[9] R.H. Goulding *et al.*, *Power Compensators for Phased Operation of Antenna Arrays on JET and DIII–D*, in Proc. 10th Top. Conf. on RF Power in Plasmas, Boston (1993), to be published.

[10] W.W. Pfeiffer *et al.*, *ONETWO: A Computer Code for Modeling Plasma Transport in Tokamaks*, General Atomics Report GA-A16178 (1980).

[11] Y.R. Lin-Liu, *Control of Current Density Profile by RF Current Drive in DIII–D*, presented at 10th Top. Conf. on RF Power in Plasmas, Boston (1993).

[12] H. St.John *et al.*, *Coupled MHD and Transport Analysis of Improved Confinement DIII–D Discharges*, this conference.

[13] S.C. Chiu *et al.*, Nucl. Fusion **29** (1989) 2175.l

[14] S.P. Hirshman and D.J. Sigmar, Nucl. Fusion **21** (1981) 1079.

[15] W.W. Pfeiffer *et al.*, *Giant Sawtooth Oscillations in the Doublet III Tokamak*, Nucl. Fusion **25** (1985) 655.

[16] A.D. Turnbull, General Atomics, private communication.

TABLE I
SIMULATION OF FWCD SUSTAINED HIGH-ℓ_i H-MODE IN DIII–D

Power		Current	
FW	4.6 MW	FWCD	0.37 MA
NB	2.5 MW	NBCD	0.09 MA
		BS	0.50 MA
		Ohmic	0.08 MA
			1.04 MA

Parameters					
a	= 0.60 m	B_T	= 2.1 T	$\beta(0)$	= 6.7%
R	= 1.70 m	n_e	= 4.6×10^{19} m^{-3}	$\langle\beta\rangle$	= 2.0%
κ	= 2.2	$\langle Z_{eff}\rangle$	= 1.8	β_N	= 2.3
ℓ_i	= 1.4	$q(0)$	= 1.0	β_p	= 2.1
I_p	= 1.0 MA	q_{95}	= 9.1	H	= 2.5

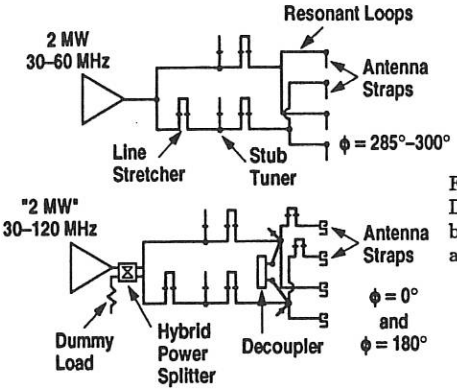

FIG. 1. (a) existing FWCD system on DIII-D; (b) two new systems like this to be added in 1994. Toroidal locations (ϕ) of antennas are given.

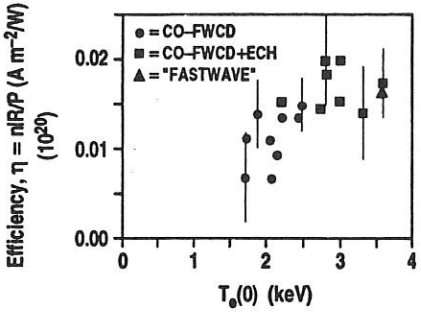

FIG. 2. Fast wave current drive efficiency versus central electron temperature. I_P = 0.4 MA, B_T = 1.1 T, $\bar{n}_e = 1 \times 10^{19}$ m^{-3}.

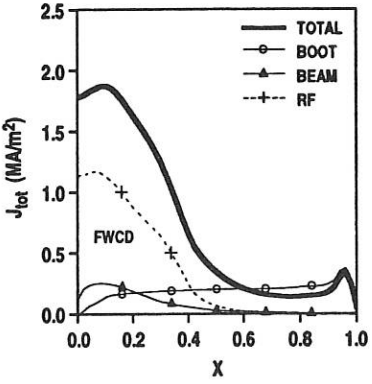

FIG. 3. Final state current density profile from simulation for FWCD applied to a κ-ramped target plasma, for coordinates of Table I.

EFFECTS OF ION BERNSTEIN WAVE HEATING ON ION TEMPERATURE AND PLASMA DENSITY IN PBX-M*

W. Tighe, N. Asakura,[a] R. Bell, S. Bernabei, L. Blush,[b] R. Cesario,[c] T. K. Chu, R. Conn,[b] R. Doerner,[b] J. Dunlap,[d] A. England,[d] H. Fishman, J. Harris,[d] R. Hatcher, G. Henkel,[d] H. Herrmann, R. Isler,[d] R. Kaita, S. Kaye, H. Kugel, B. LeBlanc, M. Okabayashi, H. Oliver, M. Ono, S. Paul, F. Paoletti,[e] A. Post-Zwicker,[d] P. Roney, N. Sauthoff, L. Schmitz,[b] S. Seki,[f] S. Sesnic, Y. Sun, H. Takahashi, G. Tynan[b] and the PBX-M Group.

Princeton Plasma Physics Laboratory, Princeton, NJ, USA [[a]JAERI (Japan), [b]UCLA (USA), [c]Euratom-ENEA(Italy), [d]ORNL (USA), [e]MIT (USA), [f]NIFS (Japan)]

ABSTRACT

Ion Bernstein Wave Heating (IBWH) experiments in PBX-M have demonstrated bulk ion heating along with density profile peaking. With averaged densities, n_e, of ~3 x 10^{13} cm^{-3}, the central ion temperature, increasedby 350 eV when 0.6 MW of IBWH was applied. Profiles of ΔT_i indicated that the IBWH power was deposited in a well-localized, off-axis region. During IBWH, the density first rises uniformly across the profile, but evolves to a very peaked profile (similar to supershots). The density gradient reaches ~5 x 10^{12} cm^{-4} in the core region. The density peaking indicates that IBWH is influencing central plasma transport in the core region, and may be important for controlling the bootstrap current profile. Finally, during IBWH, the the edge density drops consistent with the ponderomotive force of the antenna near field.

INTRODUCTION

To provide pressure profile control[1] through localized bulk ion heating[2] and density profile control,[3] an ion Bernstein wave (IBW) heating system has been installed on the PBX-M tokamak. With IBWH, localized ion heating is achieved by matching the frequency of the ion Bernstein wave to the ion cyclotron harmonic resonance for a selected ion species at specific locations within the plasma. Density profile control is based on modified Ohmic discharges.[1]

The IBW system presently consists of two antennas, each connected to the 2 MW, 40-80 MHz FMIT transmitter. The IBW antenna elements are phased (0-π) to reduce the low-$n_{||}$ related edge losses,[4] and the antennas are placed in the outer mid-plane region to optimize accessibility of IBW to the plasma core.[5]

ION TEMPERATURE PROFILE CHANGES

For this study, the IBW pulse duration was 200 ms. The highest power level was 0.7 MW. The IBW frequencies were 47 and 54 MHz at B_T = 1.2 T and 1.4 T, respectively, which correspond to the $5\Omega_D$ resonance near the plasma center. Ray-tracing calculations show that for these conditions, the IBWH power deposition is off-axis, centered ~10 cm (see Fig. 1) from the magnetic axis at 165 cm. The calculations also show that under these conditions the power is deposited primarily to the ions. Bulk ion temperature radial profiles were measured by CHarge Exchange Recombination Spectroscopy (CHERS).[6] Fifty time frames are available during each discharge. Integration times of 10 or 20 ms per frame were used. CHERS uses a heating neutral beam with 1 MW injected power (~0.7 MW absorbed).

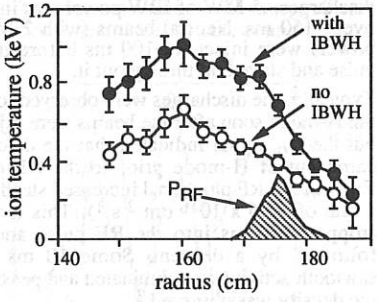

Fig. 1. Ion temperature profile taken with and without IBWH. The IBWH power deposition is also shown

As noted, there are changes to the density profile during IBWH (see next section). For the discharges discussed here, no peaking was observed and density changes could be compensated by gas

* Supported by USDOE Contract No.DE-AC02-76-CHO-3073

puffing. Both the line density and the density profiles were matched.

As IBWH power is increased, the temperature difference between discharges with and without IBWH increases from ~150 eV at 0.22 MW to more than 350 eV at 0.6 MW. Figure 1 shows the T_i profile with 0.6 MW of IBWH. The ion temperature increases across the profile. There is a broadening of the profile and a steepening of the gradient near the half-radius region. The steepened gradient points to the location of heat deposition. For the case shown in Fig. 1, the central electron temperature increased from 550 eV to 750 eV. Since the central ion temperature was ~1 keV, the heat flow would be from the ions to the electrons.

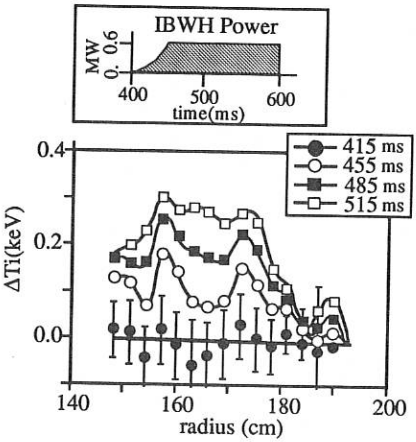

Fig. 2 ΔT_i profiles taken early in the RF phase.

In cases where the density is not matched, the product of the ion temperature and density can be used to measure the additional stored energy due to IBWH power. $T_i(0)$ was averaged over a 10 cm central plasma region. $T_i(0)$ and n_{el} were averaged over a 20 ms time window. These values were then used to evaluate $\Delta\langle n_{el} T_i(0)\rangle$. This parameter increases linearly with IBWH power in the range of power used in these experiments.[3]

The profiles shown in Fig. 1 are taken towards the end of the RF pulse. Examination of the change in T_i (T_i[with IBWH] - T_i[without IBWH]) in the early stages of IBWH provides a clearer indication of the location of heating.[2] This is shown in Fig. 2. At t=415 ms, while the IBWH power is near zero, no heating occurs. At t=455 ms, as the IBWH power reaches its operational level, the rise in ion temperature is localized in the off-axis region (~8 cm from the axis). As with those given in Fig. 1, these results are in good agreement with the calculated IBWH power deposition. In time, the central ion temperature rises and the profile fills in.

DENSITY EFFECTS

Density peaking during IBWH was observed in Ohmic discharges[4]. A study was undertaken to determine the effect of IBW on the density profile in a beam-heated discharge. For these discharges, .5 MW of IBW power was injected over ~150 ms. Neutral beams (with 2 MW of power) were injected ~100 ms before the RF pulse and stayed on throughout it.

Typically, the discharges were observed to enter the H-mode soon after the beams were injected, but the D_α signal indicated that the discharge came out of H-mode prior to the RF phase. Early in the RF phase, n_{el} increased steadily (at a rate of ~1.6 x 10^{16} cm^{-2} s^{-1}). This increase stopped ~50 ms into the RF pulse and was followed by a descent. Some 10 ms later, sawtooth activity was eliminated and peaking of the density was observed.[3]

Figure 3 shows the time evolution of the electron density profile. This is based on Thomson scattering profiles[3] from equivalent

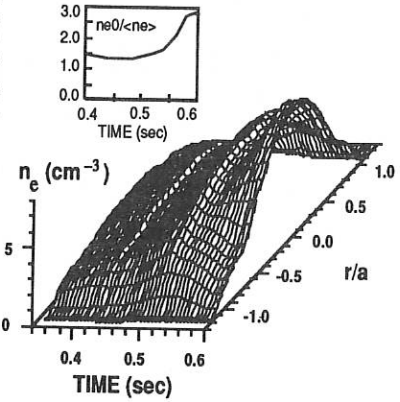

Fig. 3. Time history of n_e profile against normalized minor radius, a/r.
Inset: $n_{e0}/\langle n_e\rangle$ against time.

discharges (time points: 0.4, 0.44, 0.48, 0.54, and 0.575 s) and line-integrated density measurments for interpolation between time points. A sawtooth associated with the H-mode transition (0.425 s) and a hump (at 0.51 s) corresponding to the $n_e l$ rollover are visible. Peaking starts at ~ 0.52 s. During peaking, the shape parameter $n_{e0}/\langle n_e \rangle$ (see inset) reaches 2.7. The central density n_{e0} rises steadily to a maximum of 8.0×10^{13} cm^{-3} while T_{e0} remains constant at ~1.0 keV and T_{i0} rises to its maximum of 1.8 keV. There is some indication that the central Z_{eff} increased during the RF pulse. Spectroscopic data shows that this behavior is more likely associated with low Z impurities such as oxygen and carbon.

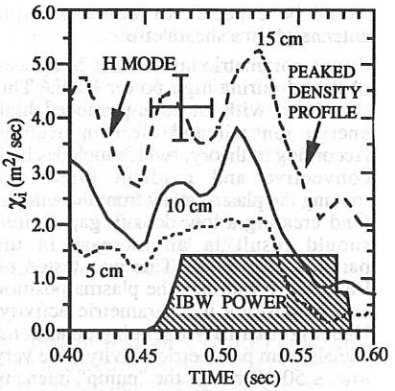

Fig. 4. Core χ_i as a function of time: 5, 10, and 15 cm from the plasma center.

The experimental results are suggestive of an improvement of the confinement in the core region. The TRANSP code[3] was upgraded to read in the IBW power deposition profile. Figure 4 shows the temporal evolution of the ion effective thermal diffusivity, χ_i, at radial locations 5, 10, and 15 cm from the magnetic axis corresponding to the inner half of the plasma. A significant drop of χ_i began at ≈ 0.52 s and marked the onset of the peaking phase. The ion diffusivity dropped over the three minor radii shown. At 10 cm, χ_i fell from 3.5 m^2/s to values around 1 m^2/s.

Associated with the peaked profile are large values of the local spatial gradient, ∇n_e, of the electron density. The ∇n_e profile (along with the RF power deposition profile, P_{IBWI}) is plotted in Fig. 5. There is a spatial correlation between the high gradients and the large values of P_{IBWI}. TRANSP calculations show that the central current density profile broadened noticeably during the IBW coupling due to the generation of bootstrap current in the mid-minor radius region. These calculations further indicate that q(0) rises above 1. This is supported by the suppression of sawtooth activity.

ION CYCLOTRON EMISSION

IBWH requires that the RF power has good accessibility to the plasma core, where absorption and heating are desired. The long-wavelength RF wave emitted from the antenna is mode-converted to a shorter wavelength ion Bernstein wave which then propagates directly to the resonant layer. Observation of ion cyclotron emission (ICE) from a tokamak can be considered as the reverse of this process. In this case, heated ions in the core excite IBW at the appropriate harmonic, and only waves which have the associated "good accessibility" will escape. These waves can propagate along the midplane to an edge location where there is easier coupling to the electromagnetic wave, and they can then be observed outside the tokamak. The IBW antenna can detect this ICE, and identify the most suitable frequency for use in IBWH. Results are given in Fig. 6.[7]

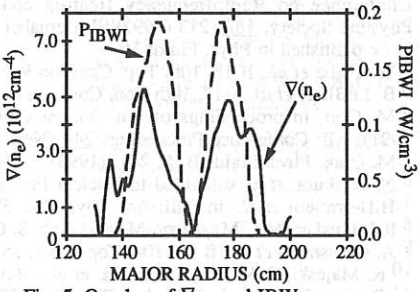

Fig. 5. Overlay of ∇n_e and IBW power deposition profile.

EDGE PLASMA EFFECTS AND PARAMETRIC INSTABILITIES

Edge plasma interaction physics during IBW has been studied.[8,9] Most importantly, the edge scrape-off density (measured by a fast reciprocating probe) has been observed to drop significantly during IBW. This reduction is in good agreement with a model employing the ponderomotive force to move the edge plasma.[10] A reduction in edge plasma density

would be expected to reduce parasitic antenna-plasma sheath effects.

Strong parametric instabilities have been observed during high power IBW.[8] This correlated with an edge-produced high energy ion tail and electron heating. According to theory, (which includes both convective and gradient effects),[11] moving the plasma away from the antenna (and creating a low density gap region) should result in an increase in the parametric activity. This was tested on PBX-M by varying the plasma position and monitoring the parametric activity. Under normal IBW operating conditions, signals from parametric activity were very low, ≤ 50 dB below the "pump" intensity (at $\omega \approx \omega_{rf}$). However, when the plasma edge was moved away from the antenna by about 10 cm, the parametric instability activity increased to ~20 dB of the pump.[11] This shows that parametric instabilities can be controlled during IBW. Probe measurements have shown no edge electron heating, nor significant changes in the floating potential during IBW.

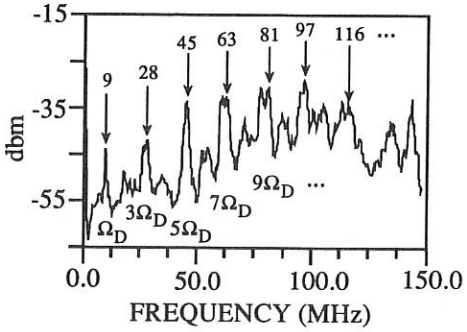

Fig. 6. Spectrum of Ion Cyclotron Emission from a D-H plasma showing harmonics every ~9 MHz. Only odd harmonics are labelled.

DISCUSSION AND CONCLUSIONS

With the application of IBWH on PBX-M, we have observed off-axis, localized ion heating and ion temperature profile modification. This may allow control of the pressure profile which is required for full-volume second stability conditions.

A peaking of the density profile is observed with the application of IBW. The confinement barrier (region of large ∇n_e) coincided with the region of absorption of IBW power, and as the density profile was peaking, χ_i fell at the radial position of peak IBW power deposition. The peaking may be related to the poloidal velocity shear stabilization of turbulence by IBW. The model predicts that due to a non-linear plasma response to the IBW wave field, a poloidal velocity shear layer can be created near the power absorption region. Predictive calculations suggest that with higher beam heating, the peak bootstrap current fraction should be ≈ 70% of the local current density and over 50% of the total current in PBX-M.

A reduction of the edge scrap-off density using IBW has been demonstrated and may be used, for example, in controlling the heat flux into the divertor plates. Careful placement of the plasma with respect to the RF antenna can strongly affect the growth of parametric instabilities.

REFERENCES

[1] M. Ono, S. Bernabei, N. Asakura, *et al.*, in the Proceedings of the Europhysics Topical Conference on Radiofrequency Heating and Current Drive of Fusion Devices, European Physical Society, 16E, 213 (1992); S. Bernabei , *et al.*, in Bull. Am. Phys. Soc. 37, 1437 (1992), to be published in Phys. Fluids B.
[2] W. Tighe *et al.*, B 18, 10th Top. Conf. on R-F Power in Plasmas, (Boston, 1993).
[3] B. LeBlanc *et al.*, B17, 10th Top. Conf. on R-F Power in Plasmas (Boston, 1993).
[4] M. Ono, in proceedings of 9th Topical Conference on R-F Power in Plasmas (Charleston, 1991), AIP Conference Proceedings 244 (New York, 1992), p223.
[5] M. Ono, Phys. Fluids B 5, 241 (1993).
[6] N. Asakura..*et al.* submitted to Nuclear Fusion, (1992).
[7] H.Herrmann *et al.* in Bull. Am. Phys. Soc. 37, 1572 (1992).
[8] R.I. Pinsker, M.J. Mayberry, M. Porkolab, S. C. Chiu, and R. Prater, Ref. 4, p169.
[9] A. Grossman, *et al.*, B 19, 10th Top. Conf. on R-F Power in Plasmas (Boston, 1993).
[10] R. Majeski, P. Robert, T. Tanaka, *et al.*, Bull. Am. Phys. Soc. 36, 2419 (1991).
[11] R. Cesario, *et al.*, in Bull. Am. Phys. Soc. 37, 1572 (1992).

ICRF HEATING OF TFTR PLASMAS IN THE SUPERSHOT REGIME

G. Taylor, J.R. Wilson, R.C. Goldfinger**, J.C. Hosea, D.J. Hoffman**, R. Majeski, C.K. Phillips, D.A. Rasmussen**, J.H. Rogers, G. Schilling, J.E. Stevens, M.G. Bell, R.V. Budny, C.E. Bush**, Z. Chang*, D. Darrow, D.R. Ernst***, E. Fredrickson, G. Hammett, K. Hill, A. Janos, D. Jassby, D.W. Johnson, L.C. Johnson, S.S. Medley, H.K. Park, J. Schivell, J.D. Strachan, E. Synakowski, and S. Zweben

Princeton Plasma Physics Laboratory, Princeton, New Jersey 08543, USA
**University of Wisconsin, Madison, Wisconsin 53706, USA*
***Oak Ridge National Laboratory, Oak Ridge, Tennessee 08731, USA*
**** Massachusetts Institute of Technology, Cambridge, Massachusetts 02139, USA*

Introduction

One of the major objectives of the ion cyclotron range of frequency (ICRF) program [1,2] on TFTR is to enhance the alpha particle parameters in deuterium-tritium (D-T) plasma experiments, which are scheduled to commence later in 1993. The increased core electron temperature produced by ICRF heating (ICRH) of D-T neutral beam injection (NBI) heated plasmas is expected to increase the alpha particle slowing down time and hence enhance the central alpha particle pressure. In preparation for D-T operation, experiments were conducted on TFTR to explore the effect of ICRH on the performance and stability of low recycling, deuterium supershot plasmas [3] in the helium-3 minority heating regime.

Experimental Results

The plasmas in these experiments were run so that the majority of the power flow was to the inboard bumper limiter. The natural plasma oblateness, which develops as the plasma stored energy ramps up at the start of NBI, was employed to move the plasma outboard edge towards the four ICRH antennas. Although supershots are characterized by low edge recycling and hence low edge density, after 100-200 ms sufficient density had built-up in front of the antennas to allow efficient coupling of ICRH power [4]. Up to 7.4 MW of 47 MHz ICRH power has been coupled into R~2.62 m, a~0.96 m TFTR, deuterium, supershot plasmas at an axial toroidal magnetic field of ~4.8 T. Experiments were performed at plasma currents of 1.85 and 2.2 MA. The Shafranov shift on axis was 0.2-0.25 m and 0.16-0.2 m for the 1.8 MA and 2.2 MA plasmas, respectively. The helium-3 resonance was within 0.1-0.15 m of the plasma core.

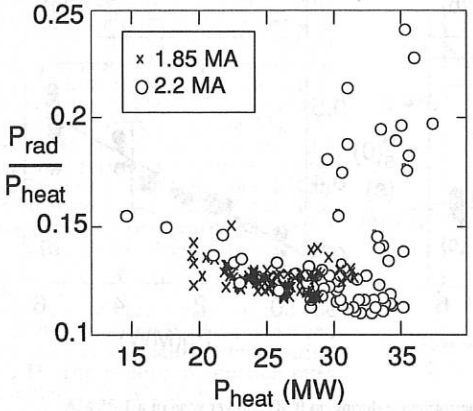

Fig.1 Radiated power fraction versus total heating power for He-3 minority, D supershots at 1.85 and 2.2 MA. For most plasmas the radiated power fraction was 10-15%, but above 30 MW some 2.2 MA plasmas exhibited radiation blooms. Data is at the time of maximum stored energy.

Combined ICRH and NBI powers reached levels of over 37 MW, about 5 MW larger than previous TFTR beam-only experiments. This allowed an exploration of the power loading limits for the carbon limiter tiles.

Fig. 1 shows a plot of the radiated power fraction versus the total heating power at the time of maximum stored energy. The radiated power fraction remained below 15% for the 1.85 MA plasmas up to the highest input powers of 32 MW. However, some of the 2.2 MA plasmas exhibited radiation blooms at heating powers above ~30 MW. The radiation blooms were accompanied by a significant increase in carbon light. Vertical plasma position shifts of 2-3 mm were found to reduce or eliminate the radiation bloom. This behavior is consistent with a steep power scrape-off at the plasma edge.

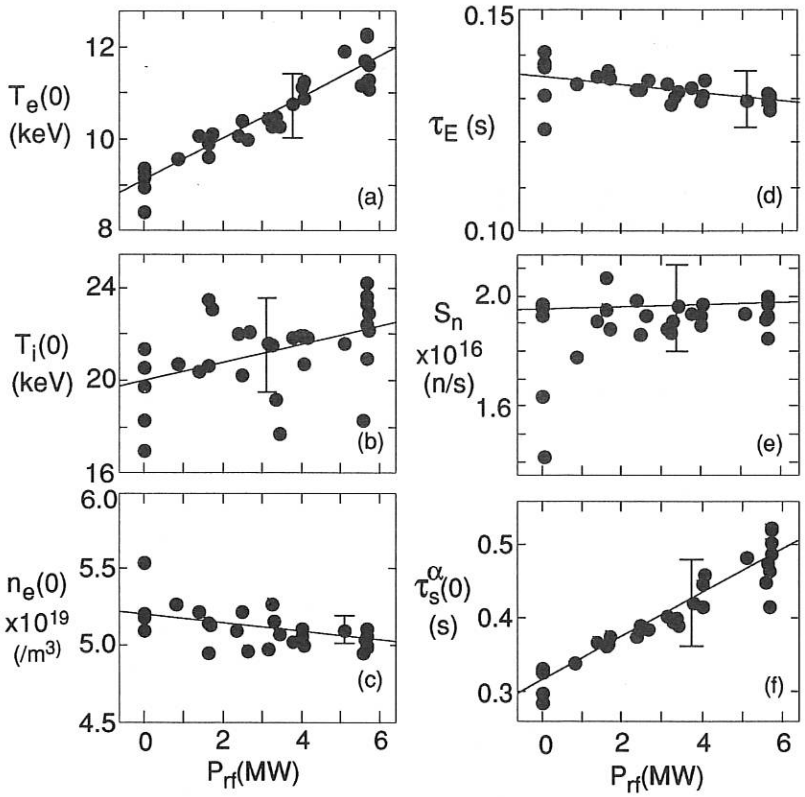

Fig. 2 Summary of plasma performance during an ICRH power scan of a 1.85 MA D-D supershot with 22-23 MW of NBI. Data was obtained at the time of maximum stored energy. (a) Central electron temperature, (b) central ion temperature, (c) central density, (d) global energy confinement time, (e) neutron production rate and (f) projected alpha energy slowing down time for a D-T plasma are plotted versus coupled ICRH power. A linear fit has been made to the data for each plot, the error bars represent typical uncertainties.

A 100 ms duration, 1Tl/s, helium-3 puff was introduced into the discharge about 0.5 s before the start of the NBI pulse. This puff was sufficient to produce a helium-3 concentration equal to about 1.5-2.5% of the peak electron density. The puff degraded global energy confinement by ~5% and decreased plasma reactivity by ~10%. Fig. 2 summarizes the results (at the time of peak stored energy) for an ICRH power scan of 1.85 MA supershot plasmas with 22-23 MW of NBI. The fraction of NBI power in the direction of the plasma current was kept relatively constant at a value of ~0.6. The maximum ICRH power coupled into a 1.85 MA supershot plasma was 5.7 MW. Core electron temperature (Fig. 2a) measured from electron cyclotron emission (ECE) [5] was increased ~40% with the application of the maximum ICRH power. Although Thomson scattering measurements were generally not taken at the time of peaked stored energy, temperature profile comparisons with ECE at other times in the pulse gave core Thomson scattering temperatures which were systematically 15-20% lower. The change in central ion temperature (Fig. 2b) was within the ±10% measurement errors of the charge exchange recombination spectroscopy (CHERS) diagnostic [6]. There was an ~4% drop in the core electron density (Fig. 2c) and ~10% drop in density profile peakedness ($n_e(0)/\langle n_e \rangle$) determined from multi-channel far-infrared interferometer (MIRI) data [7]. The peakedness degradation was due in part to an increase in edge density, this was correlated with a small increase in Z_{eff} (~5%) and an enhancement of the titanium concentration, consistent with some of the impurities coming from the ICRH antennas. The decreased core density could result from reduced beam penetration due to the higher edge density and/or Z_{eff}.

The global energy confinement times (τ_E), calculated by the SNAP [8] equilibrium code using a 2% helium-3 concentration, and the measured profiles of ion temperature (from CHERS), electron temperature (from ECE) and electron density (from MIRI) agreed within 5-10% with diamagnetically measured values. τ_E decreased ~5% as the ICRH power was increased (Fig. 2d), this τ_E degradation is less than the ~10% decrease expected from Goldston empirical L-mode scaling [9]. The measured plasma reactivity (Fig. 2e) appeared relatively unaffected by the presence of ICRH. Since the slowing down time of the 100keV NBI ions should already be insensitive to further increases in the electron temperature above that seen in the NBI-only plasmas (~9 keV), no significant increase in reactivity would be expected as a result of the enhanced central electron temperature during ICRH. The neutron production rates calculated by SNAP were found to agree with the measured values (within ~15%). The calculated neutron production rate comes approximately equally from beam-beam and beam-target reactions, with <10% from thermonuclear reactions. In addition to uncertainties in estimating the helium-3 concentration, additional uncertainties remain in the measured Z_{eff} and its

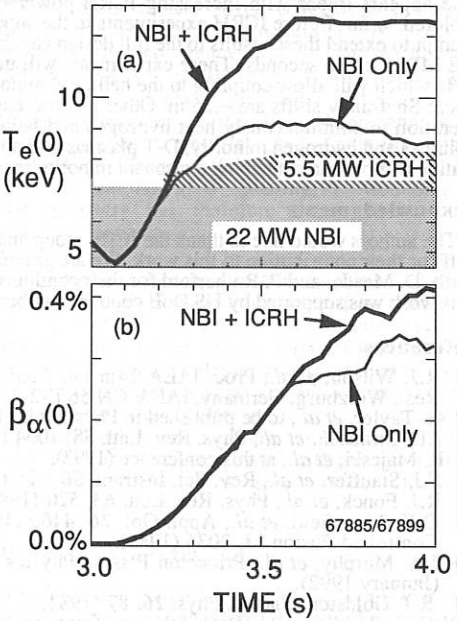

Fig.3 D-T simulation using measured D-D plasma parameters up to 3.7s and an extrapolation to steady state after that. (a) Enhancement of the central electron temperature with application of ICRH. (b) This results in a 30% increase in projected central alpha pressure due to lengthened alpha slowing down time.

profile shape, which may affect the calculated reactivity.

Discussion and Future Work

Fig. 2f shows the projected core alpha energy slowing down time calculated for D-T equivalent plasmas, with the same central density and temperature measured during the D-D experiments. A 60% enhancement in the core alpha particle slowing down time was calculated for equivalent D-T plasmas at the highest ICRH powers for the 1.85 MA supershots. Similar results were obtained for the 2.2 MA supershots, where coupled ICRH powers were extended to 7.4 MW. However, the higher current data was less reproducible due to the radiation blooms mentioned earlier. The effect of this increased slowing down time on central alpha pressure has been investigated with a time-dependent equilibrium code, TRANSP [10]. The results from one of these D-T plasma simulations are shown in Fig. 3. The simulation used measured D-D plasma parameters up to 3.7s. After that, an extrapolation was made to a steady state condition. Fig. 3 shows a comparison of two plasmas, one with both 5.5 MW of ICRH and 22 MW of D-T NBI and the other with D-T NBI alone. The time evolution of the central electron temperature is shown in Fig.3a. The central electron temperature, and hence the alpha slowing down time is enhanced early in the ICRH pulse. However, the central alpha pressure does not increase until ~0.5s after the start of the ICRH pulse. The central alpha pressure was enhanced by ~30% in this simulation. The enhancement in projected core alpha slowing down time appears linear with increasing ICRH power (Fig. 2f) up to the ICRH power levels explored so far. Future ICRH experiments in the supershot regime in both D-D and D-T will attempt to extend these results to the full design capabilty of the TFTR ICRH system, which is ~12 MW for two seconds. These experiments will utilize a lower operating frequency of 43 MHz which will allow coupling to the helium-3 minority resonance at the magnetic axis even where Shafranov shifts are ~.25 m. Other planned experiments will combine 43 and 64 MHz operation to simultaneously heat hydrogen and helium-3 minority species. Experiments on helium-3 and hydrogen minority, D-T plasmas will allow the study of second harmonic tritium heating in a plasma containing a resonant minority species.

Acknowledgments

The authors would like to thank the ICRF group and TFTR project engineering and technical staff for their contribution to this work. We are grateful to Drs. R. Davidson, R. Hawryluk, H. Furth, D. Meade, and P. Rutherford for their continued support of the ICRF research program. This work was supported by US DoE contract number DE-AC02-76-CHO-3073

References

[1] R.J. Wilson, *et al.*, Proc. IAEA 14th Int. Conf. on Plasma Phys. and Cont. Nucl. Fus. Res., Wurzburg, Germany, IAEA-CN-56/E-2-2, (October 1992).
[2] G. Taylor, *et al.*, to be published in Phys. Fluids B (July 1993).
[3] J.D. Strachan, *et al.*, Phys. Rev. Lett. **58**, 1004 (1987).
[4] R. Majeski, *et al.*. at this conference (1993).
[5] F.J. Stauffer, *et al.*, Rev. Sci. Instrum. **56**, 925 (1985).
[6] R.J. Fonck, *et al.*, Phys. Rev. Lett. **63**, 520 (1989).
[7] D.K. Mansfield, *et al.*, Appl. Opt. **26**, 4469 (1987) and H.K. Park, Plasma Phys, and Controlled Fusion **31**, 2035 (1989).
[8] J.A. Murphy, *et al.*, Princeton Plasma Physics Laboratory Report No. PPPL-TM-393 (January 1992).
[9] R.J. Goldston, Plasma Phys. **26**, 87 (1984).
[10] D.N. Smithe, *et al.*, Proc. 8th Top. Conf. on RF Power in Plasmas, Irvine, Cal. (AIP, NY, 1989), p. 338., R.C. Goldfinger, *et al.*, Proc. 10th Top. Conf. on RF Power in Plasmas, Boston (1993) and G.W. Hammett, Ph.D. Thesis, Princeton University (1986).

ICRF ANTENNA AND RF-EDGE PLASMA STUDIES IN TFTR.

R. Majeski, D. A. D'Ippolito*, Y. L. Ho**, J. Hosea, S. S. Medley, M. Murakami***, J. R. Myra*, C. K. Phillips, J. H. Rogers, G. Schilling, J. Stevens, G. Taylor, J. R. Wilson, and the TFTR Group.

Princeton Plasma Physics Laboratory, Princeton, New Jersey 08543, USA
**Lodestar Research Corp., Boulder, Colorado 80301 USA*
***Science Applications International Corp., San Diego, California, 92121 USA*
****Oak Ridge National Laboratory, Oak Ridge, Tennessee 08731 USA*

Introduction

The TFTR ICRF system has now demonstrated power coupling at the 11.4 MW level into an L-mode plasma in a hydrogen minority heating regime[1]. Up to 7.4 MW of rf power has been coupled into ^{3}He minority supershot discharges[2] and 3 MW during direct electron heating experiments[3]. During the upcoming deuterium-tritium (D-T) phase operation at increased power levels in supershot and direct electron heating scenarios is desired. Operation at phasings other than the presently utilized 180° is needed for fast wave current drive (FWCD) experiments. With these requirements in mind, two of the four antenna matching systems have been modified to allow operation at either of two frequencies, 43 or 63.6 MHz. These antennas can operate at arbitrary relative phase with sufficient loading. Feedback systems are being implemented to maintain constant relative antenna phase and constant antenna loading. Prior operation of the Bay M antenna at 0° phasing produced an influx of Faraday shield material and "antenna glow" phenomena at powers in excess of 1 MW[4]. Sheath effects [5,6] for 90° phasing for a two-strap antenna are expected to be similar to 0° phasing[7]. Modelling of rf-driven sheath effects for the TFTR geometry has therefore been undertaken in order to better predict future antenna performance.

The TFTR ICRF system consists of four two-strap antennas driven by six generators. Two antennas are driven by pairs of rf generators (one per strap) and can be operated at phases other than 180°. These generators are tunable over 40-80 MHz. The remaining two antennas are each driven by a single fixed-frequency generator and operate at fixed 180° phasing. Total available generator power is 16 MW. All the antennas are equipped with titanium carbide coated Faraday shields and graphite frame limiters. The antennas are center-grounded and end-fed using a resonant transmission line loop which is in turn fed near a high-impedance point. Impedance matching to the resonant loop utilizes a quarter-wave impedance transformer, a line stretcher, and a stub tuner. Operating frequency has been 47 MHz.

Experimental results on rf power limits from 1992.

A maximum of 11.4 MW of rf power has been coupled to an L-mode plasma with B_T=3.4 T, and I_p=1.85 MA in a hydrogen minority heating regime (Fig. 1 a&b). Antenna loading under these conditions was high and relatively constant, ranging from 20 - 40 × vacuum values. However, the rf-produced increase in stored energy exhibits a rollover as power increases (see Fig. 2) which is believed due to instability-induced tail ion losses[1]. Power coupled into a supershot plasma has reached 7.4 MW[2] with B_T=4.7 T and I_p=1.85 MA in a ^{3}He minority heating regime. In this case the neutral beam-fueled density ramp produced a time-varying loading resistance which complicated antenna matching and limited coupled power. For ^{3}He minority plasmas with low beam power (<15 MW), antenna

cross-coupling, in which rf power injected by one antenna is coupled to a second antenna and appears as reflected power, limited injected power. In direct electron heating experiments with no minority population, up to 3 MW of rf power has been coupled[3]. In this case low loading and antenna cross coupling limit power.

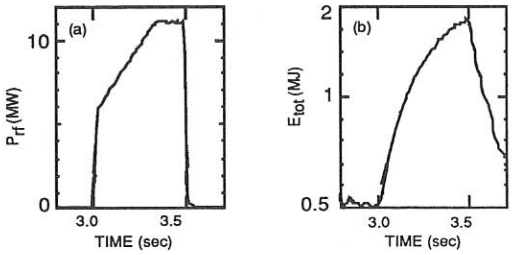

Figure 1. Coupled power (a) and stored energy (b) for an L-mode discharge with hydrogen minority ICRH.

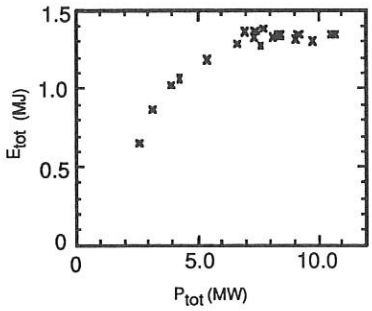

Figure 2. Stored energy as a function of ICRF power for a sequence of L-mode discharges.

Modifications to the ICRF system for 1993.

The antennas which are driven by paired generators will now be capable of operation at either 43 or 63.6 MHz[8]. In order to obtain a second operating frequency for the resonant-loop matching systems the length of the transmission line which comprises the loop was increased to resonate at 21.5 MHz. The loop is therefore 2λ long at 43 MHz and nominally 3λ long at 63.6 MHz. The resonant loops are fed with a tapered impedance quarter wave transformer optimized for operation at 43 and 64 MHz. The remaining two, single generator-driven antennas will operate at 43 MHz. Simultaneous operation at 43 MHz and 63.6 MHz will permit simultaneous H and ^{3}He minority heating with the ion resonances at high toroidal field (4.2 T) and split the power input between the two minority species. Figure 2 clearly indicates the advantages of limiting power input to the hydrogen minority to <7-8 MW. Cross coupling between the ^{3}He minority heating systems will be at the least simplified, since only two antennas and generators are involved. Direct fast wave heating of electrons at 63.6 MHz will be aided by the higher loading resistance afforded by the frequency increase.

Two major feedback systems are also being implemented. The plasma major radius will be feedback controlled to maintain constant antenna loading. This will aid in antenna matching during the beam-fueled supershot density ramp. A second

feedback system will maintain constant strap to strap phase during rf injection by varying the relative phase of the synthesized rf sources. The phase control system will ease operation at 90° phasing, which has already been demonstrated at the 1.2 MW level using one antenna.

Antenna-edge plasma effects.

Impurity influx during ICRF heating with 180° phasing in TFTR has been minimal[9]. However, initial operation at P_{rf}>1 MW in 0° phasing using the Bay M antenna produced a region of strong interaction with the edge plasma on the titanium carbide-coated Faraday shield face[4], and a resultant titanium influx[9]. Since operation at 90° phasing is expected to produce edge interactions similar to the 0° case[7], we attempt to explain past observations of edge plasma interactions at the Faraday shield through rf sheath effects[5]. In this model rf voltages are inductively generated across sheaths at bounding surfaces in the scrape-off layer (SOL) plasma. An increase in the time-average SOL space potential (rf self-bias) to a value on the order of the rf sheath voltage results, to limit electron losses across the sheath and maintain charge neutrality in the SOL. The increased space potential in turn accelerates ions across the sheath and produces an rf-driven impurity influx.

During the 0° phasing experiments the Bay M antenna design permitted the SOL magnetic field lines to link the Faraday shield face with a nearby limiter. This linkage was subsequently eliminated by a modification to the graphite frame which surrounds the antenna. Hence for the original Bay M geometry we first consider rf sheath effects produced in the SOL between the antenna Faraday shield and a nearby limiter (shield-limiter or S-L sheaths). For the present Bay M antenna geometry rf sheath generation at the Faraday shield face occurs only along SOL magnetic field lines which produce linkage across the "Vee" shaped Faraday shield (shield-shield or S-S sheaths). For either antenna geometry rf sheath generation also occurs along SOL field lines which link the sides of the graphite antenna frame and neighboring limiters.

The calculated poloidal distribution of rf sheath voltages on the Faraday shield

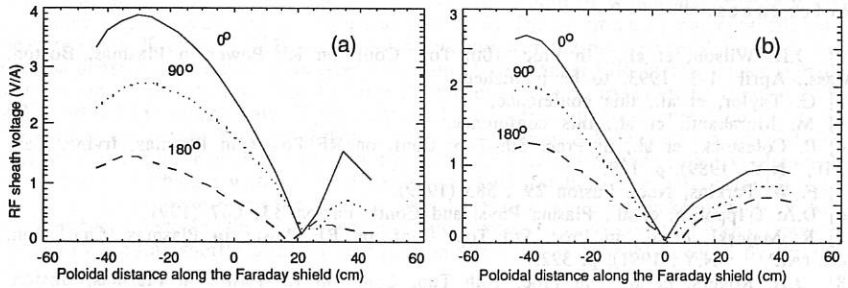

Figure 3. (a) Calculation of the rf sheath voltage on the Faraday shield, above the antenna strap, for the old Bay M geometry, and (b) along the toroidal edge of the graphite antenna frame for both the old and new geometries.

over the antenna strap for the original Bay M antenna geometry for 0° phasing is shown in Fig. 3(a). The peak in the calculated rf sheath voltage occurs on the Faraday shield near the lower end of the antenna strap, at a position which corresponds to the experimentally observed interaction region[4]. Note that typical antenna currents for 1 MW operation are in the 500 A range (0-peak), implying that the predicted sheath voltages and the associated self-biases are typically several kV. Figure 3 also displays calculations for 90° and 180° phasings. For 180° a factor of three reduction in the sheath voltage from the 0° value is predicted. Poloidal and toroidal variations in the self-bias potentials also lead to E×B driven plasma convection [10] which can be estimated for TFTR parameters to be 10-20 × Bohm, producing large density modifications at the Faraday shield.

A modified version of an rf sheath impurity influx model[6] which takes into account the TFTR geometry, has been used to approximately estimate the rf-driven impurity influxes at the shield. For the old Bay M geometry, the model predicts an influx $\Phi=1\times10^{19}$ Ti atoms sec^{-1} (65% from the S-L sheaths, 35% from the S-S sheaths) for 0° phasing, and $\Phi=4\times10^{18}$ Ti atoms sec^{-1} (all from the S-L) sheaths in 180° phasing. For the new graphite frame geometry, the elimination of the S-L sheaths reduces the predicted influx to $\Phi=4\times10^{18}$ Ti atoms sec^{-1} in 0° phasing (comparable to the old 180° case) and negligible levels in 180° phasing. 90° operation in the present geometry should not therefore result in a large Ti influx.

Sheath effects on field lines linking the graphite frame and the limiter still occur in the new geometry. A calculation of the poloidal distribution of this rf sheath voltage along the toroidal edge of the graphite antenna frame is shown in Fig. 3(b). The rf voltages are somewhat smaller and would produce a carbon rather than Ti influx. Preliminary data from operation of the Bay L antenna which is similiar to the rebuilt Bay M antenna at 90° phasing and 1.2 MW showed no significant enhancement in Ti influx over 180° operation.

Acknowledgments.

The authors gratefully acknowledge the support of the full TFTR group. This research was sponsored by the Office of Fusion Energy, US Department of Energy, under contract DE-AC02-76-CHO-3073.

References.

[1] J.R. Wilson, et al., in Proc. 10th Top. Conf. on RF Power in Plasmas, Boston, Mass., April 1-3, 1993, to be published.
[2] G. Taylor, et al., this conference.
[3] M. Murakami, et al., this conference.
[4] P. Colestock, et al., in Proc. 8th Top. Conf. on RF Power in Plasmas, Irvine, Cal., (AIP, N.Y., 1989), p. 189.
[5] F. W. Perkins, Nucl. Fusion **29** , 583 (1989).
[6] D.A. D'Ippolito, et al., Plasma Phys. and Contr. Fusion **33**, 607 (1991).
[7] R. Majeski, et al., in Proc. 9th Top. Conf. on RF Power in Plasmas, Charleston, S.C. (AIP, N.Y., 1991), p. 322.
[8] J.H. Rogers, et al., in Proc. 10th Top. Conf. on RF Power in Plasmas, Boston, Mass., April 1-3, 1993, to be published.
[9] J.E. Stevens, et al., Plasma Phys. and Contr. Fusion **32**, 189 (1990).
[10] D.A. D'Ippolitto, et al., in Proc. 14th IAEA Conf. on Plasma Phys. and Contr. Nuclear Fusion Res., paper IAEA-CN-56/E-3-9 (1992).

ICRF Direct Electron Heating Experiments in TFTR

M. Murakami,[a] E. Fredrickson, E. F. Jaeger,[a] D. A. Rasmussen,[a] F. G. Rimini,[b] J. R. Wilson, M. C. Zarnstorff, D. B. Batchelor,[a] M. G. Bell, R. Budny, C. E. Bush,[a] D. Darrow, R. C. Goldfinger,[a] D. J. Hoffman,[a] J. C. Hosea, A. Janos, R. Majeski, D. Mansfield, H. Park, C. K. Phillips, J. H. Rogers, S. Sabbagh,[c] G. Schilling, S. C. Scott, J. E. Stevens, E. Synakowski, G. Taylor, R. W. Wieland, and S. Zweben

Princeton Plasma Physics Laboratory, Princeton University,
P.O. Box 451, Princeton, New Jersey 08543
[a] Oak Ridge National Laboratory, Oak Ridge, Tennessee 37831
[b] JET Joint Undertaking, Abingdon, Oxfordshire, United Kingdom
[c] Columbia University, New York, New York 10027

Introduction

Direct electron damping[1–3] of the fast wave is a prerequisite to a viable current drive scenario for future steady-state tokamaks. It is also an attractive heating alternative to the standard ion resonance heating methods for DT experiments on TFTR because it does not require the addition of non-reactive ion species and avoids minority ion tails during studies of alpha-particle effects. The absence of minority ions in direct elctron heating (DEH) also allows the use of RF power modulation to determine power deposition profiles and to carry out modulation transport studies to characterize electron transport in supershot plasmas, as described in this paper.

Experimental Conditions

Direct electron heating experiments have been conducted in the ^{3}He minority regime (B_T = 4.6 T at R_0 = 2.62 m and a = 0.96 m) but with no ^{3}He present. The only ion resonance is the deuterium fundamental resonance on the high field side. Figure 1 shows the RF power waveform and time evolution of several plasma parameters, together with analysis results using a time-dependent transport analysis code, TRANSP.[4] D^0 NBI of 24 MW into a low edge recycling D^+ plasma creates a supershot[5] plasma with high central electron temperature $T_e(0)$ = 8 keV and high central density $n_e(0) = 6 \times 10^{19}$ m^{-3}, both of which are necessary for reasonable single-pass absorption (calculated to be ≈8%). The electron temperature profile was measured by a 20-channel ECE grating polychromator with 0.2-ms time resolution, and the electron density was derived from Abel-inversion of 10-channel FIR interferometer signals with 0.5-ms time resolution. The 47-MHz RF power is ≈100% modulated (ΔP_{FW} = 1.65 MW) with a 5-Hz square wave. $T_e(0)$ increases by 1.5 keV, and stored energy continues to rise, with a confinement time better than L-mode by a factor of 2. However, shortly (≈30 ms) after the first RF pulse ends, the supershot performance starts to degrade (the degradation is not unique to discharges with RF) owing either to MHD instabilities or to increased limiter recycling. The central electron temperature starts decreasing, while the peaked density profile becomes broad, reducing the central density. Density modulation concomitant with RF power modulation begins shortly after the degradation starts and is probably caused by limiter recycling.

Electron Heating Power Profiles

The power per unit volume absorbed by electrons can be inferred from the change in the time-derivative of the electron energy density $U_e = (3/2)n_eT_e$ through $\Delta q_e = \Delta(\partial U_e/\partial t)$ at the time when the RF power is turned on or off, assuming that the heat transport remains constant during the RF power transition. Details of the measurements are discussed elsewhere.[6] Figure 2 shows the power deposition profiles analyzed for the last three pulses (3.8 to 4.4 s) in the discharge. The profile shown by solid dots was obtained by taking into account both the electron temperature and density changes. Comparing this with the power deposition profile solely based on $\Delta(\partial T_e/\partial t)$ (which agrees well with a Fourier transform technique), we observe

that the density modulation has little effect on the q_e profiles within normalized radius $\rho = 0.3$, but has substantial effects on the volume-integrated power $P_e(\rho)$ at outer radii. The total electron absorbed power $P_e(a)$ is 60(±10)% of the incident RF power, of which about 30% is due to the density modulation at outer radii. The total (electron and ion) power deposited in the plasma can be inferred from the magnetic measurements (diamagnetism and equilibrium). These measurements show that the total absorbed power $P_{tot}(a)$ is 80(±10)% of the input power. The difference (≈20%) between this value and the total electron absorbed power (≈60%) could be attributed to the power absorbed by D^+ ions in the fundamental resonance, although time resolution and statistics in the ion temperature measurements are insufficient to detect the modulation in the presence of large heat input from NBI.

The measured power deposition profiles are consistent with those predicted by a 3-D full-wave code, Poloidal Ion Cyclotron Expansion Solution (PICES),[7] with 100 toroidal modes. The predicted power deposition profiles are centrally peaked with the volume-integrated power of 75(±10)% of the input power. The fundamental deuterium ion resonance at the normalized radius $\rho \approx 3/4$ is predicted to absorb 20(±10)% of the input power. The power deposition measured in the core (within $\rho = 1/4$) increases with increasing central electron pressure [product of $n_e(0)$ and $T_e(0)$], as expected from the increase in the electron damping with increasing electron beta. These measured electron heating power profiles are used to interpret transport properties of the supershot plasma.

Transport Studies

The centrally peaked RF power deposition to electrons represents a large perturbation to electron heating in NBI-heated plasmas, even with modest RF power. Figure 3(a) shows the profile of the total input power density to electrons (a solid bold line), which is the sum of terms for the electron-ion equilibration ($q_{i\to e}$), the beam-power to electrons (q_{be}), and the measured DEH power ($q_{e,FW}$) during the first RF pulse. Figure 3(b) illustrates the resultant electron temperature profile $T_e(\rho)$ compared with that before the RF pulse. The $T_e(\rho)$ profile in the core responds to the addition of the RF power, but the T_e increase is not saturated before the RF power is turned off, and the heat capacity term (dU_e/dt) at the end of the RF pulse is as large as a half of the RF power to electrons [as illustrated by the bold broken lines in Fig. 3(a)]. When the measured RF power deposition profiles are incorporated in the post-TRANSP analysis, there are no substantial discontinuities in the calculated thermal diffusivity $\chi_e(\rho,t)$ at the time of the RF power transitions. This verifies the a priori assumption of constant transport in the previous deduction of the power deposition profiles.

Modulation of the RF power also allows modulation transport studies of the supershot plasma. Both the electron temperature and density at a given radius are Fourier analyzed to obtain the phase and amplitude of the fundamental frequency (5 Hz) components for the last three pulses (3.8 to 4.4 s). The T_e modulation amplitude profile is the one used to calculate the power deposition profile in Fig. 3(b). The observed phase profile is roughly constant in the core ($\rho \le 0.4$) region, confirming the extent of the centrally peaked power deposition profile. Outside this region, the phase lag increases roughly linearly with radius, while the amplitude decays exponentially with radius, indicating that the heat propagation is diffusive. Interpreting the radial dependence of the phase and amplitude as being due to thermal diffusion, we find $\chi_e \approx 6.8$ and 4.6 m^2/s, respectively. These values agree (to within a factor of 2-3) with the χ_e value inferred from the power balance, as shown in Fig. 4. The discrepancy between the χ_e value based on the (transient) heat wave analysis and on the (equilibrium) power balance is smaller than that for the χ_e derived from sawtooth-induced T_e perturbation in TFTR (with the ratio typically >5).[8] The phase of the electron density wave is observed to decrease with the radius, indicating that the density wave propagates inward. The radial dependence of the phase lag and amplitude corresponds to $D_e \approx 1.0$ and 1.7 m^2/s, respectively. These values agree (to within factor of 2) with those derived from the (equilibrium) particle balance in TRANSP, as shown in Fig. 4. We also note that the ratio D_e/χ_e is between 1/3 and 1/5.

The changes in the T_e gradient with the DEH modulation provide an opportunity to test the critical temperature gradient (Rebut-Lallya-Watkins) model.[9] The temperature gradient $|\nabla T_e|$ observed in this experiment exceeds the critical temperature gradient $|\nabla T_e|_c$ throughout the plasma (with the ratio decreasing radially from 4 - 5 at the core to ≈1 at the edge). The

profiles (with and without RF) of the total (conductive and convective) heat flux $q_{e,tot}(\rho)$ from the experiment is compared in Fig. 5 with those calculated from the RLW model, $q_e^{RLW} = n_e\chi_{e,an}(|\nabla T_e|-|\nabla T_{e,c}|) + 5/2\,\Gamma T_e$, using experimentally obtained parameters. The radial behavior of $q_{e,tot}(\rho)$ is different from the model. Similarly, loci of q_e as a function of $-n_e\nabla T_e$ (whose slope gives the effective heat conductivity) at a fixed radius (e.g., $\rho = 0.25$) during the different phases of the discharge behave somewhat differently from predictions of the RLW model. Therefore this interpretive analysis indicates that the RLW model fails to describe the experiment. However, we note that the model analysis could be sensitive to some parameters [e.g., q/∇q] and more detailed elements of the model (beyond the published formula[9]) may need to be implemented in our simulation.

Summary and Conclusion

Direct electron heating with the fast wave has been observed in TFTR under conditions with minimal ion damping and at high electron temperature. Application of ≤3-MW RF power of 47 MHz to NBI-heated supershot deuterium plasmas with no resonant minority ions increased the central electron temperature by up to 2.5 keV. The electron power deposition profile was measured with modulation of RF power at 5 Hz, showing strongly peaked profiles in the core with a total integrated power of up to 80% of the applied power. The magnitude and profile shape agree well with those predicted by a 3-D, full-wave ICRF modeling code. The centrally peaked power absorbed by electrons represents a large perturbation to electron heating in NBI-heated plasmas even with modest RF power. Modulation of RF power enabled an estimate of thermal diffusivity (χ_e) from the heat wave analysis, which agrees with that derived from the power balance analysis ($\chi^{HW}/\chi^{PB} \approx 2$). Particle diffusivity derived from analysis of the density wave concomitant with the ICRF modulation is also in agreement with that from the particle balance analysis. Electron transport with the measured heating power profiles are not in agreement with the critical temperature gradient model.

In the forthcoming TFTR DT operation period, these DEH experiments will be extended to include modulation of RF power in DT supershot plasmas. The presence of tritium second-harmonic resonance may help to increase the antenna loading and to alleviate the problem of antenna cross-talks which limited the RF power during the present DEH experiments.[10] The electron heating will increase alpha population by increasing alpha slowing down time without complications of minority ions.

Acknowledgments

We wish to acknowledge the ICRF group and TFTR project engineering and technical staff for their contribution to this work. We are grateful to Drs. R. Davidson, R. Hawryluk, H. Furth, K. McGuire, D. Meade, and P. Rutherford for their continued support. The research was sponsored by the Office of Fusion Energy, U.S. Department of Energy, under contract DE-AC02-76-CHO-3073.

References

1 D. F. H. Start et al., Nucl. Fusion **30**, 2170 (1990).

2 T. Yamamoto et al., Phys. Rev. Lett. **63**, 1148 (1989).

3 C. C. Petty et al., Phys. Rev. Lett. **69**, 289 (1992).

4 R. J. Hawryluk, in Physics of Plasma Close to Thermonuclear Conditions (Proc. Course Varenna, 1979) Vol. 1, CEC, Brussels, 19 (1980); R. J. Goldston, in Basic Physical Processes of Toroidal Fusion Plasmas (Proc. Course and Workshop Varenna, 1985), Vol. 1, Monotypia Franchi, Perugia 165 (1986).

5 J. D. Strachan et al., Phys. Rev. Lett. **58**, 1004 (1987).

6 M. Murakami et al., to be published in Tenth Topical Conference on Radio Frequency Power in Plasmas, Boston, AIP Conf. Proc. (1993)

7 E. F. Jaeger, D. B. Batchelor, and D. C. Stallings, Nucl. Fusion **36**, 179 (1993).

8 E. D. Fredrickson et al., Nucl. Fusion **26**, 849 (1986).

9 P.-H. Rebut et al., Phys. Fluids B **3**, 2209 (1991).

10 R. Majeski et al., this conference.

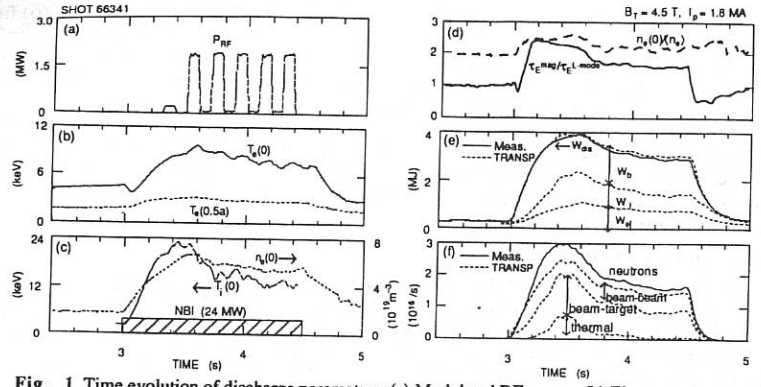

Fig. 1 Time evolution of discharge parameters: (a) Modulated RF power; (b) Electron temperature; (c) Central ion temperature and electron density; (d) Enhancement factor of global energy confinement time over Goldston L-mode scaling, and density peaking factor; (e) Stored energy measured and calculated; and (f) Neutron emission rates measured and calculated.

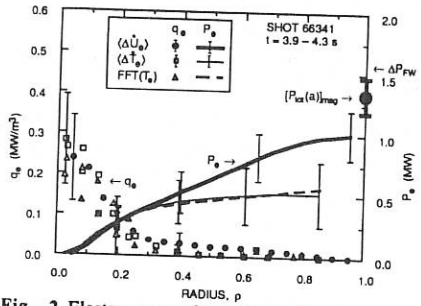

Fig. 2 Electron power deposition profiles (power density and volume-integrated power) average over the last three pulses (t = 3.9 – 4.3 s). The total absorbed power measured magnetically is also shown by the large dot.

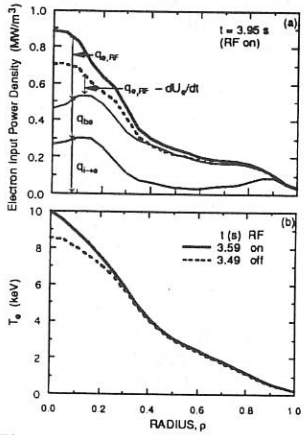

Fig. 3 (a) Electron heating power density and its components; (b) Electron temperature profile before and during the first RF pulse.

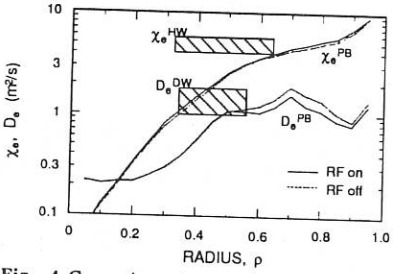

Fig. 4 Comparison of electron heat diffusivities (χ_e) and particle diffusivities (D_e): χ_e derived from power balance (PB) and heat wave (HW) analysis and D_e from particle balance (PB) and density wave (DW) analysis.

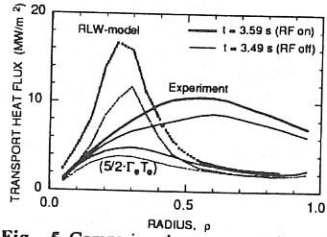

Fig. 5 Comparison between experimental electron heat flux and predictions of the RLW model.

ICRF "3-D" Antenna Coupling and Fast Ion Heating Models for Fusion Plasmas*

J. E. Scharer, M. Bettenhausen, N. T. Lam and R. S. Sund
University of Wisconsin, Madison
and
O. Sauter, General Atomics

Abstract

Analysis and computer simulation is presented for investigating coupling of Ion Cyclotron Range of Frequency (ICRF) waves to tokamak plasmas using phased coil antenna arrays. The model accounts for 3-D antenna and feeder current effects, an antenna cavity which is finite in all three dimensions and warm plasma effects. The effect of the three-dimensional cavity on the parallel wavenumber spectrum of the coupled power is investigated. We also consider the problem of fundamental and second harmonic deuterium and fast tritium beam heating for ITER and TFTR plasmas in the presence of a population of fast alpha particles. A range of D/T ratios and deuterium tail temperatures are examined for ITER for a range of alpha particle concentrations. We find that the region near the two-ion D-T hybrid resonance can provide a substantial enhancement of the alpha particle absorbed power and wave reflection. We also to describe second and higher harmonic heating of the deuterium, tritium and alpha particles for the case of the TFTR supershot. We find that a significant (> 5%) alpha particle heating occurs for the second harmonic deuterium heating case.

I. Description of the Antenna Model and Results. Accurate modeling of ICRF antennas is of interest to support operation and understanding of existing ICRF experiments and to aid in the design of future ICRF systems. The model presented here is an extension to the models developed by Brambilla[1] and Chiu et al[2]. The model incorporates a finite length antenna in a three-dimensional recessed cavity and includes parallel electric field and warm plasma effects. A rectangular coordinate system is assumed with x, y and z corresponding to the radial, poloidal and toroidal directions, respectively. Figure 1 shows the geometry used and defines various parameters.

The electric fields excited by the assumed antenna current distribution are calculated by solving Maxwell's equations in four separate regions: in the plasma, $x > 0$, and in the three vacuum regions as labeled in Fig. 1. Boundary conditions are applied between adjacent regions to produce a unique solution. The plasma wave fields are calculated using the model developed by Brambilla[1]. These results are used to calculate a plasma surface impedance relating the electric and magnetic fields at the vacuum-plasma interface.

The boundary conditions at the Faraday shield assume that the shield acts as a perfect conductor parallel to the shield bars and as a perfect insulator perpendicular to the bars. The tokamak and cavity walls are also assumed to be perfectly conducting so that the tangential electric fields are zero on the

$n_{\alpha f}/n_e$ (%)	D (%)	α (%)	e (%)	R (%)
0.1	36	9.9	18	36
0.2	34	18	17	31
0.3	32	25	16	26
0.4	31	31	15	22

Table 2.

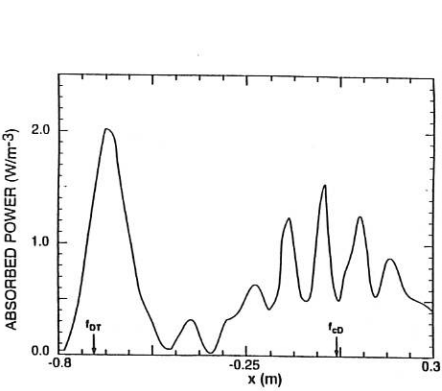

Figure 3. ITER fundamental deuterium heating.

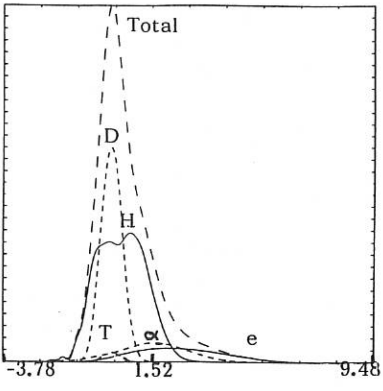

Figure 4. TFTR Supershot at $\omega = 2\omega_{CD0}$.

III. Summary. We are developing a "3-D" antenna code for studies of cavity effects and shield alignment for studies of cavity effects and shield alignment for coupling to edge density profiles on TFTR, JET and TPX. The initial results show significant effects on the antenna spectrum at low and high k_z. The influence of alpha particle absorption on ICRF fundamental and second harmonic deuterium heating can be significant and must be considered for ITER and TFTR supershot scenarios.

Acknowledgments. The authors thank D. Batchelor, M. Carter, D. Stallings and R. Majeski for useful discussions and helpful suggestions and for the use of the 2D antenna coupling code RANT for benchmarking our code. We appreciate the assistance of C. Phillips, R. Majeski and R. Wilson in determining the TFTR ICRF experimental parameters. This research is supported by U.S. DOE Grant Nos. DE-FG02-86ER53218 and DE-FG02-93ER54196 and Princeton Contract S-03587-G.

References.

1. M. Brambilla, Nuclear Fusion, 28, 549 (1988).
2. S.C. Chiu, M.J. Mayberry and W.D. Bard, Nuclear Fusion, 30, 2551 (1990).
3. R. S. Sund and J. E. Scharer, Physics of Fluids B 3, 1326 (1991).
4. O. Sauter and J. Vaclavik, Nuclear Fusion 32, 1455 (1992).

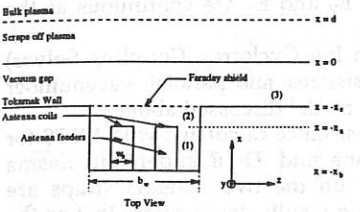

Figure 1. Antenna model geometry.

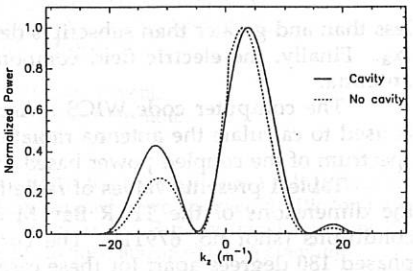

Figure 2. Wavenumber spectrum for coupled power with $(0,\pi/2)$ phasing.

magnetic field and second order gyroradius effects for cases where $(k_\perp \rho_{\alpha t})^2 << 1$. For the second harmonic regime where the third harmonic for tritium and alpha particle higher harmonics are included we utilize the SEMAL[4] code.

We consider the case of fundamental deuterium and alpha particle heating in a tritium plasma with ITER parameters. We assume the plasma to have n_e=9 x 10^{13}/cm^3, B=4.85 T, R_0=6 m, n_D/n_T=0.5, T_e=T_T=10-15 keV and T_D=10-50 keV with a corresponding fast alpha particle concentration of $n_{\alpha f}$=0.1-0.4 % n_e. The two ion hybrid resonance lies at x=-0.7 m towards the high field side from the fundamental resonance on the axis. The corresponding left-hand circularly polarized component peaks in a localized region near the two ion hybrid resonance. The Maxwellian equivalent alpha particle distribution is chosen to have the same number of resonant particles in this region as the slowing down distribution. The $|E_{left}|$ peak extends over a comparatively narrow interval near the two-ion hybrid resonance, and most of the power that goes to the alphas is absorbed in that narrow region. Consequently, we choose the number of resonant particles at x_p, the location of the $|E_{left}|$ peak, to be the basis of equivalency between two distributions.

Table 2 shows the total power absorption for each species for $k_{||}$=6 m^{-1} for the case of the lowest temperature plasmas noted above. Note that a substantial fraction of the incident power can be absorbed by the fast alphas when the absorption by the deuterium and electrons is not complete. Figure 3 shows the total absorbed power density over the region where it is significant. Figure 4 corresponds to a TFTR supershot with n_{eo} = 9 x 10^{13}/cm, T_e = 10 keV, T_H = 50 keV, T_D = T_T = 20 keV, n_D/n_T = 1, n_H/n_e = 2%, n_α/n_e = 0.25% @ T_α = 800 keV. The wave frequency corresponds to $\omega = 2\omega_{CD0}$ on axis at B_0 = 4.5T utilizing the SEMAL code. Note the significant alpha particle heating on the low field side (9%) as well as comparable hydrogen and deuterium heating.

walls. A jump condition is applied at the antenna current elements such that $\hat{x} \times (\vec{B}_> - \vec{B}_<) = \mu_0 \vec{J}_s$ where $\vec{J}_s$ is the surface current on the antenna and the less than and greater than subscripts denote the valued of $\vec{B}$ for $x < -x_a$ and $x > -x_a$. Finally, the electric field components E_y and E_z are continuous at the antenna.

The computer code WICS (Wisconsin Ion Cyclotron Coupling Solver) is used to calculate the antenna radiation resistance and parallel wavenumber spectrum of the coupled power based on the model discussed above.

Table 1 presents values of radiation resistance calculated with WICS for the dimensions of the TFTR Bay M antenna and TFTR supershot plasma conditions (shot no. 67911). The currents on the two antenna straps are phased 180 degrees apart for these cases. The results demonstrate that as the cavity height is increased the radiation resistance increases due to smaller return currents on the cavity walls. Similarly, as the length of the antenna is increased the radiation resistance per meter antenna length increases provided the ends of the antenna are far enough from cavity walls. This result is due to the decreased importance of end effects due to the radial feeders and the finite antenna length.

R_A (Ω)	b_h (cm)	h (cm)	R_A/m (Ω/m)
4.1	81	38	5.4
8.7	550	38	11.4
11.8	550	50	11.8
20.7	550	100	10.4

Table 1. Variation of radiation resistance with antenna and cavity height.

Figure 2 shows the parallel wavenumber spectrum of the coupled power spectrum for the TFTR Bay M antenna for a 90 degree phase difference between currents on the straps. The spectrum has been normalized to give a maximum of 1.0 for each case. The presence of the cavity increases the coupled power in the secondary lobe of the spectrum at negative k_z. The differences in the spectrum shown in the figure is primarily due to a reduction in the power coupled to low k_z rather than an increase in the power coupled to higher k_z. This is consistent with the reduction in radiation resistance due to the cavity as discussed above.

II. ICRF Heating and Applications to ITER and TFTR. We consider the effects of a small concentration of alpha particles on ICRF wave propagation and absorption for an ITER plasma at the fundamental deuterium cyclotron resonance. We then consider the cases of second harmonic deuterium for the TFTR supershot case. For the fundamental and second harmonic regimes we utilize the XWAVE[3] code which includes perpendicular gradients in the

20th EPS Conf. on Controlled Fusion and Plasma Physics, 26-30 July 1993, Lisboa Portugal

Recent progress in ICRF heating experiments on JT-60U

Saigusa M., Kimura H., Fujii T., Moriyama S., Nemoto M.,
Sato M., Hamamatsu K., Hosogane N., Isei N., Kamada Y.,
Koide Y., Sugie T.,Takeuchi H., Yoshino R.

Naka Fusion Research Establishment,
Japan Atomic Energy Research Institute,
Naka-gun, Ibaraki, 311-01, JAPAN

Sawtooth stabilization experiments by ICRH has been performed at high density and low q regimes in JT-60U. The maximum coupled power reached 5 MW for 1.15 sec at out-of-phase. Typical gaps between separatrix and Faraday shield are about 13 cm for out-of-phase and 27 cm for in-phase due to good antenna-plasma coupling.

1. Introduction

Coupling is important item for designing realistic ICRF antenna in fusion reactor. JT-60U ICRF antenna was designed for obtaining high loading resistance even if a wide gap exists between antenna and plasma [1].

The stabilization of MHD instability is important point for good energy confinement. Sawtooth stabilization experiments by ICRH at the fundamental minority heating regime has been investigated in JET [2] and TFTR [3]. Theory suggested that the high energy trapped ions by ICRH suppress the sawtooth instability by stabilizing the m=1 internal kink mode due to the conservation of the third adiabatic invariant which is the flux of the poloidal magnetic field through the area defined by the toroidal precession of the trapped particle orbit centers [4]. The minority second harmonic ICRF heating, which is suitable for producing the high energy ions in the high density plasma, has been investigated at the frequency of 116 MHz in JT-60U [5, 6].

2. Coupling Properties

JT-60U ICRF heating system has 8 tetrods (Eimac 8973) and two antennas which are 2×2 toroidal and poloidal loop antenna array. Eight tetrods can generate 6 MW for 10 seconds and 8 MW for 3 seconds with dummy load at the frequency of 116 MHz. Tuning system consists of eight stub tuners, eight phase shifters and the frequency feedback control function.

Maximum coupled powers increase to 5 MW (at generator output of 5.8 MW) for 1.15 sec in the case of out-of-phase ((π,0) phasing) and 4.4 MW for 0.23 sec in the case of in-phase ((0,0) phasing). The arcing in the tetrods caused by the impedance mismatching disturbed power up for the (π,0) phasing. The fluctuation of loading resistance due to the weak single pass absorption is trouble for keeping good matching during RF pulse for the (0,0) phasing.

The loading resistance (Rc) is defined by $Rc = 2P \cdot (Z_0/V_{max})^2$ on each element, where P, V_{max} and Z_0 (50 Ω at JT-60U) are a through power into a stub tuner, the maximum voltage and the characteristic impedance of transmission line connected to the antenna, respectively. Figure 1 shows the dependence of loading resistance on the line average electron density at the Ip=2~3 MA, Bt_0=3.83~4.05T, where Bt_0 is defined as the toroidal magnetic field on a machine center (R=3.32 m). The open and closed circles show the experimental data of loading resistance for the (π,0) and (0,0) phasings, respectively The solid line is the loading resistance for (π,0) phasing calculated by coupling code assuming that the separatrix electron density is one tenth of central electron density, the gradient of peripheral electron density is $0.9 \cdot n_e(0)/21$cm. The loading resistance for (π,0) phasing is 3.5~6 Ω over the wide density range of $\bar{n}_e$=1~5.5×10^{19} m^{-3} at the separatrix-wall distance of 9~11 cm (Separatrix-Faraday shield distance =12~14 cm).

Dependence of loading resistance on the gap between the separatrix and the first wall on the mid-plane is shown in Fig.2. The antenna is installed to the mid-plane port, and Faraday shield surface is located on 3 cm outer on major radial direction from the first wall. The open and closed circles indicate the average loading resistance of current straps for (π,0) and (0,0) phasings, respectively. The solid lines shows the calculated loading resistances for (π,0) phasing, the dashed line shows the fitted line for (0,0) phasing. The loading resistance is over 4 ohms at the separatrix-wall distance of 10 cm for (π,0) phasing and 30 cm for (0,0) phasing at the plasma current of 2MA. Heating responses were observed in the high energy proton tail and the plasma stored energy in both phasings, clearly. The reason of good coupling properties of JT-60U is explained as the wider and longer current strap and the longer interval of the toroidal adjacent straps, because the cut-off density of $N_{//}$=3 spectrum, which is the peak of coupled $N_{//}$ spectrum for (π,0) phasing, is very low (~1.5×10^{18} m^{-3} at the axial toroidal magnetic field of 4T).

3. Radiation Losses

The ratio of incremental radiation loss from main plasma to the incidental ICRF power at on-axis and off-axis heatings is shown in Fig.3. The ratio of the incremental radiation loss to net ICRF power ($\Delta P_{rad}^{main}/P_{IC}$) was almost 30 percents in JT-60 limiter discharge with carbon wall and carbon guard-limiter [7]. On the other hand, ($\Delta P_{rad}^{main}/P_{IC}$) decreases with increasing ICRF power in the range below 1.5 MW and gradually decreases to 10 % above 1.5 MW with the on-axis-heating in JT-60U. The reason of high $\Delta P_{rad}^{main}/P_{IC}$ in low RF power is thought as the multipactoring discharge or the weak single pass absorption without high energy ion tail, because the multipactoring discharge has been observed below the same power threshold and a Fokker-Planck code predicts the weak single pass absorption in low RF power level.

The power dependence of $\Delta P_{rad}^{main}/P_{IC}$ and the incremental spectral intensity of Ni+24 is not clear in the case of off-axis heating regime. However, the $\Delta P_{rad}^{main}/P_{IC}$ and the incremental spectral intensity of Ni+24 for only off-axis heating regime increases with the average electron density of a target plasma as shown in Fig.4. Therefore, the impurity generation for the off-axis-heating is caused by the some mechanism (parametric instability or ripple trapped high energy ions in peripheral region) concerned with the cavity resonance in vacuum vessel due to the weak single pass absorption. The observed Nickel ion during ICRF pulse may be generated from Faraday shield made of copper plated Inconel 625.

4. Sawtooth Stabilization by Minority 2 ω_{CH} ICRH

Extension of the operation range for the sawtooth stabilization by the minority $2\omega_{CH}$ heating has progressed substantially in recent high power experiments with coupled power up to 5MW. We could obtain the sawtooth stabilization at q_{eff} down to 3.5 (q_{95}>2.8) and $\bar{n}_e$ up to about $5\times10^{19}m^{-3}$.

Figure 5 shows the typical waveform of sawtooth stabilization experiments by ICRH (out-of-phase) at q_{eff}=3.5, Ip=3 MA and Bt_0=3.97 T. W* is the plasma stored energy, $\bar{n}_e$ is the line average electron density, $T_e(0)$ is the central electron temperature measured by the electron cyclotron emission, P_{IC} is the coupled ICRF power. A stable period of about 1 sec was obtained for $\bar{n}_e$=4.8 $\rightarrow$ $4.5\times10^{19}m^{-3}$ with P_{IC} of 4.8MW. The sawtooth inversion radius over plasma minor radius (r_{inv}/a) expanded from about 0.3 to about 0.4 during the stable period.

Figure 6 shows the operation range for the sawtooth stabilization by minority $2\omega_{CH}$ heating in $1/q_{95}$ -$<n_e>$ plane, where the data of sawtooth period > 0.6 sec are plotted for comparing with the JET results, because of almost same plasma volume (~90 m^3). Thus the wide operation range for the sawtooth stabilization by the minority $2\omega_{CH}$ heating was confirmed in low-q and high $<n_e>/P_{tot}$ regime, i.e.q_{95} > 2.8 and $<n_e>/P_{tot}$ <

0.9×10^{19} m^{-3} MW^{-1}. The results imply that the sawtooth stabilization is realized in low-q and high density regimes more efficiently (with less power) by the minority $2\omega_{CH}$ heating.

The sawtooth stabilization tend to be stabilized more easily at high electron density in JT-60U. In fact, the sawtooth-free periods become longer with increasing $\bar{n}_e$ as indicated in Fig.7. The results also indicate that the sawtooth stabilization of low current plasma (2MA) is easier than that of high current one (3MA), because of the inversion radius of 3MA plasma is larger than that of the 2MA plasma.

Figure 8 indicates the sawtooth-free period against the RF power in low density region ($\bar{n}_e$=1.7~2.6$\times10^{19}$m^{-3}). The sawtooth-free periods increases with RF power without RF power threshold in contrast with the clear power threshold observed in JT-60 in high density region [8], and TFTR at minority ω_{CH} heating regime [9].

5. Conclusion

Operation range for the sawtooth stabilization by the second harmonic minority ICRH has been enlarged to the high density ($\bar{n}_e$~5$\times10^{19}$m^{-3}) and low q (q_{eff}=3.5) with high efficiency ($\langle n_e\rangle/P_{tot} < 0.9\times10^{19}$ m^{-3} MW^{-1}) in JT-60U. The maximum coupled power reached 5 MW for 1.15 seconds at out-of-phase and 4.4 MW for 0.23 sec at in-phase. Typical gaps between separatrix and Faraday shield are about 13 cm for out-of-phase and about 27 cm for in-phase due to good coupling. The radiation loss over the RF power decreases to 10 % with increasing RF power.

REFERENCES

[1] Saigusa, M., et al., "Electrical design and test of ICRF antenna for JT-60U" submitted to Fusion Engineering and Design (1993).
[2] Campbell, D.J., et al., (1988) Phys. Rev. Lett., 60, 2148.
[3] Hosea, J.C., et al., Plasma Phys. and Controll. Fusion Research 1990, Vol.1 IAEA, Vienna, (1991) 669.
[4] Porcelli, F., et al., Plasma Phys. and Controll. Fusion Research, **33**, (1991) 1601.
[5] Kimura, H., et al., 10 th Topical Conf. of Radio Frequency Power in Plasmas, Boston, "Sawtooth Stabilization experiments by ICRF Heating alone and its combination with NBI or LHCD in JT-60U", (1993) to be published.
[6] Fujii, T., et al., 10 th Topical Conf. of Radio Frequency Power in Plasmas, Boston, "Lower Hybrid Current Drive and ICRF Heating Experiments on JT-60U", (1993) to be published.
[7] Saigusa, M., et al., (1992) Proc. EPS Top. Conf. on RF Heating and Current Drive of Fusion Devices (Brussels, 1992), EPS, 45.
[8] Kimura, H., et al., "Higher Harmonic ICRF Heating Experiments in JT-60" to be published in Plasma Phys. and Controll. Fusion Research (1993).
[9] Phillips, C.K., et al., 9th Topical Conference of Radio Frequency Power in Plasmas, Charlston " ICRF Heating on TFTR", (1991) 88.

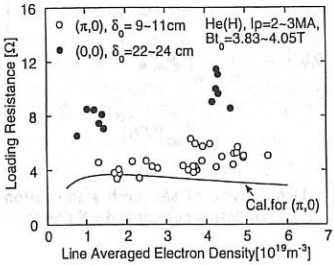

Fig.1 Dependence of loading resistance on the line average electron density.

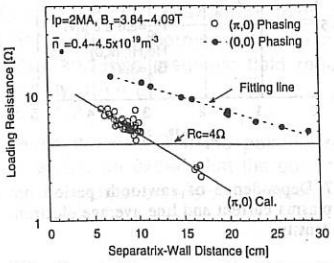

Fig.2 Loading resistance versus the distance between separatrix and first wall on mid-plane.

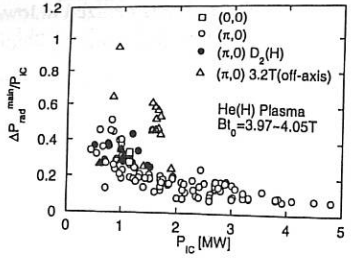

Fig.3 Incremental radiation loss over ICRF power versus ICRF power.

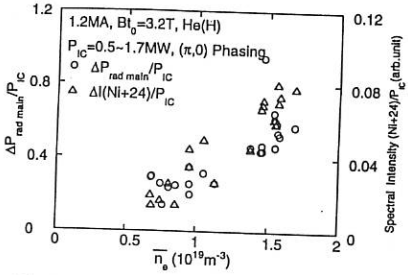

Fig.4 Incremental radiation loss over line average electron density in the case of off-axis heating.

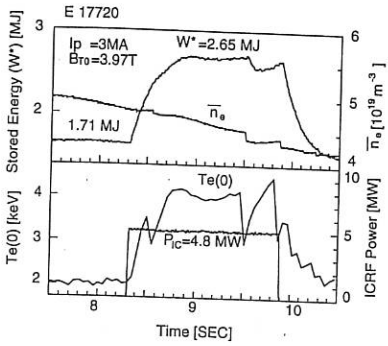

Fig.5 Typical discharge of sawtooth stabilization by ICRH at q_{eff}=3.5, Ip=3 MA and Bt_0=3.97 T.

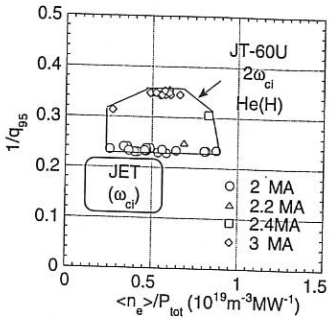

Fig.6 Comparison of operation ranges for sawtooth stabilization by ICRH in JET and JT-60U.

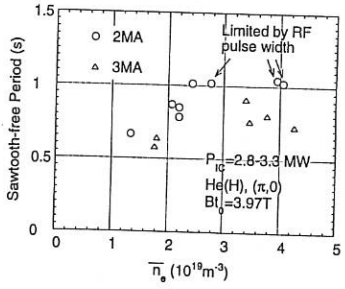

Fig.7 Dependence of sawtooth period on plasma current and line average electron density.

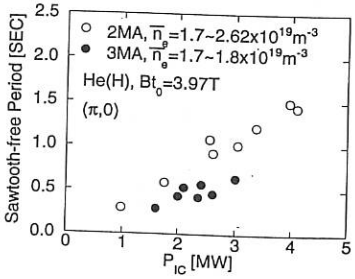

Fig.8 Dependence of sawtooth stabilization effect on Plasma current and RF power.

FAST WAVE AT 433 MHz ON FTU BY A FOLDED WAVEGUIDE LAUNCHER

E. Barbato, F. De Marco, E.F.Jaeger+, M.D.Carter+, D.J.Hoffman+, F.W.Baity+, R.Goldfinger+, D.B.Batchelor+

Associazione EURATOM-ENEA sulla Fusione, Centro Ricerche Energia Frascati
C.P. 65, 00044 Frascati, Rome, Italy

1-INTRODUCTION

The use of fast wave (FW) power to interact directly with electrons is a useful tool for central heating of high density, high temperature plasmas and for electron current drive (CD). Direct electron heating by FW has been observed on JET and TFTR and, although FW absorption is weak at low β, successful electron heating and CD have been achieved on DIII-D[1] at Te=2-3keV. The folded waveguide (FWG)[2] is a promising new concept for ICRF launchers having the advantage of compact, rigid structure and very low impedence (E_y/H_z) at the plasma edge. The FWG is particularly attractive for FTU since loop antennas suffer efficiency degradation at high frequency due to poloidal current decrease, whereas the RF flux coupled by a FWG is more poloidally uniform.

Here we consider the possibility of injecting ~ 1 MW of FW at 433 MHz into the FTU-Tokamak using the FWG as a launcher. Besides testing the FWG, and studying the FW electron heating regime, an other interesting issue of this experiment would be the study of possible sinergy between FW and the lower hybrid wave (LHW) at 8 GHz which is also available on FTU. The main parameters of FTU are a=30 cm, R_0=90 cm, B_T=4-8 T, I_P<1.5MA, n_e=0.4-2.0 $10^{14}cm^{-3}$.

2-FTU-FWG LOADING CALCULATION

Power supplies are available (3 Klystrons, delivering 0.6 MW each, 1 s pulse length) on FTU at 433 MHz. At B_T=7 T this frequency corresponds to the 8th harmonic of the deuterium at the plasma centre and to the 6th harmonic at the plasma periphery, on the low field side. The LH resonance layer of the slow wave branch is localized at the plasma periphery.

The toroidal dimension of the FTU port (Δz=8 cm, Δy=40 cm) fixes the FW parallel wavevector $k_{||}$ at the rather high value of $k_{||}$=45 m^{-1}, corresponding to a toroidal modenumber n_ϕ=40 and to $n_{||}$=5. High frequency and high magnetic field require high density for FW propagation (k_r^2>0) with a cutoff density given by:

$$\omega_{pe}^2(cutoff)=\omega\omega_{ce}(n_{||}^2+n_\theta^2-1)^{1/2}(n_{||}^2-1)^{1/2}. \qquad (1)$$

In order to minimize the cutoff density and increase the coupling, the poloidal refractive index n_θ must be as low as possible. According to eq.(1), we expect that the power per unit antenna length increases as a function of the antenna poloidal extension. Therefore a single FWG is proposed as high as the port.

+ Oak Ridge National Laboratory, Oak Ridge, Tennnesse 378311-8071

To calculate the plasma impedence a cold plasma model is assumed with an outgoing boundary condition far from the plasma edge. A parabolic density profile ($n_o=1.10^{14}$ cm^{-3} and $n_{edge}=1.5\ 10^{13}$cm^{-3}) matched to an exponential profile in the scrape off layer (λ=0.6cm) has been used. Once the impedence is calculated, the vacuum fields distribution inside the cavity and in front of the FWG is calculated using the MAnTIS-3D antenna code [3]. The result of the calculation is the ratio $\frac{P_c}{E_c^2} \sim 0.2 Wm^2V^{-2}$ where P_c is the coupled power and E_c the corresponding electric field inside the FWG, calculated by the code. Up to now, the maximum electric field achieved in a FWG before arcing was $E_{MAX}=2\text{-}3\ 10^6$ V/m[4]. Therefore ~0.5 MW should be coupled to the FTU plasma at the electric field limit. This corresponds to a power flux of 4 KWcm^{-2} and and a vacuum electric field in front of the FWG E_y~1.7 KVcm^{-1}.

3-POWER ABSORPTION CALCULATIONS

The real and the imaginary parts of $n_\perp$ are given by:

$$n_\perp^2=[(S-n_{||}^2)^2-D^2]\ [S-n_{||}^2]^{-1} \qquad (2)$$

$$Im(n_\perp)=0.25\ \pi^{1/2}\ \beta\ \xi\ \exp(-\xi^2)n_\perp(1+\alpha^{-2}) \qquad (3)$$

where $\beta=\frac{8\ \pi n_e T_e}{B_T^2}$, $\xi=\frac{c}{n_{||}v_{the}}$, $\alpha=\frac{P}{D}(S-n_{||}^2)\frac{v_{the}^2}{2c^2}\frac{\omega}{\omega_{ce}}$, $v_{the}^2=\frac{2Te}{m_e}$

and S,D,P, in the frequency range of interest here ($\omega^2>>\omega_{ci}^2$) read: $S=-\omega_{pi}^2\omega^{-2}$, $D=\omega_{pe}^2(\omega\omega_{ce})^{-1}$, $P=-\omega_{pe}^2\omega^{-2}$ with the ordering $P>D^2>>S$ (S~10, D~10^2,P~10^5). Since $\alpha^2\sim[(S-n_{||}^2)v_{the}^2/(2c^2)]^2<<1$ holds, only the second term survives in eq.(3) that becomes:

$$Im(n_\perp)=0.5\ \pi^{1/2}\ \beta\ \xi^3\ \exp(-\xi^2)\ n_\perp\ \frac{n_{||}^2}{(S-n_{||}^2)} \qquad (4)$$

where the Landau Damping dominates. Since $n_\perp$ scales like B_T^{-1}, $Im(n_\perp)$ scales like B_T^{-3}

There is a remarkable analogy between the DIII-D and the FTU experiment, as far as the non-dimensional parameters involved in the absorption (ω/ω_{ce}, β, ξ_e) are concerned. In particular, the corresponding set of parameters are: f=60 MHz, B_T=1 T,$n_e=1.410^{13}$ cm^{-3}, $n_{||}$=9, T_e>1keV for DIII-D and f=433 MHz, B_T=7 T, $n_e=1.10^{14}$ cm^{-3}, $n_{||}$=5, T_e> 3.2keV for FTU. In fig.(2) $n_\perp$ and $Im(n_\perp)$ (eq.(3)) are plotted, as a function of ξ, for different FTU parameters. According to eq.(4) $Im(n_\perp)$ has a maximum at $\xi^2\sim3/2$ corresponding to $n_{||}$=6 for FTU (at T_e=4keV), and $n_{||}$=10 for DIII-D (at T_e=1.5keV). On DIII-D successful heating is observed when T_e>1keV, i.e.when the maximum of $Im(n_\perp)$ starts to overlap with the maximum of launched $n_{||}$-spectrum. When this condition is fullfilled, in spite of the smallness of first pass absorption calculations, 80% of the power is estimated to be absorbed independent of the magnetic field. The non-dependence on B_T suggests that multiple pass absorption occurs. Toroidal effects can upshift $n_{||}$ along the ray trajectory and therefore also the power launched at low $n_{||}$ has some chance to be absorbed.

From the analogy of the FTU experiment parameters with those of DIII-D, we could expect heating on FTU when launching $n_{||}$=6 into the FTU plasma target previously given. In fact, according to the Lackner-Gottardi[5] scaling for the energy confinement time, 0.5MW of additional power, at q=3, B_T=6T and $n_e=1.10^{14}$ cm^{-3}, lead to an increment of the central

electron temperature of 0.4Kev. Indeed the monopole spectrum, launched by the FWG, is peaked at $n_{||}$ somewhat lower than 6 so the estimate of the FW absorbed power may be optimistic. However, the extent to which the low $n_{||}$ are absorbed is not clear. As already pointed out, toroidal effects can lead to an enhanced absorption of low $n_{||}$. Ray tracing calculations for FTU showed that a ray with $n\phi$=30, whose first pass absorption was less than 1%, suffered 7% of power absorption after 3 ray passes. Similarly a ray with $n\phi$=40 showed 25% absorption after few ray passes, while the first pass absorption was 7%. The ray tracing results definitely tell us that a full wave analysis is required because several wall reflection are needed in order to damp the rays. In a full wave code the $n_{||}$ variations are taken into account by retaining the coupling in the m_θ modes. A few runs have been done for FTU with the PICES[6] code just to show the role of the m_θ coupling ($n_{||}$ upshift) in the absorption of low $n\phi$. When the m_θ coupling is on, a higher plasma resistance is found (19 Ω, corresponding to 30KW for a 0.18 long strap antenna at the the electric field limit) and low $n\phi$ modes appear in the coupled (absorbed) spectrum.

Up to now we considered FW absorption on a maxwellian plasma target neglecting kinetic aspects. Indeed LHW strongly modifies the electron distribution function and this may affect the absorption especially of low $n_{||}$. Quasilinear calculations of the electron distribution function[7] show that the simultaneous application of both waves induces an enhancement, up to a factor 200, in the absorption of FW when these latter travel faster than the LHW. This is due essentially to the increment of the suprathermal population interacting with FW, induced by LHW. In fig.(2) the FW absorbed power is plotted as a function of the LHW power for two values of the launched FW power. In this calculation the power flux of the wave are calculated at r=a/2 and the absorbed power is obtained multiplying the power density, calculated by the code, by the volume $V=\pi^2 R_0 a^2/2$.

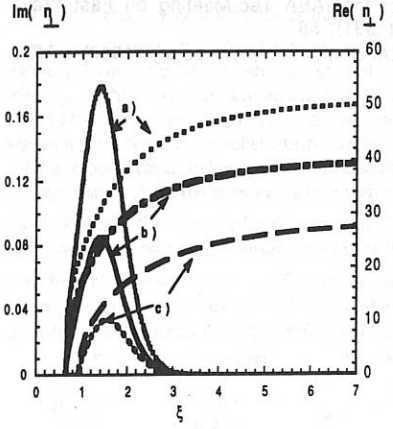

Fig.1 $Re(n_\perp)$ and $Im(n_\perp)$ vs. ξ at a)B_T=5.5T, T_e=3.5keV, n_e=$2\,10^{14}$cm^{-3} b)B_T=7T, T_e=3.5keV, n_e=$2\,10^{14}$cm^{-3} c)B_T=7T, T_e=3.5keV, n_e=$1\,10^{14}$cm^{-3}.

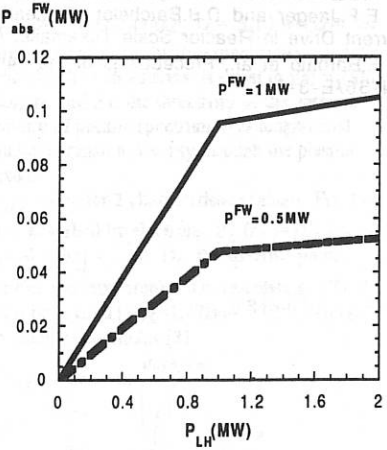

Fig.2: QLFP Calculations: FW absorbed power vs P^{LH} ($n_{||}^{FW}$=3, $\Delta n_{||}^{FW}$=0.5, $n_{||}^{LH}$=4, $\Delta n_{||}^{LH}$=1) at Te=3.5keV and n_e=$1\,10^{14}$cm^{-3}.

4- CONCLUSIONS

The possibility of injecting Fast Waves at 433MHz into FTU by means of a FWG has been analyzed. In order to minimize the poloidal mode number and increase the loading per unit poloidal length, a single FWG in a port is proposed, having a monopole polarizing plate with a poloidal extension of 0.4m. In this case 0.5MW are estimated to be coupled to the plasma at the electric field limit. The monopole spectrum extends in $n\phi$ from -60 to +60 corresponding to $n_{||}$=7.5. In spite of the smallness of first pass absorption (few percent) high $n_{||}$ (>5) are expected to be absorbed on FTU in analogy to what observed on DIII-D. Furthermore there are indications, from ray tracing, full wave calculations and Fokker-Plank calculations, that low $n_{||}$ (<5) may also be absorbed. 0.5MW absorbed by a typical FTU plasma produce an increment of the central electron temperature of 400eV. Furthermore in a LH driven plasma at relatively high density and low magnetic field, FW at low $n_{||}$ (monopole spectrum) could enhance the current drive efficiency.

REFERENCES

[1] R. Prater et.al., Plasma Phys. and Controlled Fusion **35** (1993), A53
[2] T.L.Owens, IEEE Transactions on Plasma Science**14** (1986), 934
and G.L.Chen et al., IEEE Transactions on Plasma Science**16** (1988),301
[3] M. D.Carter et al., AIP Conference Proceedings 244, RF Power in Plasmas, Charleston (1991), 164 , also 10th Topical Conference on RF Power in Plasmas, Boston (1993)
[4] R.H.Goulding et al., AIP Conference Proceedings 244, RF Power in Plasmas, Charleston (1991), 287
[5] K.Lackner and N.A.O.Gottardi, Nuc. Fus. **30** (1990), 767
[6] E.F.Jaeger and D.B.Batchelor, Proceedings of the IAEA Tec-Meeting on Fast Wave Current Drive in Reactor Scale Tokamaks, Arles (1991), 86
[7] E.Barbato et al., Proceedings of the 14th IAEA Conference, Wurzburg (1992), IAEA-CN-56/E-3-3.

Fast wave excitation and absorption in TJ-1U torsatron in the frequency range $\omega >> \omega_{ci}$

Dyakov V.E., Longinov A.V.,Tsurikov V.A. (Khfti.Kharkov.Ukraine)
Ascasibar E., Castejon F., Rodriguez R.L. (CIEMAT.Madrid.Spain)

Introduction. Investigation of excitation, propagation and absorption of electromagnetic waves in stellarator-type traps requires the complete solution of Maxvell equations accounting for 3-D nonuniformity inherent in these systems in plasma as well as in antenna arrays. However because of mathematical difficulties of exact solving such a problem (in particular even contemporary powerful computers have limited capabilities for solution of such problems) even attempts are absent presently to solve them. Even for tokamaks that are simpler from this point of view (2-D nonuniformity) there are presently available only the first attempts to solve such a problem with the simplified problem setting. Therefore the various approximate methods(models) and especially their combinations may play an important role. Such an approach permits to find out some other phenomena at the qualitative level , some of them being clarified with sufficiency good accuracy. This report gives the results of studying the scenario of heating electrons utilizing fast waves (FW) in the range $\omega >> \omega_{ci}$ in the TJ-1U torsatron (a=15cm ,R=60cm ,B_0=0.5T). The studies nave used the above approach with the 1-D model of FW excitation by an antenna array and with the 3-D model of FW propagation and absorption employing the ray tracing technique.

FW propagation and absorption . Ref.[1] has considered earlier the optional scenarii of RF heating in the TJ-1U using the ray tracing technique. In contrast to Ref.[1] here we study in more detail the regime with f=60MHz in the high gas kinetic pressure plasma β when the Shafranov shift is of value. The radiation of the actual antenna has been simulated by multitude of rays starting from different points of the radiating surface. Though the application of such an approach has not a sufficient theoretical ground , it seems, in any case that this method may be sufficiently accurate for regime when sufficiently slowed-down waves are excited (e.g., with $\lambda_{||} < a$, a is the antenna scale size).

Below we give the results for the asymmetric initial spectrum over the longitudinal wave- number $k_{||}$ .Due to the antenna symmetry the change of sign of initial wavenumbers (k_ζ, $k_\zeta \approx k_{||}$) will give the similar ray trajectory with the change of sign of tangential wavenumbers (with respect tj the magnetic surface). Hence ,e.g., the steady current excited in plasma by the real antenna, is equal to $j(a)=j_c(a)d$, where j_c is the current density obtained in these calculations and d is the directivity of the antenna. Ref.[1] has already noted that due to the 3-D nonuniformity of plasma spectrum over longitudinal wavenumbers symmetries substantially as a result of multiple transit of the ray through the plasma column cross section. Below we give the calculation results

15 rays starting from the antenna surface with equal $N_{||0}$ value for 2 characteristic regimes. Fig. 1-4 gives : $P_e(z_e)$, the integrated spectrum of the RF power absorbed by electrons; $P_e(z_e)=\int P_e(z_e,a)da$ is the spectral power on the surface marked with a $Z_e = \omega/\sqrt{2}K_{||} V_{te}(a)$, D_e the specific power absorbed by electrons; ΔTe(a), the enhancement of the electron temperature. On calculating ΔTe the scaling coefficient of the electron thermoconductance has been used [2],$\chi=1.47B_T^{0.84}R^{-0.75}n(a)^{-0.69}$;j(a), the steady current density calculated according to empirical formulas [3]

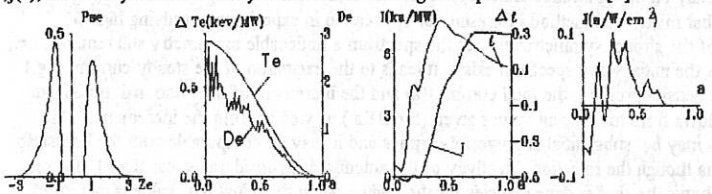

Fig1

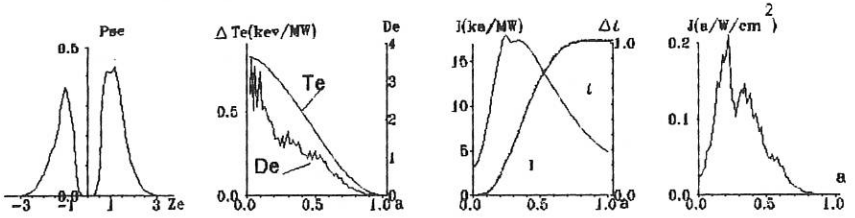

Fig.2

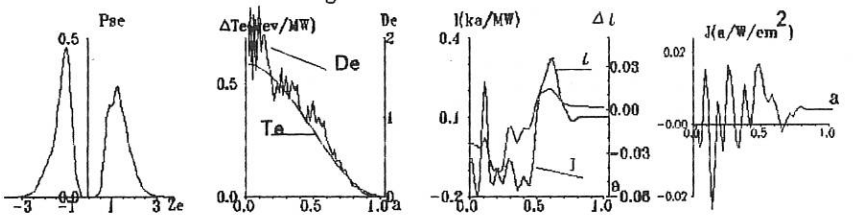

Fig.3

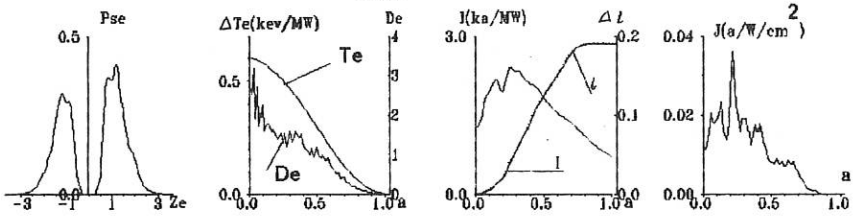

Fig.4

neglecting the trapped particles; I(a), the total steady current inside the surface with the mark a; $\Delta\iota$,the increment of the rotational transform angle due to the steady current.The plasma density profile is $n_e=n_e(0)\ (1-a^2)^{1/2}$,$T_e=T_e(0)(1-a^2)$, $T_e(0)$=1KeV,B_0=0.5T ,f=60MHz.

Low density regime ($n_e\ (0)=10^{13}$ cm^{-3} , $T_e(0)$=1KeV). Fig.2 shows the calculation results for 15 rays with the initial value $N_{||}$ =5. It follows from the dependence $P_e(z_e)$ that for the monochromatic initial spectrum in plasma a strong broadening of the spectrum occurs as well as its almost total symmetrization. The Cherenkov absorption occurs mainly due to particles with $V_{||}<V_{te}$, i.e., by the bulk of the electron distribution function. It is a consequence of a relatively small Cherenkov absorption of FW. The resulting energy deposition profile D_e is peacked sufficiently well. This profile feature does not depend practically on the Shafranov shift (β). This self-adjustment of the profile is similar to the OH like regime what makes this method promising for application in experiments studying high β regimes. In spite of the strong symmetrization of the spectrum a noticeable asymmetry still remains, i.e., the memory about the initial wave spectrum exists. It leads to the excitation of the steady current. Fig.1 shows the current density profile j, the total current I(a) and the increment of the rotational transform angle $\Delta\iota$. As it follows from the current values given (I=6.3Ka.) as well as from the increment $\Delta\iota$ the current generation may be substantial in powerful regimes and it may be comparable with the bootstrap current phenomena though the radiation directivity of the antenna d is considerably less than 1 (for real antennas). Fig.2 shows the similar dependencies for the regime when the initial $N_{||}$ value is increased

($N_{||}$ =15). As is seen from Fig.2 the energy deposition profile and ..Te depend on $N_{||}$ weakly. However the current generation is considerably more efficient (approximately in 2.5 times).

High density regime ($n_e(0)$=2 10^{13} cm^{-3}, Te(0)=0.5KeV) Fig.4 depicts the calculation results for this regime for $N_{||}$ =15. The energy deposition profile and ΔTe change weakly compared to the low density regime. The steady current value lowers mainly due to the density increase. However when the $N_{||}$ value lowers in the high density regime, the current value decreases sharply. Fig.3 shows the calculation results for $N_{||}$ =5 for all rays. In this case the practically total symmetrization of the spectrum occurs and the current generation efficiency is very low.

FW excitation by antenna arrays. The problem of FW excitation in the nonuniform plasma has been studied using the 1-D model of plasma and the 3-D model of the antenna array in the approximation of the solenoidal current surface and of the straight plasma cylinder [4]. This code has been amended by the account of the poloidal magnetic field, the TJ-1U-like profile of which having been taken. Under these conditions the solution of the wave equation in plasma has been obtained for one wave (FW, in the approximation $m_e \to .0$) whereas in the vacuum region two waves (TM and TEM) have been employed. As in ref. [4] the FW damping has been accounted for by introducing the effective collision frequency ν_{eff}/ω. However because of the complicated pattern of FW propagation in a real system (due to 3-D nonuniformity) it is difficult to determine the quantity ν_{eff}/ω. equivalent to the real

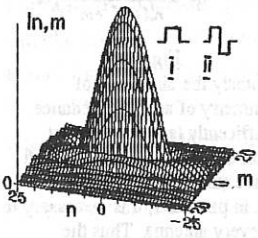

Fig.5

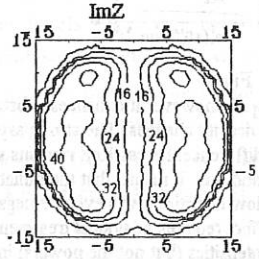

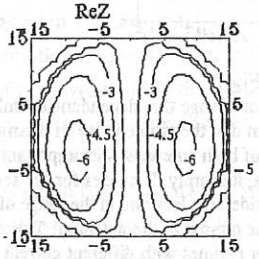

Fig.6

(Cherenkov) damping mechanism. Therefore the calculations have been performed for various ν_{eff}/ω. what permits to estimate the situation with TJ-1U. Below we consider the results for sufficiently large ν_{eff} .values when the excitation of eigenmodes don't occur. The calculations have been carried out for the parabolic profile of plasma density at B_0=0.5T. Two types of antennas have been studied: a long wavelength one (type 1) and a short wavelength one (type 2). Fig.5 shows the driving current distribution for these antennas. To control the spectrum including the generation of directed radiation it is possible to use two antennas located in adjacent horizontal branch pipes. The location and size of antennas are chosen similar to ones for antennas designed for TJ-1U [5], vessel radius a_c=17.5cm plasma column radius a_p=10cm, the gap between the plasma boundary and the current surface h=1cm, diameter of the current surface (property of TJ-1U antennas) D=15cm, the spacing between adjacent antennas l=60cm. The circular configuration of the current surface leads to the peculiar form of the driving current spectrum j(n,m), i.e., the spectrum form in the wave space is similar to the antenna form in the real space (see Fig.5 where the spectrum j(n,m) for a single antenna of type 1 is shown). Fig.6 depicts the local impedance distribution on the current layer surface in case the type-2 antenna is used with the density $n_e(0)$=2 10^{13} cm^{-3}. As is seen the quality factor Q=ImZ/ReZ determining the efficiency of the antenna performance is sufficiently low. The averaged active impedance ReZ may be somewhat enhanced (that is equivalent to the lowering of the averaged quality factor Q) due to the decrease of effect of central part of the antenna if similar to Ref. [4] one optimizes the driving current distribution. Fig.7 shows the dependencies of ReZ and ImZ versus the plasma density $n_e(0)$. As is seen, in spite of

the large slowing-down $N_{||}$ the quality factor remains sufficiently low even at low plasma densities. Plasma gyrotropy in the presence of the poloidal magnetic field leads to that even with symmetric spectrum of the antenna a directed radiation arises in plasma. Though the directivity value d in this case is not large (Fig 8), the regimes are possible when this quantity may increase substantially (e.g., when natural modes are excited). Fig 7 shows the similar dependencies for 2 antennas of the 1st type with the phase shift $\pi/2$. Here the broken lines mark the corresponding ReZ and ImZ for one antenna and the solid lines are related to another antenna. There attracts attention the weak dependence of ReZ on density what is a consequence of low Bo and relatively large gap between the current surface and chamber wall. The directivity of radiation d is very low. The directivity may be improved remarkably is the phase shift is increased. Fig. 7 shows with broken lines the quantity d for the phase shift $\varphi=0.7\pi$. Low value of directivity is due to the relatively large spacing between antennas. Fig 9 gives the calculation results for two antennas of type 1 with the phase shift $\pi/2$, however the spacing between antennas is decreased in 2 times (l =30cm). As is seen, such a change

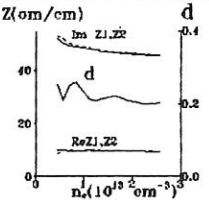

Fig.7

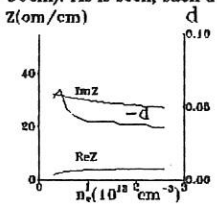

Fig.8

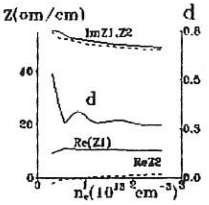

Fig.9

does not change the dependencies ImZ_1,Z_2 however it enhances substantially the directivity of radiation d in the whole range of plasma density changes. The strong asymmetry of active impedance values of both antennas is its important difference. hereas ReZ remains sufficently large for the first antenna, it sharply decreases for the second one. It means that the radiation of the second antenna will be considerably less and in the range of low densities it will even be negative (the energy flux is directed from the plasma to the antenna). This effect requires additional treatment, in particular, it is necessary to consider regimes with different current intensities (but not the powers) in every antenna. Thus the antenna efficiency in the regime with f=60MHz appears sufficiently high even when one uses the short wavelength current layer. The option to control the directivity of the radiation is rather limited because of the large spacing between antennas.

References.

1. Dyakov V.E.,Longinov A.V.,Castejon F.,Ascasibar E.,Rodrigues R.L. Proc. Europ. Top. Conf. on RF Heating and CD of Fus. Devices,Brussels,1992,vol.16E,p.145
2. A.V.Longinov,E.I.Kolosenko,Rodriguez R.L.,Ascasibar E.,Castejon F. ibid,p.157.
3. S.C. Shu, C.F.F. Karney, R.W. Harvey, T.K. Mau ,ibid,p.173.
4. K.Yamazaki, T. Amano Nuclear Fusion V.32, N4, p.633, 1992.
5. A.V.Longinov,V.A.Tsurikov, Jornal "Plasma Physics"(Russian),vol.15, N3,p.
6. A.V.Longinov,E.I.Kolosenko,G.A.Miroshinichenko et al., Proc. 13th Conf. on Contr. Fusion and Plasma Physics, Schliersee,1986,vol.2, p.201(1986)

THE INFLUENCE OF FINITE ORBIT EFFECTS ON THE ICRH POWER DEPOSITION

T. Hellsten, L.-G. Eriksson* and J. Carlsson
Royal Institute of Technology, S-10044 Stockholm, Sweden
*JET Joint Undertaking, Abingdon, OXON, OX14 3EA, UK.

Abstract
The deviation between the drift orbits and the magnetic surfaces gives rise to a number of effects for ICRH, the power absorption profile deviates from the power transfer profile, spatial diffusion of the resonating ions appears and for an asymmetric spectrum there is also a radial drift. A code, FIDO, has been developed to study these effects being based on a mapping technique. The effects of the RF-induced drift are studied for resonating ions near the magnetic axis.

INTRODUCTION – Ion Cyclotron Resonance Heating, ICRH, can be modelled with combined codes calculating the power deposition and velocity distribution of resonating ions. For low to moderate power levels good agreement between experimental results and calculations has been found with such a code [1,2]. An assumption frequently used in Fokker-Planck codes calculating the velocity distributions is that of zero width of the drift orbits, i. e. the zero banana width approximation. For larger coupled powers or longer slowing down times this assumption no longer holds [2]. The inclusion of finite width of the drift orbits gives rise to a number of effects, such as RF-induced diffusion [3,4], deviation between power absorption and power transfer profiles. These effects have previously been studied by using a 2D-code [5] (in r and v) and an orbit following Monte-Carlo code HECTOR [6]. The RF-induced quasi-linear diffusion becomes 3D when the finite width of the drift orbits is taken into account. One can solve the resulting orbit averaged Fokker-Planck equation either with finite element/ finite difference methods in a suitable space of orbit invariants or by a Monte-Carlo technique. An advantage with the Monte-Carlo approach is that it avoids the rather complicated boundary conditions which has to be imposed on the 3D diffusion problem. To speed up the computations so that more particles can be used when simulating ICRH an alternative method is suggested. Instead of following the drift orbits after random interactions by collisions and RF-wave fields we propose to calculate the changes of the invariants of the unperturbed orbits. This corresponds to solving the bounce averaged Fokker-Planck equation. The evolution of the particle distribution in the space of the invariants is then simulated by adding increments to the invariants by interpolating from values in a precalculated table. In this way one avoids time consuming recalculations of similar orbits. The latter being a severe limitation of traditional Monte-Carlo methods when only a small fraction of the particles constitutes the energy ions forming the tail, which describe the physics of interest.

CHANGES IN THE INVARIANTS – A particle orbit in an axisymmetric toroidal geometry can be described by three invariants, exact or adiabatic. Here we use as the invariants the energy, E, the toroidal angular momentum, P_ϕ, and an angle like variable, Λ, where $\Lambda = \mu B_0/E$, B_0 is the magnetic field strength on the magnetic axis and μ the magnetic moment. The changes of the magnetic field over a gyro radius is assumed to be small so that the magnetic moment and Λ can be regarded as exact invariants.

A problem that appears when representing the obits of the particles by their invariants is that there is not a unique relation between particle orbits and invariants, co and counter passing orbits may have the same invariants. To distinguish them we represent an orbit by a quadruplet $\underline{X} = (E, P_\phi, \Lambda, \sigma)$ where σ separates the different kinds of orbits. Certain regions in the invariant space are not represented by any orbits, so called forbidden regions.

The orbit invariants will change due to Coulomb collisions and interaction with the RF-field at the resonances. We assume the changes in the invariants, $\Delta\underline{X}(\underline{X})$, to be small during a poloidal turn of the drift orbit. The changes in the invariants due to Coulomb collisions can then be calculated by integrating the quasi-linear Coulomb operator for a test particle along a poloidal turn of the unperturbed orbits. The RF-contributions are calculated by integrating the RF-interaction across the resonance. The increments of the invariants have to be separated into drift contributions (deterministic) and diffusion contributions (random processes). The drift contributions, which usually are second order terms are additive and can be straightforwardly integrated along the unperturbed drift orbit. The diffusive contributions are first order effects but the sign and magnitude changes randomly. The changes of the invariants during one orbit is then calculated as $\underline{X}_{n+1} = \underline{X}_n + \Delta\underline{X}_1(\underline{X}_n) + \alpha\Delta\underline{X}_2(\underline{X}_n)$ where α is a random number between -1 and 1, $\Delta\underline{X}_1$ and $\Delta\underline{X}_2$ represents the drift and the diffusive contributions, respectively. The increments of the invariants can then be straightforwardly accelerated by multiplying the drift contributions with $\sqrt{\tau_{step}/\tau_{orbit}}$ and the diffusive contributions with τ_{step}/τ_{orbit}. The step length τ_{step} has to be sufficient small so that $|\Delta\underline{X}_i|/|\underline{X}_i| << 1$.

When adding finite increments to the invariants it may lead to that the quadruplet $\underline{X}$ will take values which do not correspond to an orbit. Particles may then unphysically disappear into the magnetic axis or into an "orbit" having $v_\perp > v$ at the mid plan on the low field side or so that the "orbit" corresponding to $\underline{X}$ either has r, E or Λ less than zero. As the particles are advanced in time the quadruplet has to be controlled so that it does not move into the forbidden regions of the invariant space because of the finite increments used. When going from trapped to passing a random number has to be used to determine whether the orbit goes to a co or to a counter passing orbit.

RF-INDUCED DRIFT – Absorption of waves with finite toroidal mode numbers gives rise to an increase of the parallel as well as the perpendicular energy. The increase of the parallel velocity $\Delta v_{\|} \approx k_{\|} v_{\perp} \Delta v_{\perp}/\omega$ becomes important only for high energy ions. This increase gives rise to a radial drift for an asymmetric spectrum. To illustrate the importance of the radial drift on the formation of high energy ion tails we have plotted the evolution of single particles in the absence of diffusive contributions caused by Coulomb collisions and RF-interactions in Figs. 1 and 2. This gives us a picture how the particles on averaged evolve in E and r, where r denotes the minor radius of the turning point of a trapped particle and the minor radius at $\theta = \pi/2$ for a passing particle, θ being the poloidal angle. The particles are started with E_0=50 keV, $\Lambda_0 = 0.2$ and n_φ=30, except for those indicated. First the energy increases and r is approximately constant, then there is an abrupt change in r when the orbit changes from passing to trapped, which has to do with the definition of r. As the energy of the particles exceeds 100 keV the radial diffusion becomes important. As the particle moves radial outwards the power absorption and as a consequence the particle's energy decreases and the radial drift vanishes. For the calculations we have chosen an electric wave field corresponding to a flux surface averaged power absorption density $p=p_0 \exp(-17.3r^2)$, in the absence of finite deviation of the drift orbits from the flux surfaces. In these calculations we have assumed that $k_{\perp}$=0, the density of the resonating species is $n_H=10^{18}m^{-3}$, and $n_D=10^{19}m^{-3}$, $T_e=T_i$=10 keV, I=3 MA, B_0=2.2 T and f=33 MHz. In Fig.1, where $p_0=0.1MW/m^3$, the central orbit reach high energy without turning into a trapped particle. This is because as the perpendicular energy increases the parallel energy increases too. For this particle P_ϕ increases without significantly changing its radial location. A large fraction of the central orbits may not turn into trapped particles for antennae launching waves with large toroidal mode numbers. For particles with higher Λ_0 the RF-heating will turn them into trapped ions which will drift as is illustrated with a particle starting with $\Lambda_0 = 0.9$.

The RF-induced drift becomes more important as the power density increases even for a constant temperature profile which is illustrated in Fig. 2, where the evolution of typical orbits are shown in the absence of diffusion. The higher the power density is the further out the ions drift. Although the power density increases with a factor 5 the maximum energy increases only with 3.8. We have used constant temperature profiles to separate the drift effects from the effect, that as the width of the banana orbits increases the ions slow down on cooler electrons further out. If a non-constant temperature profile is used of the form $T_\alpha=T_0 (1-(r/a)^2)$, with T_α =10 keV, the maximum energy is reduced further to increase only by 3.4.

The radial drift of the resonating ion drift orbits results in that power being absorbed in the centre and transferred further out. The finite width of the banana orbits yields a similar effect.

For symmetric spectrum the drift term cancels and only the diffusive term remains, but the parallel energy will still increase which will reduce the number of trapped ions in the centre.

SUMMARY – The finite deviation of the drift orbit from the magnetic flux surfaces plays an important role for hot plasmas with peaked power deposition profiles. The drift caused by an asymmetric spectrum drives the particles radially outwards and thereby curtailing the formation of high energy ion tails. However, for the central ions the increase of the parallel velocity may prevent these ions from being trapped and drifting outwards. The increase in parallel velocity also reduce the anisotropy in the velocity distribution resulting in an under estimation of the high energy tail by measurements which measure the anisotropic energy content.

ACKNOWLEDGEMENTS – The FIDO code has been developed under JET contract JT2/10726.

REFERENCES

[1] L.- G. Eriksson, T. Hellsten, D.A. Boyd, et al Nuclear Fusion, **29**(1989)87.
[2] L.- G. Eriksson, T. Hellsten, and U. Willén, submitted to Nuclear Fusion.
[3] S. Riyopoulos, T. Tajima, T. Hatori and D. Pfirsch, Nuclear Fusion, **26**(1986)627.
[4] L. Chen, J. Vaclavik and G. Hammett, Nuclear Fusion, **28**(1988)389.
[5] T. Hellsten, Plasma Physics and Controlled Fusion, **31**(1989)1391.
[6] M. Kovanen, W. Core and T. Hellsten, Nuclear Fusion, **32**(1992)787.

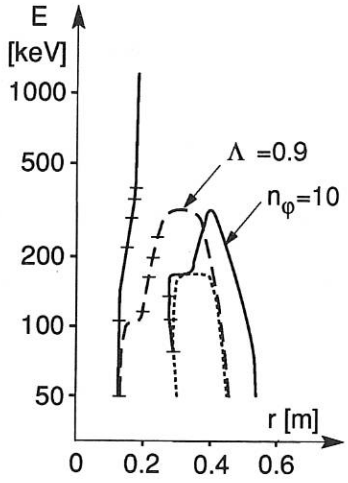

Fig.1 The evolution of E and r for RF-heated ions. Λ_0=0.2 and n_φ=30 except for indicated orbits.The first bars denote time steps of 0.2 s.

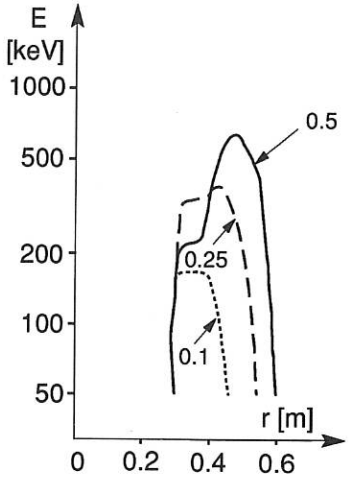

Fig. 2 The evolution of E and r for different power density profiles ,where $p=p_0\exp(-17.3r^2)$ p_0 =0.1, 0.25 and 0.5 MW/m^3.

Minority Cyclotron Absorption in Finite Larmor Radius Wave Equations

M.J. Alava[1], J.A. Heikkinen[1] and T. Hellsten[2]

[1]Helsinki University of Technology, Department of Technical Physics, SF-02150 Espoo, Finland

[2]Royal Institute of Technology, Alfvén Laboratory, S–10044 Stockholm, Sweden

The heating of plasmas in the ion cyclotron range of frequencies has become one of the most succesful methods for achieving reactor temperatures. The main absorption mechanisms of the heating power are absorption at the fundamental harmonic resonance of a minority ion species, at the second harmonics of the majority and mode conversion to an electrostatic ion Bernstein wave. The estimation of the power deposition profile can be carried out by several methods. The currently most comprehensive in terms of physics included is the numerical calculation of the absorption and mode conversion by solving the wave electric fields from wave equations. In the most widely used form, the equations are obtained by expanding the plasma dielectric tensor to second order in the ion Larmor radius [1,2]. Such equations can account for absorption of the fast magnetosonic wave at the first and second harmonic resonances, mode conversion to electrostatic waves, electron Landau damping and transit time magnetic pumping. In the following, we discuss some less–well known features of the second order finite Larmor radius (FLR) equations. These consist of negative absorption around the cyclotron resonance of a minority ion species, and mode conversion to spurious electrostatic modes at the same location.

To study the absorption, we write the dielectric tensor for a Maxwellian plasma to all orders in ion Larmor radius [3]

$$\epsilon_{ij} = \delta_{ij} - \sum_{\alpha} \frac{\omega_{p\alpha}^2}{\omega^2} \{ - \sum_{n=-\infty}^{\infty} a_{0\alpha} \Pi_{\alpha ij}(\beta_\alpha a_{n\alpha}; n) Z(a_{n\alpha}) - a_{0\alpha}^2 \hat{z}\hat{z} \} \tag{1}$$

Here $a_{n\alpha} = \frac{1 - n\Omega_\alpha/\omega}{n_z v_{T\alpha}/c}$. ω, $v_{T\alpha}$, $\omega_{p\alpha}$ and Ω_α are the heating frequency, thermal velocity, plasma frequency and cyclotron frequency of the α'th species. Z is the plasma dispersion function, and n_z and $\hat{z}$ are the refractive index of the wave and the unit vector in the direction of the the background magnetic field. In the perpendicular direction, the matrix Π_α reduces to

$$\Pi_{(\alpha xy)} = \begin{pmatrix} \frac{n^2}{\beta_\alpha} \Lambda_n(\beta_\alpha) & in\Lambda_n'(\beta_\alpha) \\ -in\Lambda_n'(\beta_\alpha) & \frac{n^2}{\beta_\alpha} \Lambda_n(\beta_\alpha) - 2\beta_\alpha \Lambda_n'(\beta_\alpha) \end{pmatrix}. \tag{2}$$

We have $\beta_\alpha = k_\perp^2 v_{T\alpha}^2 / 2\Omega_\alpha^2$ and $\Lambda_n(\beta_\alpha) = I_n(\beta_\alpha)\exp(-\beta_\alpha)$.

The corresponding absorbed power density reads $p = \epsilon_0 \omega \mathrm{Im}(\vec{E}^* \cdot \epsilon \cdot \vec{E})$. By transforming the coordinates so that the base vectors coincide with the eigenvectors $\hat{e}_i$ of the anti–Hermitian part of the tensor ϵ one obtains $p = \epsilon_0 (\omega_{p\alpha}^2/\omega) a_{0\alpha} \mathrm{Im}[Z(a_{n\alpha})](\mu_1 |E_1|^2 + \mu_2 |E_2|^2)$.

Here μ_i, $i = 1,2$, are the eigenvalues of the tensor $\mathbf{\Pi}_\alpha$, and the electric field can be written with $\vec{E} = E_1\hat{e}_1 + E_2\hat{e}_2$ in terms of the corresponding eigenvectors $\hat{e}_i$. We have considered a cyclotron resonance of only one ion species α. To discuss the minority absorption with $n = 1$, we expand $\mathbf{\Pi}_\alpha$ to second order in ion Larmor radius (first order in β_α), and obtain

$$\mathbf{\Pi}^{(1)}_{\alpha(xy)} = \begin{pmatrix} \frac{1-\beta_\alpha}{2} & \frac{i(1-2\beta_\alpha)}{2} \\ -\frac{i(1-2\beta_\alpha)}{2} & \frac{1-3\beta_\alpha}{2} \end{pmatrix}. \tag{3}$$

The eigenvalues of the expanded tensor read $\tilde{\mu}_{1,2} = (1 - 2\beta_\alpha)/2 \pm \frac{1}{2}\sqrt{1 - 4\beta_\alpha + 5\beta_\alpha^2}$. These are compared to those of the original tensor in Eq. (2) with $n = 1$ in Fig. 1 as a function of β. While the eigenvalue $\tilde{\mu}_1$ approximates well at small β the corresponding eigenvalue μ_1, the second eigenvalue $\tilde{\mu}_2$ has a wrong sign, indicating negative absorption. In practice, the sign of the absorption as predicted by the FLR expanded dielectric tensor is a complicated matter. E.g., for a single Fourier–mode, the sign of the absorption depends on the concentration of the minority species, as the eigenvector of $\tilde{\mu}_2$ corresponds to the left–handed component of the field, which dominates at high minority concentrations. The presence of more than one mode leads to additional interference effects.

The phenomenon of negative absorption is highlighted in Fig. 2, which shows the behaviour of the radial electric field E_x calculated from the FLR wave equations in a 1–D slab geometry. The parameters and the geometry are chosen to model an isolated deuterium cyclotron resonance in a 50 % – 50 % DT–plasma. As the figure demonstrates, the magnetosonic wave entering the slab couples to two electrostatic modes, carrying energy both to right and left from the resonance. This is a manifestation of the wrong dispersion of the electrostatic mode, resulting from the breakdown of the FLR expansion for modes with a large $k_\perp$. This leads to the existence of the electrostatic mode on the both sides of the cyclotron resonance. In addition, the solution displays clear negative absorption: the decomposition of the modes at the slab ends reveals that the outgoing modes carry about 8 % excess energy compared to the fast mode entering. This is in marked contrast to the expected result of a fast wave being transmitted and slightly attenuated at the resonance due to the small Doppler broadening at $n_z = 2$.

The mode conversion to the spurious mode can be analyzed by writing the FLR equations around the cyclotron resonance, assuming $E_z = 0$, in the approximate form [4]

$$\begin{aligned} E_y'' + \Delta^2 E_y &= -\frac{i\Delta^2}{2}E + i(\sigma E')' \\ (\sigma E')' + SE &= \frac{i\Delta^2}{2}E_y - i(\sigma E_y')'. \end{aligned}$$

We define $E = E_x + iE_y$, $\Delta^2/2 = S + D$ and utilize the fact that $S + D$ is roughly constant. Here, S and D are the dielectric tensor elements according to the Stix' notation [3]. We use the approximation $\delta = -2\sigma$, $\sigma' = 3\sigma$ and $\sigma = -\sigma_1$ for the FLR corrections [1], as is appropriate around the resonance where the fundamental resonant terms dominate. In this form the equations describe two modes connected by the coupling terms on the RHS.

To remove the mode conversion, the intermode coupling by the FLR corrections should be reduced. This can be accomplished by symmetrizing δ and σ' by $\delta = -\sigma$ and $\sigma' = \sigma$. Then the modified equations read

$$\begin{aligned} E_y'' + \Delta^2 E_y &= -\frac{i\Delta^2}{2} E \\ (\sigma E')' + SE &= \frac{i\Delta^2}{2} E_y. \end{aligned}$$

Now the coupling terms are typically about two decades less in magnitude compared to the dominant original ones, as can be seen from their ratio $\Delta^2/|2\sigma n_B^2|$. The effect resulting from the diminished coupling is shown in Fig. 3. The radial electric field E_x displays a clear reduction in the conversion to the electrostatic mode, compared to Fig. 2. We have in addition made the modification $\sigma_1 \to \mathrm{Re}[\sigma_1]$, which makes the fundamental absorption resulting from the FLR corrections positive definite everywhere.

The problems in the minority absorption are sensitive to the boundary conditions and the parameters of the heating scenario being simulated. In the latter, the most important parameter is the minority concentration [5]. To render the spurious effects insignificant, we suggest modifying the FLR corrections in the wave equations by setting $\mathrm{Im}\,\lambda_1 = 0$ in σ, δ and σ' and using the definition $\delta = \delta_2 - \delta_1$ and $\sigma' = 2\lambda_0 + \sigma_2 - \sigma_1$. This method makes the calculations of mode conversion and absorption at e.g. large deuterium minority concentrations in DT–plasmas feasible, in contrast to the original FLR equations [5].

It is a well known fact that the FLR equations do not produce a correct, expected picture of fast wave absorption and, moreover, do not give a correct dispersion relation for the electrostatic modes [6]. In this study we have shown that the problems encountered in full wave solutions of wave propagation result from a combination of negative absorption and mode conversion to a spurious electrostatic mode. These can be overcome by modifying the FLR corrections to the dielectric tensor elements at the fundamental resonances in a conceptually simple, easy to program manner, compared to adding artificial damping to the equations. Such changes do not affect the fast wave absorption at fundamental or second harmonic resonances, which are modelled by the other tensor elements with sufficient accuracy. In addition, the mode conversion at e.g. ion–ion hybrid resonances is given correctly, without resorting to the numerically demanding integrodifferential formulation for the wave propagation problem [7].

References

[1] T. Martin and J. Vaclavik, Helv. Phys. Acta **60** (1987) 471.
[2] M. Brambilla, Plasma Phys. Contr. Fusion **31** (1989) 723.
[3] T.H. Stix, The Theory of Plasma Waves, (Mc Graw–Hill, 1962).
[4] M.J. Alava, J.A. Heikkinen and T. Hellsten, submitted to Phys. Fluids B.
[5] M.J. Alava, J.A. Heikkinen and T. Hellsten, submitted to J. Comp. Phys.
[6] C. Chow, V. Fuchs and A. Bers, Phys. Fluids **B2** (1990) 1089.
[7] O. Sauter and J. Vaclavik, in Theory of Fusion Plasmas, Proc. of Joint Varenna – Lausanne Int. Workshop, Varenna, 1990 (Eds. E. Sindoni, F. Troyon and J. Vaclavik) Bologna 1990, 403.

Table 1 Parameters for the T(D)–example

ω	1.4325×10^8 s^{-1}
n_y	0
n_z	2
B_0	3.0 T
R_0	3.0 m
$T_e = T_i$	5 keV
n_e	5×10^{19} m^{-3}
n_D/n_e	0.5
n_T/n_e	0.5
L	0.25 m
R_{left}	3.1 m

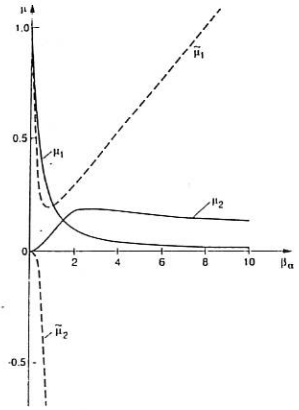

Figure 1. The eigenvalues of the tensors in Eqs. (2) (solid curve) and (3) (dashed curve) as a function of β_α.

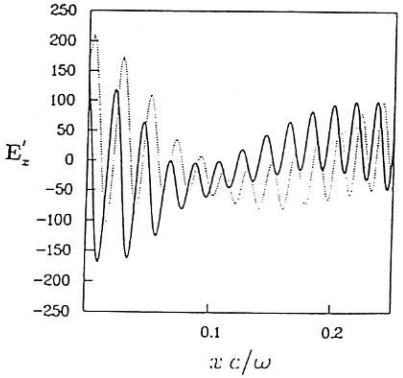

Figure 2. E'_x calculated from the FLR equations around the separated cyclotron resonance layer. Other parameters as in Table 1. Solid curve: Re[E'_x], dotted curve: Im[E'_x].

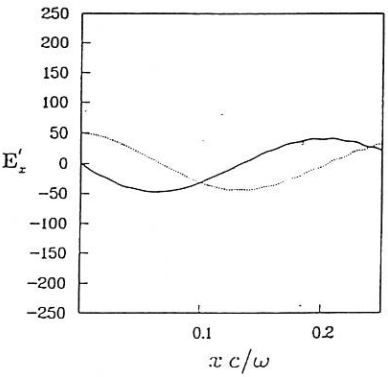

Figure 3. As in Fig. 2 , but with the modified FLR corrections and with the imaginary parts of δ_1, σ'_1 and σ_1 set to zero.

THEORY OF TRAVELLING WAVE ANTENNA FOR ICRH AND FAST WAVE CURRENT DRIVE IN TOKAMAKS

V.L.Vdovin

NFI RNC Kurchatov Institute, Moscow

Tokamaks FWCD antennae require many loops with significant diffi culties of location of large coaxes in a region of first wall and their matching with a generator due to mutual coupling between loops (LMC) (mainly through the plasma). It is natural to convert LMC from a defect into advantage by feeding a periodical structure at the edge loop [1] creating the travelling wave. In this work we will give the self consistent theory of poloidal loop antennae with a Faradey screen (FS) loaded at the edges by lumped capacitances (Fig., equatorial cross section).

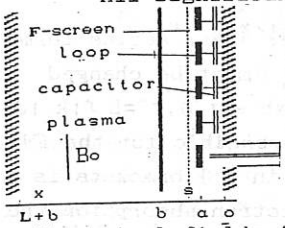

All significant features of a travelling Fast Wave (FW) antenna are obtained in a flat layer of hot plasma near of that with a period T the thin conductors elongated in a poloidal direction (y) are located, on distances a and FS s from the wall. Plasma edge is located at the distance b (plasma thickness $2a_o = L$). Electrical fields in the vacuum layers and plasma are given by

$$E_y^{(v)} = \sum_n (A_n e^{\varkappa x} + B_n e^{-\varkappa x})\, F(y)\, e^{i(k_{no}+\beta)z},$$

$$E_y^{(p)} = \sum_n (C_n e^{i\int k_\perp dx} + D_n e^{-i\int k_\perp dx})\, F(y)\, e^{i(k_{no}+\beta)z}$$

$$E_z^{(v)} = \sum_n (A_n e^{\varkappa x} + B_n e^{-\varkappa x})\, F(y)\, e^{i(k_{no}+\beta)z}, \quad (E_z = 0,\ x > s)$$

$$F(y) = (G \cos k_y y + H \sin k_y y)\, e^{-i\omega t}$$

where $k_{no} = 2\pi/T\ n$, $\varkappa_n^2 = -k_o^2 + k_y^2 + (k_{no}+\beta)^2$, $k_y = n_y k_o$, $k_o = \omega/c$, $n = 0, \pm 1, \ldots$, β - Flocke multiplier that must be found, $k_n = 2\pi n/T + \beta$.

$$k_{\perp o}^2 = ((\varepsilon_{11} - k_n^2) - \varepsilon_{12}^2)/(\varepsilon_{11} - k_n^2), \quad k_\perp = k_{\perp o}(1 + i\sqrt{\pi}/4\beta_e \xi e^{-\xi^2})$$

$\xi = \omega/k_n v_{Te}$. The excitation currents in the loops with 2w wide, also expanded in Fourier series, define the derivative jumps ($[A] = A_2 - A_1$)

$$\left[\frac{dE_y}{dx}\right]_{x=a} = 4\pi i(k_o^2 - k_y^2)\, j_y/ck_o, \quad \left[\frac{dE_z}{dx}\right]_{x=a} = -4\pi i k_n k_y j_y/ck_o$$

From here it is clear that for excitation in plasma $E_y \neq 0$ (FWaves) it is necessary the poloidal slow down $k_y > k_o$ to provide, for ex.

by Faradey screen (in [1] assumption $k_y=k_o$ is wrong). Taking $E_y(0)=E_z(0)=0$, $[E_y]_{x=a}=0$, $[E_z]_{x=a}=0$, $[B_y]_{x=a}=0$, $[E_y(x=b)]=0$, $[\partial Ey/\partial x]_{x=b}\equiv 0$ $[E_y(x=L+b)]=0$ and making use $U_m/I_m=1/i\omega C_o$ at the end of loop with a length 1 the dispersion relation (DL) is obtained. It defines the Flocke multiplier $\beta(\omega)$:

$$\frac{1}{\omega C_o}\,tg\,k_y l=\frac{4\pi n_y(n_y^2-1)k_o^2}{c\,T}\sum_n\frac{sh\varkappa a}{\varkappa^3}\Big\{\Big|\frac{Y}{X}\Big|_n\frac{\cos\phi_1\cos\phi_2\,ch^2\tau+\sin\phi_1\sin\phi_2\,sh^2\tau}{(ch2\tau+\cos2(k_\perp L+\phi_D))/2}+\frac{sh2\tau\,\sin(\phi_D-\phi_N)}{ch2\tau+\cos2(k_\perp L+\phi_D)}\Big\}+\frac{k_y^2k_n^2}{k_o^2(k_o^2-k_y^2)}\,\frac{sh\varkappa(s-a)}{sh\varkappa s}\Big\}_n\frac{\sin k_{no}w}{k_{no}w}\,,\quad(\equiv Z(\beta)) \tag{1}$$

where in right part, that we will name by a wave antenna impedance $Z(\beta,\omega)$, $\tau_n=\int_o^L \mathrm{Im}\,k_\perp dx$ is the optical thickness (plasma density in H-mode is a constant one), $\phi_1=k_\perp L+\phi_N$, $\phi_2=k_\perp L+\phi_D$; phase displacementsof vacuum fields $tg\,\phi_N=-\varkappa\,cth(\varkappa\Delta)/k_\perp$, $tg\,\phi_D=-\varkappa\,cth(\varkappa b)/k_\perp$, $\Delta=b-a$;
$|Y/X|=(sh^2\varkappa\Delta+\varkappa^2/k_\perp^2 ch\,\varkappa\Delta)^{1/2}/(sh^2\varkappa b+\varkappa^2/k_\perp^2 ch^2\varkappa b)^{1/2}$. For series terms $|n|>n_{cr}$, when $k_\perp^2<0$, expression $|Y/X|\,[\ldots]_n$ must be changed to $(sh\varkappa\Delta\,ch\tau'+\varkappa/k_\perp ch\varkappa\Delta\,ch\tau')/(sh\varkappa b\,ch\tau'+\varkappa/k_\perp ch\,\varkappa b\,sh\tau')$, $\tau'=L\int_o|k_\perp|dx$. The imaginary term, proportional $sh\tau_n$, is responsible for the FW absorption (i.e. $\beta=\beta_o+i\,\beta'$). The second term in { } brackets is a vacuum E_z fields contribution. For a pure electron absorption the optical thickness $\tau_n<1$ even in a reactor. In large tokamaks (DIII-D,...) $\tau_n<<1$. Then the denominator in { } brackets $(1+\tau_n^2+\cos2(k_\perp L+\phi_D))/2$ is small one when $2(k_\perp L+\phi_N)=\pi/2+\pi m$, $m=0,\pm1,..$ The numerator also strongly oscillate ($\sim\cos\phi_1\cos\phi_2$) and in a rare plasma when FW modes with different n are well separated the slow down is imposed by plasma itself (!) but not by antenna structure. In a dense large plasma the resonant denominators are "overlapped" (so called modes' overlapping [2]) and the expression in squared brackets behaves more smoothly, the regime similar to radiation into half space is realized [2], although $\tau_n<<1$. In that case (1) must be solved numerically (and poloidal harmonics accounted for).

In order to obtain the analytical results we consider $\tau_n>1$ (for example FW CD under minority ions $\omega=\omega_{ci}$). Then first term in the squared brackets (1) is simplified:
squared brackets (1) is simplified: $|Y/X|\cos(\phi_D-\phi_N)$, a plasma contribution into slow down $\beta(\omega)$ is more smooth. FW attenuation ($\beta'<\beta_o$) is obtained from (1):

$$\beta' = -\sum_{n\neq n_{cr}} \frac{sh\varkappa a}{\varkappa^3} D_n \left|\frac{Y}{X}\right| \frac{B_o}{den} \Big/ \sum_n \frac{k_n D_n}{\varkappa} \left\{ \left|\frac{Y}{X}\right| \frac{A_o\tilde{A}_1 + B_1 - B_o\tilde{A}_5}{den\ \varkappa} + 2\frac{sh\varkappa(s-a)}{sh\varkappa s} \right\}_n \frac{sh\varkappa a}{\varkappa^3}$$

(2)

where $B_o/den = sh2\tau_n \sin(\phi_D - \phi_N)/(\cos 2\tau_n + \cos 2(k_\perp L + \phi_D))$, $D_n = \sin k_{no} w / k_{no} w$ $A_o = sh\tau_n \cos(\phi_D - \phi_N) + \cos\phi_1 \sin\phi_2$, $\tilde{A}_1 = -3 + |\varkappa| a\ cth\varkappa a$, $B_1 = \varkappa b |X1/X| (sh\tau_n * \sin(\phi_D - \phi_N) - \cos\phi_1 \sin\phi_2)$, $\tilde{A}_5 = -\varkappa b |X1/X| sh2\tau_n \cos(\phi_D - \phi_N)/den_n$. The all quantities at right depend on β_o, derived from (1) at $\beta' = 0$. The dominant dependence β' over parameters is given by the multiplier $\varkappa\ sh\varkappa a |Y/X| sh2\tau_n \sin(\phi_D - \phi_N) = \varkappa^2/k_\perp/(1+\varkappa^2/k_\perp^2 cth\ \varkappa b) e^{-2\varkappa(b-a)} sh2\tau$, ($\varkappa(a+b)>1$), i.e. an attenuation by the divertor layer size $(b-a)(k_{no}+\beta)$ and by plasma dissipation $sh2\tau_n$ are defined. Here it is seen: $\beta' \sim \varkappa^2 \sim \beta_o^2$ up to $\varkappa|_{max} = k_\perp^2 \Delta/(1+k_\perp^2\Delta^2)$, ($\Delta = b-a$, $k_\perp^2 > \varkappa^2$).

Let us estimate an antenna frequency broad band. At small β from (1), taking n=0 plasma term (and all vacuum terms), one has:

$$\beta^2/k_o^2 \cong (\alpha \frac{1+\frac{\Delta}{b}}{1+\frac{\Delta}{b}} \frac{b k_\perp^2}{k_\perp^2} + \alpha\frac{s-a}{a}(\frac{T}{2w} - 1) - 1)(n_y^2 - 1)/$$

$$(1 - \alpha\frac{s-a}{a}(\frac{T}{2a} - 1) - \alpha\frac{s-a}{s}) \qquad (3)$$

where $\alpha = 4\pi n_y C_o tgk_y l/T$, $k_\perp \cong \omega/V_A$. Lower boundary frequency ω_1 ($\beta_o = 0$) is defined by equation $1/\omega C_o tgk_y l = 4\pi n_y a/T * ((1+\Delta b k_\perp^2)/(1+b^2 k_\perp^2) + \Delta s/a(T/2w-1))$, (4). The upper boundary frequency ω_2, when $\beta = \pi/T$ ($0,\pi$-phasing for the ICRH), is derived from (1) considering the plasma terms n=0, n=-1 (because of $\varkappa_o = \varkappa_{-1}$) and all vacuum terms:

$$\frac{1}{tgk_y l} = \frac{8ny}{(\pi/T)^2}(\frac{n_y^2-1}{})^2 C_o k^3 \frac{sh\varkappa a}{sh\varkappa b} \frac{\varkappa\Delta}{th^2\varkappa b} \frac{th\varkappa b + \varkappa^2/k_\perp^2}{+\varkappa^2/k_\perp^2} + 4\pi C_o \frac{k_o}{T}(s-a)(\frac{T}{2w} - 1) \qquad (5)$$

Practically for an electrical strength required $C_o \leq 1$ (and RHS<<1) So the antenna considered is sufficiently narrow band one ($n_y k_o l \cong \pi/2$ для ω_1 и ω_2).

Broad band antenna. Let us couple two considered above simple LC-antennae inductively, i.e. load by lumped capacitances near-by loops asymmetrically: first loop by a capacitance at the loop down and near-by loop - by a capacitance at a loop top. To provide the periodicity constraint for a such two against installed simple LC-antennae we take a solution in the form ($0 < x < a$):

$$E_y^{(v)} = -2\sum_n sh\varkappa_n x[(A\ cosk_y y + B\ sink_y y) e^{i(k_{no}+\beta)z} +$$

$$-2\sum_n sh\varkappa 1_n x\ (C\ cosk_y y + D\ sink_y y)e^{i(k_{no}+\beta+\pi/T)z}$$

$\varkappa 1^2 = (k_{no}+\pi/T)^2 + k_y^2 - k_o^2$. Requiring $U(a,y=0,z_m) = U(a,y=1,z_m+T/2)=0$, $(U=-\int_o E_x dx)$, after tedious but straight algebra we obtain the DR:

$$\frac{1}{tg^2 k_y 1} = \omega^2 C_o^2 Z(\beta)\ Z(\beta+\pi/T) + \frac{1}{4}\frac{(Z(\beta+\pi/T)-Z(\beta))^2}{Z(\beta)\ Z(\beta+\pi/T)}, \quad (6)$$

where $Z(\beta)$ is given (1). Taking $\beta=0$ and $Z(0)$, $Z(\pi/T)$ from (4),(5) one has

$$\frac{1}{tg^2 k\ 1}\Big|_{\omega=\omega_1} = \omega^2 C_o^2 Z(0)Z(\pi/T) + \frac{1}{4}\frac{b-a}{s-a} + \frac{b}{4a}\frac{s-a}{b-a} - \frac{1}{2} \sim 1$$

For $\beta \neq 0$ the right part of (6) is minimal at β , determined by an equation $Z(\beta) = Z(\beta+\pi/T)/\sqrt{1+4\omega^2 C_o^2 Z^2(\beta_{cr}+\pi/T)}$. Then (6) takes form $1/tgk_y 1 = (\sqrt{1+4\omega^2 C_o^2 Z(\beta_{cr}+\pi/T)} - 1)/2$. Choosing the capacitances C_o being small so $4\omega^2 C_o^2 Z^2(\beta_{cr}+\pi/T) < 1$, we have $1/tg^2 k_y 1 \cong \omega^2 C_o^2 * Z(\beta_{cr}+\pi/T) << 1$, i.e. $n_y \omega_2/c1 \cong \pi/2$. Consequently this is a broad band antenna with $(\omega_2-\omega_1)/\omega \sim 1$ and with its help it is possible to investigate as CD scenario ($\beta/k_o \sim 3-5$, $\omega \neq \omega_{ci}$) and a scenario of ion heating ($\beta/k_o \sim 10$, $\omega = \omega_{ci}$).

Conclusions. Travelling Wave antennae radiating FW significantly simplify current drive and plasma heating in large tokamaks and reactor. The theory developed gives the possibilities to calculate optimal parameters of loop antennae. The main results are the wave impedance expression and dispersion relation (1) defining the toroidal slow down β/k_o over a generator frequency. FW attenuation $Im\beta/k_o$ (2) depends not only from dispersive properties and plasma optical thickness τ but also from the antenna-plasma distance b-a (more exactly, $(b-a)\varkappa$). The simple LC-antenna is a narrow band one: $\Delta\omega/\omega << 1$. Two such inductively coupled simple LC-antennaeas shows an analysis of DR (6) for the combined antenna (loops are installed against each other) are significantly frequency broader: $\Delta w/\omega \sim 1$. Such an antenna can be used as for current drive ($\omega \neq \omega_{ci}$) and for a plasma heating ($\omega = \omega_{ci}$)

1.C.P.Moeller et al, Eur.Topical RF Conf.,Brussels 1992
2.V.Vdovin et al, 4th Int.Symp.on Heat.Toroid.Plasmas,1978,v.2,447

Slow wave antenna for plasma production and heating in the U-2M torsatron (design and theory)

Longinov A.V., Chmyga A.A., Gribok V.A., Koba I.I., Kolosenko K.I., Lukinov V.A. and Nizhnick G.Ya.
(KhFTI, Kharkov, Ukraine)

Introduction. The option to apply SW (IBW) in the range $\omega \sim \omega_{ci}$ for plasma heating has been first demonstrated on the "Sirius" stellarator [1], the "Saturn" torsatron [2]. In recent years it has been studied in a number of interesting experiments on stellarators [3], and, especially on tokamaks [4,5]. However this heating technique is studied much less than methods applying FW that have helped to obtain a number of impressive results on large tokamaks (especially on JET). One of the reasons is the considerably more complicated problem, that one for FW, for designing antenna arrays connected with IBW properties. This report gives the results of developing the powerful antenna array of a new type for the U-2M torsatron ($R = 1.7$m, $a_c = 34$cm, $B_{max} = 2.5$ T, $l = 2$) and of theoretical studies of its electrodynamic characteristic. As shown the recent theoretical studies, along with the main problem to produce plasma [5] such an array may be applied for heating ions as well as electrons [6].

Antenna design. The choice of type and design of antenna is determined by the following main factors:

1) the necessity to design a large area of the radiating surface, because the value of the specific power with IBW excitation may be substantially limited (nonlinear effects, inflow of impurities, etc.)
2) the account of the real helical geometry of the plasma column
3) the option to optimize the radiating surface from the point of view of achieving the well-peaked profile of energy deposition in plasma[6]
4) the option of creating the asymmetry of absorption spectrum over longitudinal wave numbers (for steady current generation)
5) small size of the branch pipe for coupling RF energy into the vacuum chamber, etc.

In the SW antenna design the "surface wave antenna" principle [7] is used (first used in Ref.[1]) with a new element, i.e., the "comb-like" system [8]. Fig.1 shows the antenna location in the U-2M device chamber.

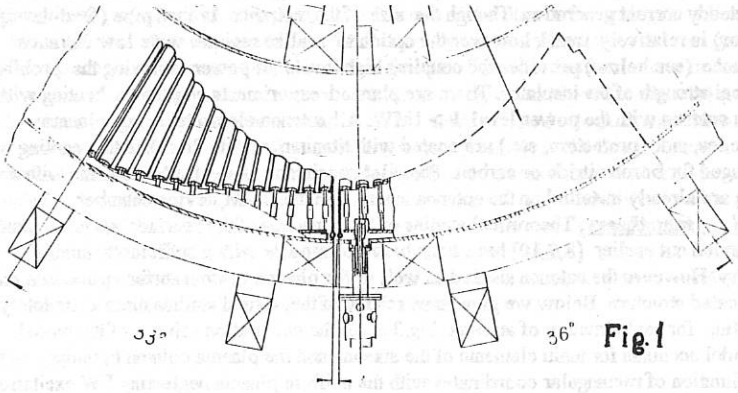

Fig.1

Antenna is located in the helical space between the boundary of the outer magnetic surface located inside the chamber and the vacuum chamber wall (a_c = 34cm) preferentially from the outer side of the torus, the radiating surface being located mainly under the helical pole of the helical winding (in the region of the minor half-axis of the plasma column cross section). On one hand, this provides for the IBW excitation with a more peaked energy deposition profile [6]. On the other hand, it permits to locate the antenna elements in the space with maximum dimensions between the plasma boundary and the vacuum chamber wall. The comb electrodes possess a regulating element permitting to control the shape of the radiating surface (for different k_φ values) and to provide for non uniformity of radiation over the antenna surface (see Fig.2).

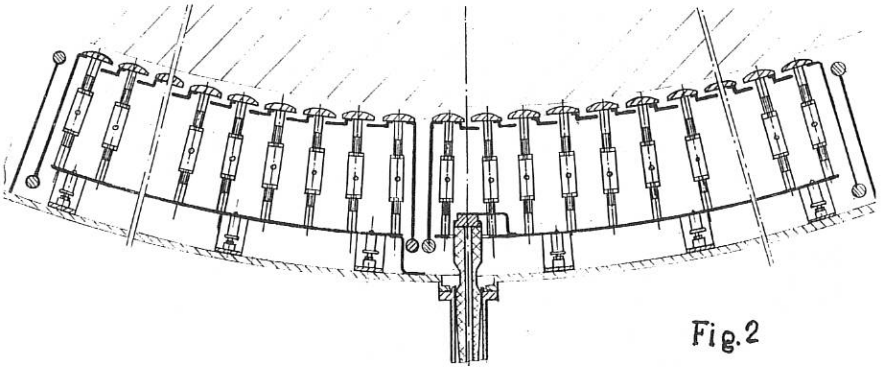

Fig.2

The last circumstance is important for optimizing the RF energy deposition profile in plasma [6]. Such regulation permits to create a different gap for every half of the antenna between the radiating surface and plasma boundary. Along with different lengths of every half this circumstance gives the option of exciting every half with different intensities (see below). As is shown in Ref. [6] the excitation asymmetry of antenna halves permits to ensure the asymmetry in the absorption spectrum over longitudinal wave numbers what leads to the steady current generation. Though the size of the entrance branch pipe (feed-through insulator) is relatively small, however the option to realize regimes with low entrance impedance (see below) provides for coupling high levels of power removing the problem of electrical strength of the insulator. There are planned experiments on plasma heating with such an antenna with the power level P > 1MW. All antenna elements facing plasma (electrodes, side protectors, etc.) are coated with titanium nitride. In future this coating will be changed for boron nitride or carbon. The pilot specimens of electrode elements with such coating are already installed on the antenna mounted in the U-2M device chamber.

SW antenna theory. Theoretical studies of SW antennas of the "surface wave antenna" type carried out earlier [8,9,10] have been based on models with a sufficiently simple geometry. However the antenna studied as well as the plasma column surface possess a more complicated structure. Below we give some results of theoretical studies more completely accounting for real structure of antenna. Fig.3 gives the calculation scheme of the model. The model accounts for main elements of the antenna and the plasma column boundary in the approximation of rectangular coordinates with the uniform plasma neglecting FW excitation

and assuming $k_y = 0$. The main feature of the model is the account of the non uniform antenna structure and the plasma column surface (the varying gap between the plasma boundary and chamber wall). The latter has been accounted for in the model by introducing the array of bumps modeling the regions where the plasma column touches the vacuum chamber wall (distributed diaphragm). The model of the antenna with the comb accounts for the option of various gap between the plasma and the comb for every half of the antenna and of various lengths of these halves.

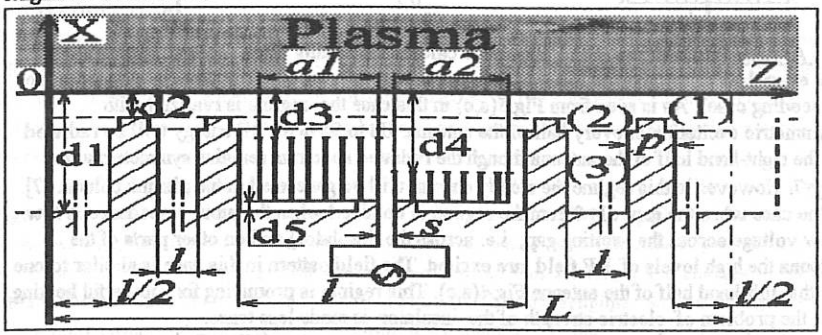

Fig. 3

The method of solving Maxwell equations is similar to one in Ref. [10], in particular, the presence of SWE and SWK (IBW) were accounted for in plasma. The method of partial regions has been used with corresponding lacing of Ez and Hy components of the electromagnetic field at boundaries of such regions. The model contains 15 regions. Application of Fourier expansion reduces the problem to the solution of matrix equations for the coefficients of spatial harmonics. In every region up to 200 harmonics have been used. The large number of parameters (sizes) leads to a large diversity of operation regimes. Below, as an example, we limit ourselves to the investigation of 2 particular cases to illustrate some options of such antenna.

Symmetric antenna. Fig.4 gives the calculation results for the following parameters: Antenna array sizes: a1=a2=120cm, d1=21cm, d2=0.1cm, d3=d4=0.7cm, d5=1.5cm, s=5cm, p=15cm, l=255cm, L=11m, plasma density: $n=10^{11}$ cm^{-3}, ion temperature: Ti=200eV, H=1T, h-plasma,ω/ω_{ci}=1.95. The potential difference at the place of coupling the RF source is 10 kV. Fig.4(a,c) gives the modules of the Ex and Hy components of the electromagnetic field for the most typical region (1). As is seen from the figure the field structure in this region is close to the TEM wave structure with the slowing-down $N_{||}$=7 (comb role) (see Fig.4b where there is shown the power spectrum of IBW radiated into plasma). The surface wave penetrates a little into the region outside the comb, mainly, to the first diaphragm. The high intensity of the field Ex in the region of diaphragm 1 is a consequence of it. This effect may enhance the inflow of impurities. To remove the impurities a special distributed diaphragm is provided with TiN coating and even surfaces. The case considered corresponds to the regime with the large input impedance (almost resonant regime). The input resistance of the slot Z=28+i46(ohm*m). With input voltage 10 kV across the slot, the power coupled to plasma amounts to1MW per 1cm length in the Y-direction.

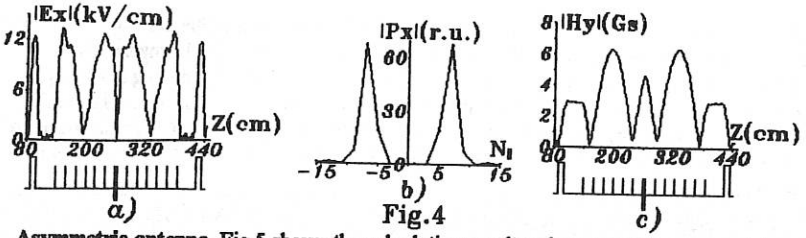

Fig.4

Asymmetric antenna. Fig.5 shows the calculation results when separate gaps are taken for every half of the antenna (d3 = 0.7cm, d4=1.2cm, the rest of parameters is similar to the preceding case). As is seen from Fig.5(a,c) in this case the regime is realized with asymmetric excitation of every half of the antenna. Up to 95% of RF energy will be radiated by the right-hand half of the antenna though the radiated spectrum remains symmetric with $N_{\parallel}=7$. However in this regime the steady current will be generated in the plasma column [7]. In the case when the gap d1=0.1cm the regime is obtained when the input impedance is low (low voltage across the exciting gap, i.e. across the insulator) and on other parts of the antenna the high levels of RF field are excited. The field pattern in this case is similar to one for the left-hand half of the antenna Fig.4(a,c). This regime is promising for powerful heating, i.e., the problem of electric strength of the insulator is made less tense.

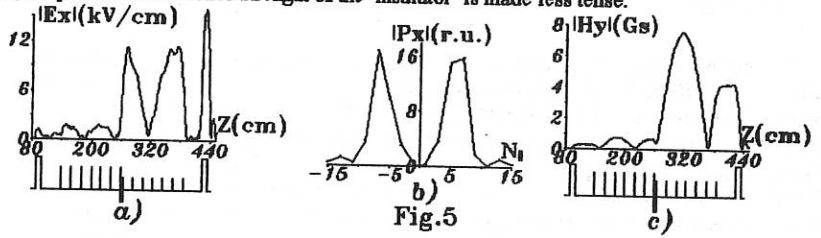

Fig.5

References

1. Burchenko P.Ya., Volkov E.D., Kramskoi E.D., et al. Pisma v JETF, 1972, v.15, n.5, p.250.
2. V.S.Voitsenya, A.Yu.Voloshko, A.V.Longinov; et al., In Proc. 5th Europ. Conf., France, 1972, v.1, p.111
3. K.Nishimura, R.Kumazawa, et al. In Proc 8 Stellarator Workshop, Kharkov, 1991, p.235.
4. M.Ono, P.Biersdorfer, et al., In Proc. 11th Int. Conf., Kyoto, 1986, v.1, IAEA, Vienna(1987), p.477.
5. T.Seki, R.Kumazawa, et al., Nuclear Fusion, v.32, n.12, 1992, p.2189.
6. A.V.Longinov, D.V.Berezov, A.A.Chmyga et al. In Proc 8 Stellarator Workshop, Kharkov, 1991, p.219.
7. V.E.Dykov, A.V.Longinov In Proc 9 Stellarator Workshop, Garching, 1993.
8. Longinov A.V., JTF, n.42(1972), p.1591.
9. A.V.Longinov, V.A.Lukinov In Proc. 16th Europ. Conf., Venice, 1989, v.3, EPS(1989), p.1101
10. V.A.Gribok, A.V.Longinov, V.A.Lukinov In Proc. 19th EPS Conf., Innsbruck, 1992, v.16c, part 2, p.929

DEPENDENCE OF FLR EFFECTS ON RF POWER IN ICRH TOKAMAK PLASMAS

Caigen LIU Qingdi GAO

Southwestern institute of physics, P. O. Box 432, Chengdu, Sichuan 610041, P. R. China

1 INTRODUCTION

In the tokamak experiments, the RF wave heating in the ion cyclotron range of frequencies (ICRH) have been one of the chiefly auxiliary heating manners [1,2]. A large quantity of tail energetic ions (i. e. tail ion) can be induced during ICRF ion heating in two compenent plasmas, These energetic ions play an important role in electron heating, background ion heating and fusion reactivity enhancement[3,4,5].

During ICRF minority heating, the minority ions absorb RF wave power and diffuse onto high energy, in the meanwhile, colliding with background particles and suffering a variety of ion losses, This is the basic physical process of formation of the tail ions, which can be described by the kinetic theory. Because of their high energy, the cyclotron radii of tail ions are large, and changes of physicsal variables in the range of a cyclotron radius may be obvious and unnegligible. So it necessary to consider the finite larmor radius (FLR) effects during ICRF minority heating.

With the ion loss being neglected, the FLR effects have been studied by D. Anderson[4]. But in tokamak plasmas, the formation of energrtic ion can be severely affected by a variety of ion losses which cause energy and particle loss from the tail ions. In this paper, based upon the quasilinear kinetic Fokker-Planck equation including collision, ion loss and RF diffusion operators, we study the characteristics of FLR efects in more detail and its dependence on RF power during ICRF minority heating in tokamak with the ion loss taken into account.

2 BASIC EQUATIONS

After minority ions absorb RF power, they diffuse in the velocity space. We describe this diffusion process by means of the quailinear kinetic Fokker-Planck equation including collision, RF diffusion and ion loss. This equation was firstly introducced by T. H. Stix [3] to study the evolution of the velocity distribution function of the heated particles in the presence of the ICRH in tokamak. Taking average over a magnetic surface, the Fokker-Planck equation is as follows

$$\frac{\partial f}{\partial t} = C(f) + Q(f) + L(f) \tag{1}$$

where C(f), Q(f) and L(f) are the collision, RF diffusion and loss operators respectively [3,4]. In tokamak, there are a lot of loss mechanisms which make both particles and energy escape from tokamak plasma and L(f) is of different forms for different losses.

We average eq. (1) over μ, where μ is the cosine of the pitch angle, which is similar to that done in many papers [3,4], let $f_0 = \int_0^{+1} f d\mu$, in the case of fundamental heating, we obtain

$$\frac{\partial f_0}{\partial t} = \frac{1}{v^2}\frac{\partial}{\partial v}(Af_0 + B\frac{\partial f_0}{\partial v}) + L(f_0) \tag{2}$$

where,

$$A = \sum C_f G(l_f v) m v^2 / m_f v_{Tf}^2$$

$$B = \sum C_f G(l_f v) v/2 + 1.5 K_1 F_1 v^2$$

$$F_1 = \int_0^1 (1-\mu^2)\{J_0^2(X) + (E_-/E_+)^2 J_2^2(X) d\mu$$

$$C_f = (n_f Ln\Lambda/2\pi)(Z_e Z_f/m\epsilon_0)^2$$

$$G(y) = [\Phi(y) - y\Phi'(y)]/2y^2$$

where Σ represents summation over subscript f (f=i, e), the argument of the bessel function is $X = k_\perp \rho_i \sqrt{(1-\mu^2)}$, Ln$\Lambda$ is the Coulomb logarithm, $\Phi(y)$ is the error function, $K_1 = P_1/3n_1m_1$, P_1 is the absorbed RF power density which is averaged over a flux surface without the FLR effects during minority fundamental heating, m_1、n_1 are the mass and density of minorty ion respectively, $l_f^2 = m_f/2T_f$.

In the eq. (2), the first term represents the collision slowing down term. For tail ions, the collision coefficient of background ions is far smaller than that of electrons, therefore, the slowing down of tail ion is dominated by electron. In the steady state and without ion loss, assuming $X \ll 1$, the tail ion distribution function $f_0 \sim \exp(-\int A/Bdv)$ can be derived from eq. (2). Because of $l_e v \ll 1$, we get $G(y) \approx 2y/3\sqrt{\pi}$ for electrons. Therefore, the tail ion distribution is approximately Maxwellian and the tail temperature is equal to $T_{tail} = T_e(1 + P_1 t_S/3n_i T_i) = T_e(1+\xi)$, *where* t_S is electron slowing down time. The tail temperature is defined as $T_{tail} = -(dLnf/dE)^{-1}$, where E is the ion energy.

If both particle loss and energy loss are considered, the loss operator may be taken the form used by J. Killeen[8]

$$L(f) = -\frac{1}{\tau_p} f + \frac{1}{v^2}\frac{\partial}{\partial v}\left[\left(\frac{1}{\tau_E} - \frac{1}{\tau_p}\right)\frac{v^3}{2} f\right] \tag{3}$$

where τ_E is the energy confinement time, τ_p is the ion confinement time.

3 CHARACTERISTICS OF FLR EFFECTS AND ITS DEPENDENCE ON RF POWER

During ICRF minority heating, the energy of tail ions may reach several hundred kev, $K_\perp \rho_i$ can not be regarded as a small quantity any longer, Fig. (1) shows the ralation between the ion energy and $X = K_\perp \rho_i$ for different toroidal magnetic field. For hydrogen, $K_\perp = 50/m$, $B = 3T$, only when $E <$ 200kev, we get $X < 1$. But during minority heating, the ion energy often exceeds 200kev[7].

It is shown in eq. (2) that the FLR effects is directly relevent to the value of the bessel function and the polarity of the electric field (E-field), According to the character of bessel functions, when $X > 0.5$, J_0^2 decreases rapidly, J_2^2 increases steadily. In tokamak plasma, the value of E_-/E_+ is large, therefore, the increase of J_2^2 is amplified by the E-field polarity. The curves of F_1 shown in Fig. (2) indicate that when $E_-/E_+ = 3$, F_1 is approximately equal to 2/3 in a wide range of ion energy, and it is expected in spite of how high heating power density is, the FLR effects won't change the heating results significantly.

The E-field polarity is related to the plasma components. In the cold plasma case, a simple formula of the E-field polarity derived from the wave equation reads as follows[3]

$$E_-/E_+ \geqslant (\omega + \omega_{ci})/(\omega - \omega_{ci})$$

where, ω, ω_{ci} are the majority and minority ion cyclotron frequencies, respectively. So we can predict how the FLR effects affect the heating results through the plasma components.

Up to now, we have analysed the velocity space characteristics of the FLR effects. And then, we are to analyse the correlation bewteen the FLR effects and the ICRH power. In a steady state, the ion

distribution function can be approximately written as Maxwellian, that is $f_0 \sim \exp(-v^2/2T_{tail})$. The FLR effects varies with the quantity of tail ions which are in the energy range where the value of F_1 changes obviousely. When $X_{tail} > 0.5$, a quite large quantity of tail ions exist, so the FLR effects must be considered. Based on the discussion of the last section, the critical RF power above which the FLR effects may play an important role can be written as follows

$$\xi_{cr} = 1.2 \times 10^4 (\frac{B}{K_\perp})^2 \frac{m_p}{m_i T_i(kev)} \tag{4}$$

where, m_p is the mass of proton, $\xi_{cr} = P_{cr} t_s / 3 n_i T_i$.

In the absence of ion losses, Numerical calculation of eq. (2) with the FLR effects taken into account is shown in Fig. (3). The power which transfers to electron by collision is defined as $P_{ec} = \int 0.5 m V^2 C_e(f) d^3V$ (*where* $C_e(f)$ is the electron collision coefficient). Fig. (3) indicates that the curve of $E_-/E_+ = 3$ approaches the curve of without FLR effects.

In tokamaks, there are a lot of ion losses which suppress the formation of tail ions, especially when the loss plays a preferential role in energetic ions[6]. Therefore it weakens FLR effects. If only considering pure ion energy loss, in the steady state without the FLR effects, substituting eq. (3) to eq. (2) and integrating eq. (2), we can get ion tail temerature as $T'_{tail} = T_{tail}/(1+\delta)$, $\delta = T_e v / m \tau_E C_e G(l_e v)$. Therefore, the critical heating power for the FLR the effects becomes

$$\xi'_{cr} = \xi_{cr}(1+\delta) \tag{5}$$

Compared with the case without ion loss, the critical power increase by a factor of $1+\delta$. If τ_E is independent on the ion energy, δ can be written as $\delta = 5.51E18 m_p T_e^{1.5}(kev)/mC_e\tau_E$, when τ_E is equal to ∞, 0.1s and 0.03s respectively, P_{cr} is 1.9E5w/m^3, 3.2E5w/m^3 and 6.2E5w/m^3 correspondingly. Fig. (4) shows the numerical results of the eq. (2) in the different ion energy confinement time, the effective temperature of the minority ion, T_{eff}, is defined as $T_{eff} = \int 0.5 m v^2 f d^3 v$. With decrease of τ_E, ξ'_{cr} increases. It also indicates that our analytical expression about the critical heating power is also in good agreement with the numerical results.

Generally speaking, τ_E is dependent on ion energy. In the most ion losses, such as the neoclassical transport or toroidal field rippling trasport, the loss of energetic ions is easier than that of bulk ions, τ_E decreases with the increase of the ion energy. In theses case, ξ_{cr} will increase. If we include particle loss, the qualitative character of the FLR effects would not change, because when $L(f) = -f/\tau_p$, we can get similarly $T''_{tail} = T_{tail}(1+\delta')$, (where δ' is a parameter dependent on τ_p and the distributional function f).

4 CONCLUSION

We have discussed the characteristics of FLR effects and its dependence on RF power in tokamaks during ICRF minority ion fundamental heating. During high RF power heating, there are numerous tail energetic ions whose energy may reach several hunderd kev. Therefore, it is necessary to consider the FLR effects in analysing the ion distribution and the heating results. Though, in the presence of the ion loss, the FLR effects can be weakened.

The FLR effects are dependent on the polarity of the E-field. When E_-/E_+ is far larger or smaller than 3, the FLR effects may be greatly enhanced or suppressed the formation of energetic ion correspondingly and affect the heating results and different polarities of E-field can be implemented by con-

trolling plasma compenents.

The FLR effects are dependent on RF heating power, A expression for critical heating power above which FLR effects may play an importment role is given. As the loss of ion energy is taken into account, the critical power is increased by a factor of $1+\delta$. It is also shown that the critical powers are in good agreement with the numerical results.

REFERENCES

(1) K. Steinmetz, H. Niedermeyer, J.-M. Noterdaeme et al., Nucl. Fusion 29(1989) 277.

(2) R. Koch et al., Nucl, Fusion 29 (1989) 59.

(3) T. H. Stix, Nucl. Fusion 15 (1975) 737.

(4) D. Anderson, W. Core, L.-G. Eriksson et al., Nucl, Fusion 27(1987) 911.

(5) M. Yamagiwa, T. Takizuka, Y. Kishimoto, Nucl. Fusion 27 (1987) 1773.

(6) K-Itoh, S.-I. Itoh, A. Fukuyama, Nucl, Fusion 28 (1988) 779.

(7) G. A. Cottrell, V. P. Bhatnagar, M. Bures et al., Pl. Phys. & Controll. Fusion 31 (1989) 1727.

(8) J. Killeen, Methods in Computational Phys. Vol. 16, Controll. Fusion, Academic Press, New York (1976) 400.

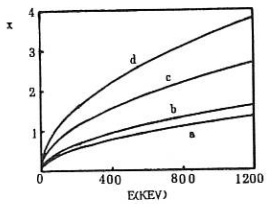

Fig. 1. $X=K_{\perp}V/\omega_{ci}$ versus the ion energy. a) $B_t=3T$, $K_{\perp}=25/m$, hydrogen; b) $B_t=5T$, $K_{\perp}=50/m$, hydrogen; c) $B_t=3T$, $K_{\perp}=50/m$, hydrogen; d) $B_t=3T$, $K_{\perp}=50/m$, deuterium.

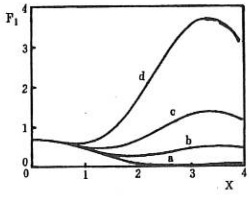

Fig. 2. Relation bewteen F_1 and X. For D(H), $T_e=$ 2kev, $T_i=1$kev, $n_e=5E19/m^3$, $n_H/n_e=0.02$, $B_t=3.4T$. a) $K_{\perp}=50/m$; $(E_-/E_+)^2=0$; b) $K_{\perp}=50/m$, $(E_-/E_+)^2=3$; c) $K_{\perp}=50/m$, $(E_-/E_+)^2=9$; d) $K_{\perp}=50/m$, $(E_-/E_+)^2=25$.

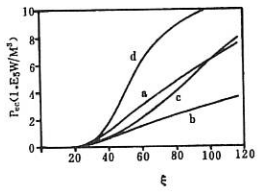

Fig. 3. RF power transfering to electron, P_{ec}, versus ξ. The parameters are the same as in Fig. 2, but the curve a does not take the FLR effects into account.

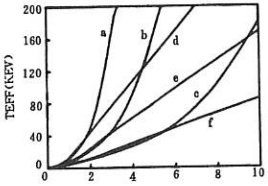

Fig. 4. Effective ion temperature T_{eff} versus P_1. For T (D), $T_e=T_i=2$kev, $n_e=5E19/m^3$, $n_T/n_e=0.02$, $B_t=3.4T$, $K_{\perp}=50/m$, $(E_-/E_+)^2=25$. a、b、c with FLR effects; d、e、f without FLR effects. a、d) without loss; b、e) $\tau_E=0.1$(s); c、f) $\tau_E=0.03$(s).

STUDY of EC CURRENT DRIVE EFFICIENCY and BOOTSTRAP CURRENT by POWER MODULATION EXPERIMENTS

V. Erckmann, U. Gasparino, H. Maaßberg, W7-AS Team
Max-Planck Institut für Plasmaphysik
Association EURATOM-IPP, D-85748 Garching, Germany

ECRH Group
Institut für Plasmaforschung, Universität Stuttgart, Germany

• INTRODUCTION •

In Stellarators, the absence of a strong "obscuring" Ohmic component permits the experimental investigation of small non-inductive currents with a precision difficult to be obtained in an equivalent Tokamak /1/. In the W7-AS Stellarator (R = 2 m, < a > ≤ 0.18 m, $P_{ECRH} \leq 800$ kW) we have performed a systematic study of Electron Cyclotron Current Drive /2,3/.

Uncertainties in the measurements of the ECCD efficiency, η_{ECCD}, are introduced by the unavoidable presence of the boostrap current (and, eventually, an Ohmic one) and by the strong coupling between confinement properties and rotational transform, which is typical for low-shear vacuum magnetic field configurations, as W7-AS /4/. To improve the accuracy, we have applied a new perturbative procedure for the determination of η_{ECCD}.

The method is based on the independent launch of two microwave beams. While one of the two beams is launched with a toroidal angle of injection corresponding to co-current drive (with respect to the bootstrap current direction) the second one is injected in the opposite direction (counter-current drive). In absence of effects perturbing the symmetry (e.g., strong $E_{||}$ as in Tokamaks, or strong anisotropic electron distribution functions as in presence of LHCD) the two r.f. beams are equivalently absorbed and the two driven currents compensate. Through a modulation of the powers in both beam with same amplitude but opposite phase, the modulated ECCD contribution can be discriminated from the unaffected bootstrap and Ohmic ones. Furthermore, the time delay between the modulated power and the response of the loop voltage contains information about the radial localization of the modulated ECCD-current /5/.

The choice of the optimal modulation frequency depends on the electric conductivity of the target plasma and on the radial localization of the modulated current profile. For on-axis ECRH in W7-AS, modulation frequencies $\nu_{mod} \leq 10$ Hz have to be chosen to avoid substantial inductive screening.

• THEORETICAL DESCRIPTION •

The current profile is described as the superposition of a bootstrap, an Ohmic and an EC-driven component. These three components are evaluated independently in the frame of the linearized neoclassical theory in the long mean free path regime /2/.

The current diffusion is evaluated by a numerical solution of the diffusion equation for the voltage $V_l(r,t)$:

$$\frac{\partial}{\partial t}\left[\,\sigma \cdot V_l\,\right] = \frac{c^2}{4\pi}\frac{1}{r}\frac{\partial}{\partial r}\left[\,r\frac{\partial V_l}{\partial r}\,\right] - 2\pi R_0 \cdot \frac{\partial J_{ext}}{\partial t}$$

with boundary conditions:

$$\left.\frac{\partial V_l}{\partial r}\right|_{r=0} = 0 \qquad V_l|_{r=a} + \frac{c^2}{4\pi}\frac{a}{R_0}L_{ext}\left.\frac{\partial V_l}{\partial r}\right|_{r=a} = V_{ext}$$

Here a and R_0 are the minor and major radius, σ the neoclassical electric conductivity, L_{ext} the external inductance, J_{ext} the external current source ($J_{ext} = J_{boot} + J_{ECCD}$) and V_{ext} the externally applied loop voltage ($V_{ext} = 0$ for operation with open OH-transformer). The second boundary condition follows directly from $V_l(a) + L_{ext}dI/dt = V_{ext}$.

During the antiphase power modulation of the two microwave beams, the temporal changes in J_{ECCD} will induce a local V_l. The associated $E_{||}$ could in principle affect η_{ECCD} itself.

Due to the perturbative nature of the experiments, this effect has been neglected in the present study, where η_{ECCD} has been assumed to be constant during the modulation. It was verified a posteriori that the perturbed quantities are indeed small.

Using the measured $n_e(r)$ and $T_e(r)$-profiles ($T_{e,0} \simeq 1.2$ keV, $n_{e,0} \simeq 1.4 \cdot 10^{19}$ m^{-3}) and assuming a uniform $Z_{eff} = 1, 2, 3$, respectively, (which is the uncertainty in the experimental determination of the Z_{eff}-profile) neoclassical theory predicts a bootstrap current $I_{boot} \simeq 7.3, 5.4, 4.5$ kA and a resistance $R \simeq 12, 20, 27$ $\mu\Omega$.

Following linear ECCD theory, including trapped particles effect in the long mean free path /2/, η_{ECCD} shows a maximum $\eta_{ECCD} \simeq 11$ A/kW for a toroidal angle of injection $\varphi_{tor} \simeq 10°$ and $Z_{eff} = 1$. At higher φ_{tor}, η_{ECCD} rapidly decreases reaching $\eta_{ECCD} \simeq 2.7, -0.3$ A/kW at $\varphi_{tor} \simeq 20°, 30°$, respectively. η_{ECCD} scales $\propto 1/(5 + Z_{eff})$

• EXPERIMENTAL CONDITIONS •

The experiments were performed with 2nd-harmonic, (X)-mode injected from low field side. The $\pm$ symmetry in the toroidal angle φ_{tor} couldn't be fulfilled. A power $P^{ctr} \simeq 200$ kW generated by the first gyrotron was injected at $\varphi_{tor} \simeq -10°$ (EC driven current opposite to the bootstrap current) while the power generated by the second source, $P^{co} \simeq 170$ kW, was injected at $\varphi_{tor} \simeq 35°$. Following the theoretical predictions and the results of previous ECCD experiments /3/, η_{ECCD} should become negligible at $\varphi_{tor} = 35°$. Therefore, P^{co} is injected not to drive any relevant ECCD but with the aim of limiting the excursion in $T_e(r)$ (and consequently J_{boot}) during an antiphase modulation cycle. Modulating the two beams in antiphase, ($\nu_{mod} = 10$ Hz, $|\Delta P^{co}| = |\Delta P^{ctr}| \simeq 60$ kW) a $\delta T_e/T_e \leq 5\%$ was measured by ECE which is to be compared to $\delta T_e/T_e \simeq 30\%$ in case of in phase modulation. Thus, for antiphase modulation, changes in I_{boot} are assumed to be negligible compared to the induced modulation in I_{ECCD}. Experiments using the exact launching symmetry, where the previous assumption becomes unnecessary, are in program and will permit more definite conclusions.

• EXPERIMENTS WITHOUT CURRENT CONTROL •

In this first kind of experiments, the total injected power $P_{inj} = P^{co} + P^{ctr}$ was kept constant (within ± 10 kW) but the relative contribution from the two sources ($P^{co} + \Delta P$ and $P^{ctr} - \Delta P$) was varied from shot to shot. Because the pulse length of 1.1 s was too short to reach a steady state current, see Fig. 1, the asymptotic steady-state current I_0, the plasma resistance R and inductance L were determined by means of a least square fitting of the time traces of the net current I_{pl} and the loop voltage V_{loop} with $I_{pl}(t) = I_0 \cdot \{1 - exp[-(t - t_0)/(L/R)]\}$ and $V_{loop} = -L \cdot dI/dt$, respectively. An example of the fit for I_{pl} is seen in Fig. 1, which gives $L/R \simeq 430$ ms ($L \simeq 5.8$ μH, $R \simeq 13.5$ $\mu\Omega$, respectively). This experimentally determined R corresponds to the neoclassical value if a uniform $Z_{eff} \simeq 1.2$ is assumed. However, allowing for the enhancement in the conductivity related to the r.f. induced deformations of the electron distribution function /6/, similar R-values could be obtained with higher Z_{eff}. After wall boronization, $< Z_{eff} > \simeq 2$ are inferred from spectroscopy measurements for this type of discharges.

The extrapolated value, I_0, for the steady state current can be interpreted as:

$$I_0 = I_{boot} + \eta^{co}_{ECCD} \cdot (P^{co} + \Delta P) + \eta^{ctr}_{ECCD} \cdot (P^{ctr} - \Delta P)$$

Assuming that I_{boot} doesn't change significantly during the ΔP-scan (note that $P_{inj} = const$) the changes in I_0 with respect to the reference case with $\Delta P = 0$ will give a measurement of $\eta^{co}_{ECCD} - \eta^{ctr}_{ECCD}$ through the linear relation $\Delta I_0 = \{\eta^{co}_{ECCD} - \eta^{ctr}_{ECCD}\} \cdot \Delta P$.

As expected a linear relationship, corresponding to $\eta^{co}_{ECCD} - \eta^{ctr}_{ECCD} \simeq 8.5$ A/kW, is found between ΔP and ΔI_0, as seen from Fig. 2. For $|\Delta I_0| \geq 150$ A the diamagnetic energy start to show a response, limiting the $|\Delta P|$-window where this technique can be applied. $|\Delta I_0|$-window of similar width are observed also under current controlled operation where the linear relationship between the increment in ΔV_{loop} and the induced ΔI_{pl} is used to determine the plasma resistance from $R = \Delta V_{loop}/\Delta I_{pl}$. It is a consequence of the strong relationship between confinement properties and boundary rotational transform ι_a.

The derived efficiency $\eta^{co}_{ECCD} - \eta^{ctr}_{ECCD} \simeq 8.5$ A/kW, is in good agreement with the values obtained by the linear model (once trapped particles effects are taken into account).

Ray-tracing calculations predict infact $\eta^{co}_{ECCD} \simeq -0.3$ A/kW and $\eta^{ctr}_{ECCD} \simeq -11$ A/kW, for $Z_{eff} = 1$.

• EXPERIMENTS WITH CURRENT CONTROL •

The uncertainty introduced by the strong dependence of the confinement properties on the net current itself can be alleviated by keeping $I_{pl} = 0$ by a feed-back induced Ohmic component, i.e., $\iota_a = const$ during the discharge. The disadvantage of this operational scenarios is that the determination of the non-inductive current, will now rely on the knowledge of the plasma resistance R. For launching conditions equivalent to the $I_{pl} \neq 0$ case, a $V_{loop} \simeq -38$ mV has to be applied to keep $I_{pl} = 0$. For a consistency check, we assume that the non-inductive current is that observed under $I_{pl} \neq 0$ operations, $I_0 \simeq 2.8$ kA, this should imply $R = V_{loop}/I_0 \simeq 13.6\ \mu\Omega$, in excellent agreement with the value inferred in the previous Chapter. Fig. 3 shows the loop voltage for a discharge where at $t = 630$ ms, P^{ctr} is reduced from 205 to 170 kW while P^{co} is simultaneously increased from 120 to 155 kW ($\Delta P = 35$ kW) to keep the total power constant. After having relaxed to the new steady state, an higher $V_{loop} \simeq -44$ mV is necessary to counterbalance the increase in the non-inductive component. This corresponds to an increment of the non-inductive current $\Delta I_0 \simeq 400$ A, using the experimetally determined $R \simeq 13.6\ \mu\Omega$. Under the usual assumptions, this should be interpreted as $\Delta I_0 = \{\eta^{co}_{ECCD} - \eta^{ctr}_{ECCD}\} \cdot \Delta P$ and consequently $\eta^{co}_{ECCD} - \eta^{ctr}_{ECCD} \simeq +11$ A/kW, again in good agreement with the previous and the theoretical estimations.

• EXPERIMENTS with PHASE and ANTIPHASE power MODULATION •

Fig. 4 compares the response of the loop voltage when the r.f. power injected by the two gyrotrons is square wave modulated in phase or in antiphase, respectively ($\nu_{mod} = 10$ Hz, $|\Delta P^{co}| = |\Delta P^{ctr}| \simeq 50$ kW). For in phase modulation the total injected power $P_{inj} = P^{co} + P^{ctr}$ is also modulated so that the temperature profile and consequently the bootstrap current, shows a relatively large excursion ($\Delta T_{e,0} \simeq 300$ eV) during the modulation phase. This is reflected by the strong and immediate response of V_{loop} seen in Fig. 4. In case of antiphase modulation P_{inj} remains constant and the loop voltage shows a delayed and considerably smaller response. This is consistent with the assumption that J_{boot} remains nearly uneffected by the modulation while J_{ECCD} reacts in phase with it. As the J_{ECCD} is driven close to the plasma axis (where the power is absorbed) with a narrow radial profile of $\simeq 3$ cm, the time delay between the gyrotron modulation and the response of V_{loop} reflects the current diffusion time. A time dependent simulation is shown in Fig. 5, where the centrally peaked current profile evaluated by the ray-tracing is used. The total current was fixed to $I_{ECCD} = 500$ kA in agreement with the efficiency of $\eta^{co}_{ECCD} - \eta^{ctr}_{ECCD} \simeq +10$ A/kW determined in the previous experiments.

• CONCLUSIONS •

Preliminary experiments have shown the potential of perturbation experiments for the analysis of electron cyclotron current drive, bootstrap current, plasma resisitivity and their radial profiles. Although we have not used symmetric launch a separation of the different current components was possible.

The results from three different perturbative experiments were found to be consistent with the neoclassical linear modelling of ECCD, bootstrap current and electric conductivity. In particular the deduced value for the ECCD-efficiency shows a good agreement with the expections of linear theory, when trapped particle effects are included.

The time traces of the loop voltage during in phase and antiphase modulations are consistent with a current profile formed by an ECCD-profile peaked on-axis and a broad boostrap component as expected from the W7-AS T_e- and n_e-profiles.

Experiments with off-axis and using symmetric launch are under way.

• REFERENCES •

/1/ V. Erckmann et al., Plasma Phys. Contr. Fus. 34 (1992), 1917
/2/ U. Gasparino et al., Theory of Fusion Plasmas, Varenna 1990, 195
/3/ V. Erckmann et al., (Proc. 13th IAEA, Washington 1990), Vol. II, 555
/4/ H. Ringler et al., Plasma Phys. Contr. Fus. 32 (1990), 933
/5/ U. Gasparino et al., ETC on r.f. Heating and Current Drive, Brussels 1992, Vol. 16E, 301
/6/ N.J. Fisch, Phys. Fluids, 28 (1985), 245

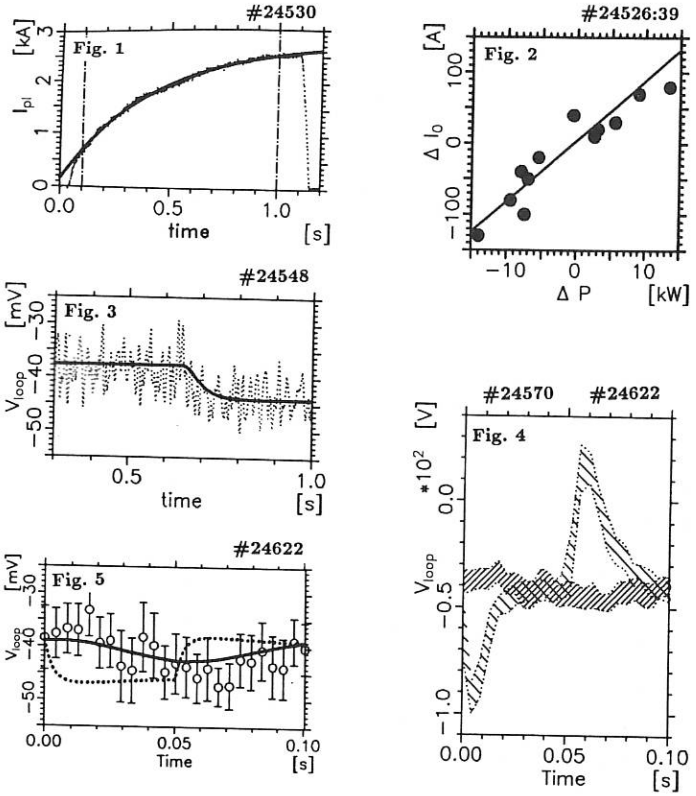

Fig. 1 Time traces of the net toroidal current for a discharge where no external loop voltage is applied. From the fit (full line) the asymptotic steady-state current I_0 and the L/R time scale are determined.

Fig. 2 Reaction of the extrapolated net current I_0 to a variation in the co- and counter-injected powers. While keeping the total power $P^{co} + P^{ctr}$ constant, the power responsible for co-current is changed to $P^{co} - \Delta P$ simultaneously to a variation $P^{ctr} + \Delta P$ in the counter-injected power.

Fig. 3 Reaction of the loop voltage when, at the time $t = 0.63$ s, the co- and the counter-injected powers are varied by an amount $\Delta P \simeq 35$ kW (keeping the total inject power constant). The full line refers to a simulation, using a ΔJ_{ECCD} in agreement with theoretical predictions (see Fig. 5).

Fig. 4 Response of the loop voltage to a square wave modulation ($\nu_{mod} = 10$ Hz) of the co- and counter-injected powers. In case of in phase modulation a strong and immediate response is seen, while for antiphase modulation V_{loop} shows a delayed and considerably smaller response.

Fig. 5 Analysis of the antiphase modulation of Fig. 4. The full line shows the theoretical expectations. In this case only the EC-driven current is modulated with $J_{ECCD}(r)$ in agreement with ray-tracing calculations. The dotted line is shown as reference and corresponds to the response in V_{loop} if the modulated current had a profile proportional to $J_{boot}(r)$.

PROPAGATION OF ELECTRON CYCLOTRON WAVES IN NON - MAXWELLIAN, WEAKLY RELATIVISTIC VLASOV - PLASMAS WITH TEMPERATURE ANISOTROPY

F.Moser

Institut für Plasmaforschung der Universität Stuttgart
D-7000 Stuttgart-80, Pfaffenwaldring 31, Fed. Republic of Germany

ABSTRACT:
The distribution functions of the electrons determine the properties of electromagnetic wave propagation in weakly relativistic Vlasov - Plasmas especially in the frequency range of the electron - cyclotron resonances and their harmonics. The dielectric tensor due to Bornatici et al. (1) is used to investigate numerically the dispersion and absorption of the electromagnetic waves propagating obliquely to a constant magnetic field.
For the fast ordinary wave propagating perpendicularly to the magnetic field anomalous dispersion is obtained in a small range around the electron - cyclotron - resonance. For the fast extraordinary R - wave (right - hand circular polarized wave) such an anomalous dispersion is found in the frequency range around the second harmonic.

THE DIELECTRIC TENSOR:

The plasma is assumed to be homogeneous in a constant magnetic field $\vec{B}_0$. Due to Bornatici (1) and Deike (2) the dielectric tensor element ε_{zz} for a weakly relativistic plasma with a Bi - Maxwellian distribution function of the form:

$$f_0(p_\perp, p_\parallel) = \frac{1}{(2\pi m)^{\frac{3}{2}}} \cdot \frac{1}{T_\parallel^{\frac{1}{2}} \cdot T_\perp} \exp\left(-\frac{p_\parallel^2}{2mT_\parallel} - \frac{p_\perp^2}{2mT_\perp}\right) \qquad (1)$$

for a propagation exactly perpendicular to the magnetic field ($\Phi = 90°$) is given by:

$$\varepsilon_{zz} = 1 - \left(\frac{\omega_p}{\omega}\right)^2 \left\{ 1 + \frac{mc^2}{T_\perp} \sum_{n=1}^{\infty} \frac{n\omega_c}{\omega} \sum_{k=0}^{\infty} \frac{(-1)^k [2(n+k)]!}{[(n+k)!]^2 \cdot (2n+k)!k!} \cdot 2^{-(n+k)} \cdot \lambda_\perp^{n+k} \cdot \right.$$

$$\left. \left[\frac{T_\parallel}{T_\perp}\right]^{n+k+1} \cdot \sum_{s=0}^{\infty} \frac{(n+k+s)!}{s!} \cdot \left[1 - \frac{T_\parallel}{T_\perp}\right]^s \left(\mathfrak{Z}_{n+k+s+\frac{3}{2}}(z_n) - \mathfrak{Z}_{n+k+s+\frac{3}{2}}(z_{-n}) \right) \right\} \qquad (2)$$

The other tensor elements ε_{ij} are given by analogous formulae (s. Bornatici (1) and Deike (2)).
The elements ε_{ij} are described by a development in the harmonic order (index n), in the Landauparameter $\lambda_\perp$ (index k) and a development in the factor of anisotropy $(1 - T_\parallel / T_\perp)$ (index s).

$\vec{p} = p_{\parallel}\hat{e}_{\parallel} + p_{\perp}\hat{e}_{\perp}$ is the electron momentum in units of $m \cdot c$, m is the electron rest mass, c is the speed of light in vacuum. The indices $\perp$ and $\parallel$ refer to the directions perpendicular and parallel to the magnetic field $\vec{B}_0$. $T_{\parallel}$ and $T_{\perp}$ are the electron temperatures, ω_p is the plasma frequency, ω_c the electron cyclotron frequency, ω is the frequency of the electromagnetic wave field,

$\lambda_{\perp} = \left(\frac{\omega}{\omega_c}\right)^2 \cdot \frac{n_{\perp}^2 \cdot T_{\perp}}{mc^2}$ is the Landau parameter with $\vec{n} = \frac{\vec{ck}}{\omega}$ (3a)

and $z_{\pm n} = \frac{mc^2}{T_{\parallel}}\left(1 \mp n\frac{\omega_c}{\omega}\right)$. (3b)

$\mathfrak{F}_r(z)$ are the generalized, relativistic dispersion functions due to Shkarofsky (3) and Robinson (4).

The WAVE - EQUATION and the DISPERSION - EQUATION:

If the dielectric tensor $\varepsilon(\omega, \vec{k})$ is known, the wave equation for the electric wave field is given by:

$$\vec{k} \times \vec{k} \times \delta\vec{E} + \left(\frac{\omega}{c}\right)^2 \varepsilon(\omega, \vec{k}) \cdot \delta\vec{E} = 0. \quad (4)$$

The dispersion equation results from (4) to be:

$$\text{Det}\left|\Lambda_{ij}\right| = 0 \quad (5a)$$

with $$\Lambda_{ij} = n^2\left(\bar{k}_i\bar{k}_j - \delta_{ij}\right) + \varepsilon_{ij}(\omega, \vec{k}). \quad (5b)$$

NUMERICAL SOLUTION and RESULTS:

The dispersion equation (5a) together with the wave equation (4) are solved numerically using the method of complex residual calculation in the root finding code and the recursion formulae for the generalized relativistic dispersion functions due to Shkarofsky (3) and Robinson (4).

Two characteristic examples are shown in the figures 1) and 2). In Fig.1) the anomalous dispersion and damping rate for the fast O. W. is shown for a propagation exactly perpendicular to the magnetic field for $T_{\parallel} / T_{\perp} = 1.5$. There is no double peak structure in the damping rate in contradiction to the results of Arunasalam et al. (5) and in agreement with the results of Fidone et al. (7). Fig.2) shows the anomalous dispersion curves of the fast, extraordinary R - wave in the frequency range $\omega \approx 2\omega_c$ for $\Theta = 90°$ and $T_{\parallel} / T_{\perp} = 0.5$. $\bar{\omega}_{cR}$ is the cut - off frequency of the right hand circular polarized X - wave. For isotropic temperatures ($T_{\parallel}/T_{\perp} = 1$) there is agreement with the results of Bornatici et al. (7).

REFERENCES:

(1) M. Bornatici et al. , J. Plasma Physics (1990), **44**, part 2, 319.
(2) R. A. Deike, Diplomarbeit, Universität Stuttgart, 1992.
(3) I. P. Shkarofsky, J. Plasma Physics (1986), **35**, part 2, 319.
(4) P. A. Robinson, J. Math. Phys. (1986), **35**, 1206.
(5) V. Arunasalam et al., Phys. Rev. (1988), A **37**, 2063.
(6) I. Fidone et al., Phys. Fluids B1 (1989) , **9**, 1937.
(7) M. Bornatici et al. , J. Plasma Physics (1981), **23**, 89.

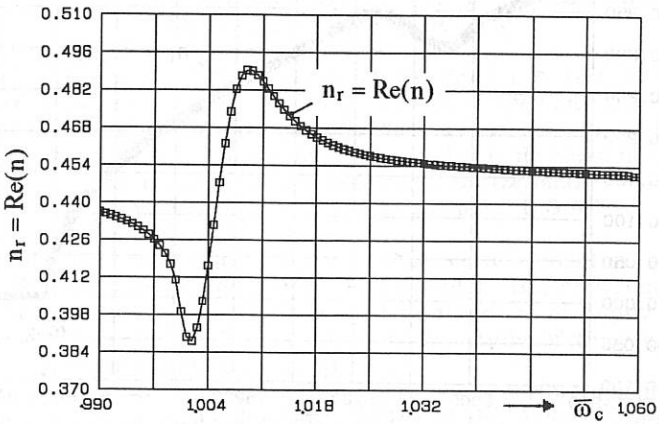

Fig. 1a) Anomalous dispersion of the fast ordinary wave (O. W.) in the frequency range $\omega \approx \omega_c$. Real part of the index of refraction $n_r = Re(n)$ versus the normalized frequency $\overline{\omega}_c = \frac{\omega_c}{\omega}$ for a Bi - Maxwellian distribution function with a temperature anisotropy $T_\parallel / T_\perp = 1.5$.
(plasma parameters: $\overline{\omega}_p^2 = 0.8, T_\parallel = 1\text{keV}, \Theta = 90°$ with $\overline{\omega}_p = \frac{\omega_p}{\omega}$)

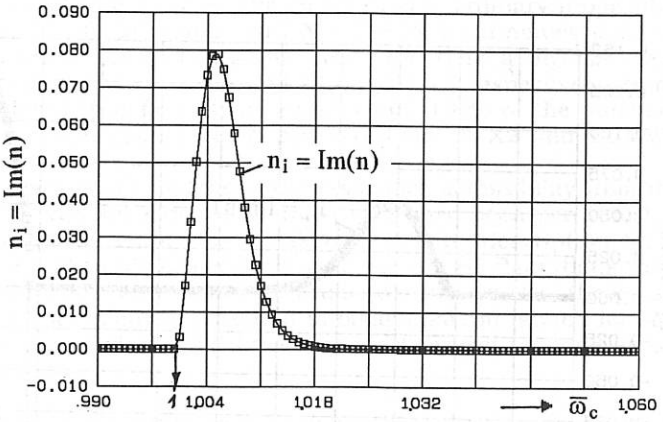

Fig. 1b) Damping rate $n_i = Im(n)$ for the fast ordinary wave (O. W.) in the frequency range $\omega \approx \omega_c$ versus the normalized frequency $\overline{\omega}_c$ for a Bi - Maxwellian distribution function with a temperature anisotropy $T_\parallel / T_\perp = 1.5$ without double peak structure!
(plasma parameters as in Fig. 1a)

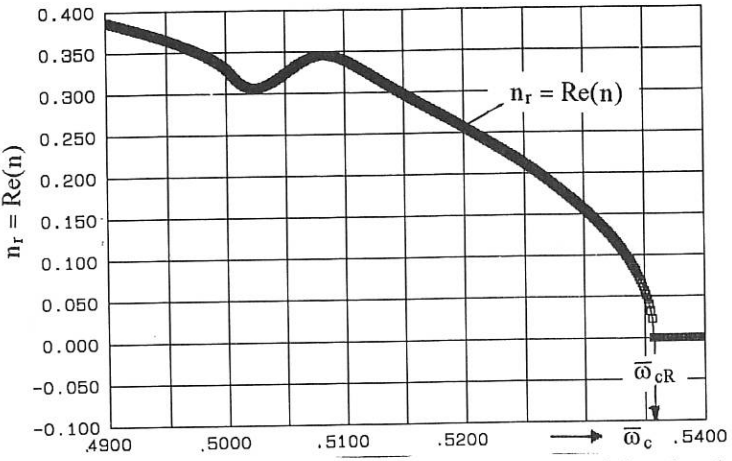

Fig. 2a) Anomalous dispersion of the fast, extraordinary, right - hand circular polarized wave (R - wave) in the frequency range around the second harmonic ($\omega \approx 2\omega_c$). $\overline{\omega}_{cR}$: cut - off - frequency, $\overline{\omega}_{cR} = \frac{\omega_{cR}}{\omega}$. Real part of the index of refraction $n_r = Re(n)$ versus the normalized frequency $\overline{\omega}_c$ for a Bi - Maxwellian distribution function with a temperature anisotropy $T_{\parallel} / T_{\perp} = 0.5$.
(plasma parameters: $\overline{\omega}_p^2 = 0.49, T_{\parallel} = 1\text{keV}, \Theta = 90°$)

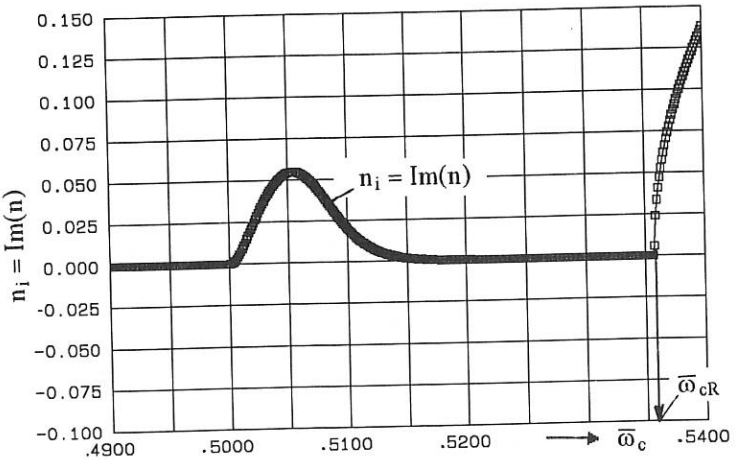

Fig. 2b) Damping rate $n_i = Im(n)$ for the fast, extraordinary R - wave in the frequency range around the second harmonic ($\omega \approx 2\omega_c$) versus the frequency $\overline{\omega}_c$ for a Bi - Maxwellian distribution function with a temperature anisotropy $T_{\parallel} / T_{\perp} = 0.5$.
(plasma parameters as in Fig. 2a)

ELECTRON CYCLOTRON RESONANCE HEATING CALCULATIONS FOR TCV

A. Pochelon, K. Appert, T.P. Goodman, M. Henderson, A. Hirt, F. Hofmann, A. Kritz*, J.-M. Moret, R.A. Pitts, M.Q. Tran, H. Weisen and D.R. Whaley
Centre de Recherches en Physique des Plasmas, Association EURATOM - Confédération Suisse, Ecole Polytechnique Fédérale de Lausanne, 21, Av. des Bains, CH-1007 Lausanne, Switzerland
* Lehigh University, Bethlehem, Pennsylvania, U.S.A.

The TCV objective is to study the influence of elongation and strong shaping on tokamak performance. In particular, the experimental programme will concentrate on the creation and control of highly elongated plasmas ($\kappa \equiv b/a \leq 3$, $R/a=3.7$, $B=1.43T$), on the study of their operational limits and on their confinement properties.

As a consequence both of the large variety of possible plasma configurations and because of its flexibility, ECRH is the most suitable heating system for the TCV tokamak. All plasma shapes, including those with high elongation, can be heated using rotatable mirrors. In addition, the localization of the energy deposition possible with ECRH can be used for modification of the current profile (through control of the electron temperature profile) and hence for the creation of the broad current profiles necessary for vertical stability at high elongation [1]. An ECRH pulse length of 2s has been chosen so as to be of the same magnitude or greater than current diffusion times.

For the EC frequencies, the choice of extraordinary propagation modes in second X2 (83GHz) and third X3 (118GHz) harmonics permits heating at the nominal toroidal magnetic field (1.43T) in a high density plasma. With cut-off densities of 4.3 and $11.5\times10^{19}m^{-3}$ respectively, combined X2 and X3, heating at fields between 90% and 100% of the nominal value is possible at high elongation. A power of 3MW in X2 and 1.5MW in X3 is planned.

Ray-tracing calculations of the resonance accessibility from the various TCV ports with realistic beam divergence have been performed using the TORAY code [2], employing (weakly) relativistic description for both dispersion and absorption. Accounting for plasma configurations from circular to fully elongated and imposing various density profiles, these calculations lead to the selection of horizontal to oblique lateral launch for second harmonic heating and current drive and quasi-vertical top launch for X3 high density heating.

X2 heating: Wave power in X2 can reach any region of the plasma when launched from the upper lateral ports, since room for mirror adjustment permits a wide range of poloidal launch angles. The EC power is nearly 100% first-pass absorbed and can be deposited in the central region ($x \equiv r/a \leq 0.4$) if the density is below cut-off on axis. By adjusting the mirror, X2 launched from the same upper lateral ports, can efficiently be absorbed close to the plasma edge at high density (70% first-pass absorption limit at

x~0.85-0.9 in ohmically heated plasma at κ=2), making it appropriate for profile control.

The effect of refraction due to relativistic effects was analysed in detail for O1 in [3]. For X2, ray-tracing results based on both the cold plasma and the relativistic plasma approximation are compared in Fig. 1. At incidence angles very oblique to the resonance, relativistic effects profoundly modify the ray trajectory and hence the absorbed power. Refraction including relativistic effects restricts somewhat power deposition at x=0 just below cut-off density on axis, due to the reflection at the resonance. Higher T_e results in more rounded trajectories with refraction being experienced earlier.

X3 heating: In contrast to X2, X3 is launched from a port at the top of the vessel giving a beam path quasi-parallel to the resonance, Fig. 2. This results in geometrically enhanced first-pass absorption [4], even for mildly elongated plasmas. Launched from the top port, X3 power results in efficient central deposition for a broad range of density. With a moderate elongation, κ=2, and density $n_{eo} \leq 7\times10^{19}$ m^{-3}, first-pass absorption of 60% is achieved in an ohmically heated plasma (see Fig. 3) and is more than 95% absorbed in a supplementary heated plasma ($T_e \sim 2\times T_{eOH}$). For full elongation κ=3, first-pass absorption increases to 80% and 100%, respectively. Due to the small imaginary refractive index, relativistic effects on refraction are not significant in X3 and there is no visible change of ray trajectory at the resonance.

Combination of X2-X3 heating: The accessible density ranges and corresponding radial deposition locations of X2 and X3 permit the simultaneous use of X2 and X3 gyrotrons for combined heating in plasmas with central density below $n_{eo} \sim 7\times10^{19}$ m^{-3}.

Maintaining n = 0 vertical stability at high elongation and low plasma current requires current profile tailoring. Off-axis heating is used to produce a local decrease of resistivity. An estimate of the power deposition profile required to obtain stable current profiles has been made assuming the Rebut-Lallia transport model. This power deposition profile is compatible with EC absorption calculations and, for a particular case at κ=2.5, vertical stability is achieved with 4MW of ECRH power.

Power loading on the walls: A simple 1D model of the scrape-off layer, together with field line tracing of various magnetic equilibria, is used to compute the total power conducted and convected to the divertor target tiles for the case of 2s ECRH pulses at the full power of 4.5MW. The calculations predict peak power densities of 1 to 7MW/m^2, the power deposition depending strongly on the divertor configuration (principally X-point to wall separation). Estimates of the resulting temperature rise indicate this is always below the threshold for the carbon bloom in the absence of severe tile misalignments.

TCA X1-O1 HFS heating results: The results of X1 and O1 heating at 39GHz in TCA can be used as an indication of the validity of the relativistic effects on refraction observed in X2 ray-tracing calculations. The beam in TCA was launched from a top high field side (HFS) steering mirror [5] movable in both the toroidal and poloidal directions. Thomson scattering and a soft X-ray absorber method were used to measure electron temperatures [5].

The effect of perpendicular ($\varphi=0^{o}$) and toroidally oblique ($\varphi=24^{o}$) injection on the central electron temperature in a series of TCA shots with varying density with X and O-mode HFS launch was examined. It was observed that the X-mode behaved as expected classically, with small first-pass absorption for perpendicular injection and increasing absorption with increasing toroidal angle (see Fig. 4). The same trend is obtained in (relativistic) TORAY runs, in which rays cross the resonance without refraction.

In contrast, the O-mode was not observed to behave classically. The latter implies maximum absorption for perpendicular injection and monotonically decreasing absorption for an increasing toroidal angle. This is not shown by the measurements in Fig. 4, where $O(0^{o})$- and $O(24^{o})$-results are compared. However, the experimental trend agrees with TORAY single-ray simulations, Fig. 5a, showing: **a)** a maximum in the absorption for toroidal angles φ between 15^{o} - 30^{o} (due to geometrical absorption enhancement), **b)** an abrupt 3D "relativistic" direction change at the resonance, further increasing absorption for rays at angles between $\varphi \sim 15^{o}$-20^{o} (see Fig. 5b-5c) and **c)** a decrease in the absorption below the classical level (horizontal injection) for angles $\varphi<10^{o}$. Multiple-ray calculations are in progress to complement these single-ray results, which show that, in the case of HFS O-mode injection, relativistic effects on refraction can result in a decreased absorption for small angles and an increased absorption for medium and large angles, a general trend which appears to be confirmed by the experimental results.

Acknowledgements: This work was partially supported by the Swiss National Science Foundation.

References

[1] G. Erickson, A. Bondeson, D.J. Ward, F. Hofmann and L. Villard, Proc. EPS Conf. on Plasma Phys., Insbruck (1992)343.

[2] R.C. Myer, M. Porkolab, G.R. Smith, A.H. Kritz, Nucl. Fus. **29** (1989) 2155, and S. Yue, A. Kritz, G. Smith, 10th. Top. Conf. on Applic. of RF Power to Plasmas, Boston 1993.

[3] S. Pesic et al., 14th. IAEA Conf., Würzburg 1992, paper D4-12.

[4] R.L. Meyer et al, 7th. Top. Conf. on Applic. of RF Power to Plasmas, Kissimee, AIP Conf. Proc. **157**(1987)73.

[5] A. Pietrzyk, A. Pochelon et al., Nucl. Fus. **33**(1993)197.

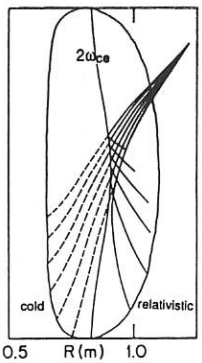

Fig. 1

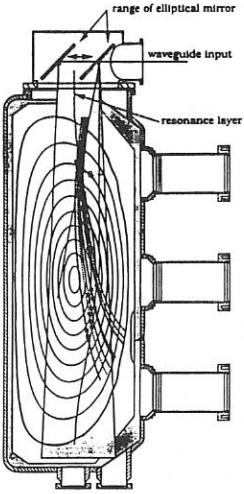

Fig. 2

Fig. 1: X2 oblique launch for cold and relativistic dispersion (1keV, $2\times10^{19}m^{-3}$). The knees at the resonance are sharper at low temperature, but disappear in the cold calculation.

Fig. 2: X3 top launch in the TCV vessel (118 GHz, $n_{eo}=7\times10^{19}\ m^{-3}$).

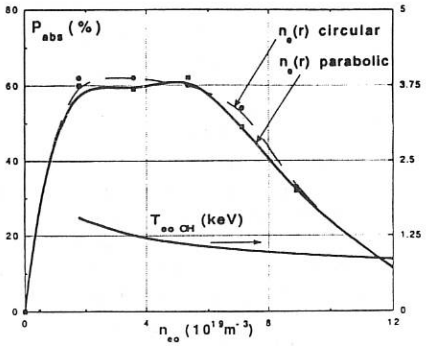

Fig. 3: First-pass absorption in X3 top launch, κ=2, ohmic temperatures, parabolic $T_e(r)$, parabolic and circular $n_e(r)$.

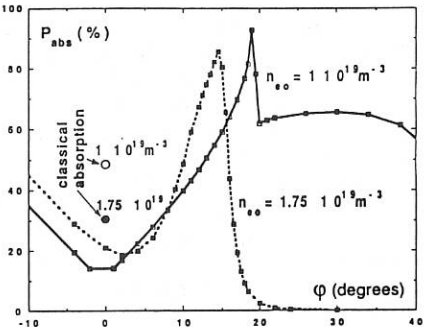

Fig. 5: a) TORAY single-ray first-pass absorption calculations for TCA O-mode cases at two densities, toroidal angle scan. Different types of refraction at the resonxance are shown in b) poloidal c) toroidal projection ($n_{eo}=1\times10^{19}m^{-3}$, $T_{eo}=1.2keV$).

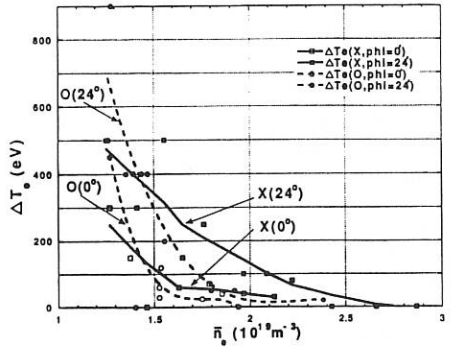

Fig. 4: Soft X-ray electron temperature increment $\Delta T_e=T_{eECRH}-T_{eOH}$ for toroidal angles $\varphi=0^0$, 24^0, for X1 and O1 HFS launches in TCA.

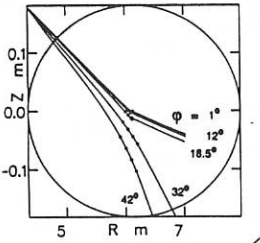

Fig. 5b)

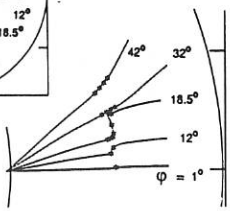

Fig. 5c)

ECRH EXPERIMENT AT 140 GHz ON FTU TOKAMAK: STATUS AND RECENT DEVELOPMENTS

L.Argenti, A.Bruschi, S.Cirant, G.Granucci, S.Nowak, A.Orefice, A.Simonetto, G.Solari,
Istituto di Fisica del Plasma, CNR, Milano, ITALY
A.Figueiredo, *Centro de Fusao Nuclear, Lisboã, PORTUGAL*

MILLIMETER WAVE SYSTEM

Four gyrotrons at 140 GHz will deliver in total 2 MW of electromagnetic power for 0.5 s, to perform ECRH experiments on the FTU tokamak in Frascati. The waves, at the frequency corresponding to the fundamental electron cyclotron resonance, chosen to exploit the maximum possible electron density, will be launched from the low magnetic field side polarized as the O-mode. The millimeter wave system /1/ was designed to achieve the best localization of the absorbed power in order to perform, besides electron and ion heating at high density, detailed studies of energy confinement in tokamaks. The antennas, one for each gyrotron and transmission line, are installed in one port of the FTU vacuum vessel (Fig.1) to launch converging microwave beams. The beam waists, with a radius between 18 and 20 mm, are formed in the centre of the chamber and can be moved vertically by tilting the final mirrors. Oblique injection can be achieved at fixed angles by multiple reflections on the vertical walls of the vacuum port. Mechanical stresses due to thermal expansions or movements of the vacuum vessel, which could determine unwanted bends on the waveguide, are released by using sliding joints and rotating mitre bends /1/.

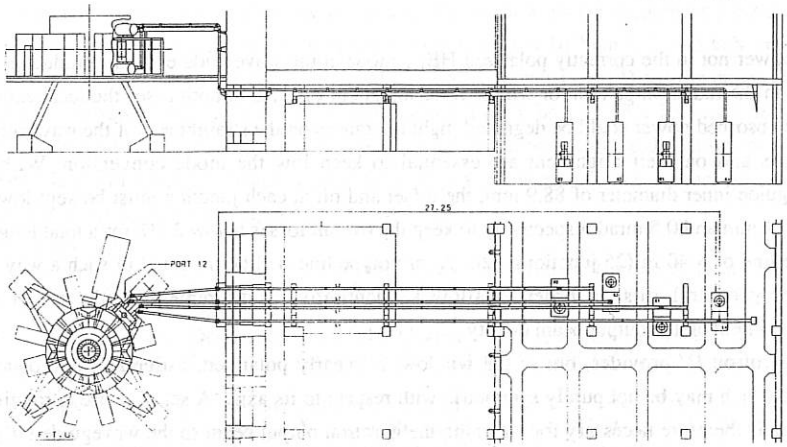

Fig.1 - Layout of the FTU tokamak and of the four transmission lines at 140 GHz

The power distribution at the beam waist has been measured at low power (Fig.2), with the whole launching system installed in a mock-up of the FTU port. The interference with the entrance aperture is limited to a negligible distortion of the Gaussian shape of the microwave beams both in cases of perpendicular (Fig.2a) and oblique launch (Fig.2b).

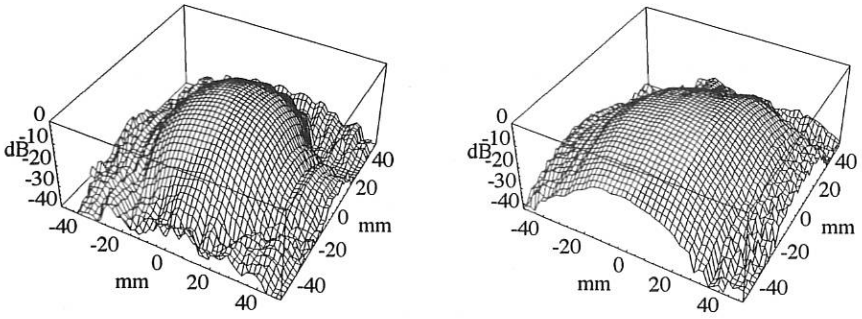

a) b)

Fig.2 - Radiation pattern of the injected beam in the central region of the vacuum vessell. In a) the beam axis is normal to the toroidal field and the pattern is taken close to the beam waist. In b) oblique launch is achieved after 3 reflections on the vertical walls of the port; the pattern is broader because of the longer path from the antenna to the receiver, which is now far from the beam waist.

The power not in the correctly polarized $HE_{1,1}$ mode at the waveguide end will produce side lobes in the radiation pattern, or will be reflected at cut-off. As in both cases the localization of the absorbed power could be degraded, tight tolerances on the straightness of the waveguide sections and on their alignment are essential to keep low the mode conversion. With a waveguide inner diameter of 88.9 mm, the offset and tilt at each junction must be kept lower than 0.1 mm and 0.5 mrad respectively to keep the overall losses below 2.5% for a total length of the line of $\approx$ 40 m (25 junctions) /2/. A prototype line will be mounted in such a way to precisely control tilts, in order to allow a quantitative measurement of the effect of misalignment on the output beam quality.

The gyrotron /3/ provides, out of the window, a linearly polarized, astigmatic microwave beam, which may be not purely symmetric with respect to its axis. A set of phase correcting mirrors is therefore necessary for matching the gyrotron output beam to the waveguide $HE_{1,1}$ mode. The correct polarization is provided by a polarizer consisting either in a pair of corrugated mirrors or in a wire-grid beam-splitter over a flat adjustable reflector /4/.

ANALYSIS OF GAUSSIAN BEAM BEHAVIOUR

Although the theory of ECW absorption and emission /5/ and of the propagation /6/ of single rays (within the limits of the geometrical optics approximation) in magnetoactive plasmas is nowadays well established, we are not so much interested in the features of single rays as in those of beams of limited transverse extent, which may be often described by a field amplitude of the form $\exp(-r^2/w^2)$ (whence the name of Gaussian Beams). Here r is the transverse coordinate on the beam cross section, and w is the distance from the beam axis at which the field is reduced by a factor 1/e (thus embedding the 86.5% of the travelling wave power).

The main effect of the Gaussian nature of a beam, i.e. the formation of a waist where a focus would be given by a standard geometrical optics treatment, is expected to significantly affect both the wave transmission and absorption processes. In a previous work /7/ the quasi-optical approximation required by a treatment of GB aiming to share with ordinary optics the property of avoiding (as far as beam trajectory and absorption are concerned) the complete solution of Maxwell's equations, was analyzed for a 2-D configuration. Suitable methods were presented which, starting from a generalized formulation of the ray-tracing equations, allow to follow the full set of rays composing a GB through inhomogeneous and anisotropic media. Linking here such a ray-tracing procedure to the general theory of resonant plasma-wave interaction, we show in Fig.3a the beam trajectories on a poloidal FTU cross section of a GB (thick lines) and of the corresponding standard optical beam (thin lines). Perpendicular injection of each beam (represented by its outermost rays) is performed from the low field side into a toroidal plasma column with circular concentric magnetic surfaces, at 140 GHz, in the first harmonic O-mode polarization, 5 cm below the mid-plane. The beam waist (in vacuum) is placed at R = 105.5 cm, z=-5 cm. The ray paths are obtained for $n_0 = 2.0 \times 10^{14}$ cm^{-3}, $T_0 = 3$ keV and $B_0 = 4.5$ T. Fig. 3b represents the relevant absorption coefficients (in cm^{-1}) for the upper (1) and lower (2) peripheral beam rays. Fig.4 is analogous to Fig. 3 for $n_0 = 2.3 \times 10^{14}$ cm^{-3} and $B_0 = 5$T. We would like to observe, in conclusion, that between the expected deviations due to the beam Gaussian nature, substantial modifications in the wave-plasma interactions may be foreseen at further beam passages after wall reflections.

REFERENCES

1) L.Argenti et al., The 140 GHz, 1.6 MW, Electron Cyclotron Resonance Heating system for the Frascati Tokamak Upgrade, Proc. 17th Symposium on Fusion Technology, Rome, September 14-18, 1992
2) L. Argenti et al., Design Review of the Millimeter-Wave System for ECRH on the FTU Tokamak, Proc. 17th Int. Conference on Infrared and Millimeter Waves, Pasadena 1992, p.425.
3) A.Litvak et al., EPS Topical Conf. on RF Heating and Current Drive, Brussels, July 1992.
4) L.Argenti et al., Polarization Sensitive Reflectors Made by Grids of Thick Wires, Proc. 17th Int. Conference on Infrared and Millimeter Waves, Pasadena 1992, p.108.
5) A.Orefice, Il Nuovo Cim., **13D**, 1141 (1991)
6) S.Nowak, A.Orefice, Report FP 91/13 (1991)
7) S.Nowak, A.Orefice, to appear on Phys. Fluids.

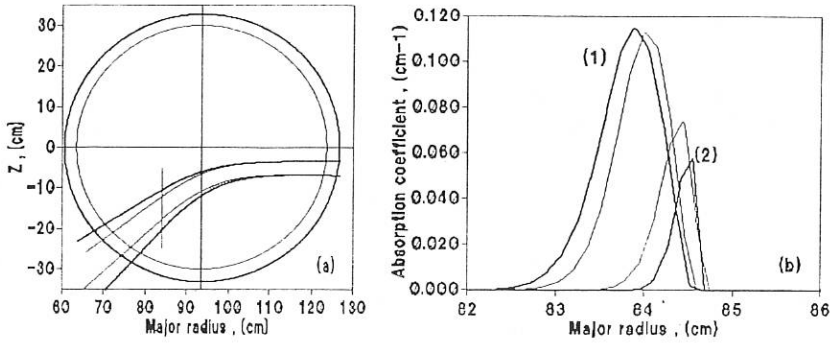

Fig.3 - Poloidal beam trajectories (a) and absorption coefficients (b) for quasi-optical (thick lines) and optical (thin lines) treatment. Each beam is represented by its outermost rays. The resonant position is marked by a vertical segment in Fig. 3a; in Fig. 3b the upper and lower peripheral rays are labelled by (1) and (2), respectively. The ray paths are obtained for $n_0 = 2.0 \times 10^{14}$ cm^{-3}, $T_0 = 3$ keV and $B_0 = 4.5$ T.

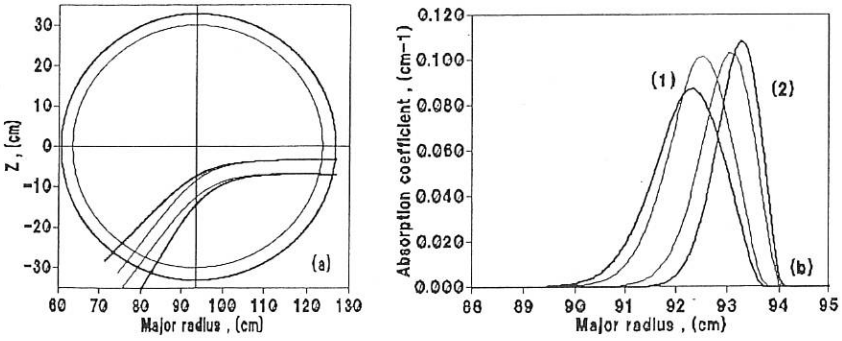

Fig.4 - Same as Fig. 3 for $n_0 = 2.3 \times 10^{14}$ cm^{-3} and $B_0 = .5$ T.

Toroidal asymmetry in ECRH produced nonthermal populations in tokamaks

A.G. Peeters, E. Westerhof, T.J.Schep

FOM-Instituut voor Plasmafysica 'Rijnhuizen', Association Euratom-FOM
P.O. Box 1207, 3430 BE Nieuwegein, The Netherlands

In the study of nonthermal effects in tokamaks, toroidal symmetry is nearly always assumed. This paper describes a toroidal asymmetry of the trapped particle distribution that is generated by the toroidal localization of electron cyclotron resonant heating (ECRH). Non-rational safety factors are assumed so that the orbits of passing particles extend over the entire flux surface, and their distribution function is symmetrized due to their fast motion along field lines. In the absence of plasma rotation and toroidal drifts, trapped particles remain tied to the same field line. Hence, their distribution function inside and outside the beam region will be different.

Timescales of processes involved

Several processes involving transport in the toroidal direction, or in velocity space, determine the toroidal asymmetry. The characteristic time in which the trapped particle orbits move around the torus, either through the drift of the orbit (τ_{drift}) or through the plasma rotation (τ_{rot}), is to be compared with the collisional relaxation time. The fastest collisional timescale on which the toroidal asymmetry is destroyed is the time in which a trapped particle is scattered to the passing particle region (τ_{detrap}). Equilibrium in velocity space between wave diffusion and collisions will therefore be established on this timescale. The equilibrium depends on the resonant energy and on the wave power, which must be sufficiently large to create a significant nonthermal distribution. If the de-trapping time τ_{detrap} is shorter than the time it takes for a resonant trapped particle to drift around the torus, a toroidal asymmetry will be generated.

The drift of the orbit around the torus is due to the inhomogeneity of the magnetic field. The characteristic time τ_{drift} is approximately [1]

$$\tau_d = \frac{4\pi\omega_c R^2 \epsilon}{qv^2} = 0.0225\,\mathrm{s}\,\frac{\epsilon}{q}\left(\frac{\omega_c}{100\,\mathrm{GHz}}\right)\left(\frac{R}{1\,\mathrm{m}}\right)^2\left(\frac{1\,\mathrm{keV}}{\mathcal{E}}\right). \tag{1}$$

The plasma rotation frequency is observed to be in the range $f_{rot} = 1 - 20$ kHz. The lower frequencies apply to the larger tokamaks. The higher frequencies occur during neutral beam injection.

Using the high velocity limit of the Fokker-Planck collision operator and considering an average scatter in pitch angle of $\Delta\theta \approx \sqrt{\epsilon}$ required for de-trapping, one obtains for the de-trapping time

$$\tau_{detrap} = 1.03 \cdot 10^{-4}\,\mathrm{s}\,\frac{\epsilon}{1+Z_{eff}}\left(\frac{\mathcal{E}}{\mathrm{keV}}\right)^{3/2}\left(\frac{16}{\ln\Lambda}\right)\left(\frac{1\cdot 10^{19}\,\mathrm{m}^{-3}}{n_e}\right). \tag{2}$$

The model

As described above, the passing particle distribution is assumed to be symmetric, while the trapped particle distribution is not. The bounce averaged Fokker-Planck equation is used to describe the evolution of the distribution function [2].

It is assumed that the drift velocity is small. The diffusion tensor, that models the effect of the waves for all orbits that cross the beam is approximated by the averaged diffusion operator $\overline{D}_{EC}$

$$\overline{D}_{EC} = \frac{1}{\Delta\varphi} \int_{\Delta\varphi} \mathrm{d}\varphi \, D_{EC}(\varphi). \tag{3}$$

Here, the toroidal angle φ labels the orbits and the integration is over the interval $\Delta\varphi$ of toroidal angles for which the orbits cross the beam. In the case of toroidal symmetry the integration extends from 0 to 2π. Therefore, in the asymmetric case the effective power that heats the trapped particle region in the beam is a factor $2\pi/\Delta\varphi$ larger.

With these approximations there are two trapped particle distributions, only one of them being heated by the wave. Both of them are collisionally coupled to the same passing particle distribution. The validity of this model requires that the heated trapped particles are de-trapped before they drift out of the beam.

It is also assumed that the collisions can be described with a Maxwell background collision operator, where density and temperature are independent of the toroidal angle. This assumption is reasonable because of the extreme high power levels required for the quasi-linear modification of the bulk distribution. With the bulk distribution being toroidally symmetric the asymmetry in the pressure will be small. Therefore, the magnetic field structure can be taken to be symmetric and the usual bounce average of the Fokker-Planck equation can be performed.

Simulations

As a first example of the difference between the symmetric and the asymmetric case simulations are performed for the following parameters: $R = 1.5$ m, $a = 0.6$ m, $B_\varphi = 4$ T, $T_e = 1$ keV, $n_e = 1 \cdot 10^{19}\,\mathrm{m}^{-3}$, $Z_{eff} = 1$, $q \approx 1$, $\omega = 105$ GHz, $P = 1$ MW, O-mode injected in the equatorial plane perpendicular to the magnetic field lines, (half) spread of the beam: toroidal 3 degrees, poloidal 2 degrees. A 100 times 150 grid in pitch angle-momentum space is used, with $p_{max}/mc = 0.3$, and three surfaces with radii $r = 10, 9.5, 9$. No power is absorbed before the beam reaches each of the surfaces.

For the parameters given above $2\pi/\Delta\varphi = 8$. The drift and de-trapping times are $\tau_{drift} = 3.54\,\mathrm{ms}\,(1\,\mathrm{keV}/\mathcal{E})$, $\tau_{detrap} = 3.43\,\mu\mathrm{s}\,(\mathcal{E}/1\,\mathrm{keV})^{3/2}$. The model is valid for $\mathcal{E} < 7$ keV, at this energy $\tau_{drift}/8 = \tau_{detrap}$. This also sets the limit of 2 kHz on the plasma rotation. Figure 1a and 1b show the distribution function in and outside the beam. The difference in the trapped particle region is clearly visible. This difference also shows up in the perpendicular temperature as a function of parallel momentum shown in figure 2.

Because the electron cyclotron emission in second harmonic X-mode is proportional to $p_\perp^4$ it is expected to be affected by the toroidal asymmetry. The ECE emissivity in second harmonic X-mode from the three surfaces is shown in figure 3. It is clear from this figure that the difference in emission in and outside the beam is significant. It should be noted that the emission for $\omega_c/\omega > 0.507$ is from electrons with an energy greater than 7 keV, where the model is not valid.

Next we consider electron cyclotron current drive using downshifted X-mode from the high field side. The parameters are: $R = 2.25$ m, $a = 0.7$ m, $B_\varphi = 4.5$T, $\epsilon = 0.133$, $n_e = 4 \cdot 10^{19}\,\mathrm{m}^{-3}$, $Z_{eff} = 1$, $2\pi/\Delta\varphi = 8$, $\omega_c/\omega = 1.039$, $\Delta\omega_c/\omega = 0.00175$,$N_\parallel = 0.156$ and 0.206, and $\Delta N_\parallel = 0.035$. For these parameters the model is valid for energies $\mathcal{E} < 17$ keV.

The current drive efficiency (η) is calculated for three injected powers: P_i = 10 kW, 1 MW and 10 MW. The results are given in table 1, together with the results from the toroidally symmetric calculations. For small power densities the current driven by the EC waves is linear in the power density. In this case the current density can be calculated from the linear response and a Maxwellian background distribution. The driven current is therefore the same for the toroidally symmetric and asymmetric cases. In general, downshifted resonances have a drawback. Due to the heating, the population of passing particles at the trapped-passing boundary, that carries current in the direction of the net plasma current, is increased. As a result, more of these particles are being trapped, leading to a lower current drive efficiency. In the high power asymmetric case the wave heats the trapped particles in the beam more efficiently and a larger nonthermal trapped particle population is formed. Therefore, the flux of passing particles over the trapped-passing boundary, caused by the wave driven diffusion, is smaller or even reversed. The number of passing particles contributing to the plasma current is reduced by a smaller amount compared with the symmetric case, and therefore the current drive efficiency remains larger. Also the larger quasi-linear saturation of the trapped particle distribution in the asymmetric case makes that less energy is absorbed by electrons who do not carry current. This also increases the current drive efficiency. It should be noted that the influence of the asymmetry on the current drive efficiency is only important in the cases where the efficiency is already low. This is because the toroidal asymmetry occurs only for moderate trapped particle energies, whereas the resonant curve should cross the trapped passing boundary at high energies for a large current drive efficiency.

Table 1. Current drive efficiency

		$T_e = 2$, $N_\parallel = 0.206$		$T_e = 1.4$, $N_\parallel = 0.156$		$T_e = 1.4$, $N_\parallel = 0.206$	
P_i		P_a	η	P_a	η	P_a	η
0.01	Sym	27.9	2.9	6.50	50.7	14.3	27.7
	aSym	27.9	2.9	6.50	50.7	14.3	27.7
1	Sym	2770	0.67	662	42.6	1450	23.0
	aSym	2590	1.7	637	45.2	1420	24.0
10	Sym	-	-	6530	16.9	14000	-28.0
	aSym	-	-	5030	25.9	11300	10.6
P_i in MW, P_a (absorbed power density) in kW/m^{-3}, η in 10^{-4} A/W, T_e in keV							

Conclusion

This preliminary investigation indicates that, as a result of the localized heating with electron cyclotron waves, there are regimes where the trapped particle distribution is toroidally asymmetric. This asymmetry is sufficiently large to be observable with the ECE diagnostics. The current drive efficiency for downshifted resonanees at large wave powers is affected by the asymmetry because of the change in the wave driven particle flux over the trapped-passing boundary and the larger quasi-linear saturation of the trapped particle distribution in the beam.

References

[1] B.Coppi, G.Rewoldt, *Advances in plasma Physics* Vol **6** p. 523 (Wiley 1976)
[2] E.Westerhof, A.G.Peeters, W.L.Schippers, *Rijnhuizen Report* RR 92-211 (1992)

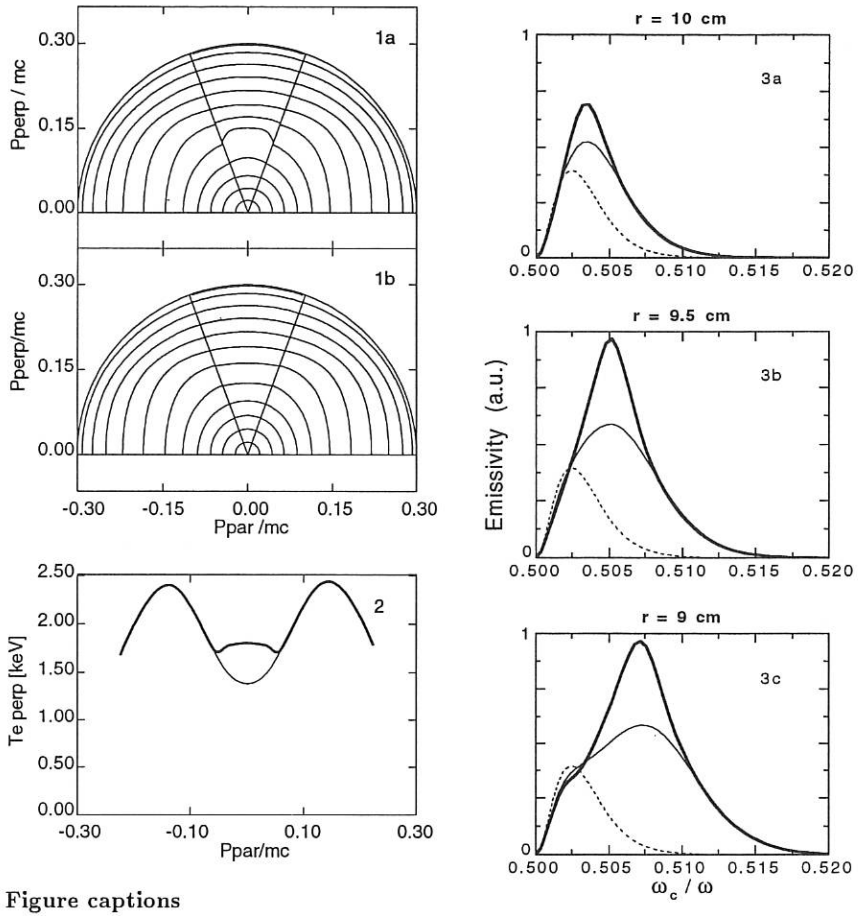

Figure captions

Figure 1a and 1b. Contour plot of the distribution function at $r = 9.5$ cm in the beam (1a) and outside the beam (1b), as a function of normalized parallel (Ppar) and perpendicular (Pper) momentum.

Figure 2. Perpendicular temperature as a function of normalized parallel momentum for the distribution in the beam (heavy line) and outside the beam ($r = 9.5cm$).

Figure 3. Emissivity in second harmonic X-mode as a function of gyro over wave frequency for the three surfaces. The heavy line gives the emissivity in the beam region, the thin line outside this region, and the dotted line the thermal emissivity.

Acknowledgements This work was performed under the Euratom-FOM Association agreement, with financial support from NWO and Euratom, and was sponsored by the Stichting Nationale Computerfaciliteiten (NCF) for the use of supercomputer facilities.

Transport of Non-thermal Electrons in Tokamaks

D C Robinson, M R O'Brien, C A Gardner and M Valovic

AEA Technology Fusion, Culham Laboratory, Abingdon, UK
(UKAEA/Euratom Fusion Association)

1 Introduction

It is likely that the anomalously high electron energy losses observed in tokamaks and other magnetic pinches are caused by magnetic and/or electrostatic turbulence [1,2]. If electrostatic turbulence is responsible, energetic electrons should be better confined than thermal electrons. Conversely, if magnetic turbulence is responsible, energetic electrons should be more poorly confined. The radial diffusion coefficient may be expected to vary as:

$$D \sim \pi R q \left\{ \frac{1}{|v_{\|}|} \left(\frac{\delta E_{\perp}}{B} \right)^2 + |v_{\|}| \left(\frac{\delta b_{\perp}}{B} \right)^2 + 2 \frac{\delta E_{\perp}}{B} \frac{\delta b_{\perp}}{B} \cos \alpha \right\} \quad (1)$$

Edge probe and core scattering measurements give $\delta E_{\perp} \sim 3\mathrm{V/m}$: Fig. 1 shows the energy dependence of the first, electrostatic, term in eq(1) for this value. Also shown is the energy dependence of the second, magnetic turbulence, term, D_M, using $\delta b_{\perp}/B \sim 5 \times 10^{-5}$ as measured at the edge of tokamak plasmas. The magnitude of $\delta b_{\perp}/B$ in the core has not been measured, and even if it had been one could not be sure that the magnetic surfaces were broken by the perturbations. However from equipartition of fluid and magnetic motions, expected to apply for 3D and near 2D MHD turbulence [3], $\delta b_{\perp}/B$ is not expected to be much larger than at the edge. It is possible that D_M is not as simple as given in eq(1): plasma effects (e.g. rotation and pressure gradients) may reduce D_M and its velocity space dependence may also differ from that given (see Discussion below). The third, cross-correlation, term in eq(1) might arise from finite β or pressure effects for example ($\alpha = \pi/2$ in Fig. 1). Figure 1 indicates that runaway electrons (provided their orbit shifts are smaller than the structure size of the turbulence) should be sensitive to magnetic turbulence as should the 'fast' electrons ($E \sim 100\mathrm{keV}$) created in Lower Hybrid Current Drive (LHCD) experiments. 'Warm' electrons ($E \sim 10\mathrm{keV}$) are particularly interesting as they are sensitive to both types of turbulence and will not be sensitive to orbit averaging effects (except possibly in tokamaks with Electron Cyclotron Resonance Heating (ECRH) where the banana widths of 'warm' trapped electrons might approach the turbulence scale size).

Experimental evidence on fast electron transport in tokamaks is conflicting: JET [4] and TORE SUPRA [5] data indicate that fast electrons are more poorly confined than bulk electrons, whereas ASDEX Ohmic [6] and LHCD [7], RTP [8] and TEXT [9] data suggest the reverse (see Fig. 1). In contrast in Reverse Field Pinches, measurements of large fast electron fluxes at the edge [e.g. 10], together with the high level of magnetic perturbations routinely observed, appear to indicate that fast electrons are more rapidly

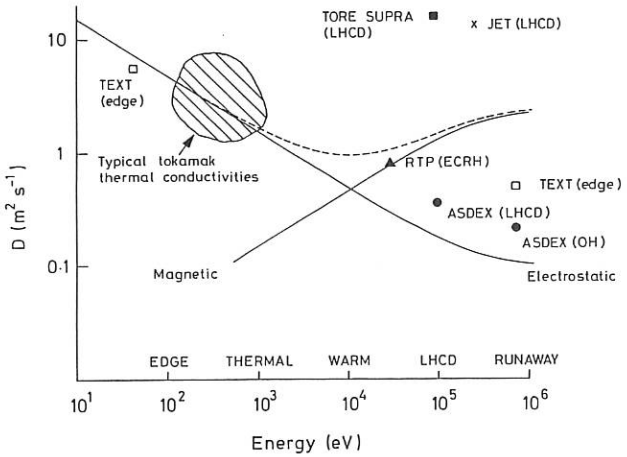

Figure 1 The dependence of electrostatic, magnetic and total radial diffusivities on electron energy from eq(1), taking $\delta E_\perp = 3\mathrm{V/m}$, $B = 1\mathrm{T}$, $\delta b_\perp/B = 5\times10^{-5}$, $q = 1$, $R = 1\mathrm{m}$. The perpendicular energy is assumed small, the magnetic turbulence is assumed weak and collisionless with no correlation with the electrostatic turbulence. Drift orbit effects, which may be important at high energies, are ignored. Relativistic effects weaken the energy dependence above $\sim 100\mathrm{keV}$. Experimental diffusivities are shown for comparison.

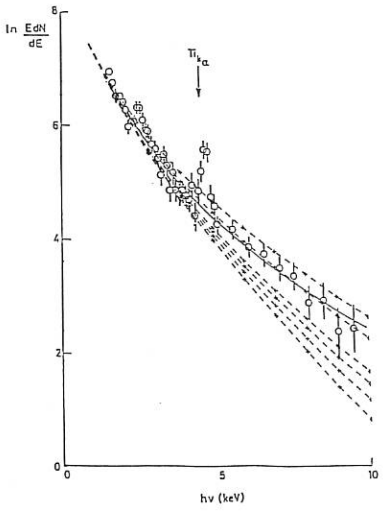

Figure 2 Experimental Bremsstrahlung spectrum (solid line) for the CLEO tokamak heated with 60GHz ECRH [13] compared with calculated spectra (dashed lines) for different levels of electron transport. The top dashed line is for $D = 0$: the remainder have $n_e(r)D(r) = 10^{19}\mathrm{m^{-1}s^{-1}}$ for energies $< 4T_{eo}$ with for higher energies, reading from the top, $D = 0$, $D \propto 1/v$, D independent of v, $D \propto v$ and $D \propto v^2$. An additional calculation for $D \propto [1 + v/(3v_{th})]^2/v$ for $v > v_{th} = (2T_{eo}/m_e)^{\frac{1}{2}}$ to better model eq(1), gave a spectrum (not shown) very close to that for D independent of v.

transported than slow electrons and hence that magnetic turbulence is responsible for electron transport in RFPs.

In this paper, the 3D electron Fokker-Planck code BANDIT-3D is used to test the sensitivity of the fast electron population in Ohmic and ECRH heated tokamaks to the velocity space dependence of the radial diffusivity. The code calculates the electron distribution function as a function of energy, pitch-angle and flux surface radius with full treatment of collisional and trapped particle effects. The ECRH is modelled by a self-consistent ray tracing/Fokker-Planck calculation and Ohmic heating is also included. The radial transport term used is of the form $\left(\frac{\partial f}{\partial t}\right)_{Tr} = \frac{1}{g_{rr}r}\frac{\partial}{\partial r}\left[rD\frac{\partial}{\partial r}(g_{rr}f) + Vg_{rr}f\right]$, with g_{rr} a metric coefficient and the balance between diffusion D and the inward pinch speed V determining the density profile. For collisionless weak magnetic turbulence for example (cf. eq(1)) $D \sim D_M \sim \pi Rq|v_{\|}|\,(\delta b_{\perp}/B)^2$. We do not allow for the influence of the radial electric field E_r on the transport: whilst an outward E_r that confines electrons could be derived self-consistently by using quasi-neutrality and neglecting ion dynamics [11], in the experiments we model, E_r is determined by the ion dynamics and is inwards, confining ions and losing electrons. For further details of the BANDIT-3D code see reference [12]. The energy dependence of the Bremsstrahlung emission is calculated from the predicted distributions, and this is compared with soft X-ray spectra measured on a number of tokamaks, with ECRH in CLEO given as an example below.

2 ECRH Spectra from CLEO

Bremsstrahlung spectra from X mode second harmonic ECRH experiments on the CLEO tokamak ($R/a = 0.9/0.13$m), using both 28 and 60 GHz waves [13], have been compared with those predicted by BANDIT-3D. The ECRH was modelled by using ray tracing data to construct the quasilinear diffusion coefficients in velocity space, the calculation then yielding a self-consistent absorption profile [12]. The experimental parameters used for the 60 GHz case were $n_e(r) = (0.1 + 1.1(1 - (r/a)^2)^{2.5}) \times 10^{19}\mathrm{m}^{-3}$, $T_e(r) = 1.0(1 - (r/a)^2)^3$keV, $V_L = 0.4$V, and $Z_{eff} = 1.6$, and the total current calculated, 15 to 17 kA depending on the transport assumed, was close to the experimental value (17kA). The waves were launched perpendicular to B with total power 150kW. The bulk radial diffusivity was taken to have a typical tokamak value ($n_e(r)D(r) = 10^{19}\mathrm{m}^{-1}\mathrm{s}^{-1}$), and for energies $> 4T_{eo}$ (i.e. $v > 2v_{th}$, $v_{th}^2 = 2T_{eo}/m_e$) D was given a power dependence on v. The pinch speed satisfied $D\partial n_e/\partial r + Vn_e = 0$, approximately maintaining the given density profile. If D and V are independent of velocity space then it is easy to show that $\partial n_e T/\partial t = 1/r\partial/\partial r[rDn_e\partial T/\partial r]$, so D acts as a thermal diffusivity. For the results in this paper V was independent of v, though runs with V having the same energy dependence as D gave very similar results. Figure 2 shows the experimental and calculated spectra for this 60GHz case. Choosing a diffusivity increasing with energy gives a poor fit to the data, implying that magnetic turbulence is not responsible for the 'warm' electron losses.

3 Discussion

In addition to the CLEO ECRH shot discussed above, simulations of Ohmic shots in the ST [14] and CLEO tokamaks, and 28GHz ECRH experiments in CLEO, have all shown that calculated and experimental spectra are closest if the transport either decreases with increasing energy, or is independent of energy, indicating that electrostatic turbulence is responsible for the transport. The fact that all our simulations indicate that the diffusivity is independent of or drops with energy is evidence that electrostatic turbulence is responsible for anomalous energy losses. If the orbit width $\gtrsim L_\perp$ the perpendicular correlation length of the turbulence, then the transport will be reduced [e.g. 6]. However, for the warm electrons modelled in this paper, $E \sim 10$keV, the orbit shift is between 0.2 and 0.7mm - with the banana widths of trapped electrons ($\sim 1 - 2$mm) $\ll L_\perp$ for the magnetic fluctuations measured at the edge. Thus averaging affects are unlikely to explain the good confinement of warm electrons in these and other experiments [7,8].

However, the characteristics of the turbulence can affect the associated transport giving a $|v_\parallel|$ dependence differing from that in eq(1). For example, theoretical models have indicated $D_M \sim |v_\parallel|^\lambda$ with $\lambda \sim 0.7 \longrightarrow 2$ depending on whether the turbulence is weak or strong, collisional or collisionless, whether it is high frequency leading to rapid decorrelation, or whether percolation theory applies [15]. Thus, although this and other research (though with several exceptions) suggest that electrostatic rather than magnetic turbulence governs thermal transport [2], further theoretical and experimental studies are required to confirm this.

Acknowledgments This work was funded jointly by the UK Department of Trade and Industry and Euratom.

REFERENCES

[1] J D Callen, Physics of Fluids B, 4 (1992) p2142.
[2] J W Connor, invited talk, this meeting.
[3] D Biskamp, Proc. Workshop on Magnetic Turbulence and Transport, Cargese 1992.
[4] A Gondhalekar et al., Proc. 1992 Int. Conf. on Plasma Phys, Innsbruck 1992, Vol I p147.
[5] D Moreau et al., Plasma Physics and Controlled Fusion, **33** (1991) p1621.
[6] O J Kwon et al., Nuclear Fusion **28** (1988) p1931.
[7] E Barbato et al., Proc. 18th Euro. Conf. on Contr Fusion and Plasma Phys, Berlin 1991, Vol III p417.
[8] B C Schokker et al., ibid. Vol I p125.
[9] A J Wootton et al., Plasma Physics and Controlled Fusion, **34** (1992) p2023.
[10] V Antoni, M Bagatin and E Martines, Proc. 1992 Int. Conf. on Plasma Phys, Innsbruck 1992, Vol I p631.
[11] G Giruzzi et al., Nuclear Fusion **32** (1992) p1011.
[12] M R O'Brien et al., Proceedings of IAEA Techn Committee Meeting on Advances in Simulation and Modelling Thermonuclear Plasmas, Montreal, June 1992.
[13] T Edlington et al., Proc. 12th European Conf. on Controlled Fusion and Plasma Physics, Budapest 1985, Vol II p80.
[14] W Stodiek et al., Proc. 5th European Conf. on Controlled Fusion and Plasma Physics, Grenoble 1972, Vol II p1.
[15] M B Isichenko, Plasma Physics and Controlled Fusion, **33** (1991) p795 and p809.

INVERSE PROBLEM FOR NON-THERMAL ELECTRON CYCLOTRON EMISSION DURING RF HEATING AND CURRENT DRIVE

V. Krivenski and V. Tribaldos

Asociación EURATOM/CIEMAT para Fusión, CIEMAT, Madrid

It is shown that the inverse problem for the electron distribution function is exactly soluble, i.e., given a set of non-thermal radiation spectra it is possible to determine uniquely the structure of the distribution function whose emission generates them.

The result makes it possible to avoid the use of phenomenological approaches, in which the fitting model artificially determines what is measured, (i.e., the adjustable parameters of the model), and allows to compare directly the *experimental distribution function,* with the predicted ones, obtained from theoretical models and Fokker-Planck calculations.

1. Normal Emission (Transmission) Measurements and Legendre Expansion

When the emitted (transmitted) radiation propagates normally to the magnetic field, the resonant electrons are located, in the velocity space, along circles of constant energy. It is therefore natural to consider a Legendre expansion of the distribution function,

$$f(r,u,\theta)=\sum a_n(r,u)\ P_n(\cos\theta)\ .$$

Inserting this expansion in the expression for the absorption and emission coefficients, α and β,[1] the resulting integrals can be readily performed analytically. Since the kernels are even functions of the parallel momentum, and within good approximation proportional to $u_\perp^{2s}$ (where s is the harmonic number), α and β can be expressed as a sum of even Legendre coefficients, in which only the first $2s+1$ terms, for extraordinary polarization, and $2s+2$ terms, for ordinary polarization, give a finite contribution.

For a typical experimental set-up, in which 1st harmonic ordinary mode, or 2nd harmonic extraordinary mode is used, the general form of the emission, and absorption coefficients is:

$$\beta_O = c_{\beta_o}\,\tilde{\beta}_O \approx c_{\beta_o}\,u^5\,\left[a_0(r,u)+1/7\,a_2(r,u)-4/21\,a_4(r,u)\right]\ ,$$

$$\beta_X = c_{\beta_x}\,\tilde{\beta}_X \approx c_{\beta_x}\,u^5\,\left[a_0(r,u)-2/7\,a_2(r,u)+1/21\,a_4(r,u)\right]\ ,$$

$$\alpha_O = c_{\alpha_o}\,\tilde{\alpha}_O \approx c_{\alpha_o}\,u^3\,\left[-9/7\,a_2(r,u)-20/21\,a_4(r,u)+u\,\partial\tilde{\beta}_O/\partial u\right]\ ,$$

$$\alpha_X = c_{\alpha_x}\,\tilde{\alpha}_X \approx c_{\alpha_x}\,u^3\,\left[-3/7\,a_2(r,u)+5/21\,a_4(r,u)+u\,\partial\tilde{\beta}_X/\partial u\right]\ ;$$

the terms $c_{\alpha,\beta}$ are slow functions of the plasma parameters, independent of the form of the distribution function, and $u=\sqrt{\left[s\omega_c(r)/\omega\right]^2-1}$ is the resonant momentum. Experimentally, the optical depth, and the radiation temperature can be determined within a range of frequencies, and then related to the distribution function by the equations:

$$\tau = \int c_\alpha\,\tilde{\alpha}\,dl \approx \int n_e\,dl\ \langle c_\alpha\rangle_r\langle\tilde{\alpha}\rangle_r\ , \qquad (1)$$

$$T_{Rad}/\left[1-\exp(-\tau)\right] \approx c_\omega\left\langle c_\beta\,\tilde{\beta}/c_\alpha\,\tilde{\alpha}\right\rangle_r \approx c_\omega\langle c_\beta\rangle_r\left\langle\tilde{\beta}\right\rangle_r/\langle c_\alpha\rangle_r\langle\tilde{\alpha}\rangle_r\ , \qquad (2)$$

which determine the average value of the Legendre coefficients a_n along the viewing path. For observation along a path of constant magnetic field, the space-averaged value of the Legendre coefficients can be determined as a function of the energy. Spatial resolution can be achieved by viewing the plasma along different paths.

Since bremsstrahlung emission perpendicular to the magnetic field is determined only by the coefficient a_0, one concludes that the most general structure of the distribution function, that can be observed and measured, by the combined use of normal electron cyclotron emission, transmission, and X-ray emission, has the general form:

$$f_{observable}(r,u,\theta) \equiv a_0(r,u)P_0(\cos\theta)+a_2(r,u)P_2(\cos\theta)+a_4(r,u)P_4(\cos\theta) \ .$$

It is worth mentioning that none of the phenomenological model distributions today in use can reproduce the previous functional dependence.[2-4] An example of inversion procedure, and determination of the *experimental distribution function*, is given in Figs. 1-4.

2. Upshifted Electron Cyclotron Emission

In hot and large plasmas it is possible to conceive a new method for measuring the distribution function, with both energy and space resolution at once, based on a similar principle to the one used for the determination of the bulk electron temperature, by electron cyclotron emission.

In the latter, all the observed emission comes from a thin layer near the position of the cold resonance x_c (defined for a given frequency ω by $\omega = s\omega_c(x_c)$), since the relativistic resonance condition, for normal observation, ensures that no contribution to the emission exists for $x > x_c(\omega)$, and emission coming from $x < x_c(\omega)$ is reabsorbed by the plasma, if $x_c - x$ is finite. Because for $x \approx x_c$ the resonant energy is low, the emitting electrons belong to the Maxwellian bulk, and the radiation temperature equals the bulk temperature in x_c .

If we now consider the previous scenario, but for a set of oblique observation angles, the emission process can still be spatially well localized, but spanning a range of higher resonant energies. In fact, the emission region is still limited to the right by the relativistic resonance condition, $x < x_0(\omega, N_\parallel)$, where x_0 is defined by $\left(s\omega_c(x_0)/\omega\right)^2 - 1 + N_\parallel^2 = 0$, and to the left by plasma reabsorption. The optical depth of bulk electrons is in general a decreasing function of $|N_\parallel|$; however, in hot and large plasmas, it is still sufficiently large to ensure that emission coming from $x < x_c(\omega)$ is completely reabsorbed, for $|N_\parallel|$ smaller than a critical value determined by the specific conditions. The electrons responsible for the observed radiation are therefore located in the region $x_c < x < x_0$, where ω is *upshifted* with respect to ω_c (i.e., $\omega > s\omega_c(x)$). The maximum resonant energy over this interval is an increasing function of $|N_\parallel|$, and all the emitting electrons have a parallel momentum with definite sign, according to the sign of $N_\parallel$ (sign $u_\parallel$ = sign $N_\parallel$).

Following this scheme, with a suitable set of radiation temperatures $T_{rad}(\omega_i, N_{\parallel i})$, it is possible to measure, at a given position in the plasma, averages of the electron distribution over distinct energy intervals ($\Delta E_{\parallel i}$, $\Delta E_{\perp i}$), for positive and negative parallel velocities. The resulting set of averaged values of the distribution function contains sufficient information to reconstruct, radially, the form of the electron distribution for energies below a certain threshold. Although we do not have a mathematical proof of the general applicability of the reconstruction process, the power of the algorithm discussed in the next section is intriguing.

3. Reconstruction of the Electron Distribution

Emission profiles at upshifted frequencies have a spatially peaked structure, which makes it natural to relate the radiation temperature for a frequency ω, to the distribution function at the point of maximum contribution, $x_m = x_m(\omega)$, through the equation:

$$T_{Rad}/\left[1-\exp(-\tau)\right] \approx T_{Rad}^{loc}(x_m) \equiv c_\omega\, \beta(x_m)/\alpha(x_m) \ .$$

A Taylor expansion of the non-Maxwellian part of the distribution function,

$$\ln\left[f_{NM}(r)\right] \equiv \ln\left[f(r) - C_{Norm}(r) f_M(r)\right] \approx c(r) + c_{\|}(r)\left[u_{\|} - u_{\|0}(r)\right] + c_{\perp}(r) u_{\perp}^2 + \\ + c_{\|\|}(r)\left[u_{\|} - u_{\|0}(r)\right]^2 + c_{\|\perp}(r)\left[u_{\|} - u_{\|0}(r)\right] u_{\perp}^2 + c_{\perp\perp}(r) u_{\perp}^4 + \ldots , \qquad (3)$$

valid whenever f_{NM} is positive, is a rapidly converging representation of the distribution function for $u = p / m_e c < 1$, (and convenient for $T_e < 20$ keV). Upon substitution of this expansion in the integrals defining the absorption and emission coefficients, α and β,[1] the following Kirchhoff-like law is obtained:

$$1/T_{Rad}^{loc} = \left[1 - 1/(1+\beta_M/\beta_{NM})\right] 1/T_e + 1/(1+\beta_M/\beta_{NM})\ 1/T_{NM} \ ,$$

$$1/T_{NM} = 2/m_e c^2 \left\{ (s\omega_c/\omega)\left[c_{\perp} + c_{\|\perp}\left\langle u_{\|} - u_{\|0}\right\rangle_f + 2\, c_{\perp\perp}\left\langle u_{\perp}^2\right\rangle_f + \ldots\right] + \right. \\ \left. + N_{\|}\left[\tfrac{1}{2} c_{\|} + c_{\|\|}\left\langle u_{\|} - u_{\|0}\right\rangle_f + \tfrac{1}{2} c_{\|\perp}\left\langle u_{\perp}^2\right\rangle_f + \ldots\right]\right\} .$$

This equation relates the expansion coefficients to the radiation temperature in a non trivial way, since to perform the averages, $\langle\ \rangle_f$, and find x_m and β_{NM}, one actually needs to know the solution of the problem, $f(r)$. A numerical solution is therefore sought, through an iterative algorithm, that minimizes the difference between the exact value of T_{Rad}, and the one obtained from the truncated Taylor representation of the distribution function.

An example of reconstruction of the distribution function, from a set of upshifted radiation spectra, is given in Figs. 5-8.

References

1 I. Fidone, and G. Giruzzi, Nucl. Fusion **30**, 803 (1990).
2 K. Kato, and I. H. Hutchinson, Phys. Fluids **30**, 3809 (1987).
3 S. Ide et al., Nucl. Fusion **29**, 1325 (1989).
4 K. Ogura et al., Nucl. Fusion **31**, 1015 (1991).

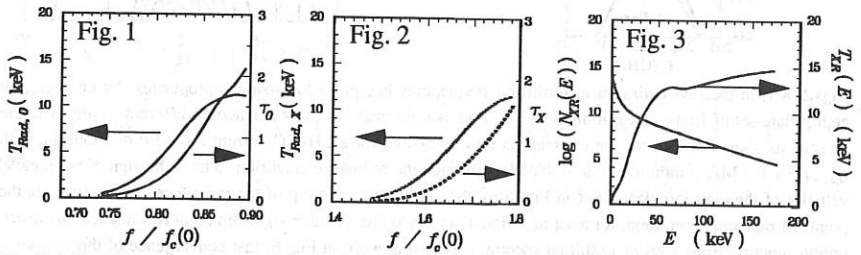

Figs.1-3 Non-thermal spectra are calculated from a Fokker-Planck distribution function, describing a lower hybrid current drive regime: Tore Supra parameters are considered, with $N_{\|1} = 2$, $N_{\|2} = 6$, $I_{LH} = 1$ MA, $T_e = 3$ keV, and $n_e = 2\ 10^{13}$ cm^{-3} . The plasma is viewed along a vertical chord, normally to the magnetic field. Ordinary mode, extraordinary mode emission and transmission spectra, and X-ray spectra are respectively shown.

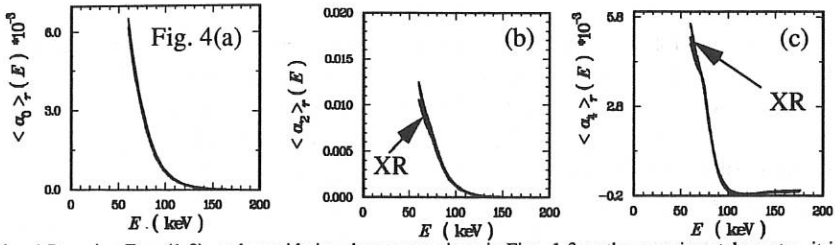

Figs.4 By using Eqs. (1-2), and considering the spectra given in Figs. 1-3 as the experimental spectra, it is possible to obtain the three coefficients $< a_0 >_\tau$, $< a_2 >_\tau$, $< a_4 >_\tau$. Two approaches have been followed: *i*) combine the experimental information contained in the two emission and transmission measurements; *ii*) combine the ordinary mode emission and transmission data, with the $< a_0 >_\tau$ calculated through an exponential fitting of the X-ray spectrum. The inverted coefficients practically coincide with the exact ones, also plotted, the error being larger in case *ii*). These coefficients allow to calculate interesting physical quantities, such as the number of suprathermal electrons and the distribution function anisotropy, at different energies.

Fig. 5

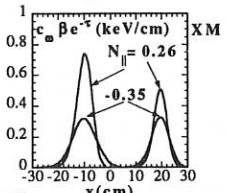

Fig. 6

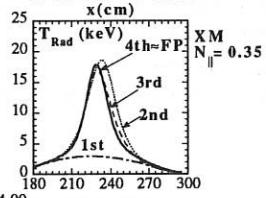

Fig. 7

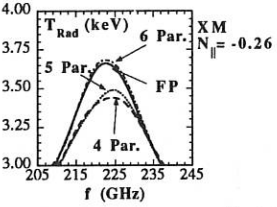

Fig. 8(a)

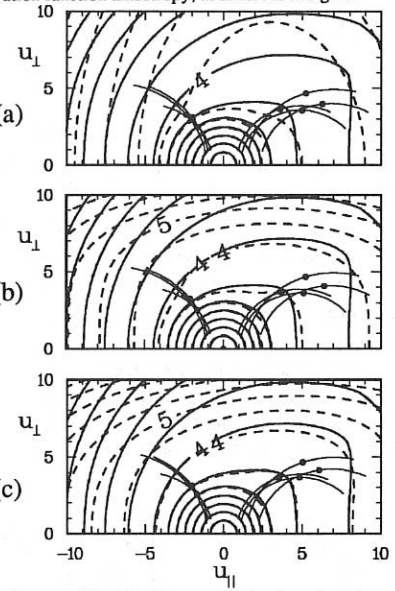

Figs.5-8 Non-thermal emission at upshifted frequencies has good localization properties: by choosing an appropriate set of frequencies, it allows to observe non-thermal electrons situated at different positions in the plasma, as shown in Fig. 5 (the emission is now computed for a LH+EC current drive FP distribution, with I_{LH+EC} = 0.9 MA); moreover, the sign of $N_\parallel$, through the resonance condition, selects the sign of the parallel velocity of the emitting electrons (in Fig. 8(a), the markers (•), on top of the resonance curves, indicate the points of maximum emission, for a set of different angles). The iterative algorithm, that reconstructs the distribution function from a set of upshifted spectra, is shown at work in Fig. 6: fast convergence of the simulated emission spectra to the FP one is apparent. Six parameters have to be retained in the expansion (3), in order to get the correct emission (Fig. 7): this corresponds also to a good reconstruction of the original distribution function, see Figs. 8, where the solution (dashed line) is plotted for 4 (a), 5 (b), and 6 parameters (c).

ELECTRON CYCLOTRON HEATING AND CURRENT DRIVE SCENARIOS FOR THE TOKAMAK ISTTOK[1]

C.A.F. Varandas, J.A.C. Cabral, A. Figueiredo, A. Moreira, J. Belo
S. Cirant*, S. Novak* and A. Orefice*

Associação EURATOM/IST, Centro de Fusão Nuclear, 1096 Lisboa Codex , Portugal
*Instituto di Fisica del Plasma, CNR, Milano, Italy

1. INTRODUCTION

Plasma heating and current drive by electron cyclotron resonance and its harmonics (ECRH and ECCD) has been performed in several plasma fusion experiments. ECRH has been used successfully to perturb the plasma electron component, bulk heat the electrons and stabilize the MHD activity. ECCD experiments have been made in small tokamaks, namely, TOSCA, CLEO, WT-3 and THOR.

The follow-up of the scientific programme for the tokamak ISTTOK (R=0.46 m, a=0.085 m, B_t=0.5 T, $n_e(0) \simeq 1.0 \times 10^{19}\ m^{-3}$, $I_p \simeq 7$ kA, $T_e(0) \simeq 250eV$, $T_i(0) \simeq 300eV$ and discharge duration $\simeq$50 ms) [1] includes the injection of RF power aiming at the enlargement of the discharge duration by ECCD, injected from the low B-field side. In similar tokamaks, like TOSCA, the RF power injection into the plasma after ohmic heating power demonstrated that plasma current can be sustained for a fairly large time.

The low values of the ISTTOK temperatures can be an advantage when transport phenomena are to be studied, since, in this case, the atoms of impurities are mostly weakly ionized, exhibiting high levels of excited states. Increasing the discharge duration the great potencialities of spectroscopic techniques like, for instance, laser induced fluorescence, can be fully exploit by adequate photon accumulation.

2. NUMERICAL RESULTS

Preliminary calculations based on ray-tracing codes give us estimates of the effectiveness of wave absorption, as measured by the percentage of the deposited power after a first passage of the waves through the plasma. Calculations showed that first harmonic O-mode sould be discarded due to low power deposition. The best results concerning power absorption are achieved with 2^{nd} harmonic X-mode interaction. The features of the used 3D ray-tracing code allow for simulations with arbitrary wave injection angle and the

[1]This work has been supported by "Instituto Superior Técnico", "Junta Nacional de Investigação Científica e Tecnológica" and European Atomic Energy Community.

inclusion of a second passage through the plasma after reflection at the wall. The path, as well as the absorption efficiency and power deposition profiles, are obtained.

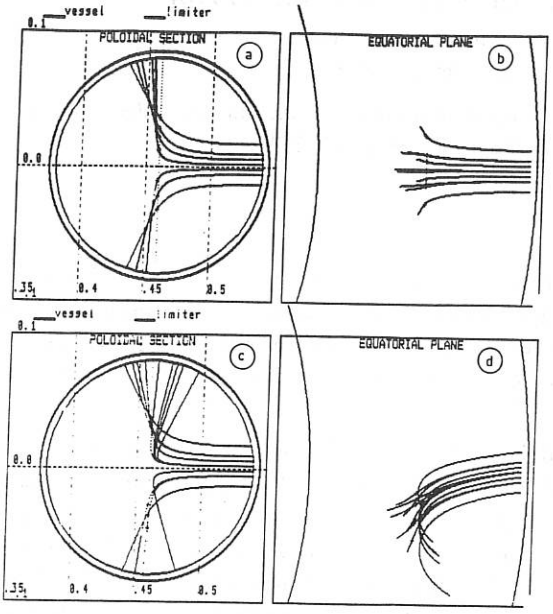

Figure 1

For perpendicular 2^{nd} harmonic X-mode injection (Fig. 1a,b), the best results predict a power absorption of 76% for $n_e = 5 \times 10^{18}\ m^{-3}$ and T_e=250 eV. The radial deposition profile is narrow and located at $0.5 < r < 2.5\ cm$ (Fig. 2a). For an oblique injection (15°) (Fig. 1c,d) the deposition profile is much broader ($2.0 < r < 6.5\ cm$) (Fig. 2b) and the absorption is larger (81%) although the existence of the close cutoff layer may reduce, in this case, our confidence on this value. It should be noted, however, that suprathermal electron populations were not taken into account, and these could modify the heating localization. Fig. 3 presents the variation of the power absorption (PA) with T_e (for $n_e = 5 \times 10^{18}\ m^{-3}$) and n_e (for $T_e = 250\ eV$).

Estimates of current drive efficiency can be made applying scaling laws from similar tokamaks experiments (Table 1). We may use:

$$\eta_{ECCD} = I_p\,(kA)\,\bar{n}\,(10^{20}\ m^{-3})R(m)\ {P_{RF}}^{-1}\,(kW) \qquad (1)$$

TOKAMAK	R(cm)	a(cm)	f(GHz)	$P_{RF}(kW)$	η_{ECCD}
TOSCA	30	8	28 ($2f_{ce}$)	180	2×10^{-4}
CLEO	90	13	60 ($2f_{ce}$)	180	10^{-3}
WT-2	40	9	35.6 (f_{ce})	60	10^{-4}
WT-3	65	20	56 (f_{ce})	120	10^{-3}
THOR	52	16	28 (f_ce)	140	-
ISTTOK	46	8.5	28 ($2f_ce$)	200	-

Table 1

The more optimistic estimates indicate that 4 kA may be achieved for $P_{RF} = 200$ kW, assuming $\eta_{ECCD} = 10^{-3}$. The expected presence of an energetic tail in the previously ohmic heated plasma will enhance the experimental results due to the fact that asymetric EC absorption by this tail is strong. More accurate estimates are to be obtained through numerical simulations using Fokker-Plank codes in conjunction to ray-tracing for the ISTTOK scenarios.

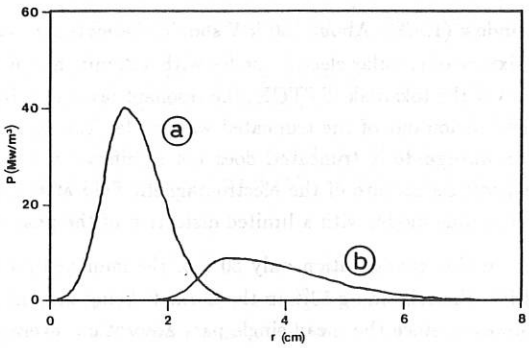

Figure 2

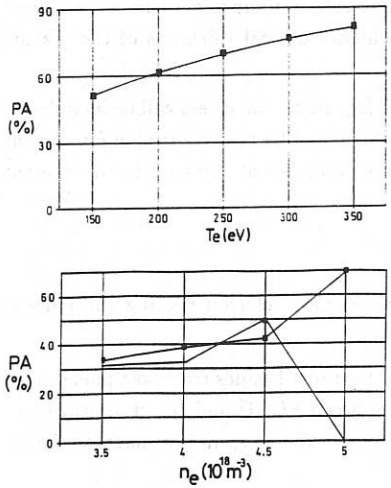

Figure 3

3. THE MILLIMETER WAVE SYSTEM

The proposed experiments will be performed using a 28 GHz gyrotron, delivering 200 kW of RF power for 40 ms mostly in the TE_{02} (81.4 %) circular electric mode, coupled to the output smooth wall waveguide with diameter of 63.5 mm through a single disk, edge-cooled BeO window.

A first version of the transmission line and launching system will use already available components, built by IFP Milano and IPF Stuttgart for ECRH experiments on THOR tokamak [2]. After a filter section for non-circular modes, the waveguide is tapered down to 35 mm to allow the insertion of three small-radius 90° bends in corrugated waveguide, optimized for TE_{02} transmission. The radius is tapered up again to 63.5 mm at the waveguide end to match with the $TE_{02} \rightarrow TE_{01}$ mode converter and the barrier window. The overall expected losses are ≈10.5%, due to filtering of spurious modes at the gyrotron output (6.5%), resistive wall losses along the 10 m of the transmission line (1%), mode conversion at the bends (1.5%) and to dielectric/reflection losses in the barrier

window (1.5%). About 180 kW should therefore be avaiable for ECRH and ECCD, in a mixture of circular electric modes with a dominance of TE_{01} (> 87 %). Due to the small size of the tokamak ISTTOK, the resonant layer seen by the wave is well within the near field region out of the truncated waveguide. Taking into account that the way in which the waveguide is truncated does not significantly interfere with the wall currents, the expected structure of the electromagnetic field at resonance is very similar to the TE_{01} waveguide mode, with a limited distortion of the phase fronts and polarization.

In this configuration only 50% of the launched power is available for direct current drive, the remaining 50% in the O-mode being insignificantly absorbed at the first pass. However, since the mean single pass absorption, averaged over the polarizations and an isotropic distribution of the propagation directions can still be significantly higher than the mean resistive losses at wall reflection ($\approx$10% considering the ports in the vessel as black holes), a large fraction of the power transmitted after the first pass is expected to be absorbed at resonance [2]. Although no net current is driven by this residual wave dumping after multiple reflections, the resulting electron temperature increase should indirectly help current drive by determining an higher optical thickness of the plasma itself.

In a second phase, $TE_{02} \rightarrow TE_{01}$ and $TE_{01} \rightarrow TE_{11}$ mode converters will be included in the 35 mm section, together with an elliptical polarizer. The power avaiable for current drive should therefore be incresed up to the maximum extent foreseen in the present estimates.

4. CONCLUSIONS

These preliminary results show the feasibility of electron cyclotron heating and current drive in ISTTOK, even at such a low magnetic field.

In these non-inductive regimes we are thinking to study, besides transport phenomena as was previously referred the synergetic effects between ECCD and the stabilization of the MHD activity and the influence of current profile in the β_{limit} in low magnetic fields.

REFERENCES

1 - J.A.C. Cabral et al., (1993) "Limiter biasing experiments on the tokamak ISTTOK", paper presented at this conference.

2 - A. Airoldi et al., Suprathernal effects in ECRH experiments on THOR tokamak, Plasma Physics and Controlled Fusion, 30, 681 (1988).

VLASOV–POISSON SIMULATION OF WAVE-INDUCED VELOCITY DIFFUSION OF ELECTRONS IN A COLLISIONAL PLASMA

J.T. Berndtson[1], J.A. Heikkinen[1], S.J. Karttunen[2], T.J.H. Pättikangas[2] and R.R.E. Salomaa[1]

[1]Department of Technical Physics, Helsinki University of Technology, Finland
[2]Nuclear Engineering Laboratory, Technical Research Centre of Finland, Finland

1. Introduction

The theory of current drive by plasma waves in tokamak plasmas relies on the quasilinear velocity diffusion of the resonant electrons against collisions. Usually, the driven current is estimated from the Fokker–Planck equation by assuming that the wave-induced diffusion can be described by the quasilinear diffusion term. In a previous paper [1], we investigated the validity of the quasilinear theory by one-dimensional Vlasov–Poisson simulations. For a fairly small number of large-amplitude waves, the diffusion was found to be slightly different from quasilinear.

We have now included a simplified Balescu–Lenard collision term in the Vlasov–Poisson code. In the following, we investigate the formation of a steady-state current with Vlasov simulations. We compare the distribution function and the current obtained from simulations with the more conventional Fokker–Planck approach.

The present simulations deal with the electron plasma waves. In the high-frequency limit, the lower hybrid waves can be approximated by magnetized electrostatic electron plasma waves. In this limit, the dispersion relation of the lower hybrid waves is approximately $\omega^2 = \omega_p^2 k_\parallel^2/k_\perp^2$, where $k_\parallel^2 \ll k_\perp^2$, and $k_\parallel$ and $k_\perp$ refer to the wave numbers parallel and perpendicular to the magnetic field, respectively. Our one-dimensional Vlasov–Poisson simulation is therefore analogous to solving the velocity distribution of the electrons in the direction parallel to the magnetic field for lower hybrid waves.

2. Collisional Vlasov–Poisson Code

We consider the Boltzmann equation that is obtained from the relativistic Vlasov equation by adding a one-dimensional collision operator for the electrons:

$$\frac{\partial f}{\partial t} + \frac{p_\parallel}{m_e \gamma}\frac{\partial f}{\partial z} + q_e E_\parallel \frac{\partial f}{\partial p_\parallel} = \left(\frac{\partial f}{\partial t}\right)_c. \tag{1}$$

The electrostatic field is solved self-consistently from the Poisson equation. As a collision term we have used the Landau limit of the relativistic Balescu–Lenard collision operator [2] where nonrelativistic (background) field particles have been assumed. After integration over the perpendicular momenta the collision term has the form

$$\begin{aligned}\left(\frac{\partial f(p_\parallel)}{\partial t}\right)_c &= \frac{\partial}{\partial p_\parallel}\{\int_0^\infty 2\pi p_\perp D_\parallel G(p_\perp) dp_\perp \times \frac{\partial f(p_\parallel)}{\partial p_\parallel} \\ &+ \int_0^\infty 2\pi p_\perp [D_\times \frac{\partial G(p_\perp)}{\partial p_\perp} - A_\parallel G(p_\perp)] dp_\perp \times f(p_\parallel)\},\end{aligned} \tag{2}$$

where the terms $D_\times$, $D_{||}$ and $A_{||}$ are the elements of the diffusion tensor and the friction vector [3]. The two-dimensional electron distribution function has been assumed to have the form $F(p_{||}, p_\perp) = f(p_{||})G(p_\perp)$, where $G(p_\perp) = (2\pi m_e^2 v_e^2)^{-1} \exp[-p_\perp^2/(2m_e^2 v_e^2)]$ is the virtual Maxwellian electron distribution in the perpendicular direction.

The numerical solution of Eq. (1) is based on the fractional step method [4,5]. The collision term is treated by generalizing the method that was introduced by Demeio for the simple Krook collision term [6]. Detailed description of these numerical methods and code has been given in Ref. [7].

3. Comparison with the Fokker–Planck Solution

We consider the one-dimensional Fokker–Planck equation which is obtained by space-averaging Eq. (1), and by making the quasilinear approximation on its left-hand side. As the collision operator we take the nonrelativistic high-velocity limit of the Balescu–Lenard collision operator (2). The nonrelativistic Fokker–Planck equation for the space-averaged distribution function f_0 then reads

$$\frac{\partial}{\partial t} f_0 = \frac{\partial}{\partial v} D_{QL}(v) \frac{\partial}{\partial v} f_0 + \frac{\partial}{\partial v}\left(D_c \frac{\partial}{\partial v} + D_c \frac{v}{v_e^2}\right) f_0 \,, \tag{3}$$

where D_{QL} is the quasilinear wave-induced diffusion coefficient. The collisional diffusion coefficient is $D_c = (Z_i + 2)\nu_0 v_e^5/v^3$, where $\nu_0 = \omega_p^4 \ln \Lambda_{ei}/(4\pi n_e v_e^3)$.

In the steady state, the well-known solution of Eq. (3) is [8]

$$f_0(v) = f_0(0) \exp\left\{ -\frac{1}{v_e^2} \int_0^v \frac{v\,dv}{1 + (D_{QL}/D_c)} \right\} \,, \tag{4}$$

where $f_0(0)$ is determined by normalization. In Eq. (4), D_{QL} is typically much larger than D_c in the region of the wave spectrum.

In our periodic collisional Vlasov code, the distribution function approaches a Maxwellian as $t \to \infty$. To investigate the formation of the steady-state current, we turn on external fields in the beginning of the simulation and keep them on all the time, which makes it possible to achieve a nontrivial steady state in the simulations. The total electric field in the plasma is then $E_{||} = E_{ext} + E_{ind}$, where the external field is of the form $E_{ext}(z,t) = \sum_{k>0} E_k(t) \cos(kz - \omega_k t - \varphi_k)$, and E_{ind} is the induced field. Since the collisional time scale is much longer than the length of our simulation, we multiply the collision term in Eq. (2) by an acceleration factor $A = 333$. Correspondingly, the collisional diffusion coefficient D_c in Eq. (4) is multiplied by the same factor. To exclude relativistic effects, we choose a low-temperature plasma with $T_e = 100$ eV.

The time evolution of the electron distribution which is initially Maxwellian is illustrated in Fig. 1 for a simulation of nine externally excited modes with wave numbers between $k\lambda_D = 0.3$ and 0.4. Initially, the current increases rapidly when a plateau forms, but between $\omega_p t = 1000$ and $\omega_p t = 2000$ the distribution changes only very little. The amplitude of the electrostatic wave also achieves a steady state by $\omega_p t = 2000$.

In Fig. 2a, the simulation result is compared to the steady-state distribution of the analytical Fokker–Planck model. The analytical steady-state (4) has been calculated by using the electrostatic spectrum of the simulation at $\omega_p t = 2000$. In Fig. 2a, the

two curves run very close to each other, but still two characteristic differences can be observed. Firstly, the plateau obtained in the simulation is somewhat higher than that of the analytical model. Secondly, at very high values of momentum, the analytical model predicts higher values of the distribution function than is observed in the simulation.

The height of the plateau is affected by several factors that are not included in the analytical model (4). In our simulation with high field amplitudes, the modes with finite trapping widths trap electrons that have velocities smaller than the phase velocity of the mode. Therefore, the lower boundary of the plateau is at smaller velocity in the simulation than in the analytical model, and the height of the plateau becomes correspondingly larger.

In Fig. 2a, we have overestimated the diffusion at high values of momentum, when we have calculated the Fokker–Planck estimate (4). In Fig. 1b, we can see that the overlap criterion is not valid for the modes near $k\lambda_D \simeq 0.2$ at $\omega_p t = 2000$. Therefore, the quasilinear diffusion coefficient should in fact be $D_{QL} = 0$ in this region. Since this was not taken into account when the Fokker–Planck result was calculated, the tail of the distribution function is too high at very large values of momentum. This also decreases the height of the plateau obtained from the analytical model.

The time evolution of the current density is shown in Fig. 2b. At $\omega_p t = 2000$, the current has achieved an almost steady-state value of 2.63 MA/m^2. The current obtained from the analytical model (4) is 2.84 MA/m^2, which is slightly larger than the simulation result.

4. Summary

We have included the Landau limit of the Balescu–Lenard collision term in a Vlasov code by generalizing the ideas introduced by Demeio for the Krook collision term [6]. This makes possible a detailed comparison of the Vlasov simulations with Fokker–Planck results. In steady state, we have found a good agreement between these two approaches. The current obtained from the Vlasov simulation of Fig. 2b was only 7% smaller than the Fokker–Planck result. This difference is most likely due to the discrete spectrum in the Vlasov simulation.

Acknowledgements: The authors would like to thank Prof. P. Bertrand and Dr. L. Demeio for useful discussions. This research was partly supported by the Academy of Finland and the Finnish Ministry of Trade and Industry.

[1] J.T. Berndtson et al., submitted to Plasma Phys. Controlled Fusion (1993).
[2] L.D. Landau, Phys. Z. Sovjetunion **10** (1936) 154.
[3] T.J.M. Boyd and J.J. Sanderson, *Plasma Dynamics*, Nelson (1969) p. 288.
[4] C.Z. Cheng and G. Knorr, J. Comput. Phys. **22** (1976) 330.
[5] R.R.J. Gagné and M.M. Shoucri, J. Comput. Phys. **24** (1977) 445.
[6] L. Demeio, J. Comput. Phys. **99** (1992) 203.
[7] J.T. Berndtson, J.A. Heikkinen and T.J.H. Pättikangas, Report TKK-F-C144, Helsinki University of Technology (1992) 22 pp.
[8] N.J. Fisch, Phys. Rev. Lett. **41** (1978) 873.

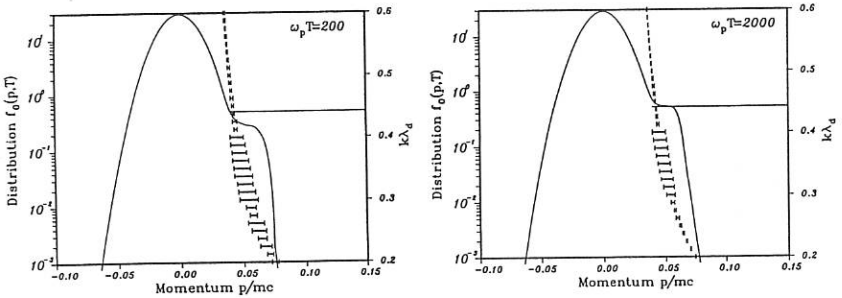

FIG. 1. Distribution function obtained from the simulation $\omega_p t = 200$ and 2000. The trapping regions of the electrostatic modes are shown on the right-hand scale ($n_e = 10^{20}\,\mathrm{m}^{-3}$, $T_e = 100\ eV$, $\ln\Lambda_{ei} = 15$ and $A = 333.33$).

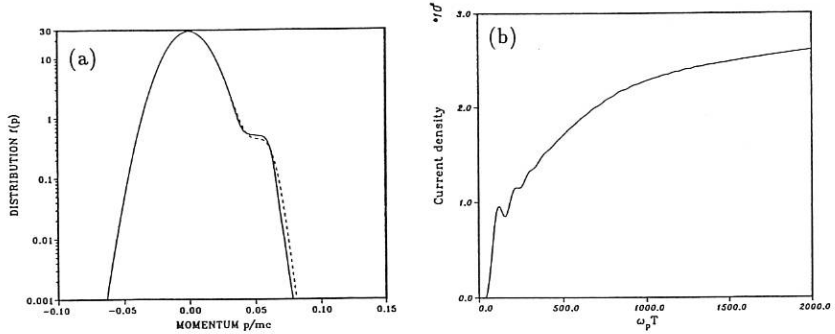

FIG. 2. a) Distribution function obtained from the simulation at $\omega_p t = 2000$ (solid) and from the analytical model (4) (dashed).
b) Time evolution of the current density (MA/m^2) in the simulation.

DISCHARGES WITH A HIGH FRACTION OF NON-INDUCTIVE CURRENT ON T-10

V.V.ALIKAEV, A.A.BAGDASAROV, A.A.BORSHCHEGOVSKIJ, V.V.CHISTYAKOV, M.M.DREMIN, Yu.A.GORELOV, Yu.V.ESIPCHUK, D.B.EVDOKIMOV, D.A.KISLOV, V.A.KRUPIN, S.E.LYSENKO, G.E.NOTKIN, Yu.D.PAVLOV, K.A.RAZUMOVA, I.N.ROI, A.N.SUSHKOV, P.V.SAVRUKHIN, V.M.TRUKHIN, N.L.VASIN, V.A.VERSHKOV
Russian Research Center "Kurchatov Institute", Moscow, Russia

C.FOREST, J.LOHR *General Atomic, San Diego, USA*

1. INTRODUCTION

An interest in the experimental study of discharges with the high fraction of a bootstrap current $f_{BS}=I_{BS}/I_p \sim 1$ has recently been aroused, because these may be keys to creating a steady state tokamak reactor.

The study of discharges with high $q \approx 5\text{-}12.5$ (plasma current $I_p=140\text{-}60$kA), where the high β_p values and hence the fraction of a bootstrap current

$$f_{BS} \cong K_{BS}\beta_p\sqrt{\varepsilon} \qquad (1)$$

are attainable has been performed on T-10. A gyrotron set, including four gyrotrons at f=140GHz (second ECR harmonic), 0.9MW per tube [1] was used to heat the plasma and to increase β_p. The experiments were conducted in parallel with the second harmonic ECCD study [1].

The main goals of the study were as follows:

1. The realization of discharges with a complete replacement of the inductive current by the sum of the bootstrap current I_{BS} and the ECCD current I_{CD}, i.e. attainment of the loop voltage $V_0<0$ in the steady state. Investigation of the discharge stability at a hollow current profile.

The preliminary estimations using the value of $f_{BS}=0.7\sqrt{\varepsilon}\,\beta_p$ and the T-10 scaling [2] have shown that the discharges with $f_{BS} \simeq 1$ and $P_{HF} \geq 2$MW can be realized in the parameters range: $I_p=100$kA ($q_L \approx 7.5$), $\bar{n}_e \geq 3\times10^{19}$ m^{-3} $\approx 14B_T/q_L R$; $I_p=75$kA ($q_L \approx 10$), $\bar{n}_e \geq 2\times10^{19}$ m^{-3} $\approx 11B_T/q_L R$. The realization of discharges with $(I_{BS}+I_{CD})/I_p \approx 1$ (under the experimental ECCD efficiency [1]) is possible with a lower power $P_{HF} \leq 1.5$ MW.

2. The direct experimental determination of I_{BS} (in discharges with $V_0<0$) as $I_{BS}=I_p-I_{CD}$, where I_{CD} is determined by the technique of co- and counter-ECCD [1]. The comparison with the neoclassical predictions [3,4].

3. The determination of the temperature T_e, density n_e and pressure p profiles, study of confinement in discharges with high q_L.

4. The estimation of potentialities of such discharges for meeting conditions

$$f_{BS}=1, \quad K_{ig}=P_\alpha/P_{tot}=1, \qquad (2)$$

(P_α is the α-particles power) in ITER.

The parameters of the T-10 discharges are given in Table 1. The input power was varied within the range P_{HF}=0.7-1.1MW. The absorbed HF power P_{ab}=0.45-0.7MW [1] was not sufficient for solving the problems 1 and 2.

TABLE 1

I_p kA	B_T T	q	$\langle n_e \rangle$ 10^{19} m^{-3}	P_{tot} MW	β_p	τ_E ms	$T_e(0)$ keV	$n_e(0)$ 10^{19} m^{-3}
146	2.45	5.0	0.83	0.58	0.5	13.9	5.65	1.2
146	2.45	5.0	1.2	0.58	0.57	15.4	4.2	1.65
147	2.44	5.0	1.95	0.59	0.84	23.2	3.4	2.65
144	2.47	5.1	1.5	0.7	0.79	17.5	4.4	1.95
76	2.48	9.8	1.2	0.49	1.2	10.7	3.8	1.6
75	2.48	9.9	1.2	0.66	1.31	8.4	4.3	1.7
75	2.47	9.9	1.2	0.65	1.53	9.9	4.6	1.7
78	2.46	9.5	1.3	0.69	1.41	9.4	4.45	2.1
78	2.45	9.5	1.9	0.7	1.45	9.5	3.0	2.6
60	2.49	12.5	1.2	0.57	1.76	8.4	4.15	1.7

2. EXPERIMENTAL RESULTS

1. Fig.1,a shows that in the experiments with I_p=75kA and P_{ab}=0.65MW the loop voltage at co-ECCD (directed along the inductive electric field) does not exceed 0.1V. The difference in V_o under co- and counter-ECCD (Fig.1,b) allows us to estimate the current I_{CD}=33±5kA. In this regime the fraction of non-inductive current $(I_{BS}+I_{CD})/I_p$=0.7 was insufficient for the direct experimental determination of I_{BS}. Therefore we deduced I_{BS} from theory [3], using the experimental profiles of T_e, T_i and n_e.

2. Typical profiles of the electron temperature and the density are shown in Fig.2. The characteristic feature of discharges with high q_L is a strong peakedness of the profiles, rising with an increase in q_L. Fig.3 shows the peakedness of the temperature and pressure profiles $K_T=T_e(0)/\langle T_e \rangle$ and $K_p=T_e(0)n_e(0)/\langle n_e T_e \rangle$, respectively, as a function of q_L. One can see that at q_L=10 the pressure peakedness attains the value K_p=10.

3. Fig.4 shows that in discharges with high q_L (q_L>5) the energy confinement time τ_E is satisfactorily described by the ITER-89-L scaling [5]. The spread in points at q_L=5 (I_p=140kA) is related to the increase of τ_E^{exp} with the plasma density $\bar{n}_e$ under ECRH (see Table 1).

Co- and counter-current drive in these experiments affects the peakedness of T_e profile and also changes the internal inductance l_i in the range $1.4<l_i<2.3$. But in the steady state the confinement is independent from l_i.

4. The parameter K_{BS} in Ex.(1) was determined from I_{BS} value, calculated in accordance with [3]. Fig.5,a shows K_{BS} as a function of q_L. The K_{BS} value is noticeably lower than K_{BS}=0.7 (usually used in estimates) and slightly

decreased with a rise of q_L and density $\tilde{n}_e$.

The bootstrap current profiles $j_{BS}(r)$ are shown in Fig.5,b for various q_L. The hollow profile of j_{BS} takes place only in a narrow zone close to the centre ($r/a<0.1$) in the discharges with $q_L \geq 5$.

3. ESTIMATIONS OF ITER PARAMETERS IN DISCHARGES WITH HIGH q

Assuming that the same temperature and density profiles as observed in the experiment could be realized in discharges with high q_L on ITER, we considered the problem of simultaneous fulfillment of conditions (2) in such discharges. The results of calculations for ITER (R=7.75m, a=2.8m, k=1.6, B_T=6T) are given in Table 2 and in Fig.6. Here τ_E denotes the energy confinement time necessary for fulfilling conditions (2). Note, that the relation $\tau_E/\tau_E^{ITER-89-L}$ is independent from K_{BS}, where $\tau_E^{ITER-89-L}$ is determined by the scaling [5].

TABLE 2

q	5			9.5			12.5		
I_p, MA	10.8			5.7			4.3		
K_{BS}	0.51			0.4			0.36		
f_{BS}	1	0.8	0.6	1	0.8	0.6	1	0.8	0.6
β_p	2.9	2.32	1.74	3.7	3.0	2.22	4.11	3.3	2.47
$P_{tot}=P_\alpha$ [MW]	1390	890	500	240	150	90	110	70	40
τ_E, s	0.9	1.1	1.5	1.8	2.3	3.1	2.6	3.2	4.4
$\tau_E/\tau_E^{ITER-89-L}$		1.66			2.44			2.93	

These results allow one to make the following conclusions.

1. If the confinement corresponds to L-mode, the fulfillment of the conditions (2) is impossible in the discharges with high q_L on ITER.

2. From the viewpoint of fulfilling the conditions (2) these discharges are less favorable in comparison with the standard ITER regimes ($q_L \simeq 2.5$-3) because the relation $\tau_E/\tau_E^{ITER-89-L}$ rises with q_L increase.

3. However, if we assume that the H-mode would be attained in such discharges, then the fulfillment of (2) is possible up to q_L=7 that allows us to reduce the current in ITER down to $I_p \simeq 8$MA. Here the confinement time in H-mode estimated from the scaling [6], $\tau_E^H = 1.5\, \tau_E^{ITER-89-L}\, k^{0.63}$.

REFERENCES

[1] V.V.Alikaev, A.A.Bagdasarov, et al, this conference.
[2] Yu.V.Esipchuk, et al, J. Moscow Phys. Soc. 1(1991)119.
[3] F.L.Hinton, R.D.Haseltine, Rev. Mod.Phys 48(1976)239.
[4] S.P.Hirshman, Phys. Fluids 31(1988)3150.
[5] P.N.Yushmanov, et al, Nucl. Fusion 30(1990)1999.
[6] Yu.V.Esipchuk, A.N.Chudnovskij, Rus. J. Plasma Phys. 19(1993)481.

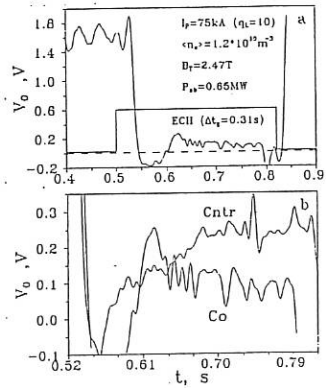

Fig.1. The loop voltage V_0 under co- (a,b) and counter-ECCD (b), I_{CD}=33±5kA, I_{BS}=19kA, $(I_{BS}+I_{CD})/I_p$=0.7, β_p=1.3.

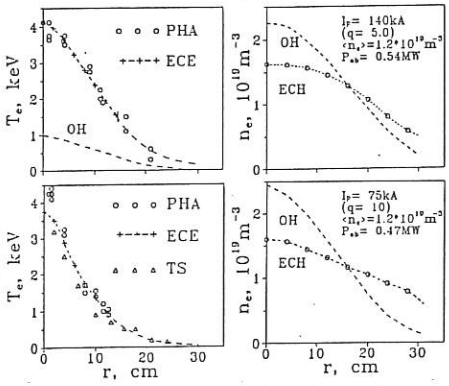

Fig.2. Temperature and density profiles

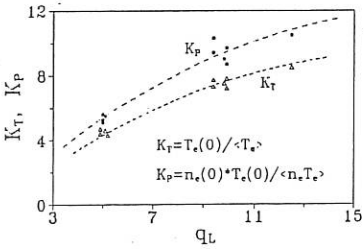

Fig.3. Temperature and pressure peakedness parameters vs q_L.

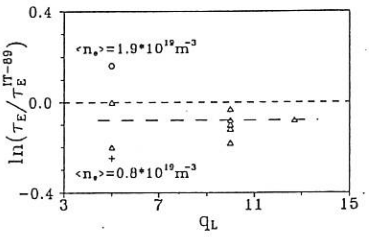

Fig.4. The experimental confinement time vs ITER-89-L scaling.

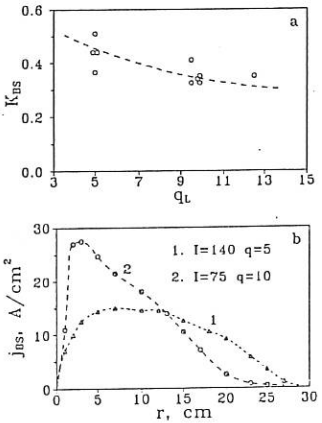

Fig.5. a) K_{BS} as a function of q_L; b) the bootstrap current profiles.

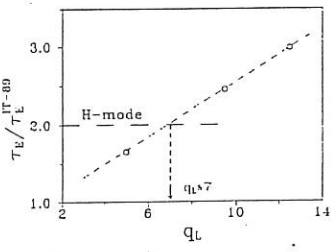

Fig.6. The relation of the confinement time, necessary to fulfillment the conditions (2), to the scaling ITER-89-L vs q .

EFFECTS OF RADIAL DIFFUSION ON RF CURRENT DRIVE IN TOKAMAK PLASMAS

A.G.Shishkin, A.P.Smirnov and V.V.Parail*

Moscow State University, Moscow, Russia
*I.V.Kurchatov Institute of Atomic Energy, Moscow, Russia

Abstract

The effects of radial electron diffusion on electron cyclotron current drive in tokamak plasma are considered. The computer code **QUARK3D** (**QU**asilinear **A**nd **R**adial **K**inetics) to simulate numerically the process of current generation is developed. The code includes: 1) the determination of wave trajectories and the absorption of RF power within the framework of geometric optics; 2) the solution of 3D bounce-averaged Fokker-Planck equation with the terms of quasilinear diffusion of electrons on EC waves and of radial diffusion. The results of numerical calculations that have been carried out for the parameters of T-10 Tokamak are presented.

Model

The basic equation of the model is a bounce-averaged Fokker-Planck equation for the electron distribution function f_e:

$$J_1 \cdot \frac{\partial f_e^{\pm}}{\partial t} = L_{coll}[f_e^{\pm}] + L_{ec}[f_e^{\pm}] + L_{rad}[f_e^{\pm}] , \qquad (1)$$

where "0", "+" and "-" correspond to trapped and to passing particles moving along the magnetic field and in opposite direction respectively. As independent variables in Eq.(1) we choose the time t, the module of velocity v, the normalized magnetic moment $s=v_1^2 B_0/v^2 B$ and the distance from the magnetic surface to the magnetic axis r. $L_{coll}[f_e^{\pm}]$ is the bounce-averaged linearized Fokker-Planck operator of Coulomb collisions of suprathermal electrons with Maxwellian background [1]. $L_{ec}[f_e^{\pm}]$ is the quasilinear diffusion operator for electron cyclotron waves [1,2]. The value of the quasilinear diffusion coefficient $\hat{D}_{ec}(r,\theta,v,s)$ is determined by the absorbed power, its poloidal localization on magnetic surface (θ is a poloidal angle) and the form of resonance region in velocity space:

$$k_{\parallel}(\rho,\theta)v_{\parallel} = \omega-\Omega_e(1 - v^2/c^2)^{1/2}, \quad \Omega_e=eB(\rho,\theta)/m_ec.$$

To determine the coefficient $\hat{D}_{ec}$ the geometric optics equations were solved for M rays. As a result the value and the localization of input RF power on a given magnetic surface were found. The total coefficient $\hat{D}_{ec}(r,v,s)$ was obtained by the poloidal averaging over all rays.

$L_{rad}[f_e^{Q}] = \frac{1}{r}\cdot\frac{\partial}{\partial r}\left(rD_{rad}(r,v,s)\cdot\frac{\partial f_e^{Q}}{\partial r}\right)$ is a operator of radial diffusion. J in Eq.(1) is given in [1].

Numerical results

To investigate the effects of radial transport on current drive numerical calculations have been performed.For the quasi-linear diffusion coefficient $\hat{D}$ the simple model was chosen:

$$\hat{D}_{ec}=D_0\cdot\frac{v_{eo}^2}{\tau_{eo}}\,\delta(r-a/2)\cdot H(v_{\parallel}-v_{1ec}), \qquad (2)$$

where H(x) is the Heaviside function, $v_{eo}=\sqrt{2T_o/m_e}$ and $\tau_{eo}=v_{eo}^3m_e^2/4\pi n_oe^4\ln\Lambda$ are the thermal velocity and the typical Coulomb collision time in the tokamak centre, a is the minor radius. The model (2) corresponds to uniform related to the poloidal angle θ absorption of EC power on a magnetic surface of radius r=a/2. To reduce the effects of temperature and density gradients the following flat profiles were used:

$$n_e(r)=n_o[0.7(1-(r/a)^6)+0.3];$$
$$T_e(r)=T_o[0.7(1-(r/a)^6)+0.3]\ . \qquad (3)$$

The coefficient of radial diffusion was taken in the form:

$$D_{rad}=D_{r_o}\cdot H(v_{\parallel}-v_{1r}), \quad D_{r_o}=a^2/\tau_c,$$

where τ_c is the life time of suprathermal electrons. The computations were carried out for $D_o=0.01$, $v_{1ec}=1.5v_{eo}$, $\tau_{eo}D_{r_o}/R_o^2=4.2\cdot10^{-3}$ (that corresponds to the following parameters of T-10: τ_c=5ms, $n_o=10^{13}$om^{-3} and T_o=5keV).Here R_o is the major radius.

Three different cases were considered:

I - $D_{rad}=0$, i.e. the absence of radial diffusion;
II - radial diffusion influences on electrons whose velocity exceeds the resonant one $v_{1r}=2.3v_{e0}>v_{1ec}$;
III - radial diffusion takes effects starting from the thermal electron velocity $v_{1r}=v_{e0}<v_{1ec}$.

In Fig.1 for the cases II and III the current profiles $j(r)$ normalized to the current density j_I in the absence of radial diffusion are presented. It can be seen that in case III the current profile is similar to that given in [3]. The current density on the magnetic surface where the heating is localized ($r=a/2$) is negative in case II. This phenomenon is explained by Figs.2 and 3 where the spectrums of current density $F(v,r)=2\pi\int v_{\parallel}(f_e^+ - f_e^-)ds$ and of the function $g(v,r)=\int_0^v F(v,r)dv$ on radius $r=a/2$ are shown. Note that $g(\infty,r)=j(r)$.

In the region $v<v_{1ec}$ the negative spectrum of current is created $F(v)<0$; for $v>v_{1ec}$ - the spectrum is positive. In case II the current density $j(r)$ is negative for $r=a/2$ since the particles that carry the current ($v>v_{1ec}$) are taken away to other magnetic surfaces due to the effect of radial diffusion. On the contrary, the particles whose velocity satisfies the condition $v<v_{1ec}$ and that make the negative contribution to the current are not influenced by the radial diffusion.

In Table 1 for the cases II and III the total current I_{ec}, the absorbed power P_{ec} and the efficiency $\eta=I_{ec}/P_{ec}$ normalized to the correspondent values for the case I are presented.

Table 1

	I_{ec}	P_{ec}	η
II	0.44	0.86	0.51
III	0.27	0.53	0.51

The degradation of absorbed power is due to the reduction in density of resonant electrons for $r=a/2$ owing to the radial diffusion.

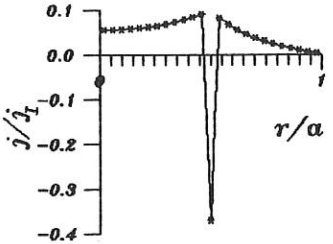

Fig.1 a)

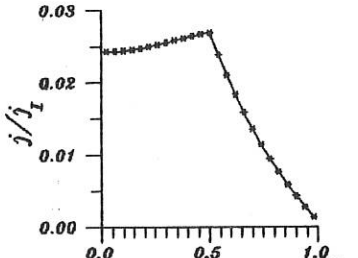

Fig.1 b)

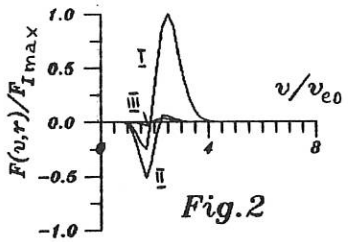

Fig.2

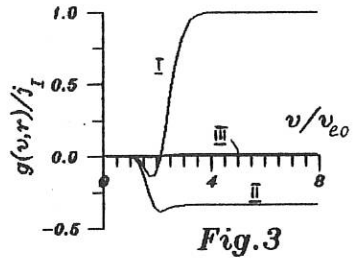

Fig.3

Fig.1 Driven current profiles: **a)** case II; $v_{1r}=2.3v_{e0}$; **b)** case III; $v_{1r}=v_{e0}$.

Fig.2 The spectrums of current density F(v,r) normalized to $F_{Imax}=\max_{v} F_I(v,r)$ for cases I, II and III.

Fig.3 The function g(v,r) for all three cases.

References

1. Dnestrovskij Yu.N., Kostomarov D.P., Shishkin A.G. and Smirnov A.P. In: Proc. of 17th EPS Conf. on Control. Fusion and Plasma Heating,Amsterdam,1990,v.14B,pt.III,p.1239-1242.
2. Dnestrovskij Yu.N., Kostomarov D.P., Shishkin A.G. and Smirnov A.P. In: Proc. of 18th EPS Conf. on Control. Fusion and Plasma Heating, Berlin, 1991, V-4, E-5, p.265-268.
3. O'Brien M.R., Cox M., McKenzie J.S. Nuclear Fusion, 1991, v.31, p.583-588.

CURRENT DRIVE WITH THE SECOND ECR HARMONIC ON T-10

V.V.Alikaev, A.A.Bagdasarov, A.A.Borshchegovskij, N.L.Vasin, V.A.Vershkov, M.M.Dremin, D.B.Evdokimov, Yu.V.Esipchuk, Yu.A.Gorelov, A.V.Gorshkov, A.Ya.Kislov, D.A.Kislov, P.E.Kovrov, V.A.Krupin, L.K.Kuznetsova, S.E.Lysenko, A.A.Medvedev, A.Yu.Novikov, G.E.Notkin, Yu.D.Pavlov, V.I.Poznyak, K.A.Razumova, I.N.Roy, V.V.Sannikov, A.V.Sushkov, V.M.Trukhin, V.V.Chistyakov and T-10 team
Russian Research Center (Kurchatov Institute), Moscow, Russia

C.B.Forest, J.Lohr, T.C.Luce, and R.W.Harwey
General Atomics, San Diego, California, U.S.A.

B.Grek
PPPL, Princeton, New Jersey, U.S.A.

ABSTRACT. The experiments on ECCD at the second harmonic were done. The current of about 35 kA was generated. The efficiency of ECCD and its dependencies on plasma parameters were measured. Not all observed phenomena may be explained by the predictions of a linear theory.

ECR current drive at the fundamental harmonic was observed in tokamaks [1,2] with efficiency η_{CD} near that predicted by the linear theory:

$$\eta_{CD} \equiv \frac{I_{CD}}{P_{ab}} \sim \frac{T_e}{n_e (Z_{eff}+5)} \cdot \langle \xi \rangle . \qquad (1)$$

Here I_{CD} is the generated current, P_{ab} the absorbed power, T_e, n_e the electron temperature and density, Z_{eff} the effective plasma charge, and $\langle \xi \rangle$ the coefficient depending on a CD generation method. For the experiments with a high plasma density the EC second harmonic CD is preferable. The mechanisms of the plasma HF power absorption for the fundamental and the second harmonic are different, as the rate of electron energy changing is proportional to $V_{\parallel} V_{\perp}$ and $V_{\perp}^2$, respectively ($V_{\parallel}$, $V_{\perp}$ are the parallel and perpendicular velocities). Analytical estimation [3] gives a two times higher value for η_{CD} for the fundamental harmonic than for the second one.

In the T-10 experiments it was necessary: (1) to demonstrate the fact of ECCD at the second harmonic; (2) to measure the value of η_{CD}; (3) to find its dependence on n_e, T_e, P_{ab} and the resonance position within the plasma.

Four gyrotrons with frequency f=140GHz and $P_{HF} \leq 1.2$MW were used. A metallic mirrors reflect the waves to direct them at the 24° angle to the major radius R at the outermost flux surface. The P_{ab} value was measured from the derivative of plasma diamagnetism at the start of the EC pulse and from the derivative of $\beta_p + \ell_i/2$ (inferred from the control fields for plasma

equilibrium at the same time. Simultaneously the injected HF power (P_{HF}) was measured calorimetrically at the ceramic window of tokamak. Taking into account that P_{HF} increases by 15% to 20% during the HF pulse, one can say that P_{ab} was about $0.8P_{HF}$. The I_{CD} value was determined by comparison of loop voltages registered in two opposite directions of the inductive plasma current for a constant direction of I_{CD} (co- and counter- experiments). The analysis assumed that the OH regimes are identical, which was verified experimentally, and that I_{CD} does not depend on co- and counter- directions. The model calculations of I_{CD} values were made using the experimental profiles of plasma parameters and the $j_{CD}(r)$ was chosen in the form which reproduces the measured time behavior of experimental loop voltage $U(t)$ and parameter $\beta+\ell_i/2$ in both directions. Fig.1 demonstrates the difference in U and $\beta+\ell_i/2$ behavior in co- and counter-experiments. The increase in $\beta+\ell_i/2$ is due to ℓ_i increasing associated with $j(0)$ rising during co-ECCD near the plasma center. Sawtooth oscillations were generated in this case and were absent in the counter case.

Fig.2 demonstrates the dependence of I_{CD} and normalized $\hat{\eta} = \eta_{CD}[n_e(0)/T_e(0)]$ on $n_e(0)$ when the resonance $\omega=\omega_{ec}$ is near the plasma center. $\hat{\eta}$ does not depend on $n_e(0)$ when $n_e(0)\geq 1.5\times10^{13}$ cm^{-3} and decreases when $n_e(0)$ decreases. The same was found in the fundamental harmonic experiments. The observed decrease of $\hat{\eta}$ at a low plasma density may by associated with the following: 1) increase of Z_{eff} with decreasing n_e; 2) the confinement time of resonance electrons τ_e in the plasma center becomes comparable with the collision time τ_{col}, that should be accounted in (1) by the factor $1/(1+\tau_{col}/\tau_e)$. Both reasons are estimated to give approximately the same decrease of η at a low plasma density. Fig.2 also shows that the value of $\hat{\eta}$ obtained previously in ECCD experiments at fundamental harmonic is in a factor of ~1.6 higher than that at the second harmonic.

Fig.3 shows the I_{CD} and $\hat{\eta}$ dependence on P_{ab}. In accordance with the linear theory $\hat{\eta}(P)$=const, however an increase of $\hat{\eta}$ with power is clearly indicated. The TORAY code based on the linear theory with relativistic effects [4] gives in ~2 times higher $\hat{\eta}$ than that measured at low P_{ab} (~0.5MW) and approximately the same $\hat{\eta}$ values at P_{ab}~0.7MW. This increase of $\hat{\eta}$ may be due to nonlinear effects. The increase of P_{ab} is accompanied by the increase of the suprathermal tails on spectra of a soft X-ray emission.

In Fig.4 one can see the dependence of P_{ab}, $T_e(0)$, I_{CD}, and $\hat{\eta}$ on the B_z value, i.e., on the resonance $\omega=\omega_{ce}$ position. The values of I_{CD} and $\hat{\eta}$ were normalized by T_e and n_e values in the point of a calculated maximum of $j_{CD}(r)$. For comparison, in Fig.4 the same dependencies calculated by TORAY code are shown. At the maximum of I_{CD} measured $\hat{\eta}$ is ~2 times lower than the calculated one. One of the reasons for that may be associated with the plasma MHD activity (sawtooth oscillations) [5].

Fig.5 shows the profiles of $nT\cdot(1/I_{SXR})\cdot(dI_{SXR}/dt)$ which is proportional to $P_{ab}(r)$ for B_z=2.3T and 2.6T. These profiles were obtained from the measurements by a pinhole chamber of soft X-ray intensity in the 4-10keV energy range. As one can see, these profiles are in rather good accordance with the theoretically predicted ones.

SUMMARY

1. The possibility of second harmonic ECCD has been demonstrated. $I_{CD}\approx$35 kA and $\eta_{CD}\approx$0.05 A/W were achieved.
2. The second harmonic efficiency is factor of 1.6 lower than the fundamental efficiency for I_{CD} generated near the plasma center.
3. The second harmonic η_{CD} dependence on absorbed power is not in accordance with the linear theory predictions.
4. The results permit planning the experiments with high n_e and hence high β using $j(r)$ profiling with the second harmonic ECCD.

ACKNOWLEDGEMENT

This work was sponsored in part by the U.S. Department of Energy under Contract DE-AC03-89ER51114.

REFERENCES

1. Alikaev, V.V., et al., Nucl. Fusion **32** (1992) 1881.
2. Luce, T.C., et al., in Plasma Phys. and Control. Nucl. Fusion Research, Vol. 1, IAEA, Vienna (1991) 631.
3. Cordey, J.G., Edlington,T., Start, D.F., Plasma Physics **25** (1982) 447.
4. Cohen, R.H., Phys. Fluids **30** (1987) 2442.
5. Forest, C.B., et al., in 10th Topical Conference on RF Power in Plasma, April 1-3, 1993, Boston, MA, U.S.A.

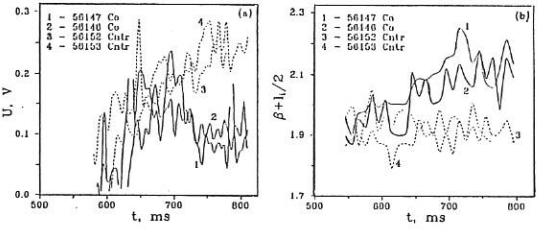

Fig. 1. (a) Loop voltage U behavior during ECCD for co- and counter-experiments. (b) The same for $\beta+\ell_i/2$. I=75kA, $n_e(0)=1.7\times10^{13}cm^{-3}$, B_z= 2.47T, P_{ab}=0.6MW. HF pulse starts at t=500ms.

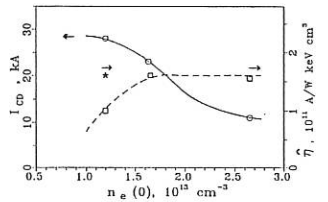

Fig.2. Dependence of I_{CD} and $\hat{\eta}$ on $n_e(0)$. I=140kA, B_z=2.48T, P_{ab}=0.56MW, * is η value at fundamental harmonic.

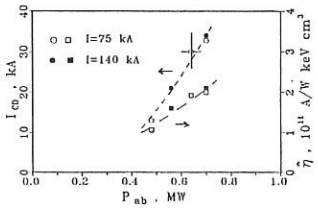

Fig.3. I_{CD} and $\hat{\eta}$ dependence on P_{ab}. $n_e(0)=1.7\times10^{13}cm^{-3}$, B_z=2.48T.

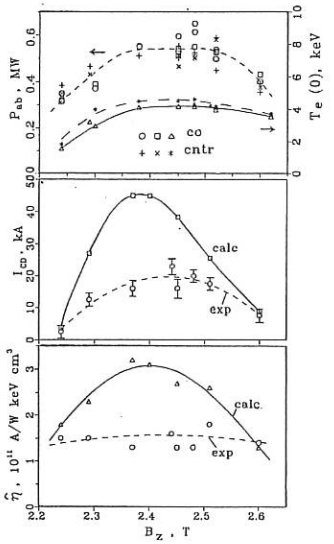

Fig.4. Dependence of P_{ab}, $T_e(0)$, I_{CD}, and $\hat{\eta}$ on B_z. I=140kA, $n_e(0)=1.7\times10^{13}cm^{-3}$

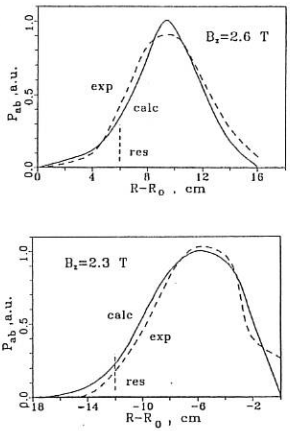

Fig. 5. Calculated profiles of P_{ab} and measured profiles of $nT\cdot(1/I_{SXR})\cdot(dI_{SXR}/dt)\sim P_{ab}$ for two resonance $\omega=\omega_{ce}$ positions.

Topic 6

Diagnostics

CHARGE EXCHANGE SPECTROSCOPY RESULTS OF JET NEUTRAL HELIUM BEAM HEATING EXPERIMENTS

M.G. von Hellermann, W.G.F. Core
U. Gerstel, L. Horton, R. König, A. Maas
JET Joint Undertaking, Abingdon, OX14 3EA, UK

Introduction

Helium beam fuelling experiments provide an ideal test bed for the investigation of slowing-down low energy alpha particles (< 145 keV) and their velocity distribution functions as well as their radial distribution. Considerable progress has been achieved in the modelling of the expected charge exchange spectra observed parallel and perpendicular to the magnetic field and the development of suitable spectral analysis procedures /1/. The first full analysis of radial profiles of temperature and slowing-down and thermalised alpha particle densities has however revealed several puzzling results, such as anisotropic ion temperatures and phase differences in the sawtooth oscillation of fast and thermal particles which require intense future modelling efforts.

Results

The fast particle component in the observed charge exchange spectra ($He^0+He^{2+}\rightarrow He^{2+}+He^{+,*}$, n=4→n=3, at λ=4685Å) is found to be in excellent agreement with predictions which are based on anisotropic velocity distribution functions obtained from the analytical solution of the neutral injection Fokker Planck equation /1,2/. Independent numerical calculations solving the Fokker Planck equation /3/ have confirmed that numerical and analytical solution agree in a first approximation (cf. Fig.1). The complete velocity distribution function covering the energy range up to the neutral beam injection energy may therefore be represented as the sum of an anisotropic slowing-down function and a Maxwellian thermal distribution function. This implies that analytical expressions may be used for the calculation of the expected charge exchange spectra cf. /1/ and usable plasma parameters such as ion temperature, thermal ion density and fast particle density can be extracted from a non-linear least square parameter fit to the observed spectra.

The effects of collision energy dependent charge transfer cross-sections on the intensity and shape of the observed spectrum is taken into account. Similar to the thermal case, where the observed spectrum maintains its Gaussian character, the predicted slowing-down spectrum is essentially unaffected in its spectral form but is modified in its amplitude and peak position (Fig.2). The spectral fit involves therefore only the determination of an amplitude factor (i.e. fast particle density) and the actual shape is calculated on the basis of known geometry factors (pitch angle etc.), electron temperature data and neutral beam injection energy.

Radially and temporally resolved measurements of fast and thermal helium ion density profiles have shown that the injection process is characterised by a change-over from a distinctly non-

Maxwellian alpha particle velocity distribution function to a dominantly Maxwellian distribution function (Fig.3). A novel result, which is confirmed by a range of pulses with different target densities and helium beam powers, is that in the first few hundred milliseconds following the start of injection the ion temperature $T_{i,||}$ deduced from an observation parallel to the toroidal magnetic field is distinctively lower than the ion temperature $T_{i,\perp}$ deduced from a spectrum observed perpendicular to the magnetic field. The values of central electron temperature based on ECE measurements appear to follow a value in between $T_{i,\perp}$ and $T_{i,||}$ (Fig.4).

The ion temperature anisotropy observed in the initial helium beam fuelling phase is contradicting a classical ion-ion isotropisation time of the order 30 to 40 msec. The slowing-down time is of the order 0.3 to 0.6 sec (Fig.5). A further interesting experimental result is the phase difference between thermal and non-thermal particle densities which was reported already for a single central channel in a previous paper /2/. The present results (Fig.6) show clearly the sawtooth propagation over the radius. It is important to note that the fast particle density sawtooth activity is in phase with ion and electron temperature, but out of phase with the thermalised alpha particle density.

The fast ion density profile (Fig.6) which is rather peaked at the start of neutral beam injection is broadened subsequently but increases only slightly in its amplitude for the case of an approximately constant source rate and target density. Fig.7 shows the ratio of fast to thermal population for three different radii (r/a=0.14, r/a=0.26 and r/a=0.51 respectively).

References:

/1/ M von Hellermann et al., JET-P(92)95, Pl.Phys. Contr.Fus.1993

/2/ W.G.F. Core, JET-P(93)19

/3/ B.Wolle, L.Eriksson, JET-P(92)30, Pl.Phys.Contr.Fus.1993

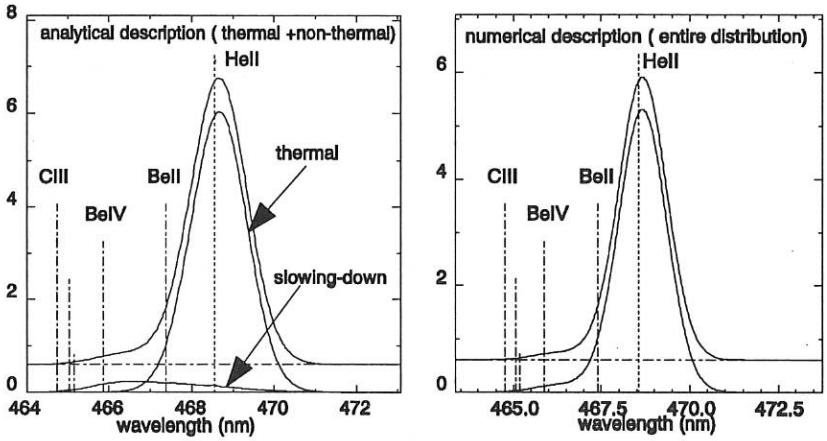

Fig.1

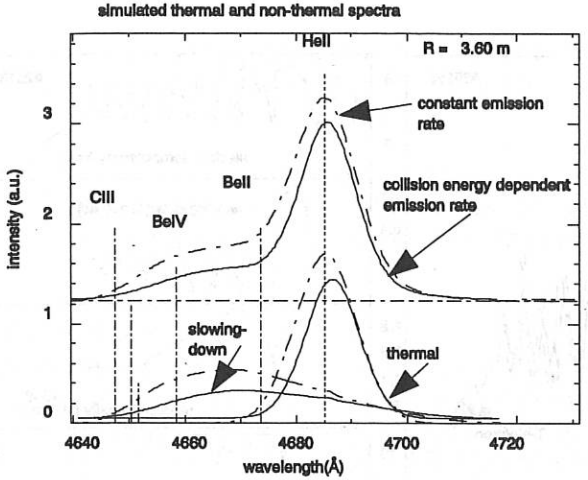
simulated thermal and non-thermal spectra
HeII
R = 3.60 m
constant emission rate
collision energy dependent emission rate
CIII
BeII
BeIV
slowing-down
thermal
intensity (a.u.)
wavelength(Å)

Fig.2

Fig.3

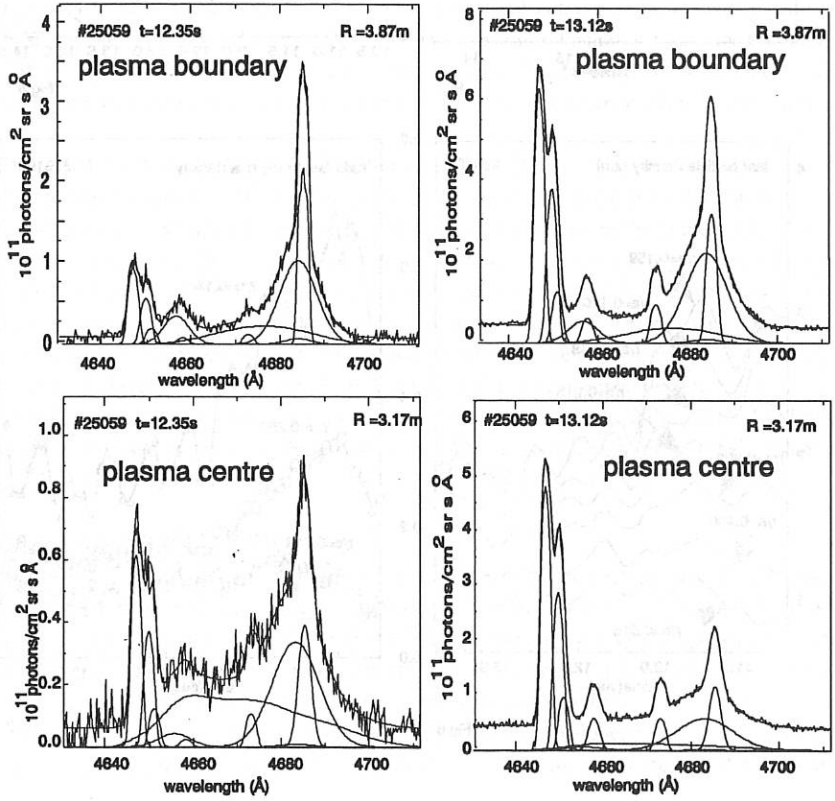
#25059 t=12.35s
R =3.87m
plasma boundary
#25059 t=13.12s
R =3.87m
plasma boundary
#25059 t=12.35s
R =3.17m
plasma centre
#25059 t=13.12s
R =3.17m
plasma centre
wavelength (Å)

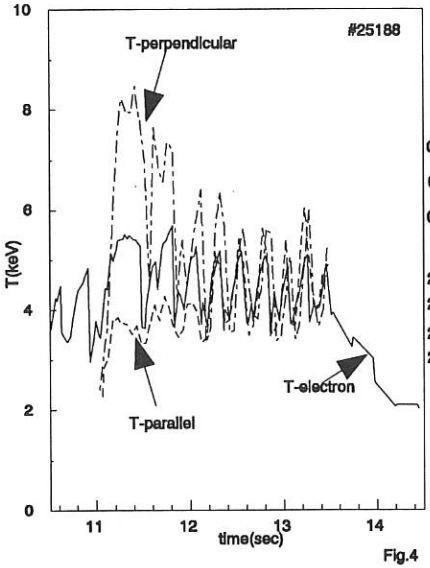

Fig.4

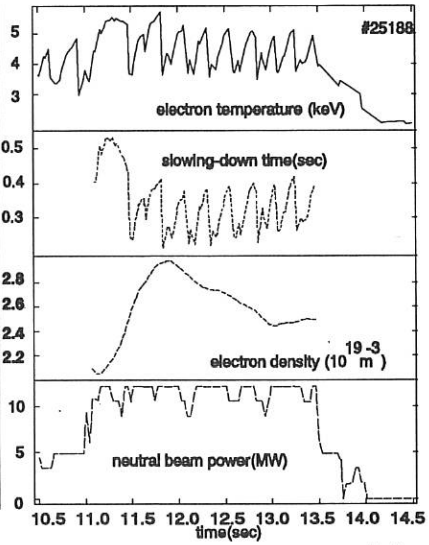

Fig.5

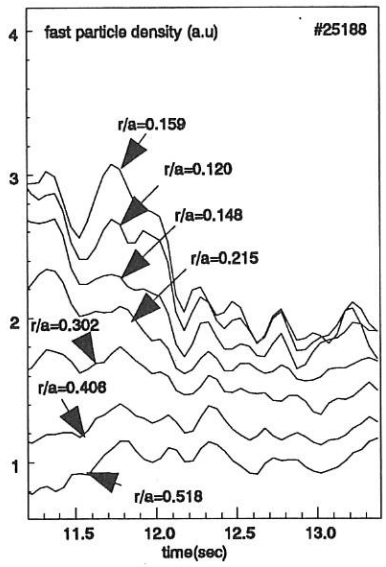

Fig.6

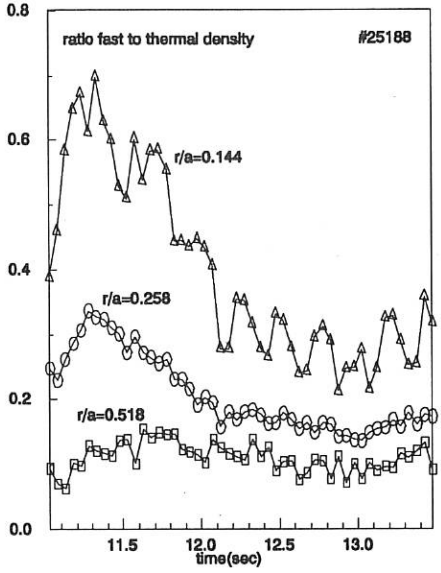

Fig.7

ANALYSIS OF REFLECTOMETER DENSITY PROFILE MEASUREMENTS IN JET

A.C.C. Sips and G.J. Kramer[1]
JET Joint Undertaking, Abingdon, Oxon, OX14 3EA, UK
[1]: On attachment from the FOM-Instituut "Rijnhuizen", Holland

INTRODUCTION

Reflectometry is a useful tool to diagnose the electron density in fusion plasmas. Various methods in reflectometry are used to obtain information on the electron density profile [1, and refs. therein]. However, routine measurements of the density profile on a Tokamak plasma have not been reported. All measurements of the density profile rely on the phase change of the probing microwave beam, along the propagation path, induced by sweeping the source frequency. In general, difficulties in the measurement and analysis of reflectometer data are caused by the effects of plasma fluctuations. In this paper a technique for measuring the density profile is given which combines the swept frequency and fixed frequency measurements. The results of the analysis are described and discussed, followed by the conclusions of this paper.

THE MULTICHANNEL REFLECTOMETER AT JET

With the twelve-channel reflectometer, that has been developed and constructed for JET [2,3], the plasma is probed along the midplane of the torus. The frequencies lie in the range 18 to 80 GHz, with radiation polarised in the O-mode, corresponding to densities in the plasma between $4x10^{18}$ m^{-3} and $8x10^{19}$ m^{-3}. The density profile can be measured by sweeping the sources over narrow frequency ranges (typically 100 MHz), while local variations in the electron density are monitored using the fixed frequency mode. The reflectometer has two detection systems. Coherent detectors, which measure both the wave amplitude and phase with a minimum sample time of 2 μs., are used to study density fluctuations in the plasma [4]. Fringe counters are used to measure phase with an accuracy of 1/128 of a fringe with a minimum sample time of 10 μs.

MEASUREMENT TECHNIQUE

The measurement of electron density profiles in JET, using reflectometry, encountered major difficulties due to the effects of the density fluctuations in the plasma. The effects of the density fluctuations is reduced by positioning of the launch and receive antennas close to the plasma, by strong filtering of the input signals to the fringe counters (bandpass of 3 kHz) and by maximising the dynamic range of the system, using high gain amplifiers.

A special technique for the frequency sweeps has been developed in which each sweep of the source frequency (up or down) is followed by a fixed frequency period of comparable

length in time which in effect generates upper and lower baselines. This operation mode is called trapeze sweep (Fig. 1), and can give continuous information in time on the electron density profile.

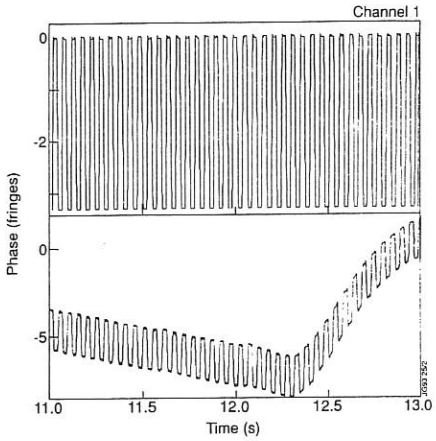

Figure 1 Two examples of the trapeze sweep mode of operation. In the upper trace the measurement of a fringe counter is given for a calibration measurement from the inner wall. The lower trace shows the measurements of channel 1 during pulse 24116

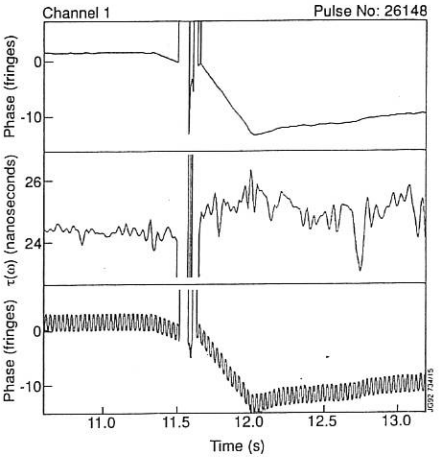

Figure 2 The propagation delay τ can be calculated continuously from the data by dividing the phase difference between the two baselines by the frequency sweep (middle trace). The top trace shows the evolution of the phase at the source frequency.

ANALYSIS METHOD

All measurements of the phase variations in the trapeze sweep mode of operations are carried out by the fringe counters. First, single fringe jumps and phase run-away periods as a result of the plasma fluctuations are eliminated or identified. Second, in the trapeze sweep mode of operation the evolution the density profile is monitored alternately at the source frequency and at the source frequency plus the magnitude of the frequency sweep. The propagation delay τ can be calculated continuously from the phase difference between the two fixed frequency baselines (Fig. 2). The resulting uncertainty on these τ values is still substantial ($\approx$ 1 nanosecond) . However, from the measured phase variation at the fixed source frequency (top trace Fig. 2) the evolution of τ can be determined. In this case the absolute value is determined by all the frequency sweeps during the total time interval of the analysis. This technique calculates the density profile and measured changes to the density profile consistently.

A computational sequence can be set up in which the τ values are Abel inverted to generate a density profile. This is followed by a new calculation of the τ values using the phase variation at fixed frequency and the refractive index calculated from the estimated density profile. This sequence is repeated until a stable and consistent solution is obtained. For the

Abel inversion routine continuous information on τ versus probing frequency between the integration boundaries is obtained by interpolating the τ values between channels. Below the lowest probing frequency the edge profile is assumed to be linear with a chosen edge gradient.

Two corrections to the density profile calculation can be implemented. A correction for the finite frequency sweep of the sources (the reflection layer moves during the sweep), and a correction to the refractive index due to relativistic effects for O-mode radiation [5]. This relativistic correction can be implemented with the knowledge of the electron temperature profile as measured by the ECE diagnostics in JET.

RESULTS

The analysis of the reflectometer data is carried out routinely, without manual intervention. An example of a result is given in Fig. 3. The evolution of the density profile can be monitored throughout the measurement interval, which is typically 6 to 8 seconds.

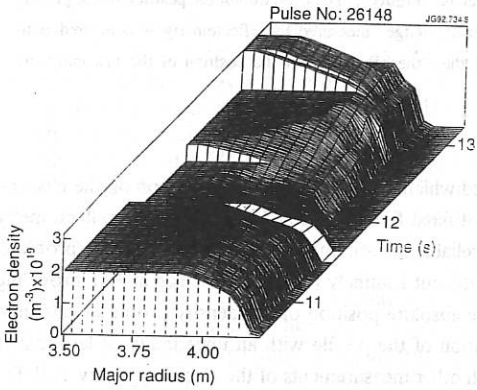

Figure 3 An example of the measured density profiles for pulse 26148. The measurements show the formation of the X-point and the steeping of the gradient of the electron density profile at the edge of the plasma during the H-mode. Note that the profiles do not extend to the centre of the plasma, which is typically at 3.1 m.

One aspect of the measurements of the reflectometer is that the radial position is measured for certain density layers. In the case of a steep density gradient in the measurement region, the uncertainties on the positions can lead to a density profile which is multiple valued at one radius. In this case the uncertainties on the measurements allow one or more density layers to be closer to the antenna than a layer with a lower density. During the calculation sequence of density profiles these non-monotonic density profiles are constrained to be monotonic.

An important check on the accuracy of the calculated electron density profiles is a comparison with the data from other diagnostics which measure the electron density at JET, such as LIDAR Thomson scattering and the multichannel interferometer. An example is given in Fig 4. The measurement of the electron density profiles by the reflectometer are independent of the reconstruction of the magnetic field measurements in JET. As a result we can compare the position of the last magnetic flux surface with the position of the edge of the reflectometer density profiles (Fig 5).

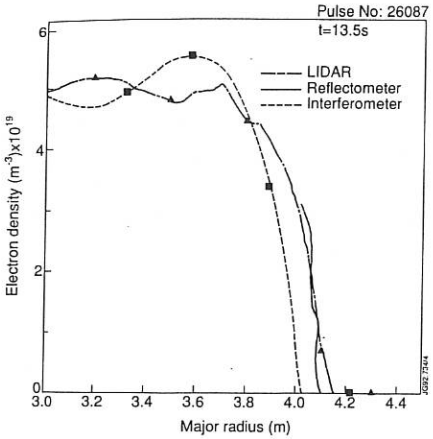

Figure 4 The density profile of the reflectometer is compared to the measurement of the electron density by means of LIDAR Thomson scattering and the multichannel interferometer at JET.

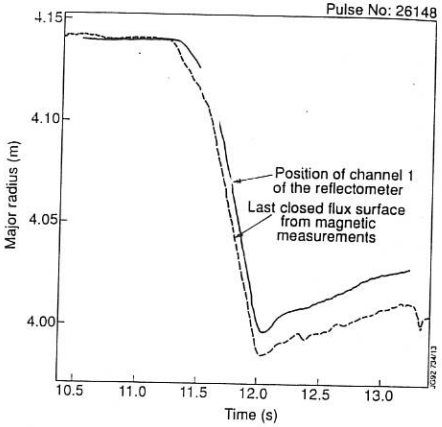

Figure 5 The evolution of the position of the plasma edge measured by reflectometry is compared with the calculation of the position of the last magnetic flux surface.

CONCLUSIONS

A new measurement technique is described which gives continuous information on the electron density profile in time. The combination of fixed frequency and swept frequency reflectometry measurements results in an accurate and reliable measurement of the electron density profile in JET. The analysis of the data can be carried out routinely for each discharge at JET providing the plasma edge is not too turbulent. The absolute position of the density profile is measured with an accuracy of 3 cm, and the evolution of the profile with an uncertainty of less than 1 millimetre. The profiles compare well with other measurements of the electron density at JET.

ACKNOWLEDGEMENTS

The authors would like to thank Drs H. Bindslev, A. Colton, A.E. Costley, N. Deliyanakis, D. O'Brien, R Prentice and P.E. Stott for the useful discussions on the interpretation of the data.

REFERENCES

[1] A.E. Costley, Diagnostics for Contemporary Fusion Experiments, International School of Plasma Physics, edited by P.E. Stott et al, Varenna (1991) 113.

[2] R. Prentice, et. al., Course and Workshop on Basic and Advanced Diagnostic Techniques for Fusion Plasmas, Varenna (1986), EUR 10797 EN Vol II 451.

[3] C.A.J. Hugenholtz and A.J. Putter, Course and Workshop, on Basic and Advanced Diagnostic Techniques for Fusion Plasmas, Varenna (1986), EUR 10797 EN Vol II 469.

[4] G.J. Kramer, A.C.C. Sips, and N.J. Lopes Cardozo, JET-P(92)97, December 1992.

[5] H. Bindslev, Plasma Physics and Controlled Fusion, Vol 34, 11, 1601.

SPECTROSCOPIC STUDY OF CX EXCITED IMPURITY IONS IN MARFES AND DETACHED PLASMAS OF TORE SUPRA

HESS W.R., MATTIOLI M., GUIRLET R., DRUETTA M.*,
Ass. EUR-CEA DRFC CEN-Cadarache
F-13108 St Paul-lez-Durance France
* Université de St Etienne, France

This work has been stimulated by the increasing interest in diagnostic methods capable of measuring the density and temperature of divertor plasmas which are characterised by low electron temperature and high neutral density. Our study of the highly radiating cold and dense edge layers sustained by the ergodic divertor (ED) of TS [1] has shown the importance of CX excited highly ionised impurities in this zone. Spectroscopic measurements of MARFE and detached plasma radiation show the existence of a highly ionised carbon flux from the hot plasma core into the cold edge layer. Space and wavelength resolved measurements of CVI (8-7, 5290 Å) and (2-1,Lyα) radiation have clearly shown the difference between CX and electron collision excitation. Whereas electron collision excitation occurs in a corona with Te~χ_i(CVI), CX collisions occur further out at the overlap of the neutral density layer and the outstreaming C^{6+} ions. Fig.1 shows the geometry of the 9 viewing lines in a poloidal plane. Each viewing line is linked via an optical fiber to a spectrometer with a 2-dimensional CCD camera [2]. **Results:** Fig.:2 shows a high density discharge with a MARFE and a detached plasma. As is seen on the radial profile of CVI (5290 Å) radiances (fig.3), a MARFE develops first on the high field side. An estimation of the neutral hydrogen density inside the MARFE using an impurity transport code together with the measured radiances gives values of n_{oM}~3.10^{17}-10^{18} m^{-3}. During the subsequent detachment, the radial profile shrinks (Δr=8cm) and the CVI radiance becomes nearly symmetric. A second type of discharge with pellet injection and ED activation shows again the importance of CX processes (fig.4 Ip=1.5MA, B_t=3.4T). During the current plateau 7 deuterium pellets are injected, three of them during ED activation. Fig.4 shows the reduction of CVI Lyα always observed during ED activation. This is interpreted as an indication of Carbon screening induced by the ED [3]. On the other hand peripheral carbon lines as CIII (977Å) increase, which indicates increased recycling at the edge with little penetration towards the center. The dips in Hα and CIII radiances show that H and C recycling is temporarily reduced at the moment of pellet injection especially during ED activation. The initial level is recovered within 180 ms which is close to τ_p the mean particle life time. Before ED activation the CVI (5290 Å) profile is poloidally symmetric as seen in fig.3 at 4.4s. During ED activation the poloidal symmetry is lost. As with the MARFE the enhanced signal of fibers B, C, D is caused by CX with increased neutral deuterium density. This is consistent with increased Hα/Dα recycling seen on fig.4. As

already stated the CVI Lyα profile remains poloidally symmetric in all situations. The reduction of CVI Lyα is not seen on the visible CVI (8-7) line, which increases during ED activation. This increase can only be due to CX with supplementary n=2 neutral excited Deuterium at the plasma edge. However, opacity of the Lyα line cannot be excluded. An estimation based on a simple absorption formula confirms this hypothesis (n_{ocrit}~5 $10^{18}m^{-3}$). It would increase the n=2 population by more than an order of magnitude.

Precise analysis of the CVI (8-7) line shape, measured with a polarizer for 9 poloidal viewing lines (fig.1), provides plasma edge temperature profiles (fig.5). Surprisingly low ion temperatures of 7 to 10 eV consistent with Langmuir probe T_e measurements in a detached plasma are observed. It may be speculated that the C^{6+} ion energy loss must occur by the following path: low temperature neutral hydrogen flux leading through resonant charge transfer to deuteron cooling and then deuteron/C^{6+} elastic collisions leading to carbon cooling. The cooling processes must occur on a timescale faster than the recombination time. Furthermore, during these discharges, characterised by a high neutral density at the plasma edge, a number of unidentified spectral lines are observed. The most persistent line at 5304.6±0.2Å (fig.6) is tentatively identified as CIII ($1s^2 2s$,7-5). Our measurements indicate a high abundance of C^{6+}, C^{4+} and C^{3+} at the plasma edge. In view of developing methods for probing the neutral density at the plasma edge, the reported results on highly excited CX lines indicate that new calculations of CX cross sections at low particle energy are necessary. A possible application would be for the low temperature high neutral density plasma encountered in the axisymmetric divertor region.

Ref.: [1] J.C.Vallet et al, Phys.Rev.Let.,vol.67,no 19 (1991) 2662
[2] W.R.Hess et al, EUR-CEA-FC-1477(1993)
[3] C.Breton et al. Nucl.Fus. 31, 1774 (1991)

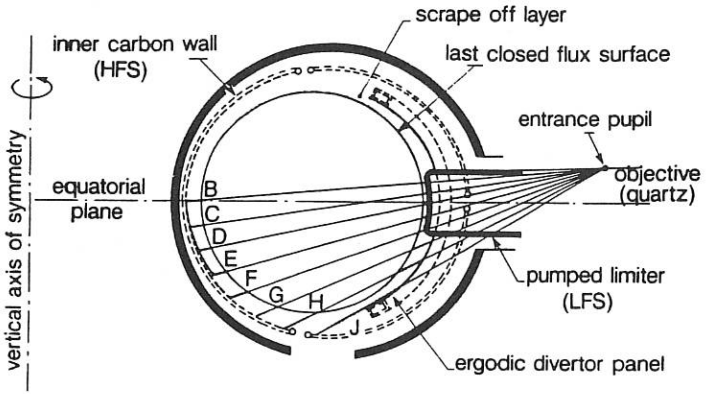

Fig 1 VIEWING GEOMETRY OF FIBERS B → J IN POLOIDAL PLANE

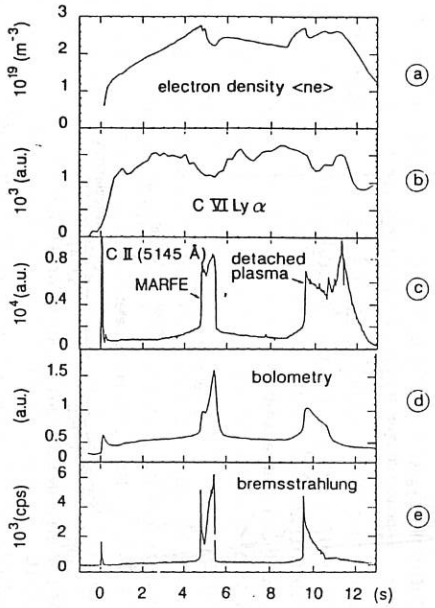

Fig. 2

Ip = 1 MA, Bt = 3 T, Ro = 2.39 m
LFS limiter a = 0.75 m

TS 6851 HIGH DENSITY DISCHARGE (D_2) WITH MARFE AND DETACHED PLASMA

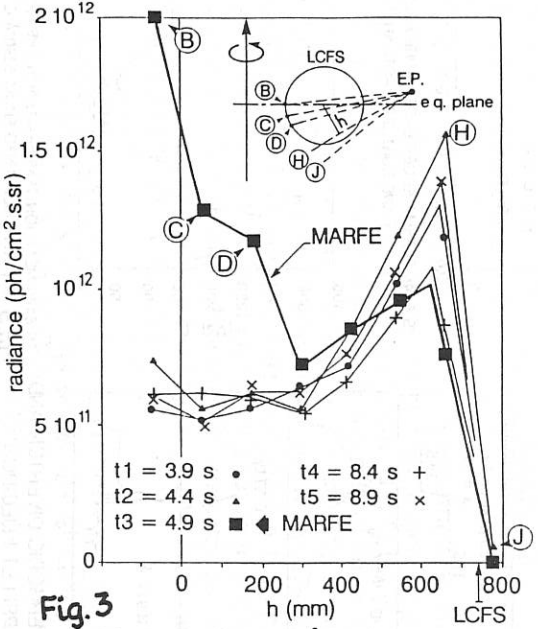

Fig. 3

TS 6851-C VI 5290 Å RADIANCES AS FUNCTION OF VIEWING LINE POSITION h

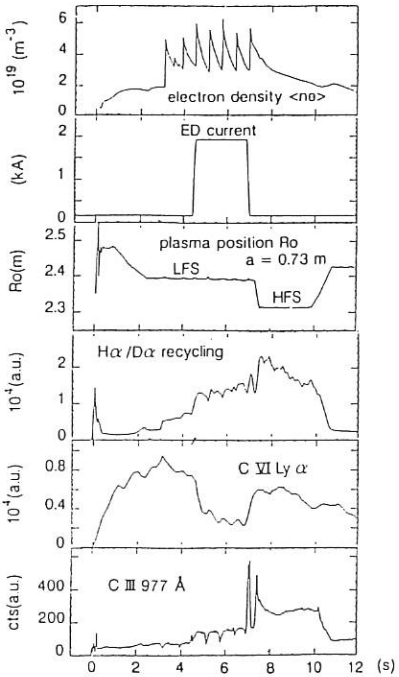

TS 6446 ERGODIC DIVERTOR AND PELLET INJECTION

Fig.4

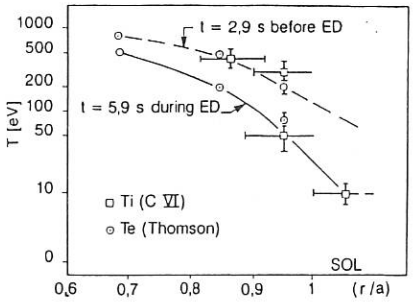

TS 6446 PLASMA EDGE TEMPERATURE PROFILE BEFORE AND DURING ED ACTIVATION

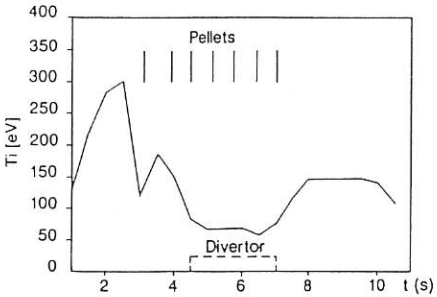

TS 6446 MEAN ION TEMPERATURE IN THE ERGODIC LAYER (FIBER H) MEASURED FROM 5290 Å C VI LINE

Fig.5

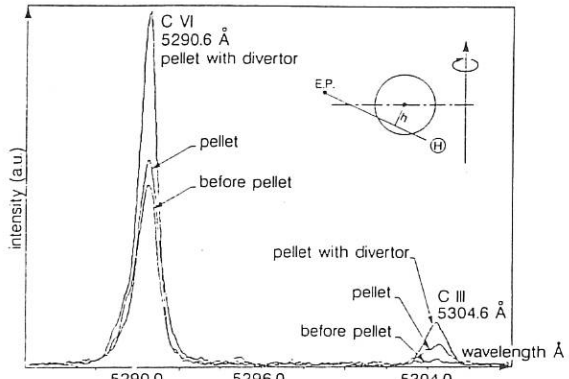

Fig.6

TS 6446-C VI 5290 AND C III 5304 Å EDGE VIEWING LINE H

High-resolution X-ray line spectroscopy on TORE SUPRA

P.Platz, A.Béraud, M.Hesse, J.-Ch.Mafféo, and B.Moulin

Association EURATOM-CEA sur la Fusion ; CEN Cadarache
13108 St.Paul lez Durance (France)

Introduction. Line spectra from the n=2-n=1 transitions in the helium-like charge state of impurity elements have been observed on several tokamaks, in particular on TFR (Ar,Sc,V,Cr,Mn) /1/, PLT and TFTR (Ti, Cr,Fe,Ni) /2/.Because of the considerable interest of these spectra in atomic physics and plasma diagnostics /3,4/,we have developed a high-resolution,Johann-type spectrometer covering the range $1.4 < \lambda < 4$ Å by use of a multi-crystal configuration.Particular design features are:full remote operation (including the loading of the appropriate crystal between shots) and heavy (n,γ)–shielding.We also discuss diagnostic applications of the spectra from Ar16+,Mn23+,Fe24+,Ni26+ and Cu27+ recently observed on TORE-SUPRA (TS).

Description of the spectrometer. Considerations on the resolving power of crystal spectrometers has led to the use of quartz laminae (30x50 mm2, thickness 0.4 mm) at Bragg angles, θ , between 65°and 71°,having radii of curvature,R,of about 3150 mm/5/.In the He-filled spectrometer,the crystals are bent by sucking them against cylindrically shaped supports /5/.This simple bending device allows for a compact 8-crystal magazine to be mounted into the spectrometer.The standard loading is specified in table I, where λ_W is the wavelength of the resonance line n=2-n=1 from the helium-like ion ($\lambda_W = 2d \sin\theta_W$) and hkl is the diffracting plane.The radii of curvature of the cylindrical supports (there are 6 glass and 2 diamond-machined-brass supports) range from 3130 to 3212 mm (table I).We have taken profit by this spread in combining supports and crystals to get almost identical $R\sin\theta_W$ products.This allows a fixed crystal-to-detector distance,which simplifies the necessary movement of the detector arm with its heavy (n,γ)-shielding (a 4π– shielding with 50 cm of borated polyethylene and 10 cm of lead) to a purely angular movement of 12°. Finally,crystals for other ion species than those listed may also be loaded,in particular for the following ions (λ, hkl and θ are given in parenthesis) : Ar17+(3.733Å;201;70.5°),Sc19+(2.872Å;211;68.7°) and Kr34+(0.9455Å 446;68.7°). The detector is a position-encoding proportional counter (with delay line read-out),intercepting a wavelength interval of roughly $0.012\ \lambda_W$,which includes the transitions (w,x,y,z) from the heliumlike

ions and the associated satellite lines (q,j,k,r,...).The resolving power of the instrument is approximately 13000.The fast timing signals from the delay line (which translates photon position into a time interval) are fed to a CAMAC station by a low-jitter, 100 m long fiberoptic link /6/.At present, the acquisition system takes 128 full spectra in the histogram mode,and the total intensities of four prominent lines are simultaneously followed by fast multichannel scalers (or MCS; dwell time >= 1 ms). The line of sight of the spectrometer makes an angle of 67° with the toroidal field(at R=236 cm).

Observed spectra and diagnostic applications.In TS,the most abundant metallic impurity in ohmically heated plasmas is iron.Fig.1 shows two spectra (normalised to the same intensity of w) from plasmas of different electron temperatures (see /4/ for standard line notations). The spectra consist of the heliumlike lines w,x,y and z ($1s^2\,^1S_0$-$1s2p\,^1P_1$, $1s2p\,^3P_2$, $1s2p\,^3P_1$ and $1s2s\,^3S_1$) and the associated satellites from the 1s2nl-1s2pnl transitions (with n>=2) in lithiumlike ions .These lines are produced by collisional excitation from the groundstate and recombination (w,x,y,z), innershell ionisation (z), innershell excitation (q,t,r) and dielectronic recombination (j,k,r,.., and n>=3) . The potential of these spectra for plasma diagnostics may be fully worked out by least-squares fits to synthetic spectra with the free parameters Ti, Te, and N_{Li}/N_{He}.However,to first order,the intensity ratio j/w yields Te (1800 and 2300eV for the plasmas of Fig.1), and the intensity ratio q/w equals $0.66*N_{Li}/N_{He}$. Notice that q/w decreases with increasing Te (Fig.1), indicating an increasing degree of ionisation.The w line of iron is very suitable for routine measurements of Ti and of toroidal rotation velocities. Fig.2 shows an example taken from preliminary ICRF experiments.Notice the blueshift by 1 channel (.059 mÅ) when ICRF is applied, indicating a change in toroidal velocity by 25 km/s (antiparallel to Ip).The line broadening yields ΔTi =350 eV.

Occasionally,the spectra from a minor component of stainless steel may be quite intense. Examples are the two Mn-spectra of Fig.3 from an ohmic and a LH-heated plasma (in a narrow interval between the n>=3 and x lines ,the background level has been recorded by placing a mask on the focusing circle). Again we may deduce Te values from the j/w intensity ratio : 1700eV (2500eV) for the ohmic (LH-heated) plasma.The q/w ratio yield N_{Li}/N_{He}=0.7 (0.4), i.e. roughly twice the values expected for coronal equilibrium conditions.

Another feature of LH-assisted discharges is the intense spectrum of copper, observed for the first time on a tokamak; Fig5. As expected, /1/,the increasing x-y, r-q, and j-k distances due to the Z^4-scaling of spin-orbit interaction leads to an overlap of the lines r and j (also of y and q) in the Cu spectrum. Therefore, an accurate value for Te may be

extracted from the observed spectrum only by comparison with a synthetic spectrum, calculated using a complete atomic -physics code,not yet available at this writing. However, a rough estimation gives Te=3800+-400eV.(Thomson scattering data,averaged over the cord segment -0.2a<r<+0.2a, yields 4000eV).
Finally,applications of the MCS are demonstrated in Fig.4 and 6. Fig.4 shows the fast decrease of the w-line of Fe24+ due to the cooling of the central plasma by a fast pellet (1.9 km/s).The collapse of the count rate to 20% of its initial value indicates a ΔTe in the 1keV range, in agreement with Thomson scattering data. The pre-injection level is restored with a time constant of 350ms. Fig.6 shows the time evolution of Ni27+ in a laser-injection experiment.The maximum of the signal is attained in 35ms.The signature of sawtooth crashes is quite evident (the time markers have been taken over from a central X-ray diode signal). The resident time (1/e) of the Ni27+ impurity ions is 200 +-20 ms.

.**Acknowledgements** to J.P.Coulon and Y.Tosolini for their contributions to this diagnostic, and to F.Dauvergne and A.Gabriel (both at EMBL Grenoble) for assistance in detector developments.

/1/ TFR Group,M.Cornille,J.Dubau,M.Loulergue;
Phys.Rev. **A 32**, 3000 (1985)
/2/ M.Bitter et al.; Rev.Sci.Instrum.**59**, 2131 (1988)
/3/ S.von Goeler et al.; in "Diagnostics for Fusion Reactor Conditions" Varenna, 6-17 Sept.1982, Report 8351-I EN; CEE, Bruxelles
/4/ J.Dubau,S.Volonté;Rep.Prog.Phys.**43**,199 (1980)
/5/ P.Platz,J.Ramette,E.Belin,C.Bonnelle,A.Gabriel;
J.Phys.E : Sci.Instrum.; **14**, 448 (1981)
/6/ J.P.Coulon,M.Hesse,P.Platz; Nucl.Instr.Methods; **274**, 291 (1989)

ion species	λ [Å]	hkl	2d [Å]	θw [°]	R [mm]	Rsinθw
Ar 16+	3.9482	200	4.256	68.1	3165	2936
Ti 20+	2.6097	212	2.764	70.8	3130	2956
V 21+	2.3812	104	2.5760	67.6	3195	2954
Cr 22+	2.1814	310	2.3604	67.5	3200	2956
Mn23+	2.0055	312	2.1632	68.0	3195	2962
Fe 24+	1.8498	115	1.9762	69.2	3142	2937
Ni 26+	1.5879	116	1.6916	69.8	3140	2947
Cu 27+	1.4771	420	1.6082	66.7	3212	2950

Table I

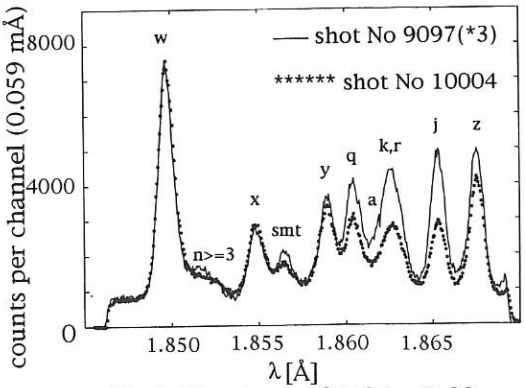

Fig.1 Spectrum of Fe24+, Fe23+

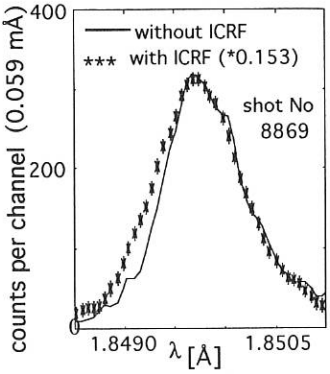

Fig.2 w line of Fe24+

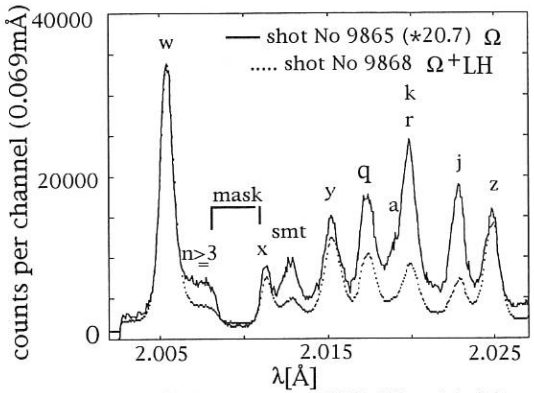

Fig.3 Spectrum of Mn23+, Mn22+

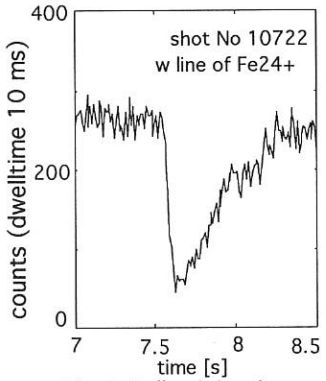

Fig.4 Pellet injection

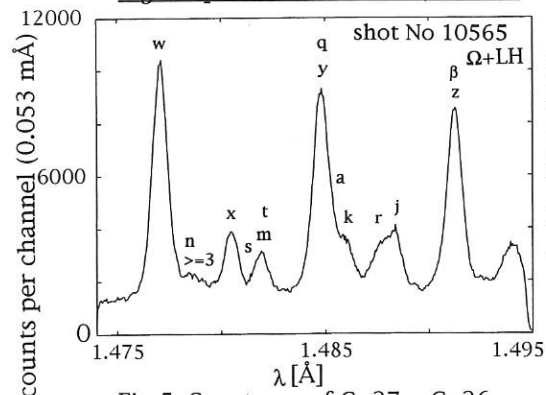

Fig.5 Spectrum of Cu27+, Cu26+

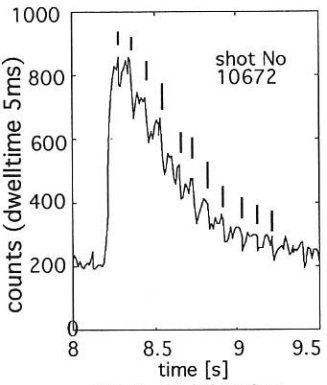

Fig.6 Ni injection

TOROIDAL AND POLOIDAL PLASMA ROTATION MEASUREMENTS IN TORE SUPRA

HESS W.R., GARBET X., GUIRLET R., HESSE M., PAYAN J.
Ass. EUR-CEA , DRFC ; CEN-Cadarache , F-13108 St Paul-lez-Durance France

Introduction: Plasma rotation measurements by visible spectroscopy and by a CO_2-laser scattering experiment (ALTAIR) [1] are presented. The ALTAIR diagnostic is used to study the turbulence changes at the plasma edge during operation of the ergodic divertor (ED). Heterodyne detection allows discrimination between waves propagating in the electron or in the ion diamagnetic direction.

The spectroscopic measurements take advantage of long discharges (t ~10s). During one shot a number of poloidal and toroidal viewing lines can be analysed:1) An "in situ" optical fiber is used which views the plasma edge at the low field side. It is aligned with the magnetic field and views the plasma in the direction of the plasma current (co-direction). 2) A tangential viewing line in the equatorial plane traverses the plasma in the counter direction. 3) A set of 9 poloidal viewing lines is coupled to a 2-dimensional CCD camera. 4) Within the throat of the outboard pump limiter, two viewing lines (on the electron and ion side) are centered on the neutralizer plates. They fix the position of the unshifted lines with an error bar of ±1km/s. The relative error bars for strong spectral lines with a good signal to noise ratio are ±0.8km/s which is still too high for poloidal rotation measurements.

Toroidal rotation: The behaviour of the wavelength shift of all analysed ions (CIII, CVI and HeII) is similar i.e. only rotation in the co-direction is observed. During current ramp up a strong rotation (~15 km/s, HeII 4686Å) in the toroidal co-direction is observed. It decreases to a non negligible value of ~3 km/s at the beginning of the current plateau of ohmic discharges and then stays constant with a constant plasma density. During current ramp down the toroidal velocity increases again to ~11 km/s and then decreases within ~1s to zero. This behaviour is shown on fig.1 in an ohmic He-discharge with a density ramp during the current plateau. A red-shift is observed with the "in situ" fiber (n°1). It is also seen that the toroidal velocity decreases with increasing density, but never changes its sign, different from observations reported in the TCA-tokamak [2]. The plasma edge ion temperature T_i, obtained from the Doppler broadening of the HeII-line (4686Å) decreases with increasing density as is always observed in ohmic discharges.

On fig.2 the blue-shift of the CIII (4647Å) line for the tangential viewing line which views the plasma in counter direction (n°2) is shown. The activation of the Ergodic Divertor (ED) quenches the toroidal rotation which decreases within ≤200ms to zero. Rotational damping in connection with the "bundle divertor" of DITE has been reported in [5], but in this case a strong toroidal rotation was

induced by neutral beam injection in co-direction. The ion temperature, as measured by the Doppler broadening of the CIII line, decreases from ~50 to 30eV during ED activation [3]. This produces an inward shift of the emitting ion-shell.

Poloidal rotation: Whereas the toroidal rotation is slowed down to a value close to zero, an enhancement (Δv=1.2±0.8km/s) in the ionic diamagnetic direction (v_θ<0) is observed on both diagnostics during ED activation. Considering the radial component of the electric field E_r and neglecting frictional forces the equation of motion for an ion of species i becomes: $E_r+v_\theta B_\phi-v_\phi B_\theta=\nabla p/eZ_i.n_i$. Extending this result to the ED phase with v_ϕ~0 and v_θ<0 a positive electric field (E_r>0), as observed by ALTAIR, is correctly deduced. Presently, the spatial resolution (Δr~6cm) is not sufficient in order to evaluate the radial position of the emitting ion-shells and the possible corrections due to diamagnetic and pseudo velocities [6]. As already mentioned, the ion and electron temperature within the ergodic zone decreases during ED activation. This produces an inward shift of the emitting ion-shell, but as shown in the next paragraph, the emission is still outside the inversion radius.

Due to the spatial resolution of ALTAIR, it can be shown that the inversion radius ρ_S of the electric field E_r is moving toward the plasma center during activation of the ED. The value of ρ_S experimentally deduced by fitting the spectra (fig.3) is ρ_S=0.93±0.05 without and 0.80 with the ED. For this purpose we consider a pure electronic turbulence assuming that the ionic turbulence is unlikely [4]. We have also observed the relative change of the fluctuation level $\langle\delta n^2\rangle/\langle n\rangle^2$ with the average density. The above model allows us to differentiate between the relative levels coming from the inside ($r/a<\rho_S$) and that coming from the outside ($r/a>\rho_S$). When the ED is activated, we observe a drop of the inside relative turbulence level, while the outside level remains constant (fig.4).

Ref.:[1] P.Devynck et al, Plasma Phys. Contr.Fus.**35** (1993) 63
[2] B.P.Duval et al; Nucl. Fus. **32** (1992) 1405
[3] W.R.Hess et al, EUR-CEA-FC-1477 (1993)
[4] Garbet X. et al., Nucl.Fus. **32** (1992) 2147
[5] N.C.Hawkes et al, Nucl.Fus. **25** (1985) 971
[6] A.R.Field et al, IPP III/165 (1990)

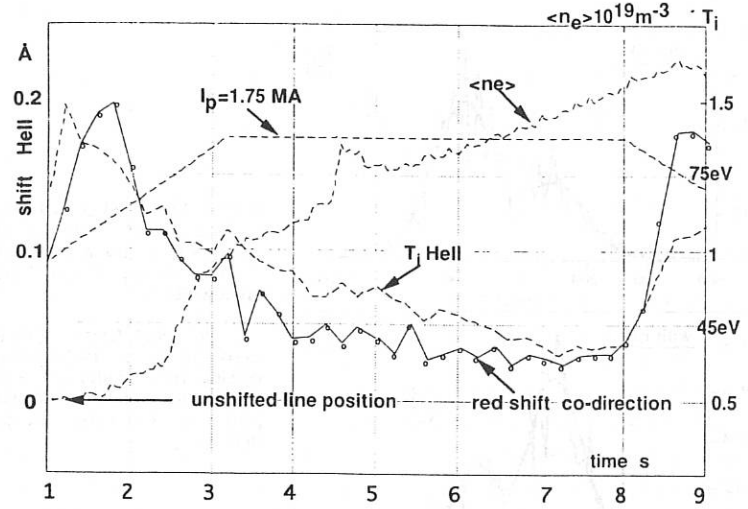

Fig. 1 Toroidal plasma velocity with density ramp He-plasma

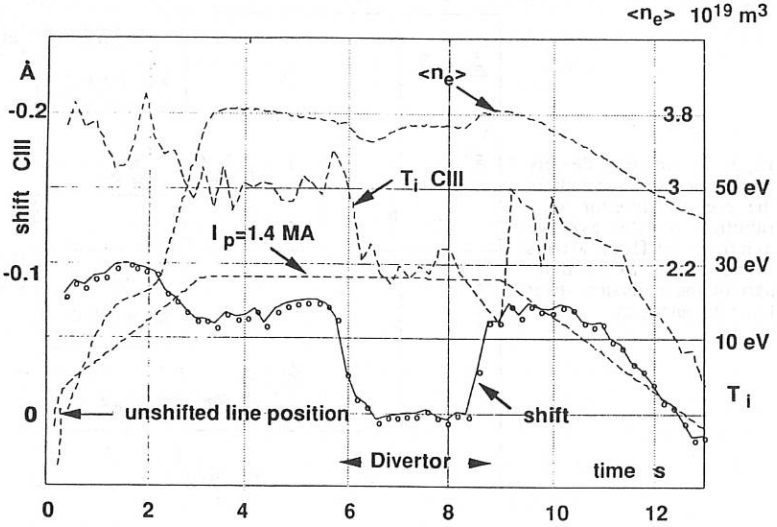

Fig.:2 Toroidal plasma rotation with Ergodic Divertor D2-plasma

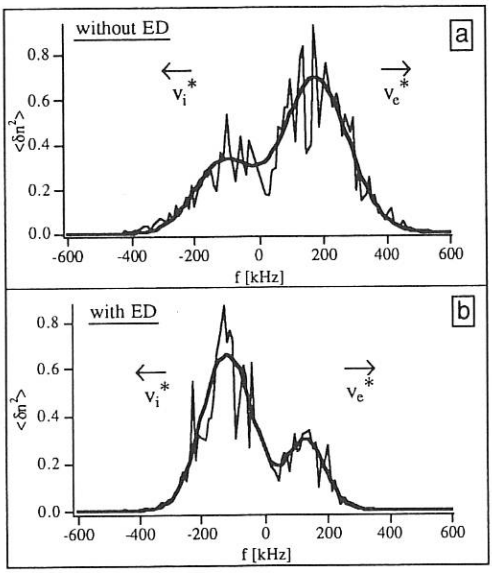

Fig3. - Measured (thin lines) and calculated (thick lines) frequency spectra without (**a**) and with (**b**) application of the ergodic divertor.

The left peak (resp. right) is associated to turbulence outside (resp. inside) the shear layer with a radial electric field pointing outward (resp. inward).

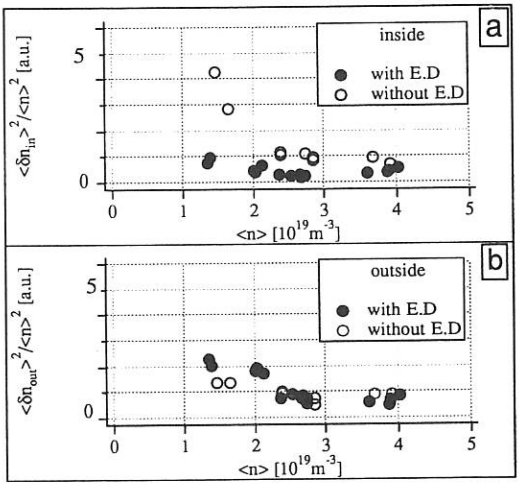

Fig4. - Relative density fluctuations with and without the ergodic divertor as a function of the average density: **a)** fluctuations corresponding to the inner part of the inversion shear layer; **b)** outer part.

Direct observation of the magnetic fluctuation spectra in Tore Supra

ZOU X.L., PAUME M., CHAREAU J.M., LAURENT L., GRESILLON D.*

Association EURATOM-CEA sur la fusion contrôlée
DRFC SPPF CE Cadarache BPN°1
13108 St Paul lez Durance France

* *Laboratoire PMI (UPR 287 du CNRS), Ecole Polytechnique, 91128 Palaiseau, France*

1) Introduction

Electrostatic turbulence has been intensively studied experimentally both at the edge and in the core of the tokamak, while the magnetic turbulence is only measured at the edge by magnetic coils[1], or determined indirectly from the transport of runaway electrons[2]. As no local measurements of magnetic turbulence exist, it has been difficult to establish the relationship with the anomalous heat transport[3][4]. Some experiments performed in TCA[5] ASDEX[6] suggest that two magnetic turbulences of different nature exist. One at low frequency (<100 KHz) located at the edge of the plasma is not correlated to the electron heat transport; another one at high frequency (>100 KHz) originates from the gradient region, and is very sensitive to the variation in the plasma parameters (n_o, B_o, I_p) and to the confinement regime change (L, H). This indicates a possible correlation between the magnetic turbulence in the gradient region and the confinement time. The cross polarization scattering diagnostic (**CPSD**), recently installed on the Tore Supra tokamak, is precisely intended to measure the internal magnetic turbulence. The principle of CPSD is based on the polarization change of the e.m. wave scattered by magnetic fluctuations.

2) Diagnostic

It has been shown that the polarization of the wave scattered by magnetic fluctuations $\tilde{B}$ is orthogonal to the polarization of the incident wave, when there is no change in polarization for scattering by density fluctuations $\tilde{n}$[7][8]. In the geometry in figure 1, the wave polarization is characterized by two eigenmodes: ordinary mode O and extraordinary mode X. The scattering processes can be described as follows: $O_i + \tilde{n} \rightarrow O_s$, $O_i + \tilde{B} \rightarrow X_s$ for an incident ordinary wave, and $X_i + \tilde{n} \rightarrow X_s$, $X_i + \tilde{B} \rightarrow O_s$ for an incident extraordinary wave. As the magnitude of magnetic fluctuations is small ($\tilde{B}/B_o = 10^{-4} - 10^{-5}$) relative to the density fluctuation ($\tilde{n}/n = 10^{-2} - 10^{-3}$), it is necessary to eliminate the like polarized scattering by using a **polarizing mirror effect (PME)**[7]: the incident wave (O_i, X_i respectively) is launched in such a plasma, so that it meets a cut off layer where it is reflected, as is the wave scattered by $\tilde{n}$ (O_s, X_s resp.). Hence only the wave scattered by $\tilde{B}$ in the other eigenmode (X_s, O_s resp.) crosses this layer (see figure 1).

The CPS diagnostic consists of three main parts[9]: a microwave source, a gaussian optic lens-antenna (GOLA) and a heterodyne detection system. The power source is an Extended Interaction Oscillator (EIO) at a frequency f = 60 GHz with a power P = 30 W. The total loss in

waveguides and microwave components for going out and returning lines is estimated to be 23 dB. The wave pattern launched by GOLA has a high directional precision, the semi-angle of divergence being less than 2°. The linear polarization of GOLA is better than 30 dB. The polarization control is ensured by a motorized rotary joint which allows a match of the antenna electric field to the total magnetic field direction at the plasma edge to within 1°. The frequency difference between the EIO and the local oscillator is stabilized at 48 MHz by a phase locked loop. The signal is detected at a balanced mixer, the output signal (around 48 MHz) being sent directly to a spectrum analyser. The display parameters are: bandwidth=30 KHz, frequency scanwidth = 500 KHz/div, scantime = 2 msec/div. The sensitivity of this detection system is measured by the $NEP_H = 10^{-18}$ W/Hz.

3) Results

Figure 2 shows the different cut off frequency profiles in the plasma as a function of vertical position. The critical density n_c corresponding to the 60 GHz O mode cut off is 4.45 10^{19} m^{-3}, and the critical magnetic field B_c corresponding to the existence of an X mode upper cut off layer crossing the beam is 2.14 T. To obtain a O mode cut off, the plasma must have a central density higher than n_c, and to obtain an X mode cut off, a magnetic field lower than B_c. Shots corresponding to the four processes have been analysed: $O_i + \tilde{B} \rightarrow X_s$, $X_i + \tilde{B} \rightarrow O_s$, $O_i + \tilde{n} \rightarrow O_s$, $X_i + \tilde{n} \rightarrow X_s$. All the results have been obtained from ohmic plasmas, the plasma parameters being: major radius = 2.462 m, minor radius = 70 cm.

Figures 3 and 4 show the spectra obtained in the same plasma for the two scenarii: $X_i + \tilde{B} \rightarrow O_s$, $O_i + \tilde{n} \rightarrow O_s$ respectively. The fluctuation spectrum obtained by cross polarization scattering (Fig.3) is broader (2 MHz) than that obtained by forward like polarization scattering (< 1 MHz) (Fig.4). The initial explanation is that CPSD selects large wavenumbers due to mode conversion, from $K_O - K_X = 0$ in vacuum to $k_o = \omega/c = 12.56$ cm^{-1} at the cut off layer for going path, and from 12.56 cm^{-1} to 25.12 cm^{-1} for back path, while forward propagation depends on wavenumbers in the range of 0 to 2/D= 0.5 cm^{-1} (where D is the antenna diameter). The dramatic change in the spectra can be considered as the signature of the CPS process. Similar features are noticed in the cases $O_i + \tilde{B} \rightarrow X_s$ (low amplitude, broad spectrum), and $O_i + \tilde{n} \rightarrow O_s$ (large central peak, smaller base), but the magnetic fluctuation spectrum is very irregular in this case. The best scenario is therefore $X_i + \tilde{B} \rightarrow O_s$ in the presence of an X mode cut off.

4) Estimate of the magnetic fluctuation level

The detected scattered power is related to the magnetic fluctuation form factor S_b by the simplified equation:

$$dP_s = P_i \, d\Omega \, df \, n_e L \, r_o^2 \, u/(1-u)^2 \, S_b$$

where S_b is defined as:

$$S_b(k,\omega) = \lim_{T,V\rightarrow\infty} \frac{n_e}{TV} \left\langle \frac{\tilde{B}(k,\omega)\tilde{B}^*(k,\omega)}{B_0^2} \right\rangle$$

and P_i is the effective incident power, $d\Omega$ is the solid angle of the antenna, df is the bandwidth of the spectrum analyser, L is the scattering volume length, and $u = (\omega_{ce}/\omega_i)^2$. Taking the measured value of dP_s, one finds S_b of order of 10 sec. To deduce from S_b, one needs to know the frequency-wavenumber volume relative to this fluctuation. If the values $\Delta f = 2$ MHz, $\Delta k_r = \Delta k_\theta = 10\ cm^{-1}$, $\Delta k_\parallel = 0.1 cm^{-1}$ are used one finds $\tilde{B}/B_o = 10^{-4}$. This value is comparable to that measured at the edge of the plasma by magnetic coils in different tokamaks[10][11][12]. The anomalous electron heat diffusivity in Tore Supra is measured to be $\chi_e = 1\ m^2.s^{-1}$, which can be explained by this magnetic fluctuation level if we use the quasilinear expression of χ_e due to $\tilde{B}$[13].

5) Conclusions

Three important results have been obtained:

a) The cross polarization scattering effect has been shown by comparing the configurations: (I) $X_i + \tilde{B} \rightarrow O_s$, (II) $O_i + \tilde{n} \rightarrow O_s$. The fluctuation spectrum (2 MHz) obtained in (I) is larger than that obtained in (II) (< 500 KHz). The spectacular broadening effect is considered to be the most prominent feature of the magnetic turbulence measured by CPSD. The difference in the frequency spectra reflects the different Bragg selection rules.

b) To obtain a pure CPS a cut off layer (X or O) is required to provide a perfect mode selection. The best scenario is $X_i + \tilde{B} \rightarrow O_s$ in presence of an X mode cut off.

c) These measurements are compatible with a level of 10^{-4} of magnetic fluctuations in the outer half of the plasma. The anomalous electron heat diffusivity in Tore Supra could be explained by this magnetic fluctuation level.

References

1) Zweben S.J., Menyuk C.R., Taylor R.J. (1979) Phys. Rev. Lett., **42**, 1270

2) Mynick H.E. and Krommes J.A. (1979) Phys. Rev. Lett., **43**, 1506

3) Liewer P.C. (1985) Nucl. Fusion, **25**, 543

4) Wootton A.J. *et al.* (1990) Phys. Fluids B2, **12**, 2879

5) Hollenstein C.H. *et al.*, in *Turbulence and Anomalous Transport in Magnetized Plasmas*, Cargèse Workshop 1986, edited by D. Grésillon and M. Dubois (Ecole Polytechnique, Palaiseau, France, 1986), p.181

6) Giannone L. IPP Report, IPP III/138, 1989

7) Lehner T., Rax J.M., Zou X.L. (1989) Europhys.Lett., **8**, 759

8) Zou X.L., Laurent L., Rax J.M. (1991) Plasma Phys. Contr. Fusion, **33**(8), 903

9) Paume M., Zou X.L., Laurent L. (1990) 15th Int. Conf. on Infrared and Millimeter Waves, Vol.1514, p756-758

10) Malacarne M., Duperrex P.A.(1987) Nucl. Fusion, **27**, 2113

11) Zweben S.J. *et al.* (1987) J. Nucl. Mater., **144-147**, 250

12) Wootton A.J. *et al.* (1988) Plasma Phys. Contr. Fusion, **30**, 1479

13) Rochester A.B. and Rosenbluth M.N. (1978) Phys. Rev. Lett., **40**, 38

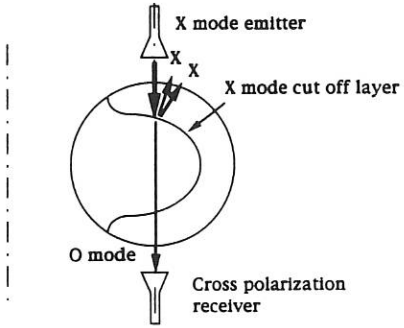

Figure 1. Scheme describing the polarizing mirror principle with an X mode cut off layer.

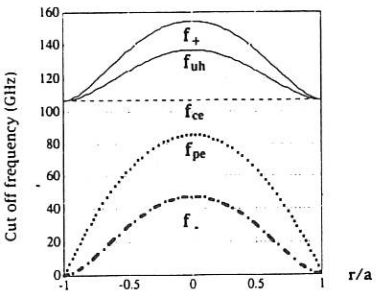

Figure 2. Vertical cut off frequency profiles. The central density is 9.10^{19} m^{-3}, the magnetic field is 3.82 T. f_+, f_- are the X mode upper and low cut off frequencies, the plasma frequency f_{pe} is also the O mode cut off frequency, f_{ce} is the electron cyclotron frequency, and f_{uh} is the upper hybrid frequency.

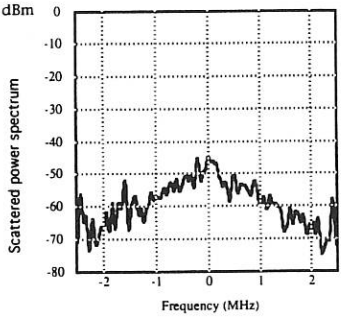

Figure 3. Scattering spectrum obtained with the scenario: $X_i + \tilde{B} \rightarrow O_s$. The vertical origin corresponds to a power level of -80 dBm (0 dBm =1 mW) for a bandwidth of 30 KHz.

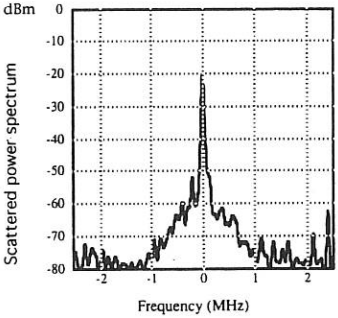

Figure 4. Forward scattering spectrum due to the density fluctuations. The scenario is $O_i + \tilde{n} \rightarrow O_s$.

Measurement of fast electron dynamics on Tore Supra

T. Dudok de Wit, Y. Peysson, J.-L. Ségui, P. Bibet,
G. Giruzzi, D.Moreau, C. Pocheau, D. Vézard

Association EURATOM-CEA sur la Fusion Contrôlée
Centre d'Etudes Nucléaires de Cadarache
13108 Saint-Paul-lez-Durance (France)

Lower Hybrid Power modulation experiments have been carried out on the Tore Supra tokamak to study the dynamics of the suprathermal electrons. Two diagnostics offering a measurement of the parallel suprathermal electron distribution function have been compared : one is an electron cyclotron transmission diagnostic, the other a multichannel X-ray spectrometer. Both reveal a dominant relaxation process which is attributed to the collisional slowing-down of the electrons. A smaller and much slower relaxation is also observed and its link with radial transport is discussed.

Measurement of the electron cyclotron absorption

Microwave transmission in the electron cyclotron range is a useful diagnostic method for investigating the suprathermal electron tail generated by lower hybrid (LH) waves. The electron cyclotron absorption (ECA) of the O-mode first harmonic is measured along a central vertical chord [1,2]. The probing frequency is swept periodically from 77 to 110 GHz; this corresponds to an energy range of E=40–160 keV for which the suprathermal electron distribution function is inferred from the absorption. The time resolution was in our case 8 ms.

A critical point in this measurement is the distinction between refraction and absorption losses. One approach consists of modelling the refraction with a ray-tracing code. We have made use of the different time scales on which the two loss terms behave. When the LH power is switched off after a steady-state phase, most of the suprathermal electrons relax within 20 ms whereas the refraction evolves on a longer time scale. This was verified by measuring the refraction at frequencies where the absorption is negligible ($f \gtrsim f_{ce}$). Using this approximation, the relaxation of the suprathermal electron population can be measured with reasonable accuracy for up to 30 ms following an LH phase.

Measurement of the hard X-ray spectrum

The measurement of the hard X-ray emission (HXE) provides another method for studying the dynamics of the suprathermal electrons. The HXE is measured by a

multichannel spectrometer [3] which operates between 50 and 500 keV; its 5 lines of sight probe a poloidal cross-section of the plasma and cross the midplane at $x/a \approx +0.2,\ 0.0\ -0.33,\ -0.52,\ -0.72$. The time resolution is determined by the photon counting statistics and was chosen to be 20 ms.

The experiments to be described were performed in helium plasmas with the parameters R=2.37 m, a=0.76 m, $\overline{n}_e$=2-2.5$10^{19}$ m^{-3}, B_φ=3.71 T, I_p=0.8 MA and $P_{LH} \leq 3.5$ MW. The lower hybrid waves were launched at f=3.7 GHz with a parallel wave index $n_{//}=1.8$ corresponding to a power deposition centered at E=100 keV. In these discharges the current was almost entirely driven by lower hybrid waves as indicated by the low loop voltage level : $V_l \leq 0.06$ V, Fig. 1. No sawtooth or intense MHD activity was observed during the LH phase. The duty cycle of the LH modulation pulses was varied from 20 ms up to several seconds, thereby allowing a wide range of the plasma dynamics to be explored.

The relaxation of the suprathermal electron population

When the lower hybrid power is switched off, a fast relaxation of the electron distribution function is observed both in the ECA and in the hard X-ray emission (HXE). From this a characteristic time constant τ_l is inferred. The values obtained from the two diagnostics are in reasonable agreement in the region where the energy ranges overlap, Fig. 2. One cannot make a direct comparison between the dynamics inferred from ECA and that from HXE since the former is measured at a given energy whereas the latter integrates contributions coming from higher energies. This effect was however neglected, and the relaxation time obtained here from the HXE should be considered as a slight overestimate.

The relaxation observed along a central chord in the lower energy range has been compared with simulations based on a 3-D Fokker-Planck code which includes quasilinear diffusion and Coulomb collisions [2]. The qualitative agreement is excellent as shown in Figs. 2 and 3. At high energy, τ_l increases with E, as would a relaxation based on Coulomb collisions, for which $\tau \sim E^{3/2}$. At low energy however, τ_l decreases with E. Such a behaviour cannot be explained by single particle effects and requires a detailed kinetic treatment of the electron population [2]. Moreover, measurements carried out at different electron densities show that the relaxation is faster at higher density : $\tau_l \sim \overline{n}_e^{-1\pm0.5}$. Such a dependence can be deduced indirectly from the radial profiles of the HXE, as the innermost chords (those who encounter the largest density) show a faster relaxation than the outermost ones. Finally, the rise time (measured at LH power switch-on) has been compared with τ_l. Its value must be significantly smaller since it falls below the time resolution of the diagnostics.

The effect of the dc electric field, which was not included in our Fokker-Planck simulation, may explain some of the small quantitative disagreement between the measurements and the simulation. When the LH power is switched off, the dc field increases and counterbalances the slowing-down processes. The simulated relaxation time is also sensitive to the spectral and radial power deposition profiles, which are not fully known.

The results which have been obtained so far all clearly support the collisional nature of the observed relaxation process and therefore lead us to identify τ_l with τ_{SD}, the slowing-down time of the suprathermal electrons. This identification has a direct consequence on the characteristic time scale of a concomitant radial diffusion process. Calling τ_D the slowest time constant associated with such a mechanism,

three cases may occur [4]. If $\tau_D << \tau_{SD}$, diffusion is the dominant loss mechanism and the relaxation time constants must be radially constant. If $\tau_D >> \tau_{SD}$, slowing-down predominates and the relaxation of the suprathermal electrons must bear its characteristic features, in particular a radial dependence. Finally, if $\tau_D \cong \tau_{SD}$, the two mechanisms are difficult to separate. Since our experimental results all support the second case, we conclude that collisional slowing-down is the dominant suprathermal electron loss process on Tore Supra. The condition $\tau_D > \tau_{SD}$ implies that a radial diffusion process modelled with a constant diffusion coefficient would have to satisfy $D < 10\ m^2s^{-1}$ at E=60 keV and $D < 3\ m^2s^{-1}$ at E=500 keV.

One consequence of the predominance of slowing-down losses is that the effect of radial transport should mainly appear as slow changes in the HXE profiles. Accordingly, discharges with long LH power pulses have been performed. Most plasma parameters exhibit transients at the power switch-on but a stationary phase is reached after 500 ms. During this phase, a slow and persistent flattening of the HXE profiles is observed, Fig. 1. This relaxation is particularly evident at higher energies and its corresponding time constant τ_2 does not depend significantly on the electron density or the spatial location.

Among the different mechanisms that may explain such a slow relaxation of the HXE, those based on changes in the electron density, temperature or the impurity concentration must be ruled out since their time dependence cannot be reconciled with our observations. The residual dc electric field however and its slow intrinsic diffusion offers a plausible explanation. The critical runaway energy (above which electrons are accelerated) varies from 2 MeV at the centre of the plasma to 600 keV at the edge, where it is expected to enhance the energetic HXE. Such a mechanism however, does not reproduce all the observed features and in particular fails to explain the decrease in the central emission profile, fig. 4. We therefore attribute part of the observed relaxation to a radial diffusion of the suprathermal electrons. Its long time scale implies a better confinement than that of the bulk electrons. Assuming the transport is purely diffusive, a model in which the diffusion coefficient is spatially constant would give $D=0.1–0.3\ m^2s^{-1}$ for 250<E<500 keV. This result allows us to interpret changes in the energy content previously attributed to suprathermal electron losses [5] as being due to a modification in the energy confinement.

Conclusions

The ECA diagnostic and the hard X-ray spectrometer provide a consistent picture of the suprathermal electron population dynamics which is characterised by two time scales. The dominant and smallest time constant (10-40 ms) is in good agreement with the simulated slowing-down time of the electrons. The larger one (0.5–1 s) is attributed at least partially to the radial transport of the suprathermal electrons which are better confined than the bulk electrons.

References

[1] G. Giruzzi, J.L. Ségui, A.L. Pecquet, C. Gil, Nuclear Fusion **31** (1991) 2158.
[2] G. Giruzzi, Plasma Phys. Contr. Fusion **35** (1993) A123
[3] Y. Peysson, J.P. Bizarro et al., Proc. 18th EPS Conference on Contr. Fusion and Plasma Physics, **IV** (1991) 345
[4] J.M. Rax, D. Moreau, Nuclear Fusion **29** (1989) 1751.
[5] D. Moreau and the Tore Supra Team, Phys. Fluids B **4** (1992) 2165.

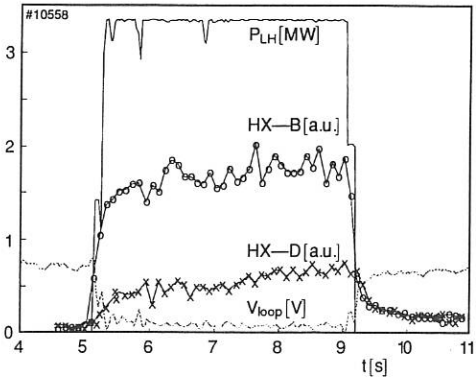

1) Temporal evolution of the plasma parameters during a long LH power pulse. A central (B) and a peripheral (D) chord of the spectrometer are shown at E=350 keV.

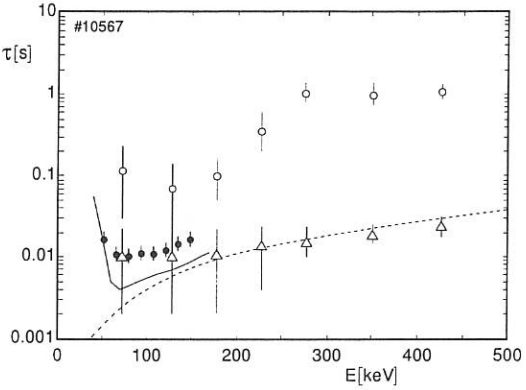

2) The energy dependence of the relaxation times, as measured along a central chord. The solid line represents the 3-D Fokker-Planck simulation, the dashed line the classical expression for the slowing-down time. Both are calculated with the experimental plasma parameters. The open symbols represent the two time constants inferred from the central HXE and the filled circles those from the ECA.

3) Simulated transmission spectra during the LH phase (dashed line) and 6 ms after switch-off (solid line). The symbols are the corresponding values measured by ECA.

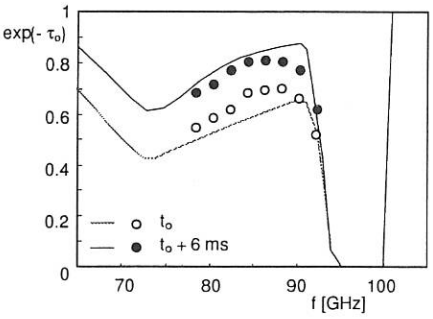

4) Reconstructed HXE profiles measured at E=350 keV at the beginning of the stationary phase, and 3 seconds later. The standard deviation results from the inversion procedure and the scatter in the HXE amplitude.

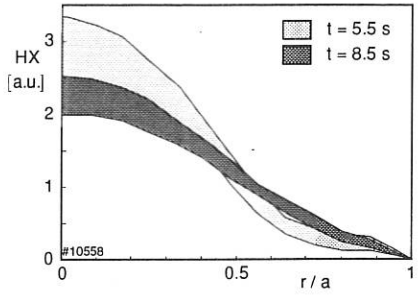

NONLINEAR FILTERING TECHNIQUES IN BROADBAND MICROWAVE REFLECTOMETRY

F. Nunes [*,+], **J. Leitão** [*,+] **and M. E. Manso** [**,+]
[*]Centro de Análise e Processamento de Sinais
[**]Centro de Fusão Nuclear, EURATOM/IST Association
[+]Departamento de Engenharia Electrotécnica e de Computadores
Instituto Superior Técnico, 1096 Lisboa Codex, Portugal

Broadband reflectometry data, used to evaluate the plasma profile, contains also information about density perturbations providing a local measurement of plasma modes and fluctuations. In order to increase the resolution of the measurement a new processing method is presented based on a stochastic nonlinear filtering approach. Structured prior knowledge about the phase/frequency evolution of the reflectometry signal is modeled as a two-dimensional Markovian process from which only one component (phase) is observed. The filter propagates the joint (phase and frequency) probability density function conditioned on the observations. The estimates are determined according to the minimum square error criterion. Results obtained from simulated and experimental data† are presented and discussed.

1. Introduction

In microwave reflectometry the plasma reflected wave is mixed with the reference wave giving rise to the (baseband) *reflectometry signal* whose relevant component has the form $y(t) = A(t)\cos\varphi(t) + n(t)$, where $A(t)$ is a random amplitude, $\varphi(t)$ (*phase shift characteristic*) is the information bearing phase both depending on the reflection conditions, and $n(t)$ accounts for an additive disturbing noise.

From the analysis of the differential phase shift characteristic versus probing frequency $\Delta\varphi(F)/\Delta F$ it is possible to study the modes that affect locally the wave propagation [1]. Magnetic modes produce periodic deformations of the plasma density profiles leading to phase and amplitude modulations of the reflectometry signals. Direct reflectometry measurements provide an estimate of the localization of magnetic modes and give complementary information about the modes, namely in conditions where the measurements with external Mirnov coils are difficult.

Standard measurements consider only the minima of the signal to evaluate $\Delta\varphi/\Delta F$. A new approach herein proposed uses all the samples of $y(t)$ to obtain an estimate of $d\varphi/dF = R^{-1}\omega(t)$, where $\omega(t) = d\varphi/dt$ and $R = dF/dt$ is the microwave sweeping rate, allowing a more detailed study of the magnetic plasma modes.

2. Problem formulation

Consider the sampled reflectometry signal: $y_k = A_k\cos\varphi_k + n_k$. (1)

If A_k is slowly variable with respect to $\cos\varphi_k$, amplitude normalization can be performed leading to the observation model: $z_k = \cos\varphi_k + v_k$, (2)

† from ASDEX tokamak, Max-Planck Institut für PlasmaPhysik, Garching.

where v_k represents the overall resulting noise, which we assume to be a zero mean white Gaussian sequence with variance r (possibly depending on the index k).

To estimate the phase/frequency evolution some prior structured knowledge about the pair $(\varphi(t), \omega(t))$ has to be assumed. The shape of the frequency characteristic usually observed in broadband reflectometry suggests that we model $\omega(t)$ as a Brownian motion with variance parameter q; this process is described, for practical purposes, by the discrete vector stochastic difference equation

$$\begin{pmatrix} \varphi_{k+1} \\ \omega_{k+1} \end{pmatrix} = \begin{pmatrix} 1 & \Delta \\ 0 & 1 \end{pmatrix} \begin{pmatrix} \varphi_k \\ \omega_k \end{pmatrix} + \begin{pmatrix} 0 \\ u_k \end{pmatrix} \tag{3}$$

where u_k is a random white Gaussian sequence with zero mean and variance $q\Delta$ (Δ is the sampling interval). This state space model, apparently restrictive, is sufficiently flexible to describe a large variety of frequency trajectories found in broadband reflectometry. There is however an important constraint: only positive trajectories of ω_k can be considered, otherwise there will be a phase indetermination. A similar problem, occurring in fixed frequency reflectometry, is overcome by observing both the inphase and the quadrature components of the signal. However, due to technical difficulties, this solution is not feasible in broadband reflectometry.

The stochastic nonlinear filtering problem is now formulated as follows: taking into account models (1) and (2) estimate, at time $t = k\Delta$, the state $\mathbf{x}_k = (\varphi_k, \omega_k)$ based on the set of past and present observations $\mathbf{Z}_k = \{z_i, 1 \leq i \leq k\}$. According to the Bayesian approach herein adopted all the information about $\mathbf{x}_k$ is contained in the conditional probability density function $p(\mathbf{x}_k/\mathbf{Z}_k)$. Propagation of this function is accomplished by recursive application of Bayes law [2]

$$p(\mathbf{x}_k/\mathbf{Z}_k) = C_k p(z_k/\mathbf{x}_k) \cdot p(\mathbf{x}_k/\mathbf{Z}_{k-1}), \tag{4}$$

and Chapman-Kolgomorov equation (the process $\mathbf{x}_k$, as given by (4), is Markovian) [2]

$$p(\mathbf{x}_k/\mathbf{Z}_{k-1}) = \int_{I\!R^2} p(\mathbf{x}_k/\mathbf{x}_{k-1}) p(\mathbf{x}_{k-1}/\mathbf{Z}_{k-1})\, d\mathbf{x}_{k-1}. \tag{5}$$

Function $p(z_k/\mathbf{x}_k)$ in (4) is an updating factor depending on the actual observation z_k and the (nonlinear) observation equation (2); C_k is a normalizing constant. Function $p(\mathbf{x}_k/\mathbf{x}_{k-1})$ in (4) is a convolution kernel reflecting the dynamics (3).The optimal estimate $\hat{\mathbf{x}}_k = (\hat{\omega}_k, \hat{\varphi}_k)$ is obtained by minimizing a suitable cost function $L(\mathbf{x}_k - \hat{\mathbf{x}}_k)$.

Practical implementation of equations (4) and (5) demmands appropriate descriptions of the involved probability density functions. In the algorithm we have developed a Gaussian sum representation able to capture the essential features of the problem at hand, and a quadratic cost function, have been adopted. This subject is addressed in a forthcoming paper. A statistical phase unwrapper, designed according to the same principles, is described in reference [3].

3. Simulation results

To test the proposed approach a simulation package was developed. Fig. 1.(a) represents the reflectometry signal y_k, as given by equation (1), with phase φ_k generated according to the dynamics (3) by setting $q\Delta = 10^{-4}$. The amplitude A_k is a low-pass random sequence and the noise disturbance n_k is made very small. An envelope $\hat{A}_k$ is

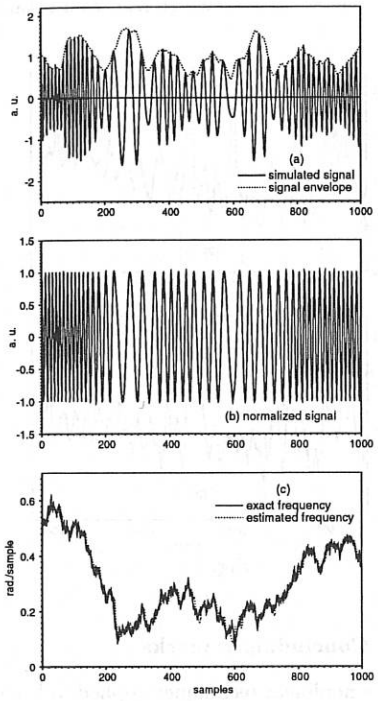

Fig. 1

obtained by fitting a piecewise straight line (or a cubic spline) to the local maxima of $|y_k|$. The amplitude normalized signal $z_k = y_k/\hat{A}_k$, shown in Fig. 1.(b), corresponds to the observation of equation (2). The additive noise v_k appears as a result of imperfect envelope fitting. Fig. 1.(c) depicts the original generated frequency trajectory ω_k (solid line) and the corresponding estimate $\hat{\omega}_k$ (dotted line) obtained by assuming an observation noise variance $r = 0.01$. (This parameter controls the filter robustness and the estimate smoothness). The estimated trajectory shows good agreement with the exact one allowing to follow the details of the Brownian motion.

4. Experimental results

Results were obtained in the ASDEX tokamak with a broadband reflectometry (O-mode) system that includes three channels probing plasma densities from $n_e \approx 0.4$ to $4.5 \times 10^{19}\, m^{-3}$. The broadband measurements concern Lower Hybrid Current Drive discharge of shot 29285. In this discharge the $m = 2, n = 1$ tearing mode was studied using the standard data analysis techniques [1].

Signals obtained in 2 ms with the Ka channel at: (a) $t_1 = 1460$ ms and (b) $t_2 = 1500$ ms are analysed. Each signal includes 1024 samples and corresponds to the linear sweeping of frequency between $F \approx 26.5$ and 40 GHz (probing density layers $n_e \approx 0.9 - 2 \times 10^{19}\, m^{-3}$).

The differential phase shift versus probing frequency characteristics resulting from applying the standard data analysis technique (detection of frequencies corresponding to 2π phase shifts) is shown in Fig. 2; the nonlinear filtering results are depicted in Fig. 3. Figures reveal that the phase shift perturbations superimposed to the slow variable curve (corresponding to the non disturbed plasma density profile), are observed with both techniques, but are more clearly resolved in Fig. 3.

Results in Fig. 3 (and curves obtained at other time instants), suggest that two perturbations exist in density regions (1) and (2). These regions are located in a typical density profile evaluated from the broadband data at = 1400 ms, as: (1) $r \approx (34 - 36cm)$ and (2) $r \approx (27 - 30cm)$, see Fig. 4. From the estimation of the radial q-profile for shot 29285 (with safety factor $q_a \approx 3.3$), these regions correspond roughly to the location of the rational surfaces $q = 5/2$ and 2. Therefore, the perturbation in region (1), seen twice at t_1 and once at t_2, should be due to the rotating island with $m = 2, n = 1$, and in region (2) to the $m = 5, n = 2$ mode. The rotating frequency inferred from the curve (Fig. 3.a) for the $m = 2$ mode is ≈ 2.5 kHz in agreement with the magnetic data. In

region (2) the perturbation exhibits high frequency oscillations which lead to a rotating frequency of ≈ 3 kHz.

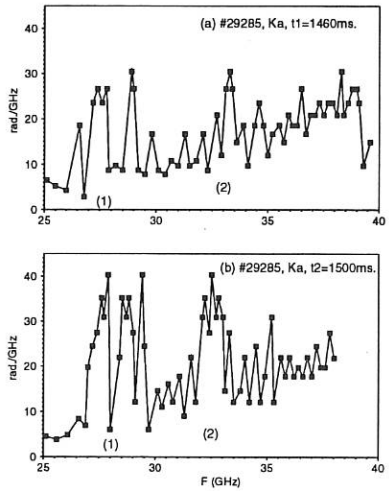

Fig. 2

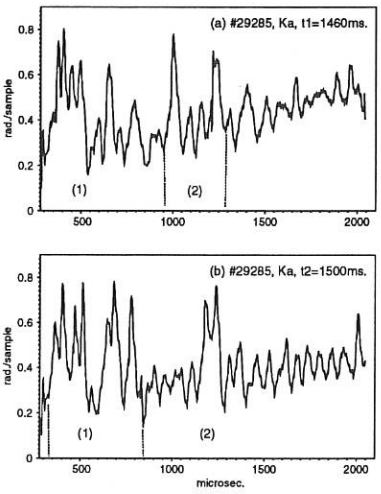

Fig. 3

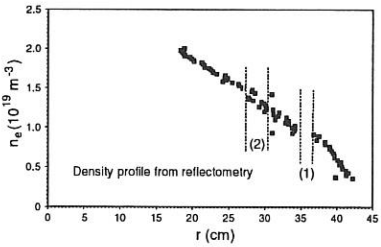

Fig. 4

5. Concluding remarks

The nonlinear techniques applied to broadband reflectometry data seem to provide an interesting tool to improve the local measurement of density perturbations due to magnetic modes. The method should be applied to a large number of broadband measurements, obtained with a high sampling rate, in order to overcome the uncertainties in the identification of the modes. Detailed measurements should be particularly important to study magnetic modes during locking and modes with higher mode numbers.

References

[1] - M. E. Manso, A. Silva, F. Serra, et al., "Changes in the Density Profile due to the $m = 2$ Tearing Mode in ASDEX", Proc. of the 17^{th} EPS Conference, Vol 14B, Part II, pp. 837, June 1990.

[2] - R. S. Bucy, "Linear and Nonlinear Filtering", Proc. of the IEEE, 58, pp. 854-864, June 1970.

[3] - J. M. F. Moura and A. B. Baggeroer, "Phase unwrapping of signals propagated under the Arctic ice crust: a statistical approach", IEEE Trans. on Acoustic, Speech and Signal Processing, 36(5), pp. 617-629, May 1988.

Langmuir Probes in Strong Magnetic Fields

A. Carlson, P. Grigull, K. Günther, D. Hildebrandt,
M. Laux, P. Pech, D. Reiner, M. Weinlich, H. Wolff
Max-Planck-Institut für Plasmaphysik, Boltzmannstr. 2, D-85748 Garching

Observed *I-V* Characteristics

In the absence of a magnetic field the *I-V* characteristic of an electrode in a plasma (a Langmuir probe) is predicted and observed to be the sum of an approximately constant ion saturation current I_i^{sat} and an electron current which grows exponentially up to a saturation level $I_e^{sat} \sim I_i^{sat}\sqrt{m_i/m_e}$. The ion saturation current is the product of ion charge, ion density, sound speed, and effective probe area. The effective area will be greater than the surface area by an amount dependent on the sheath thickness, which scales according to the Child-Langmuir law with the Debye length and the 3/4 power of the potential drop. When the sheath thickness is not negligible compared to the probe dimensions, the voltage dependence of the sheath will prevent saturation of the ion current.

In the strong magnetic fields of fusion devices, the effective area is commonly taken to be the area projected along the field, not the full surface area. Sheath effects are generally neglected because the high density results in a small Debye length and the high power density dictates the use of large probes. Additional corrections (but less than a factor of two) are made to the saturation currents due to density depletion and kinetic distribution function effects. For the case of pin-type probes, which have a fairly large area with a steep field angle, this picture appears adequate, but flush-mounted probes often show a very different behavior.

An *I-V* characteristic (Fig. 1) from a probe flush-mounted in the lower outer divertor plate of

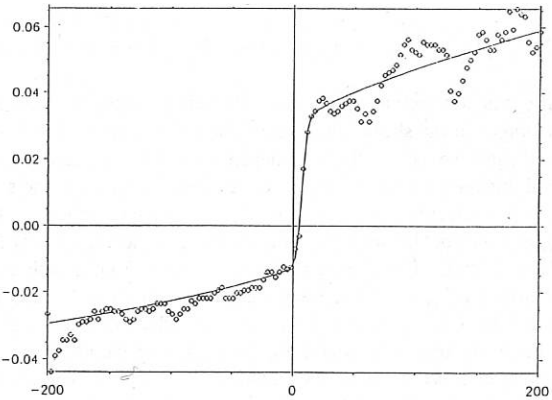

Figure 1: Current (in A) as a function of voltage (in V) for a flush-mounted probe in the lower outer divertor plate of ASDEX-Upgrade. The circles are measured values, the solid line a fit using the model described in the text.

the tokamak ASDEX-Upgrade, clearly shows two features not seen with pin-type probes: strong

non-saturation of both the ion and the electron currents, and a very low ratio of electron to ion current. Similar features are observed under a wide variety of conditions in various machines (ASDEX–Upgrade, W7–AS, DITE [1], JET, T-10) and prohibit a reliable determination of plasma parameters (n_e, T_e, and V_{pl}).

There are four Langmuir probes flush mounted on the rotatable sniffer probe head [2] used for plasma composition studies on the stellarator Wendelstein 7–AS. These probes have been used to systematically study the effects of magnetic field angle and projected area on the probe characteristics. The head was rotated from normal incidence to past grazing incidence in steps as small as 2.5°. At each angle an *I-V* characteristic was recorded and the non-saturation (Fig. 2) and the ratio of electron to ion currents parameterized. The non-saturation is a strong, but not singular, function of angle (see next section). The electron current is dramatically reduced to about 2.5 times the ion current for angles within a few degrees of grazing incidence. (Measurements on DITE [1] showed an even stronger reduction, to about 0.5.)

The Ion Branch: Non-Saturation is due to the Debye sheath.

Non-saturation of the ion current, due to sheath effects on the scale of the Debye length, is important in traditional uses of Langmuir probes [3], but not usually in fusion plasmas with high densities and large probes. In the ASDEX–Upgrade divertor plates and the W7-AS sniffer probe head, however, the magnetic field can have a very shallow angle ($\sim 1°$), so the effective probe dimension is small. Furthermore, voltages up to 50 times the electron temperature may be applied, resulting in sheaths tens of Debye lengths thick. Under such conditions a clear non-saturation can be expected and is in fact observed.

For flush mounted probes, a voltage more negative than that of the surrounding wall will result in a thicker sheath over the probe, which will pull in ions which would otherwise have skimmed by. A sheath model which ignores the electron charge density gives the following expression for the sheath thickness as a function of the voltage of the surface:

$$d(V) = \lambda_D \left(2^{3/2}/3\right) \left(\sqrt{1 - e\left(V - V_{pl}\right)/k_B T} + 2\right) \sqrt{\sqrt{1 - e\left(V - V_{pl}\right)/k_B T} - 1}\,.$$

(The sheath actually has a structure without a well-defined edge, but this formula should accurately reflect *changes* in the sheath thickness.) The sheath vanishes at $V = V_{pl}$, whereas for large negative voltages, we recover the $V^{3/4}$ dependence. We are interested in the projected area of the additional thickness of the sheath above the probe compared to the surrounding wall (which is our reference voltage); this area is $w[d(V) - d(0)] \sin\psi$, where w is the (poloidal) width of the probe (as l will be the (toroidal) length), and ψ is the angle between the magnetic field and the surface normal. The plasma potential is found from sheath theory using the measured value of current at $V_{pr} = 0$. The fractional increase of the geometrical projected area ($A_{proj} = lw \cos\psi$) will be $f(V) = \alpha \tan\psi [d(V) - d(0)]/l$, where α is an empirical correction factor. To reduce the errors arising by neglecting the physics of the electron branch (see next section), we treat the system *ad hoc* as an asymmetrical double probe with area ratio β, which results in an *I-V* characteristic of the following form:

$$I(V) = j_i^{sat} A_{proj} \frac{(1 + f(V_1)) - (1 + f(V - V_1)) \exp\left(-e(V - V_{fl})/k_B T\right)}{1/\beta + \exp\left(-e(V - V_{fl})/k_B T\right)},$$

$$V_1 = \ln 2 + V_{fl} - \ln\left(1 + \exp\left(e(V - V_{fl})/k_B T\right)\right).$$

The solid curve in Fig. 1 is such a function fitted to the data points with j_i^{sat} and T taken as free parameters. Most data from ASDEX-Upgrade can be fitted, as in this example, with $\alpha = 4$, which we consider to be a reasonable confirmation of our model. The data from W7-AS (Fig. 2) at moderate angles also fits into this picture, but the non-saturation at steep angles

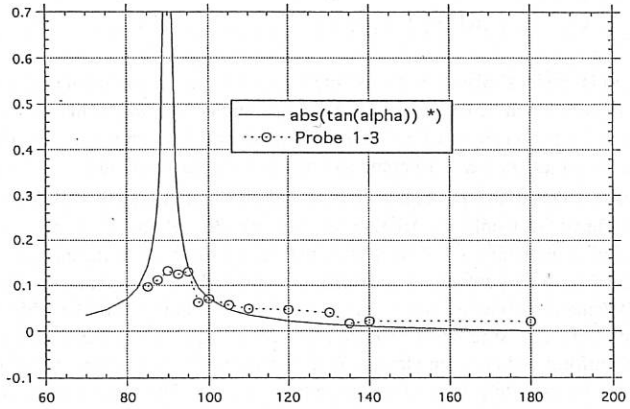

Figure 2: The non-saturation parameter $N = -(dI^{ion}/dV)_{V-\infty} * T/(I^{ion})_{V=\text{floating}}$ as a function of the angle ψ (in degrees) between the magnetic field and the surface normal. The circles are values measured using the sniffer probe on W7-AS, and the solid line is roughly the form and magnitude expected using the model described in the text.

is too large, and that at grazing angles is too small. The first discrepancy can be described by allowing the sheath to grow laterally as well as normally. The second may be related to diffusive transport across field lines [1,4].

The Electron Branch: Cross-field currents require "friction".

The electron branch is more difficult to interpret. The usual assumption is that the electrons at the probe come from a thermal distribution at the plasma potential. This assumption leads to $j_e^{sat} \sim j_i^{sat}\sqrt{m_i/m_e}$. An alternative, but equally plausible assumption is that current flows strictly along the magnetic field. In that case the current from the probe has to flow into the wall at the other end of the flux tube, so the maximum current in either direction is the ion saturation current, and the current ratio should be about unity. We have seen that the experiments show something in between, indicating that cross-field currents are inhibited by the field, but not completely. Cross-field currents exert a $\vec{j} \times \vec{B}$ force on the plasma which must be balanced (in steady state) by some kind of "friction", be it drag on neutrals, ionization, viscosity, or convective acceleration.

To investigate the consequences of this cross-field current, we have considered models which can be reduced to a 1-D non-linear ordinary differential equation. To begin with, we can eliminate the direction parallel to the field if we ignore magnetic shear and parallel resistivity. (It is not clear *a priori* from consideration of SOL plasma parameters whether or not either of these will be important.) Next we can choose either cylindrical or slab geometry, so there is an ignorable perpendicular coordinate. Finally we can restrict ourselves to steady-state to

remove the time dependence. Neglecting electron mass and ion temperature, the MHD momentum equation (with friction and viscosity terms), current continuity, and the sheath equation can be combined to yield a single equation describing the potential, from which all other quantities can be calculated:

$$\left[\left(\vec{\nabla}_\perp \Phi \times \vec{e}_z\right) \cdot \vec{\nabla}_\perp - \alpha + \beta \vec{\nabla}_\perp^2\right] \vec{\nabla}_\perp^2 \Phi = L^{-1}[-2 + \exp(V_1 - \Phi + 3) + \exp(V_2 - \Phi + 3)],$$

where $\Phi(x \text{ or } r)$ is the local plasma potential and $V_{1,2}(x \text{ or } r)$ is the potential of the first or second wall (part of which will be the probe). L is the separation of the walls, and we have replaced the velocity (to lowest order) by the $\vec{E} \times \vec{B}$ drift. Potentials have been normalized to $(k_B T/e)$ and distances to $\rho_s = \sqrt{k_B T/m_i}/\omega_{ci}$. α parameterizes the frictional force and β the viscous force.

We have investigated the *I-V* characteristics which result from solving this equation in cylindrical geometry with only the friction term on the *lhs*. If the friction arises from the ionization needed to maintain the plasma, then the curves show a significant reduction in the electron branch current for parameters in a range relevant to the SOL plasma. In a typical SOL, however, the plasma is maintained not primarily by ionization, but by turbulent diffusion. If the turbulent fluctuations are large-scale enough and slow enough, this process can be simulated by imposing a uniform and constant electric field over the probe. This case can be investigated in slab geometry by including the convection term on the *lhs*. The results lie, as do those for ionization, in a relevant region, and tend to have a form somewhat closer to those observed experimentally. The great shortcoming of these models, as well as those of other authors [5,6], is that the parameter dependence is backwards. Measurements on W7-AS and DITE [1] show a minimum in the ratio of electron to ion current at grazing incidence, but grazing incidence corresponds to a small probe dimension, while the models predict *no* reduction of the electron current in that limit.

Summary and Conclusions

In spite of the long history of Langmuir probe measurements without and with magnetic fields, there are many aspects which can not yet be adequately explained. These are not supplemental or "second order" effects, but can change the calculated plasma density and temperature by factors of two or more. We have investigated two such effects: non-saturation of the ion current and reduction of the electron current. We have found a model which explains most of the features of non-saturation, and is a useful tool to analyze data and develope further models. We have considered the role of force balance on the electron branch, and come to the conclusion that an essential element is still missing from our considerations as well as those of other authors. We believe that resolving this problem will lead to a better understanding of all plasmas with fields, flows, and a complicated geometry.

References:

[1] Matthews, G. F., *et al.*, *Plasma Phys. Cont. Fusion* **32**(1990), 1301.
[2] Wolff, H., *et al.*, *19th EPS Conf. Cont. Fusion Plasma Phys. (Innsbruck)* (1992) 1167.
[3] Johnson, J. D., and Holmes, A. J. T., *Rev. Sci. Instr.* **61**(1990) 2628.
[4] Stangeby, P. C., *et al.*, *Nucl. Fusion* **32**(1992), 2079.
[5] Sanmartin, J. R., *Phys. Fluids* **13**(1970), 103.
[6] Stangeby, P. C., *J. Phys. D: Appl. Phys.* **15**(1982), 1007.

FIRST DENSITY MEASUREMENTS WITH MICROWAVE REFLECTOMETRY ON ASDEX UPGRADE

A. Silva, M.E. Manso, P. Varela, F. Serra, L. Cupido, M. Albrecht*, F.X. Söldner*
and the ASDEX Upgrade Team.
Centro de Fusão Nuclear, EURATOM/IST Association, 1096 Lisboa Codex, Portugal
*MPI für Plasmaphysik, EURATOM/IPP Association, D-8046 Garching, FRG

A broadband one-antenna reflectometry system is under developement for the ASDEX Upgrade tokamak, to probe the plasma from the edge until the bulk region. Presently two K-band (O-mode) channels, installed respectively at the high and low sides, are in operation (broadband and fixed frequency), providing the first direct simultaneous measurements of the plasma density at both sides ($n_e \approx 0.3$ to $0.8 \times 10^{19}\ m^{-3}$).

The modifications of the inner and outer density profile due to radial displacements of the plasma column are shown. In H-mode regimes, the changes of the edge density gradients and of the level of fluctuations were studied.

I. The reflectometry system for ASDEX Upgrade

The reflectometry system for ASDEX Upgrade will operate in the frequency range 16 to 110 GHz probing the plasma from $n_e \simeq 0$ (X mode) up to $n_e \approx 15 \times 10^{19}\ m^{-3}$ (O-mode) [1]. The diagnostic includes thirteen channels with in-vessel antennae installed both at the high and low field sides. Each antenna is used both for emission and for reception thus reducing the access to the machine. Several features of the diagnostic guarantee the quality of the detected signals. The emission and detection sections are placed close to the tokamak avoiding the use of oversized waveguides that may cause spurious reflections due to higher mode propagation. The signals are generated by units that include solid state oscillators (HTO), active frequency multipliers and special drivers for fast sweep operation, $\geq 10\mu s$, (needed to minimize the effect of fluctuations in profile measurements). Up to one thousand profiles can be measured per shot, with a minimum repetition interval of $\simeq 20\mu s$. The system is totally remotely controlled through optical fiber links. Data acquisition uses a dedicated system with high computing power and data compression facilities; on-line profile evaluation is also being implemented.

II - Experimental results

Results refer to broadband swept experiments performed with $\Delta t_s = 100\mu s$ (presently the system can operate down to $10\mu s$ sweeping time). Broadband reflectometry is the only technique that fully exploits the unique capability of reflectometry to probe an "infinite" number of plasma layers with each channel. The differential phase shift $(d\varphi/df)_F$ that the waves F undergo in the plasma, which is the relevant quantity for profile evaluation, is continuously measured. Due to the detailed measurement, perturbations of the differential phase shift due to plasma fluctuations can in most cases be easily identified, enabling to obtain the plasma profile by simple filtering the disturbed characteristic [2]. From the measured differential phase shift curve it is also possible to infer the density regions where fluctuations exist, as shown in section 2.

1. Plasma radial displacements

In **Fig. 1** it is presented the spectra of the raw data signals obtained at different time instants of discharge 3068, where the plasma was horizontally displaced up to 4cm. An increase of the frequency of the main peak is observed at the low field side and a decrease is seen at the high field side. Results indicate respectively a displacement of the probed plasma region away from the outer antenna and towards the inner antenna. The measured frequency shifts agree with the evolution of the distance between the antennae and the plasma outer radius ($R_a - R_{out}$) and inner radius ($R_{in} - R_a$), as can be seen in **Fig. 2**.

The observed variations should be mainly due to changes of the vacuum distance where the probing microwaves have propagate. The evaluated profiles, however, show significant asymmetries in the outer and inner plasma. In **Fig.3** it is depicted the profiles corresponding to a radial shift of 2cm of the plasma column. The fitting of the experimental $n_e(r_i)$ points, shown in the figures, is an "average profile" that was obtained from the fitting of the measured phase shift characteristic $\varphi_i(F_i)$. The average curve $\varphi(f)$ was then processed to obtain the "average profile". Results reveal a global displacement of the profile of ~2cm at the low field side and a change in the plasma edge shape at the high field side.

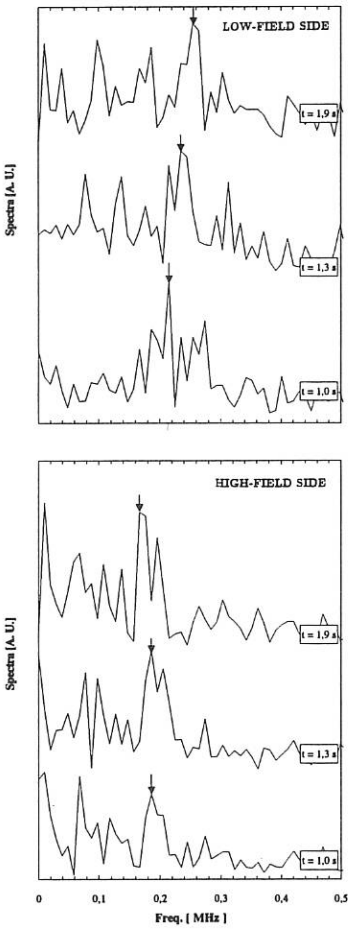

Fig 1

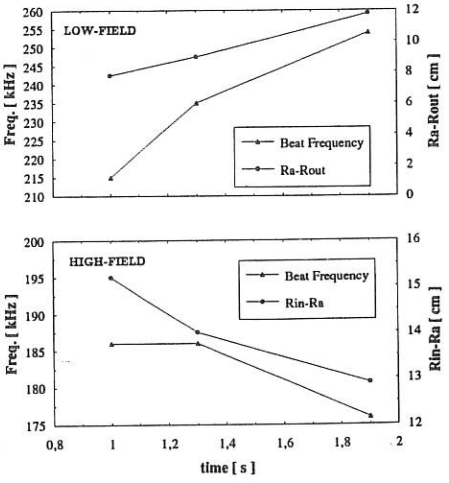

Fig 2

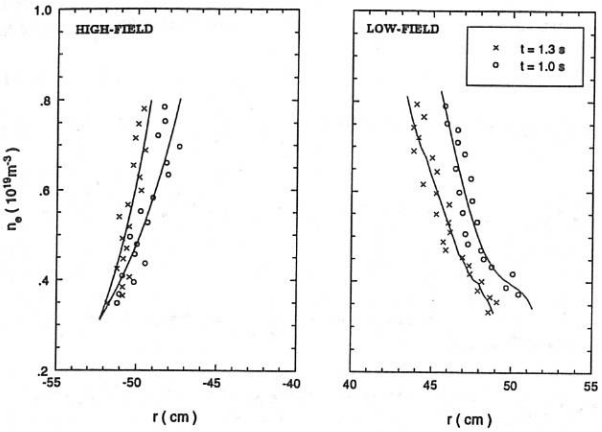

Fig. 3

2. H mode regimes

In **Fig. 4** it is presented the phase shift derivatives obtained in 100 μs and spaced by 10ms, during the ICRF heated plasma of discharge 2325. The L to H transition ocurred at t $\sim$ 1.641s. Before the transition ($\Delta t = -1ms$) the phase perturbations are observed to increase at both channels. (A similar behaviour has been observed in ASDEX with H modes achieved with neutral beam injection). Following the transition ($\Delta t = +9ms$) the perturbations decrease to levels below those observed at the L phase ($\Delta t = -11ms$). In the ELMy phase two samples are shown respectively before an ELM ($\Delta t = +259ms$) and during an ELM ($\Delta t = +269ms$). The level of fluctuations increase at both sides during the ELM, specially at the peripherie, and the edge profile flattens, as can be concluded from the corresponding profiles depicted in **Fig. 5**.

Results presented above show that the changes in density profile and fluctuations occur both at the high and low field sides (the peaking of the profile is also observed at the L to H transition in both sides). However, other measurements where samples were obtained closer ($\Delta t \leq 2ms$) to the L to H transition suggest that a delay exists between outer and inner density changes. In H modes achieved under Ohmic conditions the above density signatures of the H regimes were also found.

III - Concluding remarks

A reflectometry system is being installed in the ASDEX Upgrade tokamak. Presently two channels probing the edge plasma at the high and low field sides are in operation (broadband and fixed frequency). Results are presented showing that radial displacements of the plasma column can cause different modifications of the outer and inner plasma density profiles. In H mode regimes under ohmic conditions and with ICRF heating, the peaking (flatenning) of the profile and the decrease (increase) of the level of fluctuations at the L to H transition (during an ELM) were observed at both sides.

Results showed the great potentialities of broadband reflectometry namely to study the inner and outer asymmetries of the density profile. The diagnostic capability shall be greatly increased with the installation (by September 1993) of three channels probing inner plasma layers (O-mode) and the edge region (X mode). In particular, the spacial resolution of the measurements at the edge shall be improved with X mode operation.

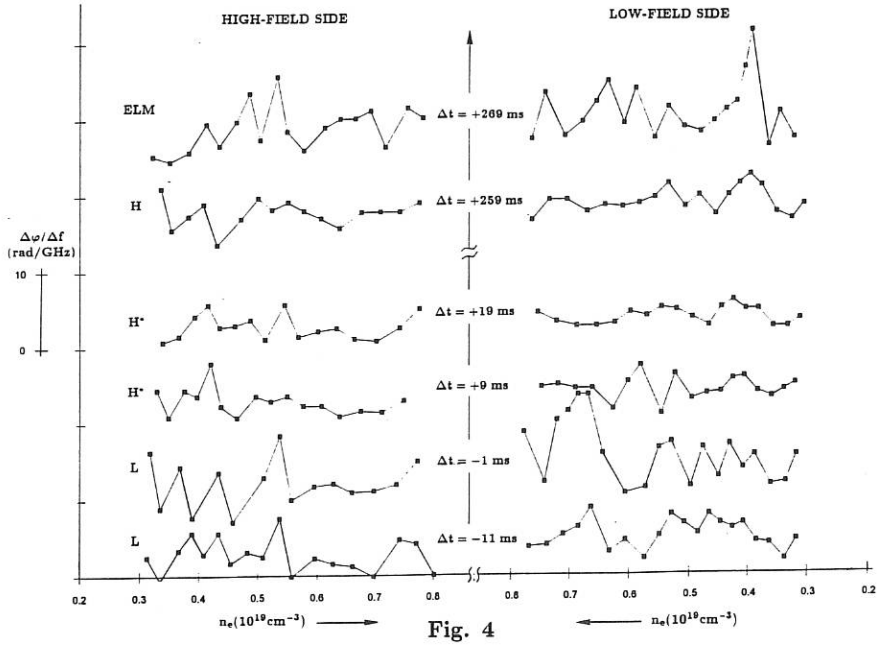

Fig. 4

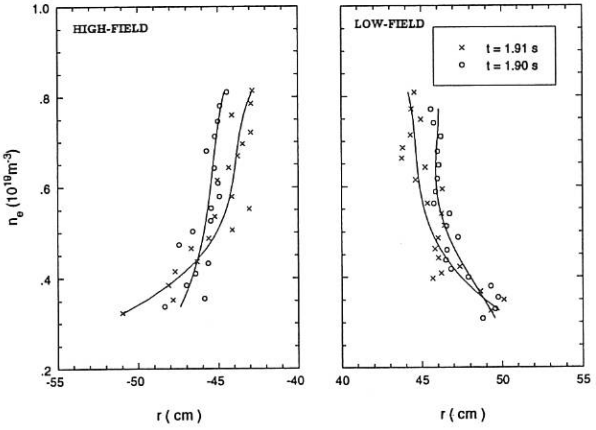

Fig. 5

REFERENCES

[1] A. Silva, L. Cupido, M.E. Manso, F. Serra, P. Varela et al., "17^{th} Symposium on Fusion Technology", Rome, 1992.

[2] M.E. Manso, Proc. IV Workshop on Magnetic Confinement Fusion: Diagnostics for Tokamaks and Stellarators, Santander, 1992.

SPECTROSCOPIC MEASUREMENTS OF ION TEMPERATURES IN THE BOUNDARY LAYER OF TEXTOR AND THEIR INTERPRETATION

J.D.Hey, Y.T.Lie, D.Rusbüldt and E.Hintz

Institut für Plasmaphysik, Forschungszentrum Jülich GmbH, Association EURATOM-KFA

1. Introduction and experimental method:

We discuss some recent spectroscopic measurements of n-α transitions (8→7 in C VI, 11→10 in Ne X, and 12→11 in Si XII), emitted through charge-exchange between impurity ions and the injected neutral hydrogen beam of TEXTOR. Derivation of radial ion temperatures from line widths requires careful consideration of the Zeeman effect, as well as the processes of l-mixing and diffusion. Since the observation direction was roughly antiparallel to the toroidal magnetic field, the experiment provided data complementary to those from lithium-beam-CXS.[1]

Profile measurements were performed with a high-aperture 3/4 m monochromator containing a 135x165 mm plane grating (1200 lines/mm, blaze angle 57°) in Littrow mounting, with an achromatic lens of 125 mm diameter as collimator. Spectral scans were made in the second order with high dispersion (reciprocal dispersion $\approx$ 4 Å mm^{-1}, slit widths $\approx$ 100 μ), the $\sigma_{\pm}$ components being the major contributors to the lines, with weak additional π components.

The optical arrangement is shown in Fig.1. Both wavelength (period 100 ms) and radial scans (period 1 s) were run simultaneously, with adequate signal reproducibility.

2. The role of the magnetic field:

A rough criterion may be formulated for judging the importance of the Zeeman effect on spectral line profiles (transition n → n' in an ion of mass μ (u), ionization stage Z), for particular values of κT (eV) and magnetic field-strength B(T). For temperatures less than:

$$\kappa T \leq \mu \left(\frac{n^4 B}{40 Z^2} \right)^2 ,$$

magnetic field effects may be expected to cause appreciable distortion of Doppler-broadened line profiles. In transitions between highly excited levels, a large number of individual Zeeman components (see Table 1) will contribute to the total line profile, and simple estimates of the ion temperature from widths of measured profiles may be rather unreliable, especially for the colder boundary layers. Calculations of theoretical profiles have therefore been undertaken in order to provide the necessary correction factors to the measured line widths. These require an accurate description of the fine-structure of hydrogenic levels[2,3], and in addition (for Li-like ions) l-dependent polarisation corrections[4] for the distortion of the Coulomb potential as a result of the presence of the pair of tightly bound 1s^2 electrons. From these unperturbed energy levels, the set of corresponding perturbed levels is determined from the solutions to the secular determinant for the Paschen-Back effect,[5,6] which accounts for the mixing of states of different J-values by the magnetic field. The corresponding perturbed line strengths are calculated according to the method described by Shortley,[6] generalised to account for simultaneous perturbation of both upper and lower states of the various components. A total theoretical profile is generated by addition of the individual Doppler-broadened σ- and π-components, where each Paschen-Back line strength carries equal intrinsic weight, i.e. where individual l-l' components are effectively weighted in proportion to their initial statistical weight (2l+1). This l-mixing assumption is considered below. The resultant line profiles for the charge-exchange lines considered here are found to be Gaussian to a good approximation, the main deviation being a slight exaggeration of the blue wing, which plays a very minor role within the half-intensity points (Figs.2-5). The correction factors (Fig.6) are derived on the assumption that a Gaussian profile has been fitted to the measured line profile, following the red wing and the peak as

accurately as possible; the 'true' temperature is obtained from the apparent temperature derived from this fit by multiplication with the corresponding reduction factor η.

Table 1: The number of Zeeman components in a hydrogenic transition.

transition	$\sigma+\pi$ components	allowed	forbidden
$n \rightarrow n'$	$2(12n'^2 - 14n' + 7)$	$2(9n'^2 - 8n' + 4)$	$2(3n'^2 - 6n' + 3)$

3. Consideration of some important physical questions:

Since electron capture in charge-exchange occurs preferentially in shells $n = n_m$ lying well below those considered here,[7,8] this process tends to populate the l-states $l = n_m$, while direct excitation from the ground-state tends to populate the p-states. For the temperature correction factors shown in Fig.6 to be applicable, it is necessary that ion-radiator collisional processes occur sufficiently frequently for the relative sublevel populations to be collisionally determined. Calculations similar to those in Ref.9, with fine-structure included, show that for our lines, the l-sublevel populations will not be fully statistical until electron densities of at least 10^{13} cm^{-3} are attained. On the other hand, the contribution to the total line intensity from the low-l substates, which tend to show the largest deviations, are very small under conditions of relative equilibrium. For typical neutral beam fluxes in TEXTOR, competition from collisional excitation[10,11] from the ground state is found to be completely negligible for both the Ne X and C VI lines in the edge region, on the assumption of roughly equal concentrations of C^{5+} and C^{6+} ions[12]; farther inwards, however, a contribution of up to 30% of the observed intensity may be expected from collisional excitation, resulting in some loss of spatial resolution.

The differential equation[13] describing the temporal temperature variation of test ions moving through a background of field ions, shows that in spite of appreciable diffusion at the plasma edge ($D_\perp \approx 10^4$ cm^{2}s^{-1}), T_i of high-Z ions is not significantly in excess of that of the background protons (deuterons). Their use for diagnostic purposes is thus justified. This is also seen from the good agreement between T_i values from C VI and from Ne X (profiles, Figs.3,4,7).

4. Interpretation and conclusions:

Fig.7 shows a series of radial measurements of T_i for various levels of neon inlet under stationary conditions, stated in Table 2 in terms of relative impurity fluxes on the ALT limiter (e.g. C/D), as well as corresponding values for T_e obtained from a thermal He-beam.[14] Convergence of the T_i profiles by minor radius r = 32 cm, i.e., steepening of these profiles towards the edge with increasing neon flux, are consistent with the concept of predominant edge cooling[15] by Li-like Ne VIII ions.[16] In contrast, the electron temperatures converge towards a lower limit of some 10 eV beyond r = 46 cm. This reflects a general steepening of the radiation potential curves for the impurities C, O, Ne with decreasing T_e,[15,16] as well as the fact that line radiation cooling primarily affects T_e, through electron-collisional coupling, while coupling to the ion velocity distribution is a secondary process. Measurements of T_i thus complement those of T_e, and provide useful data for models of the plasma boundary.

Table 2: Some information on shots relating to neon cooling (cf. Fig.7), with flux ratios.

Shot	1/e length for T_i	T_i/T_e (r=44 cm)	Ne/D (%)	C/D (%)	O/D (%)
50697	8.5 ± 1 cm	4.4 ± 1	-	-	-
51065	7.5 ± 1	4.2 ± 1	1.3	1.8	0.6
51066	6.5 ± 1	4.2 ± 1	3.3	1.4	0.5
51071	5.0 ± 1	3.8 ± 1	6.7	1.2	0.4

REFERENCES

1. R.P.Schorn, E.Wolfrum, F.Aumayr *et al.*, Nucl.Fus. 32(3), 351-359 (1992).
2. H.A.Bethe & E.Salpeter, *Quantum Mechanics of One- & Two-Electron Atoms.* Springer (1957).
3. S.Klarsfeld and A.Maquet, Phys.Lett.43 B, 201-203 (1973).
4. B.Edlén, *Handbuch der Physik (Vol. XXVII, pp.80-220)* (ed. S.Flügge), Springer, Berlin (1964).
5. E.U.Condon and G.H.Shortley, *The Theory of Atomic Spectra,* Cambridge (1951).
6. C.C.Kiess and G.Shortley, J.Res.N.B.S. 42, 183-207 (1949).
7. W.Fritsch, Phys.Rev. A30, 3324-3327 (1984).
8. R.Janev, L.Presnyakov and V.Shevelko, *Physics of Highly Charged Ions.* Springer (1985).
9. R.M.Pengelly and M.J.Seaton, Mon.Not.Roy.Astr.Soc. 127, 165-175 (1964).
10. Y.Itikawa, S.Hara, T.Kato *et al.*, At.Data Nucl.Data Tables 33, 149-193 (1985).
11. D.H.Sampson and H.L.Zhang, Astrophys.J. 335, 516-524 (1988).
12. R.P.Schorn, E.Hintz, D.Rusbüldt *et al.*, Appl.Phys.B 52, 71-78 (1991).
13. L.Spitzer, Jr., Mon.Not.Roy.Astr.Soc. 100, 396-413 (1940).
14. B.Schweer, G.Mank, A.Pospieszczyk *et al.*, J.Nucl.Mater. 196-198, 174-178 (1992).
15. U.Samm,P.Bogen, H.A.Claassen *et al.*, J.Nucl.Mater. 176 & 177, 273-277 (1990).
16. U.Samm *et al.*, Proc.14thInt.Conf.Plasma Phys.Contr.Nucl.Fus.Res., Würzburg (1992).

Acknowledgements: The authors wish to thank P.Bogen, U.Samm, B.Schweer and B.Unterberg for useful discussions and supporting data.

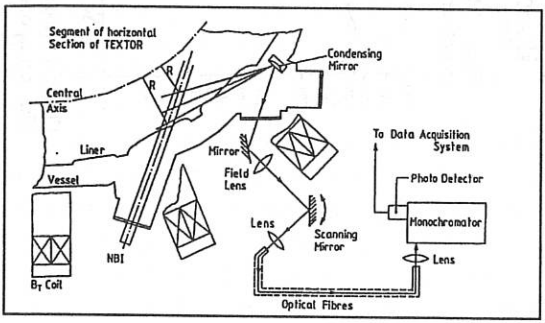

Figure 1.Schematic optical arrangement for measurements on TEXTOR.

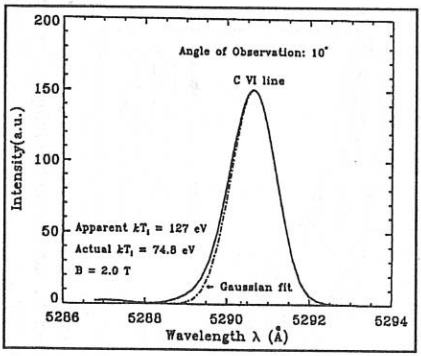

Figure 2.Theoretical profile of C VI λ5290Å for B=2.0T and 10° observation angle relative to magnetic field direction.

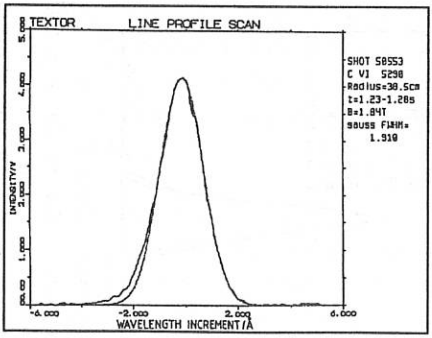

Figure 3.Measured profile of C VI λ5290Å for B=1.84T and observation angle approx. 170°.

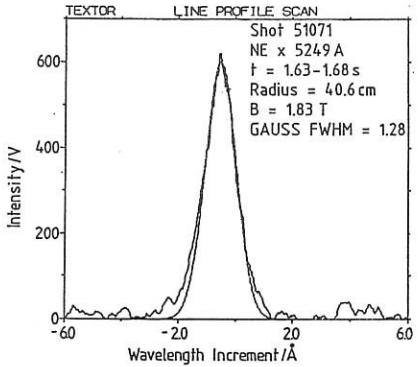

Figure 4.Measured profile of Ne X λ5249Å B=1.83T and observation angle approx. 170°.

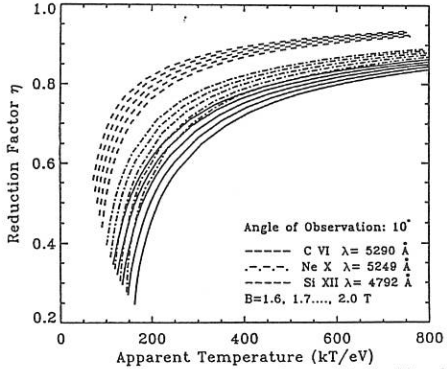

Figure 6.Correction factors η to be multiplied by the apparent temperature.

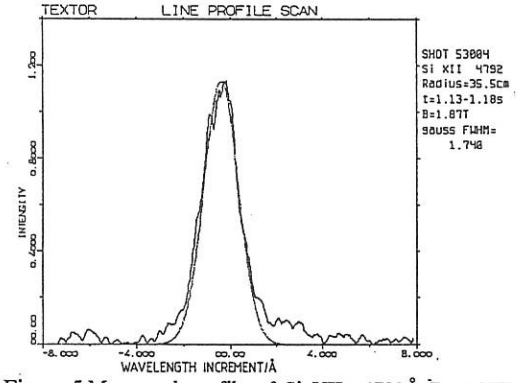

Figure 5.Measured profile of Si XII λ4792Å B=1.87T and observation angle approx. 170°.

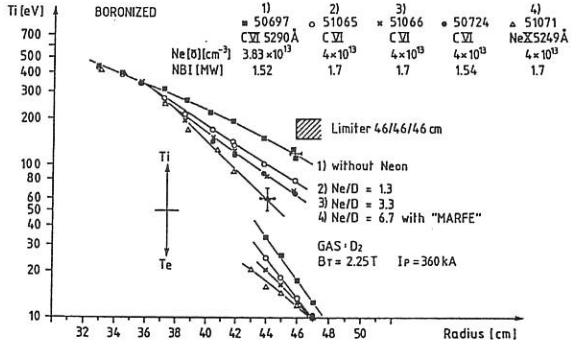

Figure 7.Measured values of Ti for a series of TEXTOR shots. The corresponding values of Te are also shown.

Mach Number Measurements of Neoclassical Plasma Flow in the Edge Plasma of the Tokamak TEXTOR

K. Höthker, W. Bieger* and H.-J. Belitz

Institut für Plasma Physik, Forschungszentrum Jülich,
Association EURATOM-KFA, Postfach 1913, D-5170 Jülich, Germany
*Fachhochschule Aachen, Abt. Jülich, Ginsterweg 1, D-5170 Jülich,

Abstract

Besides the determination of the ion temperature [1] the Rotating Electrical Double Probe is also well suited for the measurement of the Mach number of plasma flow in magnetized plasmas [2] (in addition to its simultaneous conventional application as an electrical probe). Results obtained from such probe measurements for an experimental study of the flow in the edge plasma of the tokamak TEXTOR are presented. The characteristic features of the measured flow are all consistent with expectations from neoclassical theory.

Experimental Set-up

The measurements have been performed in the edge plasma on both sides of the leading edge of the limiter ALT II in TEXTOR. Parameters of the machine and details of the probe have been described in reference [1]. The probe head consists of two cylindrical probe pins with a diameter of 5 mm, and a length of 5 mm. Their distance is 10 mm. The probe is installed in the equatorial plane of the tokamak, cf. fig. 1, with its axis perpendicular to the magnetic field and rotates around this axis during the discharge with the frequency of 2 Hz. The determination of the Mach numbers from the probe signals is performed by comparison with the theory of [3].

Experimental Results

In fig. 2 the radial profile of the Mach number of the plasma flow parallel to the magnetic field is shown for an Ohmic discharge. In the shadow of the ALTII limiter the direction of the flow can always be explained by the sink effect of the limiter. For radii smaller than that of the leading edge of limiter ALTII r_{ALTII} the characteristic features of the plasma flow are not significantly determined by the limiter: The flow

characteristics here are not changed when the nearest limiter blade of ALTII is withdrawn. The direction of the flow is always the same as the direction of the plasma current, cf. fig. 2, also for discharges with the plasma current direction opposite to that of fig. 2. However, the direction of the flow in the region $r < r_{ALTII}$ does not depend on the direction of the toroidal magnetic field as shown in fig. 3. Here the results of similar measurements as those of fig. 2 are presented, the toroidal magnetic field having, however, the opposite direction compared to fig. 2.

In fig. 4 the dependence of the Mach number at the position $r = r_{ALTII} - 1.7$ cm is shown as a function of the mean core density. With increasing density the Mach number decreases from $M \approx 0.5$ to zero.

Discussion

At the position $r < r_{ALTII}$ of the Mach number measurements the ions are in the banana/plateau regime as is evident from the measured values of the ion temperatures (>100 eV) and densities ($<4E18m^{-3}$). From neoclassical theory, e.g. [4] one expects for this regime a superposition of a plasma flow parallel to the magnetic field and of the ion bootstrap current. The direction of this flow and of the ion bootstrap current is expected to be the same as that of the plasma current and independent of the direction of the toroidal magnetic field. The measured Mach number characteristics show the same behavior. For the smaller densities the measured Mach numbers are in good agreement with the theoretical ones. Moreover, the value of the Mach number is expected to decrease with increasing density - as observed - partly due to the related decrease of the ion temperature and ion collisionality and partly due to the increase of the drag on the ions by charge exchange processes [5].

References

[1] K. Höthker, H.-J. Belitz, W. Bieger and H. Amemiya Rev. Sci. Instr. 61 (1990) 114
[2] K. Höthker, W. Bieger and H.-J. Belitz 17th EPS Conference on Controlled Fusion and Plasma Heating, Vol. IV, 1568, Amsterdam (1990)
[3] K. S. Chung and H. I. Hutchinson Phys. Rev. ABBE (1988) 4721
[4] F.L. Hinton and R.D. Hazeltine Rev. Mod. Phys. 48(1976)239
[5] P.M. Valanju, M.D. Calvin, R.D. Hazeltine, and E.R. Solano Phys. Fluids B4(1992)2675

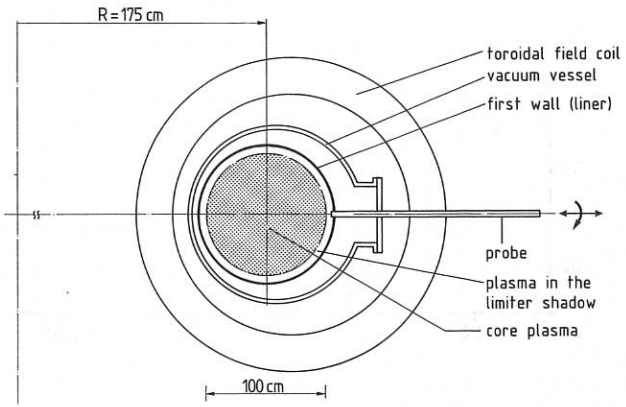

Fig. 1 Position of the rotating probe on the tokamak TEXTOR

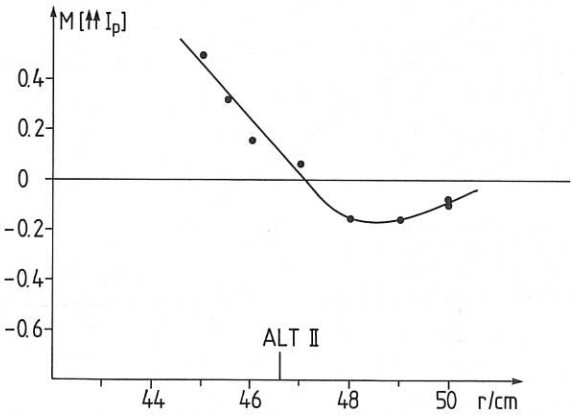

Fig. 2 Mach number of the plasma flow parallel to the magnetic field as a function of the radius, B_{tor} = 2.25 T, I_p = 0.35 MA, $\langle n_e \rangle$ = 2.3 E19 m^{-3}

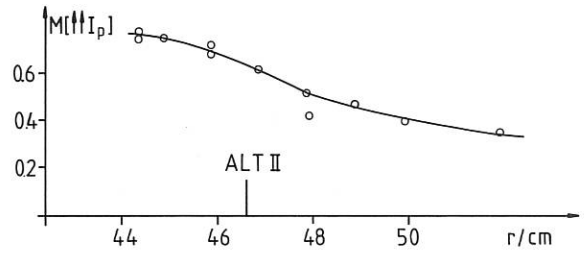

Fig. 3 Mach number of the plasma flow parallel to the magnetic field as a function of the radius, toroidal magnetic field inverted, B_{tor} = 2.25 T, I_p = 0.35 MA, $\langle n_e \rangle$ = 3.5 E19 m^{-3}

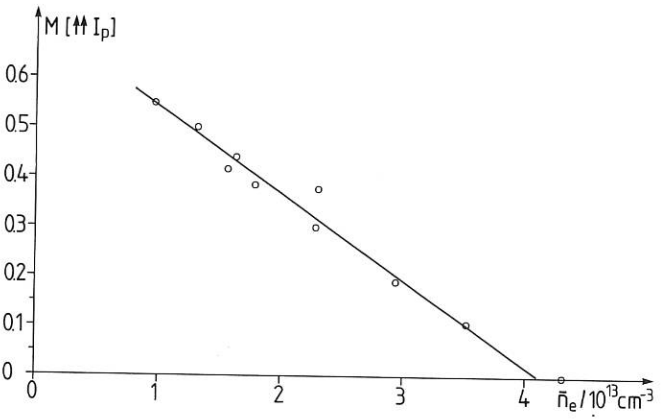

Fig. 4 Mach number of the plasma flow parallel to the magnetic field as a function of the mean core density r = r_{ALTII} - 1.7 cm B_{tor} = 2.25 T, I_p = 0.35 MA,

COLORIMETRIC DIAGNOSTCS FOR IN-SITU DETERMINATION OF EROSION AND DEPOSITION RATES IN TEXTOR

P. Wienhold[1]), F. Weschenfelder[1]), R. Möller[2])

[1]) IPP [2]) ZEL, Forschungszentrum Jülich GmbH,
Ass. EURATOM-KFA, D-52425 Jülich, Germany

1. MOTIVATION

Sputter erosion at graphite wall components is realized as a serious problem in future fusion devices. For ITER, intolerable material losses in the range of cm/day are estimated /1/ if no control techniques will be developed. In present day machines, the decrements are still much less (<1um). The eroded carbon is codeposited with hydrogen at other places of the wall surface in transparent form (a-C:H) with a carbon density of about 6.5 x $10^{22}/cm^3$ /2/. Measuring the thickness changes would yield therefore information about the carbon transport processes.
The deposits are easy to observe in day light because of the appearence of interference colors which mainly depend on thickness /3/. Deposition rates of about 5 nm/s as observed in the scrape-off layer of TEXTOR /4/ would shift an interference fringe into the next color after two discharges. This provides ideal circumstances for the use of colorimetry /5/ as a technique which can measure the colors and, hence thicknesses and rates. Observations shotwise and in dependence on plasma parameters are the first aims. Modelling of the data may later reveal ways to keep the net effects at tolerable low levels.

2. SET UP AT TEXTOR AND FIRST EROSION EXPERIMENT

The experimental set up consists of a CCD color video camera (PULNIX TMC76) which views through a top window, but declined by 7.5° against the vertical direction. The test piece is at the bottom of the torus in a total distance of about 2m from the camera. Sufficient illumination is provided vertically through a second window by means of halogene light (150 W) part of which is blocked, however, because of support structures of the ICRH antenna. The development of the fringes is monitored and recorded by video technique. Color measurements are then made off-line by computer aided image processing which implies the use of a frame grabber board (DT 2871) and the according software.
Before introduction into TEXTOR, a cylindrical graphite test piece (102 mm length, 48 mm diameter) with a half spherical end had been prepared for an erosion experiment by covering it with an a-C:H film in a laboratory plasma chamber. A thin Ti-film (few nm) sputtered before as a marker onto the graphite surface made the colors of the not homogeneous a-C:H deposit brillant. They reached yellow (140 nm) and purple (155 nm) of second interference order at the spherical end (see top view in fig.1). We restricted the later color measurements to a central area (about 30 mm in diameter) outside of which colors are shifted due to the inclining incidence.
This a-C:H covered test piece was positioned with its tip at r = 47.3 cm by means of a vacuum lock system. The toroidal limiter ALT II defined the plasma radius a = 46 cm, the neighboured limiters on electron (poloidal) and on ion drift side were

withdrawn. Plasma discharges in deuterium (n_e = 2.8 x $10^{13}/cm^3$, I_p = 357 kA, B_T = 2.25 T) lasting 3.6 s were heated by coinjecting hydrogen neutral beams with 1.3 MW over 2 s. The liner temperature was 150 °C. After the first exposure (# 54476) the probe tip was moved closer to the plasma by 5 mm (r = 46.8 cm) and exposed during the following discharges until the a-C:H deposit had partly been eroded down to the Ti-marker. Between shots, camera and illumination system were activated and short sequences recorded.

3. COLORIMETRIC MEASUREMENTS AND CALIBRATION

One single video image is sufficient for the colorimetric analysis and has to be stored in the computer. Since we observed the test piece from top the images looked similar to fig. 1, but with a changing fringe pattern. Colors were measured then along the mid part of the central diameter connecting ion and electron drift side (i an e in fig.1).

Colorimetry makes use of the facts that any visible spectral distribution creates a unique color impression in the eye of a human observer /6/ on the one hand. According to the CIE standards, this impression is described in terms of the three quantities hue (H), saturation (S) and intensity (I) of the color. On the other hand, the identical color impression can be admixed from three proper set visible wavelengths, such as emitted from the red (R), green (G) and blue (B) phosphorouses of a video screen and are quantifiable, e.g. in terms of voltages. The transitions between RGB and HSI coordinates are defined as mathematically unique. Because of technical limitations, only the hue (H) can be represented from a video system with its full natural range, not S and I. This is no restriction because H differs with thickness d remarkebly.

The calibration between H and d was made as follows. In case of a growing a-C:H film the changing hue of the interference colors can be calculated. Mainly the film thickness enters, but also its optical constants and those of the substrate, the angle of incidence (Θ), and the illuminating spectrum /3/. Fig.2 shows for two substrates (C,Si) how H, given here as a polar angle in the color circle, passes repetitively yellow, purple, blue and green sections order by order except the first which ends with the unchanged spectrum (no color). Note, that the polar angle decreases when d increases. Besides day light illumination and Θ=0° we assumed n=2.25 for the refrective constant and k=0.13 as extinction. These values and d were measured ellipsometrically on a set of Si specimen which had been covered with a-C:H together with carbon, steel and aluminum substrates in the laboratory. Since the observed relations hue-thickness agree almost perfectly with the calculated ones for all substrates up to the third order of interference the calculated relation for the carbon substrate is used in the following in order to transfer the measured H into d values. As fig.2 shows the influence of different substrates is not negligible.

4. RESULTS AND DISCUSSION

The observed spherical end of the test piece (confer fig.1) covered 5 mm radial distance only and was always located in an erosion dominated zone of the SOL. This is indicated by a decrease of all polar angles (open squares) compared to the ones measured over the virgin probe (full squares) and denoted with

1 and 0, respectively, in fig. 3a. The change on electron drift side is less compared to ion drift side, probably because of the adjacent (2.5 m) and shadowing ALT II limiter. The hue kept decreasing during exposures 2 (open) and 3 (full circles) - leaving hereby the purple range and entering the yellow - when the piece had been moved closer to the last closed flux surface (8mm distance). On the ion drift side the erosion became so rapid that the colors almost disappeared and can not be given in the figure. The total removal of the deposit on this side was later confirmed by visual inspection ex-situ.
Fig. 3b shows the thickness profiles evaluated by means of the calibration curve (fig. 2). Losses between 5 and 10 nm corresponding to 0.9 - 1.8 x 10^{16} C/cm^2s were found on ion drift side after the first exposure. They were too large to be reliably measured during the next discharge (dashed line). These numbers would correspond to an eroding hydrogen flux of 3-6 x 10^{17}/cm^2s if we neglect the erosion by impurities and the redeposition. Erosion is still present at the tangency point of the probe and shifts the maximum of the thickness distribution to the electron drift side by about 7 mm. On the sphere, this represents a position 1 mm more distant from the plasma then the tip, but still in the range of the hydrogen gyroradii /7/. On electron drift side, much less material is eroded during one exposure (1-3 nm), presumably because of the short connection to the ALT-II limiter.

5. CONCLUSIONS

In spite of the preliminary character of the data, these first results show that carbon erosion in TEXTOR can directly be measured after a single discharge by colorimetry of the interference colors as long as the carbon exists in transparent form (a-C:H). In neutral beam heated (2.6 MWs) discharges, the erosion from a test piece exceeded 10 nm when the probe came closer than 13 mm to last closed flux surface. We did not report about deposition experiments because of the lack of space.
Of particular advantage is that colorimetry can observe larger areas (>10 cm^2) little influenced by shape or surface roughness. In combination with other techniques, e.g. spectroscopy of the leaving carbon and in direct response to plasma parameter changes, the modelling of the erosion and deposition processes should be possible and is aimed at.

REFERENCES

/1/ M.F.A. Harrison, E.S. Hotston, G.P. Maddison, NET Report EUR-FU/80/90-97, May 1990
/2/ P. Wienhold, F. Waelbroeck, H. Bergsaker et al., J.Nuc.Mat. 162-164(1989)369
/3/ P. Wienhold, U.Littmark, E-MRS Symp. Proc. Vol.XVII,441, June 1987, Strasbourg, France
/4/ P. Wienhold, J.v.Seggern et al. and H. Bergsaker, M. Rubel et al., J.Nuc.Mat.176&177(1990)150
F. Weschenfelder, Thesis, Univ. Düsseldorf, 1993
/5/ e.g. D.L. MacAdam, Color Measurement, Springer-Verlag Berlin, Heidelberg, New York, Tokyo, 1981
/6/ Commission Internationale de l'Eclairage (CIE), Publication No. 13.2, Paris, 1974
/7/ J.N. Brooks, D.K. Brice, A.B. DeWald, R.T. McGrath, J.Nuc.Mat.162-164(1989)363

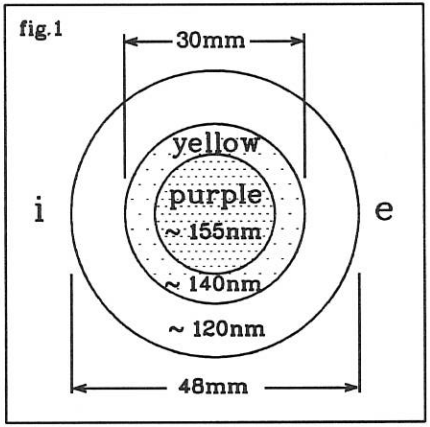

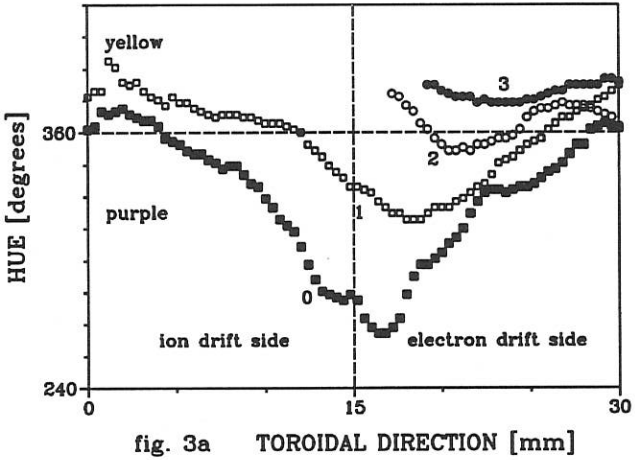

fig. 3a TOROIDAL DIRECTION [mm]

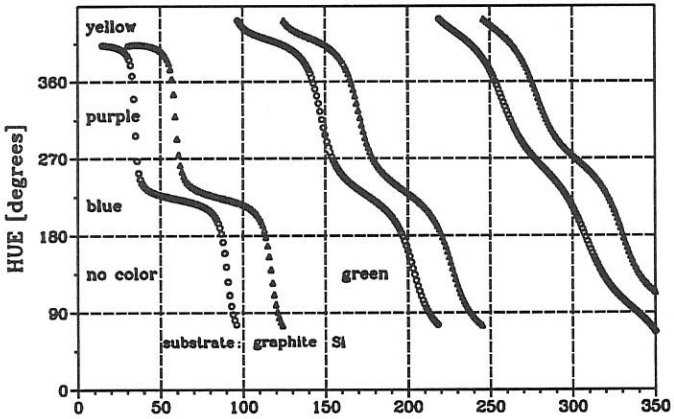

fig. 2 THICKNESS [nm] of a-C:H with n=2.25, k=0.13

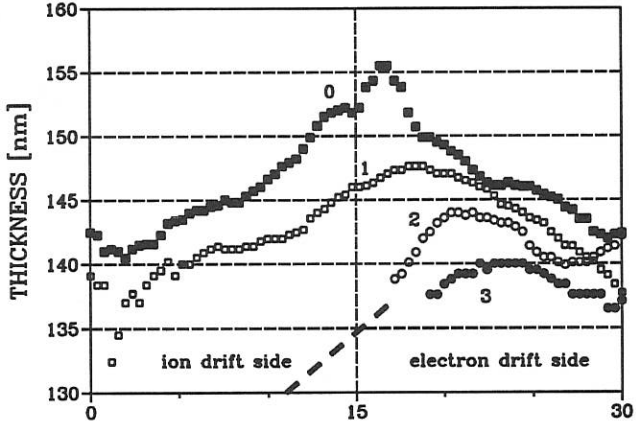

fig. 3b TOROIDAL DIRECTION [mm]

STUDY OF SPUTTERED Si-ATOMS IN FRONT OF A TEXTOR-LIMITER BY LASER-INDUCED FLUORESCENCE

Ph. Mertens, P. Bogen, B. Schweer
Institut für Plasmaphysik, Forschungszentrum Jülich, Ass. Euratom-KFA,
PF 1913, D-W5170 JÜLICH

Abstract

An optical system has been installed in the sector of the limiter lock of TEXTOR in order to study by laser-induced fluorescence the density and velocity distribution of atomic impurities in front of a test limiter. In the present case, it was a brick of silicon carbide material. Experiments were carried out on the silicon line at 251.6 nm. A pulsed dye laser was used, with a repetition rate of 20 Hz. By means of fast pressure tuning of the laser wavelength, during the flat-top of the plasma shot, spectral profiles were measured with a resolution of 1 pm, around $\overline{n}_e = 2 \cdot 10^{13}$ cm^{-3} (average line density). The profiles correspond to sputtered atoms escaping from the limiter. The velocity dependent penetration depth of these atoms was measured.

Introduction

The sputtering of impurities from the wall and limiters or divertor plates of fusion devices is becoming an increasingly important question as far as plasma contamination and recycling processes are concerned. The density and velocity distribution of sputtered atoms could so far seldom be studied in front of a tokamak limiter by other methods than emission spectroscopy [1,2].

Laser-induced fluorescence has, on the other hand, the advantage of being independent of the electron density and temperature, n_e and T_e, in a broad range of values. This criterion is met in the vicinity of the limiters in present middle-sized tokamaks ($n_e < 10^{13}$ cm^{-3}). Furthermore, the excitation takes place with a single laser line on a specific atom, which means that other decay lines, for instance from the excited dissociation of SiO molecules, can be rejected easily.

We were able to point out one work involving laser-induced fluorescence in front of a limiter-like arrangement [3]. The scarceness of similar studies is due, among other reasons, to the difficulty of installing a reasonably luminous observation system at the right place, and of operating it reliably in a tokamak environment. We could develop and install such a system in the sector of the first limiter lock on TEXTOR, and use it for measurements in front of a recently tested graphite limiter impregnated with silicon carbide.

Principles and experimental setup

The bulk material under study contained 30% of silicon imbedded, mainly in the form of SiC, in a graphite matrix (SiC30 [4]). We have carried out the whole experiment on the $^3P_2 \rightarrow {}^3P_2{}^\circ$ line of Si I at 251.6 nm in the ultraviolet. The Doppler half width of this line at room temperature amounts to the following value :

$$\Delta\lambda_D = 2\sqrt{\ln 2}\ \frac{\lambda_0}{c}\ \sqrt{\frac{2 k_B T}{m}} = 0.59 \text{ pm} \qquad (1)$$

where λ_0 represents the wavelength at rest, c the velocity of light, k_B Boltzmann's constant and m the mass of the silicon atom.

This transition has the further advantage that the Landé factors are equal in the upper and lower levels, so that the Zeeman effect can be eliminated by selecting the π-component with a polarized exciting beam, which could be performed to a large extent thanks to the high degree of polarization of our dye laser (> 90%).

The laser system consisted of a commercial, excimer-pumped, pulsed dye laser with a typical repetition rate of 20 Hz [5]. The pulse width lay around 10 ns. This dye laser was tuned by pressure variation, fast enough to record the whole spectral profile within the ~2.5 s long flat-top of the tokamak discharge. The spectral resolution of about 1 pm corresponds to a velocity interval of $1.2 \cdot 10^5$ cm/s for the detected neutrals.

As shown in fig.1, the laser beam was aligned, through an upper port of the tokamak section, onto the top of the limiter under examination. This limiter showed a slight convexity in both toroidal and poloidal directions. Taking advantage of the latter, we moved the laser spot on the limiter a few millimeters behind the crest, in order to avoid stray light to the observation system, which was installed perpendicularly to the excitation beam.

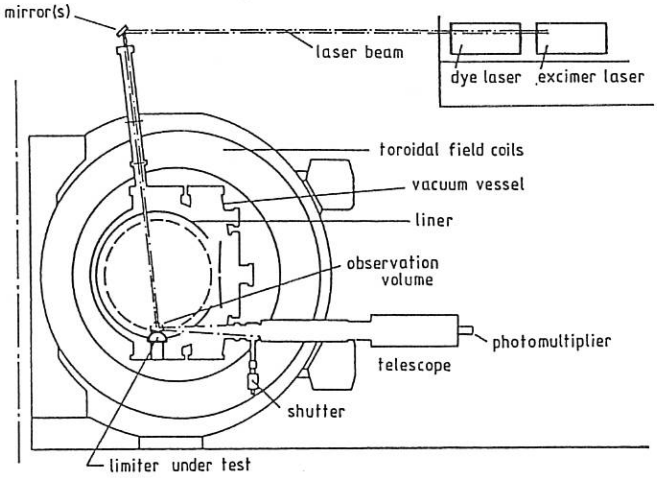

Fig. 1 Experimental setup on TEXTOR

The actual fluorescence volume was determined by the tilt of the observation telescope, a Cassegrainian arrangement, which imaged it 1:1 on a UV-photomultiplier behind a quartz window. An additional interference filter was used throughout the measurements with $\Delta\lambda$ = 3 nm. The fluorescence signal was recorded by means of a fast boxcar integrator [6] coupled to the timing and data acquisition system of TEXTOR.

The velocity profile of sputtered atoms is comprehensively discussed in the literature [7,8]. This so-called Thompson profile [9] writes

$$f(v)\,dv = (v/v_s)^2 \left[\, 1 + (v/v_s)^2 \,\right]^{-3} \quad dv \qquad (2).$$

A similar distribution, written in the form of wavelength dependence for our experimental conditions [10], was fitted to the experimental results as will be shown below.

Results and discussion

Figure 2 shows the raw fluorescence signal versus number of laser shots for a typical plasma discharge (with parameters I_p= 355 kA, $\bar{n}_e$= 1.5 · 10^{13} cm^{-3}, T_e= 1.1 keV, limiter position r_{lim}=45.5 cm, measuring point 2 mm in front of limiter top). The laser wavelength was continuously scanned over the flat-top part of the tokamak discharge.

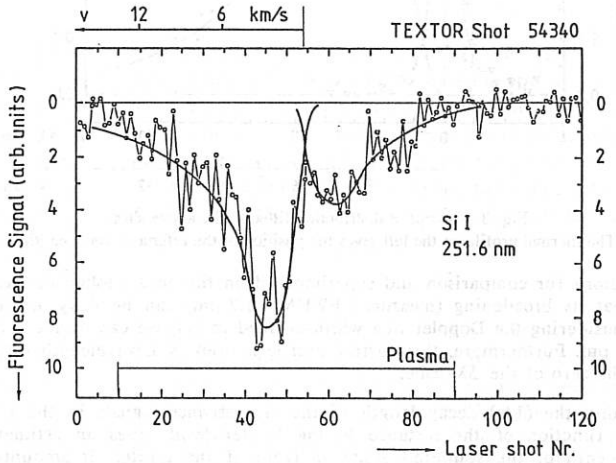

Fig. 2 Fluorescence signal from Si-atoms in front of the test limiter during the plasma discharge (on top, coarse velocity scale for the sputtered atoms)

The small open circles correspond to single laser shots, with the thin line drawn only to guide the eye. The thicker line suggests the presence of two overlapping Thompson profiles :

i) one extends far to the left of the picture, to larger wavelength shifts or higher velocities, showing sputtered atoms escaping from the limiter.

ii) the second profile comes from particles which are excited by the reflected laser light, so the Doppler shift extends in the other direction. It is indeed a mirrored image, with smaller amplitude, of the first distribution.

A Thompson distribution can be fitted to the first curve, smoothed over three shots, with a single free fitting parameter U_s, the surface energy, characteristic of the material as shown in [7-10]. This distribution is shown in figure 3 as a solid line drawn through the black dots. With a half width of about 5 pm for this Thompson profile, we come out with a value of U_s= 4.9 eV, comparable to the value of 4.8 eV measured in the laboratory by sputtering a silicon wafer with a 900 eV argon-ion beam (cf. also the value of 5.4 eV in [11]).

On the same figure, the open triangles represent the fluorescence of Si atoms in a low-current glow discharge in argon, with silicon cathode. This dashed profile was recorded

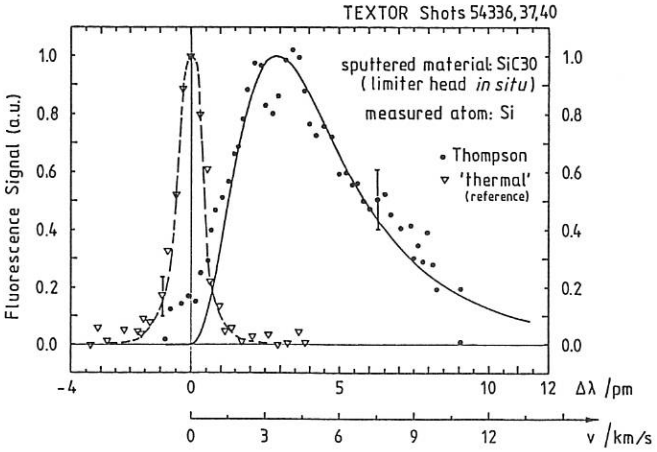

Fig. 3 Thompson distribution fitted to the above shot.
The thermal profile on the left gives the position of the reference wavelength.

in the laboratory for comparison and superimposed on the actual tokamak measurement. Assuming that its broadening (measured FWHM ~1.2 pm) can be fully ascribed to the laser, and considering the Doppler line width defined in (1), we can derive a laser width of about 1.0 pm. Furthermore, this narrow profile is used as a wavelength reference and determines the zero of the Δλ-scale.

Additionally, the (1/e)-decay length of the fluorescence signals in the plasma discharge as a function of the distance to the limiter head gives an estimate for the penetration depth of the sputtered atoms in front of the limiter. It amounts to about 7 mm. From the Doppler shift, we infer this corresponds to a velocity of $v = 3 \cdot 10^5$ cm/s.

The present results show that the laser-induced fluorescence can help to determine the values of various parameters *in situ* in front of a tokamak limiter. They will be complemented by further laboratory measurements in a later publication.

Acknowledgments

We thank Prof. E. Hintz for his support. It is also a pleasure for us to acknowledge the help of Mr. K. Klören on the technical side, of the TEXTOR team for the tokamak operation, and of Mr. M. Silz for the computer programs.

Literature

[1] A. Pospieszczyk, *in* Atomic and Plasma-Material Interaction Processes in Controlled Thermonuclear Fusion, R.K. Janev *ed.*, Elsevier (to be published in 1993)
[2] P. Bogen, D. Rusbüldt, Nucl. Fusion **32/6**, 1057-1061 (1992)
[3] U. Samm *et al.*, Plasma Phys. and Contr. Fusion **29/10A** (14th EPS), 1321-1332 (1987)
[4] SiC30 (Schunk & EBE, D-W6300 Gießen), 60% SiC and 5% free Si (weight) in graphite matrix
[5] Lambda Physik, Model FL2002, Göttingen (F.R.G.)
[6] EG&G, Model 4400, Princeton (U.S.A.)
[7] Sputtering by Particle Bombardment I, R. Behrisch *ed.*, Springer Topics Appl. Phys. **47** (1981)
[8] H.L. Bay, B. Schweer, Report of the Research Centre in Jülich, Jül-2032, 9 pp. (1985)
[9] M.W. Thompson, Phil. Mag. **18**, 377-414 (1968)
[10] Ph. Mertens and P. Bogen, Appl. Phys. **A43**, 197-204 (1987)
[11] A. Goehlich, M. Röwekamp, H.F. Döbele, J. Nucl. Mat. **176 & 177**, 1055-1058 (1990)

SILICON FLUXES IN THE TEXTOR SCRAPE-OFF LAYER FOLLOWING SILICONIZATION

M. Rubel[1], P. Wienhold[2], B. Emmoth[1], H.G. Esser[2] and J. Winter[2]

[1]Manne Siegbahn Institute of Physics, Association Euratom-NFR, Frescativägen 24, S-104 05 Stockholm, Sweden

[2]Institute of Plasma Physics, Association Euratom-KFA, D-5170 Jülich, Germany

ABSTRACT

Graphite collector probes were used at TEXTOR for detailed studies of ionic fluxes in the scrape-off layer (SOL) during the first silicon-assisted operation of a tokamak. The probe exposures were made in order to recognize the evolution of silicon fluxes and the influence of silicon on the behaviour of other impurity atoms such as boron, oxygen and metals. Comparative exposures were made during plasma pulses performed under following conditions: before the introduction of Si into the machine, with silane (SiH_4) puffing into the SOL, fully fuelled with SiH_4 and immediately after the first or second siliconization as well as long time (260 discharges) afterwards.

1. INTRODUCTION

Deposition of thin, reproducible films on a tokamak first wall is considered as one of the most advantageous methods of wall conditioning improving the operation of controlled fusion devices. Following the carbonization /1/and boronization /2/, the siliconization of the tokamak wall was made at TEXTOR /3/by rf assisted dc glow discharge in SiH_4 - H_2 gas mixture. The main goal of the process was to enhance gettering efficiency of oxygen impurity in the machine by the deposited layer. The deposition of silicon - containing film on the entire TEXTOR wall was preceded by a serie of experiments based on the puffing of different amounts of SiH_4 into the SOL and by discharges fully fuelled with SiH_4. Such gradual introduction of silicon into the tokamak allowed for detailed studies of the Si transport in the machine and its influence on the TEXTOR operation. Among numerous diagnostic techniques applied during the plasma pulses with silane and after the siliconization, the surface collector probe was also used in order to recognize: i) the evolution of Si fluxes; ii) the influence of Si on the behaviour of other fluxes like boron, oxygen and metals.

2. EXPERIMENTAL

The investigation was carried out with graphite probes exposed to the TEXTOR plasma in a time integrated mode. Single probe was facing 2 - 5 similar discharges lasting 2.9 - 3.8 s; the total exposure was 6.7 - 15.9 s. During all the exposures the plasma radius was defined by the ALT II belt limiter at r = 46 cm. Several tens of probes were exposed to the scrape-off plasma under different conditions: heating mode (ohmic and assisted with NBI or ICRH), central plasma density ($n_e(0)$ = 1.6 - 5.0 x 10^{19} m^{-3}) and gas filling (H/H+D = 0.05 - 0.92). The reference exposure was made in the presence of the B/C surrounding, whereas following exposures were done during

the silane-assisted operation, immediately after the first and second siliconization as well as hundreds of discharges later. The exposed samples were transported to the surface analysis station and examined by means of high energy ion beam techniques. The content of the deposited silicon, oxygen and metals was determined with Rutherford backscattering spectroscopy (RBS) whereas nuclear reaction analysis (NRA) was used to study the contents of boron /$^{11}B(p,\alpha)^{8}Be$, 640 keV H^+ beam/ and deuterium / $^{3}He(d,p)^{4}He$, 760 keV $^{3}He^+$/. Moreover, ion induced detrapping of the deposited D by 760 keV $^{3}He^+$ ions was studied.

3. RESULTS AND DISCUSSION

Co-deposited layers formed on the exposed graphite surfaces contain deuterium and hydrogen together with plasma impurity atoms: boron, silicon, oxygen and metals (Me=Ni+Cr+Fe) originating from the TEXTOR liner. Table 1 presents the deposition rates (F) of plasma impurity atoms measured 12 mm deep in the scrape-off layer during ohmically heated discharges fuelled with hydrogen, deuterium or silane. In all the cases the central plasma density was $2.5 \pm 0.1 \times 10^{19}$ m^{-3} making the results of respective experiments available for direct comparisons. The experiments made during the plasma pulses with additional ICR heating are reported elswhere /4/.

Table 1. Deposition rates of impurity atoms before and after siliconization.

EXPOSURE		EXPOSURE CONDITIONS	GAS (H/H+D)	DEPOSITION RATES F_B	F_{Me}	F_{Si}	F_O (10^{14} cm^{-2} s^{-1})	F_O/F_{Si}
I	B/C surrounding	Boronized (reference)	H_2 (0.66)	22.7	0.56	----	32	----
II		SiH_4 puffing (0.25×10^{20} mol.)	H_2 (0.65)	23.5	0.62	0.4	29	72.5
III		SiH_4 puffing (4.4×10^{20} mol.)	H_2 (0.70)	24.7	0.57	10.0	52	5.2
IV		Discharges in silane plasma	SiH_4 (0.72)	27.5	0.93	53.1	53	1.0
V		Changeover to hydrogen	H_2 (0.76)	30.6	0.76	22.1	53	2.4
VI	Si surrounding	After I siliconization	H_2 (0.82)	2.7	0.10	98.0	16	0.16
VII		After II siliconization	D_2 (0.07)	0.6	0.24	102.0	16	0.15
VIII		260 disch. after siliconization	D_2 (0.05)	3.4	0.50	18.2	42	2.32

Deposition rates of respective atoms vary distinctly dependently on the exposure conditions and some important tendencies may be noticed. The deposition rates of boron (F_B) are nearly constant for discharges made in the boronized machine (B/C surrounding) even when the amount of silicon in the machine increases gradually by flushing or fuelling with silane. As expected, a drastic decrease of the boron fluxes (by a factor of 10 or more) occurs following the siliconization of TEXTOR. The fluxes are low independently on the fuel (H or D) and they remain low even hundreds of dicharges after the second wall conditioning with silicon.

The depositions rates of metals (F_{Me}) behave similarly to those of boron. The amounts of metals is already fairly small in the presence of the boronized wall /5/, but siliconization reduces them furtheron. There are certain fluctuations of the metal fluxes dependently on the fuel. In the B/C surrounding the Me flux is nearly doubled in the presence of the SiH_4 plasma and similar increase, by a factor of 2, is observed in the freshly siliconized machine when the hydrogen plasma is replaced by the duterium one. The effect is probably induced by the increased sputtering of metals from the walls by SiH_4 or D_2 in comparison to sputtering in hydrogen environment. However, both the fluxes (boron and metals) are low indicating that the siliconized layer covering the wall is fairly durable and does not become eroded easily even by hundreds of discharges.

Pronounced deposition rates of silicon, F_{Si}, are observed already during the silane-assisted operation and, as expected, they increase substantially in the siliconized machine. The introduction of silicon into the plasma (exp. II-V) does not change the deposition rates of boron, but the amounts of oxygen on the collector surface are increased, what is in contradiction with spectroscopic data showing the decrease of oxygen fluxes in the plasma. Then, one may suppose: i) that oxygen is more efficiently trapped ion the probe surface by the co-deposited layer containing silicon, or ii) that the co-deposited layer with Si uptakes much oxygen from air when the samples are transported from TEXTOR to the surface analysis station /6,7/. However, in exposures III-V the amount of oxygen measured on the probes is constant independently on the amount of silicon collected indicating that the oxygen uptake from air, even if occurs, is not the main mechanism deciding the oxygen content on the probes under investigation.

In general, oxygen concentrations found on the probes' surfaces should be considered in connection to the boron and/or silicon deposition rates. Both boron and silicon getter oxygen and it has already been shown for boron containing deposits that they also uptake oxygen from air /6,7/and similar effect could be expected for silicon-containing deposits. As has been proved previously /6,7/the ratio of oxygen to boron contents on the probes exposed in the boronized TEXTOR ranges from 0.8 shortly after boronization to 2.5 hundreds of discharges later. This is exactly the case of the F_O/F_B values (1.2 - 2.1) determined after the exposures (I-V) made in the presence of the B/C surrounding, whereas the F_O/F_{Si} ratios measured in the freshly siliconized machine (exp. VI, VII) are much lower, 0.15, as the amounts of oxygen collected in the deposits is very much reduced. These small oxygen contents detected in the presence of high silicon fluxes confirm that the deposits' composition is not strongly influenced by oxygen from air. Assuming pronounced sorption of oxygen from air one would expect the oxygen content to rise parallelly with the increase of Si amount in the deposit. In contrary, less oxygen is found on the probes exposed following the siliconization. Therefore, one may tentatively conclude that the low oxygen contents on the probes reflect fairly low oxygen fluxes in the SOL due to very efficient oxygen gettering by the siliconized layers on the TEXTOR wall. This tentative statement is partly justified by the results of addditional exposures performed in the freshly siliconized TEXTOR (I siliconization, H_2 plasma) at three different plasma densities. The results are collected in Table 2.

It has been shown and discussed several times /i.e. 8,9/that the increase of the plasma density influences the reduction of ionic fluxes in the SOL. Such tendency is

fairly well reflected by the silicon (and boron to some extent) deposition rates presented in Table 2. However, the deposition rates of other species, including oxygen, remain nearly unchanged when the plasma density changes. It proves again very low contents of metals and oxygen at TEXTOR following the siliconization.

Table 2. Fluxes of impurity atoms in the SOL *versus* plasma density

Density	DEPOSITION RATES			
(10^{19} m^{-3})	F_B	F_{Me}	F_{Si}	F_O
	(10^{14} cm^{-2} s^{-1})			
1.6	2.8	0.09	121	16
2.5	2.7	0.10	98	16
3.5	2.1	0.10	58	19

Ion induced detrapping of the deuterium on the probes was studied with 760 keV $^3He^+$ beam for deposits kept at room temperature. The samples were irradiated with doses up to 2 x 10^{16} cm^{-2}. The release of D was negligible (below 10 %) from the samples exposed in the immediately after the siliconization and containing little boron (6 x 10^{15} cm^{-2}) and much silicon (2 x 10^{17} cm^{-2}). More deuterium, 15 - 23 %, was detrapped from the deposits formed during the exposures performed 260 discharges later. Nevertheless, these detrapping effects are disinctly lower than those observed for the surfaces exposed in the carbonized /10/or boronized environment when up to 60 % of deuterium was released. The studies of detrapping are considered as preliminary ones but they prove pronounced difference between the deuterium binding states in the layers with or without silicon.

The result obtained by means of surface collector probes show that fluxes of impurity atoms (boron, metals and oxygen) in the TEXTOR scrape-off layer are distinctly reduced due to the siliconization. Moreover, one can suggest that the co-deposited layers (Si/B/O/Me/- H/D) on the probes' surfaces are chemically inert when exposed to air. Further studies are under way in order to recognize the chemical state of respective atoms in the deposits.

REFERENCES

1. J. Winter, J. Nucl. Mater. 145-147 (1987) 131.
2. J. Winter *et al.*, J. Nucl. Mater. 162-164 (1989) 713.
3. J. Winter *et al.*, These Proceedings.
4. G. van Oost *et al.*, These Proceedings.
5. P. Wienhold *et al.*, J. Nucl. Mater. 176&177 (1990) 150.
6. P. Wienhold *et al.*, Vacuum 43 (1992) 745.
7. P. Wienhold *et al.*, J. Nucl. Mater. 196-198 (1992) 647.
8. H. Bergsåker *et al.*, Proc. 16th Fusion, Venice, Italy, 1989, p.1027
9. M. Rubel *et al.*, Physica Scripta 43 (1991) 508.
10. H. Bergsåker *et al.*, Proc. E-MRS 17 (1987) 433.

Measurements on the ion velocity distribution in the toroidal direction by Rutherford scattering at TEXTOR

H.F. Tammen, A.J.H. Donné, S.A.H. Moorman, T. Oyevaar and F.C. Schüller.

FOM-Instituut voor Plasmafysica 'Rijnhuizen', Associatie Euratom-FOM, P.O.Box 1207, 3430 BE Nieuwegein, The Netherlands.

Keywords

toroidal rotation velocity, ion temperature measurements

Abstract

The Rutherford scattering diagnostic at TEXTOR has been used to perform measurements on the ion velocity distribution in the toroidal direction. During injection of one neutral beam, tangential to the plasma, the obtained spectrum was found to be shifted as a result of the toroidal rotation of the hydrogenic bulk ions. In the centre of the plasma, speeds around 10^5 ms^{-1} have been found. During balanced injection no rotation was observed.

1. Introduction

The Rutherford scattering diagnostic (RUSC) at TEXTOR is primarily used for performing temporally- and spatially resolved measurements of the ion temperature /1, 2, 3/. A narrow beam of monoenergetic 30 keV helium atoms is injected vertically into the plasma. A small part of the beam particles is scattered, mainly in forward direction, through elastic collisions with the moving plasma ions, exchanging momentum and energy in the process. Particles that are scattered at a certain, adjustable angle (3°-8°) are energy analyzed by a time-of-flight analyser. For pure plasmas the width of the obtained spectra is directly related to the ion temperature in the scattering volume. Furthermore, bulk motion of the plasma ions shows up as an additional shift of the complete spectrum.

2. Toroidal rotation measurements

The present geometry of RUSC is such that the scattered particles carry information about the ion velocity distribution in the toroidal direction. Hence, any shift of the spectra is caused by bulk motion in the toroidal direction, i.e. toroidal rotation of the plasma. At TEXTOR there are two tangential neutral beam injectors, injecting in opposite directions, so the possibility exists to study toroidal rotation both during balanced injection and with only one injector.

Usually, the toroidal rotation velocity of a plasma is measured by active Charge Exchange Recombination Spectroscopy /4,5/. With this technique the rotation is inferred

from the spectral shift of impurity line emission (Doppler shift). The impurities involved are usually C or O, but also heavier elements can be used. Typical speeds measured during tangential injection of neutral particles are of the order of 10^5 ms^{-1}. With balanced injection no rotation is observed. This technique, however, does not render information about the toroidal speed of the hydrogenic bulk ions of the plasma. Hence, RUSC offers a new and independent method for the determination of the toroidal rotation velocity. Furthermore, the possibility now exists at TEXTOR to determine simultaneously the toroidal rotation velocity of hydrogenic and impurity ions, which in the near future will be exploited.

3. Results

First measurements of the toroidal rotation were performed with injection of H-particles into a D-plasma. The plasma current was 350 kA and the line-averaged electron density was 3.0 x 10^{19} m^{-3}. For experimental reasons, not discussed here, the toroidal field was only 1.8 T. Both injectors applied 1.3 MW of power, NBI-Counter from 0.8 - 1.8 s and NBI-Co from 1.3 - 1.8 s. The scattering angle was 7° and the scattering volume was positioned at the centre of the plasma. Four reproducible discharges were monitored (#54609-54612) and spectra obtained at similar time-intervals were added to improve the statistics.

Fig. 1 shows several characteristics of the measured data: a) the averaged time-of-flight of a spectrum, b) the width of a spectrum and c) the number of counts detected in a spectrum. After NBI-Counter has been switched on, the average value of the spectra is clearly seen to decrease by approximately 3 ns. This is caused by the toroidal rotation. The addition of NBI-Co leads to balanced injection, and the average almost reaches the same value as during the ohmic phase of the discharge. The increase in width of the spectra reflects the increase in the ion temperature, which is larger during balanced injection than during NBI-Counter alone. The small drop in counting rate of the diagnostic is caused by enhanced losses of the diagnostic beam, due to the changing edge layer of the plasma during NBI.

Rotation during ohmic heating is thought to be very small ($\leq 10^4$ ms^{-1}). Consequently, the average value of spectra obtained during the ohmic phase of a discharge can be used as a reference zero-level, and the change which occurs after the onset of NBI can then be used to deduce the actual toroidal speed. In this way a toroidal speed of 1.5(±0.2) x 10^5 ms^{-1} has been derived for this particlular case of NBI-Counter injection. The statistical error given is also indicative for the threshold value of observation of rotation. This is of the same order of magnitude as that which has been measured at TEXTOR by Recombination Spectroscopy /6/. Although during the balanced phase the average of the spectrum slightly differs from the ohmic phase, this is not caused by plasma rotation. Detailed analysis of the spectra revealed that the difference can be accounted for by the (weak) dependence of the average on the ion

temperature, which is mainly the result of the energy dependent efficiency of the RUSC analyser. Fits to the data from the three phases of the discharge (integrated over 0.4 s) are plotted in Fig. 2, together with the measured spectrum from the balanced heating phase to indicate the quality of the fits. The derived ion temperatures are: 0.7 keV (ohmic), 1.1 keV (NBI-Counter) and 1.6 keV (balanced heating), each with an accuracy of 10%.

The dependence of the central rotation on the injected NBI power has also been investigated. The main plasma and diagnostic parameters were similar to the ones mentioned above. Special care was taken that the density of the plasma was equal for all discharges. However, this time the NBI-Co injector was used and consequently the spectra were shifted to longer time-of-flights. The NBI power was not varied by changing the energy of the injected particles but by reducing the number of injected particles, to prevent changing the penetration depth of the beam. The results of the scan can be viewed in Fig. 3, where the central toroidal speed is plotted versus NBI power. The rotation is clearly seen to increase with injected power. A simple power fit showed that the central toroidal speed is, within statistical uncertainties, proportional to the square root of the applied NBI power for the data set under consideration: an exponent of 0.54 was found.

Finally, the radial dependence of the toroidal rotation has been investigated by adapting the position of the scattering volume on a shot-to-shot basis. Again, the same plasma parameters as before were used, with 1.3 MW of NBI-Co injection. Due to the restricted range in the plasma which in the present experimental set-up can be covered with one scattering angle, both 6° and 7° were selected. The result of the profile measurement is given in Fig. 4. The toroidal speed is seen to decrease towards the edge of the plasma, as has been observed for impurity rotation.

Acknowledgement

The authors would like to thank their colleagues from TEXTOR for their assistance and interest. This work was performed under the Euratom-FOM association agreement with financial support from NWO and Euratom.

References

/1/ A.J.H. Donné, E.P. Barbian, H.W. van der Ven, Journal of Applied Physics **62**, 3130 (1987).

/2/ A.A.E. van Blokland, E.P. Barbian *et al.*, Review of Scientific Instruments **61**, 3116 (1990).

/3/ H.F. Tammen, A.A.E. van Blokland *et al.*, Proc. 19th Conf. on Controlled Fusion and Plasma Physics, Innsbruck (1992) Vol II, p. 1091.

/4/ R.C. Isler, A.J. Wootton *et al.*, Nuclear Fusion **26**, 391 (1986).

/5/ H.J. Weisen, M. von Hellermann *et al.*, Nuclear Fusion **29**, 2187 (1989).

/6/ H. Euringer, private communication.

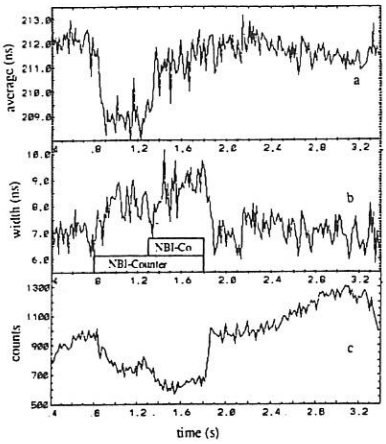

Fig. 1 *Average (a), width (b) and number of counts (c) of spectra mesaured during a discharge with NBI-Counter and balanced heating. (For the plasma parameters: see main text.)*

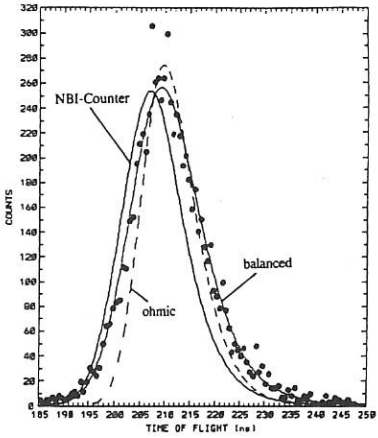

Fig. 2 *Fits to data during the ohmic, NBI-counter and balanced heating phase of the same discharge as in Fig. 1. The shift caused by toroidal rotation is clearly visible. The spectrum (black dots) was obtained during balanced heating and is shown to illustrate the quality of the fit.*

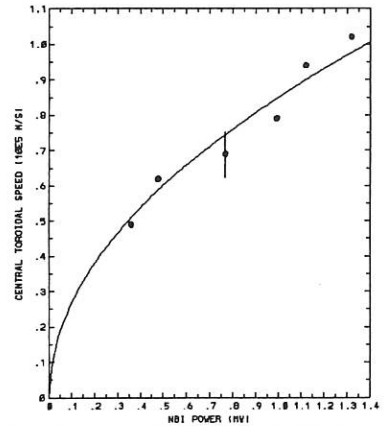

Fig. 3 *Central toroidal speed of the hydrogenic ions versus applied NBI-Co power. The fit shown is proportional to the square root of the NBI power.*

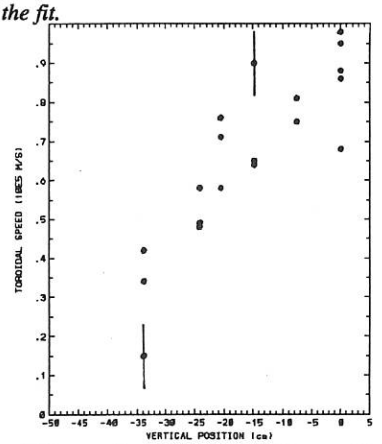

Fig. 4 *Measured vertical profile of the toroidal rotation speed. The two outermost positions were measured at a scattering angle of 6°, the others at 7°.*

MEASUREMENT OF THE LOCAL PARTICLE SOURCE INDUCED BY GAS-PUFFING IN THE FRASCATI TOKAMAK UPGRADE

V. Zanza

Associazione EURATOM- ENEA sulla Fusione, Centro Ricerche Energia Frascati, C.P. 65 - 00044 Frascati, Rome (Italy)

INTRODUCTION

The knowledge of the particle source strength is of great importance to understand the particle transport mechanisms in a tokamak. Since the ion plasma sources are due to ionization (and recombination) of neutral atoms, numerical codes have been often used to calculate the neutral atom density profile [1], whose knowledge allows, through the well known ionization and recombination cross sections, to get the particle source strength. However, the results of such codes depends on some information such as the impurity content and the distribution of external sources that are often difficult to obtain. Moreover, the measurement of neutral atom density, based on spectroscopic tecniques, is only possible in the edge of the plasma [2].

In this paper we describe a method for measuring the local neutral density and, consequently, the particle source strength directly induced by gas puffing. The measurement is performed by modulating the gas valve flow and measuring the perturbation, $\delta\Gamma$, induced in the fast neutral emission as a function of energy.

The results, which are independent of any assumption on the neutral transport in the plasma, may be used also to validate the calculation performed by numerical codes.

METHOD

As it is well known the flux of neutral atoms, $\Gamma(E)$, with energy E emitted by the plasma along a central chord is given by

$$\Gamma(E) = \frac{1}{4\pi} \int_{-a}^{a} n_i n_a \langle \sigma_{cx} v \rangle f(E, T_i)\, \eta(E,x)\, dx \qquad (1)$$

where a is the minor radius, n_i and n_a are the ion and atom density respectively, $\langle \sigma_{cx} v \rangle$ is the maxwellian averaged charge-exchange reaction rate, $f(E,T_i)$ is the local ion distribution function and $\eta(E,x)$ is the probability for a neutral atom, generated at a location x with energy E, to reach the plasma edge traveling along the line of sight.

When the neutral density is changed by a quantity, δn_a, for example by a modulation of the external sources, the induced variation of the neutral flux is

$$\delta\Gamma(E) = \int_{-a}^{a} \delta n_a\, W(x,E)\, dx \qquad (2)$$

where W(x,E) is a weight function (independent of the neutral density) given by

$$W(x,E) = \frac{n_i \langle \sigma_{cx} \rangle f(E, T_i)\, \eta(E,x)}{4\pi} \qquad (3)$$

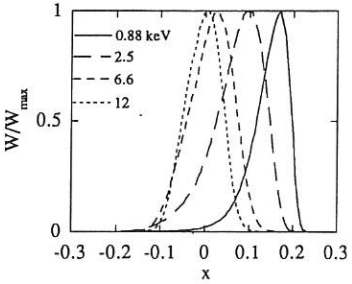

Fig. 1 – W/Wmax vs x at different energies

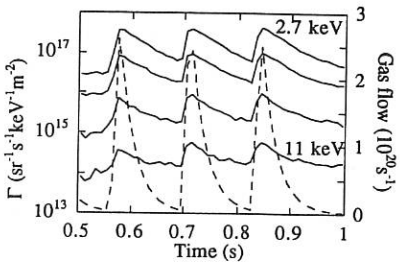

Fig. 2 – Γ, at different energies, (full line) and gas flow (dotted line) vs time

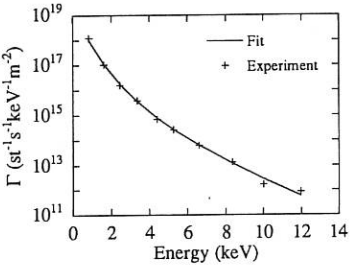

Fig. 3 – Γ vs energy

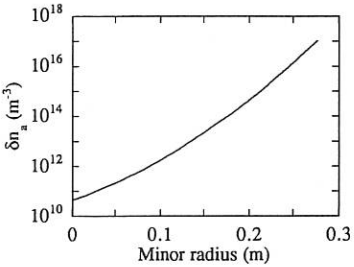

Fig. 4 – δn_a profile for the higher density discharge

In Fig. 1, the behaviour of W, normalized to unity, as a function of x is shown for different energies for a typical FTU discharge having line average density, n, of 8×10^{-19} m^{-3}. As we can see, the weight function is different from zero in a region whose location and extension depends on neutral energy. So $\delta\Gamma(E)$ contains the information about the profile of δn_a.

Using for $\delta n_a(r)$ the expression $\delta n_a=\exp(a+br+cr^2)$, the parameters a, b and c can be obtained by fitting the values of $\delta\Gamma(E)$, calculated with Eq. (2) and (3), to the experimental ones. The profile of δn_a so obtained allows, through the well known ionization and recombination cross sections, to get the perturbation, δS, induced in the particle source strength.

RESULTS

The method described above were applied to two ohmic FTU discharges. The first one having $n=8\times10^{-19}$ m^{-3} and the second one $n=4.5\times10^{-19}$ m^{-3}. To this end a few gas pulses, having a distance of 150 ms, were sent into the tokamak with a piezo-electric valve. The induced variation of the emitted neutrals were measured with a ten channels absolutely calibrated neutral particle analyser [3] located in the same valve port.

In Fig. 2 we can see the time behaviour of the neutral fluxes, at four different energies for the higher density discharge; in the same figure the behaviour of the particle inflow at the plasma edge, calculated from the valve flow taking into

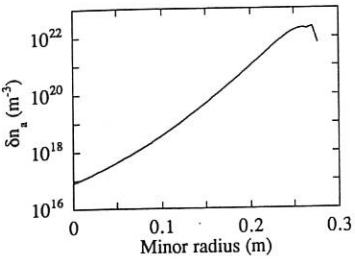

Fig. 5 – δS profile for the higher density discharge

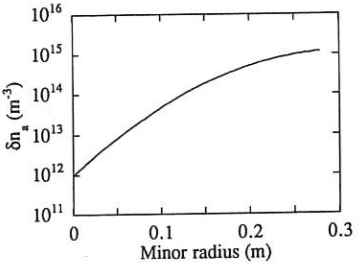

Fig. 6 – δn_a profile for the lower density discharge

account the integration due to the port volume, is also shown. In Fig. 3 the amplitude of the first harmonic of the induced neutral flux oscillation, obtained by a discrete Fourier analysis, is shown as a function of energy for the same discharge. The fitting line, obtained with the method described above, is shown (full line) in the same figure. The δn_a and the source function profiles are shown respectively in Figs. 4 and 5. In figs. 6 we show the source function profile for the lower density discharge. As it is expected, due to a better neutral penetration, the source function, in this case, is considerably higher than in the previous (higher density) case.

SUMMARY AND CONCLUSIONS

We have described a method to measure the local neutral density and particle source directly induced by the gas puffing in tokamak plasma. The method is based on the gas puffing modulation and on the measurement of the induced variation of the fast neutrals emitted by the plasma. It should be noted that the source function which enter in the particle balance equation is the surface average of S which can be obtained by measurements performed, by many analysers, at different toroidal and poloidal locations. Moreover our results are useful to test the assumptions made in the neutral particle transport codes.

REFERENCES

[1] M.H. Hughes and D.E. Post, Journal Comp. Phys. **28**, 43 (1978).
[2] R.D., Bengtson, P.M., Valangju, A., Ouroua et al., Rev. Sci. Instrum. **61**, 3110 (1990).
[3] R. Bartiromo, G. Bracco, M. Brusati et al., Rev. Sci. Instrum. **58**, 788 (1987).

STUDY OF THE SCRAPE-OFF LAYER IN COMPASS AND START TOKAMAKS

J. G. Ferreira*, S. K. Erents, R. Duck, S. J. Fielding, J. Hugill, G. M. McCracken, C. Qian
Culham Laboratory, UKAEA/Euratom Association, Abingdon, Oxon OX14 3DB, U.K.
*Keble College/University of Oxford, Oxford, Oxon OX1 3PG, U.K.

Introduction

Exhaust of particles and power in the scrape-off layer of tokamaks is presently under intensive investigation because of its importance for next-generation tokamaks. In this connection, Langmuir probes have been used to investigate the properties of the plasma at the edge of the tokamaks START and COMPASS-D at Culham Laboratory.

START is a small tokamak with some unusual features [1]: a very small aspect ratio ($A \approx 1.3$), formation and heating of the plasma by compression, a large separation between the plasma boundary and the walls of the vacuum vessel, and an interesting exhaust mechanism which works as a natural divertor configuration (Figure 1). Probe measurements have contributed to a better understanding of the formation and exhaust of the plasma in this tokamak. The existence of an exhaust "plume" around the central column is reported where $n_e \approx 5 \times 10^{18} m^{-3}, T_e \approx 15eV$ are measured.

Probes have been used in COMPASS to study the scrape-off layer of single null X-point configuration plasmas (Figure 2). A particular feature of these measurements was the use of voltage scan frequencies above $100kHz$, a range where very few measurements have been done so far. We report here measurements carried out at $200kHz$, the use of still higher frequencies being planned for the near future. With this method, fluctuations in temperature, plasma potential and density can be separated and reliable data on can be obtained to evaluate heat losses by electron conduction, possibly as important as convection in transporting heat from the confinement zone into the scrape-off layer [2]. We report here the first results obtained using this technique in COMPASS-D.

Measurements on START

Figure 1 presents a sketch of START showing a typical magnetic field configuration, the exhaust plume where intense light emission is observed, and the position of the probes used in the measurements (an array of fixed single Langmuir probes embedded in one of the bottom target plates and a movable double probe at the midplane). One of the main purposes of probe measurements in START was the investigation of how the plasma boundary and exhaust mechanism were affected by its unusual configuration. In particular, the magnitude of the plasma density outside the main core was not known before probe data was taken, making difficult for instance the interpretation of density measurements using interferometry.

One of the results of probe measurements done so far in START was to confirm the existence of an exhaust plume extending up and down along the central rod (the inner leg of the toroidal field coils). This result could in fact be expected from the pattern of magnetic flux surfaces shown in Figure 1 and is indeed confirmed by the distribution of light emission seen in CCD pictures [1]. The probe data also show clearly the evolution of the plasma formation process. (Figure 3). The time behaviour of density and temperature profiles obtained from both probes show the plasma appearing initially at the midplane in a region around $40 - 45cm$, spreading inwards and then compressing to its final "steady-

state" configuration around the central column, about $1.5ms$ after the beginning of the shot. In the "steady-state" phase, the density measured by the midplane probe decays steeply outside the main plasma core, a result which validates the use of the diameter of the main plasma seen in CCD pictures as the relevant path for density interferometry. On the other hand, surprisingly high density values were measured by the probes in the exhaust plume at the bottom of the configuration which acts as a natural divertor carrying particles away from positions just outside the last closed flux surface towards the top and bottom target plates. Another evidence of the strong link between the target region and the confined plasma is a clear increase in the probe signals in response to internal reconnections which often occur in the discharge [3].

The density decay length measured at the midplane ($\lambda \approx 35mm$) is a factor of 2.5 smaller than that measured at the targets ($\lambda \approx 90mm$). This also seems to be consistent with the predicted magnetic configuration of Figure 1, where an expansion of flux tubes is clearly seen between the midplane and the limiter. Moreover, applying a simple model of the scrape-off layer ignoring particle sources [4] to estimate the cross-field diffusion coefficient $D_\perp = \lambda^2 C_s / L_c$, where the length of the magnetic field lines $L_c \approx 5m$ is obtained from the magnetic configuration in Figure 1, gives a diffusion coefficient somewhat larger than the Bohm value, as observed in other tokamaks.

The scaling between edge and central densities in START seems to present a behaviour similar, in broad sense, to that observed in other machines. Figure 4 shows the dependence between plasma density $n(a)$ measured by the exhaust probes and density n_0 measured at the centre of the plasma using Thomson scattering, for two values of peak plasma current. A less then linear increase of $n(a)$ with n_0 is observed, as well as a weaker dependence on the input power in rough agreement with similar scaling laws obtained elsewhere, for instance, in ohmic discharges on JET [5]. An estimate of the power transported by the particles in the exhaust was obtained from the target probe data. Taking the field line angle into account, using a power transmission factor $\gamma \approx 10$ and integrating over the whole exhaust area gives a value for the exhausted power P_{exh} of the same order of magnitude as the ohmic input power ($P_\Omega = I_p V_{loop} \approx 200kW$). However, considering the large uncertainties in the estimate of P_{exh}, this exercise only shows that a significant fraction of the plasma energy is possibly exhausted by the particles escaping in the plume around the central column.

Measurements on COMPASS

Measurements using a single probe have been carried out in a single null X-point configuration on COMPASS-D (Figure 2). The probe approached the separatrix from the top (opposite to the X-point) and its position was scanned in a shot to shot basis. The probe voltage was scanned at $200kHz$ and the probe current and voltage were acquired using $5MHz$ ADC's. The plasma parameters (electron temperature T_e, plasma density n_e and floating potential V_f) were determined by fitting the characteristic curve obtained from each sweep, compensated for the stray capacitive current, to the theoretical probe curve, giving in principle a time resolution of $2.5\mu s$ (some sweeps fail to produce a good fit, making the effective time resolution slightly worse). Both average and fluctuating quantities were determined from these measurements.

Profiles of average plasma parameters are shown in Figure 5. The range of values is typical of tokamak edge plasmas ($T_e \approx 10 - 30eV$, $n_e \approx 1 - 7 \times 10^{18} cm^{-3}$, $V_f \approx \pm kT_e/e$).

A pronounced kink is observed in all the curves at a vertical position around $30cm$, which can possibly be explained by the crossing of the separatrix. Outside this kink, the decay length of density and temperature have similar values of the order of $10cm$, whereas inside it the density decay is considerably steeper ($\lambda \approx 1cm$) than that of the temperature ($\lambda \approx 2cm$). Significant fluctuations were observed in density, temperature and potential, the level of fluctuation in temperature being of the same order as that in the density.

Acknowledgements

This work is partially funded by the UK Department of Trade and Industry.

J. G. Ferreira is partially supported by INPE/SCT and FAPESP, SP, Brazil.

Thanks are given to George Vayakis for his major contributions in setting up the probe system in COMPASS and for many valuable ideas and discussions.

References

[1] **Sykes A** et al, Nuclear Fusion, Vol. 32, No. 4, p.694, 1992.

[2] **Vayakis G**, D.Phil. Thesis, Dept. of Engineering Science, Oxford, 1991.

[3] **Gryaznevich M** et al, this conference.

[4] **Stangeby P C** and **McCracken G M**, Vol. 30, No. 7, p.1225, 1990.

[5] **Erents S K** et al, Nuclear Fusion, Vol. 28, No. 7, p.1209, 1988.

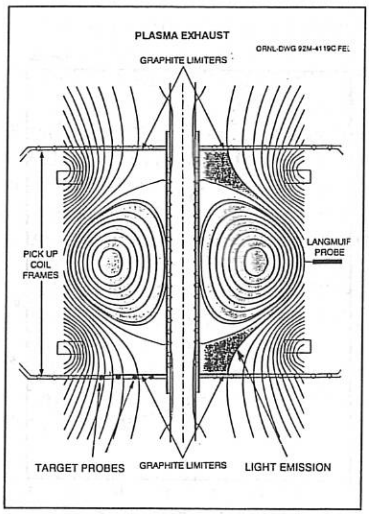

Fig 1: Sketch of START tokamak showing the position of the probes, the magnetic configuration of the compressed plasma and the target plates.

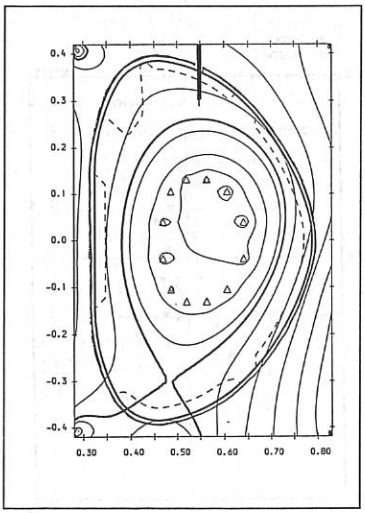

Fig 2 : Single null X-point configuration on COMPASS. The position of approach of the probe is shown at the top.

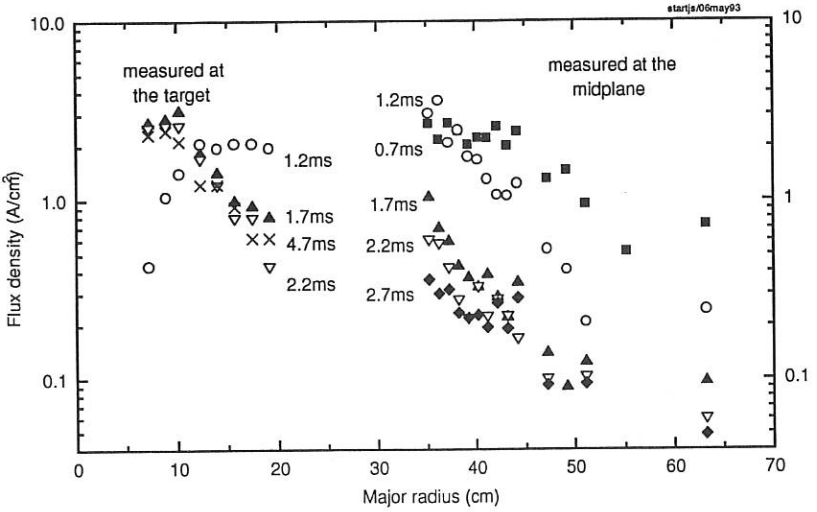

Fig. 3: Time evolution of density profiles measured at the exhaust targets and at the midplane.

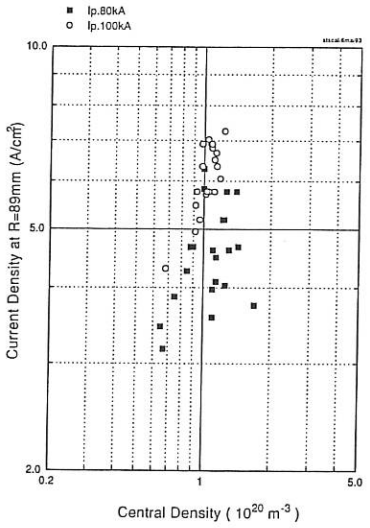

Fig.4: Scaling of edge density with central density in STAF

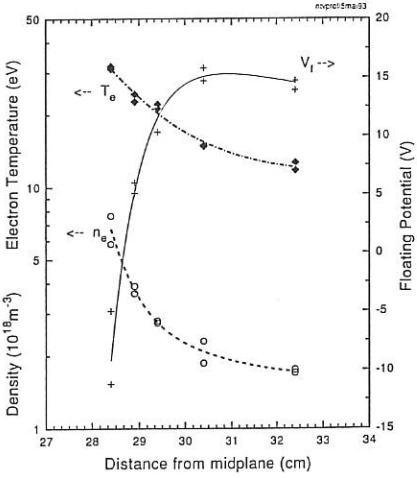

Fig. 5: Plasma density, electron temperature and floating potential profiles in the scrape-off layer of COMPASS.

Measurements with a high resolution pulsed radar reflectometer

S.H. Heijnen, M. de Baar, M.J. van de Pol and C.A.J. Hugenholtz.
FOM-Instituut voor Plasmafysica 'RIJNHUIZEN', Association EURATOM-FOM,
P.O. Box 1207, 3430 BE Nieuwegein, The Netherlands.

At the RTP Tokamak (RTP = Rijnhuizen Tokamak Project) a four-channel pulsed radar diagnostic is under development[1]. Gaussian shaped pulses, with a full width at half maximum (FWHM) of 500 ps, will be transmitted in the O-mode. The time of flight between transmission and receipt of the pulse, after it has been reflected from the critical density layer, will be measured with a resolution of < 70 ps, leading to a spatial resolution of 1 cm. The repetition rate will be $2*10^6$ pulses per second. Since in a pulsed radar system unwanted reflections, e.g. from vacuum breaks, can be separated from reflections from a density layer in the plasma, only one antenna can be used, making the access demands to the tokamak very modest.
One of the goals of this system is to study the possibilities of pulsed radar as a JET divertor diagnostic.

Design of the system

The system can be divided into two sub-systems: transmitter and receiver. The transmitter works at four different frequencies which are switched sequentially in 0.5 µs, and than modulated, see Fig. 1. The four oscillators are IMPATT oscillators of Ukraine making*. The output power is 200 mW at 29 and 33 GHz and 400 mW at 36 and 39 GHz. For switching the frequencies, a single pole four throw (SPFT) PIN-switch** is used. The insertion loss of the SPFT-switch is 3.2 dB. The fast pulse is made using a high speed PIN-modulator. The high speed modulator has a rise time of 450 ps and a fall time of 250 ps. The pulse width is 500 ps, see Fig. 2a. These rise and fall times are measured using a bipolar driving pulse, see Fig. 2b, and are a factor of four faster than when using a monopolar driving pulse as the manufacturer did. The insertion loss of the high speed modulator is 1.5 dB, and the on-off ratio is >30 dB.
Because of the losses in the SPFT-switch and in the modulator, the pulse amplitude is 68 mW at 29 and at 33 GHz, and 135 mW at 36 and 39 GHz.
The receiver consists of four IMPATT oscillators, also of Ukraine making, a SPFT PIN-switch, a mixer, and a detector. The frequencies of the local oscillators are chosen above the transmitter frequencies, to avoid problems of intermodulation and LO to IF isolation of the mixer. The transmitter and receiver SPFT switches are linked in such a way that the IF frequency of the mixer is always 18 GHz. For simplicity, amplifiers are not drawn.

---

* G.P. Ermak, Institute of Radiophysics and Electronics, Academy of Sciences of the Ukraine. Kharkov, Ukraine.

** All microwave components, except for the oscillators, are manufactured by Millitech.

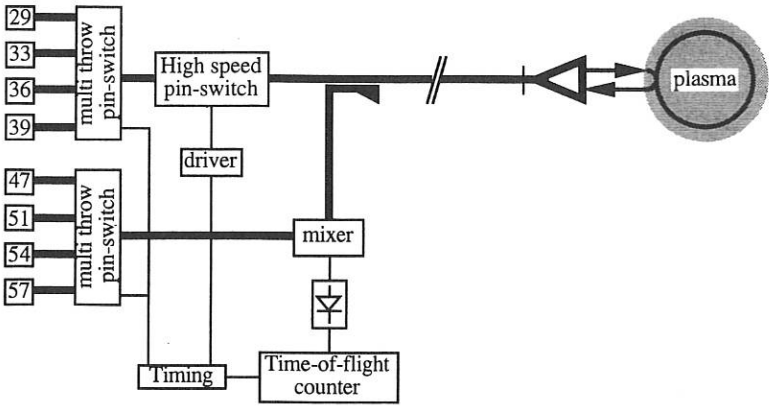

Fig. 1: Schematic representation of the four channel pulsed-radar system for RTP.

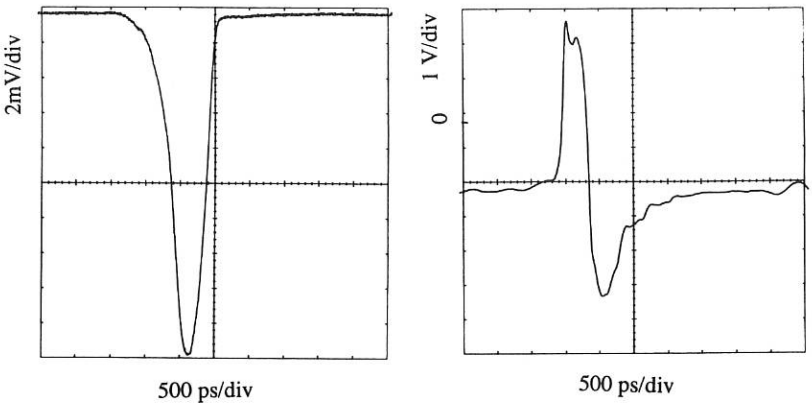

Fig.2: RF pulse, a, as generated by the fast PIN-switch, and driving pulse, b. The RF pulse is measured using a detector (Millitech: DXP-28-00) with a negative output and a sampling oscilloscope (Tectronix: CSA803).

Pulse broadening

The pulse shape will change due to dispersion. This will happen both in the plasma and in the waveguide system. In small tokamaks with high density gradients, like in RTP, pulse shape changes due to the plasma are negligible[2].
The waveguide system consists of two meter single-mode waveguide (Ka-band) and about 30 meters of over-moded waveguide (X-band). The dispersion in the waveguide will broaden the pulse from 500 ps to 660 ps.[3] Half of this broadening happens in the two meter single-mode waveguide. For this reason it was decided not to go to even larger waveguides than X-band.

TOF detection

The time of flight is detected between a reference pulse and a pulse reflecting from the plasma. As a reference pulse, the reflection from the vacuum break is taken. Therefore, on RTP, flight times in the range of one to ten nanoseconds are expected. The resolution in these flight times will be < 70 ps, corresponding to a spatial resolution better than one centimeter, when reflecting from a metal mirror. The repetition rate of the measurements is $2*10^6$ measurements per second. The four sources will be switched sequentially, so a profile can be measured in 2 μs. The combination of repetition rate and accuracy makes it very difficult to find commercially available measuring equipment. Therefore a digital counter system that measures the time between a start and a stop pulse is under development[4]. The system is based on the conventional principle of counting gated clock pulses (see Fig. 3). The resolution of this method is equal to one clock period, due to the ± 1 count ambiguity. The proposed system will employ several parallel counters instead of one single counter. Each counter is driven by the same clock, but phase-shifted. The gates are opened simultaneously during the time interval between the start and the stop pulse. The measured time-of-flight of the pulses will be equal to the average of the output of the counters. This will improve the resolution by a factor equal to the number of counters. The amount of data is reduced by adding the output of the counters. After the addition, data is stored into a memory. For a multichannel radar system data has to be demultiplexed, and synchronization with the multiplexing of the microwave sources has to be included. Other control features are also needed, e.g. if no plasma reflection is detected the gates should be closed and the counters should be reset before the arrival of the next start pulse.

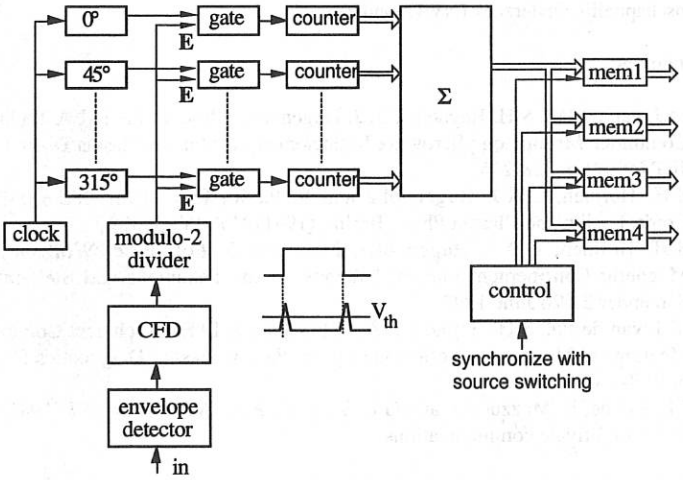

Fig. 3: Time-of-flight measurement with parallel averaging.

Amplitude fluctuations of the reflected pulse will influence the accuracy. If a threshold detector would be used, this amplitude fluctuations would result in unacceptable uncertainties in the time-of-flight measurement. Therefore a Constant Fraction Discriminator (CFD) has to be used. A CFD gives an output pulse of constant amplitude and shape, independent of the input pulse amplitude. The output pulse is generated at the moment the input pulse reaches its Constant Fraction level, which in our case will be at 50%.
It is recognized that due to dispersion in the plasma the pulse will broaden and that the CFD cannot cope with this. As mentioned before, this effect is not expected to play a significant role on RTP. The pulse broadening in the waveguide is not negligible, but as this is constant, the settings of the CFD can be corrected.

Future plans

The first high speed measurements are expected to be performed during May 1993. These measurements will be done at one frequency with a repetition rate of 500 kHz. The complete system will come into operation in September.
Investigations are underway to correct TOF measurements for finite gradient effects. Until now this is commonly done by Abel inversion techniques[5]. It appears that to use neural networks techniques can do a better job[6].

Acknowledgement

This work was performed as part of the research programme of the association agreement of Euratom and the 'Stichting voor Fundamenteel Onderzoek der Materie' (FOM) with financial support from the 'Nederlandse Organisatie voor Wetenschappelijk Onderzoek (NWO) and Euratom.

References:

[1] M.J. van de Pol, S.H. Heynen, C.A.J. Hugenholtz, Proc. of the IAEA Technical Committee Meeting on Microwave Reflectometry for Fusion Plasma Diagnostics, JET (1992) p. 228-235.
[2] S.H. Heijnen, C.A.J. Hugenholtz and P. Pavlo, Proc. 18th EPS Conf. on Contr. Fusion and Plasma Phys., Berlin, (1991) Vol. IV, p. 309.
[3] S.H. Heijnen, C.A.J. Hugenholtz, M.J. van de Pol, Proc. Workshop on Magnetic Confinement Fusion: Diagnostics for Tokamaks and Stellarators, Santander 22-26 June 1992.
[4] M.J. van de Pol, S.H. Heijnen, C.A.J. Hugenholtz, IAEA Technical Committee Meeting on Microwave Reflectometry for Fusion Plasma Diagnostics (1992), p. 228-235.
[5] J.L. Doane, E. Mazzucato, and G.L. Schmidt, Rev. Sci. Instrum. **52** (1981) 12.
[6] P. Pavlo, Private communications.

First results with the visible light tomography system on RTP

L.C. Ingesson, V.V. Pickalov*, A.J.H. Donné and D.C. Schram**

FOM-Instituut voor Plasmafysica 'Rijnhuizen', Association Euratom-FOM,
P.O. Box 1207, 3430 BE Nieuwegein, The Netherlands
*Permanent address: Institute of Theoretical and Applied Mechanics, Novosibirsk 630090, Russia
**Department of Applied Physics, Eindhoven University of Technology, The Netherlands

Introduction

A system for tomography in the wavelength range 300 – 1100 nm has been designed for the Rijnhuizen Tokamak Project (RTP). The plasma is viewed from five directions in one poloidal plane with a total of 80 *pin*-diode detectors. To obtain a sufficiently large number of photons on the detectors and to have a good spatial resolution, an optical imaging system relatively close to the emitting plasma is used to collect the light (Fig. 1). For four of the viewing directions the imaging system consists of two spherical mirrors inside the vacuum vessel; the fifth viewing direction (E) has a lens system outside the vessel. View dumps have been installed on the walls of the vessel opposite to the various detectors to reduce the unwanted background light caused by reflections on the walls. The presence of view dumps is very important as measurements that will be discussed indicate. In front of the mirrors masking apertures have been installed to reduce the effect of reflections on the walls of the ports and to stop light that is not imaged by the mirrors. The electrical system has a large bandwidth (200 kHz) so that fluctuations can be monitored on a microsecond time scale. Different wavelength regions can be selected by optical filtering, e.g. to study H_α- and Z_{eff}-profiles. The system for visible light tomography has been described in more detail in Ref. 1.

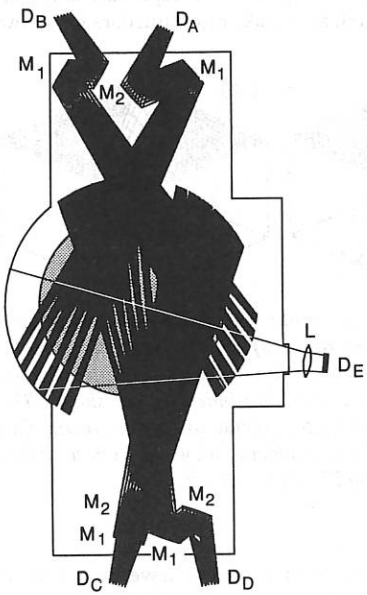

Fig. 1: *The regions seen by the detector elements in the poloidal plane of the plasma (shaded) with respect to the vacuum vessel. The detectors for the different viewing directions are numbered D_A through D_E and for four viewing directions the rays that reach every third detector element are shown. M_1 and M_2 are mirrors. For the fifth viewing direction with a lens (L) only the total region viewed is shown.*

Results of the tomographic inversion method that is being implemented for the system are shown, and measurements with the system in a table-top set-up using known light sources are discussed.

Tomography algorithms

Because of the complexity of the imaging, implementation of the system into commonly used tomography codes is not straightforward. Ray-tracing is used to calculate the contribution of the local emissivities g in the plasma to the power f measured by the various detectors [1]. This can be

expressed in the weight matrix W:

$$f_j = \sum_{i=1}^{N} W_{ji} g_i \quad , \tag{1}$$

where i is the indicator of the N cells in which the poloidal cross-section is divided, and j indicates one of the M detectors. Inversion of Eq. (1) by tomographic techniques gives an approximate emission profile.

Because of the limited number of views of the plasma, the weight matrix is not used directly to obtain a reconstruction from the measurements. Instead, as a first approach, the number of viewing directions and the number of detectors is "increased" by interpolation and smoothing of the measurements. The new interpolated viewing directions can best be chosen to be part of a detection system with parallel beams. This method has been described in Ref. 2. For the smoothing process an iterative procedure was used that includes averaging in a 3×3 window and independent spline smoothing with regularization in two directions. Boundary conditions, such as zero signal for chords looking outside the plasma region and periodicity of the solution were included. The iteration was interrupted when the norm of the residual started to increase.

After the interpolation to parallel beams the signals are used in a regularized scheme of the Filtrated Back Projection (FBP) algorithm [3]. Results for a simulated emissivity profile where information about the actual measuring system has been taken into account are shown in Fig. 2. The result for the visible light tomography system shows oversmoothing, while better results can be obtained by a similar system that is more evenly distributed. To improve the result additional *a priori* information should be included. We plan to add constraints such as energy conservation and other properties of integral projections. It should be stressed that this system was not designed to have an optimal coverage of the plasma, but especially to enable one to study fluctuations at the edge of the plasma as well as to make reconstructions of hollow profiles.

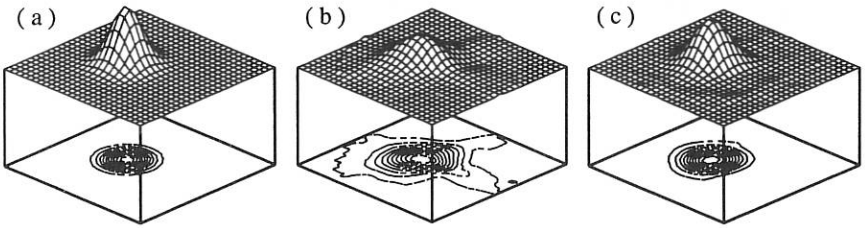

Fig. 2: *Results of tomography of a simulated off-axis circular Gaussian emission profile. Three-dimensional and contour plots of the emission profile (a), the reconstruction for the actual visible light tomography system (b) and the reconstruction for a system with the same number of viewing directions and detectors, but more evenly distributed, (c) are shown. The tomographic reconstructions (b) and (c) were obtained after calculation of the signals that would have been measured by these systems with 3% noise added, followed by interpolation to a parallel beam system with 11 viewing directions and 27 detectors each.*

Table-top measurements

Measurements with the system installed on a dummy tokamak section have been used to evaluate the performance of the hardware and software. Light sources were used to simulate

structures in the plasma region and the signals from all 80 detectors were measured simultaneously. The light sources were elongated in the toroidal direction because the detectors see a slab that is approximately 1.5 cm thick, and two views (B and C, see Fig. 1) are slightly tilted with respect to the poloidal plane. With the set-up we could study the effect of reflections on the walls with and without view dumps, and differences between the measured weight matrix and the calculated one. Also larger light emitting structures were applied to obtain measurements that could be used to investigate the performance of the reconstruction algorithms, but a complicating effect is that for this purpose only optically thick sources could be found (while in the optical wavelength range the plasma is optically thin).

To study the contribution of reflections on the walls to the signals, separate measurements of the background of reflected light and "direct" light are needed. This can be done by measuring the light from a small source: some detectors will see the source directly, while others will only measure the background light. An estimate of the total background light produced by a constant emission profile can be obtained by multiplying the measured background light averaged over all detectors by the number of times that the light source would fit into the plasma. An estimate of the direct light can be obtained by multiplying the signal of the detectors seeing the source by the number of times the source fits into the viewing region. Measurements have been taken with the source in different positions, which yield comparable results. With view dumps the background radiation was just measurable and an upper limit for the contribution of background light to the total signal of 10% is found (possibly partly containing a contribution from noise). Without view dumps (the tokamak walls were simulated by sheets of aluminium) a background level about two to three times as high was observed for the viewing directions with mirrors, while for direction E (with the lens system) it is even more. The absence of the view dumps would therefore have large effects on the interpretation of measurements.

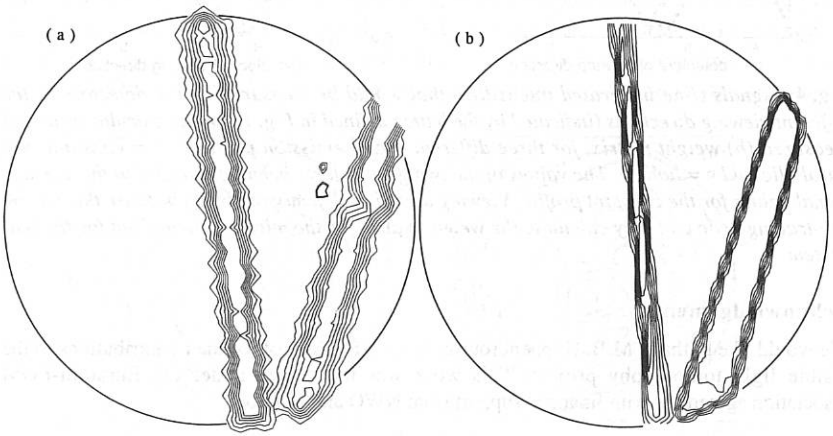

Fig. 3: *Contour plots of the measured (a) and calculated (b) weight-matrix elements for two detectors. The circle represents the plasma boundary (radius 170 mm). The "wobbly" shape and the appearance of local maxima and minima in both (a) and (b) are digitizing effects of the grid [square cells of 14 mm for (a), and 7 mm for (b)] and have no physical significance.*

The weight matrix was measured by using a cylindrical light source with a diameter of 18 mm: the source was moved in a grid in the poloidal plane and for every position the contribution to all detectors was measured. With a source of finite size a slightly smoothed matrix is obtained [Fig. 3(a)] which is quite similar to the calculated one [Fig. 3(b)]. The measured and calculated weight matrices have been used to calculate the signals that would be measured by the detectors for three different emission profiles (Fig. 4). The overall shapes of the curves are quite similar, but some effects still have to be explained. For the measured weight matrix, noise and systematic errors in the measurements, and the possibly not accurately enough known calibration factors, could cause "unsmoothness" in the curves. Errors in the measurements could include inaccuracies in the positioning of the light source, and the fact that the source is a cylindrical surface emitter of finite size while for the calculated weight matrix the average over a volume element is taken. Furthermore: (1) for the calculated case the design positions of the mirrors were taken which differ from the actual positions, (2) the ray-tracing was done for two dimensions while especially for the viewing directions that are tilted out of the poloidal plane (B and C) a three-dimensional calculation is needed, and (3) reflections where no view dump was possible (especially A) and light not imaged by the mirrors reaching the detectors (only in B) are not taken into account in the calculation of the weight matrix.

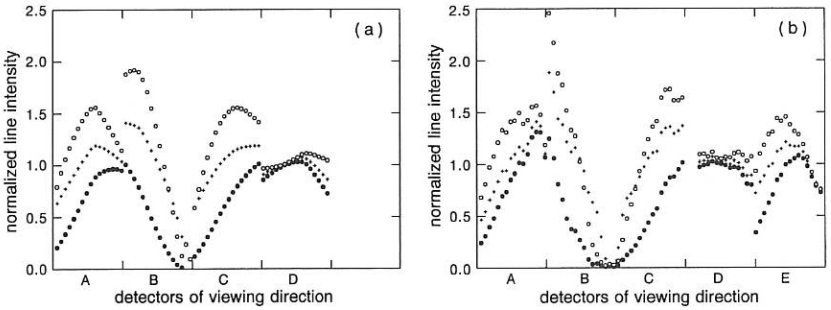

Fig. 4: *Signals (line integrated intensities) that would be measured by the detectors of the different viewing directions (indicated by the letters defined in Fig. 1) for the calculated (a) and measured (b) weight matrix, for three different radial emission profiles: + = constant, • = parabolic and ∘ = hollow. The values of the two graphs have been normalized to the average signal values for the constant profile. Viewing direction E is missing in (a) because the current ray-tracing code can only calculate the weight matrix for the mirror systems, not for the lens system.*

Acknowledgements

We would like to thank M.B. Hoppenbrouwers and G.H. Kolthof for their contributions to the visible light tomography project. This work was performed under the Euratom-FOM association agreement with financial support from NWO and Euratom.

[1] L.C. Ingesson, J.J. Koning, A.J.H. Donné, D.C. Schram, Rev. Sci. Instrum. **63**, 5185 (1992)

[2] V.V. Pickalov, L.C. Ingesson, A.J.H. Donné, D.C. Schram, Proc. 1992 Int. Conf. on Plasma Physics, Innsbruck, Part II, pp. 1143-1146

[3] V.V. Pickalov, T.S. Melnikova, Beitr. Plasmaphysik **24**, 417 (1984)

A SPACE-TIME TOMOGRAPHY ALGORITHM FOR THE FIVE-CAMERA SOFT X-RAY DIAGNOSTIC AT RTP

E.S. LYADINA(*), C.P. TANZI, D.F. DA CRUZ, A.J.H. DONNÉ

FOM-Instituut voor Plasmafysica 'Rijnhuizen'
P.O. Box 1207, 3430 BE Nieuwegein, The Netherlands

(*)On leave from Russian Scientific Center
I.V.Kurchatov Institute, Moscow, Russia

INTRODUCTION

A five-camera soft x-ray with 80 detector channels has been installed on the RTP tokamak [1] with the object of studying MHD processes with a relatively high poloidal mode number (m=4). Numerical tomographic reconstruction algorithms used to reconstruct the plasma emissivity profile are constrained by the characteristics of the system. Especially high poloidal harmonics, which can be resolved due to the high number of cameras, can be strongly distorted by stochastic and systematic errors. Furthermore, small uncertainties in the relative position of the cameras in a multiple camera system can lead to strong artefacts in the reconstruction.

NOISE FILTRATION BY SPACE-TIME TOMOGRAPHY

Elimination of noise can be excellently performed by means of space-time tomography [2]. This method is based on a statistical analysis of the time traces of the spatial expansion coefficients used in the Cormack reconstruction algorithm. Numerical simulations have been performed for the actual RTP five-camera set-up using complex spatial-temporal model profiles. Figure 1 presents the result of a simulation illustrating the advantages of the space-time tomography algorithm above the normally used Cormack algorithm in which the data are treated in separate time slices. Space-time tomography uses an adaptive filter, which effectively suppresses any noise effects in the reconstructed image.

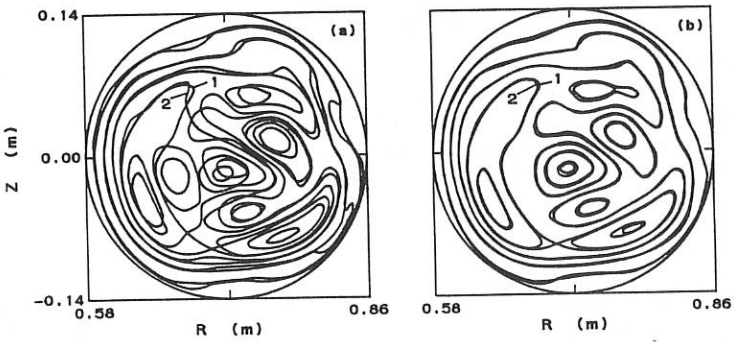

Fig. 1 *Contour plots of model (1) and reconstructed (2) soft x-ray emissivity given by the standard Cormack method (a) and by the space-time tomography method (b), using poloidal modes up to m=4 with 1% added noise.*

ELIMINATION OF SINGULARITIES

Each viewing chord is represented by a point in the p-ϕ [3] diagram (Fig. 2). Because the viewing angle of each camera is large, detectors of other cameras fall within it. This results in coincident lines of sight (i.e. points of intersection in the p-ϕ diagram). Each coincidence leads to a singularity in the reconstruction algorithm and implies that only nine (instead of ten) Fourier components (up to m=4) are available for calculation at the values of p corresponding to these points. The presence of noise and systematic errors (e.g. uncertainties in the alignment of the cameras) gives rise to areas of instability that have a finite spread around the points of intersection. Different methods to eliminate the singularities have been tested. The method which was adopted is based on finding, for each value of p, the two lines which are closest along ϕ (Fig. 2). The data from one of the two lines are omitted and nine Fourier components are calculated for this value of p using data from all other cameras. The same is done again, this time omitting the data of the second line. The average of the two results is used in the reconstruction.

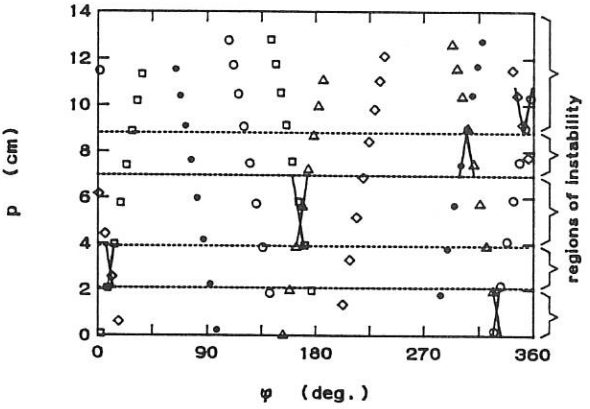

Fig. 2 *Positions in the p-ϕ space of the viewing chords of the soft x-ray detectors at RTP (p is the distance to an origin, ϕ the poloidal angle). The sets of detectors from each of the five cameras form lines of which the intersections are marked by crosses. The crosses indicate near coinciding viewing chords, which, due to noise, cause instability. For each value of p, our method removes the worst instability. Thus, five p intervals can be distinguished.*

REDUCING SYSTEMATIC ERRORS DUE TO UNCERTAINTIES IN CAMERA POSITIONS

The presence of detector elements from different cameras which are looking face-to-face along the same chord also has a fortunate advantage. The signals measured along these overlapping chords should, in first order, yield the same x-ray emissivity. However, if the design positions of the cameras are used, the calculation of the signals in the points of intersection (by means of interpolation of the signals from neighbouring detectors) shows a significant difference (Fig. 3a). This difference is mainly caused by uncertainties in both the spatial arrangement and the calibration of the cameras. Because each camera

has a point of intersection with one or more others, the reduction of the discrepancy between these signals could yield a direct criterion both for reducing the uncertainty on the camera positions and the relative calibration coefficients between cameras. Note that, due to the fan-like arrangement of chords, these coefficients may not be determined by means of normalization of the integral projections to the same value. An optimization program has been developed to deduce the detector positions (displacement and rotation) and calibration coefficients that yield a minimal discrepancy between the signals in the points of intersection. The program includes some regularizing terms, which do not allow camera positions that are unrealistically far from design values. Furthermore, it is possible to incorporate additional information about the alignment of all integral projections for discharges with an almost axially symmetric distribution. The program uses experimental data from several time windows from different discharges, chosen to include some characteristic variations (oscillations, internal and major disruptions, pellet injection). The total amount of experimental data used by the optimization program amounts to 24000 values which give a sufficiently large statistical base for making a reliable decision. Figure 3b presents the signals along the overlapping chords after refining the camera positions and calibration factors. The optimization has resulted in a significant decrease of systematic errors on the inputs of the space-time tomography procedure. An additional system of control detectors providing identical signals can be recommended for elimination of uncertainties in the camera positions in future multi-camera tomography systems.

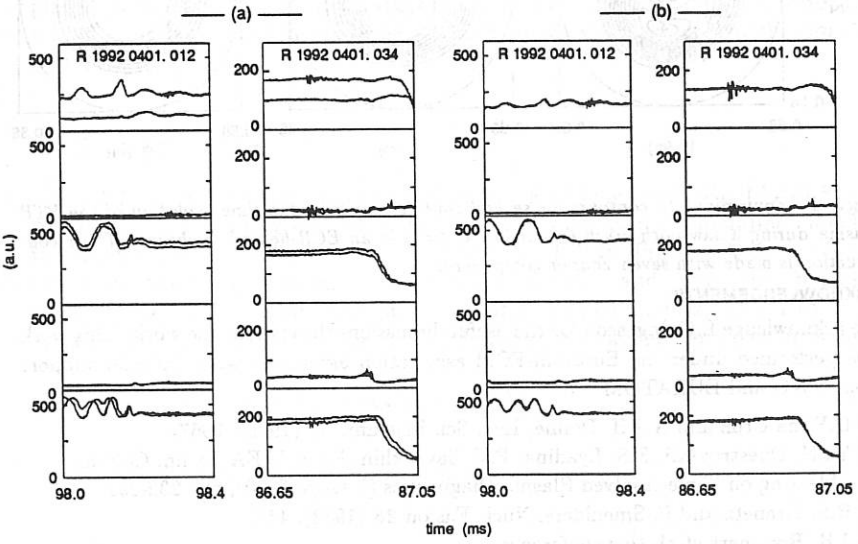

Fig. 3 *Discrepancy between the signals of two different RTP discharges in the five points of intersection before (a) and after (b) the determination of the camera positions.*

RESULTS

The first results of space-time tomography applied to major disruptions on RTP are given in Ref. [4]. In Fig. 4 the time evolution of an ECR-heated RTP plasma during a sawtooth crash is shown. This reconstruction has been made with seven Fourier components (m=3). It shows that the method described here is effective in reducing stochastic and systematic errors which may have caused artificial structures in the reconstructions with the same number of Fourier components from the Tokamak de Varennes [5,6].

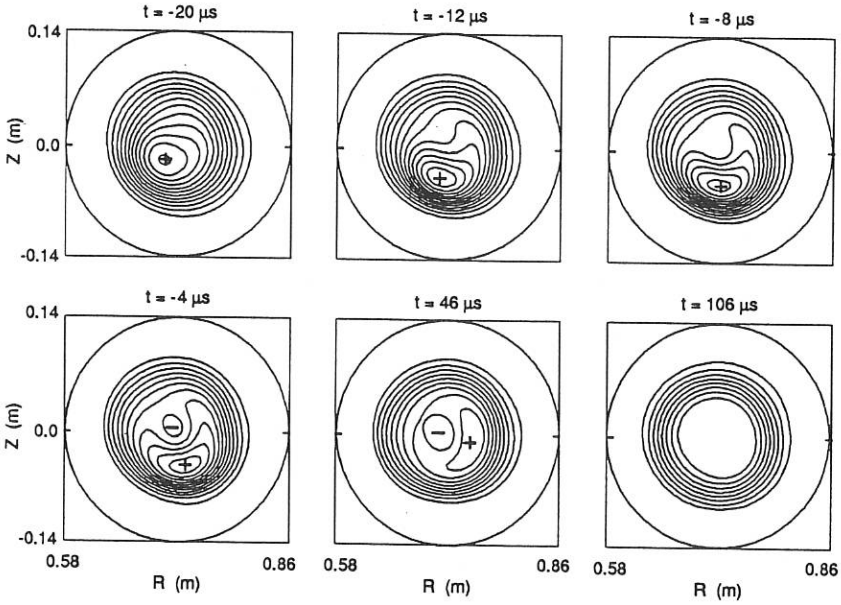

Fig. 4 *Equiemissivity contours for several time frames from the time evolution of the RTP plasma during a sawtooth crash (occurring at t=0) in an ECR-heated discharge. The reconstruction is made with seven Fourier components.*

ACKNOWLEDGEMENTS

We acknowledge L.C. Ingesson for the useful discussions throughout the work. This work was performed under the Euratom-FOM association agreement with financial support from NWO and EURATOM .

[1] D.F. da Cruz and A.J.H. Donné, Rev. Sci. Instrum. **61** (1990), 3067.
[2] Yu.N. Dnestrovskij, E.S. Lyadina, P.V. Savrukhin, Proc. IAEA Techn. Comm. Meeting on Time-resolved Plasma Diagnostics (Nagoya,1990), pp. 232-292.
[3] R.S. Granetz and P. Smeulders, Nucl. Fusion **28** (1988), 457.
[4] J.H. Rommers et al, this conference.
[5] C. Janicki, R. Décoste, and C. Simm, Phys. Rev. Letters **62** (1989), 3038.
[6] C. Janicki et al., Nucl. Fusion **30** (1990), 950.

A Method for Measuring Plasma Position in the Rectangular Tokamak TJ-I

J. Qin, E. Ascasibar, I. Pastor, A.P. Navarro, M.A. Ochando,
M.A. Pedrosa, L. Rodriguez, J. Sanchez and TJ-I team
Asociacion Euratom/CIEMAT-Fusion, 28040 Madrid, Spain.

1. Introduction

Determinations of plasma position in tokamaks are based on measuring the external magnetic field of the plasma current. Usually, the measurements are performed with magnetic coils along a closed contour around the plasma column[1,2], or with small magnetic probes in pairs positioned diametrically[3]. However, such measurements are constrained in TJ-I because of a severe restriction on installing the magnetic probes. It is only possible to install some small magnetic probes inside the vacuum vessel near its top and bottom walls where the limiters stand (see Fig.1).

In this paper an alternative method of measuring plasma position in TJ-I is presented. The plasma position can be derived from the measurements of those magnetic probes located off the equatorial plane, with the aid of a filament model. The method is proved to be reliable, and would be applied to those small-size devices with similar restrictions.

2. Method

TJ-I is a rectangular tokamak with R=30cm and b/a=12.5/9.5cm. Assuming that two pairs of identical magnetic probes installed inside the device are at the positions numbered by 1-4 in Fig.1, which pick up the horizontal components of magnetic fields, and that the plasma column has a vertical and a horizontal displacements, $\Delta_\perp$ and $\Delta_\parallel$, respectively, one can estimate $\Delta_\perp$ and $\Delta_\parallel$ by the power series as follows:

$$\Delta_\perp \approx \alpha_0 + \alpha_1 D_y + \alpha_2 D_y^2 + \alpha_3 D_y^3 ,$$
$$\Delta_\parallel \approx \beta_0 + \beta_1 D_x + \beta_2 D_x^2 + \beta_3 D_x^3 , \qquad (1)$$

where α_i and β_i are the coefficients depending on the plasma displacements, current density profile and the positions of probes, D_y and D_x are the cylindrical approximations (i.e., $R\to\infty$) to $\Delta_\perp$ and $\Delta_\parallel$, respectively. To the first order of ratios $\Delta_\perp/D<1$, $\Delta_\parallel/D<1$ and $A/D<1$ (A and D are two parameters of the probes positions, see Fig.1), we have:

$$D_y = D\,\frac{B_2 - B_4}{B_2 + B_4}$$

$$D_x = \frac{D^2}{2A}\,\frac{B_3 - B_1}{B_3 + B_1} \qquad (2)$$

where B_i(i=1,2,3,4) are the signals of magnetic field of plasma current measured by the corresponding probes. Here we have used a filament current equal to the plasma current.

The coefficients α_i and β_i in Eq.(1) can be given approximately as $\alpha_i=\alpha_i(\Delta_\parallel, D)$ and $\beta_i=\beta_i(\Delta_\perp, D, A)$ obtained from the filament model in which the plasma column current is replaced by a filament current. For example, Table-I shows the coefficients β_i(i=0,1,2,3) obtained as the vertical displacement $\Delta_\perp$ changes between ±3cm for the probes with A=2cm and D=11cm. While for D=10—12cm, only the coefficient α_1 is dominant, others remain so small that can be neglected. Also α_1 is very weakly dependent on the horizontal displacement $\Delta_\parallel$, it can be replaced approximately by the constant equal to that value obtained as $\Delta_\parallel$=2cm, for example, α_1=0.92 for D=11cm. In this case the error bars in the vertical displacements obtained are not larger than 8%, provided the horizontal displacement $\Delta_\parallel$ varies within ±3cm.

Table-I: Coefficients β_i(i=0,1,2,3) in Eq.(1), given A=2cm and D=11cm.

$\Delta_\perp$(cm)	-3.0	-2.5	-2.0	-1.5	-1.0	-0.5	0	0.5	1.0	1.5	2.0	2.5	3.0
β_0	1.06	1.01	0.96	0.91	0.86	0.81	0.76	0.71	0.65	0.60	0.55	0.50	0.45
β_1	1.49	1.39	1.30	1.21	1.11	1.03	0.95	0.87	0.79	0.72	0.64	0.57	0.51
$\beta_2(\times10^{-2})$	4.3	3.9	3.6	3.2	2.9	2.6	2.3	2.1	1.8	1.6	1.4	1.2	1.1
$\beta_3(\times10^{-2})$	1.8	1.6	1.5	1.3	1.2	1.1	0.94	0.83	0.73	0.64	0.56	0.49	0.42

3. Experiments

TJ-I is usually run at B_T=(1.0-1.4)T and I_P=(30-40)kA. The equilibrium position of plasma column in TJ-I is mainly determined by the pre-programmed vertical field and the dc horizontal field. Figure 2 shows one discharge, with the plasma displacements measured by the probes of D=11cm and A=2cm. It can be seen, during the plateau of plasma current, the plasma column stays around the center, with small horizontal and vertical displacements. However, the plasma starts moving inward from ~14ms until the end of discharge, because since then the applied vertical field exceeds the required value, as the plasma current falls faster. The minor radius of plasma column during time evolution is given by: $a_p=\min\{a-|\Delta_{\parallel}|, b_L-|\Delta_{\perp}|\}$, b_L is the limiter radius.

To check the method discussed above, comparative experiments are performed with the multichannel diagnostics of H_α observations[4] and Bolometry[5]. Under steady state conditions, the relative movement of plasma column can be figured out from the different channels of these diagnostics, by means of interactions between the plasma and the wall/limiters. For example, the inner and outer H_α channels observe the plasma column vertically near the inner and outer walls, their signals depend partly on the horizontal displacement $\Delta_{\parallel}$, while the top and bottom bolometers view the plasma column horizontally at the top and bottom limiters, the signals of which are related to the vertical displacement $\Delta_{\perp}$. Figure 3 shows the measured plasma displacements and the H_α observations. As the measured $\Delta_{\parallel}$ has indicated that the plasma column goes outward/inward, it can be found correspondingly the decrease/increase in H_α(in) and the increase/decrease in H_α(out) signals during the same periods. Further, still in this shot (not shown here), the bottom bolometer receives only the background radiation while the top one receives an increasing radiation from ~14ms, in good agreement with the vertical displacement measurement shown in Fig.3, which indicates that the plasma column is displaced upward all the time and further more upward since ~14ms of discharge.

4. Conclusion

In this paper we have shown a method of measuring the plasma position in TJ-I, under some restrictions on installing the probes. The method is simple but proved to be reliable. Although the experimental

data is interpreted by the filament model, the effect of plasma current density profile does not change the results significantly. For example, assuming a quadratic form of current density profile, rather than a filament current, the numerical simulations have shown that the modification on the horizontal displacements is only an inward-shift of less than 0.2cm from those values of filament model.

References

[1] I.P. Shkarofsky, Phys. Fluids 25, 89(1982).

[2] R.J.J. van Heijningen et al., Plasma Phys. 14, 205(1972).

[3] S.V. Mirnov, Plasma Phys. (J. Nucl. Energy, C) 7, 325(1965).

[4] F.L. Tabares, et al., J. Nuclear Materials 176/177, 899(1990).

[5] M.A. Ochando, Diagnostics for Contemporary Fusion Experiments, Varenna 1991 (ed. by P.E. Stott, et al.), p.439, Bologna.

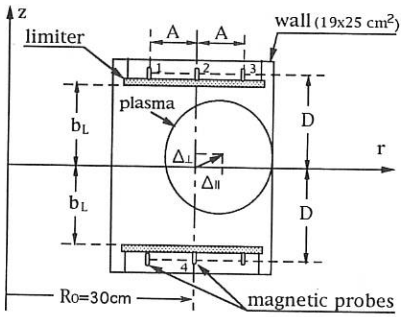

Fig.1 Schematic diagram of experimental arrangements.

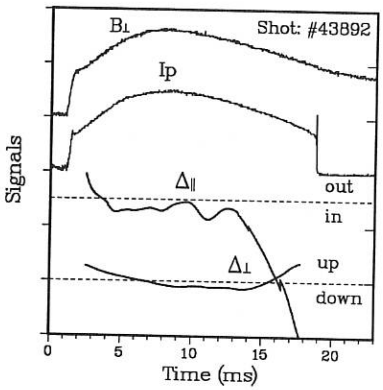

Fig.2 Vertical field $B_\perp$(200G/div), the plasma current I_P(25kA/div), and the measured horizontal and vertical plasma displacements, $\Delta_\parallel$ and $\Delta_\perp$ (2cm/div).

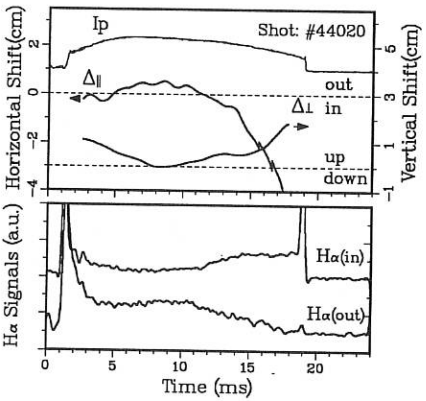

Fig.3 Comparison of the plasma displacements measured with two channels of H_α signals.

Density Profile Measurements by Amplitude Modulation Reflectometry on the TJ-1 Tokamak

E. de la Luna, V. Zhuravlev, B. Brañas, J.Sanchez, T. Estrada.
Asociación EURATOM/CIEMAT, 28040 Madrid, Spain.

J. Segovia , J.L.Oramas
Facultad de Informática, Univ. Politécnica, 28660, Madrid, Spain.

Introduction

Amplitude Modulation (AM) reflectometry has been proposed (1-2) as an alternative method to the more traditional swept frequency reflectometry systems which can be strongly affected by the presence of plasma density fluctuations. Compared to the time domain systems, the time measurements are replaced in AM reflectometry by much simpler phase delay measurements.

In AM reflectometry, the time delay of the microwave beam propagating to the reflecting layer and back is directly obtained through the phase delay of the modulating envelope, which is directly measured in a linear (0-2π) phase meter. This method avoids operation with multifringe counters and is a very attractive alternative for real time determination of the plasma position and density profile.

In order to achieve real time density profile monitoring, fast analysis methods are necessary, first results of Neural Networks application to the problem of fast inversion of the density profile are shown.

Description of the reflectometer

An AM reflectometer, has been developed to measured the density profiles on the TJ-1 tokamak (R=0.3 m, a=0.1 m B< 1.5 T), operating in the 33-50 GHz frequency range, in the extraordinary propagation mode. It uses two separate launching and receiving antennas, overcoming the problems related to the parasitic reflections coming from the vacuum window or other components of the waveguide system.

The system (Ref. 2) uses a modulator working at 232 MHz, this frequency is a compromise between the need for spatial resolution (which requires high modulation frequencies) and the 2π ambiguity which appears when too short modulation wavelengths are used. In order to improve the sensitivity of the measurements, heterodyne detection is used after the first envelope detector, to obtain the phase difference between the modulating envelopes of the launched and received beams. In addition, the use of narrowband band pass filters centered at the last IF (2 MHz) contributes considerably to enhance the signal-to-

noise ratio of the overall system. The advantages and limitations of the method are described in Ref.2.

Several tests have been performed both at the laboratory and at TJ-1. Laboratory tests (Fig.1), using a metallic mirror, show that the mirror distance can be measured with an accuracy of about one centimetre.

For calibrating the waveguide paths, sweeping frequency measurements were taken in absence of plasma (Fig.2), showing the presence of an oscillation in the measured phase caused by the interference of the main reflected signal with a secondary reflection in the chamber (no significant resonances due to the microwave circuits are observed).
Mixing of these two signals, leads to an error in the measured time delay (this effect is especially strong in small tokamaks) which appears as a modulated perturbation. In the presence of plasma, this perturbation can be minimized by averaging over many plasma fluctuations .The averaging is done at the band pass (40 KHz) IF filter used for eliminating fast amplitude modulation of the reflected signal. The value of the phase for the calibration is obtained by minimizing the sums of squares of the differences between the measured values of the phase and the calculated values of the phase knowing the waveguide system length.

Experimental results

Fig.3 shows the temporal evolution of the line integrated density measured by interferometry (3a), the output of the phase detector, which is directly proportional to the time delay $\tau(t)$ (3b) and the amplitude of the reflected signal (3c). The AM reflectometer was operating at fixed frequency (37 GHz, B=1 T) The presence of the cutoff is well identified in these signals. Before the discharge, the time delay has a constant value, which corresponds to the reflection in the opposite wall of the chamber. At t=0 ms the plasma grows up in the chamber, the group index of refraction inside the vessel begins to increase, but the beam is still reflected from the inside wall. At $t \approx 3$ ms the plasma reaches cutoff for this frequency at some radial position. As expected the delay time is always less than that from the inside wall. Moreover, it is clearly seen how the amplitude drops noticeably near cutoff, due to refraction, and then stabilizes when cutoff is achieved. At $t \approx 8$ ms, the density begins to decrease and the time delay begins to increase as the cuttof layer moves radially inwards. The loss of the cutoff as the density falls is marked by the same indications as during the density rise but in reverse. The time delay measured for this signal, is 0.36 ns. (+/- 0.05).

In fixed frequency operation, density profile can be calculated from delay time vs. frequency data $\tau(f)$, varying the input frequency, for a set of reproducible discharges. Fig. 4 shows a reconstructed density profile, using frequencies between 39 GHz and 45 GHz, the corresponding measured time delays vary from 0.3 ns to 0.5 ns. The density profile

obtained is consistent with typical profiles in TJ-1 for this type of discharges (I= 40 kA, B=1 T, $\langle n \rangle = 1.5 * 10^{13}$ cm^{-3}) (Ref. 3).

Neural Networks application

A neural network for reconstructing density profiles has been built. It has been trained using 270 examples from simulation. Several networks for O/X modes and for the different line averaged densities are used.

The net input consists of the time delays corresponding to the different microwave frequencies (33-50 GHz) calculated for TJ-I geometry.There are 35 input points and 100 output points corresponding to n(r).

The net has 160 neurons (35 at the input level , 25 at the hidden level and 100 in the output one). It makes 3750 products (also 3375 summations and 125 hyperbolic tangents). This implies a clear improvement (by about three orders of magnitude) over the classical reconstruction methods.

On fig. 5 two typical examples of original (simulated) and reconstructed density profiles are shown. A high accuracy is achieved. The thick lines correspond to the initial part of the density profile which lies below the lowest cutoff. It can be observed that even this part of the profile is properly reconstructed. According to this results, the N.N. is not only able to provide a faster reconstruction, but also able to solve the problem of the profile initialization. Further tests to confirm this feature in a broader data set are in progress as well as the application of the algorithm to real density profile data taken either form A.M or F.M reflectometry.

Summary

The AM reflectometer for TJ-I is in now in real plasma operation. The evolution of the time delay as well as the type of density profile obtained are consistent with the expected behaviour of the discharge. The results support the consideration of AM reflectometry as a realistic approach.

A Neural Network algorithm has been developed for fast density profile reconstruction, the results offer good accuracy, substantial reduction in the computing time and even an improvement in the profile initialization.

References

(1) V.A. Vershkov, V.A. Zhuravlev, Sov.Phys.Tech.Phys. 32 (5), 523 (1987)

(2) J.Sanchez, et al., Rev. Sci. Instrum. 63 (10), (1992)

(3)C. Pardo and B. Zurro, Report CIEMAT -610. Madrid.(1987)

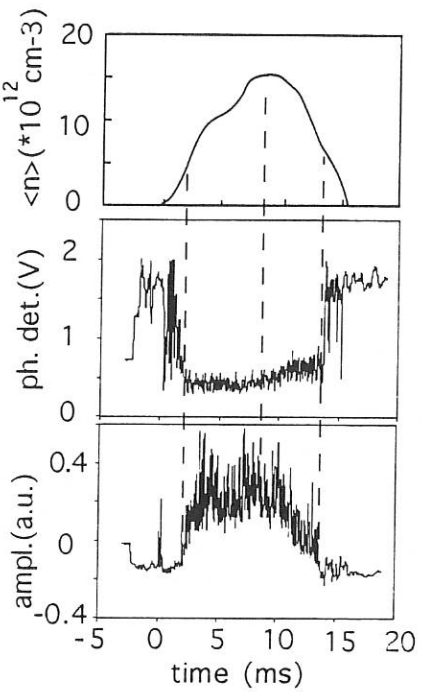

Fig.3. a)Line integrated density, b)output of the phase detector, c)amplitude of the reflected signal

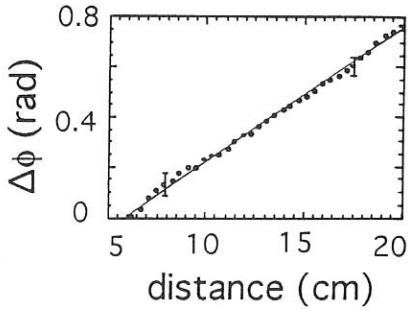

Fig 1. AM reflectometry laboratory test.

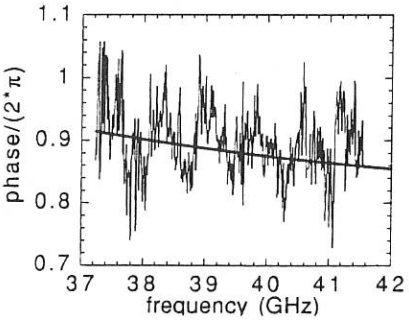

Fig.2. Signal without plasma for calibration

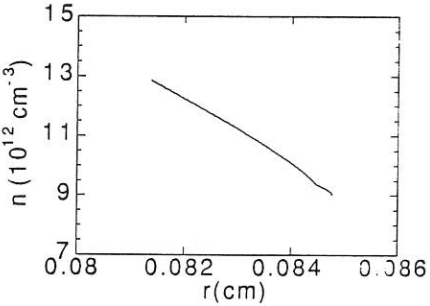

Fig. 4. Density profile reconstruction from AM reflectometry data

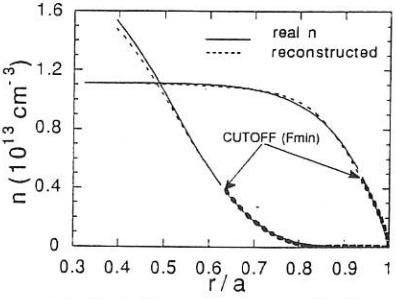

Fig 5. Profile reconstruction by Neural Network algorithm

PERFORMANCE MODELING OF THE THOMSON SCATTERING DIAGNOSTIC FOR THE TOKAMAK ISTTOK

W. van Toledo, D.E. Evans*, M.J. Forrest*, P. Wilcock*, C.A.F. Varandas, M.P. Alonso, J.L. Pinto, and J.A.C. Cabral
Associacão EURATOM/IST, Centro de Fusão Nuclear, 1096 Lisboa Codex, Portugal
*AEA Fusion, Culham, Abingdon, Oxfordshire OX 143 DB, England

1. Diagnostic set-up

A Thomson scattering diagnostic has been installed on the tokamak ISTTOK [1] to make multi-point measurements of electron temperature and density. Time variation of these parameters is obtained with reproducible discharges by firing the laser at different times. The plasma current is about 8 kA, while the central electron temperature and density range from 20 to 300 eV, and from $1x10^{18}$ to $9x10^{18}$ m^{-3}, respectively. Simultaneous measurements along two vertical lines of sight through the tokamak plasma are envisaged, carried out in the conventional way by means of 90° scattering. For that purpose a laserbeam, produced from a 25 J, 25 ns Nd:glass laser (1054 nm), is divided by a beam splitter to provide two beams of equal power passing along two vertical chords (at 5 mm and 60 mm radius) through the plasma. The spatial resolution achieved will be 6 mm per point. The scattered light is relayed by optical fibers to polychromators, one for each chord. Here, narow band optical interference filters separate the light in the blue side of the spectrum into three spectral channels. Detection is by Si avalanche photo diodes situated behind each filter. The polychromators are kept very compact by reducing the number of spectral channels to three, which is considered to be sufficient to establish temperature measurements on a Maxwellian plasma.

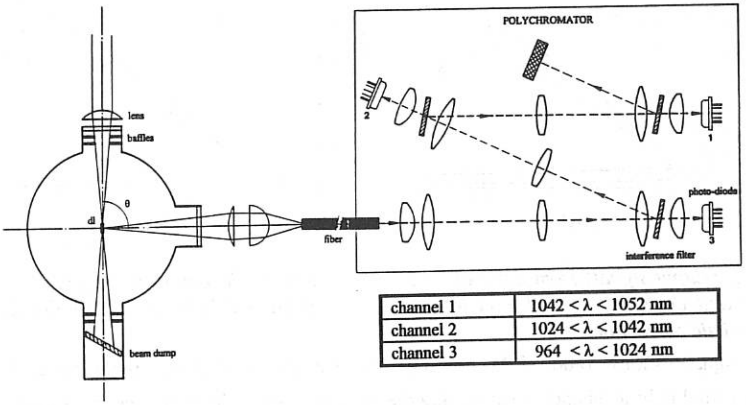

channel 1	$1042 < \lambda < 1052$ nm
channel 2	$1024 < \lambda < 1042$ nm
channel 3	$964 < \lambda < 1024$ nm

Fig. 1. The Thomson scattering diagnostic at ISTTOK.

2. Results from modeling

A numerical simulation has been done for the Thomson scattering diagnostic. For a fixed electron density of 5×10^{18} m^{-3}, the output voltage of each detector is calculated as a function of the electron temperature from

$$V_n(T_e)=\int_{\lambda_{i,n}}^{\lambda_{f,n}}\iiint P_S(T_e,\lambda_S,\theta,\phi)\,\eta(\lambda_S)\rho(\lambda_S)TR_{out}\,d\theta d\phi d\lambda_S, \qquad (1)$$

and is shown in Fig. 2 for r=5 mm. P_S is the scattered Doppler broadened wavelength spectrum [2]. The integration boundaries $\lambda_{i,n}$ and $\lambda_{f,n}$ denote the limits of the spectral sensitivity of the n-th channel (see inset Fig. 1). The polarisation angle, ϕ, is $86^0\pm7.4^0$ for r=60 mm and $115^0\pm7.4^0$ for r=5 mm. The characteristics of the avalanche photodiodes include the effective quantum efficiency $\eta(\lambda)$ and the response function $\rho(\lambda)$. The transmission T through the collection optics, the fiber optics and the interference filters is taken here as 0.5. R_{out} is the 50 Ω output impedance. Combining the output signals as

$$P=(V_2+V_3)/V_1, \qquad (2)$$

we obtain an almost linear relationship with T_e (see Fig. 3). After experimental verification of the parameters in Eq. 1, Fig. 3 can be used as a calibration curve for the temperature determination. The solid curves in Figs. 2 and 3 take into account the relativistic blue-shift [3]. We can conclude that, even for relatively low temperatures, neglecting this effect would lead to an over-estimation of the electron temperature.

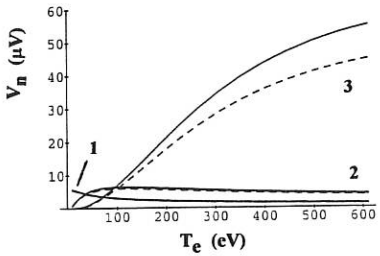

Fig. 2. Output signals from detectors 1-3. Solid and dashed line: with and without relativistic correction.

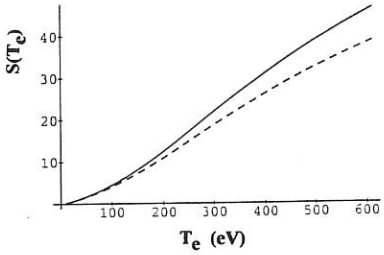

Fig. 3. The calibration curve Solid and dashed lines: see Fig. 2.

The signal-to-noise ratio (S/N, see Fig. 4) was determined by assuming a 2.5% background light level and by calculating the detector noise. The measurement accuracy is then calculated as

$$\Delta V_n=V_n\left((\Delta C)^2+(S/N)^{-2}\right)^{1/2}, \qquad (3)$$

where ΔC refers to an assumed 5% relative error in the calibration of the channel-dependent parameters η,ρ and T (see Eq. 1). Error propagation, using Eq. 2, and $\Delta T/T \approx \Delta P/P$, due to the almost linear relationship between P and T_e, gives the accuracy of T_e determination (see Fig. 5).

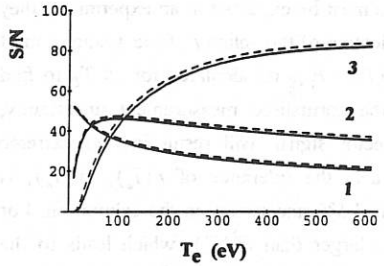

Fig. 4. Signal-to-noise ratio. Solid line: 2.5% background signal included. Dashed line: after correction for background signal.

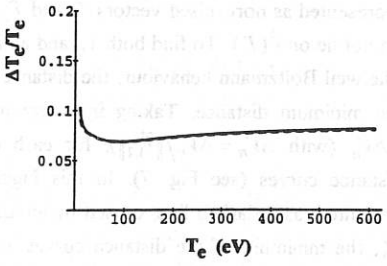

Fig. 5. Relative accuracy of T_e. Solid and dashed line: see Fig. 5.

3. Verification of the Maxwell-Boltzmann behaviour of the plasma

For any plasma condition, a measurement point P (see Eq. 2) always lies on the calibration curve of Fig. 3. However, no information is given as to whether the electron velocity distribution is Maxwellian. If there are deviations from Maxwell-Boltzmann in one or more spectral ranges, an erroneous T_e determination would be the result. To overcome

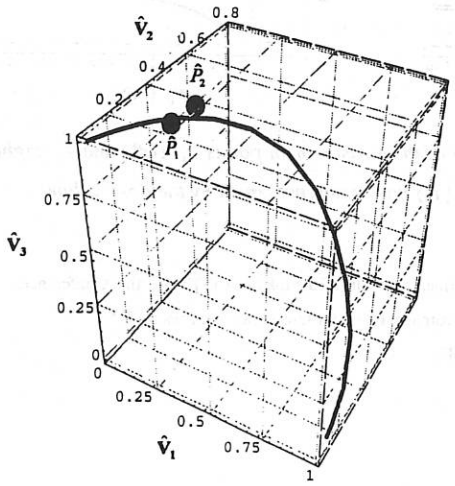

Fig. 6. Representation in 3-D space of the normalised calibration curve $\hat{r}(T_e)$ and two measurement points, $\hat{P}_1$ and $\hat{P}_2$.

this problem, the calibration curve is represented in 3-D space, putting the three output signals along the axes and suppressing the T_e axis (see Fig. 6). To cancel out all parameters which do not depend on the individual channels, the calibration curve is normalised to give $\hat{\vec{r}}(T_e)$. Every point on the curve corresponds to a unique value of T_e. In the graph two simulated measurements, P_1=(3,6,15)(μV) and P_2=(3,15,25)(μV), which are represented as normalised vectors $\hat{\vec{P}}_1$ and $\hat{\vec{P}}_2$. As must be expected in an experiment, they do not lie on $\hat{\vec{r}}(T_e)$. To find both T_e and an indication of the validity of the assumption of Maxwell Boltzmann behaviour, the distance $\|\hat{\vec{r}}(T_e) - \hat{\vec{P}}_{1,2}\|$ is calculated for all T_e to find the minimum distance. Taking into account the normalised measurement uncertainty, $\pm\Delta\hat{V}_n$ (with $\Delta\hat{V}_n = \Delta V_n / \|\vec{P}_{1,2}\|$), for each detector signal, will result in two extreme distance curves (see Fig. 7). In this Figure also the tolerance of $\hat{\vec{r}}(T_e)$, $\delta\hat{\vec{r}}(T_e)$, is presented, as a dashed line, caused by an assumed 5% uncertainty in the calibration. For P_1, the minimum of the distance curves is not larger than $\delta\hat{\vec{r}}(T_e)$, which leads to the conclusion that a Maxwell-Boltzmann distribution is valid here, and that, therefore, the measured temperature of 160 eV is meaningful. This is in contrast to P_2, in which deviations from the Maxwell-Boltzmann distribution are recognised by a minimum distance (at 140 eV) which is larger than $\delta\hat{\vec{r}}(T_e)$. If the temperature would be determined from Fig. 3, then the result would be 130 eV for P_1 and 210 eV for P_2, which shows the necessity of the followed procedure.

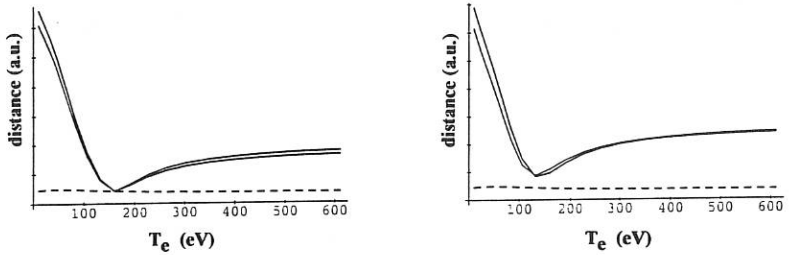

Fig. 7. Distance curves (solid lines) of the measurement points $\hat{\vec{P}}_1$ (left) and $\hat{\vec{P}}_2$ (right) as a function of T_e. The tolerance of $\hat{\vec{r}}(T_e)$ has been represented by the dashed line.

[1] C.A.F. Varandas et al., The first experimental results of the tokamak ISTTOK, this Conference.

[2] J. Sheffield, Plasma Scattering of Electromagnetic Radiation. Academic Press, 1975.

[3] J. Sheffield, Plasma Phys. **14** (1972) 783.

PLASMA STUDY AT T-11M TOKAMAK BY MICROWAVE PULSE RADAR - REFLECTOMETER

V.F.Shevchenko, A.A.Petrov, V,G.Petrov, U.A.Chaplygin

Troitsk Institute of Innovation & Fusion Research ,
142092 , Troitsk , Moscow Region , Russia

Introduction

This work has been performed within the frame of TSP program in order to study global movements and density profile of plasma under adiabatic contraction in the directions of minor and major radii of a tokamak.

The main problem to be solved in this task is to provide absolute measurements of a coordinate of a reflecting plasma layer with high temporal and spatial resolution. At the same time the method applied must be protected against the influence of false reflections and significant amplitude variations of the reflected signal. We believe that these problems should be solved by means of pulse radar reflectometry.

Description of the PRR-System

The basic scheme of the single frequency (32.1 GHz) pulse radar reflectometer (PRR) was used for O-mode measurements on the T11-M tokamak [1].

A number of methods of catching on the signal reflected from the plasma have been tested:

- double fixed threshold method,
- catching on the weight center of the signal,
- riding threshold former [2],
- locking with compensation of amplitude and rise time of the signal.

Apparently riding threshold former is most preferable for

middle sized tokamak due to its short switching time which is of about rise time of analyzing signal.

The reflectometer was linked to the tokamak with a 12 m length double-antenna waveguide system. The attenuation between the microwave generator and detector was about of 40 dB with S/N ratio over 10 dB. The single pulse time resolution was not better than 250 ps in plasma experiments due to low level of S/N ratio. Improvement of reflectometer resolution up to 100 ps (SR = 1.5 cm) has been achieved by means of time interval data averaging.

Experiments on the T-11M tokamak

The main parameters of the T-11M tokamak during these experiments were: tokamak minor radius a_0= 24 cm, plasma minor radius a = 17 cm, major radius R = 70 cm, peak electron density $N_{e,max} < 4.5 * 10^{13}$ cm^{-3} and density rise time of approximately 50 ms. The central magnetic field and plasma current were typically B_0 = 1.1 T, I_p= 70 kA.

As an example of PRR operation on the T-11M tokamak a brief overview of the Shot #4516 is presented on Fig.1. At the initial stage of discharge (12-14 ms) during few milliseconds the pulse radar operates as a double path interferometer, i.e. the time delay is increasing, then after getting the critical density level the signal is inverted and falls down to a minimum value of the time delay (30 ms). After 75 ms PRR also operates in interferometric mode so that its signal depends on integral density along the working chord. The reflectometric mode is revealed in the next time interval, when the PRR measures small values of the time delay. It can be well seen that the perturbations corresponding to MHD harmonics and density fluctuations correlate with the ones on the loop voltage, mean electron density and SXR signals (see 32 ms, 36 ms, 48 ms, etc.). After abruption at the 50th ms the temperature at the center of the plasma has dropped and

despite of the mean density has grown the time delay has also grown. It can be explained by the following: cooling of the central region of the plasma makes the electron density to increase in order to maintain the constant value of pressure n_e*T_e and, consequently the density profile is peaked. So the critical density layer is immersed deeper towards the plasma center. At the end of discharge the short surge of the SXR signal indicates plasma outflux on the wall, which is accompanied by a significant impurity influx and total cooling of the plasma.

Fig.2 illustrates the time evolution of a frequency spectrum of the PRR signal. Such analysis can provide a qualitative information about plasma oscillations. The raw PRR data have been filtered before Fourier analysis with time constant of 0.1 ms in order to avoid an intensive high frequency noise referring to a PRR jitter. The SXR signal shows that sawtooth activity appears between 45 and 65 ms. At the same time the island corresponding to the frequency of about 1 kHz occurs on the spectrum map. A high frequency wing is displayed slightly when sawteeth exist, but after 65 ms conceivably MHD activity develops which has more wide spectrum.

It should be emphasized that SNR in the PRR system is significantly higher (up to 10 times) in the constant current phase of discharge nevertheless the measured time delays scatter on this stage is stronger in comparison to the one for the reflections from the inner wall of the tokamak. Obviously this effect is due to plasma inhomogeneities.

CONCLUSION

First experiments with pulse-radar reflectometer on the T11-M tokamak have shown a feasibility of this method for fusion plasma diagnostics. The measured values of the propagation time delay are in good agreement with a calculated one.

REFERENCES

1. V.F.Shevchenko, A.A.Petrov, V.G.Petrov, Y.A.Chaplygin, Proceedings of VI Conference on Diagnostics of High Temperature Plasma., St. Peterburg, 26-31 May, 1993.

2. E.A. Meleshko. Nanosecond electronics in experimental physics. M., Energoatomizdat, 1987.

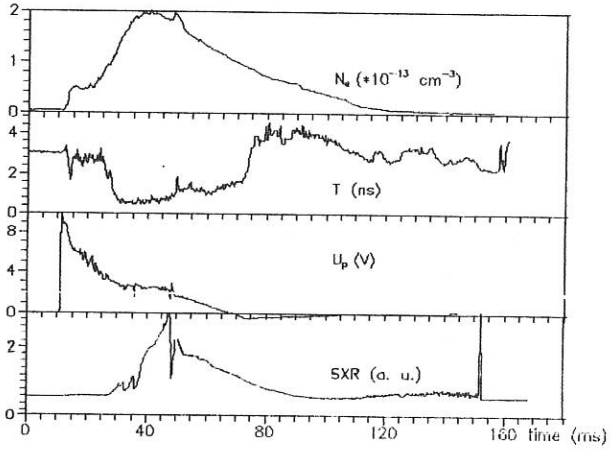

Fig. 1. Shot #4516. Time evolution of mean density N_e, PRR signal T, loop voltage U_p, soft x-ray emissivity SXR.

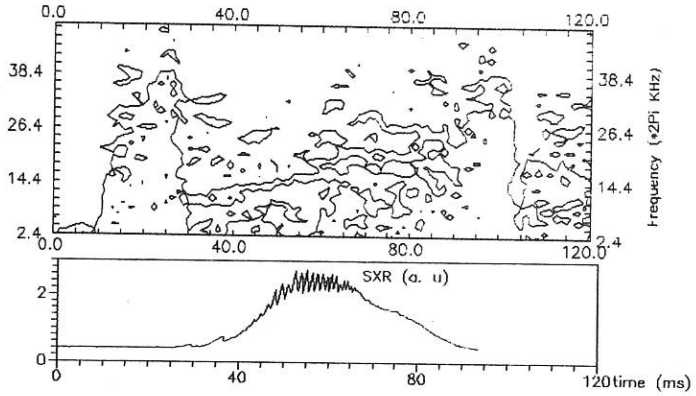

Fig. 2. Shot #4518. Time evolution of frequency spectrum of PRR signal and soft x-ray emissivity.

IMPURITY TRANSPORT STUDIES USING MICROPELLETS.

S. Zoletnik, J.S. Bakos, B. Kardon, S. Kálvin,
G. Kocsis, G. Veres

Department of Plasma Physics
KFKI–Research Institute for Particle and Nuclear Physics
P.O.Box 49, Budapest–114, Hungary, H–1525

Introduction. The investigation of radial transport processes in a tokamak plasma by tracing laser blow–off injected impurities is a widely applied method. Key techniques for such experiments are short pulse injection and good spatial resolution detection of impurity ionic line radiation. The first requirement can be fulfilled by the approximately hundred microsecond pulse length of the blow–off injection technique, while the second technique is usually provided by soft X–ray cameras. As the injected ions become ionized to high degree on a millisecond time scale, they radiate in the energy sensitivity range of the soft X–ray cameras during transport. If one tries to investigate the much faster toroidal transport processes the same way, the situation changes dramatically. The characteristic time scale of toroidal transport phenomena is in the hundred microsecond range, thus the ions get spread around the torus before they become "visible" for the X–ray cameras. The injection pulse length of the blow–off technique is comparable to the transport times, thus the time evolution of the impurity source function may also disturb the measurement.

In previous toroidal transport investigations on the MT–1M tokamak[1] it was shown that microchannel plate(MCP) cameras[2] can be used efficiently to detect the radiation of injected impurities just after the injection. In those experiments the characteristic time scales were determined, and it was shown that at least in the first step of their spreading the ions travel along magnetic field lines[3]. However, the injection pulse length in those experiments (100–300μs) was longer than the time in which the ions travelled around the torus (50μs), thus the injection could be treated rather as continuous than instantenous. To overcome this problem, a new technique has been developed to inject the impurities in the form of micropellets ($d_{pellet} < 100\mu m$) instead of a blow–off beam. The expansion and motion of the ion cloud of such pellets are investigated and presented in this paper.

Micropellet injection technique. The pellets were injected by one of the the blow–off devices of the MT–1M tokamak. Special targets were prepared to inject the material in the form of pellets, rather than a neutral beam. Basically two types of techniques were used. In the first type the pellets were formed in a random fragmentation process of a foil or bulk material (a), while in the second method pre–formed pellets (powder) were accelerated (b).

(a) It is well known that a blow–off beam, especially in the case of thick target layer, containes fragments of the foil. To increase the amount of material injected in the form of pellets, extremely thick targets were used. In the first series of experiments 5.6μm and 16μm aluminium foil was fixed onto the surface of the glass blow–off target plate by a melted 10μm mylar (composition:C,H,O) foil. In the second series, only the above mylar foil was applied. In the third series, the ruby laser was focused on to the surface of the glass plate. Depending on the target type and laser energy density, small fragments with different size and velocity distribution were detected in the tokamak. The range of velocities extended up to 4 km/s.

(b) To define the pellet size, aluminium powder with 60–100μm granule size was fixed

onto the surface of the glass target plate by a thin layer of transparent vinyl acetate (composition:C,H,O) glue. The granules were accelerated by the irradiation to 200–300 m/sec velocity, while the glue was evaporated only around the granules. The size and velocity of the pellets was much more reproducible as in the case of (a), but the velocities remained much lower.

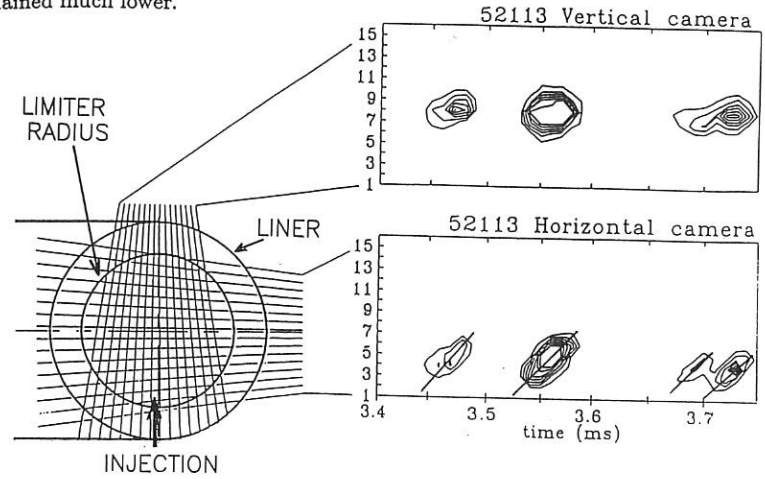

Fig. 1. The arrangement of the two MCP cameras in a poloidal cross–section of the tokamak and a contour plot of the radiation intensity distribution measured by the two cameras. The solid lines represent pellet velocities, calulated from the arrival time.

Detection technique. The radiation of the impurities was detected by two MCP cameras and in some experiments by a monochromator equipped with a photomultiplier. Each camera measured the radiation in a pinhole arrangement along 16 chords. The two cameras were mounted either in one poloidal cross–section of the tokamak (*Fig. 1.*) or in two different cross sections. In this latter case both cameras were mounted in the geometry of the horizontal camera in *Fig. 1.* The MCP detectors in the cameras are sensitive to radiation approximately in the $5eV$–$1keV$ energy interval. Different filters are used at the imaging hole to select the desired measurement energy interval within the above limits. A list of the filters applied in the present experiments along with their energy and wavelength range is shown in *Table 1.*

filter	energy range	wavelength range
Quartz	5–6eV	2000–2500Å
CaF_2 crystal	6–10eV	1200–2000Å
0.2μm C foil	80–300eV	40–150Å

Table 1. Filters used in the MCP cameras during the pellet injection experiments and their associated energy and wavelength intervals.

With the first two filters listed in *Table 1.* the cameras are sensitive to UV radiation. It was shown in previous experiments[1] for aluminium injection, that the cameras equipped with these filters detect mainly the radiation of Al^{2+}, and that this ion can travel only a few centimeters along the magnetic field lines before beeing ionized. As a

consequence, the trajectory of the pellets was determined by detecting the radiation in the UV energy range. *Fig. 1.* shows tracks of a series of small pellets. From the figure one can deduce that the trajectories are vertical straight lines in the poloidal cross section. Pellets with deeper penetration length were also observed in some measurements, but the trajectories were always found to be straight vertical lines.

Transport investigations. The experiments were performed on the MT–1M tokamak (R=40cm, a=12.5cm). The pellets were injected from the downside of the plasma along the vertical central chord of the tokamak. Typical plasma parameters during the experiments were: limiter radius r_{lim}=9cm plasma current I_p=20kA, toroidal induction B_t=1T, line averaged electron density n_e=1-3 $\times$ $10^{19}m^{-3}$.

The transport of ions evaporated from the injected micropellets was observed by using carbon filters in the MCP cameras. It is shown in Ref.[1] for aluminium injection that with this filter the cameras are sensitive to the radiation of Al^{3+} and higher ionization stages. These ions can travel several meters in the tokamak, thus their radiation can be observed at other poloidal cross–sections than that of the injection. *Fig. 2.* shows the result of a measurement with two MCP cameras mounted in two adjacent cross–sections horizontally. In this case a low–velocity aluminium pellet was injected using a blow–off target of type (b). Camera B measured the radiation of low ionization stage ions at the place of injection, while camera A simultaneously measured the radiation of higly ionized ions at a distance of 40 cm from the injection. The radiation of high ionization stages does not appear at the edge of the plasma because of the low electron temperature. The time delay in the appearance of the radiation at the same measurement channel is not more than 10μs, which is the resolution of the measurement system. From this fact one can deduce that the progagation speed of the aluminium ions in the toroidal direction is at least 4 $\times$ $10^4 m/s$. The thermalization time between Al ions and the protons of the hydrogen plasma is much longer than 10μs, thus this velocity cannot be understood if one assumes thermalization of the injected ions to the plasma ion temperature.

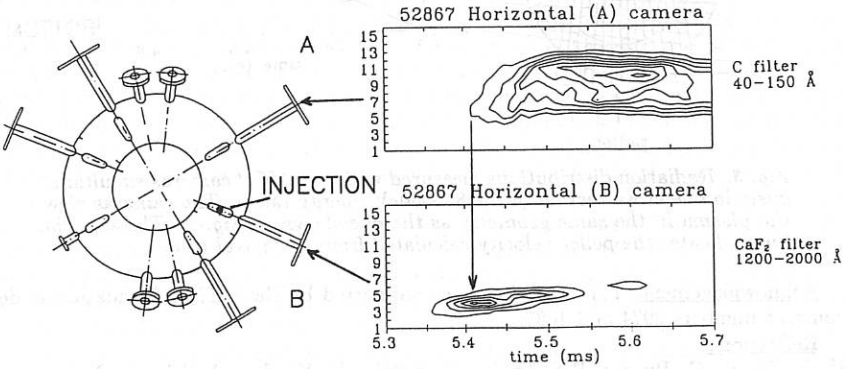

Fig. 2. Radiation distributions measured simultaneously in two cross–sections of the MT–1M tokamak. The pellet entered the plasma at section B. The time of appearance of the radiation at channel 5 is compared. For better understanding the top view of the tokamak chamber is shown. The cameras view the plasma in the same geometry as the horizontal camera in Fig. 1.

The motion of the impurity pellet cloud in one poloidal cross section was investigated by measuring with two MCP cameras located in one cross–section. The results of such a measurement is shown in *Fig. 3.* The calculated pellet velocity is indicated by the straight line. It is clearly seen that the maximum of the radiation intensity distribution shifts from the straight vertical line continuously towards the HFS. Other radiating spots also appear at different places of the cross–section. The characteristic features of this figure (continuous shift towards HFS, second spot at LFS-top) is *reproducible* in different shots and in the case of different pellets. The separate radiating spots are thought to be a consequence of the tail of the pellet cloud extending around the torus and reaching the cross–section of the injection after one toroidal turn. Hovewer, the continous shift in the radiation intensity distribution in the signal of the vertical camera cannot be interpreted this way. To understand this feature one must assume, that the pellet cloud shifts in the poloidal or toroidal direction with a velocity much lower than the velocity of the expansion along field lines. Such slow cross field shift could be attributed to a magnetic or $\mathbf{E}\times\mathbf{B}$ drift or to a drag force excerted on the pellet cloud by the streaming background plasma. The detailes of this process are subject to further examination.

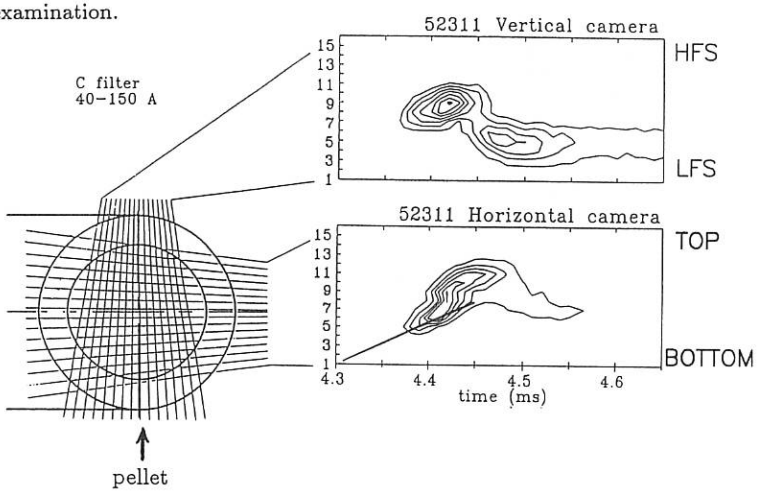

Fig. 3. Radiation distributions measured with two MCP cameras simultaneously in one cross–section in the 80–300eV energy range. The cameras view the plasma in the same geometry as the one shown in Fig. 1. The straight line indicates the pellet velocity calculated from its arrival time.

Acknowledgement. This work has been supported by the OTKA foundation under contract numbers 2974 and 4087.

References.

[1] G. Kocsis, G. Bürger, P.N. Ignácz, S. Kálvin, B. Kardon, J. Szigeti, G. Veres, S. Zoletnik and J.S. Bakos, Plasma Phys. Contr. Fus. 34 1423 (1992)

[2] S. Kálvin, J.S. Bakos, G. Bürger, B. Kardon, G. Petravich and S. Zoletnik, Rev. Sci. Instrum. 60 2857 (1989)

[3] S. Zoletnik, G. Veres, J.S. Bakos, G. Bürger, P.N. Ignácz, B. Kardon, S. Kálvin, G. Kocsis and J. Szigeti, Europhys. Conf. Abstr. 16C (Int. Conf. on Plasma Phys., Innsbruck, 1992), I. 303 (1992)

Determination of the transversal diffusion coefficient, $D_{\perp}^{e}$, from the electron saturation current to a planar Langmuir probe in a strongly magnetized D. C. discharge argon plasma

M. STANOJEVIĆ, M. ČERČEK, T. GYERGYEK,* N. JELIĆ

"J. Stefan" Institute, University of Ljubljana, Jamova 39, P. O. B. 100, 61111 Ljubljana, Slovenia (*T. Gyergyek is also with Faculty of Electrical and Computer Engineering, University of Ljubljana, Tržaška 25, 61111, Ljubljana, Slovenia.)

1 Introduction

In a highly magnetized plasma Langmuir probe makes a strong local perturbation of the plasma, so the values of the plasma parameters derived from the probe current-voltage (I-V) characteristics using the non-$\vec{B}$ theory of current collection by the probe can be significantly incorrect [8]. The theoretical study of Stangeby [5] based on the diffusion model of current collection by a planar surface perpendicular to the magnetic field direction models the complete Langmuir probe characteristic in a strong magnetic field. The expression for electron saturation current collected by the probe contains a number of parameters usually unknown in advance (the ion temperature, T_i, electron parallel-field diffusion coefficient, $D_{\parallel}^{e}$, electron cross-field diffusion coefficient, $D_{\perp}^{e}$), therefore, precise evaluation of the unknown $D_{\perp}^{e}$ from the measured electron saturation current, I_e^s, is practically impossible. In that study, the geometry of the probe, that is its size and shape, is not taken into consideration and the plasma density variation in the effective collection region of the probe is treated very approximately. However, all these effects are important, because in a strongly magnetized plasma even a small probe makes a significant spatial perturbation and in the case of the edge plasma in fusion devices, the probes must be large enough to withstand large particle and heat fluxes in the edge, which, on the other hand, brings stronger perturbation of the local plasma. In spite of the complexity, taking into consideration all these effects and solving the steady state diffusion equation for the plasma presheath with properly chosen boundary conditions, brings the possibility of reducing the number of initially unknown parameters in the expression for the electron saturation current, so $D_{\perp}^{e}$ can be simply determined from the measured characteristics [7]. The applicability of the diffusion model itself is limited by the demand that velocity distributions of the plasma particles are Maxwellian or almost Maxwellian, regardless of the dissipative mechanism for maxwellization. It can be also shown that similar approach may be used for describing net electron and net ion collection and the results can be qualitatively and quantitatively related to the results of some other models. For example, various fluid models of ion flow to a planar surface have shown that net ion collection is practically unaffected by the magnetic field or the nature of the cross-field plasma transport mechanism. Calculations for different planar probe geometries using this model show that the assumption of weak dependence on the cross-field plasma transport mechanism

implies also weak dependence on the probe geometry. Therefore, planar probes with the same effective ion collection area, S_i, which is usually equal to the probe geometrical area, S_{pr}, collect almost the same ion saturation currents despite of their different shapes. Thus, for practical purposes, that is determination of the unperturbed local plasma density, n_0, from the measured ion saturation current to a planar probe, I_i^s, one may use the expression:

$$I_i^s \doteq e\ 0.7\ n_0 \left(\frac{k_B T_e}{m_i}\right)^{1/2} S_i, \tag{1}$$

which is somehow an average value of this and various fluid and kinetic models [6]. Our experiments have shown that $D_\perp^e$ derived from the measured electron saturation currents, I_e^s, using this model, are reproducible and can be easily explained with a simple theoretical model of turbulent plasma transport.

2 Experiments

2.1 Measurements of planar Langmuir probe I-V characteristics in strong magnetic fields

Measurements of I-V characteristics of a circular disc one-sided probe with a radius $R_{pr} = 0.8\ mm$ were made in D. C. discharge argon plasma in a homogeneous magnetic field, in the range of magnetic field densities $B = 0.007 - 0.31\ T$ and on two neutral pressures, $p_n^{(I)} = 0.23\ Pa$ and $p_n^{(II)} = 0.33\ Pa$. The discharge current, I_d, was 0.6 A in both cases, except for $B \leq 0.2\ T$ on the lower neutral pressure, where $I_d \doteq 0.4\ A$. A nonlinear least-squares fit was applied to the portion of the characeristic below the floating potential, $V_{pr} < V_f$, of the form [1, 4]:

$$I = I_i^s \left[\ 1\ -\ \exp(e(V_{pr} - V_f)/k_B T_e)\ \right], \tag{2}$$

where the ion saturation current, I_i^s, and the electron temperature, $k_B T_e$, were chosen as fitting parameters. The unperturbed local plasma density, n_0, was calculated with equation (1). Measured electron temperatures, $k_B T_e$, and plasma densities, n_0, derived from measured ion saturation currents, on two neutral pressures, $p_n^{(I)} = 0.23\ Pa$ ("•") and $p_n^{(II)} = 0.33\ Pa$ ("○"), are presented in figures 1 and 2.

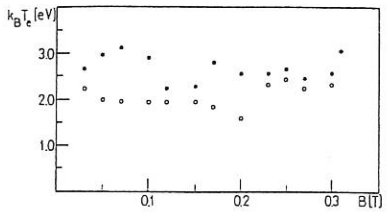

Figure 1: Dependence of the measured electron temperatures, $k_B T_e$, on the magnetic field density, B, on two neutral pressures, $p_n^{(I)} = 0.23\ Pa$ ("•") and $p_n^{(II)} = 0.33\ Pa$ ("○").

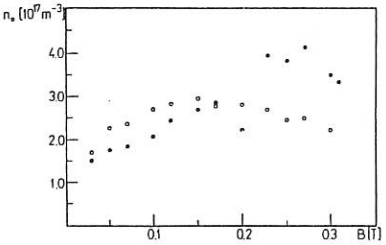

Figure 2: Dependence of the plasma density, n_0, derived from the measured ion saturation current, I_i^s, on the magnetic field density, B, on two neutral pressures, $p_n^{(I)} = 0.23\ Pa$ ("•") and $p_n^{(II)} = 0.33\ Pa$ ("○").

In both cases, the electron temperatures insignificantly depend on the magnetic field density, whereas their dependence on the neutral pressure is more essential ($k_B T_e^{(I)} \doteq 2.5 - 3\ eV$, $k_B T_e^{(II)} \doteq 2 - 2.5\ eV$), that is the electron temperature decreases with the increasing neutral pressure. The plasma density also insignificantly depends on the magnetic field density, which may be an indicator of the anomalous plasma transport. In the classical transport picture, a stronger magnetic field means smaller cross-field diffusion losses of charged particles and consequently, higher plasma density, if there are not any other changes in plasma production and confinement. On the other hand, the plasma density and potential fluctuation levels are generally increased in stronger magnetic fields. Thus, initially "quiescent" plasma (whatever that word might mean) is becoming more turbulent as the magnetic field density is increased. This results in increased charged particles' and heat cross-field losses, that is turbulent transport, which means that stronger magnetic fields do not significantly improve the plasma confinement.

2.2 Evaluation of the transversal diffusion coefficient, $D_\perp^e$, from the measured electron saturation current

Previously mentioned diffusion model gives the following expression for the electron saturation current to a circular disc one-sided probe:

$$I_e^s = -e\,\frac{1}{4}\,n_0\,\overline{c}_e\,S_e\,F_e^s, \tag{3}$$

where $\overline{c}_e = \sqrt{8k_BT_e/(\pi m_e)}$, $S_e \doteq \pi(R_{pr}+\rho_e)^2$ (ρ_e is the electron Larmor radius) and F_e^s is the electron saturation current reduction factor given by:

$$F_e^s = 1 - 4\sum_{j=1}^{\infty}\frac{1}{\zeta_{0j}^2\,(1+\zeta_{0j}^2\,\delta)}, \tag{4}$$

where ζ_{0j} are zeros of the cylindrical Bessel function of the first kind and $\delta = 4\pi z_{ff} D_\perp^e/(\overline{c}_e S_e)$. On both neutral pressures, the dissipative mechanism for maxwellization was predominantly turbulent, so the dimension of the free-fall region near the probe, z_{ff}, was determined by some characteristic spatial scale length of the turbulent plasma state, which is related to the coherence length of the plasma density fluctuations. Thus, assuming $z_{ff} \doteq \rho_s \doteq \sqrt{k_BT_e m_i}/(eB)$, which is the usual spatial scale length for the plasma density fluctuations in strong magnetic fields [2], $D_\perp^e$ can be written as:

$$D_\perp^e \doteq \frac{\delta\ e\ B\ S_e}{\sqrt{2\ \pi^3\ m_e\ m_i}}, \tag{5}$$

where δ can be numerically calculated from the measured F_e^s using equation (4). It is obvious from figure 3 that $D_\perp^e$ calculated with equation (5) are close to corresponding Bohm diffusion coefficients, $D_\perp^B = (1/16)\ k_BT_e/(eB)$, which indicates the turbulent nature of the cross-field charged particles' transport. The results can be summarized as:

$$D_\perp^e = D_\perp^t = \mathcal{K}\frac{k_BT_e}{e\ B}, \tag{6}$$

where $D_\perp^t$ is the turbulent transversal diffusion coefficient and $10^{-3} \leq \mathcal{K} \leq 5\cdot 10^{-2}$. These results can be easily related to the plasma density fluctuation level with a simple theoretical model of turbulent plasma transport [3, 7]. It turns out that $\mathcal{K} \sim \delta n/\langle n\rangle$, so $D_\perp^e \sim (\delta n/\langle n\rangle)\ k_BT_e/(eB)$. This result qualitatively explains the fact that measured plasma density insignificantly increased

with the magnetic field density, because the plasma density fluctuation level, $\delta n/\langle n \rangle$, was increased in stronger magnetic fields, therefore cross-field losses of charged particles caused by the turbulent transport increased, so the magnetic confinement was less effective.

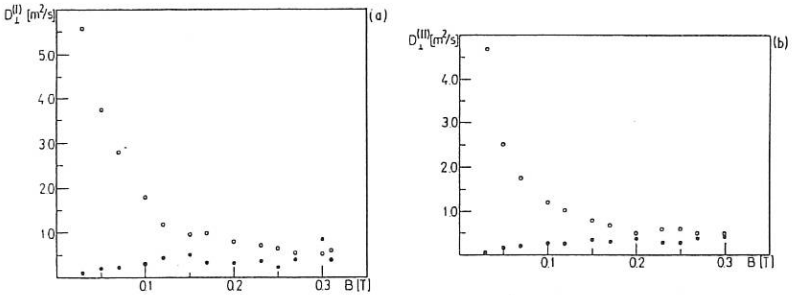

Figure 3: Cross-field diffusion coefficients, $D_\perp^e$ ("•"), calculated with equation (5) and corresponding Bohm diffusion coefficients, $D_\perp^B$ ("o").

3 Conclusion

Presented experimental study of planar Langmuir probe I-V characteristics in magnetized D. C. discharge argon plasma confirmes the possibility of deriving the transversal diffusion coefficient, $D_\perp^e$, from the measured electron saturation current using the diffusion model of current collection by a planar Langmuir probe, if some additional information about the plasma state, such as collisionality, turbulence level, etc., is available. This additional information about the plasma is usually easily obtained, at least by series of measurements of the probe characteristics with varied external parameters of the plasma system, such as, neutral pressure, magnetic field density, plasma heating, etc., as it was presented in this study.

References

[1] S. K. Erents, J. A. Tagle, G. M. McCracken, P. C. Stangeby, and L. DeKock. *Nucl. Fusion*, 26(12):1591–1603, 1986.

[2] P. C. Liewer. *Nucl. Fusion*, 25(5):543–621, 1985.

[3] V. Pericoli-Ridolfini. *Nucl. Fusion*, 31(1):127–135, 1991.

[4] R. A. Pitts and P. C. Stangeby. *Plasma Phys. Contr. Fusion*, 32(13):1237–1248, 1990.

[5] P. C. Stangeby. *J. Phys. D: Appl. Phys.*, 15(6):1007–1029, 1982.

[6] P. C. Stangeby and G. M. McCracken. *Nucl. Fusion*, 30(7):1225–1379, 1990.

[7] M. Stanojević, M. Čerček, T. Gyergyek, and N. Jelić. *submitted to Contr. Plasma Phys.*, 1993.

[8] J. A. Tagle, P. C. Stangeby, and S. K. Erents. *Plasma Phys. Contr. Fusion*, 29(3):297–301, 1987.

MEASUREMENTS OF EDGE FLUCTUATIONS BY PHASE CONTRAST IMAGING ON DIII–D*

S. CODA,†‡ M. PORKOLAB,† K.H. BURRELL, and T.N. CARLSTROM

General Atomics, San Diego, California 92186-9784, U.S.A.

1. INTRODUCTION

A novel imaging diagnostic for the investigation of edge plasma density fluctuations was recently installed on the DIII–D tokamak. The diagnostic, which is based on the Zernike phase contrast method [1–3], was developed in response to the need for spatially resolved, long wavelength fluctuation measurements. Unique features of this system include: large bandwidth (100 MHz), high sensitivity ($\tilde{n}_e \simeq 10^9\,\mathrm{cm}^{-3}$), and absolute calibration capability. Initial results are presented on the fluctuation suppression at the L– to H–mode transition and on the bursts of turbulent activity which occur during ELMs.

2. PHYSICAL PRINCIPLES

A laser beam transmitted by the plasma undergoes a phase shift [3] $\Delta\Phi(x,y) \propto \int n_e(\boldsymbol{r})dz$, where n_e is the electron density and z denotes the direction of propagation. In order to provide a direct spatial mapping of $\int n_e dz$ in the (x,y) plane, two processes are required: the phase information must be transformed into an amplitude variation, and the plasma cross section must be imaged onto a detector array capable of measuring that amplitude. The obvious choice of an imaging Mach-Zender interferometer [4] is limited in sensitivity by mechanical vibrations producing differential phase variations between the reference and the plasma arms. This problem is overcome by the choice of an internal reference interferometer, which offers better sensitivity at the expense of an absolute phase reference. This is adequate when fluctuations, rather than the bulk density, are of interest. In particular, the phase contrast method [1,2] has been shown [5] to have the unique property of creating an amplitude image directly proportional to the phase shift in the object.

The direct spatial representation is very attractive at low wave numbers, where the scale lengths of the modes may become comparable to the characteristic gradient lengths. If desired, the wave number spectrum can always be reconstructed *a posteriori* by spatial Fourier analysis, which can also yield the direction of the phase velocity. The response of the Phase Contrast Imaging (PCI) technique in wave number space (in a direction perpendicular to the direction of propagation of the beam) is essentially flat down to a cutoff value k_c which is approximately equal to 2π divided by the beam

*This is a report of work supported by the U.S. Department of Energy under Contract No. DE-AC03-89ER51114 at General Atomics and Grant No. DE-FG02-91ER54109 at Massachusetts Institute of Technology.

†Department of Physics and Plasma Fusion Center, Massachusetts Institute of Technology, Cambridge, Massachusetts 02139, U.S.A.

‡Present Address: General Atomics.

width. Thus the upper limit on the wavelength is not intrinsic to the technique, rather it is dictated by considerations of machine access.

3. EXPERIMENTAL SETUP

The light source is a 20 W, cw, CO_2 laser ($\lambda_0 = 10.6$ μm). The gaussian beam is expanded to a width of 7.6 cm by a telescope arrangement, and relayed to the DIII–D vacuum vessel by a set of mirrors. The beam enters and then exits the vessel through ZnSe windows, the direction of propagation being vertically downward, near the outer edge of the plasma (Fig. 1). The edge location ensures that the integration length is relatively short, thereby minimizing the limitation represented by the intrinsic lack of vertical resolution. The transmitted beam is then steered to the imaging optics which are located on the optical table that also supports the laser. The total beam path is approximately 10 m long.

The imaging optics consist of the following: a focusing off-axis parabolic mirror, a phase contrast filter ("phase mirror"), and two ZnSe lenses which, together with the paraboloid, form an image of the plasma midplane on the plane of the detectors. The phase mirror is located at the focus of the paraboloid. A feedback stabilization system ensures that the beam is accurately focused on the center of the phase mirror even in the presence of mechanical vibrations. The detector is a 16-element, LN_2-cooled, photovoltaic, HgMnTe linear array. The orientation of the array is generally chosen to coincide with the radial direction in the tokamak, although a toroidal mapping is also possible. The optical magnification is usually selected to project the width of the beam on the length of the array, providing a spacing of 5 mm between adjacent chords. A shorter spacing could be chosen if desired.

The frequency response of the PCI system is determined by the detector, which operates in the band 1 kHz to 100 MHz. The detector signals are processed by low noise preamplifiers, and then filtered and amplified further in the 1 kHz to 1 MHz band (after suitable heterodyne downshifting when high frequency studies are being performed). The resulting low frequency signals are then transmitted to the CAMAC acquisition electronics and digitized at 2 Msamples/sec. The extremely low NEP of the detector is reflected in an unparalleled density sensitivity which, for typical integration lengths, is presently of the order of $10^9\ \mathrm{cm}^{-3}/\mathrm{MHz}^{1/2}$and can be ultimately reduced to $< 10^8\ \mathrm{cm}^{-3}/\mathrm{MHz}^{1/2}$ by modifying the detector bias and reducing the bandwidth to ~ 20 MHz.

The PCI diagnostic can be tested on acoustic and ultrasonic waves propagating in air. Moreover, through the known dependence of the index of refraction of air on its pressure, an absolute calibration of the phase response can be carried out with the aid of a calibrated microphone. The response function in wave number space has also been measured and it has been found to agree with the theoretical one.

4. RESULTS

The PCI diagnostic has been operated in a variety of experimental conditions, and data analysis is currently in progress. The region explored extends from a few cm inside the plasma boundary to well into the scrape-off layer. In an effort to determine the wavelengths and correlation lengths of the fluctuations, the familiar techniques of two-point correlations in the frequency domain have generally been employed. Among

the preliminary results obtained thus far the most striking one is the sharp reduction in the edge fluctuation level observed at the onset of the H–mode of plasma confinement (Fig. 2). This reduction appears to be a universal feature which has long been confirmed by a variety of fluctuation diagnostics [6]. The radial resolution afforded by PCI indicates that the suppression region is localized in the proximity of the separatrix, but a more detailed analysis is needed to place this observation on a quantitative footing.

A second type of event which has displayed consistent features is the ELM. ELMs occur during H–mode and are always accompanied by a transient return to L–mode levels of fluctuations (Fig. 3). ELMs occur on a short time scale. In the case of the so-called type III ELMs, the bursts of fluctuations can occupy a time interval of less than 0.5 msec.

The spectra observed both in L– and in H–mode are generally incoherent and broad band in nature, with short correlation lengths, of the order of 1 cm or less. On occasion, however, coherent modes are detected. A large outwardly propagating wave was observed consistently during the occurrence of type III ELMs, with a frequency of 96 kHz and a wavelength of 4.4 cm. At low frequency (< 20 kHz), large level MHD events are commonly seen, which can be recognized by their simultaneous appearance on magnetic pick-up coils or soft x–ray signals. These phenomena can be remarkably coherent, as coherence values of up to 0.6 (with a 95% confidence level of 0.1) have been measured between PCI and soft x–ray signals.

A detailed and methodic analysis of past data is planned for the near future, along with a dedicated study of the spatial structure of fluctuations at the L– to H–mode transition, which will be carried out through a systematic scan of the plasma boundary position. The absolute amplitude of the fluctuations will also be estimated, using a unique capability of PCI. A multi-point system such as PCI would benefit greatly from time-domain analysis, where the envelope of the time correlation function is studied as a function of the spatial position [7]. An appropriate software package has been recently developed for this type of analysis which is also planned for the near future.

REFERENCES

[1] F. Zernike, Physica **9**, 686, 974 (1942).
[2] H. Weisen, Rev. Sci. Instrum. **59**, 1544 (1988).
[3] S. Coda, M. Porkolab, and T.N. Carlstrom, Rev. Sci. Instrum. **63**, 4974 (1992).
[4] R. Nazikian and L.E. Sharp, Rev. Sci. Instrum. **58**, 2086 (1987).
[5] H. Weisen, Plasma Phys. and Contr. Fusion **28**, 1147 (1986).
[6] K.H. Burrell, T.N. Carlstrom, E.J. Doyle, *et al.*, Plasma Phys. and Contr. Fusion **34**, 1859 (1992).
[7] J.S. Bendat and A.G. Piersol, *Random Data*, (Wiley, New York, 1986).

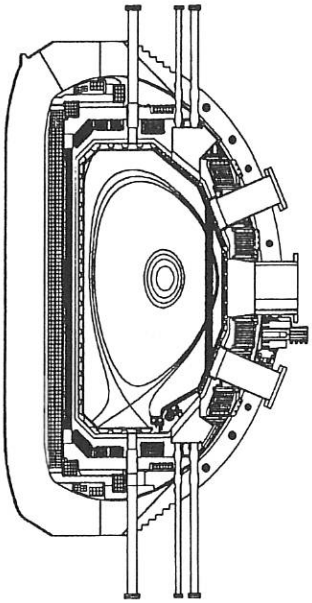

FIG. 1. Cross-section of the DIII–D vessel and laser beam path.

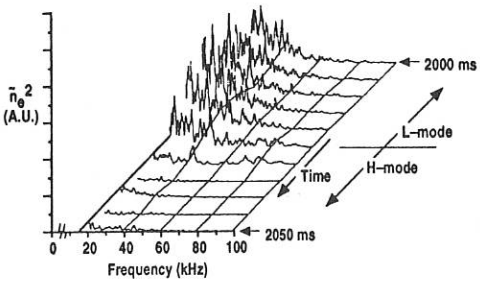

FIG. 2. Time evolution of power spectrum at one spatial location (L– to H–mode transition).

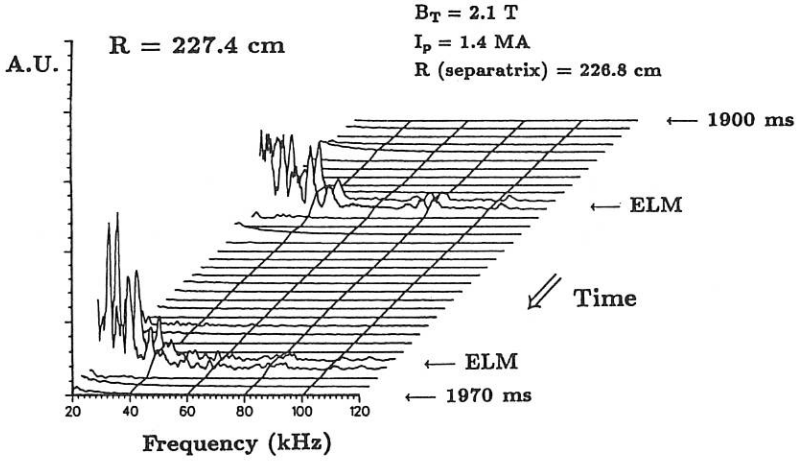

FIG 3. Time evolution of power spectrum at one spatial location (ELMing H–mode).

Initial Operation of the Alpha Charge Exchange Diagnostic Using Impurity Pellet Injection into Deuterium Plasmas on TFTR

S. S. Medley, R. K. Fisher*, A. V. Khudoleev**, D. K. Mansfield, J. M. McChesney*, P. B. Parks*, M. P. Petrov**, C. K. Phillips, A. L. Roquemore, and K. M. Young

Princeton Plasma Physics Laboratory, Princeton, NJ 08543 USA
** General Atomics, San Diego, California 92186 USA*
*** A. F. Ioffe Physical-Technical Institute, St Petersburg, Russia*

Introduction

In a collaboration between General Atomics, the A. F. Ioffe Physical-Technical Institute, and the Princeton Plasma Physics Laboratory, the feasibility of using impurity pellet injection to measure the energy distribution of the fast-confined alpha particles in a reacting plasma [1] is being investigated on TFTR. A small fraction of the alpha particles incident on the pellet ablation cloud will be converted to helium neutrals. In the case of lithium pellets, both double charge exchange ($He^{2+} + Li^{+} \rightarrow He^{o} + Li^{3+}$) and sequential single charge exchange ($He^{2+} + Li^{+} \rightarrow He^{+} + Li^{2+}$ followed by $He^{+} + Li^{+} \rightarrow He^{o} + Li^{2+}$) reactions will result in helium neutrals whose energy is essentially unchanged by the charge transfer process. Interactions with Li^{+} are of special interest because lithium pellets are used to produce beneficial wall conditioning effects on TFTR, the cross sections are relatively large (compared with B or C), and a large spatial region of the cloud is expected to be dominated by this helium-like ionization state of lithium. By measuring the resultant helium neutrals escaping from the plasma using a mass and energy resolving charge exchange analyzer, this technique offers a direct measurement of the energy distribution of the incident high-energy alpha particles. The final goal of the TFTR experiments, of course, is to measure the energy distribution of the 3.5 MeV alpha particles during DT operation.

Experimental Overview

The Alpha Charge Exchange (ACX) diagnostic that has been assembled on TFTR uses a high energy (1 to 3.5 MeV ^{4}He) neutral particle analyzer that was designed and fabricated by the Ioffe Institute and previously used on the JET tokamak [2]. The Ioffe E||B type mass and energy analyzer has eight signal channels with CsI(Tl) or ZnS(Ag) scintillator detectors whose light emission is measured by phototube/amplifier electronics operated in the analog mode with a selectable bandwidth up to 5 MHz. Principal analyzer parameters are: 1) energy range, 0.2-3.5 MeV with a dynamic range of E_{max}/E_{min} of 3.45, 2) energy resolution $3.0 \leq \Delta E/E(\%) \leq 7.1$, and 3) a maximum magnetic field of B=10 kG and electrostatic plate voltage of $V = \pm 20$ kV for detection of 3.5 MeV $^{4}He^{++}$ particles. Further details of the analyzer characteristics have been published elsewhere [2]. The Lithium Impurity Injector (LPI) that was used in conjunction with the analyzer was built by MIT and is capable of injecting Li, B and C pellets. For the experiments reported here, only cylindrical Li pellets with dimensions 1.7 mm Φ x 3 mm L containing ~ 7.3×10^{19} atoms were inject with velocities in the range of 550 ± 150 m/s. Based on this pellet speed and the digitizer time resolution of $\Delta t \sim 20$ μs, the spatial resolution of the pellet ablation cloud radial position is $\Delta r \sim 1$ cm.

A schematic of the ACX diagnostic is given in Fig. 1 and the field-of-view relative to the LPI pellet trajectory is shown in Fig. 2. The LPI axis lies on a major radius of TFTR and the ACX axis makes a selectable oblique angle of 2.75°, 13°, or 18.37° with the LPI axis, to

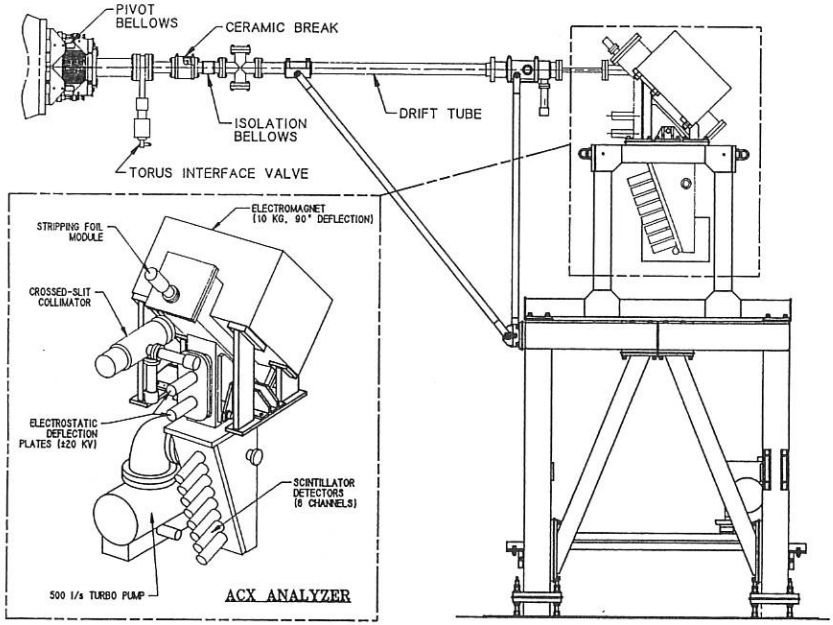

Fig. 1 Schematic of the Alpha Charge Exchange (ACX) diagnostic on TFTR

allow viewing of the cloud at different toroidal distances from the pellet. The ablated lithium leaves the pellet surface as neutrals but quickly ionizes to Li^+ and begins to expand along the magnetic field lines. Further from the pellet, the cloud will become doubly, Li^{2+}, and triply, Li^{3+}, ionized. One of the goals of the TFTR experiments is to confirm that a large spatial region of the cloud is dominated by the helium-like ionization state Li^+, because of the jump in ionization potential to the next higher level. In the work reported here, the ACX was positioned at the 13^o angle which views ~ 15 cm from the pellet at R = 3 m. This position was chosen based on pictures of 5845 A^o line radiation from pellet clouds on TFTR showing Li^+ clouds that extended ~ 30 cm from the pellet. By measuring the neutrals at different distances from the cloud, we hope to confirm a large Li^+ region and justify using a neutralization fraction for alphas incident on a Li^+ target.

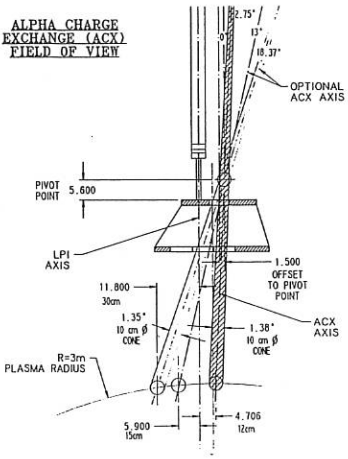

Fig. 2 Layout of the field of view for the Lithium Pellet Injector and the ACX diagnostic.

Results

During D-D operations prior to the D-T phase on TFTR, preliminary experiments were conducted to observe neutrals from the high energy ^{3}He tail produced during ICRF minority heating interacting with the ablation cloud from Li pellets. In the last few weeks of D-D operation of TFTR in the fall of 1992, initial experiments were conducted to observe neutrals from the high energy ^{3}He tail produced during ICRF minority heating interacting with the ablation cloud from Li pellets. During this period, we obtained about 30 shots with ^{3}He heating and lithium pellet injection. Many exhibited some evidence of a ^{3}He neutral signal, but only one tokamak shot, where the pellet penetrated the farthest, showed a neutral signal much larger than the measured background due to visible light from the pellet cloud. This shot is illustrated in Fig. 3, where the pellet penetrated to R = 2.74 m and during the last ~ 150 μs or ~ 9 cm of its travel, resulted in large increase in signal level. The spectum was obtained during the 2.5 s flattop phase of a deuterium discharge having salient parameters as follows: B_T = 4.8 T, I_p = 1.8 MA, R = 2.62 m, a = 0.92 m, $n_e(0) \sim 6 \times 10^{19}$ m^{-3}, and $T_e(0) \sim 2.8$ keV. The RF heating was applied from 3.0 - 4.0 s and reached a launched power of P_{rf} = 2.4 MW, but faulted to 1.1 MW from 3.6 - 4.0 s. The Li pellets were injected at 3.8 s (200 ms after the drop in RF power) and at 3.9 s. The first pellet was used for the ACX data, and a multichord photo diode array for measuring the pellet trajectory showed that this pellet had a velocity of v = 586 m/s and penetrated to R = 2.74 m (87% of the plasma minor radius). Hence the neutral signal was large only when the pellet cloud came within ~ 13 cm of the ICRF resonance layer at R = 2.70 m. Two virtually identical shots were taken, the first with the analyzer fields configured to measure the $^3He^{++}$ ions and the second with the analyzer fields zeroed to obtain a background shot used to correct the raw data for interference of pellet light scattered into the detectors. After correcting for this effect, the residual signal was analyzed using the expression:

$$dN(3He^{++})/dE = 4\pi\Sigma\, dN(3He^{o})/dE$$

$$\Sigma = [F_o(E,L^+)\Gamma(E)\Delta E\omega v_{He} A_{cloud}]^{-1}$$

where $dN(3He^{++})/dE$ is the ion distribution in the plasma in the direction of observation, $dN(3He^{o})/dE$ is the measured signal, $F_o(E,Li^+)$ is the neutral equilibrium fraction for ^{3}He incident on Li, $\Gamma(E)$ and ΔE are the calibrated detection efficiency and channel

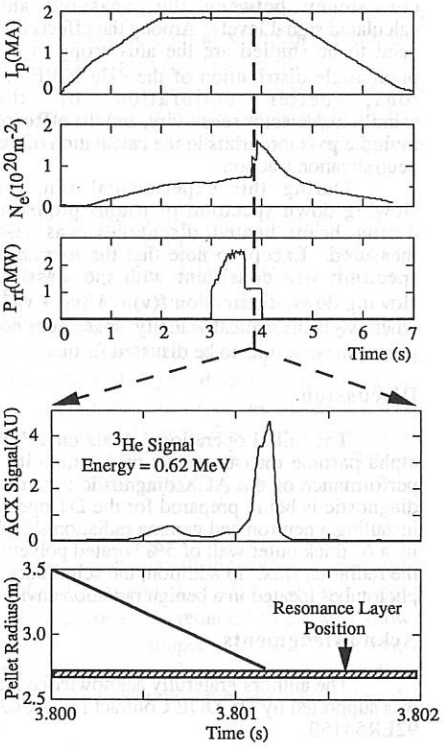

Fig. 3 Selected plasma discharge and ACX signal waveforms during ^{3}He minority heating. Also shown is the pellet position versus time.

energy width of the analyzer, ω is the solid angle of the collimator, v_{He} is the ion velocity and A_{cloud} is the area of the portion of the cloud observed by the analyzer.

The results are shown in Fig. 4 where a straight line fit to the data yields an effective $3He^{++}$ temperature of T_{tail} = 170 keV. The measurement is in favorable agreement with RF code modeling calculations which give an effective tail temperature of 170 - 200 keV. However, the amplitude of the measured signal in this preliminary operation of the ACX is significantly below our initial estimates. More detailed analysis remains to be done to obtain consistency between the measured and calculated signal levels. Among the effects that need to be studied are the anisotropy in the pitch angle distribution of the ^{3}He ICRF tail ions, better calibration of the scintillator/detector sensitivity, and the effect of multiple pass ion orbits in the calculation of the neutralization fraction.

During this experimental run, the slowing down spectrum of tritons produced during beam heated discharges was also measured. Except to note that the measured spectrum was consistent with the classical slowing down distribution $f(v) \sim 1/(v^3 + v_c^3)$ where v_c is the critical velocity, space does not permit these results to be disussed further.

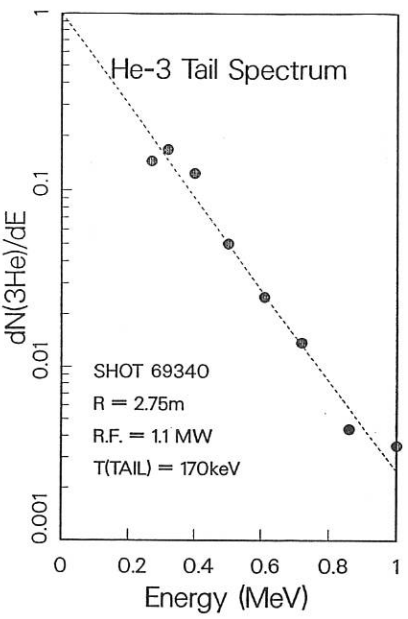

Fig. 4 Measured energy spectrum for the ICRF-generated ^{3}He minority ion tail.

Discussion

The initial operational goals on TFTR, which were to demonstrate the feasibility of alpha particle measurements using impurity pellet injection and to certify operation of the performance of the ACX diagnostic system, have been achieved. At the present time, the diagnostic is being prepared for the DT operating phase of TFTR. This preparation includes installing a neutron and gamma radiation shield consisting of a wall of 4" thick Pb encapsulated in a 6" thick outer wall of 5% borated polyethylene giving approximately 100X attenuation of the radiation flux. In addition, the scintillator light emission will be coupled by fiber optics to phototubes located in a benign radiation environment.

Acknowledgments

The authors gratefully acknowledge the support of the full TFTR group. This work was supported by US DOE Contract DE-AC02-76-CHO-3073 and US DOE Grant DE-FG03-92ER54150.

References

[1] R. K. Fisher, *et al.*, Rev. Sci. Instrum. **63** (10), 4505 (1992).
[2] A. B. Izvozchikov, *et al.*, Jet European Torus Report JET-R(91)12, (1991).

Equilibrium Reconstruction of the Q-Profile in Tokamaks from Motional Stark Effect Data

S. P. Hirshman, D. K. Lee (Oak Ridge National Laboratory)
F. M. Levinton, S. H. Batha (Fusion Physics and Technology)
M. Okabayashi, R. M. Wieland (Princeton Plasma Physics Laboratory)

The motional Stark effect (MSE) diagnostic[1,2] has been implemented on the Tokamak Fusion Test Reactor (TFTR) and the Princeton Beta Experiment (PBX-M) to obtain q-profile measurements in the presence of a finite-β plasma. A multichannel MSE polarimeter system has obtained data for several plasma conditions including L-mode, Supershot, current ramps and high β_p. Accurate measurement of the q-profile is essential for analysis of the equilibrium, stability and transport properties of a tokamak. Many externally observed phenomena, such as sawteeth and the beta collapse, can be analyzed principally in terms of the q and q' (i.e., shear) profiles. Thus, the MSE measurement supplements the standard diagnostic suite of external magnetic probes to provide a new set of *internal profile* data which was previously unavailable. Using the MSE data, together with magnetic probe data, it is possible to obtain a self-consistent equilibrium reconstruction of the q-profile.

Before describing the reconstruction technique, a brief review of the MSE diagnostic will be presented here. The motional Stark effect arises from the electric field induced on a neutral atom (in its rest frame) due to its motion across the tokamak magnetic field ($\boldsymbol{E}=\boldsymbol{V}\times\boldsymbol{B}$). The Stark electric field causes a wavelength splitting and polarization of the emitted radiation in a direction parallel to the local magnetic field. The direction of the linearly polarized radiation provides the basis of the local magnetic field pitch angle measurement. On TFTR, the diagnostic views (on the midplane) one of the deuterium neutral beams ($E_b \approx 90$-120 kV) used for heating the plasma. Due to the good penetration of the neutral beam, coverage from inboard of the magnetic axis to near the outboard edge of the plasma is obtained with a mulit-channel fiber-optic array (at ten radial midplane locations in the plasma). In summary, the MSE measurements on TFTR and PBX-M yield a set of ten magnetic pitch-angles, $\alpha(R_j, Z=0)=\arctan(B_z/B_T)$ taken along the midplane of the tokamak.

In a tokamak plasma, the magnetic pitch is inversely proportional to the local value of $q(\psi)$ through the relation $\tan\alpha = q^{-1}(\psi)(Z_\theta/R)\lambda$. Here, $Z_\theta = \partial Z/\partial\theta$, and $\lambda = \langle\Lambda\rangle/\Lambda$, where $\Lambda = \sqrt{g}/R^2$ depends on the Shafranov shift Δ. For a circular, low β_p plasma, this reduces[3] to the well-known form $\lambda \approx (1+d\Delta/dR)^{-1}$. In general, for either finite β_p or shaped plasmas, a numerical equilibrium reconstruction is necessary to determine the q-profile which accurately reproduces the pitch angle profile data. The theoretical basis and numerical implementation for this reconstruction will now be presented.

The solenoidal magnetic field **B** in a plasma can be expressed in terms of the poloidal flux function ψ as $\boldsymbol{B}=\nabla\varphi\times\nabla\psi+\boldsymbol{B}_T$. Here, the toroidal field is $\boldsymbol{B}_T = F(\psi)\nabla\varphi = q(\psi)\nabla\psi\times\nabla\theta$, where F = RB_T and θ is the poloidal angle. The ideal magnetohydrodynamic (MHD) force balance equation for an isotropic, stationary plasma, $\boldsymbol{F}_{MHD} \equiv \boldsymbol{J}\times\boldsymbol{B} - \nabla p = 0$, reduces to the Grad-Shafranov equation $\Delta^*\psi = -\mu_0 R^2 J\cdot\nabla\varphi$, where the kinetic pressure is p = $p(\psi)$ and the toroidal current density is

$J\cdot\nabla\varphi = p' + FF'/(\mu_0 R^2)$. When an equilibrium is reconstructed from experimental measurements, the heretofore *free* (unconstrained) ideal functions p and q (or F) can be determined to match the data. Typically, this matching procedure is done in a least squares sense[4] to minimize the χ^2 error (where $\chi^2 = \Sigma w_j |data_j - equil.fit_j|^2$, with weights w_j on the various data to reflect the relative experimental uncertainties.

An *iterative* numerical method is needed to perform this data matching because the data are measured in *real space*, whereas the free functions p and q (or F) must be determined in *flux* space. Consider the problem of matching the MSE pitch angle data α_j taken at radii R_j. Using the mapping $\psi(R_j,Z=0)$, one can evaluate the geometric factors which relate $q(\psi_j)$ to α_j, thereby reconstructing the q-profile at the measured points. However, this "updated" q-profile will not, in general, agree with that which was used to determine the original mapping between real and flux space by solving the Grad-Shafranov equation. Thus, one is compelled to repeat this process until the variation in the inferred q-profile from one iteration to the next is less than some prescribed tolerance. Except for the exceptional case when both p′ and FF′ are linear functions of ψ (in which case the toroidal current $J\cdot\nabla\varphi$ reduces to a linear function of ψ), the solution of the Grad-Shafranov equation must be performed numerically at each iteration.

The nonlinearity of the mapping between "measurement space" and "MHD space" is one of two factors which makes the q-profile reconstruction challenging. The other is the radial distribution and sparseness of the data. Although the MSE data generally encircle the magnetic axis (the radius where the pitch angle changes sign), there may not be any observations close to the edge of the plasma. Since the q-profile must be expanded in a set of basis polynomials $q(\psi) = \Sigma q_n T_n(\psi)$ which span the entire interval $\psi = [\psi_{axis}, \psi_{edge}]$, the lack of data near the plasma edge can lead to spurious edge oscillations in reconstructed q (Gibbs' phenomenon), with associated erroneous reversed edge currents. A way to prevent this effect, without shrinking the plasma boundary, is to provide a "phantom" edge MSE point. This is in fact provided by a measurement of the total enclosed toroidal current, which determines the magnetic pitch at the plasma boundary through the relation $I_p = q_{edge}^{-1} \oint g_{\theta\theta}/\sqrt{g}\, d\theta$. The sparseness and experimental uncertainty (0.2° or less) of the MSE angle data can also result in oscillations *between* data points if too many polynomials are used to reconstruct the data. The application of "tension" to minimize the RMS curvature of the $q(\psi)$ fit, which is accomplished by adding a penalty function proportional to $\int (q'')^2$ to χ^2, alleviates this problem.

Since the geometric factor λ, which relates the pitch angle to the local value of q, depends in a complex way on the entire q-profile, it is not possible to find *analytically* the derivative $d\chi^2/dq$ needed, in principal, to optimize the fit to the data. (In least-squares terminology, the coefficient matrix relating the q_n to the data depends itself on the q_n .) However, since λ depends primarily on the q and p through the magnetic axis (Shafranov shift), it is possible to perform a numerical *global* optimization of χ^2 by varying the magnetic axis over a finite interval around the MSE-inferred axis position. In this way, the dominant nonlinearity in the least-squares matching procedure is taken into account.

The three-dimensional Variational Moments Equilibrium Code VMEC[5] has been modified to perform equilibrium reconstruction of q and p profiles from MSE, measured thermal pressure and numerically computed fast-ion beam pressure, and external magnetics data. VMEC is an *inverse equilibrium* solver, in which the cylindrical coordinates (R,Z) are determined from the Grad-Shafranov equation in terms of the flux coordinates (ψ,θ) (with φ an ignorable coordinate in tokamaks): $R(\psi,\theta)=\Sigma R_m(\psi)\cos(m\theta)$, $Z(\psi,\theta)=\Sigma Z_m(\psi)\sin(m\theta)$. VMEC uses a form of the conjugate-gradient (steepest-descent) algorithm to determine by iteration the Fourier coefficients ("moments") of R and Z on a radial mesh which is equally spaced in the toroidal flux. The descent algorithm minimizes the MHD energy and, at completion, satisfies the MHD force balance for the cylindrical components of $\mathbf{F}_{MHD}$, $\mathbf{F}_{MHD}\cdot\nabla R = 0$ and $\mathbf{F}_{MHD}\cdot\nabla Z = 0$. Because $\mathbf{F}_{MHD}$ is evaluated *explicitly* in terms of the R_m and Z_m coefficients (there is no time-consuming *inversion* of the Δ^* operator), each iteration executes rapidly and the several hundred iterations needed to achieve equilibrium consumes typically 10-20 sec. of cpu time on an IBM RISC-6000 workstation (on the CRAY-C machine, the cpu time is reduced by a factor of ten). During the course of these descent iterations, the q and p profiles are changed incrementally to satisfy the evolving *linear* least-squares equations determining the instantaneous data match (recall that the coefficient matrix of the data fit is also evolving due to changing equilibrium state). In this way, the final equilibrium state, together with optimized q and p profiles, are achieved simultaneously.

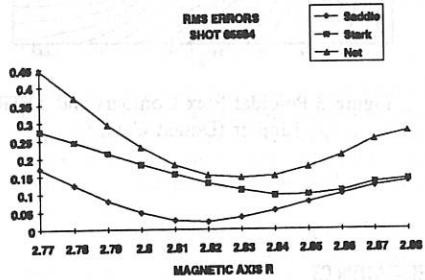

Figure 1

Figure 1 shows the effect that varying the magnetic axis has on the MSE and external magnetic flux (saddle) coil errors for a β_p = 0.75, I_p = 1.38 MA TFTR discharge. Several equilibria were computed at different *fixed* values of magnetic axis. In this case, since the MSE mismatch has a broad and shallow minimum compared with the saddle error, the "optimum" axis position (found by the numerical code) is at R_{opt} = 2.83 m, close to the saddle minimum point (2.82 m).

In addition to matching the MSE data and external magnetic flux loops, the ability to fit the diamagnetic loop measurement has also been incorporated into VMEC. This match is important for determining the total energy content of the plasma. The Shafranov relation[6] $\beta_I = \mu_I + s_I$ is used to express the diamagnetic data μ_I in terms of the VMEC variable $\beta_I \propto \int p\, dV$.

An example of a VMEC equilibrium reconstruction is shown in Figs. 2-3. These are for a high poloidal-beta TFTR current ramp-down shot, with I_p = 490 kA and $\varepsilon\beta_p \approx 1$. The open dots in Fig. 2 depict the MSE pitch angle data vs. midplane radius, and the solid curve is the reconstructed fit. The poloidal flux contours are shown in Fig. 3. The dashed curve is the TFTR limiter, while the confined plasma is bounded by the nearly circular surface inside the separatrix.

In conclusion, a fast numerical implementation of equilibrium reconstruction has been developed which incorporates q-profile information from the MSE diagnostic. Eventual real-time feedback control of the current profile is envisioned for future long-pulse devices (TPX, ITER).

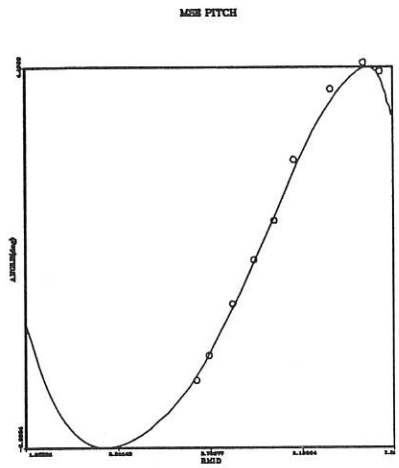

Figure 2 MSE Data (open dots) and reconstruction (solid curve)

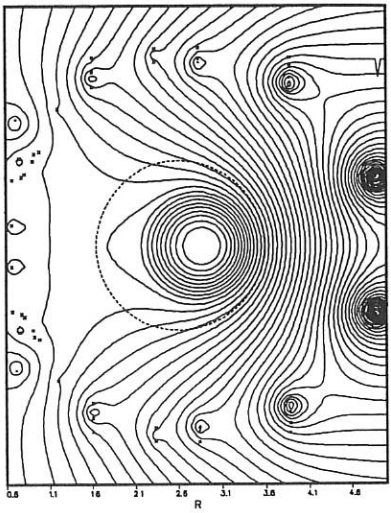

Figure 3 Poloidal Flux Contours and TFTR Limiter (Dotted Curve)

ACKNOWLEDGMENTS

Research sponsored in part by the office of Fusion Energy, U.S. Department of Energy, under contract DE-AC05-84OR21400 with Martin Marietta Energy Systems, Inc. and by Department of Energy contract No. DE-AC02-76-CHO-3073.

REFERENCES

[1]F. M. Levinton, R. J. Fonck, G. M. Gammel, R. Kaita, H. W. Kugel, E. T. Powell, and D. W. Roberts, Phys. Rev. Lett. **63**, 2060 (1989)
[2]F. M. Levinton, Rev. Sci. Instrum. **63**, 5157 (1992).
[3]J. M. Greene, J. L. Johnson, and E. Weimer, Phys. Fluids **14**, 671 (1971).
[4]B. J. Braams, Plasma Physics and Controlled Fusion **33**, 715 (1991).
[5]S. P. Hirshman and D. K. Lee, Comput. Phys. Commun. **39**, 161 (1986).
[6]V. D. Shafranov, Plasma Physics **13**, 757 (1971).

Langmuir Probe Measurement of Fluctuations in the Edge Plasma of Tokamak de Varennes

H. Y. W. Tsui[+], A. J. Wootton[+], and the TdeV team

[+]Fusion Research Center, The University of Texas at Austin, Austin, Texas 78712, USA

Centre canadien de fusion magnetique, Varennes, Quebec, J3X 1S1, Canada

Introduction

Plasma turbulence in the edge of Tokamak de Varennes (TdeV) [1] is characterized using a fast reciprocating probe system [2]. The 5-pin Langmuir probe array [3] provides simultaneous and local measurements of steady-state and fluctuating electron temperature, density, and plasma potential, as well as turbulence-induced fluxes. Much experimental evidence exists to indicate that fluctuation-driven fluxes dominate particle and energy transport in the edge of tokamaks as well as other toroidal devices [4]. However, the turbulence drive mechanisms are yet to be identified. Edge magnetic configuration differs between a divertor and a limiter tokamak. By comparing data from TdeV (with a divertor) and from TEXT (with a limiter) we hope to identify any effects caused by the separatrix configuration of TdeV.

Edge Plasma Behaviour

The TdeV device has a major radius of 0.87 m and a double-null axisymmetric divertor with closed divertor chambers. The reciprocating Langmuir probe is mounted on a top-port and is inserted vertically at R = 0.87 m into the plasma. Between the separatrix and r = 29 cm the probe is connected to the outboard divertor plate with a typical connection length of 1 m. At r > 29 cm the probe is connected to the outboard screening protective limiter with a length roughly 30 cm.

A velocity shear layer is observed near the separatrix, which is nominally located at r_s = 27 cm. The layer, characterized by a reversal of the propagation of the turbulence, has been observed near the separatrix in ASDEX [5]. Profile measurements of the power weighted phase velocity of the turbulence V_{ph} and the floating potential φ_{fl} in discharges having I_ϕ = 150 kA, B_ϕ = 1.4 T, and $\bar{n}_e = 2.5 \times 10^{19}$ m^{-3} are shown in fig. 1. Also plotted is the **ExB** rotation V_{ExB} obtained from the plasma potential using $\varphi_{pl} = \varphi_{fl} + \alpha T_e$ with $\alpha = 3$. In these discharges the velocity shear layer, where V_{ph} and V_{ExB} change rapidly, is about 1 cm wide and located outside the separatrix and has a phase velocity inversion point (i.e. $V_{ph} = 0$) at 27.4 cm. It is expected that the level of shear rate, dV_{ExB}/dr ($\approx dV_{ph}/dr$) ~ 10^5 s^{-1}, can introduce shear de-correlation. Within the shear layer, both the spectral width σ_k and σ_k/k were found to increase by some 20-40%. This impliesan increase in spatial de-correlation. A comparison of V_{ph} with V_{ExB} shows that the propagation of the turbulence in the plasma frame is in the ion diamagnetic drift direction in the scrape-off layer (SOL); a result different from that of tokamak TEXT. However, the coefficient α depends on many plasma parameters such as impurity mix, which may be different between machines. We note that there is a 5 mm difference in the location of rapid change in V_{ph} and V_{ExB}. In the experiment, it was also observed that the location of the shear layer shifts inward in discharges with higher plasma current. In the 210 kA discharges the phase velocity inversion point is at 26.5 cm and the layer, still having a width of about 1 cm, now extends across the separatrix. In these discharges, the propagation of the turbulence in the plasma frame is in the electron diamagnetic drift direction just outside the separatrix ($r \geq r_s$) and changes to the ion diamagnetic drift direction at $r \geq 28.5$ cm.

Fig. 2 shows the profiles of electron temperature T_e and density n_e and the corresponding normalized rms fluctuation amplitudes obtained from discharges with $I_\phi = 150$ kA, $B_\phi = 1.4$ T, and $\bar{n}_e = 2.5 \times 10^{19}$ m^{-3}. The profile of T_e is approximately exponential over a 5 cm range outside the separatrix while the profile of n_e can be described as exponential only for a small region close to the separatrix. The n_e profile is almost flat for $r \geq 28$ cm. Near the separatrix i.e. at $r \approx r_s$, the scalelengths for T_e and n_e are comparable (~ 2 cm) indicating that electron energy loss is principally convective. Further away, the density scalelength L_n is much longer than the electron temperature scalelength L_{Te}. The flattening of n_e profile at $r \geq 28$ cm suggests that either the presence of a significant level of ionization or a very large effective diffusion coefficient (i.e. $D \rightarrow \infty$). Significant plasma source may be expected from the close proximity to a protective limiter when $r > 29$ cm. In contrast, profile measurements in TEXT show that T_e profile tends to flatten in the SOL away from the last-closed flux surface (LCFS) and that typically $L_{Te} \geq L_n$ in that region. Using the equilibrium parameters at 27 cm (Table 1), the particle flux according to the simple SOL estimate is $\Gamma_{SOL} \approx n_e c_s \lambda / (2L_c) = 4 \times 10^{20}$ m^{-2}s^{-1} where $\lambda^{-1} = L_n^{-1} + 0.5 L_{Te}^{-1}$ and the connection length is taken to be $L_c = 5$ m. This value is consistent with the fluctuation-driven particle flux $\Gamma_{\tilde{n}\tilde{E}} = 5 \pm 1 \times 10^{20}$ m^{-2}s^{-1} derived from a cross-correlation between the fluctuations $\tilde{n}$ and $\tilde{E}_\perp$. The SOL estimate, however, departs from the measured $\Gamma_{\tilde{n}\tilde{E}}$ at $r \geq 28.5$ cm. Such departure is consistent with the idea that significant local plasma source exists at $r \geq 28$ cm. Near the separatrix the amplitude ordering of $|\tilde{T}_e|/T_e \approx 0.5\ |\tilde{n}|/n$, is similar to that observed in the edge plasma of TEXT. Further into the SOL, $|\tilde{T}_e|/T_e$ becomes comparable to or larger than $|\tilde{n}|/n$. In TEXT, $|\tilde{T}_e|/T_e$ is typically smaller than $|\tilde{n}|/n$.

Comparison between a divertor and a limiter SOL plasma

Table 1 summarizes the edge parameters near $r = r_s$ in TdeV and in TEXT where r_s is the separatrix or the LCFS. Near r_s, the effective diffusion coefficient $D = \Gamma L_n / n$ in TdeV is almost a factor of 3 smaller than that in TEXT, implying that the magnetic topology of a separatrix or a divertor improves particle confinement. In both devices, the values of L_n/L_{Te} (≈ 1) near $r \approx r_s$ indicating that convection is more effective than conduction for electron energy transport. Other differences in the equilibrium and fluctuation parameters exist when $r > r_s$. The ratio $\eta_e = L_n/L_{Te}$ is much larger than 1 in TdeV and $\eta_e \leq 1$ in TEXT. The ordering of fluctuation amplitude ($|\tilde{T}_e|/T_e \geq |\tilde{n}|/n$ in TdeV and $|\tilde{T}_e|/T_e < |\tilde{n}|/n$ in TEXT) suggests that different principal turbulence drives prevail in the divertor and in the limiter SOL plasmas. In particular, $|\tilde{T}_e|/T_e \geq |\tilde{n}|/n$ may indicate the prevalence of impurity radiation driven turbulence [6,7]. In both devices, the amplitude ordering of $|\tilde{T}_e|/T_e$ and $|\tilde{n}|/n$ is consistent with the expected difference in η_e for turbulence in the hydrodynamic regime [7], namely $|\tilde{T}_e|/T_e > |\tilde{n}|/n$ when $\eta_e > 1$.

Conclusions

A velocity shear layer, of width about 1 cm and located near the separatrix, is found in the divertor plasmas of TdeV. Varying the plasma current can change the location but not the width of the shear layer. Fluctuation-driven particle flux plays an important role in the particle transport near the separatrix.

A comparison between a divertor and a limiter edge plasma indicates that the magnetic topology of separatrix or a divertor has better edge confinement. Significant differences in the

characteristics of the turbulence have also been found in the far scrape-off-layer indicating that the principal turbulence drives could be different.

Acknowledgments

This work is supported by the Centre canadien de fusion magnetique with funds from AECL, Hydro-Quebec and INRS. The data analysis is performed under USDOE grant DE-FG05-88ER-53295.

References

[1] Décoste, R., Bolton, R., Couture, P., in Controlled Fusion and Plasma Physics (Proc. 18th Eur. Conf. Berlin, 1991) Vol 15C, Part I, p.141.

[2] Ritz, Ch. P., Tsui, H. Y. W., Rhodes, T. L., Bengtson, R. D., Lin, H., Wootton, A. J., Rev. Sci. Instr. **61** (1990) 2998.

[3] Tsui, H. Y. W., Bengtson, R. D., Li, G. X., Lin, H., Meier, M., Ritz, Ch. P., Wootton, A. J., Rev. Sci. Instrum. **63**, 4608 (1992).

[4] Tsui, H. Y. W., et al, J. Nucl. Mater. **196-198**, 794 (1992); Wootton, A. J., Tsui, H. Y. W., and Prager, S., Plamsa Physics and Controlled Fusion **34** (1992) 2023.

[5] Niedermeyer, H., Carlson, A., Endler, M., Giannone, L., Rudyj, A., Theimer, G., and the ASDEX-Team, in Controlled Fusion and Plasma Physics (Proc. 18th Eur. Conf. Berlin, 1991) Vol 15C, Part I, p.301.

[6] Ware, A. S., Diamond, P. H., Carreras, B. A., Leboeuf, J.-N., and Lee, D. K., Phys. Fluids B **4** (1992) 102.

[7] Beer, M. A. and Hahm, T. S., Phys. Fluids B **4** (1992) 2567.

	TdeV I_ϕ = 210kA $\bar{n}_e$=2.5x10^{19}m^{-3}	TEXT I_ϕ = 200kA $\bar{n}_e$=2x10^{19} m^{-3}
B (T)	1.4	2
q	3.4	3.3
n (10^{18} m^{-3})	3.5	2
T_e (eV)	25	30
L_n (cm)	2	3
L_{Te} (cm)	2	3.5
$k_\perp$ (cm^{-1})	2	2.5
$k_\perp \rho_s$	0.1	0.1
$\lvert\tilde{n}\rvert/n$	0.2-0.3	0.1-0.2
$\lvert\tilde{T}_e\rvert/T_e$	0.1-0.2	0.05-0.1
$\lvert\tilde{\varphi}_{pl}\rvert/T_e$	0.3-0.4	0.3-0.4
Γ (10^{20}m^{-2}s^{-1})	5	5
D (m^{-2}s^{-1})	3	8

Table 1: Edge Plasma Parameters at $r \approx r_s$ in TEXT and TdeV where r_s is the separatrix or the last-closed-flux surface.

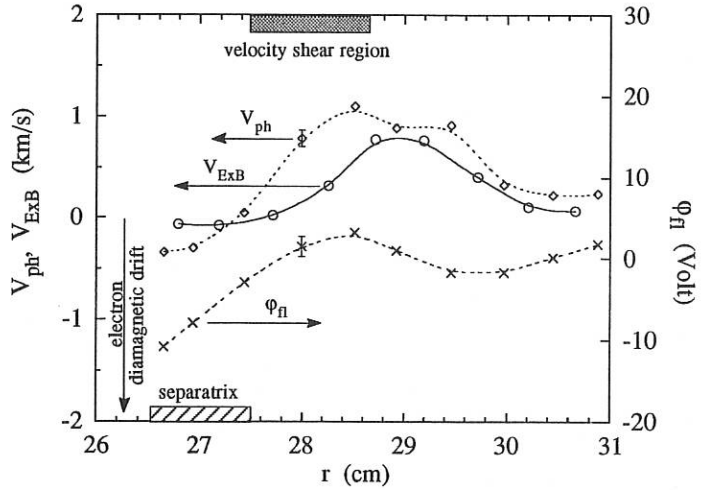

Fig. 1 Profiles of floating potential φ_{fl}, phase velocity V_{ph}, and **ExB** velocity V_{ExB} in TdeV.

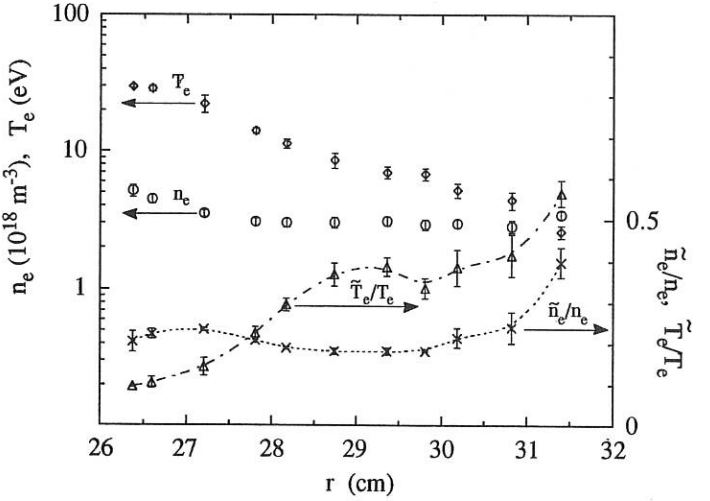

Fig. 2 Edge profiles of electron temperature and density and their normalized rms fluctuation levels. In the SOL of TdeV plasmas, density scalelength can be large and that $|\tilde{T}_e|/T_e$ can become comparable or larger than $|\tilde{n}|/n$.

Te and ne profiles on JFT-2M plasma with the highest spatial resolution TV Thomson scattering system

Toshihiko Yamauchi and TVTS team
Japan Atomic Energy Research Institute, Naka-machi, Naka-gun, Ibaraki-ken,Japan

§1. Introduction

A high spatial resolution TV Thomson scattering system was constructed on JFT-2M tokamak[1]. This system is similar to those used at PBX-M and TFTR[2]. These systems are providing complete profiles of *Te* and *ne* at a single time during a plasma discharge.

The characteristics of JFT-2M TVTS are as follows: 1.Measured points are composed of not only 81 points for the scattered light and plasma light, whose time difference is 2ms, but also 10 points for plasma light measured at the same time with scattered light. 2.Spatial resolution is 0.86cm, which is higher than any other Thomson scattering system. 3.Sensitivity of detector composed of image intensifier tubes and CCD is as high as that of photomultiplier tube.

Te and *ne* profiles have been measured over one year on JFT-2M. The line-averaged electron density measured was in the region of $5x10^{12}cm^{-3}$- $7x10^{13}cm^{-3}$ and the measured electron temperature was in the region of 50eV-1.2KeV.

§2. Overview of TVTS

TVTS is shown schematically in Fig.1. A ruby laser producing about 20J in 20ns with 0.25mrad beam divergence is focussed to below 3mm diameter over the 70cm measurement region in the horizontal mid-plane of the plasma. The image plane in the central region of 70cm are shown in a photo in Fig.2. A piece of images in a photo corresponds to one measured point. The laser beam is terminated in a beam dump designed to minimize stray laser light. A 6m long beam tube places the window at a point where the beam size is 25mm. The light scattered from the beam is collected from an f:6 cone and imaged at f:1.75, using a Bouwers concentric catadioptric mirror system [3], onto an array of 81 fiber optic bundles each of which measures 0.9x2.25mm. These bundles are then rearranged from the 0.9x191 mm input to 2.25x72.9mm at the input to the spectrometer. In addition to the data channels, ten additional channels located parallel to the beam image provide data on the plasma light and stray laser light. A relay lens then expands this image onto the input slit of the spectrometer. A simple Littrow spectrometer is used to minimize the scattering of stray laser light and the formation of secondary images by reflection. A field lens at the image plane focuses the light onto a camera lens which images the spatially resolved spectra onto the face of an 80mm diameter gateable image intensifier tube. This tube demagnifies the image of scattered signal from 80mm to 18mm within a gate duration of 120ns triggered by laser trigger spark gap. A second image intensifier tube provides further gain and further demagnifies the image from 18mm to 11mm. This image is fiber-optically coupled to a cooled CCD at -30°C. The data from the CCD are digitized and temporarily stored in the personal computer used to control the camera. The data are then passed to a Vax station 3500 to calculate Te and

ne profiles.

§3. Comparison of scattered signal with 13-point system and others

The sensitivity of the system can be compared with the 13-point system previously used on JFT-2M whose profiles are shown in Fig.3 [4]. The effective length of scattered light is 0.75-0.8cm/point which is a half length of 13-point system as described in Tab.1. The effective solid angle of scattering light collection is 2.2×10^{-2}rad and the optical transmittance is 6-8%. The detector sensitivity consisting of the image intensifier tubes and CCD is 3-10 counts/photoelectron(pe). These are similar to 13-point system [5]. The laser energy is 15 J, which is 4 times larger than 13-point system. Therefore, it is understood that the scattered signal of TVTS is 2 times larger than that of 13-point system.

On the other hand, a comparison to the PPPL TVTS systems [2] is described in Tab.1 as well as follows; The optics collects 36 % more light than the TFTR system and 10% more than the PBX-M system.

The sensitivity of the JFT-2M detectors is better than that of the PPPL ICCD detectors, but the phosphors on the anodes of two image intensifiers introduce pulse height distribution noise. The shape of the spectral sensitivity curves are very similar for both types of detector.

Table 1 Comparison of Thomson Scattering System

	detector	spatial point of profile	spatial resolution	measured length	laser energy	scale/channel
13point TS	PM	13	5.0 cm	1.7 cm	3-5 J	large
JFT-2M TVTS	II+CCD	81	0.86	0.78	15-20	compact
PPPL-TVTS	ICCD	55(PBX-M)/76(TFTR)	1.1 / 2.2-3.9	1.1 / 2.2-3.9	15-20	compact

3.1 Estimate of signal to noise ratio

The total signal includes the dark noise, stray light signal, plasma light signal and real scattered signal. For the JFT-2M system, the fluctuation of dark noise is about 1 count/pixel in the CCD temperature range of -28°C ～ -32°C (normally 30±1°C). The stray light signal is below 4 count/pixel with a high-pass filter [6]. The plasma light signal is 2-3 counts/pixel except for the signal from special point such as divertor. The S/N ratio is 18 ,determined from the real scattered signals in the red end of the spectrum which is 60 counts/pixel, the white plate calibration data 3 counts/pe and the noise of photon statistics. The contour of real scattered signal is shown in Fig.4(a). The signal of H α spectral line is excluded with a mask placed on the output image of simple Littrow type spectrometer. The vertical cross section of the contour is shown in Fig.4(b). *Te* and *ne* profiles are calculated with these scattered signals.

§4. Te and ne profiles on JFT-2M plasma

20 spectral channels out are used for the estimation of *Te* and *ne*. Figure 4 shows the scattered signals at 20 wavelength with the fitted curve at the plasma center. The error of *Te* in Fig.5 is about 5% and *ne* is 4%. The figures 6(a) and (b) show *Te* and *ne* profiles in an H-mode plasma and its pressure profile, respectively. In this H-mode, the temperature pedestal and sharp gradient at the edge profile are observed and the flat density profile and sharp gradient at the edge are also observed Figure 7 shows the profiles during ECH at ne=0.9x10^{13}cm^{-3}. These profiles measured with one shot of JFT-2M discharges, show a large improvement compared to the capabilities of 13-point system as shown in Fig.3 [4,5,7].These profiles give detailed gradients of *Te*, *ne* and *Pe*, which are very essential to estimate the χ_e and the ballooning parameter.

Acknowledgement

The high spatial resolution TVTS was developed in a collaboration with PPPL for two years. I would like to express my gratitude to Dr.K.Young in PPPL, Dr.H.Maeda in JAERI for their valuable support and Dr.D.Dimock who was TVTS project leader in PPPL.

References

[1]T.Yamauchi et al; Jpn. J. Appl. Phys. **31** (1992) 2255.
[2]N.Bretz et al; Appl. Opt. **17** (1978) 192.
[3]D.Johnson et al;Rev. Sci. Instrum. **56** (1985) 1015.
[4]T.Yamauchi, R.Neufeld and T.Ogawa;Jpn.At.En.Res.Inst. JAERI-M**89-104**(1989).
[5]T.Yamauchi and I.Yanagisawa;Appl.Opt. **24**(1985) 700.
[6]T.Yamauchi and D.Dimock;Jpn. J Appl.Phys. **29** (1990) 1345.
[7]T.Yamauchi et al;Physics Letters A **131**(1988) 301.

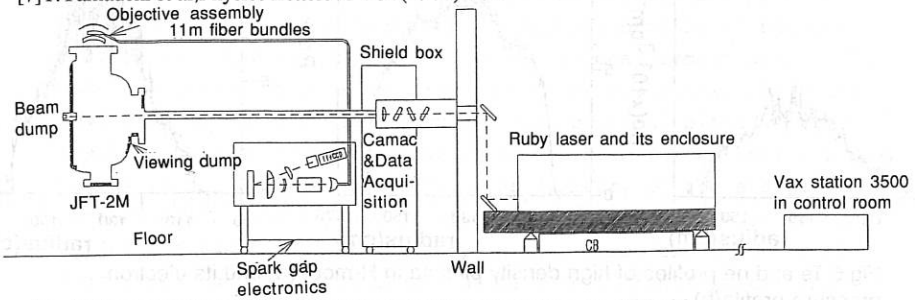

Fig.1 Elevation view of TV Thomson scattering system on JFT-2M.

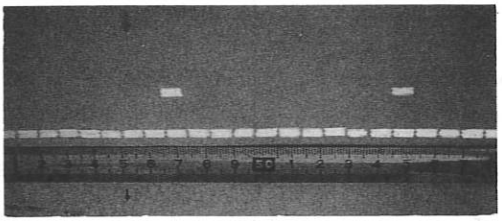

Fig.2 Image of measured point at the central region.

The 34 fibers, 4 in vertical and 8 or 9 in horizontal, are used for one spatial channel and it corresponds to an image of 3.7mm in width and 7.5-8mm in length.

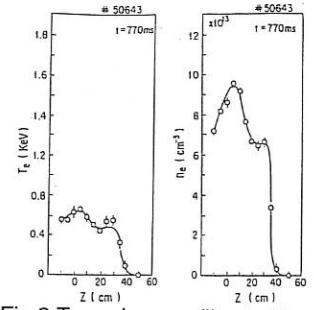

Fig.3 Te and ne profiles in H-mode with 13-point system

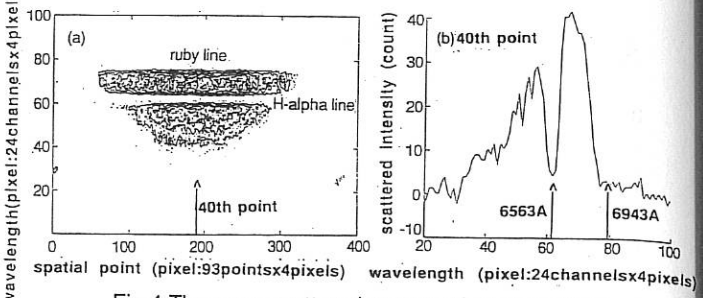

Fig.4 Thomson scattered pattern after subtracting the dark, stray light and plasma light signals(a) and the doppler broadening at the plasma center(b).

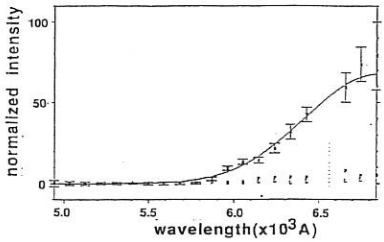

Fig.5 Fitting curve of scattered signal calculated with 20 wavelength channels

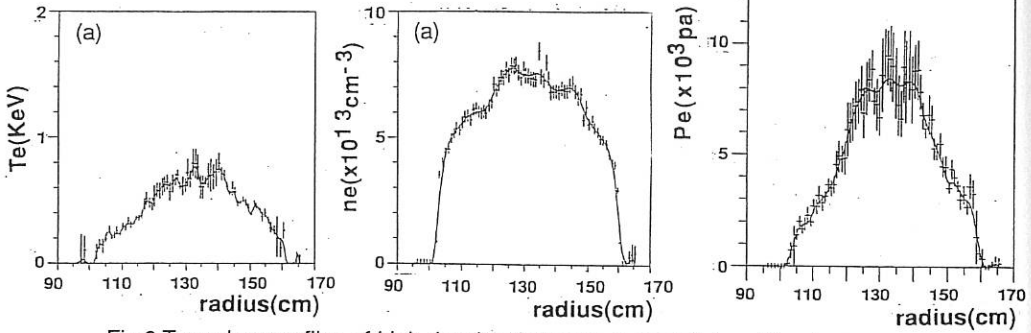

Fig.6 Te and ne profiles of high density plasma in H-mode(a) and its electron pressure profile(b).

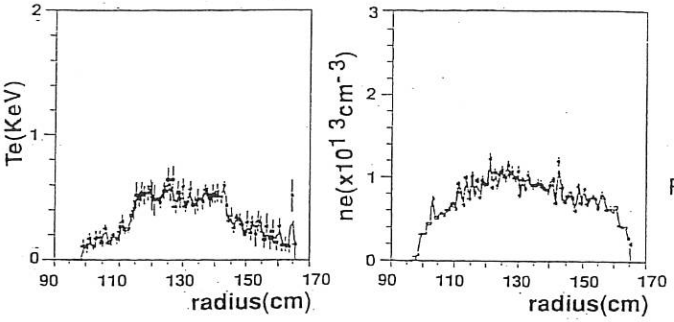

Fig.7 Te and ne profiles of low density plasma during ECH.

Study of local electric potential and turbulence of tokamak plasmas in JIPP T-IIU by heavy ion beam probe(HIBP)

Y.Hamada,Y.Kawasumi,A.Nishizawa,K.Narihara,K.Sato,T.Seki,K.Toi, H.Iguchi, A.Fujisawa, K.Adachi,A.Ejiri,S.Hidekuma, S.Hirokura, K.Ida, K.Kawahata, M.Kojima,R.Kumazawa,M.Sasao, K.N.Sato,T.Tsuzuki, I.Yamada,T.Watari

National Institute for Fusion Science

Nagoya, 464-01, Japan

By the use of simultaneous toroidal and poloidal sweeps and shaped electrode of the analyzer in the heavy ion beam probe, potential profiles in JIPP T-IIU tokamak plasma are measured at the rate of 120 profiles of plasma potentials in a second. The measured potential profile in the rather high q plasmas shows a rather large region of flat profile and a sharp decrease of the potentials in the center of the plasma. The region of the sharp change of the potential roughly coincides with the region of the hot core of the plasma. The peak potential grows appreciably by the gas puffing.

§1. Introduction

The heavy ion beam probe(HIBP) in a magnetic confinement system is particularly useful for the measurement of local electric potential and fluctuations of local plasma density and potential. The first precise measurement of a potential profile of the tokamak plasma, was performed in ST tokamak.[1] Its measurement was, however, conducted at a very low current of about 20kA where the deviation of the secondary beam from one poloidal plane was very small. It means that trajectories of the beam in the analyzer stay nearly in the analyzer plane(plane of symmetry of the analyzer and perpendicular to the plane of analyzer electrode) because of small deflection due to plasma current. In this case, the error in the measurement of total energy of the beam is insignificant, since beam velocity perpendicular to the analyzer plane, is small. In ISX-B tokamak, potential profiles of ohmic plasmas and those of plasmas with co and counter neutral beam injection, were measured by shot-to-shot basis in order to eliminate the error due to the change in entrance angles.[2] Similar measurements were performed in TM-4 and TEXT tokamaks.[3,4]

Here we succeeded in a potential profile measurement by a single poloidal sweep across plasma. This is performed by the method of the automatic compensation of the error due to the off-axis entrance angle proposed by Y.Hamada et al..[5] This method relies on the simple principles that when the beams enter the energy analyzer with various off-axis entrance angles, the parallel plate analyzer records the maximum and total energy only when the beam direction is parallel to the analyzer axis. In addition the energy analyzer with very homogeneous characteristics along the width of the intrance slit are required in this method. In our case, the uniform electric field is obtained by the shaped electrode system[6]. The detail of this method will be discussed in the different paper.

§2. Potential profiles in JIPP T-11U Plasmas

Figure 1 shows the typical raw data of normalized difference of the currents of the upper and lower detector plates as a function of time under poloidal and toroidal sweeps at various times of the discharges. The thallium beam[7] of 400keV is injected into the plasma and the toroidal and poloidal sweepers are installed at the entrance to JIPP T-11U tokamak.[8] The 2kHz toroidal sweep is applied for the compensation of the error due to the off-axis entrance angle. The radial profile of the plasma potential is approximately the dashed curve connecting small peaks induced by the toroidal sweep, since the measured energy is maximum and true energy only when the direction of the beam is parallel to the analyzer axis.

In the growing phase and decaying phase of the plasma current, the depth of the plasma potential in the center of the plasma column is small. Its depth grows as plasma current grows. The plasma potential in the center region is about -1 keV at 170kA discharge, and its depth increases during the gas puffing of the plasma. As we can see in Fig. 1, the level of plasma potential varies with time since high voltage generator is a little affected by the intense radiation at the early phase of the discharge. Accordingly we can only determine the relative change of the plasma potentials from the boundary layer to the plasma center.

Figure 2 shows the plasma potential and electron temperature versus plasma radius. The electron temperature profiles are measured by 28-spacial-points-100Hz YAG Thomson scattering apparatus. The ion temperature is determined by the Doppler width of various line emissions. The main features of the profiles are wide area of rather flat potential in the outer layer of the plasma column as was observed in TM-4 and TEXT and the sharp decrease of the plasma potentials in the center of the plasma. As we can see in Fig. 2, the region of large gradient of potentials is the region of high electron temperature. The narrow region of hot cores of the plasma column is due to the high q(=about 6) operation of the discharge. The radial profiles of the electron temperature are consistent with the prediction of profile consistency. The low electron temperature in the outer layer of the plasma column causes the low ion temperature in this layer and the potential gradients can not be large in this region.

The center ion temperature is about 400eV and the ratio of the depth of the potential to peak ion tempreature is about 2.5 in accordance with the analysis by Yang et al..[4] The positive and rather flat region is not affected by the Mirnov oscillations. This may mean that the turbulence in the plasmas outside the hot core of the plasma is not due to large-scaled instabilities and has characteristics of larger electron mobility compared to the ion mobility across the magnetic surface.

References

1) J.C.Hosea,F,C.Jobes et al.,Phys. Rev. Letts. **30** (1973) 839.
2) G.A.Hallock,J.Mathew et al.,Phys. Rev. Lett. **56** (1986) 1248.
3) V.I.Bugarya,A.V.Gorshkov,et al., Nucl. Fusion **12** (1985) 1707.
4) X.Z.Yang,B.Z.Zhang, et al., Phys. Fluids **B3** (1991) 3448.
5) Y.Hamada,Y.Kawasumi et al., NIFS-143 Research Report (1992).
6) Y.Hamada,Y.Kawasumi,et al., Rev.Sci.Instrum., **63** (1992) 4446.
7) Y.Hamada,Y.Kawasumi,M.Masai,H.Iguchi,A.Fujisawa and JIPP T-11U Group: Annual Review of NIFS (1990) p.118.
8) K.Toi,Y.Hamada,K.Kawahata, et al.,: *Proc. 13th Int. Conf. on Plasma Physics and Conrolled Nuclear Fusion Research, Washington,D.C., 1990,* Vol. p.301, IAEA, Vienna (1991).

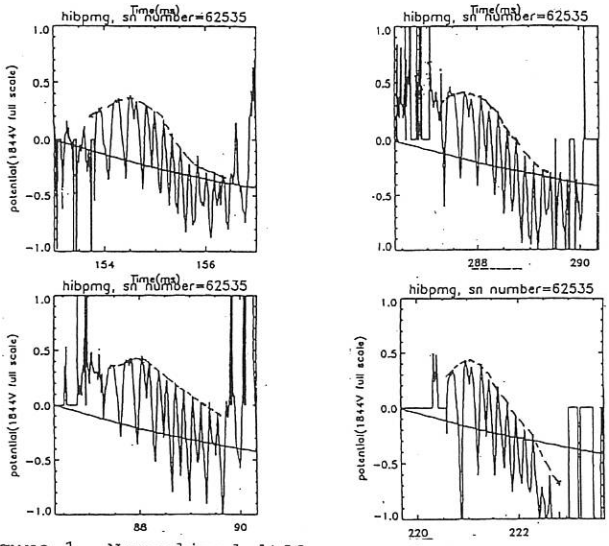

Figure 1. Normalized difference of the currents of detectors versus time under poloidal and toroidal sweeps at various times. Plasma potentials are dashed lines connecting the small peaks due to fast toroidal sweeps. Discharge parameters are B_t=3T, I_p=170kA, a_p=21cm, R_p=91cm.

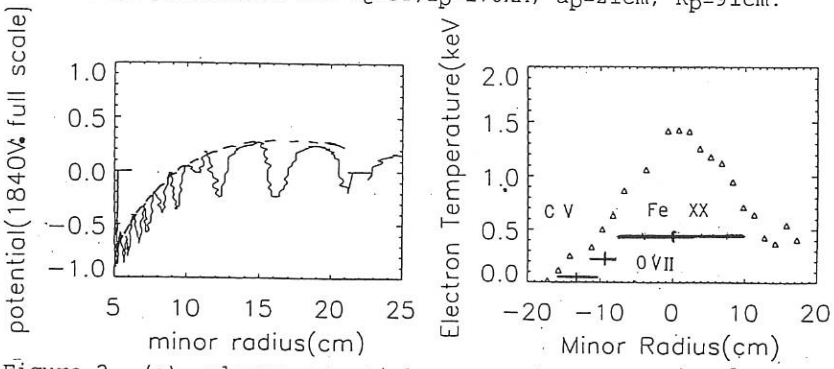

Figure 2 (a), plasma potential versus minor radius under the discharge condition of fig.1. Full scale is 1840V. Small positive potential is observed from the boundary to about r/a_p=0.5. (b), electron temperature profile and ion temperature at the same condition.

Impurity Fluxes and Profiles in Wendelstein 7-AS

J.V. Hofmann, W7-AS Team, ECRH Group, NI Group

Max-Planck-Institut für Plasmaphysik, EURATOM Ass.,
D-85748 Garching bei München, FRG

1. Introduction: Wendelstein 7-AS is a modular stellatator with 5 magnetic field periods, low vacuum magnetic shear and high aspect ratio (≥10). The minor and major radii are $a \leq 0.18$ m, $R_0 = 2.0$ m. The plasma cross section changes from nearly triangular in the middle of each field period ($\phi = 0^o$) to nearly elliptical at both ends ($\phi = \pm 36^o$).

Impurity influxes and profiles are investigated in a poloidal plane, intersecting the top limiter, close to the elliptical cross section of the plasma at $\phi = -25.4^o$. Figure 1 shows the poloidal cross section in this plane for a rotational transform of $\iota = 0.345$ together with the port axis (dashed) and the typical range of lines of sight (LoS) of the visible spectroscopy scanning mirror system (arrows). At this low rotational transform the set of nested flux surfaces within the natural separatrix (outermost plotted flux surface) would spread out to the vessel wall and has always to be restricted by a limiter (horizontal bar). Thus, the limiter determines the last closed flux surface (LCFS), indicated as a bold contour (shown here for maximum aperture). For high rotational transform ($\iota > 0.5$) the plasma is limited by a natural separatrix located inside the maximum aperture of the limiters. However, also in this case the movable limiters can be inserted to control the plasma edge. The plasma aperture can thus be varied from 18 cm ≤ a ≤ 12 cm.

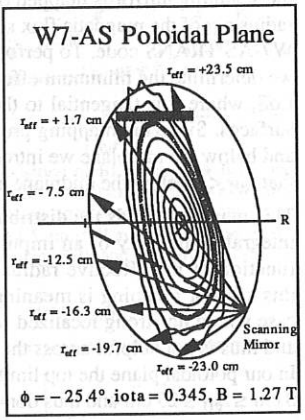

Fig.1: Poloidal cross section of W7-AS showing the magnetic flux contours, the top limiter and the LCFS, the position of the scanning mirror system and typical lines of sight.

In the following we investigate the poloidal distribution of impurity ions in this cross section to determine local sources. Then we concentrate on the localisation of the ionic shells and determine the influence of the plasma aperture on the radial location of the ions. In a next step we deduce the radial pressure profile of BIV and deduce the local diamagnetic impurity drift which is of importance for the measurements of radial electric fields. Finally we investigate the 'limiter peaks', observed for all impurity species and its dependence on limiter position. With most measurements performed on boron species we want to stress the diagnostic potential of this impurity and give a compilation of all boron transitions throughout the UV- and visible spectral range, including molecules, as measured on W7-AS.

2. Poloidal distribution of impurities: Within the geometry of fig.1 the intensity distributions across the whole poloidal cross section are measured for all ionization stages of boron (BI - BV), carbon (CII - CV) and oxygen (OI - OV) throughout the UV- and visible spectral range (200 nm ≤ λ ≤ 800 nm). In order to localize impurity sources, emission from

neutral or singly ionized species is best suited. Higher ionization stages, however, are more spread out over the flux surfaces. Poloidal scans during stationary phases of discharges and shot-to-shot scans of the LoS show that all intensities are strongly peaked at the top limiter, as shown in fig.2. While low ionization stages show relatively narrow peaks around the limiter position high ionization stages like BIV-V, CIV-V and OV exhibit a very broad radial distributon. The smaller peaks between -25 cm $\leq r_{eff} \leq$ -10 cm are attributed to the ionic shells. From these measurements the top limiter is found to be the only prominent local impurity source (deduced from BI, CI and OI signals) but the integrated influx from the wall is exceeding that from the limiter due to its much larger surface.

In order to radially localize the emission of different ionization stages the LoS coordinate of the scanning mirror is mapped onto an effective radius r_{eff} of the magnetic flux surfaces using the W7-AS TRANS code. To perform this mapping we determine the minimum effective radius of a LoS, where it is tangential to the magnetic flux surfaces. Since the mapping provides r_{eff} above and below the midplane we introduce a sign thus that $r_{eff} < 0$ below the midplane and > 0 above.

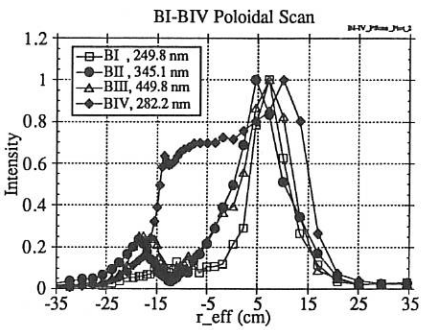

Fig.2: Boron intensities as a function of r_{eff} for full scans of the poloidal cross section. Note the very broad distribution of BIV, the 'limiter peaks' at r_{eff} >0 and the 'shell peaks' between -25 cm $\leq r_{eff} \leq$ -10 cm. The LCFS is located around -17 cm.

This mapping yields the distribution of the LoS integrated intensity of an impurity species as a function of the effective radius r_{eff}. However, this kind of mapping is meaningful only in the case where no strong localized source is present and thus is not helpful across the limiter surface. In our poloidal plane the top limiter spreads from 0 cm $\leq r_{eff} \leq$ 25 cm and thus dominates all measurements with $r_{eff} > 0$ inside the plasma.

On the other hand, since we did not find a strong localized source apart from the limiter this method allows to investigate the radial distribution of impurities in the lower half of the plasma.

3. Localization of ionic shells: While all ionization stages exhibit a strong peak at the limiter, a range of intensity maxima occurs between -25 cm $\leq r_{eff} \leq$ -10 cm, see fig.2, which correspond to the locations of the ionic shells (detailed investigations can exclude the possibility of wall reflections of the strong intensities from the top limiter). The locations of these shells are primarily a function of the electron temperature and transport processes. The electron temperature profile determines the radial range in which an ion species can exist (before it is further ionized) and transport leads to a significant spread and deformation of the shells (clearly seen in transport calculations). It should be noted, that the ionic shells are only run through when an atom or ion penetrates the plasma from outside. An ion leaving the plasma, however, will not recombine until it reaches the immediate vicinity of a surface. Thus, high ionization stages of impurities are found f.ex. near the limiter surface.

As a result of the temperature dependence of the location of the shells and the relatively high surface temperatures of the limiter ($\approx$ 100 eV) we find quite different behaviour for low and high ionization stages. Low ionization stages like (B,C,O) II-III which reside at or outside the LCFS show no significant change in their location as the plasma temperature is increased or the aperture is changed. Higher ionization stages like (B,C,O) IV-V, however, are shifted in their

radial location as the temperature increases (see also fig.5) or the aperture is changed. Fig, 3 shows the location of BII (squares + dots) and BIV (triangles + diamonds) for plasma apertures of a=17.5 cm (open symbols) and 14.4 cm (full symbols). The BII shell essentially becomes broader and the location relative to the LCFS increases while the BIV shell stays about 2 cm inside the LCFS and is shifted together with the aperture.

For more detailed investigations and for the deduction of ion temperatures (from Doppler broadening), drift velocities (from Doppler shift) and radial BIV density profiles as a function of time we performed shot-to-shot measurements on BIV and BII (also during H-mode discharges). Fig.4 shows the measured LoS integrated BIV intensity profile (dots) for a plasma with $\iota = 0.563$ and a separatrix radius of about 14 cm. The profile was taken at a time point of 0.5 s, where it is steepest, as shown in fig.5. Inversion of the intensity profiles yields the radial emissivity and thus the radial impurity density profiles. The BIV density profile (dashed line in fig.4) is located around 11 cm. BII is found to reside in these discharges around 15 cm. From the boron ion temperatures and densities the pressure profiles and the local diamagnetic impurity drifts are calculated. The local diamagnetic drift of BIV, shown in fig.4 as full line, turns out to be very steep at the outside of the profile. The drift is in ion-diamagnetic direction at the outside and changes sign when the maximum of the pressure profile is crossed. Fig. 5 shows the profile contours of the BIV shot-to-shot intensities from which the radial location and shift of the profile during the discharge as a function of time is measured. From 0.4 to 0.5 s the ECRH is increased from 0.17 MW to 0.34 MW resulting in a temperature increase and in a slow outward shift of the profile centre by 1.5 cm . However, the 0.9 intensity level at the inside shows a much more pronounced shift of over 3 cm leading to a strong change of the gradient at the inside.

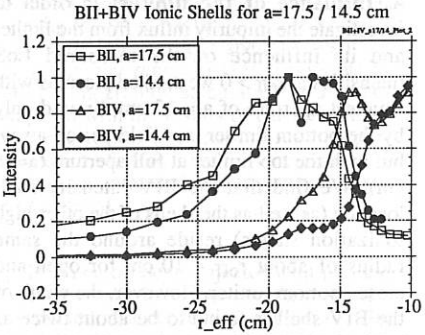

Fig.3: Radial position of BII (squares + dots) and BIV (triangles + diamonds) ionic shells as a function of r_{eff} for plasma apertures a = 17.5 cm (open symbols) and 14.5 cm (full symbols), respectively. Note the broadening of BII and the shift of BIV.

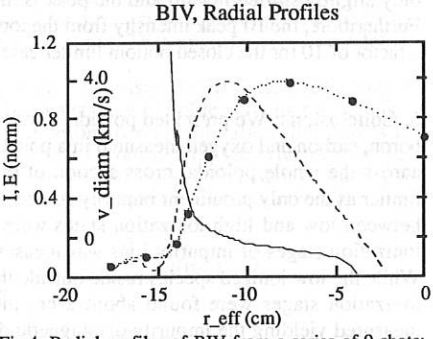

Fig.4: Radial profiles of BIV from a series of 9 shots: measured LoS integrated intensity (red dots and spline fit), emissivity (BIV density) from inversion of the intensity profile (dashed).

The measured boron ion temperatures may also be inverted to yield an ion temperature profile across the spread of the corresponding shell. With the knowledge of the diamagnetic drift of the boron ions a radial drift velocity profile due to a radial electric field in the H-mode may be inferred and thus a profile of the radial electric field.

The location of the BIV shell as measured by visible spectroscopy has been found to be in agreement with transport calculations using the measured Thomson profiles of electron density and temperature and typical transport coefficients.

4. Influence of the limiter: In order to investigate the impurity influx from the limiter and its influence on the measured LoS intensities at $r_{eff} > 0$ we studied plasmas with smallest aperture of a = 12 cm, limited only by the bottom limiter one field period away, but with the top limiter at full aperture (a=16 cm). We find that the BIV intensity shell location (as well as the shells of the other high ionization stages) reside around the same radius of about $r_{eff} \approx 10$ cm for open and closed bottom limiter. However, the width of the BIV shell is found to be about twice as wide ($\Delta r_{eff} \approx 6.5$ cm) in the case of the open bottom limiter than in the closed case. In case of the closed limiter the 'limiter peak' of BIV drops significantly by about a factor of 4 (and becoming ≈30% smaller than the 'shell peak') and is shifted inward compared to the open limiter case. For BI the 'limiter peak' is found to be only slightly shifted inward and the peak is much broader compared to the open limiter case. Furthermore, the BI peak intensity from the top limiter drops remarkably, as expected, by about a factor of 10 for the closed bottom limiter case.

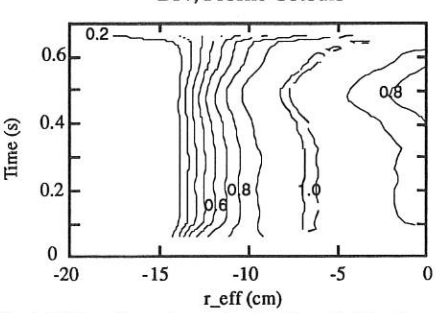

Fig.5: BIV profile contours showing the radial location and change of the intensity profile as a function of time and radius .

5. Conclusions: We presented poloidal distributions and radial profiles of the light impurities boron, carbon and oxygen measured in a poloidal cross section of the W7-AS stellarator. Scans across the whole poloidal cross section of the plasma, inner wall and limiter identified the limiter as the only prominent impurity source. Important differences of the poloidal distribution between low and high ionization states were found. The radial distribution of the different ionization stages of impurity ions was measured in one discharge or on a shot-to-shot basis. While the low ionized species reside outside the separatrix or the LCFS, BIV and other higher ionization stages were found about 2 cm inside. Density profiles of the boron ions were measured yielding the impurity diamagnetic drift. Our measurements allow for simultaneous determination of impurity densities, temperatures and drift velocities (radial electric fields) and will allow to determine radial profiles of all these quantities across the spread of the impurity shells as a function of time.

The different species and transitions of boron yield a high diagnostic potential and will always stay at a diagnostic level due to boronization. We will therefore present a compilation of all species and transitions including BH-molecules, measured recently.

CXRS-Measurement and Code-Calculation of Impurity Profiles

J. Baldzuhn, W. Ohlendorf, A. Weller, R. Burhenn, M. Kick, W7-AS-Team

Max-Planck-Institut für Plasmaphysik, EURATOM Association,
D - 85748 Garching, Fed. Rep. Germany

INTRODUCTION.

Charge Exchange Resonance Spectroscopy CXRS is performed for impurity lines of several ionization states, especially for carbon and boron, on the advanced stellarator W7-AS. These lines are excited by means of a neutral beam diagnostic injector. The spatially resolved spectroscopic observation in the visible and near ultraviolet region makes it possible to evaluate density profiles of the impurities without a tomographic calculation or an Abel inversion. The measured impurity profiles are compared with the results of calculations of the IONEQ-Code, which take into account either a neoclassical or an anomalous transport model. Thus, diffusion coefficients and convective velocities for the impurities are evaluated. Discharge scenarios before and after H-mode transitions are compared, and impurity influxes before and after boronization of the vessel wall are considered.

PROFILE MEASUREMENT.

The charge exchange CX lines are excited by a pulsed neutral beam injector with particle energies typically at about 30, 15 and 10 keV for the full, half and one third energy components, respectively. Because the beam is pulsed, background radiation can be subtracted from the CX radiation. The light is guided by means of a turnable mirror device towards a 1.26m spectrometer. Intensity can be recorded between 200 nm and 700 nm by a multi-channel photomultiplier array with 15 channels, the spectral resolution for the whole device is about 0.02 nm / channel.

We start from Thomson scattering data for electron temperature and density profiles, an assumed neutral gas background and the geometry of the experimental arrangement for the first loop of an iterative calculation of the impurity profile. A first-step attenuation profile for the neutral beam is calculated by assuming a model for a first-step impurity profile, because the impurity itself contributes to the beam attenuation, too. That impurity profile model is calculated from the electron density profile.

This first-step beam attenuation profile together with the measured CXRS are used as input data for the calculation of a second-step neutral beam attenuation profile, making possible the evaluation of a second-step impurity profile, and so on. A recursion algorithm makes it possible to calculate the n-step impurity profile, which is considered as satisfactory for the case that numerical convergence and stability for the calculated profiles, step by step, are attained for higher n. The whole problem can be condensated to the solution of the following equation:

$$\frac{N_{phot.}(l)}{n_k(l) \cdot Vol(l) \cdot \langle \sigma_{CXR}(V) \cdot V_{coll} \rangle} = Int\,(l) = \sum_{i=1}^{3} Int(l=0)_i \quad X$$

$$X \quad \exp\left\{ -1 \cdot \int_{-z_0}^{-z_0+l} \left(\sigma_{CX}(V) \cdot n_{H^+}(z) + \sum_{j=1,\, j \neq k}^{m} \sigma^j_{CX}(V) \cdot n_j(z) + \sigma^k_{CX}(V) \cdot n_k(z) \right) dz \right\}$$

Here, N_{phot} (l) stands for the CX light intensity as a function of the coordinate l along the neutral beam trace, Int(l) is the neutral beam intensity, n_k (l) is the impurity density profile for the ionization state k, Vol(l) is a geometric factor, V_{coll} is the collision velocity, $\sigma_{CXR}(V)$ is the CX cross section for the excitation of CX radiation, $\sigma^j{}_{CX}(V)$ is the CX cross section for

the neutral beam attenuation by collisions between neutral hydrogen atoms with impurity ions in the ionization state j. The summation in the first line spreads over the mentioned three energy components for the neutral beam, z is the vertical coordinate with respect to the plasma, the summation in the exponent spreads over the assumed impurities present in the plasma. The exponential factor gives the total neutral beam attenuation, the integral corresponds to a line density multiplied by a cross section. Atomic data for cross sections are taken from Barnett, and Tawara et al. (1).
Variations of that procedure consist of variations of the cross sections. Thus, we determine the influence of the absolute values of the cross sections on the final results, see Rehker and Speth (2), to be able to estimate errors stemming from possible uncertainties of the input data. Further variations are done by replacing the left sides of the following expressions by the right sides for the equation given above.

$$\text{replace} : \sum_{i=1}^{3} \sigma_{CX}(V) \rightarrow \sum_{i=1}^{3} \frac{\langle \sigma_{CX}(V) \cdot V_{coll.} \rangle}{V_{beam,i}}$$

$$\text{replace} : \sum_{i=1}^{3} \langle \sigma V \rangle \rightarrow \sum_{i=1}^{3} \int_0^{\infty} \sigma_{CX}(V_{coll.}) \cdot V_{coll.} \cdot f(V_{plas.})\, d^3V_{plas.}$$

Here, $f(V_{plas.})$ stands for a velocity distribution function, assumed for the plasma particles, the brackets < . > denote the mean defined by the integral (for monoenergetic beam particles):

$$\langle \sigma V \rangle = \int_0^{\infty} \sigma(V_{coll.}) \cdot V_{coll.} \cdot f(V_{plas.}) \cdot d^3V_{plas.}$$

Thus, the role of differing velocity distributions, and variations of it, can be estimated.
The impurity density profiles, evaluated in the described way, are then compared to IONEQ code calculations.

CODE CALCULATIONS.
The code IONEQ can, among other things, calculate impurity density profiles starting from electron density, electron temperature and background neutral gas profiles as input parameters, see Weller et al. (3). The calculation includes either an anomalous model, which needs estimated values for diffusion and convective inward velocity for the impurity under consideration, or a neoclassical ansatz. The calculated result of IONEQ can be varied by a variation of the input anomalous diffusion coefficient D for an impurity in ionization state k, the inward convective velocity V and an exponential parameter α, such that the result of the calculation fits best to the measured CXRS impurity density profiles. The inward convective velocity V for a impurity species at minor radius r is given by $V(r) = (-2D / a) \cdot (r / a)^{\alpha}$. Here, a is the minor plasma radius. First, a ansatz for diffusion and convection is made, then a set of coupled continuity equations is solved by IONEQ for each flux surface, taking into account radiation, ionization and recombination as sources and sinks from the neighbor flux surfaces. For our investigations, we first calculate anomalous transport parameters by comparison with CXRS measurements. From the impurity density profiles obtained in this way we then calculate the corresponding neoclassical values.

RESULTS.
First, we present two results for density profiles of C VII, observed by CXRS of C VI at a wavelength of 343.4 nm. The CXRS light intensity is integrated during a time interval of 50 msec, the spatial resolution in direction of the effective minor radius r_{eff} is about 1 cm. In all plots below, the plasma edge is on the right, the magnetic axis is on the left, a_{eff} is about 16 cm. The density of C VII is given in arbitrary units, absolute concentrations are for these examples about $5 \cdot 10^{17}$ m^{-3} in the plasma center, as confirmed by VUV-measurements. Each single dot with an error bar in the plot in figure 1 corresponds to one measured point,

the drawn line shows the result of the IONEQ calculation. The anomalous diffusion coefficient D, the inward velocity V and the exponential factor α are chosen such that the calculated line fits best to the measured data. Note that we do not perform a numerical fit in the usual sense, but much more only an adaptation by hand. For the example in fig. 1, we obtain an anomalous D = 1500 ± 500 cm^2 / sec, V = 2 ± 1 m/sec inward velocity at the plasma edge, α = 2.0 ± 0.5.

Figure 2 shows some data points for the density of C VII, 100 msec before (lower line) and 100 msec after H-mode transition (upper line). Typical error bars are given, too, the x-axis indicates the position z in the laboratory frame along the neutral beam. Unfortunately, due to a poor raw data basis, only 4 points are available. Apparently, the C VII profiles are much more peaked after the transition occured. This is due to severely changed transport for the impurities.

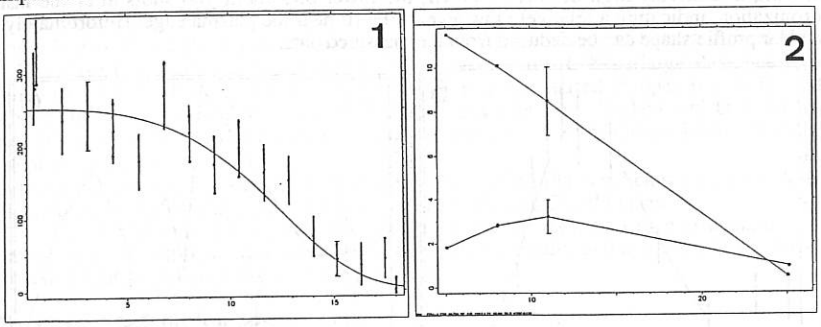

Figure 3 shows results for the density profiles of B VI, observed by CXRS of B V at a wavelength of 298.1 nm, together with the results of the code calculation, indicated by the drawn line. Once again, the calculated curve is fitted to the measured data points, indicated by single dots. We obtain an anomalous D = 1500 ± 1000 cm^2 / sec, V = 2 ± 1 m/sec inward velocity at the plasma edge and α = 2.0 ± 0.5 for the anomalous transport calculation.

Figure 4 shows a result for density profiles of B VI, observed by CXRS of B V, 150 msec before (lower line) and 100 msec after H-mode transition (upper line). Once again, severely changed transport can be observed. Unfortunately, a code calculation cannot be performed for that changed profile because of strongly changed profile shape. Some representative error bars are given again. The y-axes are in arbitrary units, the x-axes show the effective minor radius.

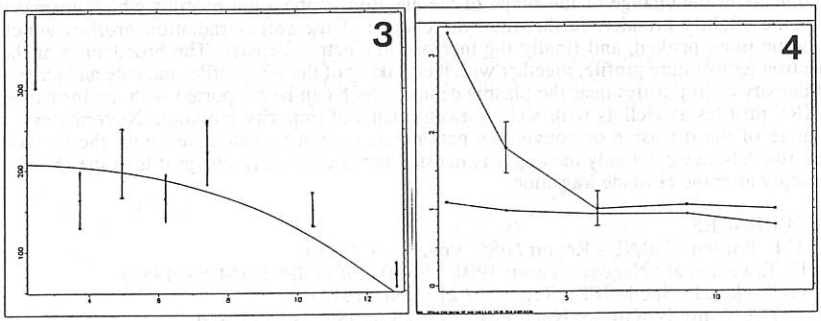

Figure 5 shows a result for a density profile of B V (H - like), measured by CXRS of B IV at a wavelength of 282.4 nm, together with the result of the IONEQ calculation. The measured data are indicated by single dots, the y-axis is in arbitrary units. Apparently, that line is observable by CXRS due to the fact, that the electron impact excited line from lower l-states is superposed by the charge exchange excited line from higher l-states. After subtraction of the background intensity, CX intensity is observable. As expected, the density profile is concentrated to a shell near the plasma edge. Anomalous values obtained from the IONEQ calculation are $D = 2000 \pm 1000$ cm^2 / sec, $V = 4 \pm 2$ m/sec, $\alpha = 3.0 \pm 1.0$.

Figure 6 shows results of passive measurements of Fe III at a wavelength of 326.7 nm near the plasma edge. The x-axis here is given in cm in the laboratory frame, effective radii cannot be calculated outside the plasma, a ≈ 30 cm. The y-axis is in arbitrary units, but the same for both lines. The upper line is taken several hundreds of shots after the last boronization, showing a relatively high density of Fe III, the lower one about 100 shots after the last boronization, indicating a relatively low level of Fe III near the plasma edge. Unfortunately, no clear profile shape can be deduced from the measured data.

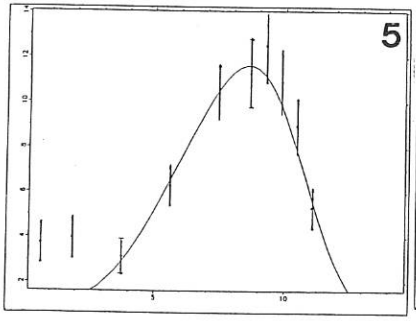

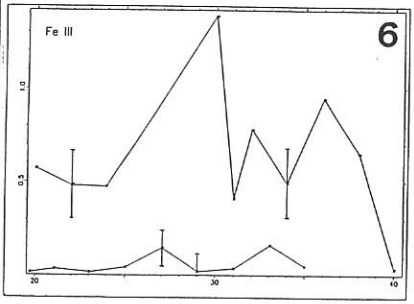

DISCUSSION.

All values obtained for anomalous D by a comparison of IONEQ calculations with the CXRS measurements are between about 1500 and 2000 cm^2 /sec. Afterward calculation for neoclassical D from the obtained impurity profiles provide almost the same values, indicating only a minor deviation between anomalous and neoclassical transport for impurities.

Passive measurement of Fe III light intensity, directly after and a long period after boronization, show a clear decrease due to the boronized vessel wall, a result which is supported by VUV measurements.

The H-mode transition, and the changed transport after the transition, are modelled by taking into account the change of the shape of the electron temperature profiles which normally become slightly broader, furthermore the change of the soft-X-radiation profiles which become more peaked, and finally the increase in electron density. The broadening of the electron temperature profile, together with the peaking of the SX-profiles indicate an increase of density of impurities near the plasma center, which can be supported with the measured CXRS profiles as well as with VUV measurements of impurity radiation. Nevertheless, a change of the diffusive or convective parameters cannot be calculated with the method described, because not only the impurity density increases, but also the profile shape changes strongly after the H-mode transition.

REFERENCES.

(1) C.F. Barnett : ORNL - Report 6086, Vols. 1 - 3, (1990)
H. Tawara et al.: Nagoya Reports IPPJ-AM-30 (1983), IPPJ-AM-56 (1987)
(2) S. Rehker, E. Speth: IPP - Report 2 / 217, Jan. (1974)
(3) W7-A Team, NI-Group: Nucl. Fus., Vol. **25,** (1985), p.1593, and
A. Weller et al.: Plasma Phys. Contr. Fus., **33** , 18.th EPS Berlin, Invited Papers (1991)

A spectrometer with multilayer filters for line intensity measurements in the RFX experiment

Andrea Murari*, Lionello Marrelli, Piero Martin§ and Gianni Gadani#

Istituto Gas Ionizzati del C.N.R., Euratom-Enea-Cnr-Università di Padova Association Padova, Italy
**Dipartimento di Ingegneria Elettrica, Università di Padova, Italy*
§Dipartimento di Fisica 'G.Galilei', Università di Padova, Italy
 # Enea-Fus, Bologna, Italy

I. Introduction

The role played by light impurities in influencing the power balance of Reversed Field Pinch (RFP) plasmas is usually very important. This is the case for RFX[1], a large Reversed Field Pinch experiment (R=2 m, a=0.457 m) which has recently started its operation in Padova, whose first wall is completely covered by 2016 graphite tiles. Carbon and Oxygen line emissions are in this initial low-current operational phase of RFX key-factors in understanding the plasma confinement[2,3]
In this paper we present a simple spectrometer with multifoil filters which we have developed as an on-line monitor of line emission from the H and He-like C and O ions.
In section II the basic principle of the measurement and the experimental apparatus are described, in section III we discuss the initial experimental results and in section IV the project for a new multichord diagnostic is briefly presented.

II. The RFX multifoil spectrometer

II.1: The principle

The basic concept on which this method is based is similar to that of the Ross balanced filters[4,5]: the same region of the plasma is observed by means of four standard Silicon SXR detectors, each covered by a different multilayer foil filter with a transmission function which has a peak of the order of 10% in correspondence of one of the energies of interest (E_{CV}=307.7 eV, E_{CVI}=367.5 eV, E_{OVII}=571.4 eV and E_{OVIII}=656.1 eV) and a much smaller value for the other three. This is obtained using the K or L absorption edges in the transmission functions of the materials. In fact each of the filters is made by a combination of thin film absorbers: the material and the thickness of each absorber is chosen in such a way that the global transmission function of the filter satisfies the previous requirements.
For this first version of the RFX multifoil spectrometer we have adopted the same filters which have been used in MST[6]. The compositions of these filters are the following:

Filter CV	4000Å Ti + 6000Å CaF_2	free standing
Filter CVI	6000Å Ti + 2000Å Cr	supported by 1000Å parylene (C_8H_8)
Filter OVII	2500Å Ni + 5000Å Cr	supported by 2000Å parylene (C_8H_8)
Filter OVIII	3000Å Ni + 5000Å Fe	supported by 2000Å parylene (C_8H_8)

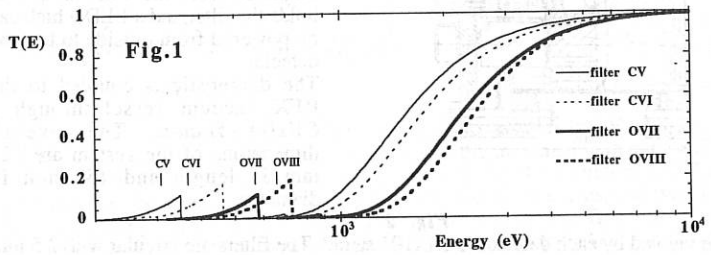

The transmission functions T(E) of these filters are shown in Fig.1 and their values in correspondence of E_{CV}, E_{CVI}, E_{OVII}, E_{OVIII} are listed in the following table:

	Transmissions T(E) @			
	E_{CV}	E_{CVI}	E_{OVII}	E_{OVIII}
Filter CV	***0.06413***	0.00444	0.00394	0.01373
Filter CVI	0.01995	***0.06210***	0.00288	0.00103
Filter OVII	0.00046	0.00424	***0.11168***	0.00079
Filter OVIII	0.00007	0.00110	0.06332	***0.12915***

As can be noted the 4x4 matrix of transmissions **T** is not exactly diagonal, i.e. each filter has a preferential transmission for one of the energies, but the values of T(E) for the remaining three is not zero. This means that in order to reconstruct the line intensities from the measured signals one has to solve a linear system of equations where the line intensities **I** are the unknowns and the measured signals **S** are known:

$$\mathbf{I}=\mathbf{T}^{-1}\bullet\mathbf{S} \qquad (1)$$

The results which one obtains from Eq. (1) are correct provided that: (i) there are not other lines strongly emitting in the energy region where the transmission functions of the 4 filters are different from zero and (ii) the continuum radiation passing through the filters may be neglected.
Hypothesis (i) is based on a spectroscopic experimental survey[1], whereas for point (ii) we have performed a calculation of the signal we should expect in the detectors with the actual geometry due to continuum spectrum at present typical RFX electron density and temperature (n_e= $3x10^{19}m^{-3}$, T_e=350 eV) and with a SXR enhancement factor ξ=4. The ratio between the expected signal due to continuum and the measured signal is approximately 0.01, a result which makes us confident that the detectors are measuring only the emission form the four H and He-like states of C and O.

II.2 The experimental set-up
A drawing of the diagnostic is shown in Fig. 2. Six detectors, (4 for the multifoil filters and 2 covered by 25 and 125 μm of Beryllium for electron temperature measurement with the absorption method) are mounted in a Macor® flange contained inside a Steinless Steel tubular structure with a diameter of 100 mm.

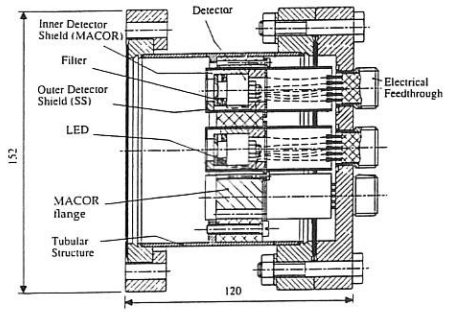

Each detector with their electrical wires are located inside a double cilyndrical shield with a pinhole. The external cylinder is SS and acts as a guarded Faraday cage; the internal container is Macor: it keeps the detector case electrically insulated from the external shield, holds the filter and a LED which can be powered from outside to test the detector.
The diagnostic is coupled to the RFX vacuum vessel through a CF100 flange. The overall dimensions of the system are 120 mm in length and 152 mm in diameter.

Fig. 2

The solid angle viewed by each detector is $1.1x10^{-2}$ sterad. The filters are circular with 2.5 mm

radius. The photodiodes are Ion-Implanted Silicon detectors with an active area of 12.6 mm^2. They are connected to a linear amplifier (OPA111) with a buffer stage (LM310) which drives the line up to analog-to-digital converter. The bandwidth of the electron is ≈10 kHz and the signals have been sampled at a frequency of 25 kHz.

III. Experimental results

An example of the experimental results obtained with this instrument is shown in Fig.3, where the reconstructed CV, CVI, OVII and OVIII lines intensity are displayed together with the plasma current I, chord averaged electron density n_e and the toroidal magnetic field at the wall $B_t(a)$ for the RFX pulse # 2074.

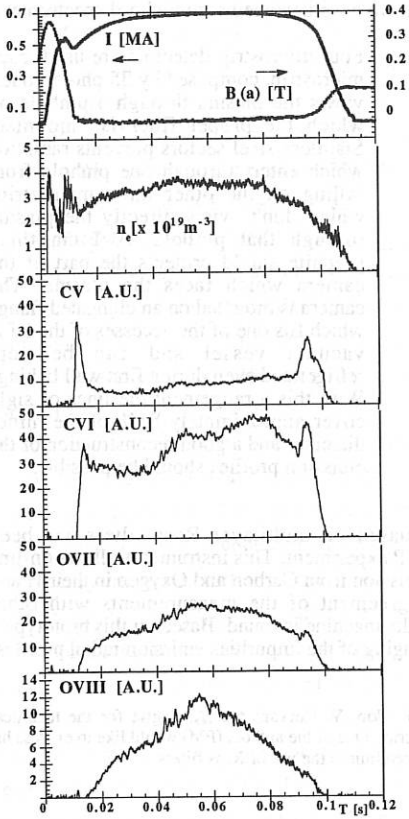

Fig. 3

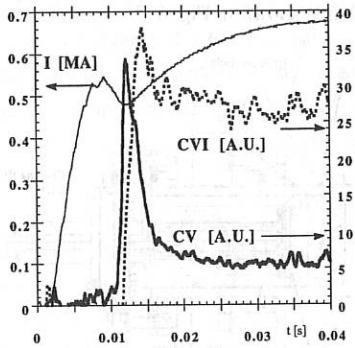

Fig. 4

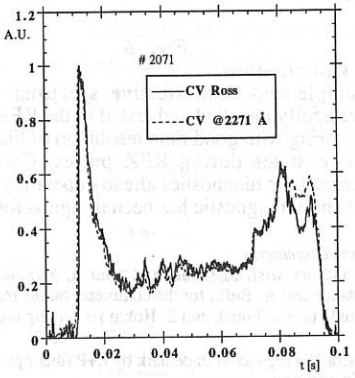

Fig. 5

We can observe, as expected, that CV emission grows faster than CVI at the beginning of the discharge. CV emission starts in correspondence of the first maximum in the plasma current. It is interesting to note in Fig. 4, a zoom on some of the waveforms of Fig. 3, that CV emission shows a peak, sometimes well pronounced, in correspondence of the shallow decrease in the plasma current occurring after the first maximum. This feature, which is typical of the present RFX start-up, is possibly indicative of a stronger plasma-wall interaction, with

an enhanced release of Carbon in the plasma due to the passage of the magnetic distribution through a series of unstable states before reaching the RFP configuration.
In Fig. 5 the CV emission as measured by the multifoil spectrometer during shot #2071 is compared with the signal from one of the RFX Czerny-Turner spectrometers[7] which is observing the 2271 Å CV line (both signals are normalised to their maximum); the good agreement existing between these two measurements performed with different instruments gives us an enhanced confidence on the reliability of the diagnostic. Good agreement is obtained also comparing measurements of OVII emission.

IV. Future developments

Considering the positive result of the prototype and the need for simultaneous on-line monitors of the H and He-like C and O emission profiles we have designed a multichord spectrometer which is shown in Fig. 6.

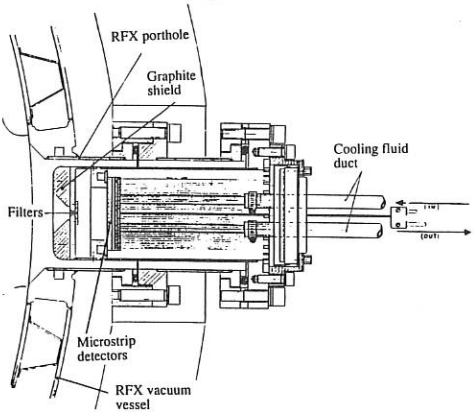

Fig. 6

Four microstrip detectors are used; each microstrip, composed by 35 photodiodes, views the plasma through a pinhole on which the proper filter is mounted. Stainless steel sectors prevents radiation which enters through one pinhole from falling on the other three microstrips which don't view directly the plasma through that pinhole. A 1 cm thick graphite shield protects the part of the camera which faces the plasma. The camera is mounted on an elongated flange which fits one of the accesses of the RFX vacuum vessel and can be kept refrigerated even during first wall baking. With this arrangement the lines of sight cover approximately 85% of the minor diameter and a good reconstruction of the emission profiles should be possible.

V. Conclusions

A simple and cost-effective spectrometer based on multilayer Ross filters has been successfully installed and tested in the RFX RFP experiment. This instruments allows on-line monitoring with good time resolution of line emission from Carbon and Oxygen in their H and He-like states during RFX pulses. Good agreement of the measurements with other spectroscopic diagnostics already operating on the machine is found. Based on this prototype a multichord diagnostic has been designed for imaging of the impurities emission radial profiles.

Acknowledgements
The authors wish to thank A. Parini, I. Molon, E. Perdon, V. Cervaro and A. Saglia for the technical assistance and A. Buffa for the comments on the manuscript. One of the authors (PM) would like to express his gratitude to R.J. Fonck and S. Hokin for having introduced him to the use of Ross filters.

®Macor is a registered trademark by E+P fiber optic AG

References

[1]The RFX Team, 'First results on the RFX Reversed Field Pinch Experiment', paper IAEA-CN-56-H-1-1,'14th IAEA International Conference on Plasma Physics and Controlled Nuclear Fusion Research', Würzburg, 1992.
[2]Paccagnella R. et al., 'Analysis of Reversed Field Pinch plasmas in RFX', this conference
[3]Carraro L., Puiatti M.E., Scarin P., Valisa M., 'Impurity behaviour in RFX', this conference
[4]Ross, P.A., Phys. Rev **28** (1926) 425.
[5]Ross, P.A., Rev. Sci. Instrum. **16** (1928) 433.
[6]Hokin S., Fonck R.J., Martin P., Rev. Sci. Instrum. **63** (1992) 5038
[7]Carraro L., Puiatti M.E., Scarin P., Valisa M., Rev. Sci. Instrum. **63** (1992) 5188

The CX - Neutral Particle Analysis of the RFX Plasmas

S.Costa, F.Frascati[1], R.Guatieri[2], I.Molon, A.Schiavi[2]
Istituto Gas Ionizzati del CNR, EURATOM-ENEA-CNR Association,
35023 Padova, Italy

Measurements and analysis of neutral atom fluxes from RFX confined plasmas are presented in this paper. Atom fluxes of energy lower than 4000 eV are measured. Neutral particles in this energy range are produced by charge exchange (CX) phenomena and are a significant component of the total energy loss of the plasma. The flux analysis provides a good estimate of the ion temperature and of the power loss.

I. EXPERIMENTAL APPARATUS

The CX neutral particle fluxes are measured by means of two neutral particle analysers covering different energy ranges: for the low energies a high resolution 4-meter-long time of flight analyser (TOF); for the high energies a 10 channels stripping cell neutral particles analyser (NPA), which can discriminate between particles of different masses and energies by a suitable arrangement of magnetic and electric fields. The lines of sight of both analysers lie on the equatorial plane and see the same cross section of the plasma through a pumping manifold. The divergence of the two lines of sight is 10°. These devices may provide complementary observations, since TOF covers the 0.02 - 2.5 keV energy range and the stripping cell NPA may be adjusted by the operator in order to cover one order of magnitude in the 0.3 - 30 keV energy range.

Time-of-flight (TOF) Analyser: this analyser (Fig.1) was realised at the Istituto Gas Ionizzati-CNR at Padova after a similar prototype performing measurements on ETA-BETA II experiment /1/. Neutral particle fluxes are detected by a Hamamatsu R595 electron multiplier after a flight along a 4-meter-long vacuum duct. Multi-

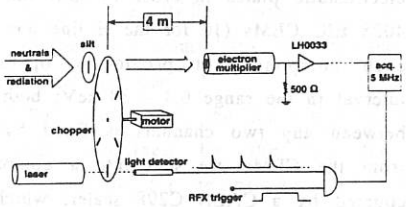

Fig.1: TOF analyser layout (schematic)

---

[1] *ENEA-Fus Bologna, Italy*
[2] *Universita' di Padova, Dipartimento di Ingegneria Elettrica, Padova, Italy*

pulsed fluxes of neutrals come in from the plasma through one of the 6 slits of the chopper wheel, spinning at 20000 rpm (each slit is 0.15 mm ×15 mm). As a consequence a window is opened every 0.5 ms, when the rotating slit overlaps the 0.15 mm fixed slit for a 3μs interval. The time of travel of the single particles from the slit to the detector is converted into energy, obtaining the energy spectrum at every window opening.

The TOF analyser detects neutral atoms of energy in the above-mentioned range, but cannot discriminate between particles with different atomic masses.

The electron multiplier, whose signal rise time is about 10 nsec, generates a current which is acquired as a voltage signal after shorting on a 500 Ω resistor. The analogue signal is then digitised at 5 MHz and stored by means of a LeCroy L6810 ADC. In order to open a 100 μs acquisition window, so that unnecessary data are lost, a laser trigger is set in coincidence with every slit overlapping.

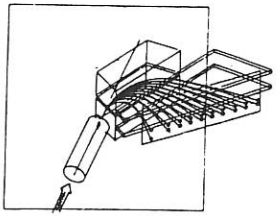

Fig.2: Stripping Cell NPA geometry

Stripping Cell Analyser: this analyser (Fig.2) was projected and realised at Laboratori ENEA at Frascati (Rome) and has already been used at JET for neutrals measurements /2,3/. The neutral atom beam is collimated by a series of three diaphragms, whose diameter is 3 mm, after a 5.2-meter-long vacuum duct. In the stripping cell the hydrogen (work pressure = $2.6 \cdot 10^{-3}$ mbar) ionises a fraction of the arriving neutral particles: the ions are deflected first by a couple of polar expansions in order to create a spread in energy, then by a couple of electrostatic plates in order to split the H and D components. A series of Galileo 4028 EIC CEMs (10 for the H line and 10 for the D line) detects the total flux of each component at previously operator-adjusted values of energy over an interval in the range 0.3 - 30 keV; both for the H and the D line, the energy ratio between any two channels is fixed by the geometry of the system. The signals from the CEMs are sent into a comparator-discriminator, whose TTL pulses are counted by a CAEN C298 scaler, which integrates the counts over a pre-set time interval (at present 5 ms).

II. MEASUREMENTS AND ANALYSIS

The parameter set for the stripping cell NPA depends on the present plasma characteristics. The typical plasma current is 600 kA; the electronic density, measured by the interferometer, is 2 to $4 \cdot 10^{19}$ m^{-3}; the electron

temperature obtained by the Si-Li detector is about 250 - 300 eV and the duration of the plasma current about 0.1 seconds.

At now the energy range expected for the CX neutrals produced by RFX plasma is lower than 4000 eV. For NPA we have chosen to operate the 600 - 7400 eV energy range, because the neutral atom fluxes with energies lower than 600 eV are too strong and saturate the CEMs. As a consequence of this choice measurements of the highest energy 4 or 5 channels have no physical meaning, because the signal is comparable with the noise due to the scattered UV radiation.

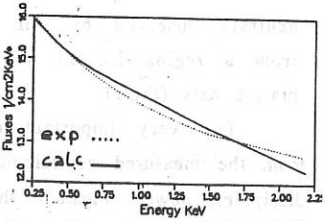

Fig.3: Example of an "off line" fit

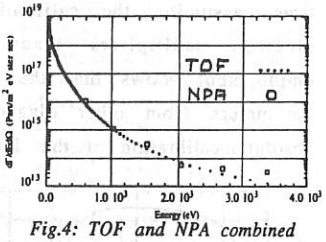

Fig.4: TOF and NPA combined energy spectra

We analyse the data in two steps. At first we evaluate in real time ("on line" analysis) the ion temperature /1/ by a fit in an energy range of about 800 - 3000 eV. After, we use a Monte Carlo simulation code (AURORA) /4,5/ ("off line" analysis) to fit an instantaneous experimental spectrum (Fig.3). The same code evaluates the output CX power, the total irradiated neutral atoms of Hydrogen, the radial distributions both of the neutral H density and of the ion and neutral H temperatures.

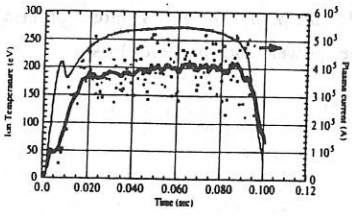

Fig.5: RFX pl. curr. and ion temp.

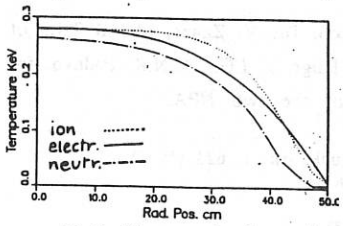

Fig.6: Electron, ion, neutral temperature profiles

We present now some experimental results. Fig.4 shows the overlapped neutral atom spectra, measured with the two analysers. In the next future, when the ion temperatures of the RFX plasma will be higher, the spectrum from NPA will be the extension of the TOF one.

In Fig.5 we present the ion temperatures versus time, obtained by the "on line" analysis: these are the temperatures of the hottest plasma region, transparent for the CX neutral atoms. Fig.6 points out that the in-axis plasma ion temperature, calculated by the AURORA code, is higher than the "on line" calculated temperature: the most energetic

neutrals observed by our instruments come from a region located at 0.25 m from the plasma axis (Fig.7).

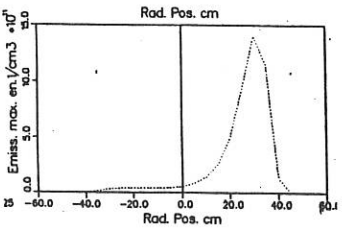

Fig.7: Diametral distribution of neutral emission

The very important quantity deducible from the measured neutral outfluxes is the CX dissipated power. Figs.8,9 show the "on line" evaluated fluxes and power emissions versus time, assuming the calibration data of the electron multipliers manufacturers. Codes employment shows that the measured flux is in agreement with the plasma parameters from other diagnostics, but it will be soon confirmed after the absolute calibration of the detectors.

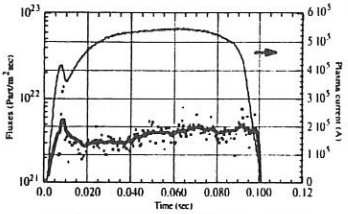

Fig.8: Neutral emission time evolution

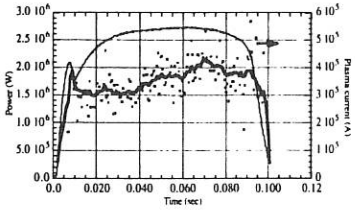

Fig.9: Power losses relating to neutral particle escape

III. CONCLUSIONS

We have described the two NPA equipment used for analysing the plasma of RFX. The first evaluations of the plasma parameters and the good agreement between the energy spectra of the two NPA systems seem to confirm the reliability of the experimental apparatus. In the near future the completion of the beam-driven apparatus for absolute calibration of the electron multipliers will allow us to get a more precise estimate of the power and particle loss.

ACKNOWLEDGEMENTS

The authors would like to thank Dr. G. Bracco, Dr. V. Zanza, Mr. B Tilia of the Laboratori ENEA, Frascati (Roma), and Eng. V. Toigo of I.G.I. C.N.R. Padova, for their irreplaceable contribution in the realisation of the two NPA.

REFERENCES

/1/ A.Schiavi , et al., 1992 Int.Conf. Plasma Phys.,Innsbruck, part I, 623 (1992).
/2/ R. Bartiromo, et al., Rev. Sci. Instrum. **58** (1987), 788.
/3/ R. Giannella,et al., Nucl. Fus., **28**, 193 (1988).
/4/ M.H. Huges, D.E.Post, Jou.of Comp.Phys.,**28**, 43 (1978).
/5/ A. Bignami,R. Chiorrini, ENEA-RT/FIMA(82) 10 (1982).

SPACE-RESOLVING FLAT FIELD SPECTROGRAPH FOR LARGE SIZED PLASMA DIAGNOSTICS

Naohiro Yamaguchi, Jungo Katoh, Yukiko Sato, Tatsuya Aota,
Atsusi Mase and Teruo Tamano

Plasma Research Center, University of Tsukuba, Tsukuba, Ibaraki 305, Japan

INTRODUCTION

Impurity line radiation and continuum radiation emitted from high-temperature plasmas fall in the spectral region from extreme ultraviolet (EUV) to soft x-ray. Therefore EUV/soft x-ray measurements are important methods to diagnose magnetically confined plasmas of the type used in fusion research. Measurements of spatial variation of radiation from plasmas are necessary for accurate determination of radiative power losses and ion density profiles which are extremely useful for understanding impurity transport, confinement and sources, and also for applications to diagnose plasma parameters. These measurements require instruments which provide simultaneous spectral, temporal and spatial coverage of the plasma.

We have developed and constructed new spatial imaging spectrographs, one of which covers the VUV spectral region from 200 Å to 1050 Å and other for the soft x-ray region from 20 Å to 350 Å. These spectrographs have been applied for measurements of a large sized plasma in the GAMMA10 tandem mirror device[1].

I. SPACE-RESOLVING VUV/SOFT X-RAY SPECTROGRAPH

The spatial imaging is realized by the optical system of an astigmatic pinhole camera, using a short entrance slit and a concave grating. Therefore key components of our spectrograph are an entrance slit of limited height, an aberration-corrected concave grating with variable groove spacing and an image-intensified two-dimensional detector. The aberration-corrected concave grating ruled by a numerically controlled ruling engine[2] is used to form a flat-field spectral output surface. Detailed ray tracing have been carried out to investigate the basic characteristics of the spectrographs in the practical geometric configuration for plasma measurement.

A. VUV SPECTROGRAPH

The conceptual drawing of the VUV spectrograph is shown in Fig. 1. The concave grating, specifically designed to cover the wavelength range from 200 to 1050 Å with an incident angle of 51°, has a radius of curvature of 500 mm, and a nominal groove density of 1200 g/mm. The entrance slit is settled about 2 m distant from the center of the plasma and has an opening of 100 μm wide by 2 mm high. The spectrograph has a field of view of 26-27 cm radius at the center of the plasma. The image of spectral line is directly detected by a 50×50 mm^2 microchannel plate (MCP) with a phosphor screen which converts a VUV spectral image to a visible image. Recording of the spectral image has been carried out by the two ways; one by the use of a solid state camera (256×256 pixels) with fast scanning controller and another by an instant photographic camera. In the former method one can obtain sequential space-resolving spectra in a single plasma shot with 9.6 ms temporal resolution, and in the latter method a snapshot with 1 ms temporal resolution can be taken.

The basic characteristics have been confirmed through calibration experiments using a DC glow discharge source. In Fig. 2 are shown the results of spatial imaging test when an

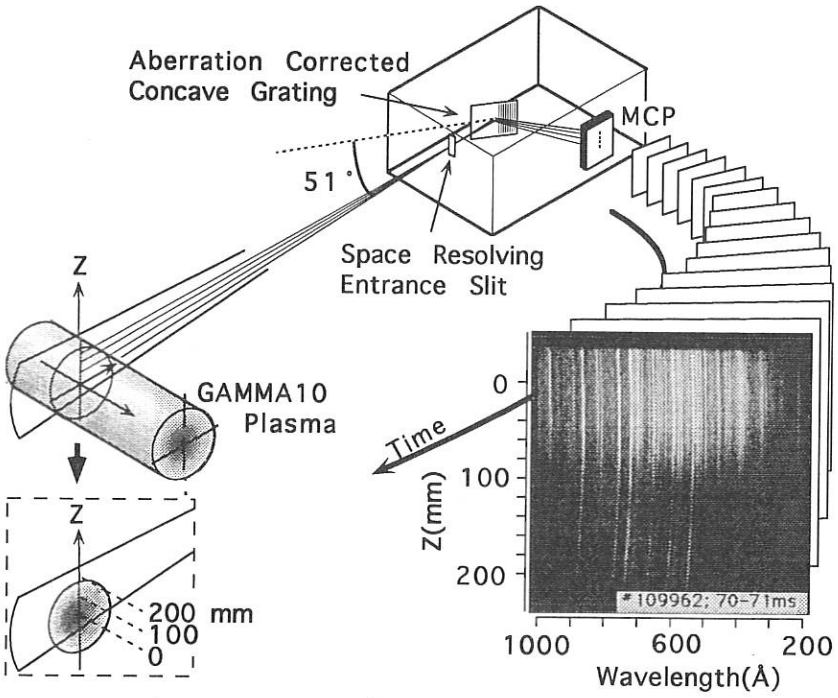

Fig. 1 : Schematic of the space- and time- resolving VUV spectrograph. The spectrograph views the upper half of the plasma.

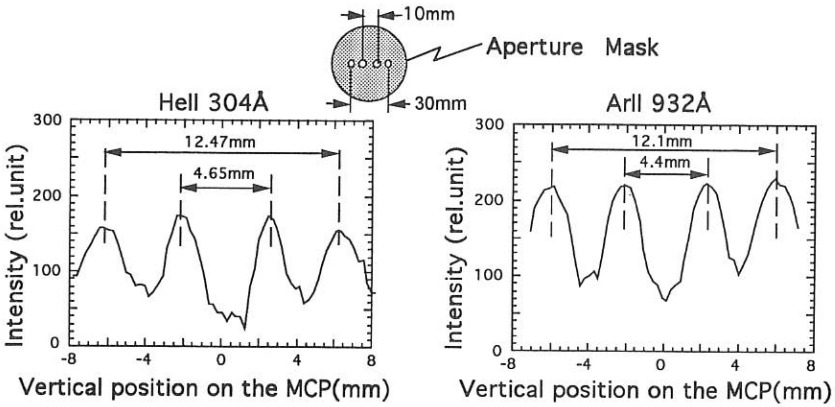

Fig. 2 : Spatial image profiles of He and Ar lines when the aperture mask is put just in front of a light source. The light source is about 1 m distant from the spectrograph.

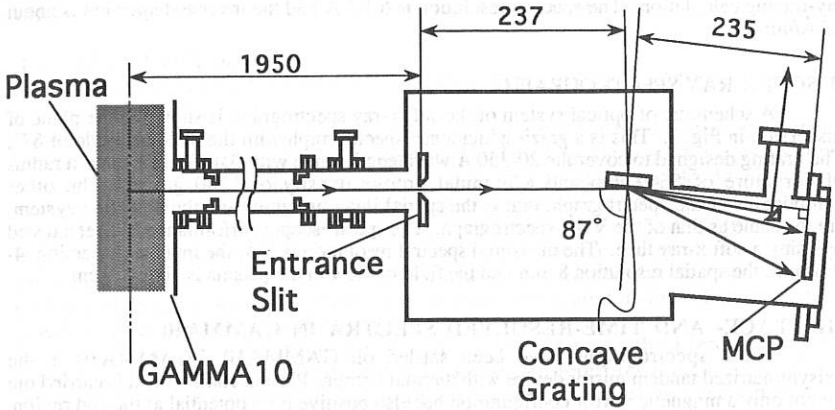

Fig. 3 : Schematic of the soft x-ray spectrograph.

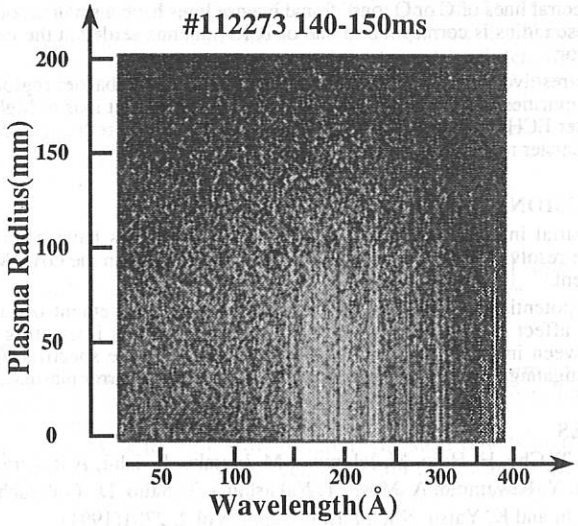

Fig. 4 : Space-resolved soft x-ray spectrum of the GAMMA10 plasma.

aperture mask is set in front of the light source. The intensity profiles are taken vertically to the direction of dispersion for He 304 Å and Ar 932 Å lines. These results lead the spatial resolution of this spectrograph is 7-10 mm at the center of plasma, which agrees well with the ray-tracing calculation. The spectral resolution is 6 ± 3 Å and the inverse dispersion is about 20 Å/mm.

B. SOFT X-RAY SPECTROGRAPH

A schematic of optical system of the soft x-ray spectrograph is shown in the plane of dispersion in Fig. 3. This is a grazing incidence spectrograph with the incident angle of 87°. The grating designed to cover the 20-350 Å wavelength range with flat focal field has a radius of curvature of 5649 mm and a nominal groove density of 1200 g/mm. The other components of the spectrograph, that is the spatial imaging optics and the detection system, are the same as that of the VUV spectrograph. The spectroscopic performance has been tested by using a soft x-ray tube. The measured spectral resolution is 3 Å, the inverse dispersion 4-9 Å/mm, the spatial resolution 8 mm and the field of view in the plasma is about 20 cm.

III. SPACE- AND TIME-RESOLVED SPECTRA IN GAMMA10

These spectrographs have been settled on GAMMA10. GAMMA10 is the axisymmetrized tandem mirror device with thermal barrier. Plasma confinement is carried out by not only a magnetic mirror configuration but also positive high potential at the end region. The plug potential is produced by means of ECH at the plug/barrier region. The main plasma confined in GAMMA10 is produced and heated by ICRF power deposition. Space- and time-resolved spectra have been obtained successfully in the GAMMA10 experiment.

A VUV spectrophotograph taken at the central cell is shown in Fig. 1. Almost all lines distribute within a region of about 10 cm radius where the main plasma exists, and identified as spectral lines of C or O ions. Some intense lines have a small second peak in the outer edge whose radius is correspond to that of ICRF antenna settled at the near end of the central cell mirror.

A space-resolved soft x-ray spectrum of the plasma at the barrier region is shown in Fig. 4. Main impurities are also C and O. It has been observed that ions of higher ionization stage appear after ECH power injection. This would relate to the production of hot electrons by ECH in the barrier region[3].

IV. CONCLUSION

New spatial imaging VUV and soft x-ray spectrographs have been constructed. Space- and time-resolved spectra have been obtained successfully in the GAMMA10 tandem mirror experiment.

Plasma potentials, which take an essential role in confinement of tandem mirror plasma, would affect distributions of impurity ions. Then it is interesting to study the correlation between impurity profiles and potential ones. These spectrographs could be utilized in investigating impurity transport phenomena in tandem mirror plasmas.

REFERENCES

[1] S. Miyoshi, T. Cho, H. Hojo, M. Ichimura, M. Inutake, K. Ishii, A.Itakura, I. Katanuma, Y. Kiwamoto, A. Mase, Y. Nakashima, T. Saito, D. Tsubouchi, N. Yamaguchi and K. Yatsu, Nucl. Fusion Suppl. Vol.2, 2781(1991).

[2] H. Harada and T. Kita, Appl. Opt. 19, 3987(1980).

[3] Y. Kiwamoto, T. Saito, T. Cho, N. Yamaguchi, A. Mase, A. Sakasai, T. Kariya, T. Kondoh, H. Gotoh, I. Katanuma and S. Miyoshi, Phys. Fluids 29, 2781(1986).

Effects of Peripheral Physical Phenomena on ECE Spectra

A.Airoldi and G.Ramponi
I.F.P. Associazione EURATOM-ENEA-CNR, Via Bassini, 15 - Milano (Italy)

Introduction- In large fusion Tokamaks the measurement of the Electron Cyclotron Emission (ECE) from the low field side, perpendicularly viewing chord, is by now a standard way of obtaining the radial electron temperature profile. In high temperature plasmas the condition of large optical thickness for the second harmonic X-mode may be easily satisfied even for frequencies corresponding to the edge plasma region, allowing the temperature profile to be inferred. Recent experimental observations of enhanced emission at frequencies associated with the extreme edge of the profile in H-mode JET plasmas have been interpreted as the effect of a small fraction of suprathermal electrons/1/.
It is well known that the ECE spectra are very sensitive to the presence of non-thermal electron components, thus it is important to interpret the ECE signals as an indication of the possible deviation of the electron distribution function from a 'pure' Maxwellian and to discern under which conditions they are a good measure of the plasma thermal energy.
To address these ECE diagnostic problems, we use a comprehensive ray-tracing, cyclotron emission and absorption code which solves the radiation transfer equation by using a relativistic calculation of the absorption and emission coefficients, both for Maxwellian and non-Maxwellian plasmas/2/. The electron distribution function is assigned as a function of the normalized flux function $\bar{\psi}$ .In the code the 'observed' radiation temperature is obtained by integrating the transfer equation along (3-D) ray trajectories by taking into account the overlapping of different harmonics as well as that of thermal and non-thermal emissions at the same frequency, and the possible double passage through resonances due to reflections at cutoff layers. Wall reflections are also taken into account through the relation:

$$T_r(f) = \frac{8\pi^3 c^2}{(2\pi f)^2} \int_0^{s_a} \beta(f) e^{-\int_s^{s_a} \alpha(f) ds'} ds \,/\, (1 - R_w e^{-\int_0^{s_a} \alpha(f) ds}) \qquad (1)$$

where $T_r(f)$ is the radiation temperature observed at the antenna($s = s_a$), s is the abscissa along the ray path, α and β are the relativistic absorption and emission coefficients respectively.
The aim of this work is to show how different physical effects at the edge plasma may cause the appearance in the observed radiation temperature spectra of peculiar features of thermal and non-thermal origin. Namely we investigate the effects due to:
i) large gradients of the edge pressure in Maxwellian plasmas;
ii) peripheral trapping of electrons
iii) presence of parallel tails in the electron distribution function.
The simulations of the spectra of radiation emitted at the second harmonic X-mode along the equatorial plane are performed by using a JET-like equilibrium plasma, characterized by the following parameters:

$$B_o = 2.2T;\ R_o = 3.29m;\ a = 1.13m;$$

$$n(\overline{\psi}) = (n_o - n_a)(1 - \overline{\psi}^{e1})^{e2} + n_a,\ n_o = 5x10^{13}cm - 3;\ n_a = .5x10^{13}cm - 3$$

$$T(\overline{\psi}) = (T_o - T_a)(1 - \overline{\psi}^{b1})^{b2} + T_a,\ T_o = 10Kev,\ T_a = 0.5Kev$$

Effects of combined relativistic downshift and large temperature gradients at the edge- We consider here a Maxwellian plasma, characterized by high values of Te and dTe/dR at the edge. In the range of frequencies corresponding to resonances near the outer edge a hump may appear (as shown in Fig.1), whose intensity increases with the steepness of the temperature profile. The nature of this hump is thermal even if the radiation temperature in this narrow frequency range is above the electron temperature of the corresponding 'cold' resonant point. The frequency position of the peak radiation temperature (f=97 Ghz in the considered cases) marks the steep transition from optically thin to optically thick radiation, as shown in Fig.2 by the corresponding values of the optical depth τ .
In fact, the high reabsorption of radiation ($\tau > 4$) for frequencies f > 98 Ghz blocks the downshifted emission of the electrons resonating at radial positions R' < R, being R' = R/ γ and γ the relativistic factor (R and R' represent the 'cold' and 'hot' resonant positions corresponding to the same frequency). On the contrary, for frequencies corresponding to the hump region where the plasma is optically thin,the downshifted emission is weakly reabsorbed and wall reflections may amplify the single pass radiation temperature to values corresponding to T(R') > T(R). (The wall reflection coefficient has been taken R_w =0.6 in present calculations).

Effects of peripheral trapping of electrons- In this and in next sections we show how the departure from isotropy of the velocity distribution of the electrons near the edge may affect the spectrum of the emitted radiation. We consider two cases of anisotropic velocity distributions. The first case refers to a distribution where the perpendicular energy of a fraction of particles is greater than their parallel energy. An important example is the case where there is a deficiency of particles with small perpendicular energy: these so called loss-cone distributions occur naturally in magnetic mirror configurations. In tokamaks they could represent the fraction of electrons trapped in local mirrors due to the ripple of the toroidal field. Having in mind the experiment with enhanced toroidal field ripple on JET plasmas (where the ripple at the position of the outer limiter was $\delta = (B_{max} - B_{min})/(B_{max} + B_{min}) =$ 12%), we calculate the spectrum of the radiation accepted by the low field side antenna by assuming that the electron distribution function contains a thermal part and a fraction w_t of trapped particles described by:

$$f_{LC} = K_{LC}\ p_\perp^{2m}\ e^{-\frac{\mu}{2}(p_\perp^2 + p_\parallel^2)}$$

where m is the loss-cone index, K_{LC} is the normalization constant and $\mu = mc^2/T$. The generalized absorption and emission coefficients are calculated in the form given in Ref./3/. By taking m=1, μ the same as that of the thermal part and the fraction w_t depending on the local magnetic ripple δ as $w_t = \sqrt{(2\,\delta/(1 - \delta))}$, we obtain the radiation spectra shown in Fig.3 . The level curves in the plane ($p_\perp$,$p_\parallel$) of the corresponding distribution function near the outer edge are shown in Fig.4. It is worth noticing that in the considered case the average perpendicular energy of the electrons is $E_\perp = (1 + mw_t)\ T$, so that the enhancement of the non-thermal

radiation temperature with respect to the thermal one shown in Fig.3 is just an indication of the difference between $E_\perp$ and T. The anisotropy of the distribution function cannot however be inferred by the observation of perpendicular ECE only.

Effects of non-thermal parallel tails- In this section we consider the case of an anisotropic distribution function where the parallel energy is dominant. Besides the thermal bulk, it contains a non-thermal tail of electrons that have been accelerated along the magnetic field. Such a distribution could simulate runaway electrons created at low densities by the toroidal electric field or LH current drive conditions. By considering a distribution function like that shown in Fig.5 (where the parallel energy of the positive tail has been limited to 60 Kev and their perpendicular temperature is 4 Kev) in the region $0.8 < \overline{\psi} < 1$, we obtain the radiation spectra of Fig.6. It may be observed that in this case the non thermal spectra look similar to the thermal of Fig.1, although the corresponding distribution functions are very different in the parallel direction. This is due to the weak dependence of perpendicular ECE on the parallel electron energy.

References

/1/ D.Bartlett et al., *Proc. of 19th European Conf. on Contr. Fusion and Plasma Phys.*, Part I p.165, Innsbruck 1992

/2/ A.Airoldi, A.Orefice and G.Ramponi, *Il Nuovo Cimento* **13D**, 517, (1991)

/3/ A.Orefice *J.Plasma Physics* **39**, 61, (1988)

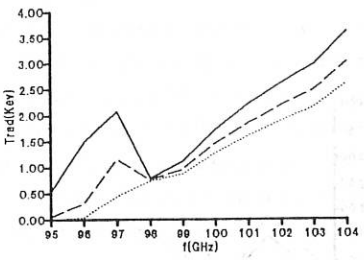

Fig.1)- X-mode radiation temperature spectra at frequencies in the second harmonic edge region, for different temperature profiles. Dotted line: b1 = 1, b2 = 1; dashed line: b1 = 1.2, b2 = 1; continuous line: b1 = 1.5, b2 = 1.

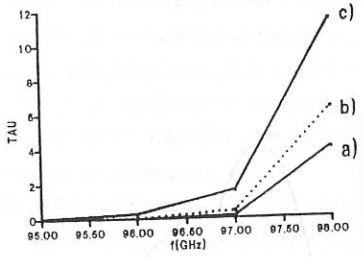

Fig.2)- Optical depth vs. frequency for the same cases of Fig.1: a) b1 = 1; b) b1 = 1.2 ; c) b1 = 1.5.

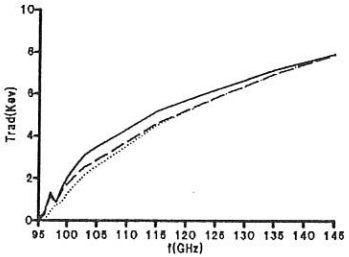

Fig.3)- Non-thermal spectra in presence of a fraction w_t of electrons having a loss-cone distribution, compared with the corresponding thermal case (dotted line). The two cases differ for the radial profile of w_t (dashed curve: w_t = 0.47 at the edge(R = 4.4 m), w_t = 0.01 at R = 3.9 m; continuous line: w_t = 0.47 at R = 4.4 m, w_t = 0.01 at R = 3.5m)

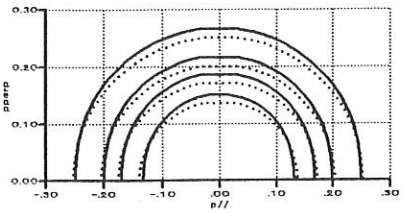

Fig.4)- Level curves in the plane ($p_\perp$, $p_\parallel$) of the electron distribution function giving the dashed spectrum of Fig.3, at R = 4.3 m (w_t = 0.3, m = 1). Dotted circles are the corresponding Maxwellian.

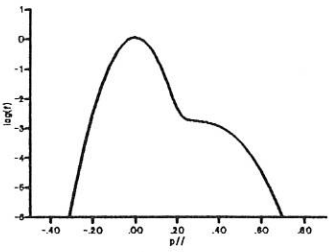

Fig.5)- Electron distribution function vs. $p_\parallel$ at $\overline{\psi}$ = 0.9, assumed to calculate the non-thermal spectra of Fig.6.

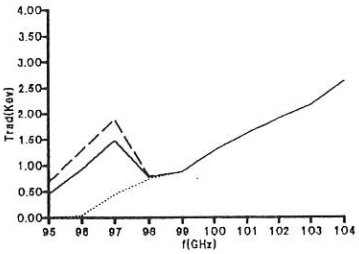

Fig.6)- Non-thermal spectra obtained in presence of a parallel tail like in Fig.5. Dashed line: fraction of suprathermals = 0.01, $T_\perp$ = 4 Kev; continuous line: fraction of suprathermals = 0.005, $T_\perp$ = 4 Kev; dotted line is the corresponding thermal spectrum.

NEXT STEP NEUTRON DIAGNOSTICS

H Condé, J Frenje, B Holmqvist, J Källne, E Nilsson, PU Renberg
Uppsala University, INF-ISV-TSL, S-751 21 Uppsala, Sweden.
G Gorini
Dept. of Physics, University of Milano, I-20133 Milano, Italy[a)]

It is recognized that the neutron emission will be one of the main means to observe burning fusion plasmas of the next step tokamaks, not only in the conventional meaning of plasma diagnosis but also for plasma control and safety monitoring purposes[1)]. High requirements on accuracy, reliability and prompt information delivery must be met by these neutron diagnostics. Moreover, information must be provided on a much more extended range of plasma parameters than present neutron diagnostics have dealt with. Tokamaks for burning plasmas will therefore require the development of next step neutron diagnostics involving the testing of hitherto unexplored measurement methods.

Future plasma neutron information will depend on the use of neutron spectrometers and neutron cameras measuring basic plasma parameters such as the ion temperature, T_i (for the thermal plasma component), the radial distribution of the neutron emission, $y_n(r)$, and the fusion power (i.e., total neutron yield, Y_n, being the volume integral $Y_n=\int y_n \cdot dV$). Here, y_n is the product of an ion velocity (or T_i) function and the (fuel) ion densities which can be derived. Additionally important derived information includes neutron source characteristics, the thermal to non-thermal fusion power ratio, etc., and α-particle effects. The quality of this information can be no better than the statistical accuracy of the data so a basic figure of merit is the number of counts recorded by the instrument over consecutive short time intervals, i.e., count rate , C_n. The interval length is the time resolution that is required in order not to have to integrate over large parameter variations of the plasma evolution[2)].

The normal operating range of the next step neutron diagnostics would start at count rates of $C_n \approx 100$ kHz and extend into the tens of MHz. This is considerably (orders of magnitude) faster than have been mastered by the present neutron spectrometers and cameras for deuterium plasmas. Therefore, new detection methods must be used that have practically no intrinsic capability limit with regard to count rate (i.e., $C_n^{CAP} >> 10$ MHz). The magnetic proton recoil (MPR) method[3)] is of this type and it has also sufficient neutron flux sensitivity (efficiency, $\varepsilon > 10^{-5}$ cm^2) so that, for anticipated collimated fluxes (F_n), the attained count rate ($C_n = \varepsilon \cdot F_n$) would fall in the stipulated operating range for burning plasma studies.

Spectrometer and camera concepts based on MPR have been presented for use on ITER and NET[4)]. A

---

a) This contribution is now part of the MPR project collaboration being formed between the Associations EURATOM-ENEA of Italy and EURATOM-NFR of Sweden.

prototype MPR spectrometer is under construction[b] and planned for use at JET during the main DT phase[5]. In this contribution we shall describe the principles of this MPR spectrometer, illustrate the projected diagnostic capabilities on JET and describe some specific tests that can be performed with relevance for the planning of spectrometers and cameras on ITER.

The MPR concept is simple. A collimated neutron beam is made to produce recoil protons in a thin target (CH_2 foil); the target is placed at the end of the collimator. The recoils arise from nuclear scatterings $n+p_H \rightarrow n'+p$ where n is the incoming neutron, p_H a target proton, n' the scattered neutron and p the recoil proton. The protons emitted in the forward direction (mean angle $\theta_p=0$) within the solid angle Ω_p are selected for momentum analysis and transport to an array of proton detectors where they are counted in a number (about 50) of narrow energy bins. The **count rate capability** is $C_n^{CAP}>5$ MHz per counter which means >25 MHz for narrow spectral features (e.g., the 'thermal' peak) and >>100 MHz for broad features extending over all 50 detector counters. The **actual count rate** is determined by the available flux from the plasma and the ε-value of the spectrometer which in turn is a function of the energy resolution ($\Delta E/E$) as has been described in detail elsewhere[2-4]. Here, however, we shall consider an issue of special relevance to the JET experiment, namely, **count rate optimization,** and its corollary, the **handling of background**.

The optimization is best expressed by noting that the count rate is proportional to the solid angle product $\Omega_p \cdot \Omega_n$ where Ω_n is the solid angle of the neutron collimator defining the incoming neutrons. It is in our case a cylinder of fixed cross section A=10 cm^2 (diameter ϕ=3.6 cm) and length l, i.e., $\Omega_n=A/l_c^2$. The two solid angles define the energy difference distribution in E_n-E_p and, hence, the kinematics contribution ($\Delta E_K/E$) to the spectrometer energy resolution ($\Delta E/E$). There are three main contributions to $\Delta E/E$, namely, the spectrometer optics ($\Delta E_s/E$) and the proton energy loss in the target ($\Delta E_t/E$), besides the $\Delta E_k/E$ contribution, each adding to $\Delta E/\Delta E$ that would typically be chosen to be around 2.5 %. The ΔE_t and ΔE_k are generic neutron detection terms, while ΔE_s is specific for MPR. Thus, for given $\Delta E/E$, one would try to optimize the count rate from a plasma of given Y_n, for instance, by opening up the neutron collimator by decreasing its length ($C_n \propto 1/l_c^2$).

There are, however, constraints on the usable size of the collimator aperture, namely, the viewing port size ($x_v \approx 25$ cm in this case) and the plasma size ($x_p \approx 50$ cm taken as FWHM of the emissivity profile). In order to use a large collimator aperture (say $l_c=l_c'=50$ cm), the MPR should be placed close to the port with the distance to the target being $l_v \approx l'_v \approx 1.8$ m which also clears the plasma size requirement (distance being about $l_p=l'_p \approx 4.5$ m for a near tangential sight line). A closer position than l' will not benefit the count rate, but removing the spectrometer would quickly reduce the count rate in proportion to l_v'/l_v^2. Thus, a Torus Hall location is required for full exploitation of the MPR and the high background radiation that comes with this location must be faced.

The MPR has a high tolerance to background since it is only necessary to detect (count) protons of specific energy (say 14-MeV) and, hence, specific pulse height. Therefore, strict (±5 %) pulse height discrimi-

---

[b] Los Alamos National Laboratory is participating in this project by contributing design efforts.

nation can be applied to reject all radiation but for the fraction of 14-MeV neutrons interacting in the scintillation detectors with the same pulse height as the protons from the target. The 14-MeV neutron flux at the detector must be reduced to a level where its contribution to the true signal rate is negligible. It is estimated that a 150 cm thick front shielding of concrete, with a 30 cm complement elsewhere, is sufficient to handle the 14-MeV neutron background and it would, at the same time, prevent other types of radiation from harming the pulse height discrimination efficiency by pile up effects. Although detailed interface checking remains, it is clear that the MPR, with its shielding, is compatible with the space limitations and the radiation levels at such a position near a JET horizontal port that would allow operation at the maximum count rate for a given total neutron yield, Y_n. The count rate would be $C_n=\eta \cdot Y_n$ with $\eta \approx 10^{-13}$ corresponding to an MPR efficiency of $\varepsilon=7 \cdot 10^{-5}$ cm^2 which is only slightly below (a factor of less than 3) the generic upper limit for neutron detection at $\Delta E/E=2.5$ %. JET will have other neutron spectrometers but these are positioned outside the Torus Hall at a distance of some 20 m from the plasma. In this case, the η–values will not exceeding the 10^{-15} range and the mentioned count rate optimization is not an issue.

The MPR would reach a count rate of about 0.2 MHz for a 10 MW DT discharge in JET and would thus open up new possibilities for neutron spectrometry observations. Since the MPR operates close to the 'theoretical' upper limits for neutron spectrometry, and since it is a novel technique to tokamak plasma measurements, certain tests are called for.

The JET set-up would have a neutron collimator with (remotely) variable length l_c=50-150 cm. This would have several objectives, namely, to study effects of neutron (back) scattering from the plasma wall, collimator in-scattering, halo effects of the beam passing through the MPR spectrometer, etc. Moreover, there would be a target changer for variation of target thickness, and hence direct variation of $\Delta E_t/E$ and ε, besides a changer for variation of Ω_s to adjust $\Delta E_s/E$ and ε. The planned mapping of operating ranges will be essential for characterizing the MPR spectrometer and to determine its performance limits. Tokamak measurements are the sole source of this information.

With the MPR, it is possible to measure the neutron spectrum over an extended energy range, say from about 5 to 18 MeV, the band width being ±20 % in each setting of magnetic field. Neutrons of 5-11 MeV are due to back scattering which will be analyzed in terms of neutron transport models. Understanding the back scattering is necessary for projecting the performance of neutron spectrometry as a fuel density diagnostic on ITER and the performance of neutron cameras as a plasma profile diagnostic.

The radiation sensitivity of the proton detector system will be studied so as to obtain numbers for the background to signal ratio for different conditions of beam flux and total neutron production as well as aperture and target settings. For 14-MeV neutrons, the background effects are not expected to be difficult to handle but they will in the measurement of 2.5-MeV neutrons from dd-reactions, as the fuel density diagnosis on ITER will require.

The diagnostic measurements of importance to the JET program will include ion temperature (T_i), the absolute value of the line integral $\int y_n(s) \cdot ds$ (along the sight line s), fusion power composition (according to its thermal and non-thermal components), etc, and additionally derived fusion reactivity information. To illustrate the quality of these measurements one can mention that if all fusion power (at its peak value) was due to the thermal

reactions, the statistics in the T_i determination would reach ±10% for a time resolution of 1 ms (or ±3 % at 10 ms, etc.). This would allow one to follow major features in the plasma variations such as the saw teeth rises even for plasma conditions of moderate fusion power levels. Similarly, as judged from the results of the preliminary tritium tests[2], the dynamic range connected with this count rate should permit measurement of T_i at its base level before the application of additional heating (for instance, neutral beam injection, NBI). In this way one could follow the energy rise in the plasma for application of given NBI power level and pulse length.

Thanks to the good statistics, the thermal peak could be distinguished even with non-thermal contributions present due to NBI or RF power injection. The non-thermal contributions would be determined and its spectral shape and amplitude (because of the absolute efficiency calibration) would be sufficiently determined for detailed and quantitative comparison with results from plasma predictive codes such as TRANSP. This information would be essential for determining the Q-value of the discharge. Neither of these aspects of plasma ion information have been purported to be available from other diagnostics.

In the conference presentation, examples will be discussed that quantify the planned test and diagnostic measurements of the MPR neutron spectrometer project on JET. We will discuss some of the technical aspects of using the MPR in the JET Torus Hall during the main DT phase and the benefit-to-cost ratio of the project. The benefit relates both to obtaining essential prototype information about the next step neutron diagnostic systems and to providing important diagnostic information to the JET program. The cost of the MPR project is not higher than typical for neutron spectrometers.

REFERENCES

1) "ITER DIAGNOSTICS", (V Mukhovatov et al), ITER document series no. 33, IAEA, Vienna, 1990.
2) "NEUTRON SPECTROMETRY CONCEPTS FOR DIAGNOSING DT PLASMAS OF Q≈1", (J Källne, G Gorini, H Condé and PU Renberg), EPS conf. Innsbruck, June 1992, Vol. II p 1047
3) "MAGNETIC PROTON RECOIL SPECTROMETER FOR FUSION PLASMA NEUTRONS", (J Källne and H Enge), Nucl Instr. Meth. **A311**(1991)595.
4) "NEUTRON DIAGNOSTICS FOR BURNING PLASMAS: SURVEY STUDIES, CONCEPTUAL DESIGNS, AND PROPOSALS OF NEUTRON DIAGNOSTICS FOR THE NET/ITER TOKAMAK", (J Källne and G Leman) Uppsala university neutron physics report (1991) UU-INF #1/91, and NET Physics Memo (1990) PM90-003.
5) "THE MPR ON JET PROJECT" (J Källne and G Leman), Uppsala University Neutron Physics Report, March 1993.

Frequency-resolved measurement of electron density, plasma potential and electron temperature fluctuations using a four-probe array technique

M. Krämer and B. Fischer

Institut für Experimentalphysik II, Ruhr Universität Bochum
D-44801 Bochum, Germany

1. Introduction. Reliable measurements of electron density, plasma potential and electron temperature fluctuations are necessary to obtain the fluctuation-induced particle and energy fluxes as well as to compare the theoretical predictions on low-frequency wave instabilities, turbulence theories, etc. with the experimental findings. Here, a new technique is proposed which uses a 4-probe-array consisting of a double probe (DP) and two reference probes (RP). Relating the spectral components of the DP current-voltage characteristics to those of the RP's we can construct time-resolved probe characteristics from which the amplitude and the phase spectra of the fluctuating quantities are computed. We believe that the proposed method yields more reliable results than /1,2/. Clearly, it only allows to measure the *coherent* part of the fluctuation spectra, which, however, is the relevant part contributing to the fluctuation-driven transport.

2. Principle of the technique. The technique uses an array of 4 Langmuir probes with the tips equally spaced in poloidal/azimuthal (θ) direction. The inner pair of probes (2 and 3) form a usual DP, whereas the outer probes (1 and 4) serving as *reference* probes are biased into the ion saturation current regime. (Note that the ion saturation currents of double and single probes are equal.) For the computations (with synthetic fluctuations) we used the ideal DP model for plane probes. In the presence of fluctuations (denoted by $\tilde{}$) we can write the current (DPC) as

$$I = \bar{I} + \tilde{I} = aAe\bar{n}\bar{T}_e^{1/2}(1+\tilde{n})(1+\tilde{T})^{1/2}\tanh\Big(0.5(u-\tilde{u})/(1+\tilde{T})\Big),$$

where $\tilde{n} = \tilde{n}_e/\bar{n}$, $\tilde{T} = \tilde{T}_e/\bar{T}_e$, $u = eU/\bar{T}_e$, $\tilde{u} = e\tilde{U}/\bar{T}_e$, , a: constant factor $O(1)$, A: probe area, n_e: electron density, T_e: temperature, U: probe voltage, $\tilde{U}$: difference of plasma potentials. The procedure is described as follows:

(1.) The voltage applied to the DP is scanned in small steps whereby a sufficient number M of time series (N samples in interval T) of the three probe currents are taken for each DP voltage. (2.) The time series are then Fourier-transformed.

(3.) The phases of the DPC Fourier components are related to the averaged phases of the RPC components. Thus, phase differences between the two probes owing to finite fluctuation wavenumbers cancel so that the reference signal is approximately taken at the DP position.

(4.) The mean values of the density and the temperature are evaluated from the time-averaged DP characteristics. The spectral components of the fluctuations $(\tilde{n}(f_n), \tilde{u}(f_n),$

and $\tilde{T}(f_n)$, $f_n = n/2T$, $n = 1, ..., N$) are then determined by adding the mean (averaged over M time series) DP spectral component $Re(\tilde{I}(U, f_n)\exp(-i\psi))$ to the time-averaged DPC and fitting this characteristic by the nonlinear algorithm of Levenberg and Marquardt (see e.g./3/). This procedure is performed for $\psi = 2k\pi/K$, ($k = 1, 2, ..., K$, $K \geq 16$) yielding the fluctuations over one oscillation period. The three spectral components are then simply determined from the first harmonic of this oscillation so that errors owing to the distortion of the DP characteristics at larger fluctuation amplitudes and/or evaluation errors are reduced.

(5.) Once the fluctuation spectra are known, the particle and heat fluxes can easily be calculated from $< \tilde{n}\tilde{u} >$ and $< \tilde{T}\tilde{u} >$.

3. Results

(a) *Synthetic fluctuations.* The method was tested with synthetic fluctuation data whose spectra are a superposition of a coherent Gaussian spectrum and an incoherent spectrum (Gaussian or white noise) assuming fixed phase differences between the three coherent spectra. With these data the DP and RP currents were generated, whereby the coherent parts of the fluctuations at the measuring and reference probes are assumed to be in phase.

In Fig.1, we show the typical numerical results. Reasonable agreement between the given and the computed spectra can be seen, particularly for smaller fluctuation amplitudes. Merely the fluxes are slightly below the values expected. Note that the shift of the phases (Fig.1e) is caused by the finite phase difference between the density and the ion saturation current fluctuations for the chosen phases. The computations with the synthetic data have been performed extensively varying all quantities of interest. The agreement between the given and the computed fluctuation spectra turns out to depend only weakly on the width of the spectra and the coherency whereas it is stronger effected by the phase differences between the three fluctuating quantities.

(a) *Measured fluctuations.* The probe measurements were performed on a ECR-produced linear plasma column ($n_e \leq 10^{17}m^{-3}$, $T_e = 3\text{–}6eV, p = 2\times10^{-3}Torr H_2$, probe position $2.5cm$ off axis, tips $\parallel B_0 = 0.22T$, $r = 0.1mm, l = 5mm$, probe distance $d_p = 2mm$). For the calculations, we have used different probe characteristics yielding the best fit for $I \propto U\,(\tanh(eU/2T_e) + const)$. That the ion saturation current increases with the probe voltage revealing essentially no dependence on T_e is confirmed by resonance cone diagnostic.

In Fig.2., we have plotted the measured spectra from which some interesting features can be inferred. The amplitudes of the plasma potential fluctuations are much larger than those of the density (normalized $|\tilde{\phi}| \approx |\tilde{u}|/(\bar{k}_\theta d_p)$). Further, there is a correlation between the dispersion curve ($\bar{k}_\theta$) and the temperature fluctuations. Finally, we note that the temperature fluctuation-driven is relatively small ($< \tilde{n}\tilde{u} > \approx 2 \times 10^{-3}$, $< \tilde{T}\tilde{u} > \approx 10^{-4}$).

References

/1/ Robinson D. C. and Rusbridge M. G. (1969) Plasma Phys. **11**, 73.

/2/ Tsui H. Y. W. et al. (1991) Nucl. Fusion **31**, 2371.

/3/ Press W. H. et al. (1989) *Numerical Recipes* Cambridge Univ. Press, Cambridge.

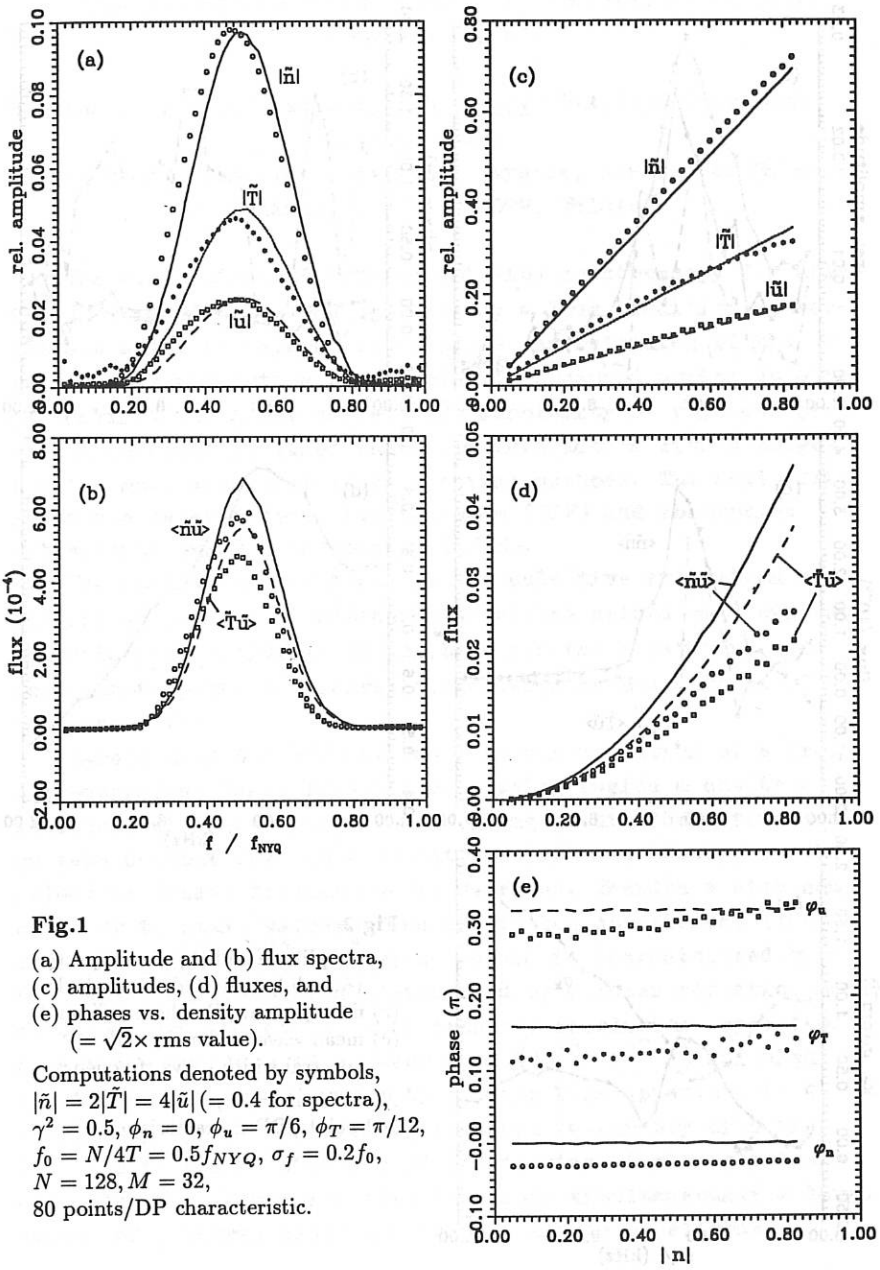

Fig.1

(a) Amplitude and (b) flux spectra,
(c) amplitudes, (d) fluxes, and
(e) phases vs. density amplitude
($= \sqrt{2}\times$ rms value).

Computations denoted by symbols,
$|\tilde{n}| = 2|\tilde{T}| = 4|\tilde{u}|\,(= 0.4$ for spectra),
$\gamma^2 = 0.5$, $\phi_n = 0$, $\phi_u = \pi/6$, $\phi_T = \pi/12$,
$f_0 = N/4T = 0.5 f_{NYQ}$, $\sigma_f = 0.2 f_0$,
$N = 128, M = 32$,
80 points/DP characteristic.

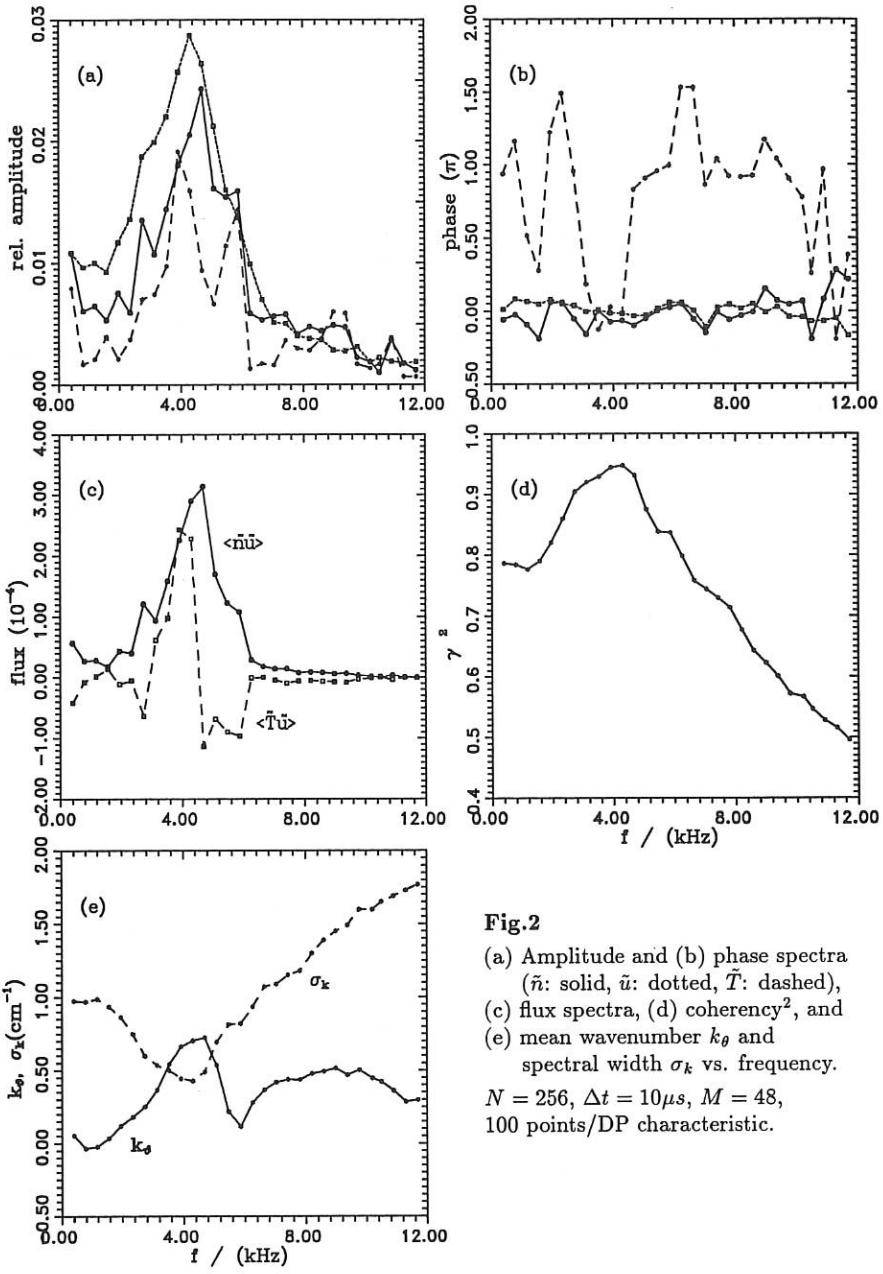

Fig.2

(a) Amplitude and (b) phase spectra ($\tilde{n}$: solid, $\tilde{u}$: dotted, $\tilde{T}$: dashed),
(c) flux spectra, (d) coherency^2, and
(e) mean wavenumber k_θ and spectral width σ_k vs. frequency.

$N = 256$, $\Delta t = 10\mu s$, $M = 48$,
100 points/DP characteristic.

LASER FLUORESCENCE AND ABSORPTION SPECTROSCOPY OF LASER ABLATION PLASMAS

V. S. Burakov, P. A. Naumenkov, S. N. Raikov, N. A. Savastenko and N. V. Tarasenko

Institute of Molecular and Atomic Physics, Academy of Sciences of Belarus, Minsk, 220072, Belarus

The application of optical emission spectroscopy for ablation plasmas diagnostics has already a long tradition. Nevertheless a lot of papers the complete understanding of the fundamental properties of the plasmas produced during ablation is lacking. The great variety and complexity of physical processes involved in laser radiation interaction with a target require more sensitive laser spectral methods. The most efficient are laser-induced fluorescence (LIF) and absorption intracavity laser spectroscopy (ICLS).

The well known LIF based on the selective excitation of plasmas species is an ultrahigh sensitive method with wide diagnostic possibilities. It has been for the first time used for high temperature plasmas diagnostics by the authors of this paper /1/.

Rarely used the ICLS is based on the variation of a frequency-dependent laser losses when placing inside a cavity a substance with absorption lines lieing within the active medium gain contour /2/. As a result, radiation weakening on the selective losses frequencies is observed. Besides a high sensitivity to small values of an absorption coefficient (the limit is 10^{-10}-10^{-11} cm^{-1}), the method is characterized by a high spectral resolution, determined by a laser radiation mode structure (~ 0.01 cm^{-1}), high temporal resolution, specified by a pulse duration of a laser used (10^{-8}-10^{-2} s) and high spatial resolution, limited by a laser beam apperture in a cavity ($\lesssim 1$ mm). The ICLS is compared favourably with the LIF, due to the possibility of diagnostics of strongly luminous plasmas. It permits also to record simultaneously a large amount of spectral lines shapes in a single experiment.

In this paper a diagnostics of model ablation plasmas has been undertaken utilizing both laser methods with the hope of their use in future for parameters measurements of a real inertial plasmas. Results on compositional analysis and temporal and spatial evolution are discussed.

Experimental. A radiation of Q-switched Nd:YAG (1.06 μm, pulse duration - 10 ns) or ruby (0.69 μm, 200 ns) lasers was focused on a surface of a Ti or Al target in air. The target surface was placed normally to the direction of laser beam propagation. The irradiation spot diameter in the focal plane of a lens was 0.4-1.3 mm. The maximal power density on the target surface was about 10 GW/cm^2.

The plasmas produced was located in a cavity of a first dye laser, radiated a smooth broadband spectrum within the range of 385-415 nm. The dye laser spectra with absorption lines were recorded by a 0.001 nm resolution spectrograph. The dye laser was calibrated against standard selective losses. As such standards we used aqueous solutions of $Eu(NO_3)_3$, having comparatively narrow unsplit absorption lines of Eu^{3+} ion.

The fundamental and second harmonics of a next dye laser radiation with linewidth of 0.02 nm was used for selective excitation of species in 550-580 and 280-320 nm spectral ranges. The calibration of LIF detectors was performed by using fluorescing dye solutions with a known quantum yield.

Both dye lasers, accurately delayed with respect to the ablation laser pulse, were used to probe the plasmas 1 mm up to 7 mm above the surface with temporal resolution of 25 ns. The probe lasers beams with a 1 mm diameters were propagated in parallel to the target surface. Simultaneously the own plasmas radiation was recorded and spectroscopically analyzed.

Results and discussion. Lasers probing of ablation plume has enabled to measure spatial-temporal profiles of heavy species and electrons as well as plasmas temperature. Apart from the absorption lines of species of the basic target material (Al or Ti) lines of impurities: Ca, Fe, Mn, K etc. are recorded in a single dye laser spectrum.

The ultimate distance from the target at which Al or Ti

species are detected is 6 mm. The maximal value of atoms density reaches $6 \cdot 10^{15}$ cm^{-3} (Al) and $1.1 \cdot 10^{15}$ cm^{-3} (Ti) near the target surface behind of the leading front of the plume as well as for singly ionized atoms - $4.5 \cdot 10^{13}$ cm^{-3} (Ti). The decay of ground and excited states of Ti or Al atoms and ions at stages of plasmas expansion and afterglow is of an exponential character. Worthy of note is a fact of measuring comparatively high density of Ti ions - 10^{12} cm^{-3} in the late afterglow: 100 μs after ablation laser pulse (the total duration of own plasmas glow was not greater than 10 μs).

Radial distribution of species in a plume has been elucidated. The whole angle of species escape is 100-110°. The axial velocity of a vapor cloud front reaches 1 km/s near the surface and sharply decreases with growing a distance from a target. The ablation laser power threshold of species detection near the target surface is 10 MW/cm^2.

Processing of the absorption lines shapes has permitted determining the electrons density from the Stark broadening and shift. At the leading front of a plume the maximal value of electrons density has been obtained - 10^{18} cm^{-3}.

Both heavy species and electrons densities measurements don't need assumptions of plasmas equilibrium state. Theoretically plasmas at electrons densities equal or higher than 10^{17} cm^{-3} are considered as a rule to be in local thermodynamic equilibrium (LTE). Therefore the value of plasmas temperature and its time dependence have been calculated assuming the reaching of LTE in plasmas at the leading front of the plume and behind it from the Boltzmann relation and Sacha equation. The maximal value of temperature is 25 kK.

In the afterglow and in the far zone of a plume the dominant mechanism of line broadening is the Van-der-Vaals interaction of target species with air atoms with the typical vapor-gas cloud temperature 0.5-1.0 kK.

The LIF measurements have confirmed the sufficient role in plasmas evolution of gas phase reactions between ablated Ti atoms and ambient oxigen. The ultimate distance from a target of TiO existence is 3 mm and molecules are detected till 70 μs

after ablation laser pulse. The made experiments allowed to establish the effect of irradiation conditions on the gas phase reactions. At the same incident laser intensity the oxidation process is more efficient within a plume with a greater initial size (irradiation spot diameter).

The dye laser excitation of separate vibrational-rotational levels of TiO β-system (0,0) band has permitted to observe the LIF as well as the collisional induced fluorescence (CIF) in 553-570 nm spectral range. The temporal profiles of CIF intensity exhibit the behaviour similar to that of the LIF to the exclusion of more rapid decay in afterglow as a result of electrons density decreasing. The collisional decay probability of TiO levels has been calculated using the dependence of the CIF amplitude from dye laser intensity: $\sim 10^{10}$ s^{-1} (10 μs after ablation laser pulse) and $\sim 10^{9}$ s^{-1} (70 μs). The time resolved rotational temperature of TiO has been measured. More systematic LIF studies are in progress in order to elucidate the role of different oxidation mechanisms.

/1/ G.T.Razdobarin, V.V.Semenov, L.V.Sokolova, I.P.Folomkin, V.S.Burakov, P.Ya. Misakov, P.A.Naumenkov, S.V.Nechaev, Nuclear Fusion 19, 1439 (1979)

/2/ V.S.Burakov, P.A.Naumenkov, S.N.Raikov, Optics Communications 80, 26 (1990)

Collective Scattering from Plasmas: Effects of Particle and Fluid Motions

Petro P. Sosenko*, Dominique Grésillon

PMI Lab, Ecole Polytechnique, F 91128, Palaiseau, France;
* also Institute for Theoretical Physics named after M.M. Boholiubov, Ukrainian Academy of Sciences, 252130 Kyyiv, Ukraine

1. Introduction. Electromagnetic wave scattering is a classical diagnostic tool for both fusion and space plasmas. As it is well known, there exist two scattering conditions: incoherent fluctuations, which are the manifestation at small scales of the plasma discrete structure and which are produced by the random motion of individual independent particles, and collective fluctuations at large scales, associated with the scattering determined by dressed particles. The scattering spectrum depends upon thermal particle motion, and the plasma temperature governs the shape of the spectral distribution of the scattered radiation over the frequency.

Meanwhile, for the conditions of some experiments, for instance tokamak microwave or infrared scattering experiments, or magnetospheric radar backscattering experiments, the scattering factor can be substantially modified due to macroscopic fluid-like flows in the plasma. The latter can appear as a result of low-frequency and large-scale electromagnetic fields, produced either by some external sources or internal factors, in particular MHD turbulence.

In this paper the effect of fluid-like plasma motion on the electromagnetic wave scattering from magnetized plasma is studied. It is suggested, that such motion perturbs the clouds of polarization charge around particles. This phenomenon of renormalized screening determines the collective scattering spectrum from the magnetized kinetically stable but MHD agitated plasma.

2. Scattering from Density Fluctuations. Let us consider the mechanism of electromagnetic wave scattering from the magnetized plasma, associated with the fluctuations of electron density δn_e [1]:

$$d\sigma = (\frac{1}{2\pi})(\frac{\mu_0 e^2}{4\pi m})^2 \mid (\vec{s}\times\vec{e})\times\vec{s}\mid^2 \langle \delta n_e^2\rangle_{\vec{k}\omega}\, d\omega_s d\Omega_s\ , \qquad (1)$$

$d\sigma$ is the differential scattering cross-section, which determines the intensity of scattered waves in the frequency band $d\omega_s$ and the solid angle element $d\Omega_s$, ω_i is the frequency of the incident wave with the wave vector $\vec{k}_i$, ω_s is the frequency of the scattered wave with the wave vector $\vec{k}_s$, $\omega = \omega_s - \omega_i$ and $\vec{k} = \vec{k}_s - \vec{k}_i$ are the changes in the frequency and the wave vector in the course of scattering respectively. $\vec{s}$ is the unit vector in scattering direction, $\vec{e}$ is the unit polarization vector for the incident wave. $\langle \delta n_e^2\rangle_{\vec{k}\omega}$ is the spectral distribution for the electron density fluctuations (which determines the scattering dynamic form factor). The time and space fluctuations of the magnetic field $\vec{B}$ will be neglected, $\vec{B} = \vec{B}_0 \equiv B_0\vec{b}$. The following notations are also used. ω_p is the plasma frequency, $\omega_p^2 = nq^2/\varepsilon_0 m$, n is the mean density, q and m are the particle charge and mass, ε_0 is the vacuum dielectric permittivity, μ_0 is the vacuum magnetic permeability. The index a labels plasma species and the subscript $e(i)$ is used for the electrons (ions), $q_e = e$.

According to the general microscopic theory of plasma fluctuations, the following representation for the density fluctuation is introduced:

$$\delta n_{aK} = \delta n_{aK}^{(0)} - (ik\varepsilon_0/q_a)\,\kappa_a^{(1)}(K)\,\delta E_K\,, \quad K \equiv \{\vec{k},\omega\}\,, \tag{2}$$

where plasma discreteness reveals itself in the incoherent density fluctuations $\delta n_a^{(0)}$, due to random motion of individual free particles, $\kappa_a^{(1)}(K)$ is the linear electric plasma susceptibility, $\delta\vec{E} = -\vec{\nabla}\Phi$ ($\delta E_K \equiv -ik\Phi_K$) is the strength of the self-consistent microscopic electric field in the plasma, which is taken to be longitudinal. The second term on the right-hand side governs plasma polarization, within the context of the self-consistent description it can be associated with a cloud of polarization charges around a test-particle in the plasma. The Poisson law enables one to determine the electric field from the density fluctuations in the system of free particles: $\delta E_K = \sum_a q_a \delta n_{aK}^{(0)}/ik\varepsilon_0\varepsilon(K)$, where $\varepsilon(K)$ is the plasma dielectric permittivity, $\varepsilon(K) = 1 + \sum_a \kappa_a^{(1)}(K)$, and to express the density fluctuations for the particles from the particular species in terms of the density fluctuations for free particles. In particular, for electrons

$$\langle \delta n_e^2 \rangle_K = \langle (\delta n_e^{(0)})^2 \rangle_K \mid 1 - \kappa_e^{(1)}(K)/\varepsilon(K) \mid^2 + \\ + \sum_{a\neq e} Z_a^2 \langle (\delta n_a^{(0)})^2 \rangle_K \mid \kappa_e^{(1)}(K)/\varepsilon(K) \mid^2 . \tag{3}$$

Taking into account the experimental observations of the low-frequency (as compared to the cyclotron frequency) fluctuations in the plasma, let us consider the scattering spectra with small changes in frequency, $\omega_s - \omega_i \sim \lambda\Omega$, $\lambda << 1$ ($\Omega \equiv qB_0/m$). In this case, the general expressions for the electrodynamic coefficients and the spectral distributions for the fluctuations in the system of free particles simplify (c.f. [2]):

$$\kappa^{(1)}(K) = \alpha(\vec{k}) - i\,\frac{\omega_p^2}{nk^2}\int d\vec{v}\; W^{(0)}(K)\; J_0^2\; k_\parallel \partial_{v_\parallel} f\,,$$

$$\langle (\delta n^{(0)})^2 \rangle_K = 2\Re \int d\vec{v} W^{(0)}(K)\; J_0^2 f\,, \tag{4}$$

where $\alpha(\vec{k}) \equiv (\omega_p^2/nk^2)\int d\vec{v}(J_0^2 - 1)\;(1/v_\perp)\partial_{v_\perp} f$, $f = f(v_\parallel, v_\perp)$ is the mean particle distribution function, $J_0 = J_0(k_\perp v_\perp/\Omega)$ is the Bessel function of zero order, and the subscript $\parallel$ ($\perp$) is used for a vector component along(across) the magnetic field. The contribution $\alpha(\vec{k})$ arises from particle polarization drift modified due to finite-Larmor-radius (FLR) effects. In the long-wave-length limit, when FLR effects are weak, the parameter $\alpha(\vec{k}) = \alpha \equiv \omega_p^2/\Omega^2$, and can be quite large. Frequently under experimental conditions for ions $\alpha_i \sim 10^3$, while α_e is of the order of unity.

The latter equations introduce the probability $W(\vec{r},t;\vec{r}',t') \equiv W^{(0)}(\vec{r}-\vec{r}',t-t')$ for the transition of the free particle from the space point $\vec{r}'$, where it is at the time instant t', to the point $\vec{r}$ at the time instant t:

$$W^{(0)}(\vec{r},t) = \vartheta(t)\delta(\vec{r} - v_\parallel t\vec{b})\,, \quad \vartheta(t) \equiv \int_{-\infty}^{t} dx\delta(x)\,, \tag{5}$$

as in the low-frequency limit the particles can be traded for the quasiparticles, - the guiding centres in this case, - which in the free state move only along the magnetic field with a constant velocity (c.f. [3]). $W^{(0)}(K)$ appears after the Fourier space-time transformation is applied: $W^{(0)}(K) = i/(\omega - k_\parallel v_\parallel + i0)$.

3. Renormalization of Particle Transition Probability. In order to explain the observations of either laboratory or space plasmas, it is possible to allow for the occurence of fluid-like turbulent motion in the plasma [4]. The latter can substantially alter the scattering of electromagnetic waves in the magnetized plasma. In the presence of fluid-like plasma motion particle trajectories modify, as a consequence the renormalization of the transition probability takes place:

$$W(\vec{r},t) = W_R(\vec{r},t) \equiv \vartheta(t)\langle\delta(\vec{r} - \vec{r}(t))\rangle \ , \tag{6}$$

where $\vec{r}(t) = v_\parallel t\vec{b} + \vec{R}_F(t)$ is the quasiparticle trajectory. $\vec{R}_F(t)$ is the macroscopic displacement across the magnetic field due to fluid-like motion. The latter can be produced by large-scale and low-frequency electromagnetic fields, generated either by some external factors or internally, for example due to magnetohydrodynamic turbulence. The variable $\vec{R}_F(t)$ is assumed to be random with some probability distribution.

The Fourier space-time component

$$W_R(K) = \frac{i}{2\pi}\int d\omega' \frac{S_F(\vec{k}_\perp, \omega' - k_\parallel v_\parallel)}{\omega - \omega' + i0} \ , \tag{7}$$

where the fluid motion spectrum appeared:

$$S_F(\vec{k}_\perp,\omega) = \int dt\, exp(i\omega t)\langle exp[i\vec{k}_\perp \cdot \vec{R}_F(t)]\rangle \ . \tag{8}$$

Therefore, the renormalization of the electrodynamic coefficients and the correlation functions takes place, and it governs the spectral distributions for fluctuations with regard to fluid-like plasma motion.

Let us study the case, when W_R is governed by the normal distribution for the velocity of fluid-like motion [4]:

$$S_F(\vec{k}_\perp,\omega) = (\sqrt{2\pi}/\gamma_F)\, exp\{-(\omega - \omega_F)^2/2\gamma_F^2\} \ , \tag{9}$$

where the mean velocity $\vec{U}$ and the root mean square u' of the velocity oscillation associated with the fluid-like motion are traded for the Doppler frequency shift $\omega_F = \vec{k}\cdot\vec{U}$, which determines the location of the spectrum maximum, and the spectrum width $\gamma_F = k_\perp u'$. For normal distribution of particles with respect to their parallel velocity, characterized by the parallel thermal velocity $s_\parallel$, the renormalization of the electric susceptibilities and the correlation functions for "undressed" particles reduces formally to the renormalization of the parallel temperature and the Doppler frequency shift:

$$T_\parallel \to T_R = C_F T_\parallel \geq T_\parallel \ , \quad \omega \to \omega - \omega_F \equiv \tilde{\omega} \ , \quad C_F \equiv 1 + (k_\perp/k_\parallel)^2 (u'/s_\parallel)^2 \ ,$$

The dependencies of the spectral distributions for the electron density and total charge density fluctuations $Y_e = \langle \delta n_e^2 \rangle_{\vec{k}x} / n_e$ and $Y = (1+\alpha_i)^2 \langle \delta \rho^2 \rangle_{\vec{k}x} / e^2 n_e$ from $x = (\omega - \omega_F)/\sqrt{2} s_{\|e} \mid k_\| \mid$ are presented for the electron-ion plasma with $\lambda_s^2 k^2 = 0.1$ ($\lambda_s^2 \equiv (1+\alpha_i)\lambda_{\|e}^2$, $\lambda_\|$ is the Debye length at the parallel temperature), and $T_{\|i}/T_{\|e} = 0.1$ for different values of C_{Fi}, when $\gamma_F \sim s_{\|i} \mid k_\| \mid$. The width of the spectral line increases with C_{Fi}, while its intensity decreases. It is to be noted that the dependence of the spectra over the frequency is symmetric with respect to ω_F.

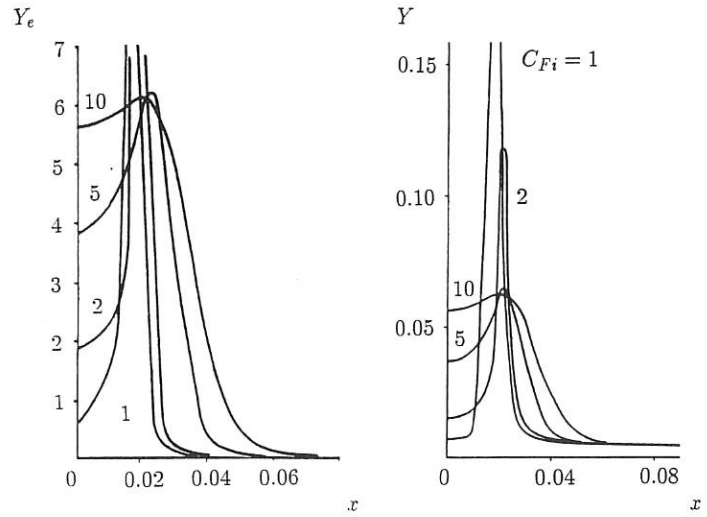

4. Summary. Thus, the renormalization can result in a self-similar transformation of fluctuation spectral distributions, which is subordinated to an effective ion temperature. In the absence of fluid-like motion the effective temperature is equal to the real one, while in the presence of such motion it can be much larger than the latter. This peculiarity is to be taken into account in the explanations of the electromagnetic wave scattering from the plasma.

[1] I.H. Hutchinson, *Principles of Plasma Diagnostics*, Cambridge University Press, Cambridge et al. (1987).

[2] O.H. Sitenko, P.P. Sosenko. Electrodynamic Properties of Inhomogeneous Magnetoactive Plasma: Low-Frequency Limit. Kyyiv, 1989. 52 p. (Ukrainian Academy of Sciences/ Preprint ITP-89-59E); Physica Scripta. **43**, 609 (1991).

[3] P.P. Sosenko, V.K. Decyk. Microscopic Description of Magnetized Plasma: Quasiparticle Concept. Rep. PPG-1427. 30 p. (IPFR-UCLA, Los Angeles, 1992); Physica Scripta **47**, 258 (1993).

[4] C. Hanuise, J.P. Villain, D. Grésillon et al. Ann. Geophysicae **11**, 29 (1992).

AUTHOR INDEX